



Palacký University
Olomouc

**TARGETING GENOTOXIC AND PROTEOTOXIC CELLULAR STRESS
PATHWAYS IN CANCER**

Habilitation Dissertation

M.Sc. Martin Mistrík, Ph.D.

Olomouc (Czech Republic) 2024

Acknowledgments

First and foremost, I would like to express my deepest gratitude to my mentor, Prof. Jiří Bártek, for his unwavering guidance and long-standing support. His mentorship opened doors for me to collaborate with prominent figures in the scientific community, both domestically and internationally. I would also like to extend my thanks to my undergraduate mentor, Prof. Miroslav Strnad, who ignited my passion for science and recommended me to Prof. Bártek's Laboratory of Genome Integrity at the Research Institute of the Danish Cancer Society in Copenhagen, where I spent three invaluable years during my PhD.

I am especially grateful to Assoc. Prof. Marián Hajdúch, not only for the cutting-edge instrumentation and resources at the Institute of Molecular and Translational Medicine (Faculty of Medicine, Palacký University), where much of my research was conducted, but also for his mentorship in designing complex experiments. His insights and guidance have been instrumental in shaping the success of many of my projects.

The quality of the research presented here would not have been possible without the collaboration of my dedicated colleagues and students at the Institute of Molecular and Translational Medicine. In particular, I would like to acknowledge Dr. Zdeněk Škrott, my former PhD student, now a valued colleague and co-author of many of my recent works. I also extend my heartfelt thanks to Dr. Katarína Chromá, Dr. Tereza Buchtová, Dr. Dušan Majera, Dr. Lucie Berésová, Dr. Eva Veselá, Dr. Pavel Moudý, MSc., Markéta Šenkyříková, MSc. Iva Protivánková, MSc. Pavlína Dušková, and MSc. Matthew Lacey, with whom I have completed numerous successful projects.

Lastly, and most importantly, I would like to thank my wife, children, and parents for their unwavering support and understanding. This work is dedicated to them.

Synopsis:

1. THE SIGNIFICANCE OF GENOTOXIC AND PROTEOTOXIC STRESSES IN CARCINOGENESIS AND CANCER TREATMENT	4
1.1. Proteostasis and proteotoxic stress.....	4
1.2. Genotoxic stress.....	12
2. ADVANCEMENTS IN TOOLS FOR INVESTIGATING GENOTOXIC AND PROTEOTOXIC STRESS INDUCTION AND RELATED CELLULAR RESPONSES	19
2.1. Replication stress inducers as the source of specific genotoxic stress.....	19
2.2. An Advanced Method for Quantifying Low-dose DNA Damage and Replication Stress Responses.....	21
2.3. Photo-manipulation DNA Damage Techniques for Cellular Research.....	22
2.4. Targeted Thermal Protein Damage for Proteotoxic Stress Research.....	23
2.5. Monitoring of Cellular Responses in Hair Follicles.....	25
3. TARGETING PROTEOSTASIS AND DNA REPAIR IN CANCER BY DITHIOCARBAMATES	26
3.1. NPL4, an adaptor of p97 segregase, as the primary anticancer target of disulfiram.....	27
3.2. Deciphering Disulfiram's Anti-cancer Mechanisms: Beyond ALDH Inhibition.....	30
3.3. Disulfiram's Targeting of NPL4 Impairs DNA Replication Dynamics and Induces ATR Pathway Malfunction.....	31
3.4. Cannabidiol Interference with Disulfiram's Anti-Cancer Efficacy Through the Metallothionein Pathway.....	33
3.5. Disulfiram's Repurposing to Overcome Resistance of Multiple Myeloma.....	35
3.6. Novel Dithiocarbamate-Copper Complexes Targeting the p97/NPL4 Pathway in Cancer Therapy.....	36
3.7. Leveraging Disulfiram, Vorinostat, and PARP inhibitors for Combating Castration-Resistant Prostate cancer.....	38
4. SUMMARY	39
5. ABBREVIATIONS	42
6. BIBLIOGRAPHY	45
7. ATTACHMENTS 1-15	50
7.1 Attachment 1.....	51-87
7.1 Attachment 2.....	88-100
7.1 Attachment 3.....	101-108
7.1 Attachment 4.....	109-116
7.1 Attachment 5.....	117-127
7.1 Attachment 6.....	128-142
7.1 Attachment 7.....	143-161
7.1 Attachment 8.....	162-173
7.1 Attachment 9.....	174-191
7.1 Attachment 10.....	192-205
7.1 Attachment 11.....	206-216
7.1 Attachment 12.....	217-242
7.1 Attachment 13.....	243-253
7.1 Attachment 14.....	254-262
7.1 Attachment 15.....	263-273

1. THE SIGNIFICANCE OF GENOTOXIC AND PROTEOTOXIC STRESSES IN CARCINOGENESIS AND CANCER TREATMENT

Our research is primarily dedicated to elucidating the nature and consequences of genotoxic and proteotoxic stresses in the context of cancer development and therapy. Preserving the integrity of both the proteome and genome requires the integration of cellular stress-responsive mechanisms and signaling pathways, which frequently utilize overlapping components¹. Cancer cells, particularly those undergoing rapid division and accumulating a high mutation burden, depend critically on maintaining proteostasis and efficiently repairing DNA to ensure survival, which fact is often explored therapeutically.

Cellular stress responses relevant to cancer progression, treatment, and this habilitation dissertation, as will be revealed further, can be categorized based on several factors, including the source of stress, which may be extrinsic (environmental) or intrinsic (metabolic) and classified as physical, chemical, or physiological. Another classification framework involves identifying the target of the stressor, whether DNA, proteins, or metabolism, and the distinct cellular pathways activated in response. These pathways may be stressor-specific or common across different types of stress.

1.1. Proteostasis and proteotoxic stress

There are several cellular pathways involved in handling protein quality. For instance, the unfolded protein response (UPR) in the endoplasmic reticulum (ER) plays a critical role in managing protein folding and maintaining protein quality control². Disruptions in this process, characterized by the accumulation of misfolded proteins, result in ER stress, a hallmark of various cancers, influencing tumor growth and chemoresistance. The UPR consists of signaling pathways activated in response to ER stress, aiming to restore cellular homeostasis or trigger pro-apoptotic pathways. Under non-stressed conditions, it is generally accepted that ER stress sensors remain inactive. In cancer, the UPR exerts a dual function: it can promote tumor cell survival and growth, but if stress remains unresolved or reaches a critical threshold, it may promote cell death³ (Figure 1). A deeper understanding of the balance between UPR's pro-survival and pro-apoptotic mechanisms is essential for the development of effective cancer therapies. Current research is exploring drugs that either induce ER stress or inhibit

components of ER stress pathways to promote cancer cell death and improve therapeutic outcomes.

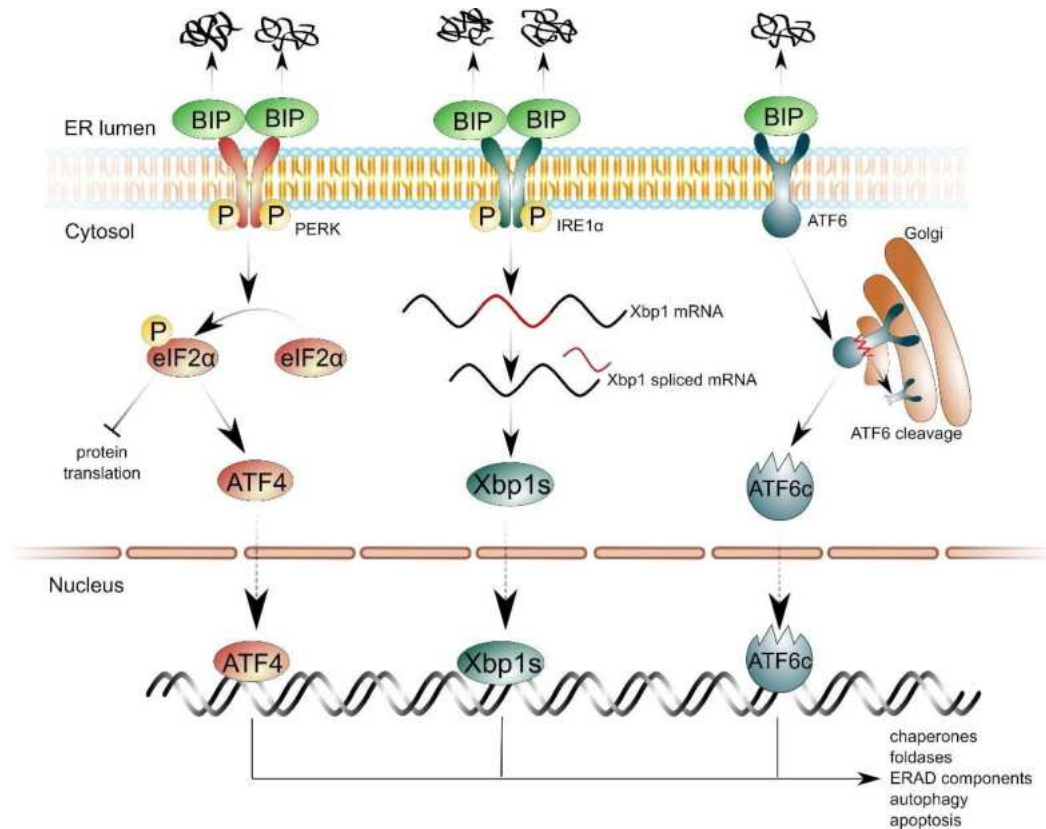


Figure 1: UPR stress response activation. Unfolded/aggregated proteins within the ER lumen are recognized by BIP protein and activate three distinct response pathways promoted by PERK, IRE1α, and ATF6 factors. The downstream factors inhibit further protein translation (by eIF2α) and trigger the expression of genes involved in protein maintenance or cell death promotion (transcription factors ATF4, Xbp1s, ATF6c).

The accumulation of misfolded or damaged proteins within the cell also activates another critical stress response pathway explored in our published works, the heat shock response (HSR). This cellular protective mechanism is characterized by the increased expression of heat shock proteins (HSPs), present at basal levels even under normal conditions but strongly overexpressed by activation of the HSF1 transcription factor (Figure 2). HSPs function as molecular chaperones, facilitating proper protein folding, maintaining the tertiary structure, and ensuring the functional integrity of various essential proteins. They play a pivotal role in cellular survival when proteins are compromised by stressors such as elevated temperature, oxidative damage, heavy metals poisoning, or genetic mutations⁴.

In the context of cancer, the relevance of HSPs becomes highly pronounced. Cancer cells, burdened with a high mutation load, frequently produce damaged or misfolded proteins, making them particularly reliant on HSPs to maintain protein homeostasis. This dependency allows cancer cells to manage proteotoxic stress, avoid apoptosis, and continue proliferating despite the presence of extensive protein damage and aggregation. Therefore, HSPs not only support normal cellular functions but also contribute to tumorigenesis by protecting cancer cells from proteotoxic damage⁵.

Given their dual role in cancer, HSPs have emerged as attractive therapeutic targets in oncology. Inhibiting HSPs can potentially disrupt cancer cell survival mechanisms, sensitizing them to proteotoxic-induced death. A range of HSP inhibitors and therapeutic agents are currently being investigated for their ability to overcome drug resistance, enhance apoptosis, and improve the efficacy of existing cancer treatments, and the first HSP90 inhibitor for clinical applications in cancer treatment (pimitespib) was approved recently⁶. These strategies offer promising avenues for novel cancer therapies, particularly in cancers that demonstrate a heavy reliance on HSP-mediated stress response pathways, such as multiple myeloma and various advanced forms of cancers typically displaying high mutational load⁷.

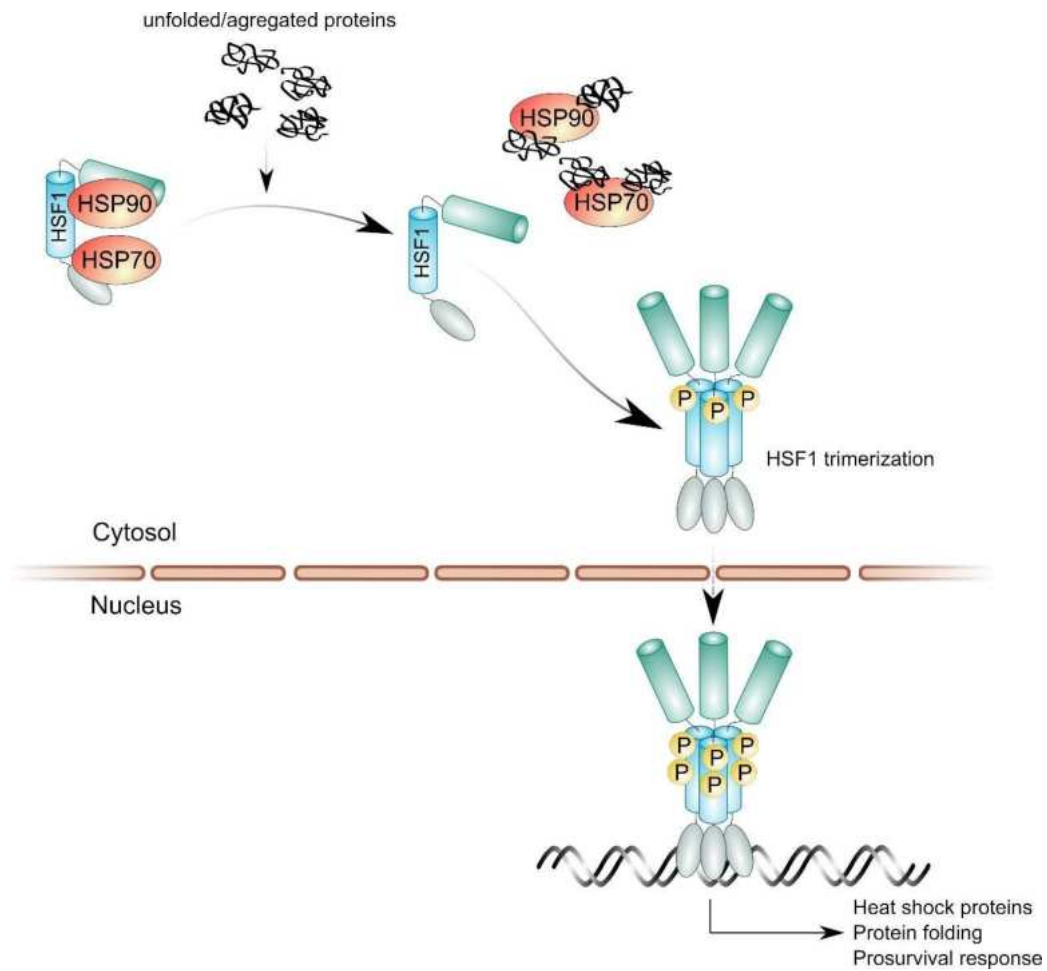


Figure 2: Mechanism of activation of HSF1 transcription factor leading to overexpression of HSP proteins. HSPs that keep HSF1 in a monomeric state are attracted to aggregated proteins. HSF1 trimerize, becoming an active transcription factor.

Another critical pathway heavily explored in our published works is the ubiquitin-proteasome system (UPS), which plays an essential role in regulated intracellular protein degradation. Cellular protein levels are tightly controlled through transcription, translation, and, ultimately, targeted degradation. The UPS is responsible for selectively degrading proteins that are damaged or no longer needed within the specialized multisubunit protein complex - proteasome (Figure 3).

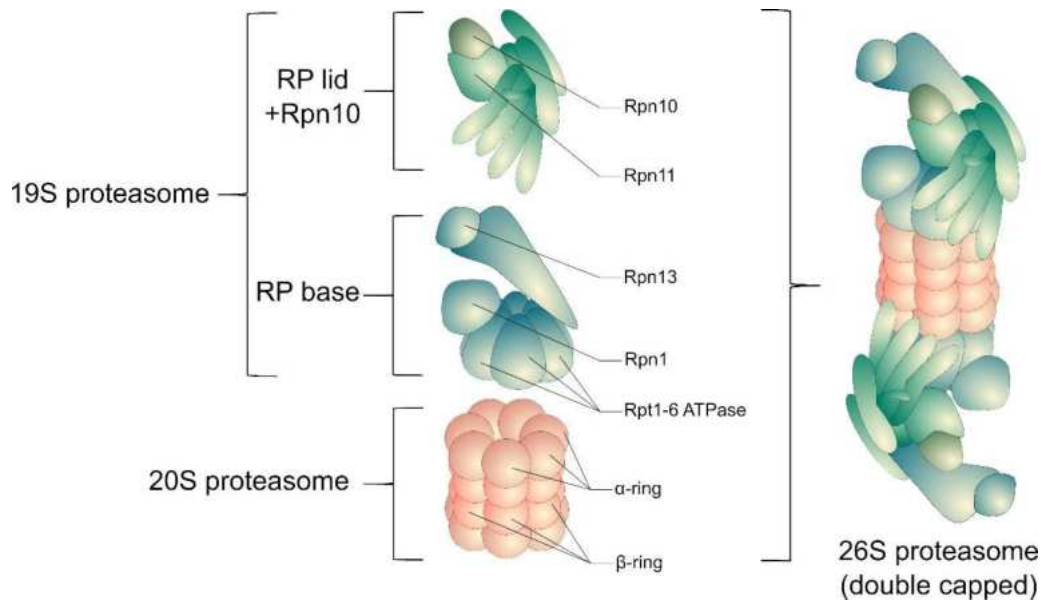


Figure 3: Schematic structure of proteasome. The barrel-like multiprotein structure (the 20S) is responsible for protein degradation, and the lids-like structures (19S) have regulatory functions. Together, they form one functional proteasome complex (26S)

Proteins dedicated to proteasomal degradation must be tagged by the K48-linked ubiquitin (Ub) chain by the cooperative action of three types of Ub conjugating enzymes termed E1, E2, and E3 (Figure 4). This system is integral to key cellular processes, such as apoptosis, cell survival, cell cycle progression, DNA repair, and antigen presentation, with the lifespan of individual proteins varying depending on their role in these processes⁸. Thus, the proper functioning of the UPS is essential for cellular health and stability.

Deregulation of the UPS can have profound implications for cancer development and progression. Aberrations in the system may result in the enhanced degradation of tumor suppressor proteins or the reduced breakdown of oncogenic proteins, thereby disrupting the balance between cell proliferation and death. Such a disruption of critical cellular pathways that control the cell cycle and apoptosis contributes significantly to tumorigenesis⁹.

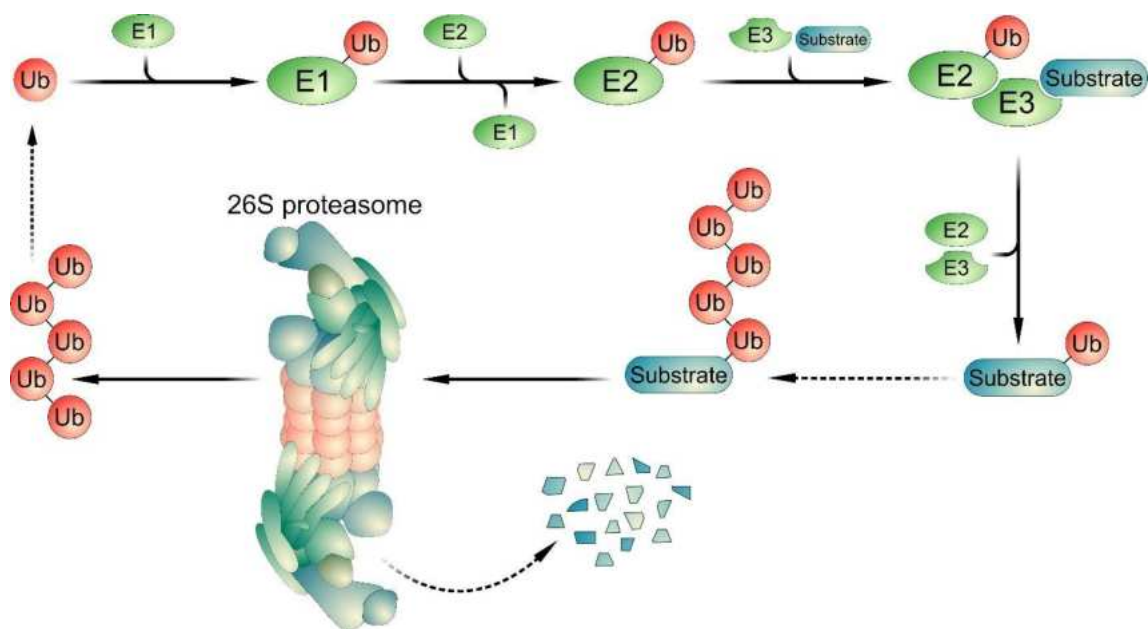


Figure 4: Schematics of tagging proteins for degradation in proteasome. The E1 ubiquitin-activating enzyme transfers Ub to E2 conjugating enzymes, which transfer Ub to E3 ligases attached to the substrate (protein dedicated to degradation). E3 ligase ubiquitinates the substrate, forming a long chain of ubiquitin proteins linked via lysine K-48. Such substrate is further recognized by 26 proteasomes and degraded. Note: Ub is not usually degraded with the substrate but is recycled.

The UPS is closely linked to the unfolded protein response (UPR) through a process known as ER-associated degradation (ERAD)². ERAD is the primary quality-control mechanism responsible for identifying misfolded or improperly processed proteins within the endoplasmic reticulum (ER) and targeting them for degradation by the proteasome in the cytosol. This connection between ER stress and the UPS ensures that damaged proteins do not accumulate within the ER, preventing further cellular dysfunction. In cancer cells, where proteotoxic stress is heightened due to increased protein synthesis and mutation-induced misfolding, the UPS and ERAD are often severely upregulated to manage the high demand for protein quality control.

Given the importance of the ubiquitin-proteasome system (UPS) in maintaining cellular protein homeostasis and its critical role in cancer progression, it represents an attractive target for therapeutic intervention. Proteasome inhibitors such as bortezomib have already demonstrated clinical efficacy, particularly in hematological malignancies like multiple myeloma⁹. These inhibitors disrupt the degradation of damaged proteins, triggering a

proteotoxic crisis (PC) that leads to cancer cell death. The rationale for targeting the UPS in cancer therapy is that cancer cells, due to their high mutation burden and reliance on proteostasis mechanisms, are susceptible to disruptions in protein degradation. In other words, as malignancies progress, the increased accumulation of misfolded and damaged proteins overwhelms cellular proteostasis systems, making cancer cells more dependent on the UPS and, thus, more vulnerable to its inhibition.

The most established class of UPS-targeting drugs in clinics and preclinical research are proteasome inhibitors, which include compounds such as MG132 and the three FDA- and EMA-approved bortezomib (Velcade®), carfilzomib (Kyprolis®), and ixazomib (Ninlaro®). These drugs selectively bind and inhibit specific subunits of the proteasome complex, leading to an accumulation of defective proteins that ultimately result in PC. Bortezomib, a first-generation proteasome inhibitor, has been a cornerstone in the treatment of multiple myeloma and mantle-cell lymphoma, showing marked clinical activity and improving patient outcomes. However, the development of resistance to bortezomib remains a significant challenge, as most patients eventually relapse after an initial positive response¹⁰. To address this, second-generation proteasome inhibitors like carfilzomib and ixazomib have been developed. These newer agents aim to offer improved pharmacokinetics, oral bioavailability (ixazomib), and the ability to overcome some of the resistance mechanisms that limit bortezomib's long-term efficacy.

Despite these advancements, the clinical success of proteasome inhibitors has been largely confined to hematological cancers, with limited efficacy observed in solid tumors. This lack of effectiveness in solid tumors may stem from various limitations, including pharmacokinetics, inadequate drug distribution, or differences in tumor microenvironment that affect drug penetration and activity. Overcoming these barriers is an area of active research, as understanding the mechanisms behind resistance to proteasome inhibition is crucial for developing more effective therapies⁹.

To improve therapeutic outcomes, researchers are now investigating alternative strategies, including inhibitors that target other components of the UPS or related protein degradation pathways. For instance, drugs that interfere with upstream regulatory elements of the UPS or target specific degradation pathways, such as ER-associated degradation (ERAD), are being explored. Additionally, the development of inhibitors against p97 (also known as

VCP), a key ATPase involved in the extraction of misfolded proteins from the ER for proteasomal degradation, represents a novel therapeutic avenue^{9,11,12} (Figure 5). These strategies aim to exploit cancer cells' reliance on efficient protein degradation pathways while minimizing the emergence of resistance.

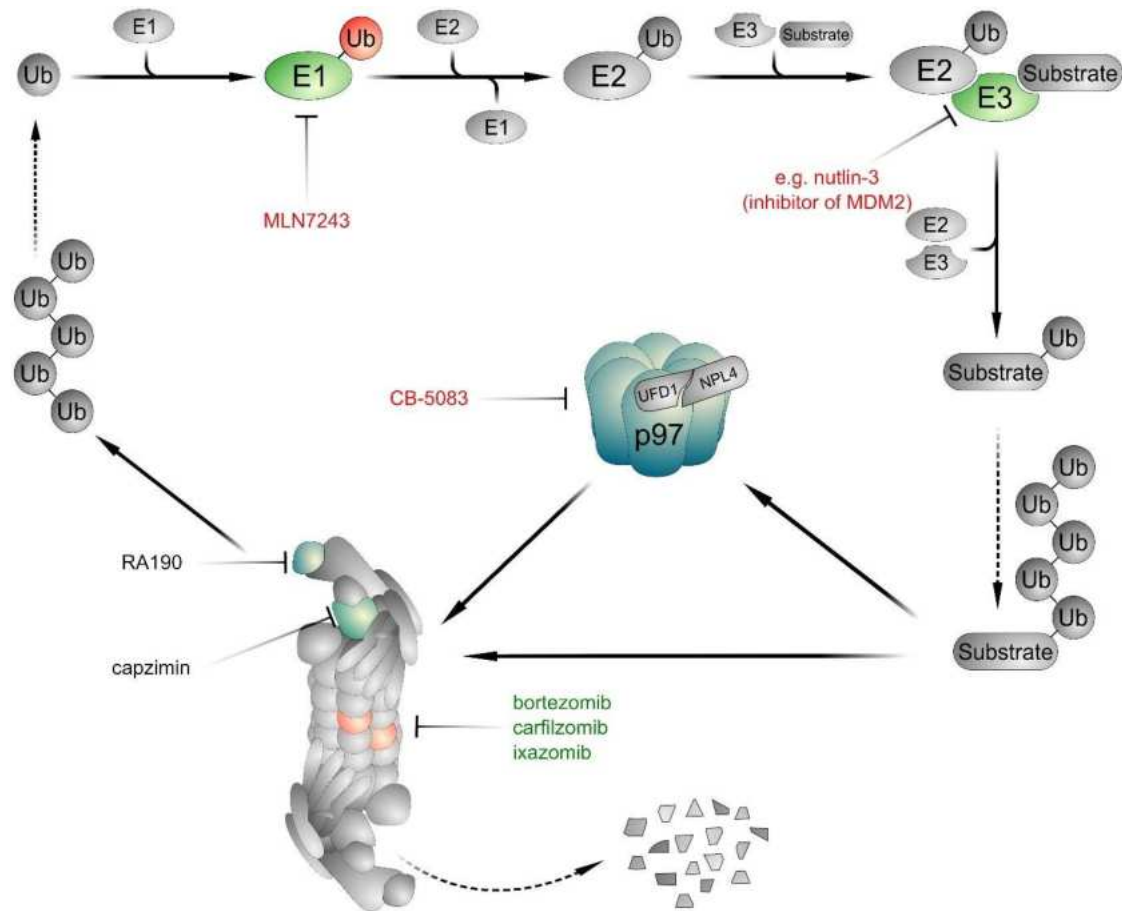


Figure 5: Various modes of UPS targeting. The UPS function can be compromised on various levels using specific drugs: Proteasome lid (19S)-targeting drugs (RA190, capzimin). Proteasome barrel (20S)-targeting drugs (bortezomib, carfilzomib, ixazomib, and MG132). Drugs interfering with the function of ubiquitination cascade (MLN7243, Nutlin-3). Drugs inhibiting p97-translocase complex (CB-5083, CuET)

1.2. Genotoxic stress

Beyond proteins, DNA is another critical macromolecule that can suffer damage from various physical and chemical agents, leading to DNA lesion induction with potentially severe cellular consequences (Figure 6).

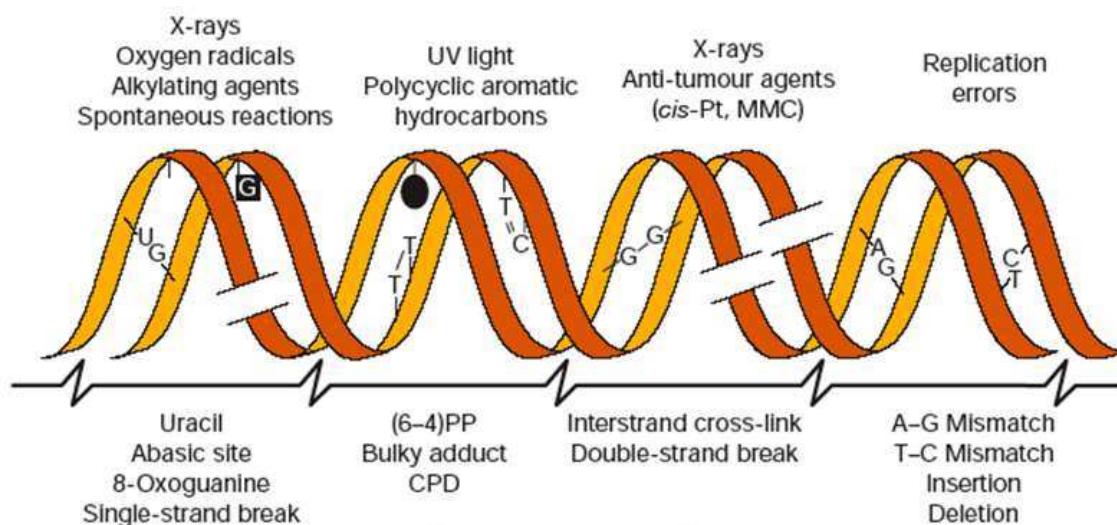


Figure 6: Sources of genotoxic stress and resulting types of DNA lesions. Natural sources, such as ionizing radiation (e.g., X-rays), are among the most common causes of exogenous DNA damage, inducing single-strand breaks (SSBs) and double-strand breaks (DSBs). UV light induces the formation of DNA lesions like 6–4 photoproducts (6–4 PPs) and cyclobutane pyrimidine dimers (CPDs). Anti-cancer drugs, such as cisplatin (*cis*-Pt) and mitomycin C (MMC), are DNA-crosslinking agents that generate covalent interstrand cross-links. Other drugs like topoisomerase inhibitors (e.g., camptothecin) block DNA-topoisomerase complexes, physically impeding the progression of replication forks, often resulting in DSBs. Anthracyclines act as intercalating agents, topoisomerase II poisons, oxidizing agents, and crosslinking agents, resulting in many different DNA lesions. Various DNA lesions can also be caused by endogenous factors, including spontaneous replication errors, hydrolytic reactions, and metabolic by-products that generate reactive oxygen species (ROS), reactive nitrogen species, lipid peroxidation products, and reactive carbonyl species. (Drawing taken from¹³)

In response to DNA lesions, cells activate a highly coordinated and complex network known as the DNA Damage Response (DDR). The DDR is central to preserving genomic integrity (GI), a state in which the genome remains stable and free of deleterious mutations. Maintaining GI involves the precise coordination of numerous processes, including DNA damage sensing, the signaling and repair of lesions, checkpoint activation to control cell-cycle progression, and, when necessary, initiating apoptosis or permanent cell cycle block

(senescence) if the damage is irreparable or too severe. Additionally, DNA repair must occur within the context of chromatin, necessitating complex interactions between DDR components and chromatin remodeling machinery to ensure that the DNA is accessible and that the repair is efficient. Integrating these processes ensures that cells can adequately respond to DNA damage, preventing the accumulation of mutations that may lead to genomic instability, a hallmark of many diseases, including cancer^{13,14}.

Among the most deleterious types of genotoxic stress are factors leading to formation of double-strand breaks (DSBs), where both strands of the DNA helix are severed. DSBs can result from exposure to ultraviolet (UV) light, ionizing radiation, DNA-damaging agents, replication obstacles, and oxidative stress. Left unrepaired, or improperly repaired, DSBs can give rise to large-scale genomic alterations, such as deletions, translocations, and aberrant DNA fusions. These events are key drivers of genomic instability, a hallmark of cancer development. The cellular response to DSBs is orchestrated by a network of kinases, including ataxia-telangiectasia mutated (ATM), ATM and Rad3-related (ATR), and DNA-dependent protein kinase catalytic subunit (DNA-PKcs). These kinases activate a broad range of downstream effectors responsible for coordinating DNA repair, cell cycle checkpoints activation, and, when necessary, apoptosis¹⁵ (Figure 7). The potential of DSBs to induce not only genomic instability but also cell death underscores the delicate balance between DNA damage and repair in cancer therapy.

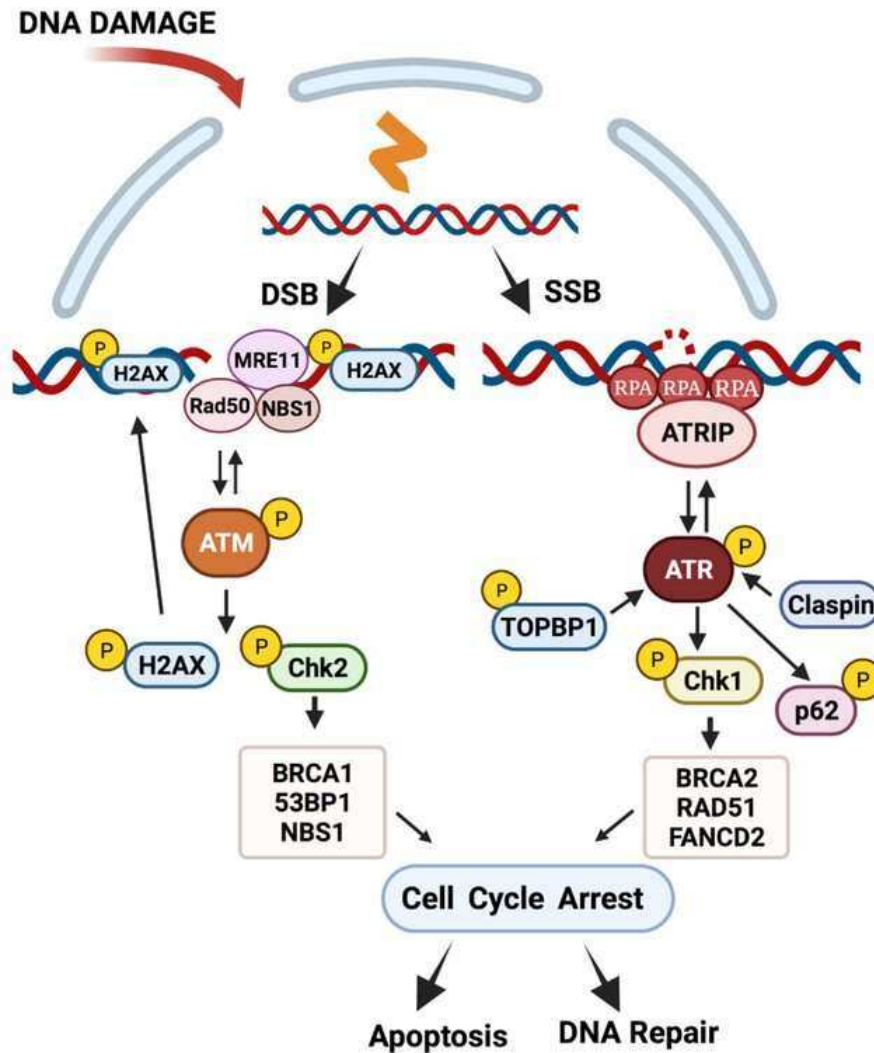


Figure 7: Simplified overview of main responsive pathways to the presence of DNA breaks. DSBs are recognized by the MRN complex, which activates preferentially ATM kinase. ATR kinase is preferentially activated in response to the presence of ssDNA in an RPA-ATRIP-dependent manner. Both kinases phosphorylate multiple downstream targets involved in DNA repair, cell-cycle regulation, and apoptosis. Both kinases may share some substrates (Drawings taken from¹⁶).

Overall, effective genomic integrity maintenance is vital for organismal health, playing a crucial role in preventing premature aging, neurodegenerative diseases, and cancer. Unfortunately, the DDR pathways can be compromised by inherited or acquired mutations in key genes, by viral infections¹⁶, or by exogenous chemical or physical interferers. In such cases, even a low amount of DNA damage can easily surpass a cell's capacity for repair. Resulting genomic

instability acts as a significant catalyst for carcinogenesis by triggering a series of events that may lead to the accumulation of pro-oncogenic mutations, allowing the cell to continue proliferation and ultimately setting the stage for complete malignant transformation.

In cancer cells, defects in the DDR are very common, which makes them genomically unstable and prone to rapid clonal evolution, which often promotes treatment evasion. At the same time, DDR defects can be viewed as a potential vulnerability and, thus, a target for therapeutic intervention. Indeed, many of the foundational therapies used to treat cancer, such as ionizing radiation and first-generation chemotherapeutic agents, challenge the DDR by introducing additional DNA damage. This approach exploits not only the intrinsic defects in DNA repair mechanisms that limit the repair efficacy but also gains from the fact that cancer cells very often exhibit elevated levels of spontaneous DNA damage¹⁷ due to various internal factors, including unscheduled or aberrant DNA replication, compromised cell cycle checkpoints, increased oxidative damage, and heightened accumulation of genotoxic metabolic byproducts. Thus, DDR defects and higher levels of spontaneous DNA damage make cancer cells more likely to succumb to additional DNA damage induced by genotoxic treatment.

The therapeutic rationale for using DNA-damaging agents and/or DDR interferers in cancer treatment mirrors the concept of exploiting proteostasis deficiencies in cancer cells, discussed in Chapter 1.1. By pushing cancer cells beyond their already compromised capacity for DNA repair, these therapies aim to induce destructive damage, leading to stable cell cycle arrest or apoptosis. However, despite their efficacy, DNA-damaging therapies come with significant challenges. Because these agents also damage the DNA of normal cells, they cause severe side effects, including myelosuppression, mucositis, and induction of secondary malignancies. Furthermore, cancer cells can rapidly develop resistance to these treatments, often by activating alternative DNA repair pathways, upregulating efflux pumps to remove the drugs, or altering the expression of DNA-damage-triggered cell death regulators.

Therefore, ongoing research seeks to deepen our understanding of DDR to develop new generations of anticancer drugs that exploit specific DDR defects. For example, tumors with mutations in DNA repair genes, such as BRCA1 or BRCA2, are particularly sensitive to intrinsic

or extrinsic genotoxic insults in case of inhibition of complementary DNA repair pathways. This concept, known as synthetic lethality, exploits the idea that cancer cells already deficient in one repair pathway become reliant on alternative repair mechanisms. By inhibiting these alternative pathways, e.g., by PARP inhibitors, cancer cells can be easily pushed beyond their repair capacity, leading to cell-cycle arrest or death¹⁸. In addition to PARP-targeted therapies, inhibitors of critical proteins in the homologous recombination DNA repair pathway, such as BRCA1 or RAD51, combined with traditional genotoxic treatments, enhance cancer cell death by further limiting the repair options available to tumor cells. Similarly, inhibitors of the ATR, Chk1, or ATM kinases, which play central roles in the DDR, are being explored for their potential to enhance the efficacy of existing treatments or overcome acquired resistance¹⁹.

A promising strategy for enhancing the efficacy of classical (direct DNA damage induction) and advanced cancer therapies (targeting DDR components) lies in the combined targeting of other cellular stress responses. Particularly, co-targeting proteotoxic and genotoxic stress pathways might improve patient outcomes significantly. This approach, which is among the primary focuses of our research, seeks to exploit the unique combined vulnerabilities of cancer cells by simultaneously inducing DNA damage (directly or by DNA repair inhibitors) and disrupting protein homeostasis. The rationale behind this strategy is based on the observation that both proteotoxic and genotoxic stress are already elevated in most cancer cells due to inherent defects in their cellular metabolic and maintenance pathways. By challenging these two critical stress responses together, we may be able to drive synergistic cancer cell death while potentially overcoming the resistance mechanisms that often limit the efficacy of individual therapies.

For instance, inhibiting the UPS or heat shock proteins impairs the cancer cell's ability to degrade misfolded proteins and trigger proapoptotic signaling, which might be compensated by anti-apoptotic regulation. If simultaneously DNA damage is introduced into the same cell, the proapoptotic signaling of these two pathways is combined, and the balance could be shifted toward cell death.

Another reason for the treatment efficacy of the convergence of these two stressors may be in the cellular resource allocation. It has been known for a long time that drugs inhibiting protein degradation, like bortezomib, can significantly alter the recruitment of essential DNA repair factors to sites of DNA damage²⁰. Mechanistically, it is due to ubiquitin

insufficiency. Ubiquitin (Ub), a small regulatory protein in eukaryotic cells, is pivotal for various cellular processes, including DNA repair and proteostasis. Ubiquitin achieves these roles by tagging proteins either for degradation by the proteasome (K-48-linked Ub chains) or for modulating protein interactions and functions (monoubiquitylations, K-63-linked and various mixed and branched Ub-chains) (Figure 8).

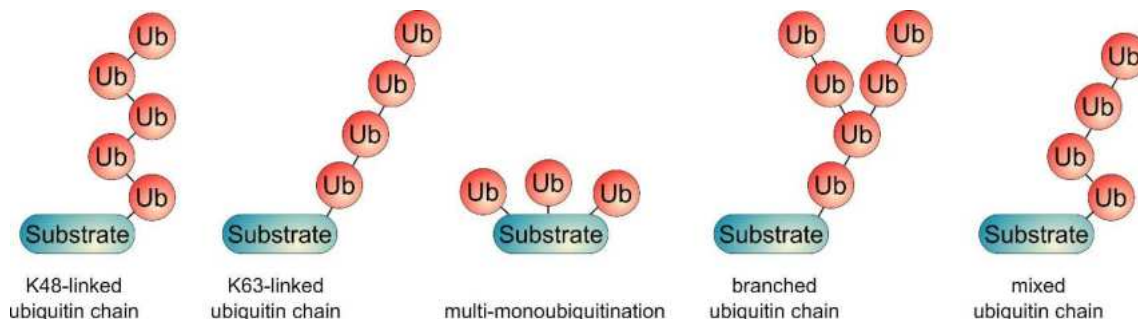


Figure 8: Scheme depicting different types of substrate ubiquitination. Long K48-linked chains ubiquitylate proteins dedicated to proteasomal degradation. Proteins involved in DNA repair signaling are mostly polyubiquitinated by K-63 linked chains or monoubiquitinated.

If the proteasome cannot degrade the polyubiquitinated proteins, large amounts of ubiquitin-tagged proteins accumulate within the cells, trapping most of the Ub in long K48-linked chains. The ubiquitin molecules are not recycled, leading to the shortage of free Ub, which limits E3-ligases such as RNF8 and RNF168, which ubiquitinate histones and other proteins within DNA damage sites to facilitate the recruitment of DNA repair factors like BRCA1 and 53BP1^{20,21}. Ubiquitination also regulates the activity of the Fanconi anemia (FA) pathway, which is crucial for repairing DNA interstrand crosslinks²². Monoubiquitylation of the FANCD2 protein is a critical step in activating this pathway, allowing for the coordination of nucleolytic incision, translesion synthesis, and homologous recombination-mediated DNA repair²².

Interestingly, the competition for ubiquitin between DNA repair and proteostasis also happens spontaneously in cancer cells due to elevated proteotoxic stress. Cancer cells often develop mechanisms that dysregulate ubiquitin usage and/or DNA repair pathways to manage this condition. Such adaptations frequently exacerbate mutations, chromosomal rearrangements, and aneuploidy, accelerating oncogenesis and contributing to poor prognosis²³.

The dual-targeting strategy aimed at DDR and proteostasis has the added benefit of potentially reducing the doses of each treatment, thereby mitigating the severe side effects often associated with genotoxic therapies. By lowering the required dose of DNA-damaging agents, we may decrease the damage inflicted on normal, healthy cells, which are more adept at handling moderate levels of genotoxic or proteotoxic stress than cancer cells.

Some preclinical studies have already shown promising results using this approach. For instance, proteasome inhibitors such as bortezomib or carfilzomib are combined with radiation therapy or DNA-damaging chemotherapeutic agents²⁴.

Despite the potential of this combined approach, there are still several challenges that need to be addressed. One of the key obstacles is understanding the complex cross-talk between the pathways regulating genotoxic and proteotoxic stress, as well as identifying the most effective points of intervention. Cancer cells are highly adaptable and may activate compensatory mechanisms to survive combined stressor assaults. Thus, a deeper understanding of the molecular mechanisms that link these two stress pathways will be critical for designing more targeted and effective therapeutic strategies.

Additionally, there is a need for the development of biomarkers that can predict which cancers are most likely to respond to this combined approach. Certain cancers may have pre-existing vulnerabilities in one or both pathways, making them more susceptible to the combined treatment. For example, tumors with deficiencies in specific DNA repair pathways, such as BRCA1/2 mutations, seem to be particularly sensitive to therapies that combine DNA-damaging agents with inhibitors of the UPS or HSR²⁵⁻²⁷.

In summary, co-targeting proteotoxic and genotoxic stress represents an exciting and innovative approach to cancer therapy, one that holds the potential to enhance treatment efficacy, overcome resistance mechanisms, and reduce side effects. By leveraging the inherent weaknesses of cancer cells in managing DNA and protein damage, this strategy offers a new avenue for combating even the most resistant and aggressive tumors. Our research gathered in the following parts of this habilitation dissertation contributes to refining this approach, bringing new methodical approaches, identifying new drugs or optimal drug combinations, and translating these findings into clinical practice to improve outcomes for cancer patients.

2. ADVANCEMENTS IN TOOLS FOR INVESTIGATING GENOTOXIC AND PROTEOTOXIC STRESS INDUCTION AND RELATED CELLULAR RESPONSES

Inducing specific cellular stresses, such as DNA or protein damage, followed by accurate quantitative monitoring of individual lesions processing and global cellular responses, are crucial for studying cancer biology, aging, and responses to genotoxic or proteotoxic agents, including anticancer chemotherapeutics. Various techniques have been developed to induce, detect, and quantify cellular stress insults, each with specific advantages and limitations. During our research, we either optimized or developed novel methodological approaches to address the limitations and challenges encountered in current DNA damage response (DDR) and proteotoxic stress research. This chapter gathers our most significant published advancements in this methodical field.

2.1. Replication stress inducers as the source of specific genotoxic stress

One of the ways DNA damage induction was studied in our research was the usage of so-called replication stress inducers. These compounds primarily interfere with DNA replication, a cornerstone of cellular proliferation, which is an energy and material-intensive process that requires precise regulation and coordination. Various checkpoints and feedback mechanisms ensure the fidelity of this process, and any perturbation or interference can lead to a cellular state generally described as replication stress (RS). More specifically, RS is characterized by the slowing down or stalling of DNA synthesis and/or replication forks, which can, in turn, threaten genome stability, jeopardize cell survival, and have broader implications for the organism, such as degenerative diseases and aging acceleration²⁸. Interestingly, replication stress is also a known result of activated oncogenes²⁹, which makes chemical factors capable of its induction a valuable proxy tool for studying various stages of the oncogenesis process. Our long-term experience and knowledge about chemical RS-inducers were gathered in a comprehensive review³⁰ (**Biomolecules, 2017, corresponding author, attachment 1**). The review outlines the mechanisms these compounds induce RS and details their effects on mammalian cells, including induced phenotypes, cellular responses, and commonly used doses in experimental setups, all based on recent research.

Interestingly, some RS inducers, such as aphidicolin, can damage DNA in a particular way, manifested by the expression of breaks, gaps, and constriction in specific DNA regions, which are evolutionary conserved and known as common fragile sites (CFSs)³¹. CFS expression is a feature that is also common for the aberrant activity of the oncogenes³². However, little is known about why such DNA breakage points exist within the human DNA and how their stability is regulated. Using a unique proteomics-based research strategy, we developed an innovative method to study CFSs induced by low doses of aphidicolin. By designing DNA sequences that emulate CFSs, particularly the human fragile site 16D sequence, we effectively utilized them as bait to 'fish' interacting proteins. This innovative methodology identified several proteins, among which Xeroderma pigmentosum protein group C (XPC) emerged as a protein of keen interest due to its previously uncharted association with CFS maintenance³³ (**Journal of Proteome Research, 2016, corresponding author, attachment 2**). XPC is primarily acknowledged for its role in the global genomic nucleotide excision repair pathway²². Our study newly links XPC's role in safeguarding CFSs during replication stress. Subsequent functional evaluations of XPC-depleted cells laid bare a spectrum of genomic anomalies associated with CFS. These encompassed aberrant checkpoint signaling, hampered replication fork progression, and the transmission of unresolved DNA replication intermediates into successive cellular generations under RS. In summary, this study accentuates the importance of XPC in safeguarding genomic integrity, especially at CFSs under RS conditions. Intriguingly, our data generated by the study also sheds light on the enigmatic evolutionary conservation of CFSs. We propose that CFC genomic loci may be an analogy to an electrical fuse that breaks upon overload. Under RS, which is not handled correctly, these structures can break and produce highly complicated and irreparable double-stranded DNA lesions, eliminating cells from proliferation via senescence or triggering apoptosis. Indeed, we confirmed in many experiments that aphidicolin is a potent inducer of cellular senescence, a form of stable proliferation arrest, and one of the most prominent mechanisms protecting organisms from cancer development³⁴. The knowledge and experience with the aphidicolin senescing properties were employed in one following study, which we used to design a screening methodology to identify compounds with senolytic properties³⁵. Senolytic drugs are a rapidly developing class of compounds that selectively induce the death of senescent cells, which accumulate within the organism during ontogenesis and may cause multiple harmful effects

by secretion of pro-inflammatory and tissue-degrading molecules known as the senescence-associated secretory phenotype³⁶.

2.2. An Advanced Method for Quantifying Low-dose DNA Damage and Replication Stress Responses

We employed and optimized many DNA damage induction methods for our experimental purposes using photon sources (UV light, X-rays, laser light), irradiation with high-energy particles (e.g., alpha particles), and various DNA-damaging chemicals. However, for quantitative analysis of DNA lesions and DNA repair kinetics, the traditional direct electrophoresis-based methods, such as the comet assay (single-cell gel electrophoresis) and field-inversion gel electrophoresis, lacked the necessary sensitivity for most of our studies. Consequently, we predominantly used indirect detection of DNA lesions via DNA damage protein markers, utilizing immunohistochemistry (IHC) followed by microscopy-based or flow cytometry-based readouts. This approach enabled more precise monitoring and quantification of DNA damage, enhancing our ability to investigate cellular responses in various contexts.

The usage of IHC, particularly the immunofluorescence-based detection of DNA lesions, pushed us to develop a new, affordable, and effective solution for quantifying the lesions in cells employing a regular fluorescence microscope and a standard personal computer with commonly available open-source image analysis software¹⁷ (**Cell Cycle, 2009, first author, attachment 3**). This publication provided an efficient alternative to expensive and specialized high-throughput screening devices. The introduced semi-automatic process allows for a sensitive, quantitative, and rapid fluorescence image analysis of thousands of adherent cells using immunofluorescent detection of serine-139 phosphorylated histone H2AX (γ -H2AX) to estimate delicate DNA breakage and extend a new dual-marker technique using RPA/Rad51 for evaluating specifically homologous recombination (HR)-based DNA repair. The method proved particularly useful in assessing low radiation doses and DNA repairing kinetics. Our collected data also provided insights into spontaneous DNA damage occurring in cancer cells and a range of HR-repair events, both constitutive and those caused by replication stress. The method also showcases the events' reliance on specific upstream factors within the DDR

system. The usefulness of this method, including various modifications, was proved in our multiple studies ^{23,26,27,33,37-50}.

2.3. Photo-manipulation DNA Damage Techniques for Cellular Research

One of the most explored tools for investigating the intricacies of DNA damage response, checkpoint signaling, and chromatin alterations in our research was the so-called laser micro-irradiation approach. This technique enables scientists to inspect how various proteins and posttranslational modifications are drawn to DNA damage sites in live or fixed cells. The principle of the method employs a laser-scanning microscope (LSM) equipped with a laser of adequate power and wavelength. Such a laser can be directed into specific subcellular areas, including the nucleus. Depending on the laser light properties, the exposed DNA can be damaged directly or after the pretreatment of cells with proper chemical photosensitizers (Figure 9).

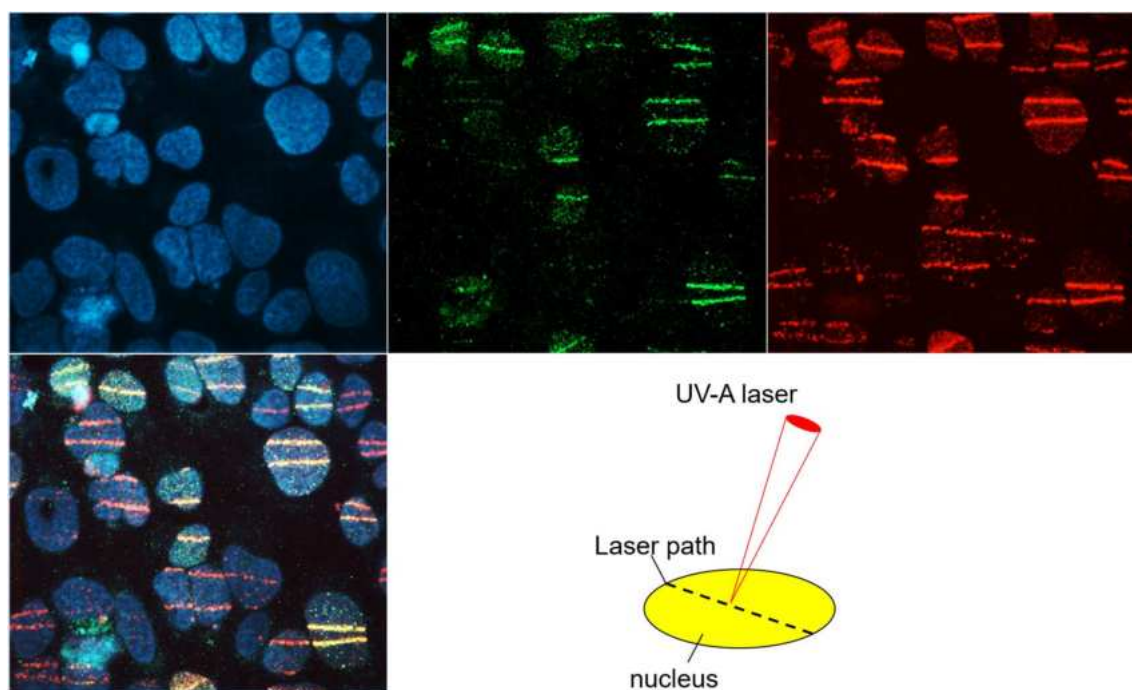


Figure 9: Example of laser micro-irradiation technique for localized DNA damage within cell nuclei. U-2-OS cells were pre-sensitized by BrdU incorporation and exposed to UV-A laser irradiation in a defined path. Visible stripes were obtained by immunofluorescence staining of proteins involved in DNA repair (green channel BRCA1, red channel γ -H2AX). The blue channel depicts DNA staining by DAPI.

The laser-induced damage assessment is done by analysis of the presence of DNA damage protein markers, which can be GFP-tagged or immunolabeled⁵¹. During our research, we used this technique routinely; however, while immensely useful, the traditional approach described in the available literature has been hampered by the cumbersome manual pinpointing of laser-targeted subcellular areas. This limitation greatly restricts the number of cells that can be laser-treated and examined in a given experiment. To overcome these limitations, we devised a solution, shifting the traditional micro-irradiation techniques to a new level, allowing rightful quantitative readouts. Instead of a few cells, our newly developed technique can leverage the capabilities of standard laser-scanning microscopes and expose up to 200 cells simultaneously to the laser⁵² (**Scientific Reports, 2016, first author, attachment 4**). Moreover, we have developed an automated quantitative readout for such laser damage assessment. The trick relies on an advanced setting of the LSM microscope when the cells are exposed to an organized pattern of collinear rays instead of manual targeting of individual cells, resulting in distinct striation patterns with known parameters. The presented software algorithm can automatically evaluate the laser-induced striation patterns and provide a quantitative understanding of various laser-induced changes in individual cells, including the time of protein recruitment to the damage sites, its quantity, and the persistence time. This automation drastically reduces the time and effort previously needed in the manual definition of laser path, amplifying the number of cells that can be included in a single experiment and allowing robust statistical testing. Overall, the "Cells and Stripes" technique, as we named it, opened a new era of microscopic micro-irradiation techniques in cellular research. We used it in follow-up studies, including works where it was adapted for an alternative photomanipulation technique known as fluorescence recovery after photobleaching^{47,53}.

2.4. Targeted Thermal Protein Damage for Proteotoxic Stress Research

By realizing how significantly laser-microirradiations shifted DNA damage research and our expertise with this technique, we devised an idea to adopt a similar methodical approach for damaging other subcellular protein-based structures. The introduction of a method to induce localized protein damage, combined with real-time observation tools, could provide a significant leap forward in the realm of cellular stress research with implications for understanding cancer and degenerative diseases. However, any attempts for direct

photodamaging proteins by LSM-embedded lasers or employment of protein-specific photosensitizers failed. Finally, we found such a solution by introducing plasmonic nanosilver technology. We covered the microscopic plates' cell cultivation surface with a thin nanosilver layer. Such a modified surface is transparent but can emit heat if hit by laser light of a proper wavelength via the plasmon resonance principle⁵⁴. Such a localized heat emission has the ability to alter or damage protein structures within its vicinity in a very controllable manner in real-time and with an achievable spatial resolution (approximately 200nm²)⁵⁵ (**Nature Comm, 2021, first author, attachment 5**) (Figure 10). The significant advantage of the method is its compatibility with standard laser-scanning microscopes, which opens it up to researchers worldwide. Using this method, we followed the recruitment of the HSP70 chaperone and its interacting proteins to the heat-damaged sites. We uncovered the kinetics of the process and some mechanistic aspects that govern the rapid HSP70 recruitment. One of the most illuminating findings from the study is the role of p97(VCP) translocase in response to local heat damage. While its involvement in various cellular processes was known, making this protein an attractive therapeutic target^{9,12}, its engagement in processing thermally damaged proteins was a novel discovery.

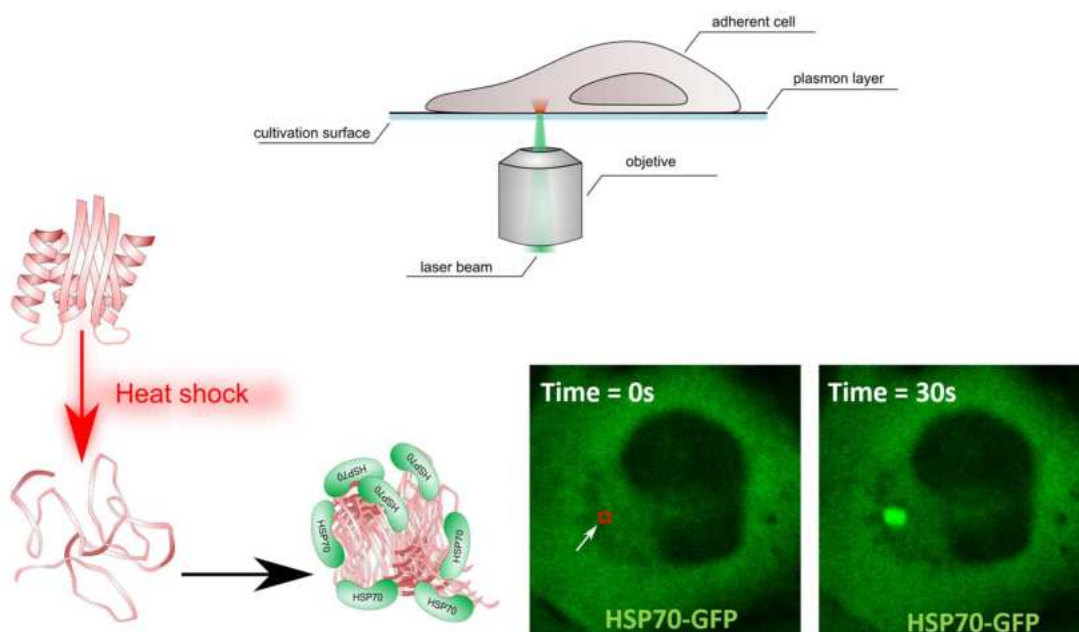


Figure 10: Overview of the method of induction localized subcellular heat damage. A laser of proper wavelength can locally burn cells in contact with the plasmon layer. Heat-damaged proteins are recognized by specific protein chaperones (e.g., HSP70). The effect can be monitored in real-time using fluorescently tagged proteins.

2.5. Monitoring of Cellular Responses in Hair Follicles

Our research occasionally transitions from cell line-based studies to preclinical and clinical models involving laboratory animals and patients. We have developed a sophisticated methodological approach utilizing follicular cells, which can be obtained non-invasively and relatively quickly. These cells can be experimentally treated in vivo or ex vivo and analyzed using various techniques for markers of DNA damage and other cellular responses. This method relies on an innovative, in-house hair follicle collection and processing device, providing sufficient biological material to replace invasive skin biopsies. The collected hair follicles contain live epithelial cells, making them particularly relevant for various cancer and aging studies. The method has been successfully tested using quantitative PCR to monitor the expression of p21 and p16, genes associated with the DNA damage response and aging, as well as immunofluorescence analysis of the DNA damage marker γ -H2AX protein for which we developed specialized image analysis software routine. Both mouse and human hair follicles have been successfully used for such procedures⁴⁵ (**Aging 2021, corresponding author, attachment 6**).

Additionally, this method has demonstrated its utility for genotyping, as the collection procedure provides sufficient DNA for standard genotyping protocols. This approach aligns well with animal research's 3Rs principle (replace, reduce, refine), offering significant ethical and logistical advantages over biopsy-based methods commonly used for genotyping (Figure 11).

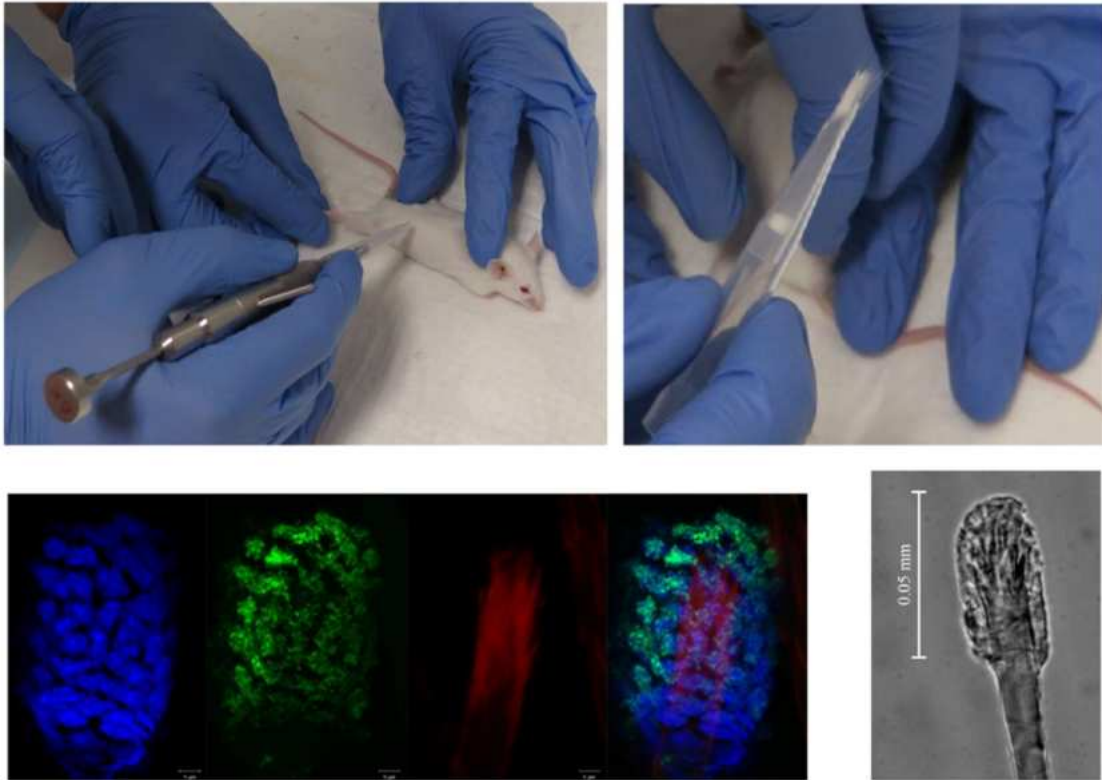


Figure 11: Overview of the method for non-invasive collection of live follicular cells from mice. An in-house developed and patented device allows an accessible collection of up to 300 hairs in a single shot. The hairs contain live follicular cells amenable to various analyses. Here is an example: immunofluorescence analysis of radiation-induced DNA damage in follicular cells of mice exposed to gamma rays (4 Gy). The blue channel depicts individual nuclei (stained by DAPI), and the green channel γ -H2AX signal. The red channel is autofluorescence of the hair structure.

3. TARGETING PROTEOSTASIS AND DNA REPAIR IN CANCER BY DITHIOCARBAMATES

The following chapter provides a comprehensive overview of our experimental work focused on targeting DNA repair and proteostasis mechanisms in cancer cells. A significant portion of our research has centered on the drug disulfiram (DSF, Tetraethylthiuram disulfide, commercially known as Antabuse), which was originally developed and remains widely used for the treatment of alcohol dependency. Our interest in DSF stemmed from an initiative to explore the potential of drug repurposing. This strategy holds great promise for addressing the urgent need for more effective cancer therapies by identifying novel uses for existing pharmaceuticals.

Disulfiram emerged as a compelling candidate not only due to a few clinical case reports suggesting its potential efficacy in cancer treatment but also reported activity against a variety of cancer types in preclinical studies⁵⁶. Beyond these observations, the published mechanistic insights proposed to explain its anticancer activity aligned closely with our research focus. In addition to its well-known role as an inhibitor of aldehyde dehydrogenase (ALDH) *in vivo*, DSF has been suggested to function as a potential proteasome inhibitor, which directly intersects with our long-standing scientific interest in the modulation of proteostasis pathways in cancer. The potential ability of DSF to influence multiple key pathways relevant to cancer progression makes it an attractive subject for further investigation, particularly in the context of targeting the fundamental cellular processes of DNA repair and protein homeostasis.

3.1. NPL4, an adaptor of p97 segregase, as the primary anticancer target of disulfiram

Before deep mechanistic insights into DSF's mode of action, we asked if its anticancer effects could be proved on epidemiological data sets. In collaboration with the Danish nationwide demographic and health registers, we performed a comprehensive nationwide epidemiological study on alcoholics undergoing DSF treatment and came to a significant finding: In case these patients got cancer and continuously used disulfiram after their diagnosis as part of their alcoholism treatment, they exhibited a lower risk of death compared to those who ceased its use upon diagnosis. This data strongly supports the potential therapeutic benefit of disulfiram in cancer treatment and asks for a deeper mechanistic explanation of DSF's anticancer properties.

Multiple preclinical studies showed a valuable fact that DSF's anticancer efficacy strongly depends on copper⁵⁷⁻⁵⁹. The copper dependency suggests that DSF might be turned into its copper complex via a simple chemical reaction involving its spontaneously forming intermediate diethyl-dithiocarbamate (DDTC), which is known as a highly potent copper chelator forming with copper ions, a stable complex – termed as CuET (diethyldithiocarbamate-copper complex). Indeed, our initial experiments with this compound confirmed potent cytotoxicity within the nanomolar scale toward various cancer cell lines.

Next, we confirmed what was already suggested from previous studies: multiple cellular phenotypes induced by CuET treatment resemble the effects of proteasomal inhibitors. Such

initial data prompt us to conclude that CuET might be the primary anticancer metabolite of DFS, and its anticancer effects imply proteostasis interference. The HPLC-MS method we developed for measuring the CuET complex in blood and other tissues confirmed that this complex is indeed formed *in vivo* and, interestingly, spontaneously also *in vitro* in cultivation media, suggesting CuET is the active molecule not only *in vivo* but also in all published DSF's *in vitro* studies.

Next, we analyzed the effect of CuET on proteasomal degradation of proteins more deeply. By systematic experiments, we surprisingly excluded that CuET inhibits proteasome directly. Instead, we identified interference with the p97 pathway working upstream of the proteasome. P97 (VCP) translocase and its cofactors are responsible for transporting degradation-tagged proteins towards the proteasome⁶⁰ (Figure 12).

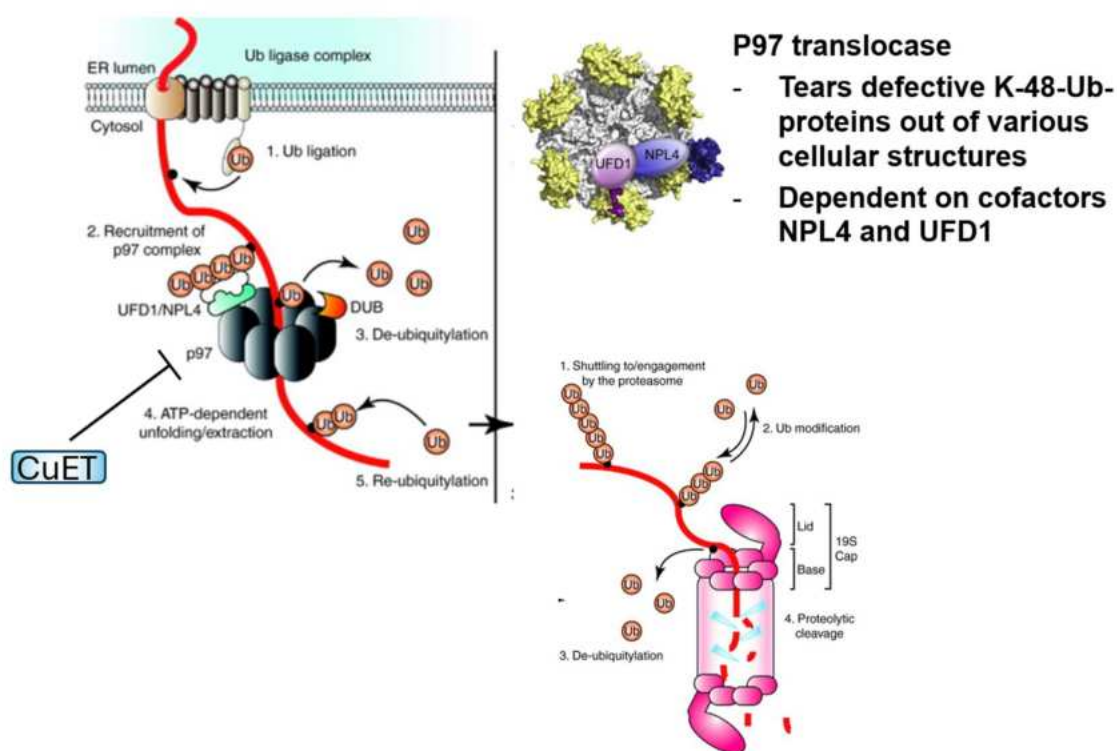


Figure 12: Effect of CuET on protein degradation via targeting p97 translocase complex. The proper function of p97 is critical for translocating defective proteins from ER to the proteasome. Therefore, inhibition of the p97 function shares multiple phenotypes with proteasome inhibitors (drawings adapted from^{2,61}).

Notably, the p97 pathway is a popular and explored focus for cancer research looking for alternatives to known proteasomal inhibitors^{9,12,62}. Next, we identified the molecular target of CuET, the NPL4 protein, an essential cofactor of p97 translocase⁶³, which directly interacts with CuET. Such interaction leads to NPL4's aggregation and formation of amorphous protein deposits (APDs) within the cells (Figure 13), ultimately leading to its loss of function and whole p97 pathway malfunction. The data were published in the prestigious Nature Journal⁵³ (**Nature 2017, shared first author, attachment 7**). Overall, this work gathers the epidemiological supportive correlation and identifies the anti-cancer metabolite of disulfiram and its molecular target. Such a revelation underscores the immense potential of drug repurposing in the battle against cancer and paves the way for harnessing the therapeutic potential of DSF, CuET, and other dithiocarbamates in oncology. This work also directly initiated a phase II clinical trial of disulfiram with concomitant copper supplementation for women with metastatic breast cancer in collaboration with three oncological centers in Czech Rep. The study aims to establish clinical evidence for introducing disulfiram and concomitant copper supplementation as an active therapy for metastatic breast cancer upon failure of conventional systemic and/or locoregional therapies. (see also for details <https://clinicaltrials.gov/study/NCT0323346>)

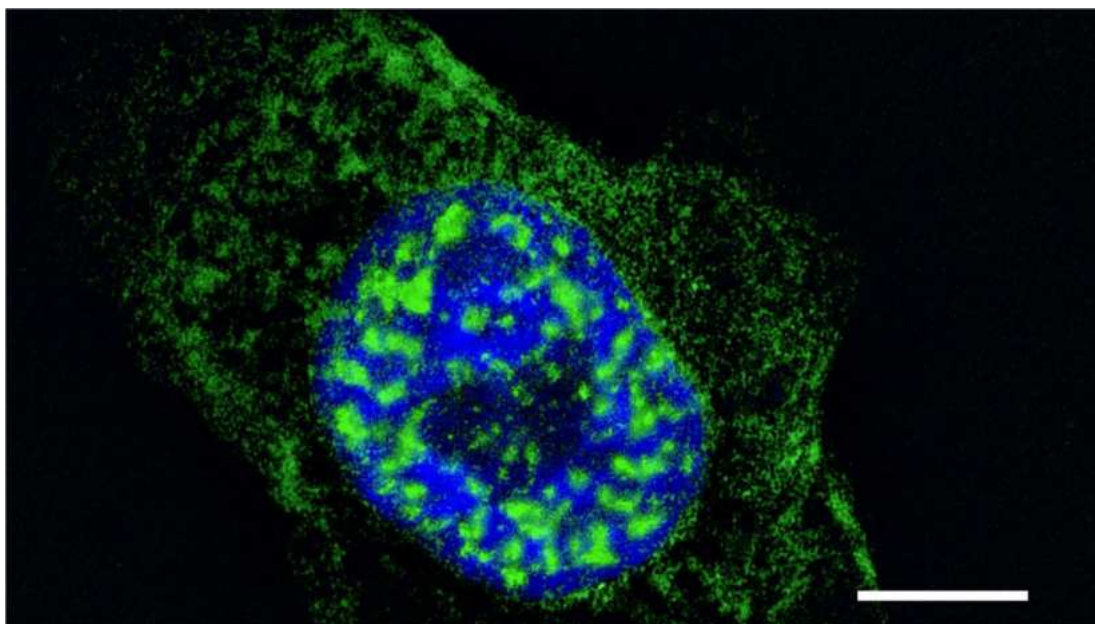


Figure 13: NPL4 protein APDs in cells treated by CuET. Detailed image of U-2-OS cell expressing GFP-tagged NPL4 protein after exposition to 1 μ M CuET for 2 hours. NPL4-GFP typically has a diffuse pattern. CuET treatment leads to the formation of nuclear and cytoplasmic deposits of the NPL4-GFP; the protein also becomes immobile and non-dissolvable. (Scale bar = 10 μ m).

3.2. Deciphering Disulfiram's Anti-cancer Mechanisms: Beyond ALDH Inhibition

Before our revelation in *Nature* in 2017 (described above), the disulfiram's (DSF) cancer-fighting abilities were initially attributed to its role in inhibiting aldehyde dehydrogenase (ALDH), a suspected biomarker and potential target for eradicating cancer stem cells⁶⁴. However, the scientific community did not wholly accept our new proposed mechanism, and some still insist on the ALDH as the primary target. One such example was a publication in a relatively prestigious *EMBO Molecular Medicine*, claiming ALDH as the primary DSF's target, providing *in vitro* evidence that DSF directly impacts ALDH activity, rendering cancer cells deficient in BRCA1 and BRCA2 tumor suppressor genes very sensitive to such treatment²⁵. Thus, we decided to investigate the DSF's ALDH-related targeting and either question this publication or accept ALDH targeting as a significant contributor to DSF's anticancer effect.

There are at least two problematic aspects of the ALDH theory for *in-vitro* studies. First is the known dependency of DSF's toxic effects on copper, which has been proven in multiple research studies and has become an accepted fact. However, there is no chemical or biological reason why adding copper ions into the culture media should render DSF an active ALDH inhibitor. The second is an often overlooked fact: DSF is not a direct inhibitor of ALDH. The mechanism of DSF's ALDH inhibitory action has been known for over two decades and, for unknown reasons, is ignored by many research teams. It involves various metabolism steps including cytochrome P450-catalyzed oxidation of S-methyl-N,N-diethylthiocarbamate and S-methyl-N,N-diethyldithiocarbamate intermediates in the liver that produces S-methyl-N,N-diethyldithiocarbamate sulfoxide, S-methyl-N,N-diethylthiocarbamate-sulfoxide and -sulfone, the fundamental metabolites that directly inhibit ALDH⁶⁵. Such a complicated chemical transformation, which would have to occur spontaneously in culture media, seems highly unlikely. Thus, we decided to adequately address this apparent inconsistency in multiple studies claiming DSF as an inhibitor of ALDH *in vitro* to demonstrate that the research teams misinterpreted their data.

Our initial focus was to establish that the *in vitro* toxicity of disulfiram (DSF) is entirely dependent on the formation of CuET. Using HPLC-MS, we confirmed that CuET forms spontaneously from DSF in standard cell culture media due to copper ions, which are always present even without an extra addition as an indivisible component of the fetal bovine serum supplement. Notably, when we removed all copper ions from the media using the metal

chelator bathocuproinedisulfonic acid (BCDS) before DSF treatment, no CuET formation occurred. DSF completely lost its toxic effects in such copper-ions-free media, including in cell lines with defective BRCA genes. In other words, we validated that BRCA-defective cells are not super-sensitive to DSF but to CuET, which is an interesting observation with significant mechanistic consequences (addressed in more detail in our follow-up publication - see further).

Subsequently, we tested the cytotoxic effects of known direct inhibitors of ALDH, including DEAB and Me-DTC-SO, which are commonly used in in vitro studies. These compounds were completely non-toxic within a rational concentration scale regardless of the cancer cells' BRCA status. These findings were later published in *Oncogene Journal*⁴⁶ (**corresponding author, attachment 8**).

Beyond its corrective function, this work serves as a pivotal turning point in understanding the role of DSF in cancer therapy. It highlights that the drug's anti-cancer effects are primarily due to its copper-laden metabolite, CuET, rather than ALDH inhibition, as was widely believed. This insight is invaluable for future therapeutic directions. Additionally, the study elucidates that the distinct cytotoxicity of DSF towards BRCA deficient cells is mediated by CuET and not due to any ALDH-inhibitory action.

3.3. Disulfiram's Targeting of NPL4 Impairs DNA Replication Dynamics and Induces ATR Pathway Malfunction

As cellular BRCA1/2 gene status was reported and further confirmed by us as an essential determinant of sensitivity to DSF's metabolite CuET (see above), we were intrigued by the mechanistic explanation. BRCA1 and BRCA2 genes are widely studied due to known mutations directly linked to many breast and ovarian cancers⁶⁶. Mechanistically, both BRCA proteins ultimately contribute to the processing of DNA damage and prevent cells from genotoxic stress and genomic instability due to their involvement in homologous recombination-mediated DSB repair and various aspects of DNA replication⁶⁷. Therefore, we logically asked if CuET activity might somehow contribute to the induction of DNA lesions and/or interfere with DNA damage response, apart from its apparent effects on proteostasis.

Notably, the target of CuET, the NPL4 protein, has also been reported to play a crucial role in protein turnover within sites of DNA damage^{68,69}.

We set essential experimental insights using our advanced methodical tools (described in more detail in Chapter 2) and found that CuET treatment effectively disrupts DNA replication dynamics. Specifically, the progression of replication forks is hindered, leading to an accumulation of single-stranded DNA (ssDNA) – a hallmark of elevated replication stress (RS), which we documented by quantification of various DNA lesion markers, especially during the S phase of the cell cycle. This damage prompts the activation of the homologous recombination (HR) DNA repair pathway and explains the heightened dependency of the cells on functional BRCA1/2 status.

More mechanistic insights revealed that the RS and subsequent DNA damage are linked to NPL4 aggregation in other ways than initially expected. We discovered that CuET treatment induces the impairment of the critical ATRIP-ATR-Chk1 signaling pathway. ATR kinase and the whole signaling pathway it mediates are essential for the proper progression of replication, particularly under the genotoxic stress conditions⁷⁰. The mode of the CuET-induced impairment was surprising and unconventional as the crucial components ATR pathway, the ATR and Chk1 kinases were found predominantly sequestered and immobilized within the NPL4 APDs formed due to CuET exposure, compromising their functionality. Overall, this study²⁶ (**Cells 2020, corresponding author, attachment 9**) offers a profound understanding of how DSF's metabolite, CuET, can be a game-changer in cancer therapy. By targeting NPL4, CuET not only induces proteotoxic stress, resembling the effects of inhibitors of proteasomal degradation, but also severely impedes replication and DNA damage via malfunction of ATR pathway-promoted inherent DNA-replication protective mechanisms. This dual action, which was further boosted by the additional discovery that NPL4 APDs also sequester p53 protein and interfere with translation⁵⁰, renders the tumor cells increasingly vulnerable, mainly if inflicted by mutations in specific genome maintenance genes, opening a promising therapeutic avenue.

3.4. Cannabidiol Interference with Disulfiram's Anti-Cancer Efficacy Through the Metallothionein Pathway

Due to our work and the contributions of other research teams, DSF has been recognized beyond its traditional role as an alcohol-aversion medication as a potentially potent anticancer drug, especially if combined with copper ions supplementation. It is now being deeply explored for its potential anti-cancer properties in multiple ongoing clinical trials⁷¹. However, while preclinical studies and limited clinical trials support its therapeutic potential in oncology, there are variations in the first published clinical outcomes from recent years. Thus, we immediately asked for potential factors limiting the efficacy of DSF treatment in patients. We realized that one such reason could be interference from other drugs often used concomitantly during cancer therapy.

To address such potential unwanted drug-drug interactions, we utilized our unique access to a high-throughput robotic screening platform accompanied by automated fluorescent microscopy evaluation. This approach allowed us to systematically screen over 1,400 biologically active compounds used in clinics or preclinical research for potential interactions. Our screening setup employed the published methodology for detecting NPL4-GFP aggregates using fluorescence microscopy, which can be quantified using microscopic fluorescence readouts.

One of the most potent hits identified in the screen was cannabidiol (CBD), a major component of *Cannabis sativa* L. (marijuana), which efficiently diminished the formation of NPL4 aggregates and also the toxic effects of DSF and its active metabolite CuET. Identifying cannabidiol as a probable agent causing resistance to DSF in clinical setups is particularly relevant because *Cannabis sativa*-derived compounds have gained increasing popularity among cancer patients for their potential to reduce cancer treatment side effects and are now more accessible due to relaxed regulations. The US Food and Drug Administration (FDA) has approved several cannabis-derived drugs for treating various conditions, including chemotherapy-induced nausea and vomiting. Notably, surveys among cancer patients revealed that cannabinoids are very often used off-label⁷²⁻⁷⁴.

Further mechanistic insights into cannabidiol's protective role against the toxic effects of CuET revealed that in the intricate cellular environment, cannabidiol triggers the expression

of metallothioneins – proteins that bind and sequester heavy metal-based substances. This is particularly significant given that CuET contains copper. Further experiments established a clear negative correlation between the levels of metallothioneins and DSF/CuET toxicity⁷⁵ (**Molecular Oncology 2022, corresponding author, attachment 10**).

Overall, this study highlights the undesirable consequences of combining marijuana products with DSF-based cancer therapy, as it jeopardizes its therapeutic efficacy. Conversely, it demonstrates that cancer cells deficient in metallothioneins are more susceptible to CuET's action. This finding also raises the prospect of using metallothionein levels to personalize DSF-based treatments, serving as a predictive biomarker for DSF's efficacy in patients. Thus, personalizing DSF therapy based on metallothionein expression could enhance therapeutic outcomes, tailor treatments to individual patient profiles, and maximize the anticancer potential of DSF.

Additionally, this research underscores the importance of considering drug-drug interactions in clinical protocols, particularly with the growing use of cannabis-derived compounds in medical settings. Further clinical studies are warranted to validate these findings and integrate them into comprehensive treatment strategies for cancer patients. This finding also serves as a cautionary note, emphasizing the need to re-evaluate the concomitant usage of marijuana-based products in various cancer therapeutic regimens, which has been largely ignored.

In response to this research need, we extended our cannabinoids investigation to other metal-containing cancer chemotherapeutics, specifically platinum-based drugs. Strikingly, cannabinoids, particularly CBD and also Cannabis sativa extracts, were found to reduce the toxicity of cisplatin, oxaliplatin, and carboplatin, the three most clinically used platinum drugs. However, in this particular scenario, the mechanistic insights did not confirm the protective role of elevated levels of metallothioneins. Instead, Inductively Coupled Plasma Mass Spectrometry (ICP-MS) analyses suggested that cannabinoids have the potency to interfere with intracellular platinum accumulation, likely through altered cellular transport and/or retention of these drugs⁷⁶ (**Biomedicine & Pharmacotherapy 2023, corresponding author, attachment 11**).

Overall, these findings highlight the complex interactions between cannabinoids and chemotherapeutic agents, necessitating careful consideration and further investigation. The potential reduction in drug efficacy, either due to stimulation of the protective metallothionein pathway or due to altered drug transport and retention mechanisms, underscores the need for a cautious approach when integrating cannabinoids into cancer treatment regimens.

As this topic was relatively new and unexplored, we compiled and published a comprehensive review of known interactions between CBD and standard-of-care chemotherapeutics⁷⁷ (**Int J Mol Sci 2023, corresponding author, attachment 12**). The review details how cannabinoids can potentially interfere with the therapeutic efficacy of many different cancer chemotherapeutics through various mechanisms. We discussed how CBD and other cannabis-derived compounds may affect drug metabolism, transport, and cellular uptake, ultimately influencing the pharmacokinetics and pharmacodynamics of these chemotherapeutic agents. Overall, we concluded that despite the benefits cannabinoids provide in alleviating chemotherapy side effects, patients and healthcare providers should reconsider or avoid combining them with ongoing chemotherapy, at least for a subset of anticancer drugs, until more is known about their interactions. Furthermore, we highlighted the need for more robust clinical trials and mechanistic studies to elucidate these interactions and their implications fully.

3.5. Disulfiram's Repurposing to Overcome Resistance of Multiple Myeloma

In our quest to identify which type of cancer diagnosis could benefit most from DSF-based treatment, we concluded that multiple myeloma (MM) might be among the primary candidates. MM is a type of blood cancer that affects plasma cells in the bone marrow, which are responsible for producing large amounts of antibodies. This metabolic demand makes them uniquely reliant on proteostasis, which makes these cells particularly prone to proteostasis dysregulation⁹. MM cells proved to be among the most responsive to CuET treatment in our panel of tested cancer cell lines⁵³.

Although there are effective drugs targeting MM, including Bortezomib (Velcade), Carfilzomib (Kyprolis), and Ixazomib (Ninlaro), which target the proteasome, MM often remains a challenge due to treatment-induced resistance. This resistance can arise from

mutations in proteasome proteins, overexpression of these proteins, or metabolic adaptations such as a reduced proteasome load due to decreased protein production¹⁰.

Therefore, instead of proposing DSF as a primary treatment for MM, we hypothesized that the unique properties of DSF's metabolite, CuET, could offer an advantage over standard proteasome inhibitors, particularly in targeting resistant MM cells. Our findings supported this hypothesis, as CuET demonstrated potent activity against MM cells that had developed resistance to frontline MM drugs like Bortezomib and Carfilzomib. Furthermore, CuET was equally effective as experimental drugs targeting protein degradation pathways upstream of the proteasome, such as p97 translocase inhibitors^{9,12}.

We further tested CuET's ability to overcome resistance mechanisms associated with reduced proteasome load, a scenario where traditional protein-turnover targeting drugs ultimately lose efficacy¹⁰. Remarkably, CuET bypassed this resistance mechanism, likely due to its additional impact on the DNA damage response we identified previously (see Chapter 3.3 for details), amplifying its therapeutic potential.

Overall, this study⁴⁹ (**Cell Death and Diseases 2022, corresponding author, attachment 13**) highlights a promising therapeutic avenue for MM patients, especially those facing disease recurrence due to treatment resistance. By repurposing disulfiram and pairing it with copper supplementation, we may be able to transform the therapeutic landscape for resistant multiple myeloma.

3.6. Novel Dithiocarbamate-Copper Complexes Targeting the p97/NPL4 Pathway in Cancer Therapy

In multiple studies (as referred above), we demonstrated the anticancer efficacy of the bis(diethyldithiocarbamate)-copper complex (CuET), a metabolic product of the anti-alcoholic drug disulfiram. Chemically, CuET belongs to a large family of dithiocarbamates (DTCs), many of which possess the capability to chelate copper, and some of them have already been investigated for their anticancer properties^{78,79}. We aimed to determine whether CuET's ability to inhibit the NPL4 protein, with proteotoxic and genotoxic consequences leading to cancer cell death, is unique to this particular dithiocarbamate or is shared by more DTC-Cu complexes.

To this end, we evaluated 20 different DTC-Cu complexes, which we obtained to determine their capacity to induce NPL4 protein aggregation.

Our findings revealed that a significant number of these complexes, despite their structural differences, could target and aggregate the NPL4 protein in cancer cells, leading to typical proteotoxic stress-related responses and cytotoxicity. Specifically, thirteen of the tested complexes exhibited these properties, mirroring the effects of CuET and demonstrating in vitro efficacy in the nanomolar range. Notably, only those complexes capable of inducing NPL4 aggregation were cytotoxic to cancer cells, underscoring NPL4 as a crucial target in their mechanism of action (Figure 14).

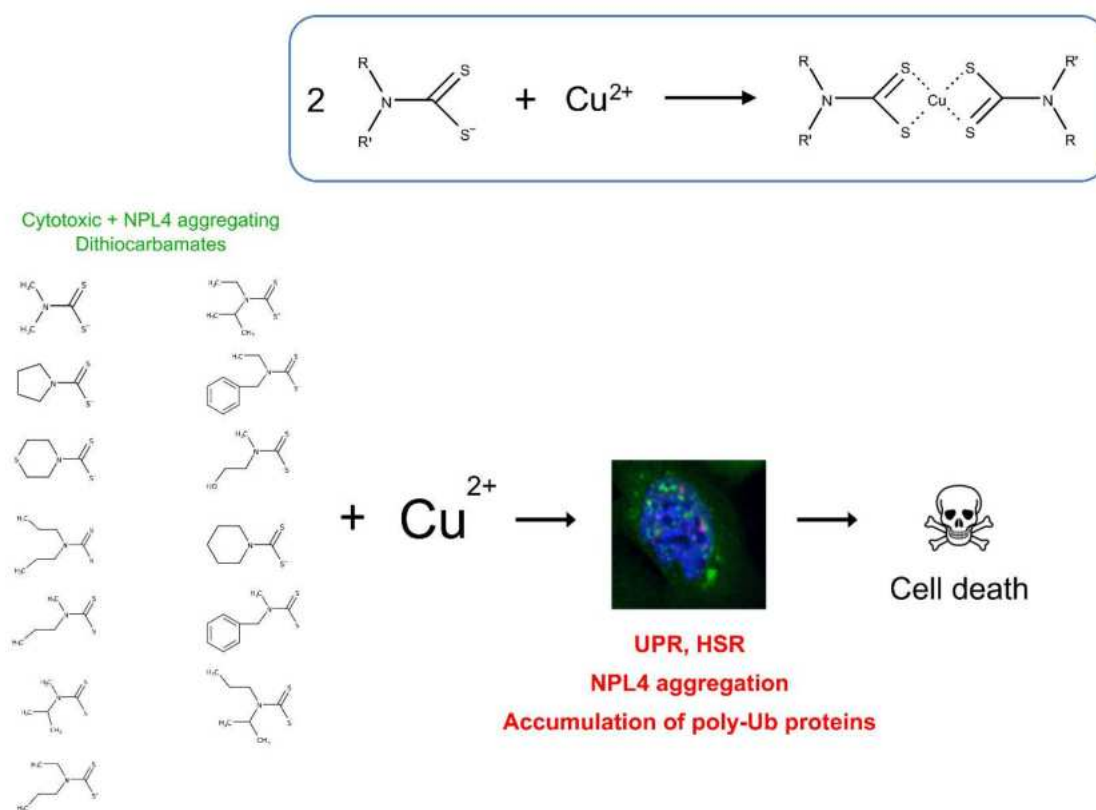


Figure 14: Overview of identified active dithiocarbamate copper complexes. Multiple structurally different dithiocarbamates make stable copper complexes, which are toxic to cancer cells, induce NPL4 protein aggregation, and are typical for proteotoxic stress.

One of the study's key conclusions explores the underlying mechanism by which these complexes affect the NPL4 protein. It seems highly unlikely that the structurally diverse DTC-copper complexes targeting NPL4 bind directly to a specific protein pocket. Instead, it appears

they just deliver cupric ions to the vicinity of the protein. NPL4 harbors two zinc-finger domains with a high affinity for bivalent metals. We speculate that at least one of these domains competes for the copper ion with the DTC-copper complexes. Once copper binds to the domain instead of zinc, the tertiary or quaternary structure of the NPL4 protein collapses, leading to aggregation and APDs formation.

Overall, this study⁸⁰ (**European Journal of Medicinal Chemistry 2023, corresponding author, attachment 14**) introduced 13 structurally diverse DTC-Cu complexes capable of effectively targeting the NPL4 protein in cancer cells, leading to proteotoxic stress and cancer cell death via the exact mechanism we previously reported for CuET⁵³. The study further reinforces the relevance of targeting proteostasis in cancer therapy and suggests that these complexes act as delivery systems for cupric ions to destabilize the NPL4 protein. The results provide a foundation for further exploration of DTC-Cu complexes in drug development, potentially enhancing anticancer treatment strategies by exploiting vulnerabilities in cancer cell proteostasis.

3.7. Leveraging Disulfiram, Vorinostat, and PARP inhibitors for Combating Castration-Resistant Prostate cancer

Castration-resistant prostate cancer (PCa) remains a formidable clinical challenge. In our research, we aimed to propose new therapeutic strategies by repurposing clinically available drugs to target specific genotoxic and proteotoxic stress responses relevant to this particular cancer subtype. We evaluated a combination of drugs, including PARP1 enzyme inhibitors (PARPi), vorinostat (a histone deacetylase inhibitor), and disulfiram (DSF), traditionally used for alcohol abuse treatment, including its active copper-chelating metabolite CuET, in conjunction with ionizing (gamma) irradiation (IR). The rationale for this selection was based on the documented anticancer effects of these drugs and their impact on DNA repair and protein turnover mechanisms.

The drugs, both individually and in combination with IR, were tested on three distinct human PCa cell lines, including the particularly challenging radio-resistant stem-cell-like DU145-derived cells. Our study used immunofluorescence and immunoblotting techniques to elucidate the cellular pathways influenced by these drugs, specifically the DNA damage repair,

proteotoxic stress markers including heat shock activation, and activated unfolded protein response (UPR) pathways.

PC3 cells exhibited increased sensitivity to the combination of PARPi and IR, which we attributed to diminished homologous recombination (HR) repair mechanisms in this cell line. Vorinostat sensitized DU145 cells to the PARPi/IR combination, reducing mutant p53 levels. Notably, it also effectively countered the radioresistance typical for the stem-cell-like DU145-derived cells.

DSF with copper and direct treatment with CuET demonstrated strong cytotoxic effects across all tested PCa cell lines. These treatments induced a robust unfolded protein response (UPR), as evidenced by markers such as ATF4, CHOP, and phospho-eIF2 α .

Our study²⁷ (**Prostate 2018, corresponding author, attachment 15**) builds a compelling case for targeting genotoxic and proteotoxic stress responses through strategic combinations of clinically available drugs. By highlighting the potential of these drug combinations, our research suggests a promising therapeutic strategy for the challenging landscape of castration-resistant PCa. The insights gained from this study can serve as a foundation for developing innovative, real-life treatment concepts.

4. SUMMARY

This habilitation thesis provides a comprehensive overview of published research focused on the cellular processes activated by proteotoxic and genotoxic stress. It highlights significant advancements in both the development of tools and methodologies for studying these stress responses, as well as novel mechanistic insights into key areas such as proteostasis, DNA repair, and tumorigenesis. Several studies have also explored the potential of targeting these pathways as therapeutic strategies for cancer.

Methodologically, we review various chemical inducers of replication stress and DNA damage used in in-vitro experiments³⁰, including aphidicolin, a compound introduced here as a promising tool for high-throughput senescence induction³⁵. Aphidicolin was also employed in our innovative proteomic approach, leading to the identification of Xeroderma pigmentosum group C (XPC) as a critical factor in maintaining common fragile sites stability³³.

Furthermore, we developed advanced tools for the induction and quantitative assessment of DNA damage, including immunofluorescence-based assays, reporter cell lines with GFP-tagged proteins, and specialized microscopy techniques^{17,52}. One notable development is our method for inducing localized subcellular heat damage, which enabled us to investigate the cellular response to damaged proteins. This work uncovered new roles for HSP70 and the p97 translocase in protein quality control⁵⁵. Additionally, we introduced a non-invasive method for collecting hair follicle cells from laboratory animals and humans, facilitating *in vivo* and *ex vivo* studies of DNA damage and other stress responses. This approach offers a valuable alternative to invasive biopsies in the context of cancer and aging research⁴⁵.

On the mechanistic side, we introduced the concept of intracellular resource allocation under conditions of elevated proteotoxic stress, particularly focusing on ubiquitin availability. We demonstrated that limited ubiquitin resources lead to changes in the expression of the RNF168 E3 ligase, with significant implications for genomic stability and sensitivity to specific anticancer therapies²³. Our research also elucidated the mechanism underlying the anticancer activity of disulfiram (DSF), a drug currently repurposed for oncological use. DSF, through its metabolite CuET, targets the p97/NPL4 pathway, disrupting proteostasis and inducing protein aggregation⁵³. Further insights revealed that NPL4 is the main target of CuET, causing its aggregation and formation of NPL4's insoluble deposits (APDs). Interestingly, these APDs sequester many other proteins, including essential factors of the ATRIP-ATR-CHK1 pathway, causing additional replication stress and DNA damage in cancer cells²⁶. This results in heightened replication stress and DNA damage, particularly in cancer cells with DNA repair defects^{27,46}, and explains the surprising efficacy of CuET treatment in multiple myeloma cells resistant to UPS inhibitors⁴⁹. Moreover, our research clarified previous misconceptions regarding DSF's role as a direct inhibitor of aldehyde dehydrogenase⁴⁶. Based on the exceptional anticancer properties of CuET, we expanded our investigations to other dithiocarbamates, revealing a shared mechanism of action for copper complexes of these compounds, which opens new therapeutic possibilities for advanced and drug-resistant cancers⁸⁰.

Overall, this habilitation thesis presents a cohesive body of work that significantly advances the understanding of cellular responses to genotoxic and proteotoxic stress, while

contributing innovative experimental tools and offering promising therapeutic strategies for cancer treatment.

5. ABBREVIATIONS

6–4 PPs	Pyrimidine(6–4)pyrimidone photoproducts (UV-induced DNA lesions)
ALDH	Aldehyde dehydrogenase
APDs	Insoluble protein deposits
ATF4	Activating transcription factor 4 protein
ATF6	Activating transcription factor 6 protein
ATF6c	Cleaved form of activating transcription factor 6
ATM	Ataxia-telangiectasia mutated kinase
ATR	ATM and Rad3-related kinase
ATRIP	ATR-interacting protein
BCDS	Bathocuproinedisulfonic acid
BIP	Binding immunoglobulin protein (GRP78, glucose-regulated protein 78)
BrdU	Bromodeoxyuridine (synthetic nucleoside used in cell proliferation assays)
BRCA1	Breast cancer 1, early onset protein
BRCA2	Breast cancer 2, early onset protein
BRCA1/2	Referring to both BRCA1 and BRCA2 genes
CBD	Cannabidiol
PCa	Castration-resistant prostate cancer
Chk1	Checkpoint kinase 1
Chk2	Checkpoint kinase 2
CHOP	C/EBP homologous protein
CFSs	Common fragile sites
cis-Pt	Cisplatin (chemotherapeutic drug)
CuET	bis(diethyldithiocarbamate)-copper complex
DAPI	4',6-diamidino-2-phenylindole (a fluorescent stain that binds to DNA)
DDR	DNA damage response
DEAB	4-(Diethylamino)benzaldehyde
DNA-PKcs	DNA-dependent protein kinase catalytic subunit kinase
DSBs	Double-strand breaks
DSF	Disulfiram, Tetraethyl thiuram disulfide, Antabuse

DTC	Dithiocarbamate
DTC-Cu	Copper complex with dithiocarbamate
DTCs	Dithiocarbamates
DU145	Human prostate cancer cell line
eIF2 α	Eukaryotic translation initiation factor 2 α protein
EMA	European Medicines Agency
ER	Endoplasmic reticulum
ERAD	ER-associated degradation
FANCD2	Fanconi anemia, complementation group D2 protein
FA	Fanconi anemia
FDA	US Food and Drug Administration agency
GI	Genomic integrity
HSP70	Heat shock protein 70
HSP90	Heat shock protein 90
HSPs	Heat shock proteins
HSR	Heat shock response
HPLC-MS	High-performance liquid chromatography-mass spectrometry
HR	Homologous recombination
IHC	Immunohistochemistry
ICP-MS	Inductively coupled plasma mass spectrometry
IRE1 α	Inositol-requiring enzyme 1 alpha
IR	Ionizing (gamma) irradiation
LSM	Laser-scanning microscope
MMC	Mitomycin C (chemotherapeutic agent)
MM	Multiple myeloma
MRE11	Meiotic recombination 11 homolog (part of the MRN complex)
MRN	MRE11-Rad50-NBS1 complex (involved in DNA repair)
NBS1	Nijmegen breakage syndrome protein 1 (part of the MRN complex)
NPL4	Nuclear protein localization 4 homolog protein
PARP	Poly(ADP-ribose) polymerase
PARPi	PARP1 enzyme inhibitors

p53	Tumor suppressor protein p53
p62	Sequestosome 1 (also known as SQSTM1, involved in autophagy)
PC	Proteotoxic crisis
PERK	Protein kinase RNA-like endoplasmic reticulum kinase
γ-H2AX	Phosphorylated histone H2AX
p97	Also known as VCP (Valosin-containing protein)
RAD51	RAD51 recombinase protein
Rad50	DNA repair protein (part of the MRN complex)
RNF8	Ring finger protein 8
RNF168	Ring finger protein 168
ROS	Reactive oxygen species
Rpn1	Regulatory particle non-ATPase 1 (part of the proteasome)
Rpn10	Regulatory particle non-ATPase 10 (part of the proteasome)
Rpn11	Regulatory particle non-ATPase 11 (part of the proteasome)
Rpt1-6	Regulatory particle triple-A ATPase subunits 1-6 (part of the proteasome)
RS	Replication stress
ssDNA	Single-stranded DNA
TOPBP1	DNA topoisomerase II-binding protein 1
U-2-OS	Human osteosarcoma cell line
Ub	Ubiquitin
UPR	Unfolded protein response
UV	Ultraviolet radiation
VCP	Valosin-containing protein, p97 protein
Xbp1s	Spliced form of X-box binding protein 1
XPC	Xeroderma pigmentosum protein group C protein

6. BIBLIOGRAPHY

Publications to which I contributed are in bold

*Publications where I'm the first or corresponding author are marked with **

1. González-Quiroz, M. et al. When Endoplasmic Reticulum Proteostasis Meets the DNA Damage Response. *Trends Cell Biol.* 30, 881–891 (2020).
2. Claessen, J. H. L., Kundrat, L. & Ploegh, H. L. Protein quality control in the ER: balancing the ubiquitin checkbook. *Trends Cell Biol.* 22, 22–32 (2012).
3. Siwecka, N. et al. Dual role of Endoplasmic Reticulum Stress-Mediated Unfolded Protein Response Signaling Pathway in Carcinogenesis. *Int. J. Mol. Sci.* 20, 4354 (2019).
4. Wu, J. et al. Heat Shock Proteins and Cancer. *Trends Pharmacol. Sci.* 38, 226–256 (2017).
5. Wu, J. et al. Heat Shock Proteins and Cancer. *Trends Pharmacol. Sci.* 38, 226–256 (2017).
6. Rastogi, S. et al. An update on the status of HSP90 inhibitors in cancer clinical trials. *Cell Stress Chaperones* 29, 519–539 (2024).
7. Yang, S., Xiao, H. & Cao, L. Recent advances in heat shock proteins in cancer diagnosis, prognosis, metabolism and treatment. *Biomed. Pharmacother.* 142, 112074 (2021).
8. Hershko, A. & Ciechanover, A. THE UBIQUITIN SYSTEM. *Annu. Rev. Biochem.* 67, 425–479 (1998).
9. Deshaies, R. J. Proteotoxic crisis, the ubiquitin-proteasome system, and cancer therapy. *BMC Biol.* 12, 94 (2014).
10. Orłowski, R. Z. Why Proteasome Inhibitors Cannot ERADicate Multiple Myeloma. *Cancer Cell* 24, 275–277 (2013).
11. Vekaria, P. H., Home, T., Weir, S., Schoenen, F. J. & Rao, R. Targeting p97 to Disrupt Protein Homeostasis in Cancer. *Front. Oncol.* 6, (2016).
12. Anderson, D. J. et al. Targeting the AAA ATPase p97 as an Approach to Treat Cancer through Disruption of Protein Homeostasis. *Cancer Cell* 28, 653–665 (2015).
13. Hoeijmakers, J. H. J. Genome maintenance mechanisms for preventing cancer. *Nature* 411, 366–374 (2001).
14. Ciccia, A. & Elledge, S. J. The DNA Damage Response: Making It Safe to Play with Knives. *Mol. Cell* 40, 179–204 (2010).
15. Durocher, D. & Jackson, S. P. DNA-PK, ATM and ATR as sensors of DNA damage: variations on a theme? *Curr. Opin. Cell Biol.* 13, 225–231 (2001).
16. Gusho, E. & Laimins, L. Human Papillomaviruses Target the DNA Damage Repair and Innate Immune Response Pathways to Allow for Persistent Infection. *Viruses* 13, 1390 (2021).
- 17.* **Mistrik, M., Oplustilova, L., Lukas, J. & Bartek, J. Low-dose DNA damage and replication stress responses quantified by optimized automated single-cell image analysis. *Cell Cycle* 8, 2592–2599 (2009).**

18. Topatana, W. et al. Advances in synthetic lethality for cancer therapy: cellular mechanism and clinical translation. *J. Hematol. Oncol.* 13, 118 (2020).
19. Hopkins, J. L., Lan, L. & Zou, L. DNA repair defects in cancer and therapeutic opportunities. *Genes Dev.* 36, 278–293 (2022).
20. Dantuma, N. P., Groothuis, T. A. M., Salomons, F. A. & Neefjes, J. A dynamic ubiquitin equilibrium couples proteasomal activity to chromatin remodeling. *J. Cell Biol.* 173, 19–26 (2006).
21. Doil, C. et al. RNF168 Binds and Amplifies Ubiquitin Conjugates on Damaged Chromosomes to Allow Accumulation of Repair Proteins. *Cell* 136, 435–446 (2009).
22. Sancar, A., Lindsey-Boltz, L. A., Ünsal-Kaçmaz, K. & Linn, S. Molecular Mechanisms of Mammalian DNA Repair and the DNA Damage Checkpoints. *Annu. Rev. Biochem.* 73, 39–85 (2004).
- 23. Chroma, K. et al. Tumors overexpressing RNF168 show altered DNA repair and responses to genotoxic treatments, genomic instability and resistance to proteotoxic stress. *Oncogene* 36, 2405–2422 (2017).**
24. Motegi, A., Murakawa, Y. & Takeda, S. The vital link between the ubiquitin–proteasome pathway and DNA repair: Impact on cancer therapy. *Cancer Lett.* 283, 1–9 (2009).
25. Tacconi, E. M. et al. BRCA 1 and BRCA 2 tumor suppressors protect against endogenous acetaldehyde toxicity. *EMBO Mol. Med.* 9, 1398–1414 (2017).
- 26.* Majera, D. et al. Targeting the NPL4 Adaptor of p97/VCP Segregase by Disulfiram as an Emerging Cancer Vulnerability Evokes Replication Stress and DNA Damage while Silencing the ATR Pathway. *Cells* 9, 469 (2020).**
- 27.* Majera, D. et al. Targeting genotoxic and proteotoxic stress-response pathways in human prostate cancer by clinically available PARP inhibitors, vorinostat and disulfiram. *The Prostate* 79, 352–362 (2019).**
28. Burhans, W. C. & Weinberger, M. DNA replication stress, genome instability and aging. *Nucleic Acids Res.* 35, 7545–7556 (2007).
29. Primo, L. M. F. & Teixeira, L. K. DNA replication stress: oncogenes in the spotlight. *Genet. Mol. Biol.* 43, e20190138 (2020).
- 30.* Vesela, E., Chroma, K., Turi, Z. & Mistrik, M. Common Chemical Inductors of Replication Stress: Focus on Cell-Based Studies. *Biomolecules* 7, 19 (2017).**
31. Glover, T. W., Berger, C., Coyle, J. & Echo, B. DNA polymerase alpha inhibition by aphidicolin induces gaps and breaks at common fragile sites in human chromosomes. *Hum. Genet.* 67, 136–142 (1984).
32. Miron, K., Golan-Lev, T., Dvir, R., Ben-David, E. & Kerem, B. Oncogenes create a unique landscape of fragile sites. *Nat. Commun.* 6, 7094 (2015).
- 33.* Beresova, L. et al. Role of DNA Repair Factor Xeroderma Pigmentosum Protein Group C in Response to Replication Stress As Revealed by DNA Fragile Site Affinity Chromatography and Quantitative Proteomics. *J. Proteome Res.* 15, 4505–4517 (2016).**
34. Bartkova, J. et al. Oncogene-induced senescence is part of the tumorigenesis barrier imposed by DNA damage checkpoints. *Nature* 444, 633–637 (2006).

35. Raffaele, M. et al. Nociceptin/orphanin FQ opioid receptor (NOP) selective ligand MCOPPB links anxiolytic and senolytic effects. *GeroScience* 44, 463–483 (2022).
36. Kirkland, J. L. & Tchkonian, T. Senolytic drugs: from discovery to translation. *J. Intern. Med.* 288, 518–536 (2020).
37. Bartkova, J. et al. Aberrations of the MRE11–RAD50–NBS1 DNA damage sensor complex in human breast cancer: MRE11 as a candidate familial cancer-predisposing gene. *Mol. Oncol.* 2, 296–316 (2008).
38. Löffler, H. et al. Cep63 Recruits Cdk1 to the Centrosome: Implications for Regulation of Mitotic Entry, Centrosome Amplification, and Genome Maintenance. *Cancer Res.* 71, 2129–2139 (2011).
39. Kurfurstova, D. et al. DNA damage signalling barrier, oxidative stress and treatment-relevant DNA repair factor alterations during progression of human prostate cancer. *Mol. Oncol.* 10, 879–894 (2016).
40. Vancurova, M. et al. PML nuclear bodies are recruited to persistent DNA damage lesions in an RNF168-53BP1 dependent manner and contribute to DNA repair. *DNA Repair* 78, 114–127 (2019).
41. Yamada, M. et al. ATR–Chk1–APC/C Cdh1 -dependent stabilization of Cdc7–ASK (Dbf4) kinase is required for DNA lesion bypass under replication stress. *Genes Dev.* 27, 2459–2472 (2013).
42. Fugger, K. et al. Human Fbh1 helicase contributes to genome maintenance via pro- and anti-recombinase activities. *J. Cell Biol.* 186, 655–663 (2009).
43. Kanu, N. et al. SETD2 loss-of-function promotes renal cancer branched evolution through replication stress and impaired DNA repair. *Oncogene* 34, 5699–5708 (2015).
44. Kumar, A. et al. ATR Mediates a Checkpoint at the Nuclear Envelope in Response to Mechanical Stress. *Cell* 158, 633–646 (2014).
- 45.* Kudlova, N. et al. An efficient, non-invasive approach for in-vivo sampling of hair follicles: design and applications in monitoring DNA damage and aging. *Aging* 13, 25004–25024 (2021).
- 46.* Skrott, Z. et al. Disulfiram’s anti-cancer activity reflects targeting NPL4, not inhibition of aldehyde dehydrogenase. *Oncogene* 38, 6711–6722 (2019).
47. Xu, G. et al. REV7 counteracts DNA double-strand break resection and affects PARP inhibition. *Nature* 521, 541–544 (2015).
48. Fugger, K. et al. FBH1 Catalyzes Regression of Stalled Replication Forks. *Cell Rep.* 10, 1749–1757 (2015).
- 49.* Chroma, K. et al. A drug repurposing strategy for overcoming human multiple myeloma resistance to standard-of-care treatment. *Cell Death Dis.* 13, 203 (2022).
50. Kanellis, D. C. et al. Actionable cancer vulnerability due to translational arrest, p53 aggregation and ribosome biogenesis stress evoked by the disulfiram metabolite CuET. *Cell Death Differ.* 30, 1666–1678 (2023).

51. Bekker-Jensen, S., Lukas, C., Melander, F., Bartek, J. & Lukas, J. Dynamic assembly and sustained retention of 53BP1 at the sites of DNA damage are controlled by Mdc1/NFBD1. *J. Cell Biol.* 170, 201–211 (2005).
- 52.* **Mistrik, M. et al. Cells and Stripes: A novel quantitative photo-manipulation technique. *Sci. Rep.* 6, 19567 (2016).**
- 53.* **Skrott, Z. et al. Alcohol-abuse drug disulfiram targets cancer via p97 segregase adaptor NPL4. *Nature* 552, 194–199 (2017).**
54. Govorov, A. O. & Richardson, H. H. Generating heat with metal nanoparticles. *Nano Today* 2, 30–38 (2007).
- 55.* **Mistrik, M. et al. Microthermal-induced subcellular-targeted protein damage in cells on plasmonic nanosilver-modified surfaces evokes a two-phase HSP-p97/VCP response. *Nat. Commun.* 12, 713 (2021).**
56. Lu, C., Li, X., Ren, Y. & Zhang, X. Disulfiram: a novel repurposed drug for cancer therapy. *Cancer Chemother. Pharmacol.* 87, 159–172 (2021).
57. Liu, P. et al. Disulfiram targets cancer stem-like cells and reverses resistance and cross-resistance in acquired paclitaxel-resistant triple-negative breast cancer cells. *Br. J. Cancer* 109, 1876–1885 (2013).
58. Wang, N. et al. Targeting ALDH2 with disulfiram/copper reverses the resistance of cancer cells to microtubule inhibitors. *Exp. Cell Res.* 362, 72–82 (2018).
59. Xu, B. et al. Disulfiram/copper complex activated JNK/c-jun pathway and sensitized cytotoxicity of doxorubicin in doxorubicin resistant leukemia HL60 cells. *Blood Cells. Mol. Dis.* 47, 264–269 (2011).
60. Song, C., Wang, Q., Song, C. & Rogers, T. J. Valosin-containing protein (VCP/p97) is capable of unfolding polyubiquitinated proteins through its ATPase domains. *Biochem. Biophys. Res. Commun.* 463, 453–457 (2015).
61. Hänzelmann, P. & Schindelin, H. Characterization of an Additional Binding Surface on the p97 N-Terminal Domain Involved in Bipartite Cofactor Interactions. *Structure* 24, 140–147 (2016).
62. Kilgas, S. & Ramadan, K. Inhibitors of the ATPase p97/VCP: From basic research to clinical applications. *Cell Chem. Biol.* 30, 3–21 (2023).
63. Bodnar, N. O. & Rapoport, T. A. Molecular Mechanism of Substrate Processing by the Cdc48 ATPase Complex. *Cell* 169, 722-735.e9 (2017).
64. Toledo-Guzmán, M. E., Hernández, M. I., Gómez-Gallegos, Á. A. & Ortiz-Sánchez, E. ALDH as a Stem Cell Marker in Solid Tumors. *Curr. Stem Cell Res. Ther.* 14, 375–388 (2019).
65. Koppaka, V. et al. Aldehyde Dehydrogenase Inhibitors: a Comprehensive Review of the Pharmacology, Mechanism of Action, Substrate Specificity, and Clinical Application. *Pharmacol. Rev.* 64, 520–539 (2012).
66. Ponti, G. et al. Hereditary breast and ovarian cancer: from genes to molecular targeted therapies. *Crit. Rev. Clin. Lab. Sci.* 60, 640–650 (2023).

67. Yoshida, K. & Miki, Y. Role of BRCA1 and BRCA2 as regulators of DNA repair, transcription, and cell cycle in response to DNA damage. *Cancer Sci.* 95, 866–871 (2004).
68. Noireterre, A. & Stutz, F. Cdc48/p97 segregase: Spotlight on DNA-protein crosslinks. *DNA Repair* 139, 103691 (2024).
69. Kröning, A., Van Den Boom, J., Kracht, M., Kueck, A. F. & Meyer, H. Ubiquitin-directed AAA+ ATPase p97/VCP unfolds stable proteins crosslinked to DNA for proteolysis by SPRTN. *J. Biol. Chem.* 298, 101976 (2022).
70. Yazinski, S. A. & Zou, L. Functions, Regulation, and Therapeutic Implications of the ATR Checkpoint Pathway. *Annu. Rev. Genet.* 50, 155–173 (2016).
71. Meraz-Torres, F., Plöger, S., Garbe, C., Niessner, H. & Sinnberg, T. Disulfiram as a Therapeutic Agent for Metastatic Malignant Melanoma—Old Myth or New Logos? *Cancers* 12, 3538 (2020).
72. Weiss, M. C. et al. A Coala-T-Cannabis Survey Study of breast cancer patients' use of cannabis before, during, and after treatment. *Cancer* 128, 160–168 (2022).
73. Hawley, P. & Gobbo, M. Cannabis Use in Cancer: A Survey of the Current State at BC Cancer before Recreational Legalization in Canada. *Curr. Oncol.* 26, 425–432 (2019).
74. Pergam, S. A. et al. Cannabis use among patients at a comprehensive cancer center in a state with legalized medicinal and recreational use. *Cancer* 123, 4488–4497 (2017).
- 75.* Buchtova, T. et al. Cannabidiol-induced activation of the metallothionein pathway impedes anticancer effects of disulfiram and its metabolite CuET. *Mol. Oncol.* 16, 1541–1554 (2022).**
- 76.* Buchtova, T. et al. Cannabis-derived products antagonize platinum drugs by altered cellular transport. *Biomed. Pharmacother.* 163, 114801 (2023).**
- 77.* Buchtova, T. et al. Drug–Drug Interactions of Cannabidiol with Standard-of-Care Chemotherapeutics. *Int. J. Mol. Sci.* 24, 2885 (2023).**
78. Milacic, V. et al. Pyrrolidine dithiocarbamate-zinc(II) and -copper(II) complexes induce apoptosis in tumor cells by inhibiting the proteasomal activity. *Toxicol. Appl. Pharmacol.* 231, 24–33 (2008).
79. Chen, D. Inhibition of prostate cancer cellular proteasome activity by a pyrrolidine dithiocarbamate-copper complex is associated with suppression of proliferation and induction of apoptosis. *Front. Biosci.* 10, 2932 (2005).
- 80.* Loffelmann, M. et al. Identification of novel dithiocarbamate-copper complexes targeting p97/NPL4 pathway in cancer cells. *Eur. J. Med. Chem.* 261, 115790 (2023).**

7. ATTACHMENTS 1-15



Review

Common Chemical Inductors of Replication Stress: Focus on Cell-Based Studies

Eva Vesela ^{1,2}, Katarina Chroma ¹, Zsofia Turi ¹ and Martin Mistrik ^{1,*}

¹ Institute of Molecular and Translational Medicine, Faculty of Medicine and Dentistry, Palacky University, Hnevotinska 5, Olomouc 779 00, Czech Republic; eva.vesela@upol.cz (E.V.); katarina.chroma@upol.cz (K.C.); zsofia.turi01@upol.cz (Z.T.)

² MRC Laboratory for Molecular Cell Biology, University College London, London WC1E 6BT, UK

* Correspondence: martin.mistrik@upol.cz; Tel.: +420-585-634-170

Academic Editor: Rob de Bruin

Received: 25 November 2016; Accepted: 10 February 2017; Published: 21 February 2017

Abstract: DNA replication is a highly demanding process regarding the energy and material supply and must be precisely regulated, involving multiple cellular feedbacks. The slowing down or stalling of DNA synthesis and/or replication forks is referred to as replication stress (RS). Owing to the complexity and requirements of replication, a plethora of factors may interfere and challenge the genome stability, cell survival or affect the whole organism. This review outlines chemical compounds that are known inducers of RS and commonly used in laboratory research. These compounds act on replication by direct interaction with DNA causing DNA crosslinks and bulky lesions (cisplatin), chemical interference with the metabolism of deoxyribonucleotide triphosphates (hydroxyurea), direct inhibition of the activity of replicative DNA polymerases (aphidicolin) and interference with enzymes dealing with topological DNA stress (camptothecin, etoposide). As a variety of mechanisms can induce RS, the responses of mammalian cells also vary. Here, we review the activity and mechanism of action of these compounds based on recent knowledge, accompanied by examples of induced phenotypes, cellular readouts and commonly used doses.

Keywords: replication stress; cisplatin; aphidicolin; hydroxyurea; camptothecin; etoposide; cancer

1. Introduction

The DNA molecule always has to keep the middle ground: it must be sufficiently rigid to maintain correct genetic information while at the same time available for ongoing processes. DNA is particularly vulnerable to insults during replication, a process where a copy of the genome is generated [1]. Replication must be tightly regulated because it is essential for genome integrity, and therefore the fate of a new cellular generation. Accurate coordination of several cellular pathways is needed to provide sufficient energy and material supply, precise timing and functional repair to overcome arising difficulties [1].

Transient slowing or disruption of replication fork (RF) progression is called replication stress (RS), which can be caused by a limitation of important factors and/or obstacles caused by intrinsic and extrinsic sources [2]. Intrinsic sources of RS involve the physiological properties of the DNA molecule, such as regions of heterochromatin structure, origin-poor regions or sites rich in some types of repetitive sequences [3–5]. Other intrinsic sources of RS are generated by deregulated pathways that cause over- and under-replication [6–8], re-replication (also known as re-duplication) [9,10], or by transcription and replication machinery collisions [9].

The most common extrinsic sources of RS are all wavelengths of ultraviolet radiation (UV) [11], ionising radiation (IR) [12] and special genotoxic chemical compounds [13] which are the main focus of this review. RS-inducing chemicals can cause a broad spectrum of DNA lesions. Alkylating

agents such as methyl-methane sulfonate (MMS) [14], temozolomide and dacarbazine [15] directly modify DNA by attaching an alkyl group that presents an obstacle to RF progression. Moreover, the bifunctional alkylating compounds (e.g., mustard gas) can cause the crosslinking of guanine nucleobases [16,17] that violate the DNA structure even further [18]. Typical crosslinking agents introduce covalent bonds between nucleotides located on the same strand (intrastrand crosslinks), like cisplatin, or opposite strands (interstrand crosslink), like mitomycin C, and psoralens [18]. Crosslinks make the strands unable to uncoil and/or separate and physically block RF progression [19]. Even a small amount of unrepaired crosslinks (approx. 100–500) is reported to be lethal to a mammalian cell [20]. Furthermore, single-strand DNA breaks (SSB) and double-strand DNA breaks (DSB) represent a specific problem for ongoing replication which is well manifested by increased sensitivity of replicating cells towards radiomimetic compounds (e.g., neocarzinostatin) [21]. Other compounds do not damage the DNA structure directly but rather interfere with replication-related enzymes. Aphidicolin, an inhibitor of replicative DNA polymerases leads to uncoupling of the replicon and generation of long stretches of single-stranded DNA (ssDNA) [22]. After hydroxyurea treatment, an inhibitor of ribonucleotide reductase (RNR), the metabolism of deoxyribonucleotide triphosphates (dNTPs) is disturbed, and subsequently, the RF progression is blocked [23]. Camptothecin and etoposide, inhibitors of topoisomerase I and topoisomerase II respectively, prevent DNA unwinding and halt relaxation of torsional stress [24,25]. The most common sources of RS are illustrated in Figure 1.

Several repair pathways are essential for rapid elimination of DNA distortions and lesions introduced by the action of RS inducing compounds [26]. Removal and replacement of single base damage (e.g., oxidised and alkylated bases), is performed by base excision repair (BER) [27]. More extensive damage affecting several adjacent bases is repaired by nucleotide excision repair pathway (NER). NER is essential for repair of UV-induced damage such as cyclobutane pyrimidine dimers, or pyrimidine-pyrimidone (6-4) photoproducts and also needed for crosslinks removal caused by for example cisplatin [28]. Single-strand break repair in higher eukaryotes rely on poly(ADP-Ribose) polymerase 1 (PARP1) and X-ray repair cross complementing 1 (XRCC1) dependent recognition of the lesion, followed by end processing and ligation [29]. Double-strand breaks (DSBs) are processed by either homologous recombination (HR), or non-homologous end-joining (NHEJ). HR is active predominantly in S and G2 phases using the sister chromatid as a template for repair with high fidelity [30]. NHEJ, considered as an error prone pathway, performs DSB repair in all cell cycle stages more rapidly by direct ligation of two unprocessed (or minimally processed) DNA ends [31].

All previously described specific structures and concomitant DNA lesions can challenge the progression of RF. If the RF encounters a lesion which the replicative polymerase is unable to process as a template, it becomes stalled [32]. Stalled RFs are vulnerable structures and may undergo spontaneous collapse which leads to DSBs and genomic instability (GI) [33,34]. To avoid the harmful consequences of stalled forks, several mechanisms—DNA damage tolerance pathways (DDT)—exist to bypass the lesions and enable fork restart. One well-described process of DDT is translesion synthesis (TLS). TLS promotes “polymerase switch” from the replicative polymerase to translesion polymerases, which are able to continue replication across the lesion. TLS polymerases possess low processivity and fidelity towards the template DNA strand. Therefore TLS is often referred to as the error-prone pathway of DDT [32,34–36]. Among the DNA lesions which block the progression of RFs, interstrand crosslinks (ICLs) belong to the most challenging to bypass [37]. Thus, a whole group of proteins called Fanconi anaemia (FA) proteins evolved to govern the bypass and the repair of ICLs. The FA network promotes the unhooking of the ICL by specific endonucleases, bypassing the lesion by TLS polymerases or the repair by HR [5–7]. Patients with a defect in the FA protein family suffer from premature ageing, show increased sensitivity to DNA crosslinking agents (e.g., cisplatin, mitomycin C) and predisposition to certain types of cancers due to increased GI [38–40]. Although the FA pathway is involved mainly in ICL repair, it contributes more generally to initial detection of RF arrest, processing and stabilisation of the forks and regulation of TLS [41,42].

DNA damage bypass can occur in an error-free manner through the activation of the other branch of DDT, called template switching (TS). The process utilises the newly synthesised strand of the sister duplex, using it as an undamaged template. TS can be promoted either by fork regression or by strand invasion mediated by HR [34,36,43,44]. RF restart can also be achieved by firing nearby dormant replication origins or by repriming events leaving behind lesion containing single-stranded DNA (ssDNA) gaps which are subsequently processed by DTT pathways [45–50]. Altogether, these processes ensure the rapid resumption of DNA synthesis, preventing prolonged fork stalling and the potentially deleterious effects of replication fork collapse. However, upon persisting RS, or non-functional RS response, the RF may fail to restart and collapse, most probably due to destabilised, dysfunctional or displaced components of replication machinery [1,50–54]. Prolonged stalled replication forks are targeted by endonucleases followed by recombination-based restart pathways [55,56].

Among the features of RS belong accumulation of long stretches of ssDNA [46,57], resulting from the uncoupled activity of DNA polymerase and progression of DNA helicase [58,59]. The persisting ssDNA is rapidly coated by replication protein A (RPA) that in turn generates the signal triggering the checkpoint response through activation of Ataxia telangiectasia Rad3-related (ATR) checkpoint kinase [60–63]. Once activated, ATR and its downstream target checkpoint kinase 1 (CHK1) help the cell to faithfully complete DNA replication upon RS [52,53,64]. In addition, ATR as the central RS response kinase contributes to the stabilisation and restart of the stalled forks even after the stress has been removed [65]. The ATR-CHK1 pathway is responsible for cell cycle inhibition, suppression of new origin firing, DNA repair and to the overall improvement of cell survival [62,66]. The role of Ataxia telangiectasia mutated (ATM), another important checkpoint kinase, upon RS conditions is not as clear and straightforward as of ATR. ATM is preferentially activated by DSBs which are generated in later stages after RS induction, mostly after the RF collapse [67,68]. There is suggested interplay between ATM and ATR during replication stress which becomes apparent under concomitant depletion of both kinases [68]. Interplay between ATM, Werner helicase (WRN) and Bloom helicase (BLM) is needed for the resolution of replication intermediates and HR repair pathway that is important for RF restart [69,70].

Chronic replication stress conditions, particularly in the absence of proper DNA repair pathway and/or non-functional checkpoint responses might result in the transfer of RS-related DNA alterations to daughter cells, inducing mutations, GI and fuelling tumourigenesis [1].

From this point of view, the RS is a strong pro-carcinogenic factor driving selective pressure for acquisition of mutations overcoming cell cycle arrest or apoptosis [71,72]. This further leads to the progression of malignant transformation and faster selection of mutations allowing development of resistance to cancer treatment [73].

However, cells typically react on the prolonged exposure to RS by triggering mechanisms leading to permanent cell cycle arrest known as cellular senescence or apoptosis [74,75] acting as a natural barrier against tumour progression [76].

Several hereditary syndromes are linked to enhanced RS and GI. The spectrum of exhibited symptoms is broad and includes premature ageing, growth retardation, neurodegeneration, immunodeficiency, cancer predisposition and others. The disorders like Seckel syndrome (deficiency in ATR kinase) [77], Ataxia telangiectasia caused (loss of ATM kinase) [78], Xeroderma pigmentosum (XP; various defects in XP protein family group) [79] are caused by aberrations in DNA damage recognition and repair enzymes [80]. Bloom and Werner syndrome (deficiency of BLM and WRN helicase, respectively) [81,82], Fanconi anaemia (FA; mutations in FA pathway proteins) [83,84], or Rothmund-Thomson syndrome (defects in RECQ like helicase 1 protein) [85,86] are related to failure of replication fork progression and restart.

In general, RS is a potent inducer of variety of hereditary and non-hereditary diseases, including the oncogenic transformation. The knowledge and understanding of the processes during RS are crucial for choosing the most efficient therapy. The in vitro-based cell studies involving models

of chemical induction of RS are unique source of information about molecular interactions and undergoing mechanisms. For this review five compounds were chosen, all of them are commonly used for cell-based experiments to induce RS. Several aspects are discussed in detail: mechanism of action aimed at replication interference, proper dosing and common experimental setups. A brief overview of the medical use and important practical hints for laboratory use are also included.

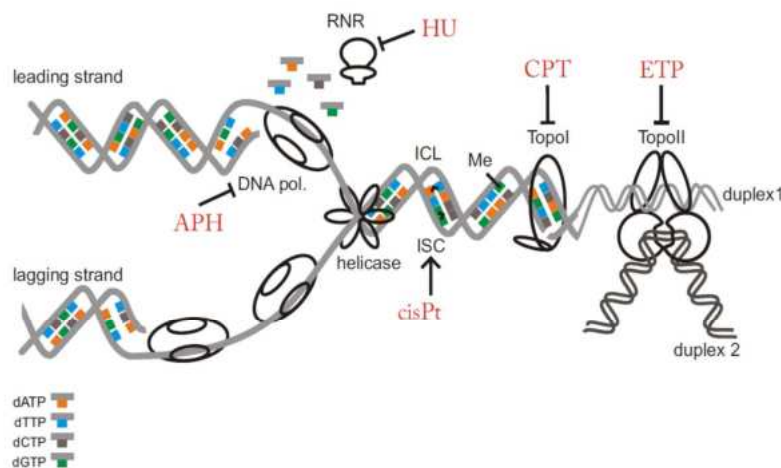


Figure 1. Schematic view of the most common lesions causing replication stress. In the scheme, several important replication stress (RS) inducing factors are illustrated: intra-strand crosslink (ISC), inter-strand crosslink (ICL), alkylated/modified base (Me) and inhibition of replication related enzymes. Compounds further described in the review are marked by red colour. RNR: ribonucleotide reductase; DNA pol.: DNA polymerase; TopoI: topoisomerase I; TopoII: topoisomerase II; APH: aphidicolin; HU: hydroxyurea; CPT: camptothecin; ETP: etoposide; cisPt: cisplatin; dATP: deoxyadenosine triphosphate; dTTP: deoxythymidine triphosphate; dCTP: deoxycytidine triphosphate; dGTP: deoxyguanine triphosphate.

2. Compounds

2.1. Cisplatin

Cisplatin (cisPt) is an inorganic platinum complex first synthesised by Italian chemist Michel Peyrone and originally known as ‘Peyrone’s chloride’ (Figure 2). The cytostatic activity of cisPt was first reported by Barnett Rosenberg and co-workers in 1965 following accidental discovery of *Escherichia coli* growth inhibition induced by the production of cisPt from platinum electrodes [87]. It is generally considered as a cytotoxic drug for treating cancer cells by damaging DNA and inhibiting DNA synthesis. cisPt is a neutral planar coordination complex of divalent platinum [88] with two labile chloride groups and two relatively inert amine ligands. The *cis* configuration is necessary for the antitumour activity [89], 3D structure of monofunctional cisPt bound to DNA structure can be found here [90].

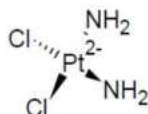


Figure 2. Cisplatin structure.

2.1.1. Mechanism of DNA Damage Induction

The cytotoxicity of cisPt is known to be due to the formation of DNA adducts, including intrastrand (96%) and interstrand (1%) DNA crosslinks, DNA monoadduct (2%) and DNA–protein

crosslinks (<1%) [91]. These structural DNA modifications block uncoiling and separation of DNA double-helix strands, events both necessary for DNA replication and transcription [92]. Inside a cell, cisPt forms an activated platinum complex, which triggers a nucleophilic substitution reaction via an attack on nucleophilic centres on purine bases of DNA, in particular, N7 positions of guanosine (65%) and adenosine residues (25%) [93]. The two reactive sites of cisPt enable the formation of the most critical crosslink between two adjacent guanines (1,2-d(GpG)), resulting in the formation of DNA intrastrand crosslinks [94]. Also, platinum can align to guanine bases on the opposite DNA strand, thus creating DNA interstrand crosslinks, present in lower percentage [95]. These cisPt crosslinks create severe local DNA lesions that are sensed by cellular proteins, inducing repair, replication bypass or triggering apoptosis [96]. Several protein families can recognise cisPt–DNA adducts, including nucleotide excision repair (NER) proteins [97], homology-directed repair proteins (HDR) [98], mismatch repair (MMR) proteins [99] and non-histone chromosomal high mobility group proteins 1 and 2 (HMG1 and HMG2) [100]. The intrastrand cisPt structural alteration stalls RNA polymerase II. It is recognised and efficiently repaired by global genome NER (GG-NER) or its transcription-coupled sub-pathway (TC-NER) [101]. The second DNA repair system predominantly involved in coping with cisPt–DNA adducts is error-free HDR, which removes DNA DSBs remaining after cisPt adduct removal [98]. In contrast to the previously mentioned repair pathways that increase cell viability, MMR proteins have been shown to be essential for cisPt-mediated cytotoxicity [99]. cisPt is reported to enhance interactions between MMR proteins MLH1/PMS2 (MutL homolog 1/PMS1 homolog 2, MMR component) and p73, triggering apoptosis [102]. Therefore, mutations in MMR genes are known to be associated with cisPt resistance [103]. HMG1 and HMG2 recognise intrastrand DNA adducts between adjacent guanines, affecting cell cycle events and subsequently inducing apoptosis [100].

In addition to the previously mentioned repair proteins, specialised translesion DNA polymerase eta (η) can be loaded onto sites of cisPt–DNA adducts promoting TLS repair pathway [104]. cisPt also induces dose-dependent reactive oxygen species (ROS), which are responsible for the severe side effects of platinum-based therapy, including nephrotoxicity and hepatotoxicity [105]. When overwhelming the reduction capacity of the cell, cisPt-induced ROS might lead to lipid peroxidation, oxidative DNA damage, altered signal transduction pathway and calcium homeostasis failure [105]. Extensive unrepaired cisPt-induced DNA damage can proceed to apoptotic cell death mediated by various signal transduction pathways, including calcium signalling [106], death receptor signalling [107] and activation of mitochondrial pathways [108]. At least two main pathways have been proposed to mediate cisPt-induced apoptosis *in vitro*. One involves the critical tumour suppressor protein p53 directly binding to cisPt-modified DNA [109] and promoting apoptosis via several mechanisms. p53 binds and counteracts the anti-apoptotic B-cell lymphoma-extra large (Bcl-xL) [110], contributes to inactivation of nutrient sensor AMP-kinase (AMPK) [111], activates caspase-6 and -7 [112] and the pro-apoptotic Bcl-2 family member PUMA α in renal tubular cells [113]. However, the role of p53 in response to cisPt seems to be controversial, as it has been described to contribute to cisPt cytotoxicity [114] and also to be involved in cisPt resistance in different cancer models [115]. The other cisPt-induced apoptotic pathway is mediated via a pro-apoptotic member of the p53 family, p73. cisPt has been shown to induce p73 in several cancer cell lines [116], which cooperates with the MMR system and c-Abl tyrosine kinase, known to be involved in DNA damage-induced apoptosis [117]. In response to cisPt, c-Abl phosphorylates p73, making it stable [118], and increases its pro-apoptotic function by binding transcription coactivator p300, which triggers transcription of pro-apoptotic genes [119]. Moreover, p73 forms a complex with c-Jun N-terminal kinase/stress-activated protein kinase (JNK), leading to cisPt-induced apoptosis [120]. Intrinsic signaling pathways involved in cisPt driven apoptosis include Akt [121], protein kinase C [122,123], and mitogen activated protein kinases—MAPK (e.g., extracellular signal-regulated kinases; ERK) [124–126], JNK [127–129] and p38 [130].

2.1.2. Other Effects

Besides DNA, the primary target of cisPt in cells, there is some evidence for the involvement of non-DNA targets in cisPt cytotoxicity [131]. cisPt interacts with phospholipids and phosphatidylserine

in membranes [132], disrupts the cytoskeleton and alters the polymerization of actin, probably due to conformational changes resulting from the formation of Pt-S bonds [133]. MicroRNAs (miR), which play a role in posttranscriptional gene silencing, have been shown to be involved in the modulation of cisPt resistance-related pathways in different cancer models. miR-378 was shown to reverse resistance to cisPt in lung adenocarcinoma cells [134], whereas miR-27a was shown to be upregulated in a multidrug resistant ovarian cancer cell line, contributing to cisPt resistance [135]. miR-21 increases the cisPt sensitivity of osteosarcoma-derived cells [136]. For references to particular studies using cisPt, refer to Table 1.

Table 1. Effects of various cisplatin treatments in vitro.

Concentration	Incubation Time	Observed Effect	Cell Line	Reference
300 μ M	2 h	increase in polyADP ribosylation	O-342 rat ovarian tumour cells	[137]
100 μ M	2 h before IR	sensitization to γ -radiation	hypoxic V-79 Chinese hamster cells	[138]
100 μ M	2 h	increase in polyADP ribosylation	CV-1 monkey cells	[139]
<20 μ g/mL (<66 μ M)	5 h	block of rRNA synthesis block of DNA replication	Hela	[140]
15 μ M	1 h	induction of SCE (sister chromatid exchange) decreased cell survival	6 primary human tumour cell culture	[141]
10–30 μ M	24 h, 48 h	induction of apoptosis	224 (melanoma cells) HCT116	[142]
10 μ M	24 h	increase in antiapoptotic Bcl-2 mRNA synthesis (regulated by PKC and Akt2)	KLE HEC-1-A Ishikawa MCF-7	[143]
2–10 μ M	72 h	induction of apoptosis	224 (melanoma cells) HCT116	[142]
5 μ M	24 h	increase in p53 stability activation of ATR increased p53(ser15) phosphorylation	A2780	[144]
5 μ M	24 h	activation of p21 activation of CHK2 increased p53(ser20) phosphorylation	HCT116	[144]
5 μ M	24 h	induction of mitochondrial reactive oxygen species (ROS) response	A549 PC3 MEF	[143]
2 μ M	24 h	G2/M arrest, subapoptotic damage	MSC	[145]
>2 μ M	24 h	decreased proliferation rate induction of apoptosis	TGCT H12.1 TGCT 2102EP	[145]
1–4 μ g/mL	2 h	block of DNA synthesis block of transcription G2 arrest apoptosis	L1210/0 cells	[146]
2 μ g/mL	48 h 144 h, 168 h	inhibition of mtDNA replication inhibition of mitochondrial genes transcription	Dorsal root ganglion (DRG) sensory neurons	[147]
1 μ g/mL	2 h	transient G2 arrest	Hela	[148]
3.0 μ M	4 h before	block of NHEJ	A2780	[138]
0.2–0.8 μ M	IR 0.5 Gy 4 h	cisPt-IR synergistic interaction	MO59J MO59K	[138]
1–2.5 μ M	24 h–48 h	block of DNA replication followed by cell apoptosis	Hela	[149]
0.3–1 μ M	overnight	inhibition of RNA polymerase II-dependent transcription	Hela XPF	[144]
0.6 μ M	2 h	90% reduction in clonogenic capacity detected after 7 days CHK1 phosphorylation causing CHK1 dependent S phase arrest	Hela	[148]
0.5 μ M	24 h 48 h	loss of telomeres (TEL), or TEL repeats cell death	Hela	[139]

ATR: Ataxia telangiectasia Rad3-related; Bcl: B-cell lymphoma; CHK1: checkpoint kinase 1; CHK2: checkpoint kinase 2; IR: ionizing radiation; mtDNA: mitochondrial DNA; NHEJ: non-homologous end-joining; PKC: protein kinase C; polyADP: poly adenosine diphosphate; rRNA: ribosomal RNA.

2.1.3. Solubility

cisPt (molecular weight (MW) 300.05 g/mol) is water soluble at 2530 mg/L (at 25 °C), saline solution with a high chloride concentration (approx. 154 mmol/L) is recommended. In the absence of chloride, the cisPt chloride leaving group becomes aquated, replacing the chloride ligand with water and generating a mixture of species with increased reactivity and altered cytotoxicity [150,151]. Commonly used solutions for laboratory use are aqueous-based solutions in 0.9% NaCl (0.5 mg/mL), pH 3.5–5. Dissolved cisPt may degrade over a short time, the storage of aliquots is not recommended. However, the stability at –20 °C in the dark is reported to be 14 days. Solutions (in 2 mM phosphate buffered saline buffer with chloride concentration 140 mmol/L) stored at 4 °C should be stable for 7–14 days [152]. Undiluted cisPt is stable in the dark at 2–8 °C for several months [121,153]. Dimethyl sulfoxide (DMSO) can also be used for cisPt dilution, however it is not recommended. The nucleophilic sulphur can displace cisPt ligands, affecting the stability and reducing cisPt cytotoxicity [154]. DMSO introduced in combination studies with cisPt does not affect its activity [152].

2.1.4. Medical Use

Following the start of clinical trials in 1971, cisPt, marketed as Platinol (Bristol-Myers Squibb, New York, USA), was approved for use in ovarian and testicular cancer by the Food and Drug Administration (FDA) in 1979 [155]. cisPt is considered one of the most commonly used chemotherapy drugs for treating a wide range of malignancies, including head and neck, bladder, oesophageal, gastric and small cell lung cancer [156,157]. Moreover, cisPt has been shown to treat Hodgkin's [158] and non-Hodgkin's lymphomas [159], neuroblastoma [160], sarcomas [161], multiple myelomas [162], melanoma [163], and mesothelioma [164]. cisPt can reach concentrations of up to 10 µg/mL in human plasma [165]. cisPt is administered either as a single agent or, in the main cases, in combination with other cytostatics (e.g., bleomycin, vinblastine, cyclophosphamide) or radiotherapy for the treatment of a variety of tumours, e.g., cervical carcinoma [153]. The most important reported side effect is nephrotoxicity, due to preferential accumulation and persistence of cisPt in the kidney [166], later ototoxicity and bone marrow depression. Pharmacokinetic and pharmacodynamic studies have shown that a maximal steady state cisPt plasma concentration of between 1.5 and 2 µg/mL has the most effective chemotherapeutic effect with minimal adverse nephrotoxicity [167]. Many cancers initially responding to cisPt treatment could become later resistant. Mechanisms involved in the development of cisPt resistance include changes in cellular uptake, drug efflux, drug inactivation by increased levels of cellular thiols, processing of cisPt-induced damage by increased NER and decreased MMR activity and inhibition of apoptosis [99,168]. To boost platinum drug cytotoxicity, overcome its resistance and achieve a synergistic effect, new platinum-based drugs, as well as their combinatorial therapy with other antineoplastic agents were developed for cancer treatment [169]. Besides of cisPt derivatives as carboplatin and oxaliplatin, are currently being used in the clinical practice, while nedaplatin, lobaplatin and nedaplatin acquired limited approval in clinical use [170,171]. Recent discoveries described the combination of cisPt with PARP inhibitor olaparib targeting DNA repair to acts synergistically in several non-small cell lung carcinoma cell lines [172]. This combinatorial therapy can be promising especially in patients with advanced breast and ovarian cancer-bearing BRCA1/2 (breast cancer 1/2) mutations [173].

2.1.5. Summary

cisPt is used *in vitro* in concentration range approx. 0.5–300 µM. The levels in human plasma can reach up to 10 µg/mL (33 µM) which should be beared in mind when interpreting *in vitro* data. Continuous treatment, or longer incubation time, or high cisPt concentration of 20 mg/mL lead to complete inhibition of DNA synthesis [174]. The concentration range of 15–30 µM results in a block of DNA replication and transcription and triggers DNA damage response (DDR) signalization

through ATM-CHEK2, ATR-CHEK1 DDR pathways resulting in p53-p21 driven cell cycle arrest or p53-mediated cell apoptosis [141–144]. However, in some cell lines also the synthesis of anti-apoptotic protein Bcl-2 was reported [143]. cisPt is in the majority of cell lines induces apoptosis above the concentration of approx. 2 μM [139,141,142,146]. cisPt block DNA replication [139,140,146] and inhibits RNA synthesis [140,175,176] and also influences the mitochondrial DNA synthesis and metabolism [147]. As a commonly used drug in clinics, many in vitro experiments have been conducted to address problems arising during treatment. Especially, the study of mechanisms underlying drug resistance [177], causes of toxic side effects [178], enhancement of synergistic effects [179] and ways how to improve drug delivery systems [180]. cisPt massively triggers the TLS repair pathways; defective FA proteins sensitise the cells towards this compound [181], defective MMR proteins establish cisPt resistance [103,182].

2.2. Aphidicolin

Aphidicolin (APH) is a tetracyclin diterpenoid antibiotic isolated from *Nigrospora sphaerica* (Figure 3) which interferes with DNA replication by inhibiting DNA polymerases α , ϵ and δ [183]. Specifically, only cells in S phase are affected, whereas cells in other phases of the cell cycle are left to continue until the G1/S checkpoint, where they accumulate [184].

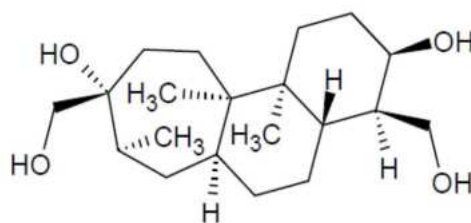


Figure 3. Aphidicolin structure.

2.2.1. Mechanism of DNA Damage Induction

APH binds to the active site of DNA polymerase α and rotates the template guanine, selectively blocking deoxycytidine triphosphate (dCTP) incorporation [185]. DNA polymerase α interacts with APH by its C18-binding OH group, APH forms a transient complex with polymerase and DNA [183]. The effect of APH on cell cultures is reversible if the cells are treated for no longer than 2 generations [186]. The exonuclease activity of APH-responding polymerases is only mildly affected, even at concentrations completely blocking the polymerase activity [183]. However, in the cell nucleus, the exonuclease activity is usually not retained because ternary complex APH–polymerase–DNA is formed and blocks the enzyme [183]; 3D structure of the complex can be found here [187].

Mechanistically, APH compromises the function of DNA polymerase, while helicase proceeds regularly (so called uncoupled/disconnected replicon), which leads to the generation of long stretches of single-stranded DNA [188]. The disconnected replicon is vulnerable structure prone for breakage preferentially at the so-called common fragile sites (CFSs) (also referred to as CFS expression) [189]. CFSs are specific genomic loci conserved in mammals generally prone to instability upon RS [190]. CFS expression is also common in precancerous and cancerous lesions [76]. Moreover, a causative role of CFS's in cancer development has been suggested [191]. APH reproducibly causes damage at the same sites, and thus low doses of APH are used to define APH-inducible CFSs, of which there are over 80 described in the human genome [22,192]. Other CFS inducers (hydroxyurea, camptothecin, hypoxia and folate deficiency) are not so specific, nor efficient as APH [193,194]. Importantly, APH efficiently induces CFS expression only when the rate of polymerase is slowed down but not completely blocked. The optimum concentration range usually spans 0.1–1 μM [195] (and refer to Table 2). Apart from disconnected replicon, there might be other explanations for the extraordinary potency of APH to induce CFS-associated genomic instability. First, APH has been shown to increase

the number of R-loops within certain CFSs, thus inducing replication/transcription collisions [196]. However, the mechanistic relationship between APH and increased R-loop formation is not clear. Second, re-licensing of replication origins is typical feature of oncogenic genetic backgrounds which are very prone to CFS expression. In such situations the CFS expression is explained as a result of DNA re-replication and subsequent collision of re-replicating forks within CFSs [10,197]. This phenomenon was studied in detail in yeasts at replication slow zones (analogous to CFSs in mammals) [198]. It is not clear whether the same re-licensing process is induced also by APH, however re-duplication would explain the reported APH-induced amplifications [191,199].

Prolonged treatment with low doses of APH induces cellular senescence response [74]. Interestingly, the most efficient doses were found to span the same range as doses used for CFS expression, which implies that CFSs might play a causative role in this process. Moreover, oncogene-induced senescence also displays increased CFSs-associated instability [10,197]. These phenotypical similarities between oncogenic stress and low doses of APH make this drug a good candidate for studying cellular processes in early stages of malignant transformation.

2.2.2. Other Effects

APH is a very specific DNA polymerase inhibitor, APH does not interact with mitochondrial DNA polymerases [186] nor proteins [200], DNA, RNA, metabolic intermediates, nor nucleic acid precursor synthesis [184,200,201]. Contradictory results have been obtained regarding the effect of APH on DNA repair synthesis (DRS). According to a radiography method, APH does not influence DRS [200], although when DRS was induced by tumor necrosis factor (TNF) or UV irradiation, APH was observed to inhibit the process [202,203]. For references to particular studies using APH, refer to Table 2.

Table 2. Effects of various aphidicolin treatments in vitro.

Concentration	Incubation Time	Observed Effect	Cell Line	Reference
0.2 mM	16 h, 10 h	formation of anaphase bridges and micronuclei	HeLa	[204]
30 μ M	6 h	stalled replication forks	HCT116	[205]
30 μ M	6 h	stalled replication forks	PD20 cells Bloom syndrome cells	[206]
5 μ g/mL (14.3 μ M)	4 h	DNA repair synthesis inhibition sensitization towards TNF treatment	L929 ovarian cancer cells A2780	[202]
5 μ g/mL (14.3 μ M)	2–8 h	S phase arrest kinetics and mechanism study	RKO 293T MEF	[207]
2.5 μ g/mL (7.15 μ M)	1 h	inhibition of DNA synthesis and DNA repair	Normal and XPA deficient human fibroblasts	[203]
10 μ M	15 h	cell cycle synchronisation at the G1/S boundary	REF-52 HeLa	[208]
5–25 μ M	24 h	inhibition of replicative polymerases	Werner syndrome cells Bloom syndrome cells	[209,210]
1 μ M	1–24 h	CFS induction	HEK293T	[210]
1 μ M	24 h	CFS induction	MEF HeLa	[211]
0.5 μ M	2 h	transient attenuation of DNA synthesis,	DT40	[212]
0.1 μ M	24 h	study of chromosome integrity and replication		
0.4 μ M	24 h	CFS induction	U-2 OS	[213]
0.1 μ M 0.2 μ M	16 h	replication stress observed on telomeres	hESC (UCSF4)	[214]
0.2 μ M	2 weeks	irreversible senescence induction	REF-52	[74]
0.2 μ M	24 h	CFS induction	BJ-hTERT	[215]
0.05 μ M 0.4 μ M	24 h	CFS induction	Werner syndrome fibroblasts AG11395 cells	[216]

Table 2. Cont.

Concentration	Incubation Time	Observed Effect	Cell Line	Reference
0.3 μ M	48 h	increased incidence of mitotic extra chromosomes replication stress	V79 hamster cell lines	[217]
0.3 μ M	72 h	replication stress	Human fibroblasts HGMDFN090	[199]
2 μ g/mL	not indicated	replication block	BJ BJ-tert HMEC	[197]
0.2 μ M	7–24 h	cell synchronization	HeLa	[184]

CFS: common fragile site; TNF: tumour necrosis factor.

2.2.3. Solubility

APH (MW 338.48 g/mol) is soluble in DMSO (up to 10 mg/mL), ethanol (up to 1 mg/mL) and methanol (freely), not soluble in water. The stability of the powder is 3 years at 2–8 °C, ethanol solution for a week at 2–8 °C, DMSO solution for 6 weeks at –20 °C [218].

2.2.4. Medical Use

APH has limited use in clinical practice owing to its low solubility. Only APH-glycinate has so far been tested in clinical trial phase I. However, fast clearance from human plasma (no drug observed after 6–8 h of APH administration) and no anti-tumour activity was observed. Its use as a single agent or even in combination with other cytostatics is no longer being considered [219]. APH is metabolised by cytochrome P-450 dependent degradation [220]. APH and its derivatives are considered as potential therapeutics for parasitic diseases, e.g., Chagas disease [221].

2.2.5. Summary

APH is used for in vitro studies in concentration range approx. 0.01 μ M to 0.2 mM. APH is mainly used for cell-based experiments involving CFS expression [222], cell cycle synchronization [223], replication fork stability and restart studies [224] and for cellular senescence induction [74]. The threshold between replication fork stalling and slowing down is around 1 μ M. Upon higher concentrations (5 μ M–0.2 mM) APH was reported to stall the DNA polymerase, leading to S phase arrest. Upon lower concentrations, when the DNA polymerases are just slowed down, CFS expression can be observed. Usually, longer incubation times (approx. one population doubling) are used, so more cells within the population are affected. APH treatment causes a significant amount of DNA damage, leading to rapid ATR kinase activation. In the case of longer APH treatment also ATM is activated probably as a consequence of DSB formed within the stalled replication forks [207]. Prolonged APH incubation in the range of days up to weeks at low concentrations (0.2–1 μ M) induces cellular senescence [74].

2.3. Hydroxyurea

Hydroxyurea (HU) was first synthesised in the 19th century (Figure 4) and inhibits the incorporation of nucleotides by interfering with the enzyme ribonucleotide reductase (RNR) [225]. RNR converts nucleotide di- and tri-phosphates to deoxynucleotide di- and tri-phosphates, which is the rate-limiting step in nucleotide synthesis [226]. Without proper levels of dNTPs, DNA cannot be correctly replicated nor repaired [227].

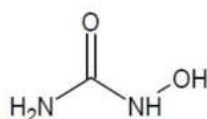


Figure 4. Hydroxyurea structure.

2.3.1. Mechanism of DNA Damage Induction

RNR is a large tetrameric enzyme comprising two R1 subunits and two small regulatory subunits R2 [228]. HU scavenges the tyrosyl radical of the R2 subunit which inactivates the RNR enzymatic activity [226]. Complete inhibition of RNR has been observed within 10 min after treatment with 0.1 mM HU and within 5 min after 3 mM of HU in murine 3T6 cells [229]. Consequently DNA synthesis is inhibited, selectively stopping the cells in S phase [230]. The inhibition is caused alterations in the dNTP pools. Each type of dNTP is affected in a different way. For example, after 280–560 μ M HU treatment for 60 min, the dTTP pool was found to increase by 50%, whereas the dCTP pool is decreased by 50% [231]. HU slows down the initiation of replication and also the progression of replication forks. Moreover, after stopping the production of dNTPs, DNA repair and mitochondrial DNA synthesis are affected in all cells, regardless of the cell cycle stage [227]. HU treatment greatly affects the choice of replication origins and origin spacing in mammalian cells [232]. Although the mechanism of DNA damage induction may look similar to that for APH, HU induces a different spectrum of fragile sites, called early replicating fragile sites (ERFs) [233]. ERFs are also induced by c-Myc expression [11,12]. It was also reported that 10 μ g/mL APH [234] (concentration that stalls the replication fork progression) leads to the generation of several kilobases long unwound DNA; however, HU treatment can generate only up to 100–200 nt long ssDNA [235].

2.3.2. Other Effects

HU induces copy number variants (CNVs) with similar frequency and size distribution as APH [236]. It was reported for yeast cells, that HU alters Fe–S centres, enzyme cofactors catalysing oxidation-reduction reactions, which interferes with various metabolic enzymes and affects the redox balance of cells. Similar mechanism is proposed also for mammalian cells [237].

HU has been negatively tested for mutagenicity, measured by single nucleotide variation (SNV) and insertion/deletion frequency [238]. On the other hand, low doses of HU have been reported to induce DNA damage [239]. Therefore, it is possible that the compound possesses some pro-mutagenic potential (see also below). For references to particular studies using HU, refer to Table 3.

Table 3. Effects of various hydroxyurea treatments in vitro.

Concentration	Incubation Time	Effect	Cell Line	Reference
200 mM	2 h	replication block	yeast cells	[240]
10–200 mM	3 h	replication block replication fork (RF) restart	yeast cells	[241]
5 mM	1 h	replication block	HEK293	[242]
2 mM	3 h	replication block		
50 μ M–5 mM	40 min–2 h	replication stress	293T mouse ES cells	[243]
2 mM	1 h, 24 h	replication stress replication block	HCC1937 MCF7	[244]
2 mM	16 h	replication block	HEK293	[245]
2 mM	24 h	DNA damage induction during S phase	U-2 OS 293T	[246]
2 mM	15 h	replication block cell cycle synchronisation at the G1/S boundary	REF-52 HeLa	[208]
2 mM	5 h	dNTP depletion	REF52	[74]
2 mM	3 h	chromosomal aberrations FANCD2 pathway involvement	lymphoblastoid cell lines	[247]
1 mM	overnight	replication block	MCF7	[248]
0.5 mM	5 h–10 h	replication block	U-2OS	[249]
2 mM	2 h–24 h	replication block		
0.5 mM	90 min	nucleotides depletion stalled RF w/o DSBs formation	MEF	[250]

Table 3. Cont.

Concentration	Incubation Time	Effect	Cell Line	Reference
0.1–0.5 mM	2 h–72 h	γ -globin gene expression	K562	[251]
0.1–0.5 mM	2 h–8 h	replication stress	PC3	[252]
0.2–0.4 mM	4 days	cell differentiation ERK signalling pathway inhibition p38 signal transduction activation	K562	[253]
0.3 mM	10 days	microsatellite instability upon FANCD2 depletion	GM08402 HeLa PD20F	[254]
0.15–0.2 mM	2 weeks	irreversible senescence induction	REF-52	[74]
0.2 mM	2 h–7 h	replication stress	MEF	[255]
0.15 mM	2 h	p53 activation	REF52	[74]
50–200 μ M	20 h	HIF1 induction eNOS induction	HUVEC	[256]
25–200 μ M	72 h	induction of apoptosis	AML cell lines (MV4-11, OCI-AML3, MOLM-13, and HL-60)	[257]
5 μ M–0.5 mM	48 h	replication stress	V79 hamster cells	[217]
2 μ M	12 h	replication stress	H1299	[258]

dNTP: deoxynucleotide triphosphate; DSBs: double-strand breaks; eNOS: endothelial nitric oxide synthase; ERK: extracellular signal-regulated kinases; FANCD2: Fanconi anaemia complementation group D2; FANCD1: Fanconi anaemia complementation group 1; HIF: hypoxia induced factor 1.

2.3.3. Solubility

HU (MW 76.05 g/mol) is freely soluble in water at 100 mg/mL, soluble also in DMSO. The powder is stable at 4 °C for 12 months. Solutions are stable for 1 month at –20 °C (after defrosting, equilibration is recommended for 1 h at room temperature). It is recommended to prepare fresh solutions before use. HU decomposes in the presence of moisture; therefore, it is recommended that it is stored in air-tight containers in a dry atmosphere [259].

2.3.4. Medical Use

HU is a commonly used medicine first approved by the FDA for the treatment of neoplastic disorders in the 1960s [260]. Common plasma levels of HU range 100–200 μ M [261]. It is used for the treatment of sickle cell disease, essential thrombocytosis [262], myeloproliferative disorders and psoriasis [260] and is commonly indicated as a cytoreductive treatment in polycythemia vera [263] and others. Synergistic effects have been reported when it is used in combination with antiretroviral pills [264] and also in indicated cases with radiotherapy [265]. HU may be used as an anti-retroviral agent, especially in HIV (human immunodeficiency virus) patients. HU may cause myelofibrosis development with increased time of use and AML/MDS syndrome (acute myeloid leukaemia/myelodysplastic syndrome) [266]. Adverse side-effects have been observed, mainly myelosuppression [267]. A 17-year follow-up study of 299 patients treated with HU as a long-term therapy showed no difference in the incidence of complications such as stroke, renal disease, hepatic disease, malignancy or sepsis [268], suggesting that HU is well-tolerated. However, CNVs are generated at therapeutic doses of HU, and data from reproductive studies and studies on subsequent generations have so far been rather limited [236,268].

2.3.5. Summary

HU is used in vitro approx. in the range 2 mM–5 mM. The most commonly used concentrations are around 2 mM. HU is used for cell cycle synchronization [269], replication fork stability studies [249,252], studies of recovery mechanisms after the release of RS [242] and checkpoint responses [241]. Lower concentrations are used for RS induction [254], induction of senescence [74], apoptosis [257],

and repair pathways induction [217]. HU reaches plasma concentrations around 0.1 mM; this should be bear in mind when interpreting the data for clinical relevance [261]. The MRN (Mre11-Rad50-Nbs1) complex members Mre11 (Meiotic recombination 11) and Nbs1 (Nijmegen breakage syndrome 1) are required for efficient recovery of replication after treatment with replication stalling agents such as hydroxyurea [12]. HU causes rapid generation of ssDNA as indicated by RPA loading 40 min after treatment [270]. Subsequently, ATR-CCHK1 signalling is activated, and HR repair pathway is induced.

Cells deficient in XRCC2 or other homologous recombination components exhibit hypersensitivity to HU [271]. It was reported that for hamster V79 cells, low concentrations of HU (5–10 μ M) mimics the replication dynamics of untreated HR deficient cells [217]. Cellular senescence after long term replication stress caused by HU is dependent on p53-p21 signalling pathway and independent of p16 [74]. HU influences multiple cellular pathways, e.g., JNK pathway, mitochondrial and peroxisome biogenesis, expression of several heat shock response proteins, autophagy pathways stimulation (beclin-1 expression), hemoglobin type F induction (in sickle cell disease, β -thalassemia patients), etc. [272]. There are several cell lines that respond to HU treatment in a specific manner, e.g., K562 cell line undergoes differentiation [253], T-cells activation is decreased [264], the morphology of vascular endothelial cells is affected [273].

2.4. Camptothecin

Camptothecin (CPT) is a pentacyclic quinoline alkaloid first isolated from the Chinese tree *Camptotheca acuminata* (Nyssaceae) by Wall et al. [274] (Figure 5). CPT has a unique intracellular target, topoisomerase I (TopoI), a nuclear enzyme that reduces the torsional stress of supercoiled DNA [24]. This activity enables specific regions of DNA to become sufficiently exposed and relaxed to facilitate essential cellular processes, such as DNA replication, recombination and transcription [275].

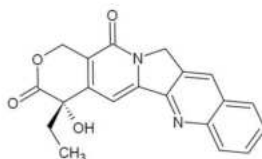


Figure 5. Camptothecin structure.

2.4.1. Mechanism of DNA damage induction

TopoI binds covalently to double-stranded DNA through a reversible transesterification reaction, generating a SSB [276], 3D structure can be found here [277]. This so-called TopoI–DNA cleavage complex (Top1cc) facilitates the relaxation of torsional strain in supercoiled DNA, either by allowing passage of the intact single strand through the nick or by free rotation of the DNA around the uncleaved strand [278]. CPT covalently and reversibly stabilises the normally transient DNA Top1cc by inhibiting religation of the scissile strand, thereby prolonging the half-life of Top1cc and increasing the number of DNA SSBs [279,280]. Moreover, trapping of the enzyme on the DNA leads to rapid depletion of the TopoI pool [281]. The effect of CPT is readily reversible after removal of the drug. However, prolonged stabilisation of Top1cc can cause multiple problems. Firstly, failure to relieve supercoiling generated by such processes as transcription and replication can lead to RS by creating torsional strain within the DNA [279,281,282]. Furthermore, the collision of the RF with the ternary drug-enzyme-DNA complex generates DSBs with serious cellular consequences, including cell death [283,284].

Because ongoing DNA synthesis is important for CPT-induced cytotoxicity, CPT is considered an S phase-specific drug. The repair of CPT-induced DSBs involves multiple DNA damage repair proteins. Recent studies have highlighted that functional cooperation between BRCA2, FANCD2, RAD18 and RAD51 proteins are essential for repair of replication-associated DSBs through HR. Loss of any of these proteins causes disruption of HR repair, chromosomal aberrations and sensitization of cells to

CPT [285]. A close link between CPT and HR has also been demonstrated in experiments measuring sister chromatid exchange events (SCEs), which are common consequence of elevated HR repair process and found to be induced by low doses of CPT [270]. CPT is applied in early S phase cells for triggering G2 arrest accompanied by blockage of the p34cdc2/cyclin B complex, a consequence of either DNA breakage, the arrest of the replication fork or both [286]. In addition, CPT driven TopoI–DNA cleavable complex and associated strand breaks were shown to increase transcription of the c-Jun early response gene, which occurs in association with internucleosomal DNA fragmentation, a characteristic mark of apoptosis [287]. Noncytotoxic concentrations of CPT can induce the differentiation of human leukaemia cells [288], and an antiangiogenic effect is suggested [289,290]. Interestingly, when used in combined treatment with APH, CPT reduces the APH-induced RPA (an indicator of ssDNA) signal and has a rescuing effect on CFS expression [291]. For references to particular studies using CPT, refer to Table 4.

Table 4. Effects of various camptothecin treatments in vitro.

Concentration	Incubation Time	Observed Effect	Cell Line	Reference
20 μ M	30 min	DNA fragmentation in G1 and S phase cells	Hela	[292]
10 μ M	24 h	increase in cell sensitivity to TRAIL-mediated apoptosis	Hep3B	[293]
10 μ M	4 h	formation of replication mediated DNA DSBs	HT29	[294]
5 μ M	60 min	inhibition of RNA synthesis	CSA	[295]
1 μ M	60 min	inhibition of DNA synthesis	CSB	[296]
1 μ M	60 min	replication block DSB formation cell death	U2OS	[297]
1 μ M	60 min	formation of stabilised TopoI-cc complex DSB formation phosphorylation of CHK1 (S317) CHK2 (T68), RPA (S4/S8)	HCT116	[294]
1 μ M	60 min	inhibition of DNA replication suggested DNA DSB formation	L1210 mouse lymphoblastic leukaemic cells	[293]
200 nM–1 μ M	50 min	DSB formation	CSB	[298]
100 nM–10 nM	60 min	DSB formation	HCT116	[299]
25 nM	60 min	checkpoint activation (ATM-CHK2, ATR-CHK1) replication fork stalling replication fork reversal formation of specific DNA structures	U-2O-S	[300]
10 nM–100 nM	60 min	inhibition of EIAV (equine infectious anemia virus) replication	CF2Th	[295]
10 nM–20 nM	60 min	inhibition of HIV-1 replication block of viral protein expression	H9	[281]
6 nM	6 h	accumulation of cells in early S phase	Normal lymphocytes	[296]
	24 h	apoptosis, DNA fragmentation	MOLT-4	
6.25 nM	48 h	specific suppression of oral cancer cells growth	KB oral cancer cells	[281]
2.5 nM	48 h	increase in SCE upon depletion of Fbh1 helicase	BJ	[281]

ATM: Ataxia telangiectasia mutated; HIV: Human immunodeficiency virus; RPA: replication protein A; SCE: sister chromatid exchange; TopoI-cc: Topoisomerase I cleavage complex; TRAIL: TNF alpha related apoptosis inducing ligand, TNF: tumour necrosis factor.

2.4.2. Solubility

CPT (MW 348.35 g/mol) is soluble in DMSO (up to 10 mg/mL), methanol (40 mg/mL), 0.1 N sodium hydroxide (50 mg/mL) or acetic acid, insoluble in water. At higher concentrations, heating is required to dissolve the product completely (approx. 10 min at 95 °C), but some precipitation occurs upon cooling to room temperature [301].

2.4.3. Medical Use

CPT cannot be used in clinical practice because of its poor solubility in aqueous solutions, instability and toxicity, but modifications at selected sites have improved the pharmacologic and activity profile [283]. Currently, three water-soluble CPT-derivates, i.e., irinotecan (CPT-11), topotecan (TPT) and belotecan (CKD-602), are available for cancer therapy. However, despite their selectivity for TopoI and unique mechanism of action, they all have critical limitations. In particular, they become inactivated against TopoI within minutes at physiological pH due to spontaneous lactone E-ring opening [302] and diffuse rapidly from the TopoI–DNA cleavage complex due to their noncovalent binding. To overcome these problems, five-membered E-ring CPT-keto non-lactone analogues S38809 and S39625 have been synthesised and selected for advanced preclinical development based on their promising activity in tumour models. Their chemical stability and ability to produce high levels of persistent TopoIcc makes them useful candidates for future treatment [303].

2.4.4. Summary

Camptothecin is used in concentration range 2.5 nM up to 20 μ M. CPT is a potent DSBs inducer in a wide concentration range, approx. 10 nM–10 μ M. Upon higher concentration (20 μ M–10 μ M), CPT was reported to be cytotoxic, increasing cell apoptosis via DNA fragmentation predominantly in S phase cells with ongoing DNA synthesis [292,293]. The most frequently used concentration of 1 μ M CPT was shown to block DNA synthesis and induce DSBs resulting from the collision of RF due to prolonged stabilisation of TopoI DNA cleavage complex. The main implication of lower CPT concentrations is the induction of replication fork slowing and reversal, as a rapid response to TopoI inhibition is the increase in topological stress of DNA locally [300]. CPT activates predominantly ATR–CHK1 and ATM–CHK2 signalling, and leading to G2 checkpoint arrest [300]. Even at low doses of CPT HR repair pathway is triggered.

2.5. Etoposide

Etoposide (ETP) is a derivative of podophyllotoxin first synthesised in 1966 and approved for treatment as an antineoplastic agent in 1983 [304]. ETP structure comprises of polycyclic A–D rings, an E-ring and aglycone core (Figure 6). ETP compromises the proper function of the enzyme topoisomerase II (TopoII), 3D structure can be found here [305]. TopoII performs cleavage of both strands of a DNA duplex and enables passage of a second intact duplex through the transient break, ATP is used to power the strand transition [306]. As a result, relaxation, unknotting and decatenation of DNA are achieved enabling processes like replication and transcription [25].

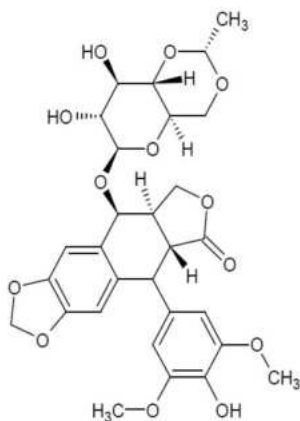


Figure 6. Etoposide structure.

2.5.1. Mechanism of DNA Damage Induction

Two modes of action were suggested for ETP to interfere with TopoII [25]. As a poison, it stabilises TopoII:DNA complexes, whereas as an inhibitor ETP interacts with the catalytic site of TopoII, decreasing the number of active cleavage complexes [307]. ETP acts as a poison by stabilizing the cleavage complex of TopoII via decoupling the key catalytic residues, thus preventing the religation of cleaved DNA ends [308]. As a result, the number of TopoII-associated DNA breaks are increased [309]. ETP's A, B and D-rings mediate the drug-enzyme interaction, whereas the aglycon core binds to DNA [262,308]. E-ring substituents are important for ETP activity but do not contribute to ETP-enzyme binding [310]. ETP is metabolised by cytochrome P3A4 (CYP3A4) to two metabolites, ETP-quinone and ETP-catechol. Both active against the TopoII enzyme. ETP-quinone is approx. 100× more efficient at inhibiting TopoII than ETP. ETP-quinone can block binding of the enzyme to DNA by stabilisation of the N-terminal clamp [307]. In cases where the enzyme still binds to DNA, the metabolite can stabilise the enzyme:DNA complex by inhibiting the religation step thus leading to higher levels of DSBs [307]. The ETP-catechol metabolite works similarly to the parent compound but can also be oxidised to the quinone [311]. ETP induces DSBs directly in all phases of the cell cycle, as observed by γ H2AX foci formation (a marker of DSBs) [312,313]. ETP does not require S-phase to induce damage, but ongoing replication enhances its cytotoxic effect [314]. ETP causes disassembly of replication factories (sites of ongoing replication), as measured by the distribution of proliferating cell nuclear antigen protein (PCNA) [315]. Moreover, the cytotoxic effect of ETP is partially reduced by inhibitors of DNA synthesis, such as APH and HU [316]. There are two isoforms of the TopoII enzyme in mammals, called TopoII α and TopoII β , sharing 68% homology [317]. TopoII α activity is upregulated during cell cycle progression, peaks in mitosis and is essential for proliferating cells [318]. TopoII β is needed during transcription and DNA repair, and its levels are more stable during the cell cycle [319]. ETP is not selective between these two paralogs, and the inhibition of TopoII β is believed to be the reason for ETP therapy-related secondary malignancies [320]. TopoII α seems to be a better target for therapy. Therefore, new compounds and analogues of ETP have been synthesised to be selective only for TopoII α [321].

2.5.2. Other Effects

A strong mutagenic effect has been measured for ETP in mammalian cells by several assays, e.g., HPRT assay (hypoxanthine phosphoribosyl transferase), SCE and detection of mutations at the locus of the adenosine kinase gene [322]. In prokaryotic organisms (*E. coli*, *Salmonella typhimurium*), no significant genotoxic effect was observed [322]. For references to particular studies using ETP, refer to Table 5.

Table 5. Effects of various etoposide treatments in vitro.

Concentration	Incubation Time	Effect	Cell Line	References
up to 450 μ M	40 min	SSB and DSB formation, induction of H2AX phosphorylation with slow kinetics	SV-40 transformed human fibroblasts G361	[323]
1–100 μ M	30 min	formation of TopoII-blocked DSBs, activation of ATM-mediated repair	MEF HEK293T BJ1 AT	[324]
2–100 μ M	6 h–48 h	senescence, apoptosis induction of p53 response	HepG2 U2OS	[325]
2–100 μ M	1–3 h	disassembly of replication factories	AT1 BR AT3 BR HeLa	[315]
50–100 μ M	3–6 h/16 h	apoptosis (activation of intrinsic (mitochondrial) pathway)	Hela HCT116	[326]
50 μ M	15 h	apoptosis	BJAB Hut78	[327]

Table 5. Cont.

Concentration	Incubation Time	Effect	Cell Line	References
50 μ M	48 h	growth arrest (accumulation of cells at G2/M boundary) induction of p53 response	MCF-7 ZR75-1 T-47D	[328]
25 μ M	1 h	SSB and DSB formation γ H2AX, pATM, pDNA-PKcs, MDC1 foci formation persisting DSBs cell death	HeLa HCT116	[329]
20 μ M	16 h	increase in γ H2AX levels reduction of proliferation rate (accumulation of cells in S and G2/M boundary)	U2OS	[330]
20 μ M	1 h	repairable DSBs	HEK293T COS-7 BJ-hTERT H1299	[331,332]
	16 h	irrepairable DSBs, ATM-dependent HIC1 SUMOylation, induction of p53-dependent apoptotic response		
20 μ M	1–5 h	apoptosis	A549 HeLa, T24	[333]
10 μ M	1 h	DNA damage induction	A549	[334]
1–10 μ M	48 h	apoptosis	HCC1937 BT-549	[335]
8 μ M	1 h	induction of p53 response,	SH-SY-5Y SH-EP1	[336]
0.75–3 μ M	72 h	senescence, apoptosis	A549	[337]
0.75 μ M	24 h	cell cycle arrest in G2/M phase, DNA damage induction, induction of p53 response	MSC TGCT H12.1 TGCT 2102EP	[145]

DSBs: Double strand breaks; HIC1: Hypermethylated In Cancer 1; MDC1: Mediator of DNA Checkpoint 1; pATM: phosphorylated Ataxia telangiectasia Mutated; pDNA-PKcs: phosphorylated DNA Protein Kinase catalytic subunit; SSB: single-strand DNA break; TopoII: Topoisomerase II.

2.5.3. Solubility

ETP (MW 588.56 g/mol) is soluble in organic solvents (ethanol, methanol, DMSO), poorly soluble in water. It is recommended that stock solutions in organic solvents be diluted so 0.1% organic solvent is present in the final solution. The stability in aqueous solution is best at pH 4–5, but it can be improved by adding polysorbate 80 (Tween80), polyethylene glycol 300, citric acid and alcohol. ETP is unstable under oxidative conditions [338]. Under acidic conditions (pH < 4), the glycosidic linkage and lactone ring are hydrolysed, whereas, under basic conditions (pH > 6), *cis*-lactone epimers are formed [304]. Aqueous solutions are stable for several hours, depending on the concentration of the solution but irrespective of the temperature. ETP is sensitive to UV irradiation, both in solution and as a powder [338].

2.5.4. Medical Use

According to pharmacokinetic studies, plasma levels of ETP peak at concentrations of 20–70 μ M [339]. ETP is approved for the treatment of refractory testicular tumors and small cell lung cancer. Various chemical modifications with potential higher efficacy have also been tested for clinical use, e.g., 4'-phosphorylation or 4'-propyl carboxy derivatives [340]. In the field of so-called personalised medicine, combined subsequent treatment of ETP and cisPt has been shown to be beneficial for patients suffering from ERCC1-incompetent lung adenocarcinoma [341]. ETP is reported to cause therapy-related leukaemias [320] and specific chromosomal translocations. Chromosomal rearrangements at the 11q23 chromosome band were found in patients and seemed to be related to the CYP3A4 metabolic conversion of ETP [342]. In mouse embryonic stem cells, an increase

in fusion chimeric products was observed at a 1.5 kb “hot spot” between exons 9 and 11 (analogous region to MLL (mixed lineage leukaemia) breakpoint cluster in human leukaemia) [343]. MLL gene encodes lysine (K)-specific histone methyltransferase 2A therefore influencing histone methylation and gene expression [344]. Leukaemogenic MLL translocations lead to expression of MLL fusion proteins. Patients with such translocations exhibit poor prognosis [345]. MLL fusion proteins are efficient in transforming the hematopoietic cells into leukaemia stem cells [346]. Many studies have attempted to solve the adverse side effects of ETP treatment and understand the underlying molecular mechanisms, e.g., multi-drug resistance [347], or unwanted toxicity [348]. The search for compounds that may improve ETP treatment usually starts with cell-based experiments, e.g., protective compounds shielding healthy cells [349], compounds selectively enhancing ETP toxicity [350] or targeted delivery [351].

2.5.5. Summary

ETP is commonly used for the induction of apoptosis [352]. Indeed, several studies reported that higher doses of the compound (25–100 μ M) activate apoptosis, mostly in a manner dependent on p53 [325–327,329]. Prolonged treatment at lower concentrations of ETP can also lead to induction of the p53 pathway, cell cycle arrest, senescence and apoptosis [145,325,330,335,337]. ETP induces the formation of irreversible DNA–TopoII cleavage complexes (TopoIIcc) and DNA damage regardless of concentration or incubation time [323,324,329–332,334,353]. The initial displacement of TopoIIcc requires the coordinated action of several processes, such as cleavage by the 5′-tyrosyl DNA phosphodiesterase (TTRAP) and proteasome-dependent degradation of TopoII [354,355]. Furthermore, the MRN complex, CtIP (RBBP8 protein) and BRCA1 play a critical role in the removal of such DNA-protein adducts [356]. The remaining DNA lesions are often referred as DSBs, which are accompanied by the activation of ATM-mediated signalling or repair pathways, usually quantified by the formation of γ H2AX [323,324,329–332]. However, several studies argue against the ability of ETP to primarily induce DSBs, showing that majority of the DNA lesions formed upon ETP treatment are SSBs [323,329]. Despite the discrepancy, pathways engaged in DSB repair are activated after the exposure to the drug, and among them, NHEJ is seemingly predominant [329,356–358]. ETP used in relatively high concentration (20–25 μ M) might lead to persistent or irreparable DSB formation [329,331,332].

3. Conclusions

Replication stress is a significant contributor to genomic instability, a major factor for the conservation of mutations [1], relevant promoter of tumorigenesis [8] and also one of the main features of cancer cells [76]. Owing to its complexity, replication can be disturbed by multiple mechanisms. In this review, we focused on several compounds known to be RS inducers and often used in cell-based assays. Some of the compounds have been shown to be effective in cancer treatment. Importantly, the chemicals have been primarily chosen to cover various mechanisms of action, resulting in different treatment-induced phenotypes resembling those of RS in carcinogenesis. Induction of RS *in vitro*, e.g., by chemicals inducing DNA damage, is a crucial research tool. Precise knowledge about the mechanism of DNA damage induction and cellular pathways involved in the RS response is particularly important for the development of appropriate cellular assays for investigating carcinogenesis and cancer treatment. The above-mentioned publications in separate compound-related tables were chosen to help with the practical aspects of such assay design. Dose and time-dependent effects related to the genetic backgrounds (i.e., dependent on the cell line used) and proper readout are important issues for experiment design. Moreover, other practical information has been included so that readers can use this review as a brief guide for choosing an appropriate model and dose scheme for cell-based studies.

Acknowledgments: The work was supported by Grant Agency of the Czech Republic 13-17555S, Internal Grant of Palacky University IGA-LF-2016-030, the Norwegian Financial Mechanism CZ09 (Project PHOSCAN 7F14061).

Author Contributions: E.V. wrote the chapter 2.3, contributed to chapters 2.2 and 2.5, prepared the figures. K.C. wrote the chapters 2.1 and 2.4, Z.T. contributed to chapter 2.5, M.M. contributed to chapter 2.2. All authors participated on the introduction part and revised the manuscript.

Conflicts of Interest: The authors declare no conflict of interest.

References

- Zeman, M.K.; Cimprich, K.A. Causes and consequences of replication stress. *Nat. Cell Biol.* **2014**, *16*, 2–9. [[CrossRef](#)] [[PubMed](#)]
- Burhans, W.C.; Weinberger, M. DNA replication stress, genome instability and aging. *Nucleic Acids Res.* **2007**, *35*, 7545–7556. [[CrossRef](#)] [[PubMed](#)]
- Huh, M.S.; Ivanochko, D.; Hashem, L.E.; Curtin, M.; Delorme, M.; Goodall, E.; Yan, K.; Picketts, D.J. Stalled replication forks within heterochromatin require ATRX for protection. *Cell Death Dis.* **2016**, *7*, e2220. [[CrossRef](#)] [[PubMed](#)]
- Gelot, C.; Magdalou, I.; Lopez, B.S. Replication stress in Mammalian cells and its consequences for mitosis. *Genes* **2015**, *6*, 267–298. [[CrossRef](#)] [[PubMed](#)]
- Krasilnikova, M.M.; Mirkin, S.M. Replication stalling at Friedreich’s ataxia (GAA)_n repeats in vivo. *Mol. Cell. Biol.* **2004**, *24*, 2286–2295. [[CrossRef](#)] [[PubMed](#)]
- Neelsen, K.J.; Zanini, I.M.Y.; Mijic, S.; Herrador, R.; Zellweger, R.; Ray Chaudhuri, A.; Creavin, K.D.; Blow, J.J.; Lopes, M. Deregulated origin licensing leads to chromosomal breaks by rereplication of a gapped DNA template. *Genes Dev.* **2013**, *27*, 2537–2542. [[CrossRef](#)] [[PubMed](#)]
- Porter, A.C. Preventing DNA over-replication: A Cdk perspective. *Cell Div.* **2008**, *3*, 3. [[CrossRef](#)] [[PubMed](#)]
- Burrell, R.A.; McClelland, S.E.; Endesfelder, D.; Groth, P.; Weller, M.-C.; Shaikh, N.; Domingo, E.; Kanu, N.; Dewhurst, S.M.; Gronroos, E.; et al. Replication stress links structural and numerical cancer chromosomal instability. *Nature* **2013**, *494*, 492–496. [[CrossRef](#)] [[PubMed](#)]
- Liu, B.; Alberts, B.M. Head-on collision between a DNA replication apparatus and RNA polymerase transcription complex. *Science* **1995**, *267*, 1131–1137. [[CrossRef](#)] [[PubMed](#)]
- Bartkova, J.; Rezaei, N.; Liontos, M.; Karakaidos, P.; Kletsas, D.; Issaeva, N.; Vassiliou, L.-V.F.; Kolettas, E.; Niforou, K.; Zoumpourlis, V.C.; et al. Oncogene-induced senescence is part of the tumorigenesis barrier imposed by DNA damage checkpoints. *Nature* **2006**, *444*, 633–637. [[CrossRef](#)] [[PubMed](#)]
- Vallerga, M.B.; Mansilla, S.F.; Federico, M.B.; Bertolin, A.P.; Gottifredi, V. Rad51 recombinase prevents Mre11 nuclease-dependent degradation and excessive PrimPol-mediated elongation of nascent DNA after UV irradiation. *Proc. Natl. Acad. Sci. USA* **2015**, *112*, E6624–E6633. [[CrossRef](#)] [[PubMed](#)]
- Mazouzi, A.; Velimezi, G.; Loizou, J.I. DNA replication stress: Causes, resolution and disease. *Exp. Cell Res.* **2014**, *329*, 85–93. [[CrossRef](#)] [[PubMed](#)]
- Jekimovs, C.; Bolderson, E.; Suraweera, A.; Adams, M.; O’Byrne, K.J.; Richard, D.J. Chemotherapeutic compounds targeting the DNA double-strand break repair pathways: The good, the bad, and the promising. *Front. Oncol.* **2014**, *4*, 86. [[CrossRef](#)] [[PubMed](#)]
- Beranek, D.T. Distribution of methyl and ethyl adducts following alkylation with monofunctional alkylating agents. *Mutat. Res.* **1990**, *231*, 11–30. [[CrossRef](#)]
- Kondo, N.; Takahashi, A.; Mori, E.; Noda, T.; Su, X.; Ohnishi, K.; McKinnon, P.J.; Sakaki, T.; Nakase, H.; Ono, K.; et al. DNA ligase IV is a potential molecular target in ACNU sensitivity. *Cancer Sci.* **2010**, *101*, 1881–1885. [[CrossRef](#)] [[PubMed](#)]
- Brookes, P.; Lawley, P.D. The reaction of mono- and di-functional alkylating agents with nucleic acids. *Biochem. J.* **1961**, *80*, 496–503. [[CrossRef](#)] [[PubMed](#)]
- Lawley, P.D.; Brookes, P. The action of alkylating agents on deoxyribonucleic acid in relation to biological effects of the alkylating agents. *Exp. Cell Res.* **1963**, *24* (Suppl. S9), 512–520. [[CrossRef](#)]
- Noll, D.M.; Mason, T.M.; Miller, P.S. Formation and repair of interstrand cross-links in DNA. *Chem. Rev.* **2006**, *106*, 277–301. [[CrossRef](#)] [[PubMed](#)]
- Schärer, O.D. DNA Interstrand Crosslinks: Natural and Drug-Induced DNA Adducts that Induce Unique Cellular Responses. *ChemBioChem* **2005**, *6*, 27–32. [[CrossRef](#)] [[PubMed](#)]
- Lawley, P.D.; Phillips, D.H. DNA adducts from chemotherapeutic agents. *Mutat. Res.* **1996**, *355*, 13–40. [[CrossRef](#)]

21. Bhuyan, B.K.; Scheidt, L.G.; Fraser, T.J. Cell cycle phase specificity of antitumor agents. *Cancer Res.* **1972**, *32*, 398–407. [[PubMed](#)]
22. Glover, T.W.; Arlt, M.F.; Casper, A.M.; Durkin, S.G. Mechanisms of common fragile site instability. *Hum. Mol. Genet.* **2005**, *14*, R197–R205. [[CrossRef](#)] [[PubMed](#)]
23. Koç, A.; Wheeler, L.J.; Mathews, C.K.; Merrill, G.F. Hydroxyurea arrests DNA replication by a mechanism that preserves basal dNTP pools. *J. Biol. Chem.* **2004**, *279*, 223–230. [[CrossRef](#)] [[PubMed](#)]
24. Hsiang, Y.H.; Lihou, M.G.; Liu, L.F. Arrest of replication forks by drug-stabilized topoisomerase I-DNA cleavable complexes as a mechanism of cell killing by camptothecin. *Cancer Res.* **1989**, *49*, 5077–5082. [[PubMed](#)]
25. Deweese, J.E.; Osheroff, N. The DNA cleavage reaction of topoisomerase II: Wolf in sheep's clothing. *Nucleic Acids Res.* **2009**, *37*, 738–748. [[CrossRef](#)] [[PubMed](#)]
26. Helleday, T.; Petermann, E.; Lundin, C.; Hodgson, B.; Sharma, R.A. DNA repair pathways as targets for cancer therapy. *Nat. Rev. Cancer* **2008**, *8*, 193–204. [[CrossRef](#)] [[PubMed](#)]
27. Krokan, H.E.; Bjørås, M. Base Excision Repair. *Cold Spring Harb. Perspect. Biol.* **2013**, *5*, a012583. [[CrossRef](#)] [[PubMed](#)]
28. Gillet, L.C.J.; Schärer, O.D. Molecular mechanisms of mammalian global genome nucleotide excision repair. *Chem. Rev.* **2006**, *106*, 253–276. [[CrossRef](#)] [[PubMed](#)]
29. Caldecott, K.W. Protein ADP-ribosylation and the cellular response to DNA strand breaks. *DNA Repair* **2014**, *19*, 108–113. [[CrossRef](#)] [[PubMed](#)]
30. Heyer, W.-D.; Ehmsen, K.T.; Liu, J. Regulation of homologous recombination in eukaryotes. *Annu. Rev. Genet.* **2010**, *44*, 113–139. [[CrossRef](#)] [[PubMed](#)]
31. Davis, A.J.; Chen, D.J. DNA double strand break repair via non-homologous end-joining. *Transl. Cancer Res.* **2013**, *2*, 130–143. [[PubMed](#)]
32. Bi, X. Mechanism of DNA damage tolerance. *World J. Biol. Chem.* **2015**, *6*, 48–56. [[CrossRef](#)] [[PubMed](#)]
33. Aguilera, A.; Gómez-González, B. Genome instability: A mechanistic view of its causes and consequences. *Nat. Rev. Genet.* **2008**, *9*, 204–217. [[CrossRef](#)] [[PubMed](#)]
34. Chang, D.J.; Cimprich, K.A. DNA damage tolerance: When it's OK to make mistakes. *Nat. Chem. Biol.* **2009**, *5*, 82–90. [[CrossRef](#)] [[PubMed](#)]
35. Ghosal, G.; Chen, J. DNA damage tolerance: A double-edged sword guarding the genome. *Transl. Cancer Res.* **2013**, *2*, 107–129. [[PubMed](#)]
36. Saugar, I.; Ortiz-Bazán, M.Á.; Tercero, J.A. Tolerating DNA damage during eukaryotic chromosome replication. *Exp. Cell Res.* **2014**, *329*, 170–177. [[CrossRef](#)] [[PubMed](#)]
37. Deans, A.J.; West, S.C. DNA interstrand crosslink repair and cancer. *Nat. Rev. Cancer* **2011**, *11*, 467–480. [[CrossRef](#)] [[PubMed](#)]
38. Longerich, S.; Li, J.; Xiong, Y.; Sung, P.; Kupfer, G.M. Stress and DNA repair biology of the Fanconi anemia pathway. *Blood* **2014**, *124*, 2812–2819. [[CrossRef](#)] [[PubMed](#)]
39. Gaillard, H.; García-Muse, T.; Aguilera, A. Replication stress and cancer. *Nat. Rev. Cancer* **2015**, *15*, 276–289. [[CrossRef](#)] [[PubMed](#)]
40. Mamrak, N.E.; Shimamura, A.; Howlett, N.G. Recent discoveries in the molecular pathogenesis of the inherited bone marrow failure syndrome Fanconi anemia. *Blood Rev.* **2016**. [[CrossRef](#)] [[PubMed](#)]
41. Kennedy, R.D.; D'Andrea, A.D. The Fanconi Anemia/BRCA pathway: New faces in the crowd. *Genes Dev.* **2005**, *19*, 2925–2940. [[CrossRef](#)] [[PubMed](#)]
42. Thompson, L.H.; Hinz, J.M. Cellular and molecular consequences of defective Fanconi anemia proteins in replication-coupled DNA repair: Mechanistic insights. *Mutat. Res.* **2009**, *668*, 54–72. [[CrossRef](#)] [[PubMed](#)]
43. Branzei, D. Ubiquitin family modifications and template switching. *FEBS Lett.* **2011**, *585*, 2810–2817. [[CrossRef](#)] [[PubMed](#)]
44. Xu, X.; Blackwell, S.; Lin, A.; Li, F.; Qin, Z.; Xiao, W. Error-free DNA-damage tolerance in *Saccharomyces cerevisiae*. *Mutat. Res. Rev. Mutat. Res.* **2015**, *764*, 43–50. [[CrossRef](#)] [[PubMed](#)]
45. Ge, X.Q.; Jackson, D.A.; Blow, J.J. Dormant origins licensed by excess Mcm2–7 are required for human cells to survive replicative stress. *Genes Dev.* **2007**, *21*, 3331–3341. [[CrossRef](#)] [[PubMed](#)]
46. Lopes, M.; Foiani, M.; Sogo, J.M. Multiple mechanisms control chromosome integrity after replication fork uncoupling and restart at irreparable UV lesions. *Mol. Cell* **2006**, *21*, 15–27. [[CrossRef](#)] [[PubMed](#)]

47. Woodward, A.M.; Göhler, T.; Luciani, M.G.; Oehlmann, M.; Ge, X.; Gartner, A.; Jackson, D.A.; Blow, J.J. Excess Mcm2–7 license dormant origins of replication that can be used under conditions of replicative stress. *J. Cell Biol.* **2006**, *173*, 673–683. [[CrossRef](#)] [[PubMed](#)]
48. Elvers, I.; Johansson, F.; Groth, P.; Erixon, K.; Helleday, T. UV stalled replication forks restart by re-priming in human fibroblasts. *Nucleic Acids Res.* **2011**, *39*, 7049–7057. [[CrossRef](#)] [[PubMed](#)]
49. McIntosh, D.; Blow, J.J. Dormant origins, the licensing checkpoint, and the response to replicative stresses. *Cold Spring Harb. Perspect. Biol.* **2012**, *4*, a012955. [[CrossRef](#)] [[PubMed](#)]
50. De Piccoli, G.; Katou, Y.; Itoh, T.; Nakato, R.; Shirahige, K.; Labib, K. Replisome stability at defective DNA replication forks is independent of S phase checkpoint kinases. *Mol. Cell* **2012**, *45*, 696–704. [[CrossRef](#)] [[PubMed](#)]
51. Tercero, J.A.; Diffley, J.F.X. Regulation of DNA replication fork progression through damaged DNA by the Mec1/Rad53 checkpoint. *Nature* **2001**, *412*, 553–557. [[CrossRef](#)] [[PubMed](#)]
52. Lopes, M.; Cotta-Ramusino, C.; Pellicoli, A.; Liberi, G.; Plevani, P.; Muzi-Falconi, M.; Newlon, C.S.; Foiani, M. The DNA replication checkpoint response stabilizes stalled replication forks. *Nature* **2001**, *412*, 557–561. [[CrossRef](#)] [[PubMed](#)]
53. Cobb, J.A.; Bjergbaek, L.; Shimada, K.; Frei, C.; Gasser, S.M. DNA polymerase stabilization at stalled replication forks requires Mec1 and the RecQ helicase Sgs1. *EMBO J.* **2003**, *22*, 4325–4336. [[CrossRef](#)] [[PubMed](#)]
54. Ragland, R.L.; Patel, S.; Rivard, R.S.; Smith, K.; Peters, A.A.; Bielinsky, A.-K.; Brown, E.J. RNF4 and PLK1 are required for replication fork collapse in ATR-deficient cells. *Genes Dev.* **2013**, *27*, 2259–2273. [[CrossRef](#)] [[PubMed](#)]
55. Hanada, K.; Budzowska, M.; Davies, S.L.; van Druenen, E.; Onizawa, H.; Beverloo, H.B.; Maas, A.; Essers, J.; Hickson, I.D.; Kanaar, R. The structure-specific endonuclease Mus81 contributes to replication restart by generating double-strand DNA breaks. *Nat. Struct. Mol. Biol.* **2007**, *14*, 1096–1104. [[CrossRef](#)] [[PubMed](#)]
56. Forment, J.V.; Blasius, M.; Guerini, I.; Jackson, S.P. Structure-specific DNA endonuclease Mus81/Eme1 generates DNA damage caused by Chk1 inactivation. *PLoS ONE* **2011**, *6*, e23517. [[CrossRef](#)] [[PubMed](#)]
57. Zellweger, R.; Dalcher, D.; Mutreja, K.; Berti, M.; Schmid, J.A.; Herrador, R.; Vindigni, A.; Lopes, M. Rad51-mediated replication fork reversal is a global response to genotoxic treatments in human cells. *J. Cell Biol.* **2015**, *208*, 563–579. [[CrossRef](#)] [[PubMed](#)]
58. Pacek, M.; Walter, J.C. A requirement for MCM7 and Cdc45 in chromosome unwinding during eukaryotic DNA replication. *EMBO J.* **2004**, *23*, 3667–3676. [[CrossRef](#)] [[PubMed](#)]
59. Byun, T.S.; Pacek, M.; Yee, M.; Walter, J.C.; Cimprich, K.A. Functional uncoupling of MCM helicase and DNA polymerase activities activates the ATR-dependent checkpoint. *Genes Dev.* **2005**, *19*, 1040–1052. [[CrossRef](#)] [[PubMed](#)]
60. Zou, L.; Elledge, S.J. Sensing DNA damage through ATRIP recognition of RPA-ssDNA complexes. *Science* **2003**, *300*, 1542–1548. [[CrossRef](#)] [[PubMed](#)]
61. MacDougall, C.A.; Byun, T.S.; Van, C.; Yee, M.; Cimprich, K.A. The structural determinants of checkpoint activation. *Genes Dev.* **2007**, *21*, 898–903. [[CrossRef](#)] [[PubMed](#)]
62. Nam, E.A.; Cortez, D. ATR signalling: More than meeting at the fork. *Biochem. J.* **2011**, *436*, 527–536. [[CrossRef](#)] [[PubMed](#)]
63. Maréchal, A.; Zou, L. DNA damage sensing by the ATM and ATR kinases. *Cold Spring Harb. Perspect. Biol.* **2013**, *5*, a012716. [[CrossRef](#)] [[PubMed](#)]
64. Lucca, C.; Vanoli, F.; Cotta-Ramusino, C.; Pellicoli, A.; Liberi, G.; Haber, J.; Foiani, M. Checkpoint-mediated control of replisome-fork association and signalling in response to replication pausing. *Oncogene* **2004**, *23*, 1206–1213. [[CrossRef](#)] [[PubMed](#)]
65. Petermann, E.; Orta, M.L.; Issaeva, N.; Schultz, N.; Helleday, T. Hydroxyurea-stalled replication forks become progressively inactivated and require two different RAD51-mediated pathways for restart and repair. *Mol. Cell* **2010**, *37*, 492–502. [[CrossRef](#)] [[PubMed](#)]
66. Labib, K.; De Piccoli, G. Surviving chromosome replication: The many roles of the S-phase checkpoint pathway. *Philos. Trans. R. Soc. Lond. B Biol. Sci.* **2011**, *366*, 3554–3561. [[CrossRef](#)] [[PubMed](#)]
67. Ozeri-Galai, E.; Schwartz, M.; Rahat, A.; Kerem, B. Interplay between ATM and ATR in the regulation of common fragile site stability. *Oncogene* **2008**, *27*, 2109–2117. [[CrossRef](#)] [[PubMed](#)]

68. Ciccia, A.; Elledge, S.J. The DNA damage response: Making it safe to play with knives. *Mol. Cell* **2010**, *40*, 179–204. [CrossRef] [PubMed]
69. Ammazalorso, F.; Pirzio, L.M.; Bignami, M.; Franchitto, A.; Pichierri, P. ATR and ATM differently regulate WRN to prevent DSBs at stalled replication forks and promote replication fork recovery. *EMBO J.* **2010**, *29*, 3156–3169. [CrossRef] [PubMed]
70. Bachrati, C.Z.; Hickson, I.D. RecQ helicases: Suppressors of tumorigenesis and premature aging. *Biochem. J.* **2003**, *374*, 577–606. [CrossRef] [PubMed]
71. Hills, S.A.; Diffley, J.F.X. DNA replication and oncogene-induced replicative stress. *Curr. Biol.* **2014**, *24*, R435–R444. [CrossRef] [PubMed]
72. Macheret, M.; Halazonetis, T.D. DNA replication stress as a hallmark of cancer. *Annu. Rev. Pathol.* **2015**, *10*, 425–448. [CrossRef] [PubMed]
73. Murga, M.; Campaner, S.; Lopez-Contreras, A.J.; Toledo, L.I.; Soria, R.; Montaña, M.F.; D’Artista, L.; Schleker, T.; Guerra, C.; Garcia, E.; et al. Exploiting oncogene-induced replicative stress for the selective killing of Myc-driven tumors. *Nat. Struct. Mol. Biol.* **2011**, *18*, 1331–1335. [CrossRef] [PubMed]
74. Marusyk, A.; Wheeler, L.J.; Mathews, C.K.; DeGregori, J. p53 mediates senescence-like arrest induced by chronic replicational stress. *Mol. Cell. Biol.* **2007**, *27*, 5336–5351. [CrossRef] [PubMed]
75. Bai, G.; Smolka, M.B.; Schimenti, J.C. Chronic DNA Replication Stress Reduces Replicative Lifespan of Cells by TRP53-Dependent, microRNA-Assisted MCM2–7 Downregulation. *PLoS Genet.* **2016**, *12*, e1005787. [CrossRef] [PubMed]
76. Bartkova, J.; Horejsi, Z.; Koed, K.; Krämer, A.; Tort, F.; Zieger, K.; Guldberg, P.; Sehested, M.; Nesland, J.M.; Lukas, C.; et al. DNA damage response as a candidate anti-cancer barrier in early human tumorigenesis. *Nature* **2005**, *434*, 864–870. [CrossRef] [PubMed]
77. O’Driscoll, M.; Ruiz-Perez, V.L.; Woods, C.G.; Jeggo, P.A.; Goodship, J.A. A splicing mutation affecting expression of ataxia-telangiectasia and Rad3-related protein (ATR) results in Seckel syndrome. *Nat. Genet.* **2003**, *33*, 497–501. [CrossRef] [PubMed]
78. McKinnon, P.J. ATM and ataxia telangiectasia. *EMBO Rep.* **2004**, *5*, 772–776. [CrossRef] [PubMed]
79. DiGiovanna, J.J.; Kraemer, K.H. Shining a light on xeroderma pigmentosum. *J. Investig. Dermatol.* **2012**, *132*, 785–796. [CrossRef] [PubMed]
80. Callén, E.; Surrallés, J. Telomere dysfunction in genome instability syndromes. *Mutat. Res.* **2004**, *567*, 85–104. [CrossRef] [PubMed]
81. Lauper, J.M.; Krause, A.; Vaughan, T.L.; Monnat, R.J. Spectrum and risk of neoplasia in Werner syndrome: A systematic review. *PLoS ONE* **2013**, *8*, e59709. [CrossRef] [PubMed]
82. Bernstein, K.A.; Gangloff, S.; Rothstein, R. The RecQ DNA helicases in DNA repair. *Annu. Rev. Genet.* **2010**, *44*, 393–417. [CrossRef] [PubMed]
83. Kim, H.; D’Andrea, A.D. Regulation of DNA cross-link repair by the Fanconi anemia/BRCA pathway. *Genes Dev.* **2012**, *26*, 1393–1408. [CrossRef] [PubMed]
84. Joenje, H.; Patel, K.J. The emerging genetic and molecular basis of Fanconi anaemia. *Nat. Rev. Genet.* **2001**, *2*, 446–457. [CrossRef] [PubMed]
85. Larizza, L.; Roversi, G.; Volpi, L. Rothmund-Thomson syndrome. *Orphanet J. Rare Dis.* **2010**, *5*, 2. [CrossRef] [PubMed]
86. Lu, H.; Shamanna, R.A.; Keijzers, G.; Anand, R.; Rasmussen, L.J.; Cejka, P.; Croteau, D.L.; Bohr, V.A. RECQL4 Promotes DNA End Resection in Repair of DNA Double-Strand Breaks. *Cell Rep.* **2016**, *16*, 161–173. [CrossRef] [PubMed]
87. Rosenberg, B.; Vancamp, L.; Krigas, T. Inhibition of cell division in *Escherichia coli* by electrolysis products from a platinum electrode. *Nature* **1965**, *205*, 698–699. [CrossRef] [PubMed]
88. Todd, R.C.; Lippard, S.J. Inhibition of transcription by platinum antitumor compounds. *Metallomics* **2009**, *1*, 280–291. [CrossRef] [PubMed]
89. Zamble, D.B.; Lippard, S.J. Cisplatin and DNA repair in cancer chemotherapy. *Trends Biochem. Sci.* **1995**, *20*, 435–439. [CrossRef]
90. Available online: <http://www.rcsb.org/pdb/explore/explore.do?structureId=3CO3> (accessed on 23 January 2017).

91. Fichtinger-Schepman, A.M.; van der Veer, J.L.; den Hartog, J.H.; Lohman, P.H.; Reedijk, J. Adducts of the antitumor drug *cis*-diamminedichloroplatinum(II) with DNA: Formation, identification, and quantitation. *Biochemistry* **1985**, *24*, 707–713. [[CrossRef](#)] [[PubMed](#)]
92. Harder, H.C.; Rosenberg, B. Inhibitory effects of anti-tumor platinum compounds on DNA, RNA and protein syntheses in mammalian cells in vitro. *Int. J. Cancer* **1970**, *6*, 207–216. [[CrossRef](#)] [[PubMed](#)]
93. Eastman, A. Reevaluation of interaction of *cis*-dichloro(ethylenediamine)platinum(II) with DNA. *Biochemistry* **1986**, *25*, 3912–3915. [[CrossRef](#)] [[PubMed](#)]
94. Sherman, S.E.; Gibson, D.; Wang, A.H.; Lippard, S.J. X-ray structure of the major adduct of the anticancer drug cisplatin with DNA: *cis*-[Pt(NH₃)₂(d(pGpG))]. *Science* **1985**, *230*, 412–417. [[CrossRef](#)] [[PubMed](#)]
95. Eastman, A. Separation and characterization of products resulting from the reaction of *cis*-diamminedichloroplatinum (II) with deoxyribonucleosides. *Biochemistry* **1982**, *21*, 6732–6736. [[CrossRef](#)] [[PubMed](#)]
96. Desoize, B. Cancer and metals and metal compounds: Part I—Carcinogenesis. *Crit. Rev. Oncol. Hematol.* **2002**, *42*, 1–3. [[CrossRef](#)]
97. Köberle, B.; Masters, J.R.; Hartley, J.A.; Wood, R.D. Defective repair of cisplatin-induced DNA damage caused by reduced XPA protein in testicular germ cell tumours. *Curr. Biol.* **1999**, *9*, 273–276. [[CrossRef](#)]
98. Borst, P.; Rottenberg, S.; Jonkers, J. How do real tumors become resistant to cisplatin? *Cell Cycle* **2008**, *7*, 1353–1359. [[CrossRef](#)] [[PubMed](#)]
99. Sedletskaya, Y.; Fourrier, L.; Malinge, J.-M. Modulation of MutS ATP-dependent functional activities by DNA containing a cisplatin compound lesion (base damage and mismatch). *J. Mol. Biol.* **2007**, *369*, 27–40. [[CrossRef](#)] [[PubMed](#)]
100. Brown, R.; Clugston, C.; Burns, P.; Edlin, A.; Vasey, P.; Vojtěšek, B.; Kaye, S.B. Increased accumulation of p53 protein in cisplatin-resistant ovarian cell lines. *Int. J. Cancer* **1993**, *55*, 678–684. [[CrossRef](#)] [[PubMed](#)]
101. Damsma, G.E.; Alt, A.; Brueckner, F.; Carell, T.; Cramer, P. Mechanism of transcriptional stalling at cisplatin-damaged DNA. *Nat. Struct. Mol. Biol.* **2007**, *14*, 1127–1133. [[CrossRef](#)] [[PubMed](#)]
102. Shimodaira, H.; Yoshioka-Yamashita, A.; Kolodner, R.D.; Wang, J.Y.J. Interaction of mismatch repair protein PMS2 and the p53-related transcription factor p73 in apoptosis response to cisplatin. *Proc. Natl. Acad. Sci. USA* **2003**, *100*, 2420–2425. [[CrossRef](#)] [[PubMed](#)]
103. Aebi, S.; Kurdi-Haidar, B.; Gordon, R.; Cenni, B.; Zheng, H.; Fink, D.; Christen, R.D.; Boland, C.R.; Koi, M.; Fishel, R.; et al. Loss of DNA mismatch repair in acquired resistance to cisplatin. *Cancer Res.* **1996**, *56*, 3087–3090. [[PubMed](#)]
104. Alt, A.; Lammens, K.; Chiocchini, C.; Lammens, A.; Pieck, J.C.; Kuch, D.; Hopfner, K.-P.; Carell, T. Bypass of DNA lesions generated during anticancer treatment with cisplatin by DNA polymerase eta. *Science* **2007**, *318*, 967–970. [[CrossRef](#)] [[PubMed](#)]
105. Brozovic, A.; Ambriović-Ristov, A.; Osmak, M. The relationship between cisplatin-induced reactive oxygen species, glutathione, and BCL-2 and resistance to cisplatin. *Crit. Rev. Toxicol.* **2010**, *40*, 347–359. [[CrossRef](#)] [[PubMed](#)]
106. Spletstoesser, F.; Florea, A.-M.; Büsselberg, D. IP₃ receptor antagonist, 2-APB, attenuates cisplatin induced Ca²⁺-influx in HeLa-S3 cells and prevents activation of calpain and induction of apoptosis. *Br. J. Pharmacol.* **2007**, *151*, 1176–1186. [[CrossRef](#)] [[PubMed](#)]
107. Shamimi-Noori, S.; Yeow, W.-S.; Ziauddin, M.F.; Xin, H.; Tran, T.L.N.; Xie, J.; Loehfelm, A.; Patel, P.; Yang, J.; Schrupp, D.S.; et al. Cisplatin enhances the antitumor effect of tumor necrosis factor-related apoptosis-inducing ligand gene therapy via recruitment of the mitochondria-dependent death signaling pathway. *Cancer Gene Ther.* **2008**, *15*, 356–370. [[CrossRef](#)] [[PubMed](#)]
108. Qian, W.; Nishikawa, M.; Haque, A.M.; Hirose, M.; Mashimo, M.; Sato, E.; Inoue, M. Mitochondrial density determines the cellular sensitivity to cisplatin-induced cell death. *Am. J. Physiol. Cell Physiol.* **2005**, *289*, C1466–C1475. [[CrossRef](#)] [[PubMed](#)]
109. Wetzal, C.C.; Berberich, S.J. p53 binds to cisplatin-damaged DNA. *Biochim. Biophys. Acta* **2001**, *1517*, 392–397. [[CrossRef](#)]
110. Kutuk, O.; Arisan, E.D.; Tezil, T.; Shoshan, M.C.; Basaga, H. Cisplatin overcomes Bcl-2-mediated resistance to apoptosis via preferential engagement of Bak: Critical role of Noxa-mediated lipid peroxidation. *Carcinogenesis* **2009**, *30*, 1517–1527. [[CrossRef](#)] [[PubMed](#)]

111. Kim, H.-S.; Hwang, J.-T.; Yun, H.; Chi, S.-G.; Lee, S.-J.; Kang, I.; Yoon, K.-S.; Choe, W.-J.; Kim, S.-S.; Ha, J. Inhibition of AMP-activated protein kinase sensitizes cancer cells to cisplatin-induced apoptosis via hyper-induction of p53. *J. Biol. Chem.* **2008**, *283*, 3731–3742. [[CrossRef](#)] [[PubMed](#)]
112. Yang, C.; Kaushal, V.; Haun, R.S.; Seth, R.; Shah, S.V.; Kaushal, G.P. Transcriptional activation of caspase-6 and -7 genes by cisplatin-induced p53 and its functional significance in cisplatin nephrotoxicity. *Cell Death Differ.* **2008**, *15*, 530–544. [[CrossRef](#)] [[PubMed](#)]
113. Jiang, M.; Wei, Q.; Wang, J.; Du, Q.; Yu, J.; Zhang, L.; Dong, Z. Regulation of PUMA-alpha by p53 in cisplatin-induced renal cell apoptosis. *Oncogene* **2006**, *25*, 4056–4066. [[CrossRef](#)] [[PubMed](#)]
114. Righetti, S.C.; Della Torre, G.; Pilotti, S.; Ménard, S.; Ottone, F.; Colnaghi, M.I.; Pierotti, M.A.; Lavarino, C.; Comarotti, M.; Oriana, S.; et al. A comparative study of p53 gene mutations, protein accumulation, and response to cisplatin-based chemotherapy in advanced ovarian carcinoma. *Cancer Res.* **1996**, *56*, 689–693. [[PubMed](#)]
115. Johnson, C.L.; Lu, D.; Huang, J.; Basu, A. Regulation of p53 stabilization by DNA damage and protein kinase C. *Mol. Cancer Ther.* **2002**, *1*, 861–867. [[PubMed](#)]
116. Gong, J.G.; Costanzo, A.; Yang, H.Q.; Melino, G.; Kaelin, W.G.; Levvero, M.; Wang, J.Y. The tyrosine kinase c-Abl regulates p73 in apoptotic response to cisplatin-induced DNA damage. *Nature* **1999**, *399*, 806–809. [[PubMed](#)]
117. Preyer, M.; Shu, C.-W.; Wang, J.Y.J. Delayed activation of Bax by DNA damage in embryonic stem cells with knock-in mutations of the Abl nuclear localization signals. *Cell Death Differ.* **2007**, *14*, 1139–1148. [[CrossRef](#)] [[PubMed](#)]
118. Tsai, K.K.C.; Yuan, Z.-M. c-Abl stabilizes p73 by a phosphorylation-augmented interaction. *Cancer Res.* **2003**, *63*, 3418–3424. [[PubMed](#)]
119. Levy, D.; Adamovich, Y.; Reuven, N.; Shaul, Y. Yap1 phosphorylation by c-Abl is a critical step in selective activation of proapoptotic genes in response to DNA damage. *Mol. Cell* **2008**, *29*, 350–361. [[CrossRef](#)] [[PubMed](#)]
120. Jones, E.V.; Dickman, M.J.; Whitmarsh, A.J. Regulation of p73-mediated apoptosis by c-Jun N-terminal kinase. *Biochem. J.* **2007**, *405*, 617–623. [[CrossRef](#)] [[PubMed](#)]
121. Hayakawa, J.; Ohmichi, M.; Kurachi, H.; Kanda, Y.; Hisamoto, K.; Nishio, Y.; Adachi, K.; Tasaka, K.; Kanzaki, T.; Murata, Y. Inhibition of BAD phosphorylation either at serine 112 via extracellular signal-regulated protein kinase cascade or at serine 136 via Akt cascade sensitizes human ovarian cancer cells to cisplatin. *Cancer Res.* **2000**, *60*, 5988–5994. [[PubMed](#)]
122. Isonishi, S.; Andrews, P.A.; Howell, S.B. Increased sensitivity to cis-diamminedichloroplatinum(II) in human ovarian carcinoma cells in response to treatment with 12-O-tetradecanoylphorbol 13-acetate. *J. Biol. Chem.* **1990**, *265*, 3623–3627. [[PubMed](#)]
123. Basu, A.; Teicher, B.A.; Lazo, J.S. Involvement of protein kinase C in phorbol ester-induced sensitization of HeLa cells to cis-diamminedichloroplatinum(II). *J. Biol. Chem.* **1990**, *265*, 8451–8457. [[PubMed](#)]
124. Wang, X.; Dhalla, N.S. Modification of beta-adrenoceptor signal transduction pathway by genetic manipulation and heart failure. *Mol. Cell. Biochem.* **2000**, *214*, 131–155. [[CrossRef](#)] [[PubMed](#)]
125. Basu, A.; Tu, H. Activation of ERK during DNA damage-induced apoptosis involves protein kinase Cdelta. *Biochem. Biophys. Res. Commun.* **2005**, *334*, 1068–1073. [[CrossRef](#)] [[PubMed](#)]
126. Nowak, G. Protein kinase C-alpha and ERK1/2 mediate mitochondrial dysfunction, decreases in active Na⁺ transport, and cisplatin-induced apoptosis in renal cells. *J. Biol. Chem.* **2002**, *277*, 43377–43388. [[CrossRef](#)] [[PubMed](#)]
127. Sánchez-Pérez, I.; Benitah, S.A.; Martínez-Gomariz, M.; Lcal, J.C.; Perona, R. Cell stress and MEKK1-mediated c-Jun activation modulate NFκB activity and cell viability. *Mol. Biol. Cell* **2002**, *13*, 2933–2945. [[CrossRef](#)] [[PubMed](#)]
128. Jones, J.A.; Stroud, R.E.; Kaplan, B.S.; Leone, A.M.; Bavaria, J.E.; Gorman, J.H.; Gorman, R.C.; Ikonomidis, J.S. Differential protein kinase C isoform abundance in ascending aortic aneurysms from patients with bicuspid versus tricuspid aortic valves. *Circulation* **2007**, *116*, I144–I149. [[CrossRef](#)] [[PubMed](#)]
129. Zanke, B.W.; Boudreau, K.; Rubie, E.; Winnett, E.; Tibbles, L.A.; Zon, L.; Kyriakis, J.; Liu, F.F.; Woodgett, J.R. The stress-activated protein kinase pathway mediates cell death following injury induced by cis-platinum, UV irradiation or heat. *Curr. Biol.* **1996**, *6*, 606–613. [[CrossRef](#)]

130. Hernández Losa, J.; Parada Cobo, C.; Guinea Viniestra, J.; Sánchez-Arevalo Lobo, V.J.; Ramón y Cajal, S.; Sánchez-Prieto, R. Role of the p38 MAPK pathway in cisplatin-based therapy. *Oncogene* **2003**, *22*, 3998–4006. [[CrossRef](#)] [[PubMed](#)]
131. Wang, S.J.; Bourguignon, L.Y.W. Hyaluronan-CD44 promotes phospholipase C-mediated Ca²⁺ signaling and cisplatin resistance in head and neck cancer. *Arch. Otolaryngol. Head Neck Surg.* **2006**, *132*, 19–24. [[CrossRef](#)] [[PubMed](#)]
132. Speelmans, G.; Staffhorst, R.W.; Versluis, K.; Reedijk, J.; de Kruijff, B. Cisplatin complexes with phosphatidylserine in membranes. *Biochemistry* **1997**, *36*, 10545–10550. [[CrossRef](#)] [[PubMed](#)]
133. Huihui, Z.; Baohuai, W.; Youming, Z.; Kui, W. Calorimetric studies on actin polymerization and a comparison of the effects of cisplatin and transplatin. *Thermochim. Acta* **1995**, *265*, 31–38. [[CrossRef](#)]
134. Chen, X.; Jiang, Y.; Huang, Z.; Li, D.; Chen, X.; Cao, M.; Meng, Q.; Pang, H.; Sun, L.; Zhao, Y.; et al. miRNA-378 reverses chemoresistance to cisplatin in lung adenocarcinoma cells by targeting secreted clusterin. *Sci. Rep.* **2016**, *6*, 19455. [[CrossRef](#)] [[PubMed](#)]
135. Zhu, H.; Wu, H.; Liu, X.; Evans, B.R.; Medina, D.J.; Liu, C.-G.; Yang, J.-M. Role of MicroRNA miR-27a and miR-451 in the regulation of MDRL/P-glycoprotein expression in human cancer cells. *Biochem. Pharmacol.* **2008**, *76*, 582–588. [[CrossRef](#)] [[PubMed](#)]
136. Vanas, V.; Haigl, B.; Stockhammer, V.; Sutterlüty-Fall, H. MicroRNA-21 Increases Proliferation and Cisplatin Sensitivity of Osteosarcoma-Derived Cells. *PLoS ONE* **2016**, *11*, e0161023. [[CrossRef](#)] [[PubMed](#)]
137. Douple, E.B.; Richmond, R.C. Platinum complexes as radiosensitizers of hypoxic mammalian cells. *Br. J. Cancer Suppl.* **1978**, *3*, 98–102. [[PubMed](#)]
138. Boeckman, H.J.; Trego, K.S.; Turchi, J.J. Cisplatin sensitizes cancer cells to ionizing radiation via inhibition of nonhomologous end joining. *Mol. Cancer Res.* **2005**, *3*, 277–285. [[CrossRef](#)] [[PubMed](#)]
139. Ishibashi, T.; Lippard, S.J. Telomere loss in cells treated with cisplatin. *Proc. Natl. Acad. Sci. USA* **1998**, *95*, 4219–4223. [[CrossRef](#)] [[PubMed](#)]
140. Jordan, P.; Carmo-Fonseca, M. Cisplatin inhibits synthesis of ribosomal RNA in vivo. *Nucleic Acids Res.* **1998**, *26*, 2831–2836. [[CrossRef](#)] [[PubMed](#)]
141. Tofilon, P.J.; Vines, C.M.; Baker, F.L.; Deen, D.F.; Brock, W.A. *cis*-Diamminedichloroplatinum(II)-induced sister chromatid exchange: An indicator of sensitivity and heterogeneity in primary human tumor cell cultures. *Cancer Res.* **1986**, *46*, 6156–6159. [[PubMed](#)]
142. Berndtsson, M.; Hägg, M.; Panaretakis, T.; Havelka, A.M.; Shoshan, M.C.; Linder, S. Acute apoptosis by cisplatin requires induction of reactive oxygen species but is not associated with damage to nuclear DNA. *Int. J. Cancer* **2007**, *120*, 175–180. [[CrossRef](#)] [[PubMed](#)]
143. Rouette, A.; Parent, S.; Girouard, J.; Leblanc, V.; Asselin, E. Cisplatin increases B-cell-lymphoma-2 expression via activation of protein kinase C and Akt2 in endometrial cancer cells. *Int. J. Cancer* **2012**, *130*, 1755–1767. [[CrossRef](#)] [[PubMed](#)]
144. Damia, G.; Filiberti, L.; Vikhanskaya, F.; Carrassa, L.; Taya, Y.; D'incalci, M.; Broggin, M. Cisplatin and taxol induce different patterns of p53 phosphorylation. *Neoplasia* **2001**, *3*, 10–16. [[CrossRef](#)] [[PubMed](#)]
145. Lützkendorf, J.; Wieduwild, E.; Nerger, K.; Lambrecht, N.; Schmoll, H.-J.; Müller-Tidow, C.; Müller, L.P. Resistance for Genotoxic Damage in Mesenchymal Stromal Cells Is Increased by Hypoxia but Not Generally Dependent on p53-Regulated Cell Cycle Arrest. *PLoS ONE* **2017**, *12*, e0169921. [[CrossRef](#)] [[PubMed](#)]
146. Sorenson, C.M.; Barry, M.A.; Eastman, A. Analysis of events associated with cell cycle arrest at G2 phase and cell death induced by cisplatin. *J. Natl. Cancer Inst.* **1990**, *82*, 749–755. [[CrossRef](#)] [[PubMed](#)]
147. Podratz, J.L.; Knight, A.M.; Ta, L.E.; Staff, N.P.; Gass, J.M.; Genelin, K.; Schlattau, A.; Lathroum, L.; Windebanks, A.J. Cisplatin induced mitochondrial DNA damage in dorsal root ganglion neurons. *Neurobiol. Dis.* **2011**, *41*, 661–668. [[CrossRef](#)] [[PubMed](#)]
148. Wagner, J.M.; Karnitz, L.M. Cisplatin-induced DNA damage activates replication checkpoint signaling components that differentially affect tumor cell survival. *Mol. Pharmacol.* **2009**, *76*, 208–214. [[CrossRef](#)] [[PubMed](#)]
149. Bürkle, A.; Chen, G.; Küpper, J.H.; Grube, K.; Zeller, W.J. Increased poly(ADP-ribose)ation in intact cells by cisplatin treatment. *Carcinogenesis* **1993**, *14*, 559–561. [[CrossRef](#)] [[PubMed](#)]
150. Jennerwein, M.; Andrews, P.A. Drug accumulation and DNA platination in cells exposed to aquated cisplatin species. *Cancer Lett.* **1994**, *81*, 215–220. [[CrossRef](#)]

151. Shirazi, F.H.; Molepo, J.M.; Stewart, D.J.; Ng, C.E.; Raaphorst, G.P.; Goel, R. Cytotoxicity, accumulation, and efflux of cisplatin and its metabolites in human ovarian carcinoma cells. *Toxicol. Appl. Pharmacol.* **1996**, *140*, 211–218. [[CrossRef](#)] [[PubMed](#)]
152. Hall, M.D.; Telma, K.A.; Chang, K.-E.; Lee, T.D.; Madigan, J.P.; Lloyd, J.R.; Goldlust, I.S.; Hoeschele, J.D.; Gottesman, M.M. Say no to DMSO: Dimethylsulfoxide inactivates cisplatin, carboplatin, and other platinum complexes. *Cancer Res.* **2014**, *74*, 3913–3922. [[CrossRef](#)] [[PubMed](#)]
153. Available online: <http://www.webcitation.org/6mEemW8DM> (accessed on 23 November 2016).
154. Massart, C.; Le Tellier, C.; Gibassier, J.; Leclech, G.; Nicol, M. Modulation by dimethyl sulphoxide of the toxicity induced by cis-diamminedichloroplatinum in cultured thyrocytes. *Toxicol. Vitro* **1993**, *7*, 87–94. [[CrossRef](#)]
155. Wiltshaw, E.; Subramarian, S.; Alexopoulos, C.; Barker, G.H. Cancer of the ovary: A summary of experience with cis-dichlorodiammineplatinum(II) at the Royal Marsden Hospital. *Cancer Treat. Rep.* **1979**, *63*, 1545–1548. [[PubMed](#)]
156. Galanski, M. Recent developments in the field of anticancer platinum complexes. *Recent Pat. Anticancer Drug Discov.* **2006**, *1*, 285–295. [[CrossRef](#)] [[PubMed](#)]
157. Lebwohl, D.; Canetta, R. Clinical development of platinum complexes in cancer therapy: An historical perspective and an update. *Eur. J. Cancer* **1998**, *34*, 1522–1534. [[CrossRef](#)]
158. Baetz, T.; Belch, A.; Couban, S.; Imrie, K.; Yau, J.; Myers, R.; Ding, K.; Paul, N.; Shepherd, L.; Iglesias, J.; et al. Gemcitabine, dexamethasone and cisplatin is an active and non-toxic chemotherapy regimen in relapsed or refractory Hodgkin's disease: A phase II study by the National Cancer Institute of Canada Clinical Trials Group. *Ann. Oncol.* **2003**, *14*, 1762–1767. [[CrossRef](#)] [[PubMed](#)]
159. Crump, M.; Baetz, T.; Couban, S.; Belch, A.; Marcellus, D.; Howson-Jan, K.; Imrie, K.; Myers, R.; Adams, G.; Ding, K.; et al. Gemcitabine, dexamethasone, and cisplatin in patients with recurrent or refractory aggressive histology B-cell non-Hodgkin lymphoma: A Phase II study by the National Cancer Institute of Canada Clinical Trials Group (NCIC-CTG). *Cancer* **2004**, *101*, 1835–1842. [[CrossRef](#)] [[PubMed](#)]
160. Pearson, A.D.J.; Pinkerton, C.R.; Lewis, I.J.; Imeson, J.; Ellershaw, C.; Machin, D.; European Neuroblastoma Study Group; Children's Cancer and Leukaemia Group (CCLG formerly United Kingdom Children's Cancer Study Group). High-dose rapid and standard induction chemotherapy for patients aged over 1 year with stage 4 neuroblastoma: A randomised trial. *Lancet Oncol.* **2008**, *9*, 247–256. [[PubMed](#)]
161. Reichardt, P. The treatment of uterine sarcomas. *Ann. Oncol.* **2012**, *23* (Suppl. S10), x151–x157. [[CrossRef](#)] [[PubMed](#)]
162. Dadacaridou, M.; Papanicolaou, X.; Maltesas, D.; Megalakaki, C.; Patos, P.; Panteli, K.; Repousis, P.; Mitsouli-Mentzikof, C. Dexamethasone, cyclophosphamide, etoposide and cisplatin (DCEP) for relapsed or refractory multiple myeloma patients. *J. BUON* **2007**, *12*, 41–44. [[PubMed](#)]
163. Glover, D.; Glick, J.H.; Weiler, C.; Fox, K.; Guerry, D. WR-2721 and high-dose cisplatin: An active combination in the treatment of metastatic melanoma. *J. Clin. Oncol.* **1987**, *5*, 574–578. [[PubMed](#)]
164. Berghmans, T.; Paesmans, M.; Lalami, Y.; Louviaux, I.; Luce, S.; Mascaux, C.; Meert, A.P.; Sculier, J.P. Activity of chemotherapy and immunotherapy on malignant mesothelioma: A systematic review of the literature with meta-analysis. *Lung Cancer* **2002**, *38*, 111–121. [[CrossRef](#)]
165. Hanada, K.; Nishijima, K.; Ogata, H.; Atagi, S.; Kawahara, M. Population pharmacokinetic analysis of cisplatin and its metabolites in cancer patients: Possible misinterpretation of covariates for pharmacokinetic parameters calculated from the concentrations of unchanged cisplatin, ultrafiltered platinum and total platinum. *Jpn. J. Clin. Oncol.* **2001**, *31*, 179–184. [[PubMed](#)]
166. Daugaard, G.; Abildgaard, U. Cisplatin nephrotoxicity. A review. *Cancer Chemother. Pharmacol.* **1989**, *25*, 1–9. [[CrossRef](#)] [[PubMed](#)]
167. Nagai, N.; Kinoshita, M.; Ogata, H.; Tsujino, D.; Wada, Y.; Someya, K.; Ohno, T.; Masuhara, K.; Tanaka, Y.; Kato, K.; et al. Relationship between pharmacokinetics of unchanged cisplatin and nephrotoxicity after intravenous infusions of cisplatin to cancer patients. *Cancer Chemother. Pharmacol.* **1996**, *39*, 131–137. [[CrossRef](#)] [[PubMed](#)]
168. Kartalou, M.; Essigmann, J.M. Mechanisms of resistance to cisplatin. *Mutat. Res.* **2001**, *478*, 23–43. [[CrossRef](#)]
169. Olszewski, U.; Hamilton, G. A better platinum-based anticancer drug yet to come? *Anticancer Agents Med. Chem.* **2010**, *10*, 293–301. [[CrossRef](#)] [[PubMed](#)]

170. Dieras, V.; Girre, V.; Guilhaume, M.-N.; Laurence, V.; Mignot, L. Oxaliplatin and ovarian cancer. *Bull. Cancer* **2006**, *93* (Suppl. S1), S35–S39. [PubMed]
171. Ganjavi, H.; Gee, M.; Narendran, A.; Parkinson, N.; Krishnamoorthy, M.; Freedman, M.H.; Malkin, D. Adenovirus-mediated p53 gene therapy in osteosarcoma cell lines: Sensitization to cisplatin and doxorubicin. *Cancer Gene Ther.* **2006**, *13*, 415–419. [CrossRef] [PubMed]
172. Michels, J.; Vitale, I.; Senovilla, L.; Enot, D.P.; Garcia, P.; Lissa, D.; Olausson, K.A.; Brenner, C.; Soria, J.-C.; Castedo, M.; et al. Synergistic interaction between cisplatin and PARP inhibitors in non-small cell lung cancer. *Cell Cycle* **2013**, *12*, 877–883. [CrossRef] [PubMed]
173. Balmaña, J.; Tung, N.M.; Isakoff, S.J.; Graña, B.; Ryan, P.D.; Saura, C.; Lowe, E.S.; Frewer, P.; Winer, E.; Baselga, J.; et al. Phase I trial of olaparib in combination with cisplatin for the treatment of patients with advanced breast, ovarian and other solid tumors. *Ann. Oncol.* **2014**, *25*, 1656–1663. [CrossRef] [PubMed]
174. Sorenson, C.M.; Eastman, A. Influence of *cis*-diamminedichloroplatinum(II) on DNA synthesis and cell cycle progression in excision repair proficient and deficient Chinese hamster ovary cells. *Cancer Res.* **1988**, *48*, 6703–6707. [PubMed]
175. Vichi, P.; Coin, F.; Renaud, J.P.; Vermeulen, W.; Hoeijmakers, J.H.; Moras, D.; Egly, J.M. Cisplatin- and UV-damaged DNA lure the basal transcription factor TFIID/TBP. *EMBO J.* **1997**, *16*, 7444–7456. [CrossRef] [PubMed]
176. Cullinane, C.; Mazur, S.J.; Essigmann, J.M.; Phillips, D.R.; Bohr, V.A. Inhibition of RNA polymerase II transcription in human cell extracts by cisplatin DNA damage. *Biochemistry* **1999**, *38*, 6204–6212. [CrossRef] [PubMed]
177. Kumar, S.; Kumar, A.; Shah, P.P.; Rai, S.N.; Panguluri, S.K.; Kakar, S.S. MicroRNA signature of *cis*-platin resistant vs. *cis*-platin sensitive ovarian cancer cell lines. *J. Ovarian Res.* **2011**, *4*, 17. [PubMed]
178. Ciarimboli, G.; Ludwig, T.; Lang, D.; Pavenstädt, H.; Koepsell, H.; Piechota, H.-J.; Haier, J.; Jaehde, U.; Zisowsky, J.; Schlatter, E. Cisplatin nephrotoxicity is critically mediated via the human organic cation transporter 2. *Am. J. Pathol.* **2005**, *167*, 1477–1484. [CrossRef]
179. Gressette, M.; Vérylaud, B.; Jimenez-Pailhès, A.-S.; Lelièvre, H.; Lo, K.-W.; Ferrand, F.-R.; Gattolliat, C.-H.; Jacquet-Bescond, A.; Kraus-Berthier, L.; Depil, S.; et al. Treatment of Nasopharyngeal Carcinoma Cells with the Histone-Deacetylase Inhibitor Abexinostat: Cooperative Effects with Cis-platin and Radiotherapy on Patient-Derived Xenografts. *PLoS ONE* **2014**, *9*, e91325. [CrossRef] [PubMed]
180. Rout, S.R.; Behera, B.; Maiti, T.K.; Mohapatra, S. Multifunctional magnetic calcium phosphate nanoparticles for targeted platin delivery. *Dalton Trans.* **2012**, *41*, 10777–10783. [CrossRef] [PubMed]
181. Kitao, H.; Takata, M. Fanconi anemia: A disorder defective in the DNA damage response. *Int. J. Hematol.* **2011**, *93*, 417–424. [CrossRef] [PubMed]
182. Sawant, A.; Kothandapani, A.; Zhitkovich, A.; Sobol, R.W.; Patrick, S.M. Role of mismatch repair proteins in the processing of cisplatin interstrand cross-links. *DNA Repair* **2015**, *35*, 126–136. [CrossRef] [PubMed]
183. Cheng, C.H.; Kuchta, R.D. DNA polymerase epsilon: Aphidicolin inhibition and the relationship between polymerase and exonuclease activity. *Biochemistry* **1993**, *32*, 8568–8574. [CrossRef] [PubMed]
184. Pedrali-Noy, G.; Spadari, S.; Miller-Faurès, A.; Miller, A.O.; Kruppa, J.; Koch, G. Synchronization of HeLa cell cultures by inhibition of DNA polymerase alpha with aphidicolin. *Nucleic Acids Res.* **1980**, *8*, 377–387. [CrossRef] [PubMed]
185. Baranovskiy, A.G.; Babayeva, N.D.; Suwa, Y.; Gu, J.; Pavlov, Y.I.; Tahirov, T.H. Structural basis for inhibition of DNA replication by aphidicolin. *Nucleic Acids Res.* **2014**, *42*, 14013–14021. [CrossRef] [PubMed]
186. Spadari, S.; Pedrali-Noy, G.; Falaschi, M.C.; Ciarrocchi, G. Control of DNA replication and cell proliferation in eukaryotes by aphidicolin. *Toxicol. Pathol.* **1984**, *12*, 143–148. [CrossRef] [PubMed]
187. Available online: <http://www.rcsb.org/pdb/explore/explore.do?structureId=4Q5V> (accessed on 23 January 2017).
188. Chang, D.J.; Lupardus, P.J.; Cimprich, K.A. Monoubiquitination of proliferating cell nuclear antigen induced by stalled replication requires uncoupling of DNA polymerase and mini-chromosome maintenance helicase activities. *J. Biol. Chem.* **2006**, *281*, 32081–32088. [CrossRef] [PubMed]
189. Sutherland, G.R. Chromosomal fragile sites. *Genet. Anal. Tech. Appl.* **1991**, *8*, 161–166. [CrossRef]
190. Shiraiishi, T.; Druck, T.; Mimori, K.; Flomenberg, J.; Berk, L.; Alder, H.; Miller, W.; Huebner, K.; Croce, C.M. Sequence conservation at human and mouse orthologous common fragile regions, FRA3B/FHIT and Fra14A2/Fhit. *Proc. Natl. Acad. Sci. USA* **2001**, *98*, 5722–5727. [CrossRef] [PubMed]

191. Hellman, A.; Zlotorynski, E.; Scherer, S.W.; Cheung, J.; Vincent, J.B.; Smith, D.I.; Trakhtenbrot, L.; Kerem, B. A role for common fragile site induction in amplification of human oncogenes. *Cancer Cell* **2002**, *1*, 89–97. [[CrossRef](#)]
192. Durkin, S.G.; Ragland, R.L.; Arlt, M.F.; Mulle, J.G.; Warren, S.T.; Glover, T.W. Replication stress induces tumor-like microdeletions in FHIT/FRA3B. *Proc. Natl. Acad. Sci. USA* **2008**, *105*, 246–251. [[CrossRef](#)] [[PubMed](#)]
193. Bristow, R.G.; Hill, R.P. Hypoxia and metabolism. Hypoxia, DNA repair and genetic instability. *Nat. Rev. Cancer* **2008**, *8*, 180–192. [[CrossRef](#)] [[PubMed](#)]
194. MacGregor, J.T.; Schlegel, R.; Wehr, C.M.; Alperin, P.; Ames, B.N. Cytogenetic damage induced by folate deficiency in mice is enhanced by caffeine. *Proc. Natl. Acad. Sci. USA* **1990**, *87*, 9962–9965. [[CrossRef](#)] [[PubMed](#)]
195. Koundrioukoff, S.; Carignon, S.; Técher, H.; Letessier, A.; Brison, O.; Debatisse, M. Stepwise activation of the ATR signaling pathway upon increasing replication stress impacts fragile site integrity. *PLoS Genet.* **2013**, *9*, e1003643. [[CrossRef](#)] [[PubMed](#)]
196. Helmrich, A.; Ballarino, M.; Tora, L. Collisions between replication and transcription complexes cause common fragile site instability at the longest human genes. *Mol. Cell* **2011**, *44*, 966–977. [[CrossRef](#)] [[PubMed](#)]
197. Di Micco, R.; Fumagalli, M.; Cicalese, A.; Piccinin, S.; Gasparini, P.; Luise, C.; Schurra, C.; Garre', M.; Nuciforo, P.G.; Bensimon, A.; et al. Oncogene-induced senescence is a DNA damage response triggered by DNA hyper-replication. *Nature* **2006**, *444*, 638–642. [[CrossRef](#)]
198. Cha, R.S.; Kleckner, N. ATR homolog Mec1 promotes fork progression, thus averting breaks in replication slow zones. *Science* **2002**, *297*, 602–606. [[CrossRef](#)] [[PubMed](#)]
199. Arlt, M.F.; Mulle, J.G.; Schaibley, V.M.; Ragland, R.L.; Durkin, S.G.; Warren, S.T.; Glover, T.W. Replication stress induces genome-wide copy number changes in human cells that resemble polymorphic and pathogenic variants. *Am. J. Hum. Genet.* **2009**, *84*, 339–350. [[CrossRef](#)] [[PubMed](#)]
200. Hardt, N.; Pedrali-Noy, G.; Foher, F.; Spadari, S. Aphidicolin does not inhibit DNA repair synthesis in ultraviolet-irradiated HeLa cells. A radioautographic study. *Biochem. J.* **1981**, *199*, 453–455. [[CrossRef](#)] [[PubMed](#)]
201. Pedrali-Noy, G.; Belvedere, M.; Crepaldi, T.; Foher, F.; Spadari, S. Inhibition of DNA replication and growth of several human and murine neoplastic cells by aphidicolin without detectable effect upon synthesis of immunoglobulins and HLA antigens. *Cancer Res.* **1982**, *42*, 3810–3813. [[PubMed](#)]
202. Gera, J.F.; Fady, C.; Gardner, A.; Jacoby, F.J.; Briskin, K.B.; Lichtenstein, A. Inhibition of DNA repair with aphidicolin enhances sensitivity of targets to tumor necrosis factor. *J. Immunol.* **1993**, *151*, 3746–3757. [[PubMed](#)]
203. Waters, R. Aphidicolin: An inhibitor of DNA repair in human fibroblasts. *Carcinogenesis* **1981**, *2*, 795–797. [[CrossRef](#)] [[PubMed](#)]
204. Wang, F.; Stewart, J.; Price, C.M. Human CST abundance determines recovery from diverse forms of DNA damage and replication stress. *Cell Cycle* **2014**, *13*, 3488–3498. [[CrossRef](#)] [[PubMed](#)]
205. Yeo, J.E.; Lee, E.H.; Hendrickson, E.A.; Sobock, A. CtIP mediates replication fork recovery in a FANCD2-regulated manner. *Hum. Mol. Genet.* **2014**, *23*, 3695–3705. [[CrossRef](#)] [[PubMed](#)]
206. Chaudhury, I.; Stroik, D.R.; Sobock, A. FANCD2-controlled chromatin access of the Fanconi-associated nuclease FAN1 is crucial for the recovery of stalled replication forks. *Mol. Cell. Biol.* **2014**, *34*, 3939–3954. [[CrossRef](#)] [[PubMed](#)]
207. Hammond, E.M.; Green, S.L.; Giaccia, A.J. Comparison of hypoxia-induced replication arrest with hydroxyurea and aphidicolin-induced arrest. *Mutat. Res.* **2003**, *532*, 205–213. [[CrossRef](#)] [[PubMed](#)]
208. Borel, F.; Lacroix, F.B.; Margolis, R.L. Prolonged arrest of mammalian cells at the G1/S boundary results in permanent S phase stasis. *J. Cell Sci.* **2002**, *115*, 2829–2838. [[PubMed](#)]
209. Basile, G.; Leuzzi, G.; Pichierri, P.; Franchitto, A. Checkpoint-dependent and independent roles of the Werner syndrome protein in preserving genome integrity in response to mild replication stress. *Nucleic Acids Res.* **2014**, *42*, 12628–12639. [[CrossRef](#)] [[PubMed](#)]
210. Nguyen, G.H.; Dexheimer, T.S.; Rosenthal, A.S.; Chu, W.K.; Singh, D.K.; Mosedale, G.; Bachrati, C.Z.; Schultz, L.; Sakurai, M.; Savitsky, P.; et al. A small molecule inhibitor of the BLM helicase modulates chromosome stability in human cells. *Chem. Biol.* **2013**, *20*, 55–62. [[CrossRef](#)] [[PubMed](#)]

211. Schmidt, L.; Wiedner, M.; Velimezi, G.; Prochazkova, J.; Owusu, M.; Bauer, S.; Loizou, J.I. ATMIN is required for the ATM-mediated signaling and recruitment of 53BP1 to DNA damage sites upon replication stress. *DNA Repair* **2014**, *24*, 122–130. [CrossRef] [PubMed]
212. Fujita, M.; Sasanuma, H.; Yamamoto, K.N.; Harada, H.; Kurosawa, A.; Adachi, N.; Omura, M.; Hiraoka, M.; Takeda, S.; Hirota, K. Interference in DNA replication can cause mitotic chromosomal breakage unassociated with double-strand breaks. *PLoS ONE* **2013**, *8*, e60043. [CrossRef] [PubMed]
213. Beresova, L.; Vesela, E.; Chamrad, I.; Voller, J.; Yamada, M.; Furst, T.; Lenobel, R.; Chroma, K.; Gursky, J.; Krizova, K.; et al. Role of DNA Repair Factor Xeroderma Pigmentosum Protein Group C in Response to Replication Stress As Revealed by DNA Fragile Site Affinity Chromatography and Quantitative Proteomics. *J. Proteome Res.* **2016**, *15*, 4505–4517. [CrossRef] [PubMed]
214. Janson, C.; Nyhan, K.; Murnane, J.P. Replication Stress and Telomere Dysfunction Are Present in Cultured Human Embryonic Stem Cells. *Cytogenet. Genome Res.* **2015**, *146*, 251–260. [CrossRef] [PubMed]
215. Miron, K.; Golan-Lev, T.; Dvir, R.; Ben-David, E.; Kerem, B. Oncogenes create a unique landscape of fragile sites. *Nat. Commun.* **2015**, *6*, 7094. [CrossRef] [PubMed]
216. Murfun, I.; De Santis, A.; Federico, M.; Bignami, M.; Pichierri, P.; Franchitto, A. Perturbed replication induced genome wide or at common fragile sites is differently managed in the absence of WRN. *Carcinogenesis* **2012**, *33*, 1655–1663. [CrossRef] [PubMed]
217. Wilhelm, T.; Magdalou, L.; Barascu, A.; Técher, H.; Debatisse, M.; Lopez, B.S. Spontaneous slow replication fork progression elicits mitosis alterations in homologous recombination-deficient mammalian cells. *Proc. Natl. Acad. Sci. USA* **2014**, *111*, 763–768. [CrossRef] [PubMed]
218. Available online: https://www.google.cz/url?sa=t&rct=j&q=&esrc=s&source=web&cd=3&cad=rja&uact=8&ved=0ahUKEwibvoX5jL_QAhULVSwKHQfLCXwQFggsMAI&url=https%3A%2F%2Fwww.sigmaaldrich.com%2Fcontent%2Fdam%2Fsigma-aldrich%2Fdocs%2FSigma%2FDataSheet%2F6%2Fa0781dat.pdf&usq=AFQjCNEPSqAi (accessed on 23 November 2016).
219. Sessa, C.; Zucchetti, M.; Davoli, E.; Califano, R.; Cavalli, F.; Frustaci, S.; Gumbrell, L.; Sulkes, A.; Winograd, B.; D'Incalci, M. Phase I and clinical pharmacological evaluation of aphidicolin glycinate. *J. Natl. Cancer Inst.* **1991**, *83*, 1160–1164. [CrossRef] [PubMed]
220. Edelson, R.E.; Gorycki, P.D.; MacDonald, T.L. The mechanism of aphidicolin bioinactivation by rat liver in vitro systems. *Xenobiotica* **1990**, *20*, 273–287. [CrossRef] [PubMed]
221. Santos, G.B.; Krogh, R.; Magalhaes, L.G.; Andricopulo, A.D.; Pupo, M.T.; Emery, F.S. Semisynthesis of new aphidicolin derivatives with high activity against *Trypanosoma cruzi*. *Bioorg. Med. Chem. Lett.* **2016**, *26*, 1205–1208. [CrossRef] [PubMed]
222. Glover, T.W.; Berger, C.; Coyle, J.; Echo, B. DNA polymerase alpha inhibition by aphidicolin induces gaps and breaks at common fragile sites in human chromosomes. *Hum. Genet.* **1984**, *67*, 136–142. [CrossRef] [PubMed]
223. Kurose, A.; Tanaka, T.; Huang, X.; Traganos, F.; Darzynkiewicz, Z. Synchronization in the cell cycle by inhibitors of DNA replication induces histone H2AX phosphorylation: An indication of DNA damage. *Cell Prolif.* **2006**, *39*, 231–240. [CrossRef] [PubMed]
224. Trenz, K.; Smith, E.; Smith, S.; Costanzo, V. ATM and ATR promote Mre11 dependent restart of collapsed replication forks and prevent accumulation of DNA breaks. *EMBO J.* **2006**, *25*, 1764–1774. [CrossRef] [PubMed]
225. Krakoff, I.H.; Brown, N.C.; Reichard, P. Inhibition of ribonucleoside diphosphate reductase by hydroxyurea. *Cancer Res.* **1968**, *28*, 1559–1565. [PubMed]
226. Reichard, P. Interactions between deoxyribonucleotide and DNA synthesis. *Annu. Rev. Biochem.* **1988**, *57*, 349–374. [CrossRef] [PubMed]
227. Håkansson, P.; Hofer, A.; Thelander, L. Regulation of mammalian ribonucleotide reduction and dNTP pools after DNA damage and in resting cells. *J. Biol. Chem.* **2006**, *281*, 7834–7841. [CrossRef] [PubMed]
228. Eriksson, M.; Uhlin, U.; Ramaswamy, S.; Ekberg, M.; Regnström, K.; Sjöberg, B.M.; Eklund, H. Binding of allosteric effectors to ribonucleotide reductase protein R1: Reduction of active-site cysteines promotes substrate binding. *Structure* **1997**, *5*, 1077–1092. [CrossRef]
229. Bianchi, V.; Pontis, E.; Reichard, P. Changes of deoxyribonucleoside triphosphate pools induced by hydroxyurea and their relation to DNA synthesis. *J. Biol. Chem.* **1986**, *261*, 16037–16042. [PubMed]

230. Skog, S.; Tribukait, B.; Wallström, B.; Eriksson, S. Hydroxyurea-induced cell death as related to cell cycle in mouse and human T-lymphoma cells. *Cancer Res.* **1987**, *47*, 6490–6493. [[PubMed](#)]
231. Akerblom, L. Azidocytidine is incorporated into RNA of 3T6 mouse fibroblasts. *FEBS Lett.* **1985**, *193*, 203–207. [[CrossRef](#)]
232. Anglana, M.; Apiou, F.; Bensimon, A.; Debatisse, M. Dynamics of DNA replication in mammalian somatic cells: Nucleotide pool modulates origin choice and interorigin spacing. *Cell* **2003**, *114*, 385–394. [[CrossRef](#)]
233. Barlow, J.H.; Faryabi, R.B.; Callén, E.; Wong, N.; Malhowski, A.; Chen, H.T.; Gutierrez-Cruz, G.; Sun, H.-W.; McKinnon, P.; Wright, G.; et al. Identification of early replicating fragile sites that contribute to genome instability. *Cell* **2013**, *152*, 620–632. [[CrossRef](#)] [[PubMed](#)]
234. Lönn, U.; Lönn, S. Extensive regions of single-stranded DNA in aphidicolin-treated melanoma cells. *Biochemistry* **1988**, *27*, 566–570. [[CrossRef](#)] [[PubMed](#)]
235. Recolin, B.; Van der Laan, S.; Maiorano, D. Role of replication protein A as sensor in activation of the S-phase checkpoint in *Xenopus* egg extracts. *Nucleic Acids Res.* **2012**, *40*, 3431–3442. [[CrossRef](#)] [[PubMed](#)]
236. Arlt, M.F.; Ozdemir, A.C.; Birkeland, S.R.; Wilson, T.E.; Glover, T.W. Hydroxyurea induces de novo copy number variants in human cells. *Proc. Natl. Acad. Sci. USA* **2011**, *108*, 17360–17365. [[CrossRef](#)] [[PubMed](#)]
237. Huang, M.-E.; Facca, C.; Fatmi, Z.; Baille, D.; Bénakli, S.; Vernis, L. DNA replication inhibitor hydroxyurea alters Fe-S centers by producing reactive oxygen species in vivo. *Sci. Rep.* **2016**, *6*, 29361. [[CrossRef](#)] [[PubMed](#)]
238. Szikriszt, B.; Póti, Á.; Pipek, O.; Krzystanek, M.; Kanu, N.; Molnár, J.; Ribli, D.; Szeltner, Z.; Tusnády, G.E.; Csabai, I.; et al. A comprehensive survey of the mutagenic impact of common cancer cytotoxics. *Genome Biol.* **2016**, *17*, 99. [[CrossRef](#)] [[PubMed](#)]
239. Mistrik, M.; Oplustilova, L.; Lukas, J.; Bartek, J. Low-dose DNA damage and replication stress responses quantified by optimized automated single-cell image analysis. *Cell Cycle* **2009**, *8*, 2592–2599. [[CrossRef](#)] [[PubMed](#)]
240. Ohou, P.Y.; Bastos de Oliveira, F.M.; Liu, Y.; Ma, C.J.; Smolka, M.B. DNA-repair scaffolds dampen checkpoint signalling by counteracting the adaptor Rad9. *Nature* **2013**, *493*, 120–124. [[CrossRef](#)] [[PubMed](#)]
241. Morafrail, E.C.; Diffley, J.F.X.; Tercero, J.A.; Segurado, M. Checkpoint-dependent RNR induction promotes fork restart after replicative stress. *Sci. Rep.* **2015**, *5*, 7886. [[CrossRef](#)] [[PubMed](#)]
242. Kim, H.-S.; Kim, S.-K.; Hromas, R.; Lee, S.-H. The SET Domain Is Essential for Metnase Functions in Replication Restart and the 5' End of SS-Overhang Cleavage. *PLoS ONE* **2015**, *10*, e0139418. [[CrossRef](#)] [[PubMed](#)]
243. Masuda, T.; Xu, X.; Dimitriadis, E.K.; Lahusen, T.; Deng, C.-X. “DNA Binding Region” of BRCA1 Affects Genetic Stability through modulating the Intra-S-Phase Checkpoint. *Int. J. Biol. Sci.* **2016**, *12*, 133–143. [[CrossRef](#)] [[PubMed](#)]
244. Yarden, R.I.; Metsuyanin, S.; Pickholtz, I.; Shabbeer, S.; Tellio, H.; Papa, M.Z. BRCA1-dependent Chk1 phosphorylation triggers partial chromatin disassociation of phosphorylated Chk1 and facilitates S-phase cell cycle arrest. *Int. J. Biochem. Cell Biol.* **2012**, *44*, 1761–1769. [[CrossRef](#)] [[PubMed](#)]
245. Awate, S.; De Benedetti, A. TLK1B mediated phosphorylation of Rad9 regulates its nuclear/cytoplasmic localization and cell cycle checkpoint. *BMC Mol. Biol.* **2016**, *17*, 3. [[CrossRef](#)] [[PubMed](#)]
246. Ahlskog, J.K.; Larsen, B.D.; Achanta, K.; Sørensen, C.S. ATM/ATR-mediated phosphorylation of PALB2 promotes RAD51 function. *EMBO Rep.* **2016**, *17*, 671–681. [[CrossRef](#)] [[PubMed](#)]
247. Molina, B.; Marchetti, F.; Gómez, L.; Ramos, S.; Torres, L.; Ortiz, R.; Altamirano-Lozano, M.; Carnevale, A.; Frias, S. Hydroxyurea induces chromosomal damage in G2 and enhances the clastogenic effect of mitomycin C in Fanconi anemia cells. *Environ. Mol. Mutagen.* **2015**, *56*, 457–467. [[CrossRef](#)] [[PubMed](#)]
248. Croke, M.; Neumann, M.A.; Grotsky, D.A.; Kreienkamp, R.; Yaddanapudi, S.C.; Gonzalo, S. Differences in 53BP1 and BRCA1 regulation between cycling and non-cycling cells. *Cell Cycle* **2013**, *12*, 3629–3639. [[CrossRef](#)] [[PubMed](#)]
249. Yamada, M.; Watanabe, K.; Mistrik, M.; Vesela, E.; Protivankova, I.; Mailand, N.; Lee, M.; Masai, H.; Lukas, J.; Bartek, J. ATR-Chk1-APC/CCdh1-dependent stabilization of Cdc7-ASK (Dbf4) kinase is required for DNA lesion bypass under replication stress. *Genes Dev.* **2013**, *27*, 2459–2472. [[CrossRef](#)] [[PubMed](#)]
250. Hu, L.; Kim, T.M.; Son, M.Y.; Kim, S.-A.; Holland, C.L.; Tateishi, S.; Kim, D.H.; Yew, P.R.; Montagna, C.; Dumitriche, L.C.; et al. Two replication fork maintenance pathways fuse inverted repeats to rearrange chromosomes. *Nature* **2013**, *501*, 569–572. [[CrossRef](#)] [[PubMed](#)]

251. Lou, T.-F.; Singh, M.; Mackie, A.; Li, W.; Pace, B.S. Hydroxyurea generates nitric oxide in human erythroid cells: Mechanisms for gamma-globin gene activation. *Exp. Biol. Med.* **2009**, *234*, 1374–1382. [CrossRef] [PubMed]
252. Vassileva, I.; Yanakieva, I.; Peycheva, M.; Gospodinov, A.; Anachkova, B. The mammalian INO80 chromatin remodeling complex is required for replication stress recovery. *Nucleic Acids Res.* **2014**, *42*, 9074–9086. [CrossRef] [PubMed]
253. Park, J.I.; Choi, H.S.; Jeong, J.S.; Han, J.Y.; Kim, I.H. Involvement of p38 kinase in hydroxyurea-induced differentiation of K562 cells. *Cell Growth Differ.* **2001**, *12*, 481–486. [PubMed]
254. Barthelemy, J.; Hanenberg, H.; Leffak, M. FANCI is essential to maintain microsatellite structure genome-wide during replication stress. *Nucleic Acids Res.* **2016**, *44*, 6803–6816. [CrossRef] [PubMed]
255. Kunnev, D.; Rusiniak, M.E.; Kudla, A.; Freeland, A.; Cady, G.K.; Pruitt, S.C. DNA damage response and tumorigenesis in Mcm2-deficient mice. *Oncogene* **2010**, *29*, 3630–3638. [CrossRef] [PubMed]
256. Da Guarda, C.C.; Santiago, R.P.; Pitanga, T.N.; Santana, S.S.; Zanette, D.L.; Borges, V.M.; Goncalves, M.S. Heme changes HIF- α , eNOS and nitrite production in HUVECs after simvastatin, HU, and ascorbic acid therapies. *Microvasc. Res.* **2016**, *106*, 128–136. [CrossRef] [PubMed]
257. Leitch, C.; Osdal, T.; Andresen, V.; Molland, M.; Kristiansen, S.; Nguyen, X.N.; Bruserud, Ø.; Gjertsen, B.T.; McCormack, E. Hydroxyurea synergizes with valproic acid in wild-type p53 acute myeloid leukaemia. *Oncotarget* **2016**, *7*, 8105–8118. [PubMed]
258. Liu, K.; Graves, J.D.; Scott, J.D.; Li, R.; Lin, W.-C. Akt switches TopBP1 function from checkpoint activation to transcriptional regulation through phosphoserine binding-mediated oligomerization. *Mol. Cell. Biol.* **2013**, *33*, 4685–4700. [CrossRef] [PubMed]
259. Available online: https://www.google.cz/url?sa=t&rc=1&q=&esrc=s&source=web&cd=3&cad=rja&uact=8&ved=0ahUKewiVt4Lulb_QAhUBGSwKHbcOB_kQFggsMAI&url=https%3A%2F%2Fwww.sigmaaldrich.com%2Fcontent%2Fdam%2Fsigma-aldrich%2Fdocs%2FSigma%2FProduct_Information_Sheet%2F%2Fh8627pis.pdf& (accessed on 23 January 2017).
260. Segal, J.B.; Strouse, J.J.; Beach, M.C.; Haywood, C.; Witkop, C.; Park, H.; Wilson, R.F.; Bass, E.B.; Lanzkron, S. *Hydroxyurea for the Treatment of Sickle Cell Disease*; Evidence Reports/Technology Assessments; Agency for Healthcare Research and Quality (US): Rockville, MD, USA, 2008; pp. 1–95.
261. Kühn, T.; Burgstaller, S.; Apfelbeck, U.; Linkesch, W.; Seewann, H.; Fridrik, M.; Michlmayr, G.; Krieger, O.; Lutz, D.; Lin, W.; et al. A randomized study comparing interferon (IFN α) plus low-dose cytarabine and interferon plus hydroxyurea (HU) in early chronic-phase chronic myeloid leukemia (CML). *Leuk. Res.* **2003**, *27*, 405–411. [CrossRef]
262. Aruch, D.; Mascarenhas, J. Contemporary approach to essential thrombocythemia and polycythemia vera. *Curr. Opin. Hematol.* **2016**, *23*, 150–160. [CrossRef] [PubMed]
263. Barbui, T.; Finazzi, M.C.; Finazzi, G. Front-line therapy in polycythemia vera and essential thrombocythemia. *Blood Rev.* **2012**, *26*, 205–211. [CrossRef] [PubMed]
264. Benito, J.M.; López, M.; Lozano, S.; Ballesteros, C.; González-Lahoz, J.; Soriano, V. Hydroxyurea exerts an anti-proliferative effect on T cells but has no direct impact on cellular activation. *Clin. Exp. Immunol.* **2007**, *149*, 171–177. [CrossRef] [PubMed]
265. Gurberg, J.; Bouganim, N.; Shenouda, G.; Zeitouni, A. A case of recurrent anaplastic meningioma of the skull base with radiologic response to hydroxyurea. *J. Neurol. Surg. Rep.* **2014**, *75*, e52–e55. [CrossRef] [PubMed]
266. Kiladjian, J.-J.; Chevret, S.; Dosquet, C.; Chomienne, C.; Rain, J.-D. Treatment of polycythemia vera with hydroxyurea and pipobroman: Final results of a randomized trial initiated in 1980. *J. Clin. Oncol.* **2011**, *29*, 3907–3913. [CrossRef] [PubMed]
267. Charache, S.; Barton, F.B.; Moore, R.D.; Terrin, M.L.; Steinberg, M.H.; Dover, G.J.; Ballas, S.K.; McMahon, R.P.; Castro, O.; Orringer, E.P. Hydroxyurea and sickle cell anemia. Clinical utility of a myelosuppressive “switching” agent. The Multicenter Study of Hydroxyurea in Sickle Cell Anemia. *Medicine* **1996**, *75*, 300–326. [CrossRef] [PubMed]
268. Steinberg, M.H.; McCarthy, W.F.; Castro, O.; Ballas, S.K.; Armstrong, F.D.; Smith, W.; Ataga, K.; Swerdlow, P.; Kutlar, A.; DeCastro, L.; et al. The risks and benefits of long-term use of hydroxyurea in sickle cell anemia: A 17.5 year follow-up. *Am. J. Hematol.* **2010**, *85*, 403–408. [CrossRef] [PubMed]

269. Darzynkiewicz, Z.; Halicka, H.D.; Zhao, H.; Podhorecka, M. Cell synchronization by inhibitors of DNA replication induces replication stress and DNA damage response: Analysis by flow cytometry. *Methods Mol. Biol.* **2011**, *761*, 85–96. [PubMed]
270. Fugger, K.; Mistrik, M.; Danielsen, J.R.; Dinant, C.; Falck, J.; Bartek, J.; Lukas, J.; Mailand, N. Human Fbh1 helicase contributes to genome maintenance via pro- and anti-recombinase activities. *J. Cell Biol.* **2009**, *186*, 655–663. [CrossRef] [PubMed]
271. Liu, N.; Lim, C.-S. Differential roles of XRCC2 in homologous recombinational repair of stalled replication forks. *J. Cell. Biochem.* **2005**, *95*, 942–954. [CrossRef] [PubMed]
272. Brose, R.D.; Shin, G.; McGuinness, M.C.; Schneidereith, T.; Purvis, S.; Dong, G.X.; Keefer, J.; Spencer, F.; Smith, K.D. Activation of the stress proteome as a mechanism for small molecule therapeutics. *Hum. Mol. Genet.* **2012**, *21*, 4237–4252. [CrossRef] [PubMed]
273. Adragna, N.C.; Fonseca, P.; Lauf, P.K. Hydroxyurea affects cell morphology, cation transport, and red blood cell adhesion in cultured vascular endothelial cells. *Blood* **1994**, *83*, 553–560. [PubMed]
274. Wall, M.E.; Wani, M.C.; Cook, C.E.; Palmer, K.H.; McPhail, A.T.; Sim, G.A. Plant Antitumor Agents. I. The Isolation and Structure of Camptothecin, a Novel Alkaloidal Leukemia and Tumor Inhibitor from *Camptotheca acuminata*^{1,2}. *J. Am. Chem. Soc.* **1966**, *88*, 3888–3890. [CrossRef]
275. Gupta, M.; Fujimori, A.; Pommier, Y. Eukaryotic DNA topoisomerases I. *Biochim. Biophys. Acta* **1995**, *1262*, 1–14. [CrossRef]
276. Champoux, J.J. Mechanism of the reaction catalyzed by the DNA untwisting enzyme: Attachment of the enzyme to 3'-terminus of the nicked DNA. *J. Mol. Biol.* **1978**, *118*, 441–446. [CrossRef]
277. Available online: <http://www.rcsb.org/pdb/explore/explore.do?structureId=1T8I> (accessed on 23 January 2017).
278. Stivers, J.T.; Harris, T.K.; Mildvan, A.S. Vaccinia DNA topoisomerase I: Evidence supporting a free rotation mechanism for DNA supercoil relaxation. *Biochemistry* **1997**, *36*, 5212–5222. [CrossRef] [PubMed]
279. Koster, D.A.; Palle, K.; Bot, E.S.M.; Bjornsti, M.-A.; Dekker, N.H. Antitumour drugs impede DNA uncoiling by topoisomerase I. *Nature* **2007**, *448*, 213–217. [CrossRef] [PubMed]
280. Staker, B.L.; Hjerrild, K.; Feese, M.D.; Behnke, C.A.; Burgin, A.B.; Stewart, L. The mechanism of topoisomerase I poisoning by a camptothecin analog. *Proc. Natl. Acad. Sci. USA* **2002**, *99*, 15387–15392. [CrossRef] [PubMed]
281. Regairaz, M.; Zhang, Y.-W.; Fu, H.; Agama, K.K.; Tata, N.; Agrawal, S.; Aladjem, M.I.; Pommier, Y. Mus81-mediated DNA cleavage resolves replication forks stalled by topoisomerase I-DNA complexes. *J. Cell Biol.* **2011**, *195*, 739–749. [CrossRef] [PubMed]
282. Palle, K.; Vaziri, C. Rad18 E3 ubiquitin ligase activity mediates Fanconi anemia pathway activation and cell survival following DNA Topoisomerase 1 inhibition. *Cell Cycle* **2011**, *10*, 1625–1638. [CrossRef] [PubMed]
283. Pommier, Y. Topoisomerase I inhibitors: Camptothecins and beyond. *Nat. Rev. Cancer* **2006**, *6*, 789–802. [CrossRef] [PubMed]
284. Tuduri, S.; Crabbé, L.; Conti, C.; Tourrière, H.; Holtgreve-Grez, H.; Jauch, A.; Pantesco, V.; De Vos, J.; Thomas, A.; Theillet, C.; et al. Topoisomerase I suppresses genomic instability by preventing interference between replication and transcription. *Nat. Cell Biol.* **2009**, *11*, 1315–1324. [CrossRef] [PubMed]
285. Tripathi, K.; Mani, C.; Clark, D.W.; Palle, K. Rad18 is required for functional interactions between FANCD2, BRCA2, and Rad51 to repair DNA topoisomerase 1-poisons induced lesions and promote fork recovery. *Oncotarget* **2016**, *7*, 12537–12553. [PubMed]
286. Tsao, Y.P.; D'Arpa, P.; Liu, L.F. The involvement of active DNA synthesis in camptothecin-induced G2 arrest: Altered regulation of p34cdc2/cyclin B. *Cancer Res.* **1992**, *52*, 1823–1829. [PubMed]
287. Kharbanda, S.; Rubin, E.; Gunji, H.; Hinz, H.; Giovanella, B.; Pantazis, P.; Kufe, D. Camptothecin and its derivatives induce expression of the *c-jun* protooncogene in human myeloid leukemia cells. *Cancer Res.* **1991**, *51*, 6636–6642. [PubMed]
288. Aller, P.; Rius, C.; Mata, F.; Zorrilla, A.; Cabañas, C.; Bellón, T.; Bernabeu, C. Camptothecin induces differentiation and stimulates the expression of differentiation-related genes in U-937 human promonocytic leukemia cells. *Cancer Res.* **1992**, *52*, 1245–1251. [PubMed]
289. Clements, M.K.; Jones, C.B.; Cumming, M.; Daoud, S.S. Antiangiogenic potential of camptothecin and topotecan. *Cancer Chemother. Pharmacol.* **1999**, *44*, 411–416. [CrossRef] [PubMed]

290. O'Leary, J.J.; Shapiro, R.L.; Ren, C.J.; Chuang, N.; Cohen, H.W.; Potmesil, M. Antiangiogenic effects of camptothecin analogues 9-amino-20(S)-camptothecin, topotecan, and CPT-11 studied in the mouse cornea model. *Clin. Cancer Res.* **1999**, *5*, 181–187. [PubMed]
291. Arlt, M.F.; Glover, T.W. Inhibition of topoisomerase I prevents chromosome breakage at common fragile sites. *DNA Repair* **2010**, *9*, 678–689. [CrossRef] [PubMed]
292. Horwitz, S.B.; Horwitz, M.S. Effects of camptothecin on the breakage and repair of DNA during the cell cycle. *Cancer Res.* **1973**, *33*, 2834–2836. [PubMed]
293. Jayasooriya, R.G.P.T.; Choi, Y.H.; Hyun, J.W.; Kim, G.-Y. Camptothecin sensitizes human hepatoma Hep3B cells to TRAIL-mediated apoptosis via ROS-dependent death receptor 5 upregulation with the involvement of MAPKs. *Environ. Toxicol. Pharmacol.* **2014**, *38*, 959–967. [CrossRef] [PubMed]
294. Strumberg, D.; Pilon, A.A.; Smith, M.; Hickey, R.; Malkas, L.; Pommier, Y. Conversion of topoisomerase I cleavage complexes on the leading strand of ribosomal DNA into 5'-phosphorylated DNA double-strand breaks by replication runoff. *Mol. Cell. Biol.* **2000**, *20*, 3977–3987. [CrossRef] [PubMed]
295. Priel, E.; Showalter, S.D.; Roberts, M.; Oroszlan, S.; Blair, D.G. The topoisomerase I inhibitor, camptothecin, inhibits equine infectious anemia virus replication in chronically infected CF2Th cells. *J. Virol.* **1991**, *65*, 4137–4141. [PubMed]
296. Bruno, S.; Giaretti, W.; Darzynkiewicz, Z. Effect of camptothecin on mitogenic stimulation of human lymphocytes: Involvement of DNA topoisomerase I in cell transition from G0 to G1 phase of the cell cycle and in DNA replication. *J. Cell. Physiol.* **1992**, *151*, 478–486. [CrossRef] [PubMed]
297. Squires, S.; Ryan, A.J.; Strutt, H.L.; Johnson, R.T. Hypersensitivity of Cockayne's syndrome cells to camptothecin is associated with the generation of abnormally high levels of double strand breaks in nascent DNA. *Cancer Res.* **1993**, *53*, 2012–2019. [PubMed]
298. Ding, X.; Matsuo, K.; Xu, L.; Yang, J.; Zheng, L. Optimized combinations of bortezomib, camptothecin, and doxorubicin show increased efficacy and reduced toxicity in treating oral cancer. *Anticancer Drugs* **2015**, *26*, 547–554. [CrossRef] [PubMed]
299. Zhang, J.; Walter, J.C. Mechanism and regulation of incisions during DNA interstrand cross-link repair. *DNA Repair* **2014**, *19*, 135–142. [CrossRef] [PubMed]
300. Ray Chaudhuri, A.; Hashimoto, Y.; Herrador, R.; Neelsen, K.J.; Fachinetti, D.; Bermejo, R.; Cocito, A.; Costanzo, V.; Lopes, M. Topoisomerase I poisoning results in PARP-mediated replication fork reversal. *Nat. Struct. Mol. Biol.* **2012**, *19*, 417–423. [CrossRef] [PubMed]
301. Available online: http://www.sigmaaldrich.com/content/dam/sigma-aldrich/docs/Sigma/Product_Information_Sheet/c9911pis.pdf (accessed on 23 November 2016).
302. Jaxel, C.; Kohn, K.W.; Wani, M.C.; Wall, M.E.; Pommier, Y. Structure-activity study of the actions of camptothecin derivatives on mammalian topoisomerase I: Evidence for a specific receptor site and a relation to antitumor activity. *Cancer Res.* **1989**, *49*, 1465–1469. [PubMed]
303. Takagi, K.; Dexheimer, T.S.; Redon, C.; Sordet, O.; Agama, K.; Lavielle, G.; Pierré, A.; Bates, S.E.; Pommier, Y. Novel E-ring camptothecin keto analogues (S38809 and S39625) are stable, potent, and selective topoisomerase I inhibitors without being substrates of drug efflux transporters. *Mol. Cancer Ther.* **2007**, *6*, 3229–3238. [CrossRef] [PubMed]
304. Hande, K.R. Etoposide: Four decades of development of a topoisomerase II inhibitor. *Eur. J. Cancer* **1998**, *34*, 1514–1521. [CrossRef]
305. Available online: <http://www.rcsb.org/pdb/explore/explore.do?structureId=3QX3> (accessed on 23 January 2017).
306. Liu, L.F.; Rowe, T.C.; Yang, L.; Tewey, K.M.; Chen, G.L. Cleavage of DNA by mammalian DNA topoisomerase II. *J. Biol. Chem.* **1983**, *258*, 15365–15370. [PubMed]
307. Gibson, E.G.; King, M.M.; Mercer, S.L.; Deweese, J.E. Two-Mechanism Model for the Interaction of Etoposide Quinone with Topoisomerase II α . *Chem. Res. Toxicol.* **2016**, *29*, 1541–1548. [CrossRef] [PubMed]
308. Wu, C.-C.; Li, T.-K.; Farh, L.; Lin, L.-Y.; Lin, T.-S.; Yu, Y.-J.; Yen, T.-J.; Chiang, C.-W.; Chan, N.-L. Structural basis of type II topoisomerase inhibition by the anticancer drug etoposide. *Science* **2011**, *333*, 459–462. [CrossRef] [PubMed]

309. Bender, R.P.; Jablonksy, M.J.; Shadid, M.; Romaine, I.; Dunlap, N.; Anklin, C.; Graves, D.E.; Osheroff, N. Substituents on etoposide that interact with human topoisomerase IIalpha in the binary enzyme-drug complex: Contributions to etoposide binding and activity. *Biochemistry* **2008**, *47*, 4501–4509. [[CrossRef](#)] [[PubMed](#)]
310. Wilstermann, A.M.; Bender, R.P.; Godfrey, M.; Choi, S.; Anklin, C.; Berkowitz, D.B.; Osheroff, N.; Graves, D.E. Topoisomerase II—Drug interaction domains: Identification of substituents on etoposide that interact with the enzyme. *Biochemistry* **2007**, *46*, 8217–8225. [[CrossRef](#)] [[PubMed](#)]
311. Jacob, D.A.; Mercer, S.L.; Osheroff, N.; Deweese, J.E. Etoposide quinone is a redox-dependent topoisomerase II poison. *Biochemistry* **2011**, *50*, 5660–5667. [[CrossRef](#)] [[PubMed](#)]
312. Rogakou, E.P.; Pilch, D.R.; Orr, A.H.; Ivanova, V.S.; Bonner, W.M. DNA double-stranded breaks induce histone H2AX phosphorylation on serine 139. *J. Biol. Chem.* **1998**, *273*, 5858–5868. [[CrossRef](#)] [[PubMed](#)]
313. Terasawa, M.; Shinohara, A.; Shinohara, M. Canonical non-homologous end joining in mitosis induces genome instability and is suppressed by M-phase-specific phosphorylation of XRCC4. *PLoS Genet.* **2014**, *10*, e1004563. [[CrossRef](#)] [[PubMed](#)]
314. Zhao, H.; Rybak, P.; Dobrucki, J.; Traganos, F.; Darzynkiewicz, Z. Relationship of DNA damage signaling to DNA replication following treatment with DNA topoisomerase inhibitors camptothecin/topotecan, mitoxantrone, or etoposide. *Cytometry A* **2012**, *81*, 45–51. [[CrossRef](#)] [[PubMed](#)]
315. Montecucco, A.; Rossi, R.; Ferrari, G.; Scovassi, A.I.; Prosperi, E.; Biamonti, G. Etoposide Induces the Dispersal of DNA Ligase I from Replication Factories. *Mol. Biol. Cell* **2001**, *12*, 2109–2118. [[CrossRef](#)] [[PubMed](#)]
316. Holm, C.; Covey, J.M.; Kerrigan, D.; Pommier, Y. Differential requirement of DNA replication for the cytotoxicity of DNA topoisomerase I and II inhibitors in Chinese hamster DC3F cells. *Cancer Res.* **1989**, *49*, 6365–6368. [[PubMed](#)]
317. Austin, C.A.; Sng, J.H.; Patel, S.; Fisher, L.M. Novel HeLa topoisomerase II is the II beta isoform: Complete coding sequence and homology with other type II topoisomerases. *Biochim. Biophys. Acta* **1993**, *1172*, 283–291. [[CrossRef](#)]
318. Niimi, A.; Suka, N.; Harata, M.; Kikuchi, A.; Mizuno, S. Co-localization of chicken DNA topoisomerase IIalpha, but not beta, with sites of DNA replication and possible involvement of a C-terminal region of alpha through its binding to PCNA. *Chromosoma* **2001**, *110*, 102–114. [[CrossRef](#)] [[PubMed](#)]
319. Ju, B.-G.; Lunyak, V.V.; Perissi, V.; Garcia-Bassets, I.; Rose, D.W.; Glass, C.K.; Rosenfeld, M.G. A topoisomerase II β -mediated dsDNA break required for regulated transcription. *Science* **2006**, *312*, 1798–1802. [[CrossRef](#)] [[PubMed](#)]
320. Azarova, A.M.; Lyu, Y.L.; Lin, C.-P.; Tsai, Y.-C.; Lau, J.Y.-N.; Wang, J.C.; Liu, L.F. Roles of DNA topoisomerase II isozymes in chemotherapy and secondary malignancies. *Proc. Natl. Acad. Sci. USA* **2007**, *104*, 11014–11019. [[CrossRef](#)] [[PubMed](#)]
321. Nitiss, J.L. DNA topoisomerase II and its growing repertoire of biological functions. *Nat. Rev. Cancer* **2009**, *9*, 327–337. [[CrossRef](#)] [[PubMed](#)]
322. Gupta, R.S.; Bromke, A.; Bryant, D.W.; Gupta, R.; Singh, B.; McCalla, D.R. Etoposide (VP16) and teniposide (VM26): Novel anticancer drugs, strongly mutagenic in mammalian but not prokaryotic test systems. *Mutagenesis* **1987**, *2*, 179–186. [[CrossRef](#)] [[PubMed](#)]
323. Muslimović, A.; Nyström, S.; Gao, Y.; Hammarsten, O. Numerical Analysis of Etoposide Induced DNA Breaks. *PLoS ONE* **2009**, *4*, e5859. [[CrossRef](#)]
324. Álvarez-Quilón, A.; Serrano-Benítez, A.; Lieberman, J.A.; Quintero, C.; Sánchez-Gutiérrez, D.; Escudero, L.M.; Cortés-Ledesma, F. ATM specifically mediates repair of double-strand breaks with blocked DNA ends. *Nat. Commun.* **2014**, *5*, 3347. [[CrossRef](#)] [[PubMed](#)]
325. Nagano, T.; Nakano, M.; Nakashima, A.; Onishi, K.; Yamao, S.; Enari, M.; Kikkawa, U.; Kamada, S. Identification of cellular senescence-specific genes by comparative transcriptomics. *Sci. Rep.* **2016**, *6*, 31758. [[CrossRef](#)] [[PubMed](#)]
326. Brasacchio, D.; Alsop, A.E.; Noori, T.; Lufti, M.; Iyer, S.; Simpson, K.J.; Bird, P.I.; Kluck, R.M.; Johnstone, R.W.; Trapani, J.A. Epigenetic control of mitochondrial cell death through PACS1-mediated regulation of BAX/BAK oligomerization. *Cell Death Differ.* **2017**. [[CrossRef](#)] [[PubMed](#)]

327. Martin, R.; Desponds, C.; Eren, R.O.; Quadroni, M.; Thome, M.; Fasel, N. Caspase-mediated cleavage of raptor participates in the inactivation of mTORC1 during cell death. *Cell Death Discov.* **2016**, *2*, 16024. [CrossRef] [PubMed]
328. Brekman, A.; Singh, K.E.; Polotskaia, A.; Kundu, N.; Bargonetti, J. A p53-independent role of Mdm2 in estrogen-mediated activation of breast cancer cell proliferation. *Breast Cancer Res.* **2011**, *13*, R3. [CrossRef] [PubMed]
329. Soubeyrand, S.; Pope, L.; Haché, R.J.G. Topoisomerase II α -dependent induction of a persistent DNA damage response in response to transient etoposide exposure. *Mol. Oncol.* **2010**, *4*, 38–51. [CrossRef] [PubMed]
330. Velma, V.; Carrero, Z.I.; Allen, C.B.; Hebert, M.D. Coilin levels modulate cell cycle progression and γ H2AX levels in etoposide treated U2OS cells. *FEBS Lett.* **2012**, *586*, 3404–3409. [CrossRef] [PubMed]
331. Dehennaut, V.; Loison, I.; Dubuissez, M.; Nassour, J.; Abbadie, C.; Leprince, D. DNA double-strand breaks lead to activation of hypermethylated in cancer 1 (HIC1) by SUMOylation to regulate DNA repair. *J. Biol. Chem.* **2013**, *288*, 10254–10264. [CrossRef] [PubMed]
332. Paget, S.; Dubuissez, M.; Dehennaut, V.; Nassour, J.; Harmon, B.T.; Spruyt, N.; Loison, I.; Abbadie, C.; Rood, B.R.; Leprince, D. HIC1 (hypermethylated in cancer 1) SUMOylation is dispensable for DNA repair but is essential for the apoptotic DNA damage response (DDR) to irreparable DNA double-strand breaks (DSBs). *Oncotarget* **2017**, *8*, 2916–2935. [CrossRef] [PubMed]
333. Sypniewski, D.; Bednarek, I.; Gałka, S.; Loch, T.; Błaszczuk, D.; Soltysik, D. Cytotoxicity of etoposide in cancer cell lines in vitro after BCL-2 and C-RAF gene silencing with antisense oligonucleotides. *Acta Pol. Pharm.* **2013**, *70*, 87–97.
334. Rybak, P.; Hoang, A.; Bujnowicz, L.; Bernas, T.; Berniak, K.; Zarębski, M.A.; Darzynkiewicz, Z.; Dobrucki, J. Low level phosphorylation of histone H2AX on serine 139 (γ H2AX) is not associated with DNA double-strand breaks. *Oncotarget* **2016**, *7*, 49574–49587. [CrossRef] [PubMed]
335. Chen, L.; Cui, H.; Fang, J.; Deng, H.; Kuang, P.; Guo, H.; Wang, X.; Zhao, L. Glutamine deprivation plus BPTES alters etoposide- and cisplatin-induced apoptosis in triple negative breast cancer cells. *Oncotarget* **2016**, *7*, 54691–54701. [CrossRef] [PubMed]
336. Rodriguez-Lopez, A.M.; Xenaki, D.; Eden, T.O.; Hickman, J.A.; Chresta, C.M. MDM2 mediated nuclear exclusion of p53 attenuates etoposide-induced apoptosis in neuroblastoma cells. *Mol. Pharmacol.* **2001**, *59*, 135–143.
337. Litwiniec, A.; Gackowska, L.; Helmin-Basa, A.; Żuryń, A.; Grzanka, A. Low-dose etoposide-treatment induces endoreplication and cell death accompanied by cytoskeletal alterations in A549 cells: Does the response involve senescence? The possible role of vimentin. *Cancer Cell Int.* **2013**, *13*, 9. [CrossRef] [PubMed]
338. Akhtar, N.; Talegaonkar, S.; Khar, R.K.; Jaggi, M. A validated stability-indicating LC method for estimation of etoposide in bulk and optimized self-nano emulsifying formulation: Kinetics and stability effects. *Saudi Pharm. J.* **2013**, *21*, 103–111. [CrossRef] [PubMed]
339. Available online: http://www.sigmaaldrich.com/content/dam/sigma-aldrich/docs/Sigma/Product_Information_Sheet/e1383pis.pdf (accessed on 23 November 2016).
340. Wrasidlo, W.; Schröder, U.; Bernt, K.; Hübener, N.; Shabat, D.; Gaedicke, G.; Lode, H. Synthesis, hydrolytic activation and cytotoxicity of etoposide prodrugs. *Bioorg Med Chem Lett.* **2002**, *12*, 557–560. [CrossRef]
341. Jokić, M.; Vlašić, I.; Rinneburger, M.; Klümper, N.; Spiro, J.; Vogel, W.; Offermann, A.; Kümpers, C.; Fritz, C.; Schmitt, A.; et al. Ercc1 Deficiency Promotes Tumorigenesis and Increases Cisplatin Sensitivity in a Tp53 Context-Specific Manner. *Mol. Cancer Res.* **2016**, *14*, 1110–1123. [CrossRef] [PubMed]
342. Felix, C.A.; Walker, A.H.; Lange, B.J.; Williams, T.M.; Winick, N.J.; Cheung, N.K.; Lovett, B.D.; Nowell, P.C.; Blair, I.A.; Rebbeck, T.R. Association of CYP3A4 genotype with treatment-related leukemia. *Proc. Natl. Acad. Sci. USA* **1998**, *95*, 13176–13181. [CrossRef] [PubMed]
343. Blanco, J.G.; Edick, M.J.; Relling, M.V. Etoposide induces chimeric Mll gene fusions. *FASEB J.* **2004**, *18*, 173–175. [CrossRef] [PubMed]
344. Thirman, M.J.; Gill, H.J.; Burnett, R.C.; Mbangkollo, D.; McCabe, N.R.; Kobayashi, H.; Ziemann-van der Poel, S.; Kaneko, Y.; Morgan, R.; Sandberg, A.A. Rearrangement of the MLL gene in acute lymphoblastic and acute myeloid leukemias with 11q23 chromosomal translocations. *N. Engl. J. Med.* **1993**, *329*, 909–914. [CrossRef] [PubMed]

345. Cerveira, N.; Lisboa, S.; Correia, C.; Bizarro, S.; Santos, J.; Torres, L.; Vieira, J.; Barros-Silva, J.D.; Pereira, D.; Moreira, C.; et al. Genetic and clinical characterization of 45 acute leukemia patients with MLL gene rearrangements from a single institution. *Mol. Oncol.* **2012**, *6*, 553–564. [CrossRef] [PubMed]
346. Krivtsov, A.V.; Armstrong, S.A. MLL translocations, histone modifications and leukaemia stem-cell development. *Nat. Rev. Cancer* **2007**, *7*, 823–833. [CrossRef] [PubMed]
347. Zhang, L.; Chen, F.; Zhang, Z.; Chen, Y.; Lin, Y.; Wang, J. Design, synthesis and evaluation of the multidrug resistance-reversing activity of pyridine acid esters of podophyllotoxin in human leukemia cells. *Bioorg. Med. Chem. Lett.* **2016**, *26*, 4466–4471. [CrossRef] [PubMed]
348. Lee, K.-I.; Su, C.-C.; Yang, C.-Y.; Hung, D.-Z.; Lin, C.-T.; Lu, T.-H.; Liu, S.-H.; Huang, C.-F. Etoposide induces pancreatic β -cells cytotoxicity via the JNK/ERK/GSK-3 signaling-mediated mitochondria-dependent apoptosis pathway. *Toxicol. Vitro* **2016**, *36*, 142–152. [CrossRef] [PubMed]
349. Pellegrini, G.G.; Morales, C.C.; Wallace, T.C.; Plotkin, L.I.; Bellido, T. Avenanthramides Prevent Osteoblast and Osteocyte Apoptosis and Induce Osteoclast Apoptosis In Vitro in an Nrf2-Independent Manner. *Nutrients* **2016**, *8*, 423. [CrossRef] [PubMed]
350. Papież, M.A.; Krzyściak, W.; Szade, K.; Bukowska-Straková, K.; Kozakowska, M.; Hajduk, K.; Bystrowska, B.; Dulak, J.; Jozkowicz, A. Curcumin enhances the cytogenotoxic effect of etoposide in leukemia cells through induction of reactive oxygen species. *Drug Des. Dev. Ther.* **2016**, *10*, 557–570. [CrossRef] [PubMed]
351. Zhang, S.; Lu, C.; Zhang, X.; Li, J.; Jiang, H. Targeted delivery of etoposide to cancer cells by folate-modified nanostructured lipid drug delivery system. *Drug Deliv.* **2016**, *23*, 1838–1845. [CrossRef] [PubMed]
352. Lindsay, G.S.; Wallace, H.M. Changes in polyamine catabolism in HL-60 human promyelogenous leukaemic cells in response to etoposide-induced apoptosis. *Biochem. J.* **1999**, *337 Pt 1*, 83–87. [CrossRef] [PubMed]
353. Kumar, A.; Ehrenshaft, M.; Tokar, E.J.; Mason, R.P.; Sinha, B.K. Nitric oxide inhibits topoisomerase II activity and induces resistance to topoisomerase II-poisons in human tumor cells. *Biochim. Biophys. Acta* **2016**, *1860*, 1519–1527. [CrossRef] [PubMed]
354. Zhang, A.; Lyu, Y.L.; Lin, C.-P.; Zhou, N.; Azarova, A.M.; Wood, L.M.; Liu, L.F. A protease pathway for the repair of topoisomerase II–DNA covalent complexes. *J. Biol. Chem.* **2006**, *281*, 35997–36003. [CrossRef] [PubMed]
355. Ledesma, F.C.; El Khamisy, S.F.; Zuma, M.C.; Osborn, K.; Caldecott, K.W. A human 5'-tyrosyl DNA phosphodiesterase that repairs topoisomerase-mediated DNA damage. *Nature* **2009**, *461*, 674–678. [CrossRef] [PubMed]
356. Aparicio, T.; Baer, R.; Gottesman, M.; Gautier, J. MRN, CtIP, and BRCA1 mediate repair of topoisomerase II–DNA adducts. *J. Cell Biol.* **2016**, *212*, 399–408. [CrossRef] [PubMed]
357. Quennet, V.; Beucher, A.; Barton, O.; Takeda, S.; Löbrich, M. CtIP and MRN promote non-homologous end-joining of etoposide-induced DNA double-strand breaks in G1. *Nucleic Acids Res.* **2011**, *39*, 2144–2152. [CrossRef] [PubMed]
358. Adachi, N.; Suzuki, H.; Iizumi, S.; Koyama, H. Hypersensitivity of nonhomologous DNA end-joining mutants to VP-16 and ICRF-193: Implications for the repair of topoisomerase II-mediated DNA damage. *J. Biol. Chem.* **2003**, *278*, 35897–35902. [CrossRef] [PubMed]

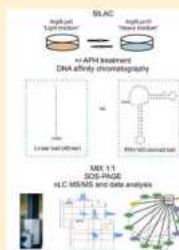


Role of DNA Repair Factor Xeroderma Pigmentosum Protein Group C in Response to Replication Stress As Revealed by DNA Fragile Site Affinity Chromatography and Quantitative ProteomicsLucie Beresova,^{†,‡} Eva Vesela,[†] Ivo Chamrad,[‡] Jiri Voller,[†] Masayuki Yamada,[†] Tomas Furst,[†] Rene Lenobel,[‡] Katarina Chroma,[†] Jan Gursky,[†] Katerina Krizova,[†] Martin Mistrik,^{‡,†,§,||} and Jiri Bartek^{‡,†,§,||}[†]Institute of Molecular and Translational Medicine, Faculty of Medicine and Dentistry, Palacky University, Olomouc, Czech Republic[‡]Department of Protein Biochemistry and Proteomics, Centre of the Region Hana for Biotechnological and Agricultural Research, Faculty of Science, Palacky University, Olomouc, Czech Republic[§]Danish Cancer Society Research Center, Copenhagen, Denmark^{||}Science for Life Laboratory, Division of Translational Medicine and Chemical Biology, Department of Biochemistry and Biophysics, Karolinska Institute, Stockholm, Sweden

Supporting Information

ABSTRACT: Replication stress (RS) fuels genomic instability and cancer development and may contribute to aging, raising the need to identify factors involved in cellular responses to such stress. Here, we present a strategy for identification of factors affecting the maintenance of common fragile sites (CFSs), which are genomic loci that are particularly sensitive to RS and suffer from increased breakage and rearrangements in tumors. A DNA probe designed to match the high flexibility island sequence typical for the commonly expressed CFS (FRA16D) was used as specific DNA affinity bait. Proteins significantly enriched at the FRA16D fragment under normal and replication stress conditions were identified using stable isotope labeling of amino acids in cell culture-based quantitative mass spectrometry. The identified proteins interacting with the FRA16D fragment included some known CFS stabilizers, thereby validating this screening approach. Among the hits from our screen so far not implicated in CFS maintenance, we chose Xeroderma pigmentosum protein group C (XPC) for further characterization. XPC is a key factor in the DNA repair pathway known as global genomic nucleotide excision repair (GG-NER), a mechanism whose several components were enriched at the FRA16D fragment in our screen. Functional experiments revealed defective checkpoint signaling and escape of DNA replication intermediates into mitosis and the next generation of XPC-depleted cells exposed to RS. Overall, our results provide insights into an unexpected biological role of XPC in response to replication stress and document the power of proteomics-based screening strategies to elucidate mechanisms of pathophysiological significance.

KEYWORDS: DNA affinity chromatography, SILAC proteomics, common fragile sites, replication stress, FRA16D, mitosis, 53BP1 bodies, γ H2AX, DNA damage response, Xeroderma pigmentosum complementation group C (XPC) protein

**INTRODUCTION**

Common fragile sites (CFSs) are defined as a nonrandom distribution of breaks, gaps, and constrictions visible on metaphase chromosomes, especially under conditions of replication stress.¹ These sites are conserved among diverse mammalian species² and have been intensively studied mainly owing to their association with chromosomal aberrations (deletions, translocations, amplifications) that are found in many types of cancer³ and may play a causative role in tumorigenesis.⁴

The molecular basis of CFS-associated chromosomal instability has been partially explained through structural analyses. Many CFSs contain AT-rich stretches that form highly flexible sequence islands. The common feature of all these atypical sequences is the formation of unusual secondary DNA structures that have been shown to compromise DNA replication *in vitro*.^{5,6} Furthermore, an increased occurrence of

replication fork collapse and DNA double strand break (DSB) formation in the flexible islands were reported for a yeast model with artificially introduced human CFS, FRA16D, upon replication stress.⁷ An additional explanation for CFSs' instability may reflect frequent collisions between DNA replication and transcription machinery due to very large genes located in some of the CFSs.⁸

Aphidicolin (APH), an inhibitor of DNA polymerases α and ϵ is the most potent inducer of the majority of known CFSs and is used at a concentration that slows but does not arrest replication fork progression.^{9,10} Such a RS scenario induces long stretches of single-stranded DNA as a consequence of the inhibited DNA polymerases lagging behind the advancing DNA helicase during DNA replication.¹¹ The cellular response to RS

Received: July 4, 2016

Published: October 30, 2016

and stabilization of CFSs involves multiple cellular factors as also documented by spontaneous expression of CFSs in cells from patients with genetic instability disorders such as Seckel syndrome.¹² Furthermore, genetic models based on experimental knock-down of checkpoint and/or DNA repair proteins like ATR or Chk1 kinases,^{13,14} BRCA1,¹⁵ FANCD2,¹⁶ SMC1,¹⁷ WRN,¹⁸ and MSH2¹⁹ show enhanced APH-induced CFS expression. Importantly, oncogenic stress evoked by mutated RAS,²⁰ Cyclin E, and E2F²¹ overexpression leads to CFS-associated instability and deletions, and rearrangements in CFS areas are often detected in human premalignant lesions and xenografts experiencing high oncogenic activity.^{22–24}

The roles of the aforementioned factors in the protection against fragility of CFSs were mostly discovered using methods of visual detection of chromosomal breaks and gaps on mitotic spreads. Several reports also utilized chromatin immunoprecipitation followed by quantitative PCR that allowed the detection of the studied protein at the CFS sequences.^{25,26} Nevertheless, an unbiased proteome-wide screening for identification of new protein candidates that could contribute to CFS maintenance has not been reported.

As shown recently, quantitative mass spectrometry in combination with nucleic acid-based affinity chromatography is a powerful tool for proteome-wide screens of specific DNA and RNA binding proteins pointing to new protein candidates for deeper functional characterization.^{27–29} In this regard, stable isotope labeling of amino acids in cell culture (SILAC) appears to be a method of choice that is straightforward, minimizes chances of bias caused by sample processing errors, and allows simple distinguishing of specific interactors from background binding proteins.^{30,31} Here, we present a new strategy combining DNA-affinity chromatography with SILAC and mass spectrometry to isolate potential CFS protein interactors. Besides the advantages mentioned above, SILAC allowed us not only to identify CFS binding factors but also to distinguish between those bound under normal unperturbed cell growth and those enriched under conditions of APH-evoked replication stress. The results obtained with our combinatorial screening approach and functional characterization of XPC as a surprising new factor involved in CFS stability and overall cellular response to RS are presented below.

MATERIALS AND EXPERIMENTAL PROCEDURES

Chemicals

All chemicals used in this study were of analytical grade and purchased from Sigma-Aldrich unless stated otherwise.

Cell Culture

In this study, the following human cell types were used: cervical cancer cell line (HeLa S3; ATCC), normal diploid fibroblast strain (TIG3, ATCC), and osteosarcoma cell line (U-2 OS; ATCC).

For the SILAC screen, HeLa S3 cells were grown in RPMI 1640 medium with omitted lysine and arginine (Biowest) supplemented with 10% dialyzed fetal bovine serum and 1% penicillin/streptomycin solution. For quantitative SILAC-based MS analysis, the RPMI 1640 medium was supplemented separately with L-arginine and L-lysine (Arg⁰, Lys⁰) or L-[U-¹³C₆, ¹⁵N⁴]arginine, L-[U-¹³C₆, ¹⁵N²]lysine (Arg¹⁰, Lys⁸) (Cambridge Isotope Laboratories, Inc.). After five cellular doublings, the success rate of protein labeling was verified by in-solution digestion and a shotgun LC–MS/MS analysis.

The other cell types were cultured in Dulbecco's modified Eagle's medium (Invitrogen) supplemented with 10% fetal bovine serum and 1% penicillin/streptomycin. The doxycycline-inducible shRNA ATR knockdown model in the U-2 OS cell line was characterized previously.³²

Affinity Ligands and Immobilization on Chromatography Media

As an affinity ligand mimicking CFS, an oligonucleotide with the sequence (5'-3') CCC CCC CCC GAT TGT GAT AAT CAT TAC ACA ATG TAT ATA GTA ATC AAA TCA TTA CTT TAT was used. With the exception of the first nine cytosines that served as a linker, the sequence corresponds to a part of the common fragile site FRA16D.⁷ The ability of the sequence to form the same secondary structures as the corresponding part of FRA16D was tested in the Mfold program.³³ Default parameters were modified to reflect our experimental conditions (150 mM Cl⁻, 1 mM Mg²⁺, 4 °C).

As a second ligand, a control oligonucleotide with linear structure, oligonucleotide (5'-3') CAA ATT TTA GCC AGT CAT CCC ATA GTA TCG TCC GTT CAA G, was used. The oligonucleotide should not be able to form stable secondary structure and was designed *in silico* as follows.

One million random 40-mers were generated and T_m (melting temperature) of the most stable secondary structure was calculated in Mfold (settings same as above). Five percent of sequences with the lowest T_m were selected, and all of the 20 bp subsequences were extracted. Another set of 40-mers was created by concatenation of random pairs from this pool. For avoiding the creation of oligonucleotides deprived of certain nucleotides or dominated by repetitions, sequences with the lowest variability (expressed as entropy) at the level of mono-, di-, tri-, and tetranucleotides were removed. After 20 rounds of this "selection" and "recombination", 100 40-mers with the lowest T_m together with their reverse sequences were selected for closer inspection. Sequences predicted to interact with single strand binding transcription factors by Transcription Element Search System web service³⁴ were removed. Final selection took into consideration the following parameters: T_m of the most stable structure, number of structures predicted by Mfold, and sequence variability. The selected 40-mer is not able to form any structure with negative ΔG , and the corresponding T_m are lower than -47 °C.

Both oligonucleotide sequences were custom synthesized and modified with biotin at the 5' end (Generi Biotech). Affinity beads were prepared by immobilization of the oligonucleotides to streptavidin-covered magnetic beads (Chemicell) according to the manufacturer's instructions. Briefly, SIMAG-streptavidin beads (1 mg) were washed three times with 1 mL of citrate buffer (150 mM NaCl, 15 mM trisodium citrate, pH 7.0) and resuspended in 0.5 mL of citrate buffer. Then, 200 pmol of the specific oligonucleotide was added, and immobilization was performed at room temperature under slow rotation of the beads in 15 min. Unbound oligonucleotides were removed by washing of affinity beads with three volumes of the citrate buffer. Before use, the prepared affinity beads were finally equilibrated to a starting condition for DNA affinity chromatography with 1 mL of a binding buffer (25 mM HEPES with 150 mM NaCl, 1 mM MgCl₂, pH 7.5) at 4 °C under slow rotation for 15 min.

Preparation of Cell Lysate and DNA Affinity Chromatography

Two differently labeled HeLa S3 cell populations, marked as light and heavy, were both cultivated with or without the presence of APH for induction of replication stress. In the first experiment, the light and heavy labeled cell populations were cultured under normal growth conditions and subsequently used in the SILAC comparative analysis of specific CFS binding proteins enriched by DNA affinity chromatography on the FRA16D fragment and control beads covered by the linear oligonucleotide. In the second experiment, both labeled cell populations were exposed to 0.4 μ M APH for 24 h before harvesting and also employed for the isolation of specific CFS binding proteins in the same way as in the first experiment.

Briefly, HeLa S3 cells, light and heavy, were harvested, and the cellular pellets were resuspended in a buffer from a NEPER nuclear and cytoplasmic extraction kit (Thermo Scientific) for isolation of nuclear proteins. The concentrations of isolated nuclear proteins were determined by Bradford protein assay (Biorad) with BSA as a standard. Equal amounts of nuclear proteins (1 mg) isolated from light and heavy cell populations were mixed with 1 mL of the binding buffer and incubated with affinity beads containing either the FRA16D fragment or a control linear sequence. The association of the nuclear proteins with oligonucleotide beads was performed at 4 °C under continuous slow vertical rotation for 1 h. After the interaction of the proteins with oligonucleotide baits, the unbound proteins were removed by washing of the beads with 1 mL of the binding buffer (repeated five times). The retained proteins were eluted from the beads directly by the addition of 25 μ L of SDS-PAGE sample buffer and boiling at 95 °C with continuous shaking for 10 min. The eluates were carefully removed from the beads and mixed 1:1. All affinity experiments were performed in two independent biological replicates. In one replicate, the FRA16D fragment was incubated with the heavy labeled nuclear proteins, and to the beads with control linear sequence, the light labeled nuclear proteins were added. In the second replicate, the labeled protein extracts added to the resins were swapped. The same SILAC comparative experiment with beads covered by the FRA16D fragment and control linear sequence was carried out with both HeLa S3 cell populations exposed to 0.4 μ M APH for 24 h. This experiment was repeated in two independent biological replicates with swapping of the labeled nuclear proteins added to the affinity beads as well.

Protein Separation and Digestion

Proteins retained and eluted from both oligonucleotide affinity beads (FRA16D fragment sequence vs linear control sequence) were mixed in a 1:1 ratio, separated on 4–16% BIS-TRIS SDS-PAGE gradient gels (Biorad), and stained with colloidal Coomassie Blue. Each sample line was divided into 13 fractions, which were further cut into small pieces. Then, proteins were destained, reduced with DDT, and subsequently alkylated with iodoacetamide and digested with rafinose-modified trypsin overnight.^{35,36} The released peptides were extracted from the gel pieces with 5% formic acid in 30% acetonitrile (v/v) and purified using C18 StageTips.³⁷

Nanoflow Liquid Chromatography Mass Spectrometry

The desalted peptides were analyzed by nanoflow liquid chromatography (nanoEASY-nLC System; Thermo Fisher Scientific) coupled to a UHR-Q-TOF maXis instrument equipped with online nanoESI source (Bruker Daltonics).

Peptides loaded on a precolumn (2 cm \times 75 μ m packed with ReproSil-Pur C18-AQ 5 μ m resin) were eluted and separated on an analytical column with a multistep gradient at a flow rate of 200 nL/min for 185 min. The gradient was created by mixing of 0.4% (v/v) formic acid (solvent phase A) and 0.4% formic acid in 80% acetonitrile (v/v) (Table S-1). The analytical column was prepared in a 15 cm fused silica emitter with an inner diameter of 75 μ m (New Objective) packed in-house with reverse phase ReproSil-Pur C18-AQ 3 μ m resin (Dr. Maisch GmbH). The MS instrument was operated in data-dependent acquisition mode using the top five precursors with charge states ≥ 2 . The selected precursors were fragmented with the use of collision-induced dissociation. The fragmented precursors were dynamically excluded for 18 s. Detailed settings of the MS analyzer are described in the Supporting Information. Each sample was analyzed in two technical replicates.

Data Processing

The collected raw data were processed using the DataAnalysis v 4.2 SP1 software (Bruker Daltonik). The XML files containing precursor and fragmentation data were created and used for consequent bioinformatics analysis. The XML files were uploaded to ProteinScape v 2.1 and searched by Mascot v2.2.07 (in-house server; Matrix Science) against a custom-prepared database containing human proteins downloaded from UniProt (20150107, 89706 seq; www.uniprot.org) supplemented with common contaminants (keratins, trypsin, bovine serum albumin) and reversed sequences of all human proteins for the determination of false discovery rate (FDR). The Mascot search was carried out with the following parameters: MS and MS/MS tolerances were set to ± 25 ppm and ± 0.05 Da, respectively; protease specificity was set to trypsin, and one missed cleavage was allowed; carbamidomethylation of cysteine was set as a fixed modification, and N-terminal protein acetylation, methionine oxidation, and heavy labeled $^{13}\text{C}(6)^{15}\text{N}(2)$ lysine and $^{13}\text{C}(6)^{15}\text{N}(4)$ arginine were set as a variable modification. Proteins identified by Mascot algorithm were subsequently processed in ProteinScape v2.1 with the following parameters: a minimum of two peptides with a score ≥ 15 and the FDR at 5% at the protein level were needed to accept protein identification. From the list of identified proteins, only those associated with at least three quantified peptide pairs were considered as quantifiable proteins and used for subsequent bioinformatics analysis.

The relative ratios of quantified proteins identified in both forward and reverse label-swap experiments were normalized by log₂ transformation and plotted in a scatter plot. For significant differences in relative protein abundance, the normalized ratios of the proteins were statistically evaluated for their normal distribution, and protein abundance was considered as significantly different ($p < 0.01$) in the case of ratios differing from the mean by 2.58σ as determined from the normalized ratio distributions of the biological replicate analyses.³⁸ Such proteins, clustered at the right top corner of the scatter plot, represent candidates for FRA16D fragment-specific interactors.

Gene Ontology Annotation Analysis

To determine the significantly enriched gene ontology (GO) molecular function and biological process terms related to FRA16D fragment-associated proteins, ClueGO,³⁹ a Cytoscape⁴⁰ plug-in, was employed. A two-sided minimal-likelihood test on the hypergeometric distribution, an equivalent to the classical Fisher's exact test, was utilized for the enrichment

analysis with the human genome set as a background gene population. The *p*-values for all enriched GO terms were adjusted with the Benjamini–Hochberg correction method.

Antibodies

For immunoblotting, the following antibodies were used: XPC (Novus Biological, NB100-477, 1:1000), pChk1 (Ser345, Cell Signaling, 2348, 1:500), Chk1 (Santa Cruz, sc-8408, 1:500), GAPDH (GeneTex, GTX30666, 1:2000), and MCM7 (Santa Cruz, sc-65469, 1:100). HRP-conjugated secondary antibodies were as follows: antimouse (GE-Healthcare, NA931 V, 1:1000), antirabbit (GE-Healthcare, NA934 V, 1:1000), and antigoat (Santa Cruz, sc-2020, 1:1000).

For immunofluorescence microscopy, the following primary antibodies were used: ATR (Santa Cruz (N-19) sc-1887, 1:250), ATRIP (Cell Signaling, 2737, 1:250), γ H2AX (pSer139, Millipore, 07-146, 1:500), 53BP1 (Santa Cruz, sc-22760, 1:500), Cyclin A (Leica, NCL-cyclinA, 1:200), and pH3 (pSer10, Millipore, 06-570, 1:1000). Secondary antimouse and antirabbit antibodies were Alexa Fluor 488 (A11001) and Alexa Fluor 568 (A11036) (Invitrogen, 1:1000).

Immunoblotting

For the analysis of checkpoint response, the same amounts of cells were resuspended in the SDS-PAGE sample buffer and incubated at 95 °C for 8 min with shaking (1400 rpm). The samples were resolved by SDS-PAGE (4–15% gradient) (BioRad) and subsequently transferred to a nitrocellulose membrane for immunoblotting detection by specific antibodies.

Gene Silencing

siGenome Human XPC (7508) siRNA SMART pool was purchased from Dharmacon (Cat. No. M-016040-01-0010), and transfection was conducted using siRNA MAX (Invitrogen) following the manufacturer's instructions. As a control siRNA, GGCUACGUCCAGGAGCGCACC from Eurofin MWG operon or siGenome RISC FREE control siRNA from Dharmacon (Cat. No. D-001220-01-05) were used. Both control siRNAs were tested to exclude cytotoxicity using the colony formation assay.

Biochemical Analysis of XPC Ubiquitination upon APH Treatment

U-2 OS were transfected with siXPC pool or control siRNA. Two days after the transfection, the cells were treated with 0.4 μ M aphidicolin for 24 h and subjected to lysis or biochemical cell fractionation and then analyzed by immunoblotting as previously described.⁴¹ The primary antibody used in this study was against XPC (Novus Biological, NB100-477).

Fluorescence Microscopy

Immunofluorescence Detection of DDR Factors. The transfected cells were seeded in 24 well plates and treated with 0.4 μ M APH or 0.5% DMSO 24 h before fixation. The cells were either fixed directly with 10% formalin, followed by 5 min permeabilization with 0.5% TritonX (staining for 53BP1, cyclin A), or fixed after pre-extraction (ATR, ATRIP). Samples were stained with primary antibodies at 4 °C overnight and then with secondary antibodies at room temperature for 1 h and incubated with Hoechst 33342 at room temperature for 5 min before mounting. Images were automatically recorded using an inverted fluorescence microscope BX71 (Olympus) and ScanR Acquisition software (Olympus), analyzed with ScanR Analysis software (Olympus), and evaluated with Statistica software (StatSoft). On the basis of DNA cyclin A

staining, the cell population was gated to G1 (cyclin A negative cells). Number of foci or signal intensity of respective markers was counted. Each experiment was performed with at least three biological replicates.

Immunofluorescence Analysis of Mitotic Cells. The transfected cells were seeded in a 24-well plate and treated with either 0.4 μ M APH or 0.5% DMSO for 24 h. After treatment, the cells were fixed with 10% formalin, permeabilized by 0.5% Triton X, and stained for the specific markers. Images were taken using an inverted fluorescent microscope (Zeiss Observer Z.1, 63 \times oil objective). The plates were placed onto the sliding table of the microscope and automatically scanned. On the basis of phospho-H3 marker positivity, approximately 150 mitotic cells were chosen and subsequently scanned for phospho-H2AX (γ H2AX) foci. γ H2AX foci were analyzed in custom-made software implemented in MatLab. Each experiment was performed with at least three biological replicates.

Flow Cytometry Analysis of pH3-Positive Cells

The transfected cells were seeded on 6 cm diameter Petri dish and treated with 0.2 μ M APH, 0.4 μ M APH, or 0.5% DMSO 24 h before fixation with 100 ng/mL of nocodazole added 6 h before fixation. The cells were trypsinized, fixed with cold (4 °C) 10% formalin for 15 min at RT, and permeabilized with 0.5% Triton X for 5 min. Samples were stained with the primary antibody against pH3 for 1 h at RT and then with the secondary antibody for 1 h. Cells were centrifuged and resuspended in PBS + 2% FBS with 0.5 μ g/mL of DAPI. Samples were analyzed with the BD FACSVerser flow cytometer, and pH3-positive cells were gated as indicated in Figure S-4.

RESULTS AND DISCUSSION

Experimental Strategy for the Identification of Potential CFS Interactors

The main goal of this work was to identify candidate CFS binding proteins and provide further insight into the biological function of selected hits. To perform the first unbiased proteome screen that would allow the detection of proteins bound to the structurally specific CFS sequence, we designed and performed DNA affinity chromatography³⁸ in combination with SILAC-based quantitative proteomics^{42,43} (Figure 1).

The crucial step of our experimental approach was the DNA affinity chromatography that demanded the design and synthesis of baits suitable for isolation of specific CFS interacting proteins. We based our bait on the concept that CFSs arise as a consequence of specific DNA sequences, which under replication stress create stable secondary structures that are difficult to replicate. Thus, we used a fragment mimicking the high-flexibility island within the well-characterized CFS, FRA16D,⁷ as the specific DNA bait. The ability of this sequence to form the hard-to-replicate secondary structure under our experimental conditions was verified in the Mfold program,³³ (for the final form, see Figure S-1). For distinguishing the candidate-specific CFS interactors from common DNA binding proteins, control bait with linear structure was designed and employed in parallel. Moreover, the nucleotide order was selected in a way to avoid resemblance with known promoters (for further details on control bait construction, see the Experimental Procedures). Both baits were modified at the 5' end by adding biotin to facilitate their immobilization to streptavidin-covered magnetic beads. To identify FRA16D

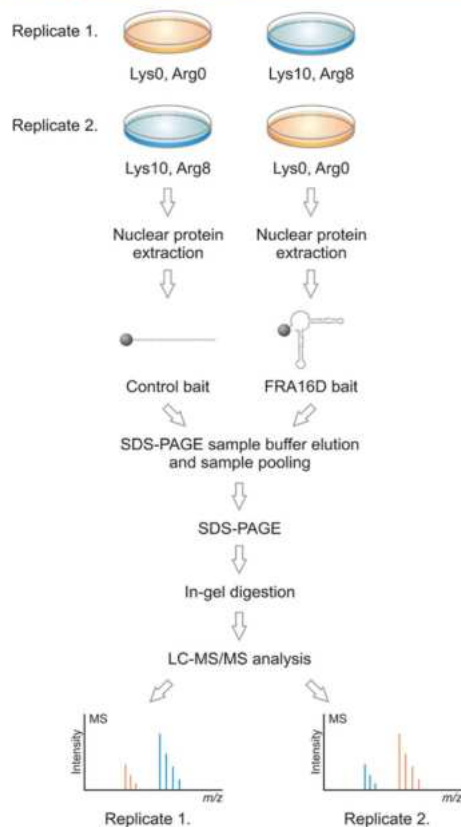


Figure 1. Experimental strategy for identification and quantification of specific FRA16D fragment interactors. Cells were grown in the SILAC “heavy” and “light” medium. The extracts of nuclear proteins were added to the resins covered by a specific FRA16D fragment as a bait and control linear sequence. After the affinity purification step, the eluates were mixed 1:1, separated by SDS-PAGE, and in-gel digested. Resulting peptide mixtures were analyzed by LC-MS/MS. The workflow was performed with cells cultured under normal conditions and also upon 0.4 μ M APH for 24 h.

fragment binding proteins, we used the following experimental strategy.

First, we performed an experiment to obtain a list of nuclear proteins interacting with the FRA16D fragment-specific bait from lysates of HeLa S3 cells grown under normal conditions. In the next experiment, the HeLa S3 cells were exposed to replication stress induced by 0.4 μ M APH, a concentration of the drug that reliably induces CFS expression.^{9,10} Importantly, a comparison of FRA16D fragment interactors from cells under normal versus replication stress conditions revealed multiple interacting proteins (Figure 2), some of which have not yet been associated with CFS biology.

Analysis of CFS-Enriched Proteins

Using a stringent threshold for FDR at less than 5%, we identified in total 655 and 282 proteins binding to the FRA16D bait in APH-treated and control cells, respectively. Protein ratios for FRA16D fragment-specific versus control bait beads could be assessed for at least 559 and 228 proteins from the above two groups, of which 410 and 150 were detected in independent biological replicates. As documented by scatter plots of \log_2 transformed ratios (Figure 2), 13 distinct proteins appeared to specifically and robustly interact with the FRA16D fragment but not with the control bait.

Among these 13 selected hits, two and eight proteins were bound to FRA16D exclusively under normal and APH-induced stress conditions, respectively, and three proteins interacted with FRA16D under both conditions (Figure 3). A validation in the form of a proof of principle for our screen was provided by the following two results. First, examination of the GO annotations of the candidate CFS binders revealed a high enrichment of proteins involved in binding to various DNA structures and proteins implicated in mechanisms responsible for genome maintenance (Figure 4A and B). This is in agreement with the use of structured DNA as the specific bait. A second and possibly even more important validation was provided by the fact that our list of 13 hits included Werner helicase (WRN) and mismatch repair protein 2 (MSH2), both proteins previously characterized for their biological functions in the maintenance of CFS stability.^{18,19}

According to the Kyoto encyclopedia of genes and genomes (KEGG) enrichment analysis, our 13 selected candidate FRA16D interactors play roles in several DNA repair pathways, including nonhomologous end-joining (NHEJ), mismatch repair (MMR), base excision repair (BER), and nucleotide excision repair (NER) (Figure 4C). The last mentioned, NER, is the pathway that operates anywhere within the genome to eliminate “bulky” DNA lesions.⁴⁵ DNA damage-binding protein 1 (DDB1), XPC, and Centrin-2 (CETN2) form the so-called initiation complex of global-genome NER (GG-NER), whereas XRCC1 and LIG3 are involved in sealing nicks or gaps after excision of the nucleotides.^{46–49} Our observation that these proteins together accumulate at the FRA16D fragment under replication stress conditions together with their high interconnectivity (Figure 3) may suggest that GG-NER could be involved in resolution of DNA structures that occur within CFS regions under replication stress.

The GG-NER initiation is supported by XPC ubiquitylation, which is promoted by the UV-DDB-ubiquitin ligase complex.⁴⁷ This UV-DDB-mediated recognition of DNA damage by XPC is particularly observed in the case of UV-induced cyclobutane pyrimidine dimers and lesions that cause low distortion of DNA helix,⁵⁰ whereas direct recognition of (6–4) pyrimidine-pyrimidone photoproducts and some other lesions caused by chemical adducts could be UV-DDB independent. To verify whether the DNA structures created upon APH treatment in CFS loci are recognized through a process that involves XPC ubiquitylation, we performed cell fractionation and assessed the ubiquitylation status of chromatin-bound XPC after APH treatment through the electrophoretic mobility of XPC. In contrast to UV-induced ubiquitylation-mediated electrophoretic mobility shift, XPC did not show such altered mobility upon treatment of cells with APH (Figure S-2), indicating a mechanism distinct from the UV response and potentially direct recognition of these replication barriers by XPC.

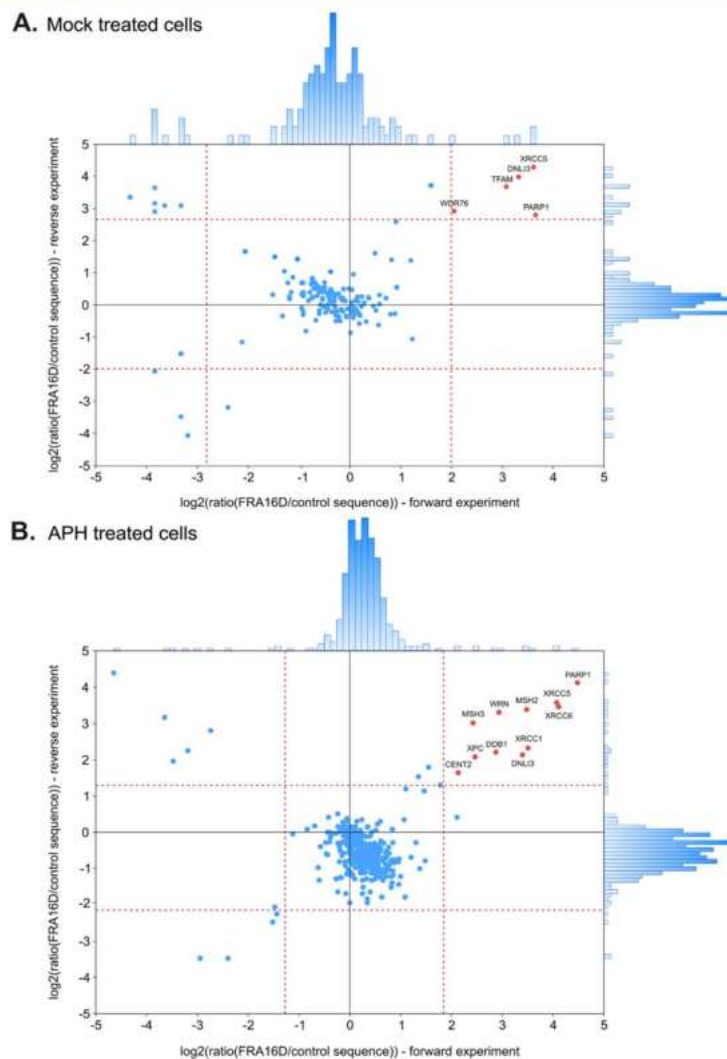


Figure 2. Determination of FRA16D fragment interaction partners. Graphs contain logarithmic ratios from both replicates “forward” H/L and “reverse” L/H plotted against each other. The specific FRA16D fragment interactors are clustered in the upper right corner (red points) because of the high ratio in both replicates of the experiment. Background proteins are centered to the origin with a 1:1 ratio in both replicates, and contaminants are observed in the upper left corner with a high ratio in the light form in both repetitions. (A) Cells cultured under normal conditions. (B) Cells exposed to 0.4 μ M APH for 24 h.

Recent studies indicate that XPC is not only the main initiator of NER, but thanks to its substrate versatility, it seems to be a general sensor of aberrant structures such as DNA cross-links and various “DNA bubbles”^{51,52} with the potential to be involved in other cellular mechanisms besides NER.⁵³ It

was shown that XPC plays a role in the elimination of oxidative damage by regulating BER,^{54,55} in chromatin remodeling and checkpoint response,^{56,57} in regulation of transcription,⁵⁸ and in the maintenance of telomere stability.⁵⁹ On the basis of these emerging reports, we next developed an automated approach to

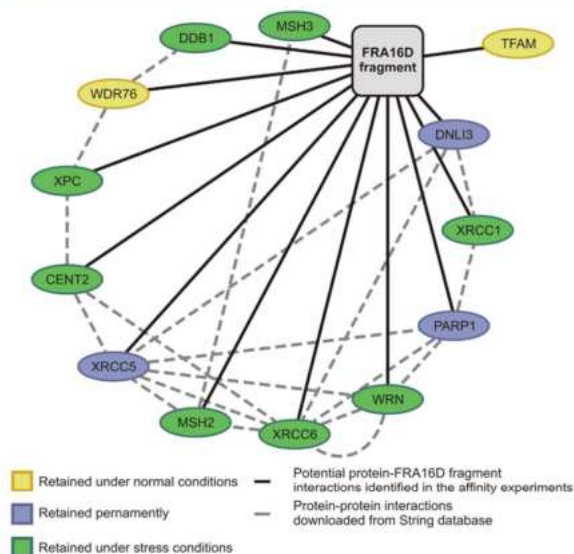


Figure 3. FRA16D fragment retained proteins and their mutual interactions. Interaction network for the proteins specifically enriched by the FRA16D fragment under normal and replication stress conditions. The depicted interactions were drawn in Cytoscape software⁴⁰ after importing the data from Figure 2 and downloading the protein–protein interactions from the String database.⁴⁴

assess mitotic CFSs and tested the possibility that CFS regions (especially under replication stress) generate some secondary DNA structures that are “sensed” by XPC.

Method for Automated Evaluation of CFS Expression in Mitosis

The involvement of proteins in the maintenance of CFS stability is usually determined by scoring for chromosomal aberrations under unperturbed control and replication stress conditions with the protein of interest either absent (mutant, deleted, or knocked down) or overexpressed. For better resolution of individual CFS regions, Giemsa staining or the FISH method on mitotic spreads is usually used.^{14,16,18} A major technical shortcoming associated with such standard approaches is high demand for the quality of mitotic spreads. Furthermore, such evaluations are very time-consuming, and a subset of smaller lesions may remain undetected. For these limitations to be overcome, a more precise method for the detection of phosphorylated histone H2AX (γ H2AX) in mitosis was developed⁶⁰ and further optimized in our present project for our purposes (Figure S-5). γ H2AX foci are commonly accepted as a marker of DNA double-stranded breaks,⁶¹ and quantification of γ H2AX immunofluorescence signal intensity, or rather the number of foci, can be used to estimate the extent of DNA damage or repair kinetics.⁶²

Our quantitative method for CFS expression is principally based on the fact that, in APH-treated human lymphoblasts, the 20 most expressed CFSs account for 80% of all detectable mitotic DNA double strand breaks.¹ Because these mitotic breaks are marked by the γ H2AX signal (Figure S-5A), the overall quantification of γ H2AX foci in mitosis after APH treatment correlates with CFS expression. Our method was

further optimized by combined immunofluorescence staining for γ H2AX and serine 10-phosphorylated histone H3 (pH3), the latter a recognized marker of mitosis. Such a setup allows for high throughput analysis using automated microscopy-based detection of mitotic cells within the cell population followed by detailed γ H2AX foci scoring selectively in the mitotic cells (Figure S-5B). The feasibility of our method for identification of factors involved in CFS stability was validated in a cellular model allowing inducible knockdown of ATR by shRNA. APH treatment resulted in an increase of γ H2AX in mitotic cells that was strongly augmented after ATR depletion (Figure S-5C), consistent with published data regarding the ATR kinase and its involvement in CFS stability.¹³

XPC Participates in Replication Stress-Induced DNA Damage Response and in the Maintenance of CFS Stability

For testing if XPC plays a role in CFS stability, the human U-2 OS cells depleted of XPC by RNAi-mediated knockdown were treated with 0.4 μ M APH for 24 h. The mitotic γ H2AX foci were quantified by the automated routine described above. Surprisingly, in an analogous experiment as with ATR knockdown, XPC deficiency caused a significant decrease in the number of γ H2AX foci after APH treatment (Figure SA,B). This observation has two possible explanations. Either the depletion of XPC leads to such a prominent form of CFS-associated instability that the G2/M checkpoint blocks such cells from mitotic entry or the CFS-associated aberrant DNA structures are sensed by a cellular mechanism that may involve XPC and that is required for the signaling from such aberrant DNA structures and thereby for generation of the ensuing enhanced γ H2AX signal. To address this intriguing observation further, we also compared the number of γ H2AX foci in XPC-

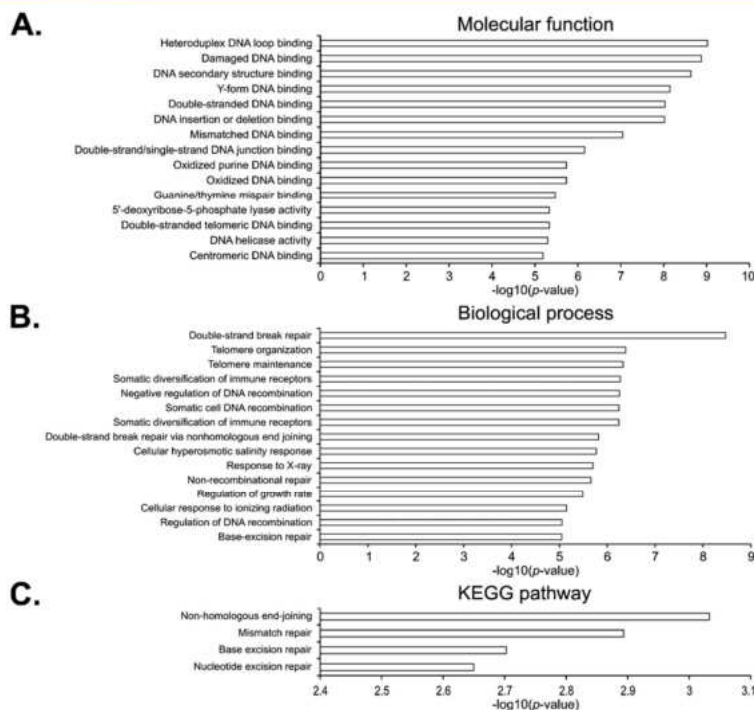


Figure 4. Gene ontology annotation enrichment analysis of identified FRA16D fragment interaction partners. Most significantly enriched terms of identified interaction proteins reveal structured DNA affinity, DNA damage signaling, and repair signatures as depicted in the graphs. (A) Molecular functions, (B) biological functions, and (C) significantly enriched KEGG pathways with significance expressed as $-\log_{10}$ of the respective p values.

depleted and ATR/XPC codepleted U-2 OS mitotic cells after APH treatment. XPC depletion resulted in decreased γ H2AX foci in mitotic cells compared to that in control mock-depleted cells (Figure S-6). In addition, depletion of XPC in cells codepleted for ATR further decreased the number of γ H2AX foci in mitotic cells compared to cells depleted of ATR alone (Figure S-6).

Given that ATR is the major checkpoint kinase whose signaling ensures arrest of cells with damaged DNA at the G2/M boundary,⁶³ we argued that the observed decrease or loss of mitotic γ H2AX signaling might reflect a previously unrecognized positive role of XPC in promoting checkpoint signaling within CFSs. On the basis of our results with mitotic γ H2AX, we suggest the possibility that XPC may bind to stalled replication forks to initiate incision of the DNA structures, which are difficult to replicate, such as the high-flexibility islands within CFSs. The XPC-driven incision process could then initiate and/or contribute to activation of the DDR signaling and create structures marked by γ H2AX foci in mitosis. Thus, in the absence of XPC, at least a fraction of stalled replication forks are not turned into such "visible" lesions, leading to insufficient checkpoint response documented here by the impaired γ H2AX signal. Provided that this proposed scenario is correct, XPC-deficient cells exposed to

replication stress should accumulate unresolved replication fork intermediates, particularly in the vulnerable genomic loci in the vicinity of CFSs. Importantly, ineffective checkpoint signaling due to XPC depletion would make such cells largely unresponsive ("blind") to the accumulating aberrant and potentially hazardous structures at CFSs and allow entry into mitosis despite the danger of breaking the chromosomes.

To test if such unresolved abnormal replication intermediates are indeed present and transferred through mitosis to the next cell generation, we scored the so-called 53BP1 bodies in G1 cells, a commonly recognized feature of cells undergoing enhanced replication stress in the previous cell cycle.⁶⁴ Mechanistically, unresolved aberrant underreplicated loci that escape into mitosis may result in DNA double strand breaks during mitosis and then were recognized and stabilized in early postmitotic daughter cells by 53BP1 and related proteins, forming the microscopically recognizable G1 53BP1 bodies.⁶⁴

Indeed, quantification of 53BP1 bodies in G1 cells in our experiments revealed a significant increase in the XPC-depleted cells upon 0.4 μ M APH treatment, a result which is fully in line with the above hypothesis (Figure 5C,D).

On the basis of the obtained data, we conclude that XPC participates in detection and/or resolution of replication

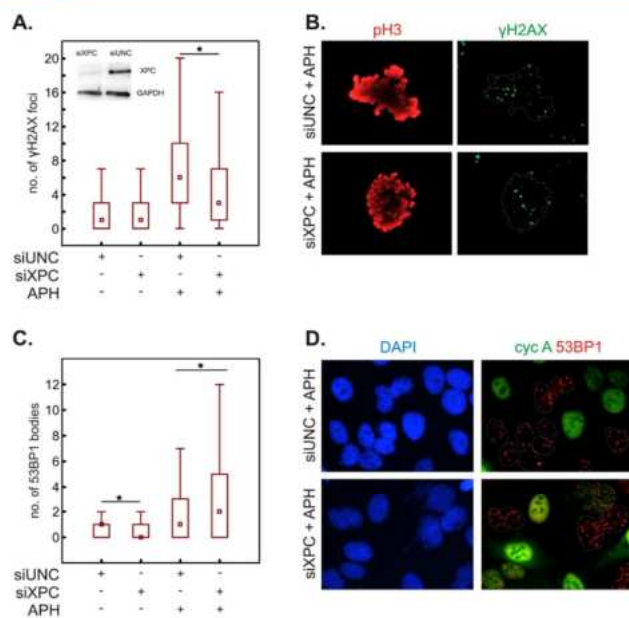


Figure 5. Analysis of DNA damage in XPC-depleted cells. Replication stress-induced DNA damage signaling is significantly altered in XPC-silenced cells. (A) Immunofluorescence detection shows a significant decrease of γ H2AX foci signal in XPC-depleted mitotic cells. (B) Illustrative pictures depicting the evaluation based on pH3 immunostaining of mitotic cells and γ H2AX foci. (C) Immunofluorescence detection shows a significant increase in G1 phase-associated 53BP1 bodies in XPC-depleted cells. (D) Illustrative pictures depicting the evaluation based on immunostaining of the S-G2 marker (Cyclin A) and 53BP1 bodies. Only cells negative for Cyclin A (encircled) were analyzed. The asterisks mean significance with a p -value < 0.05.

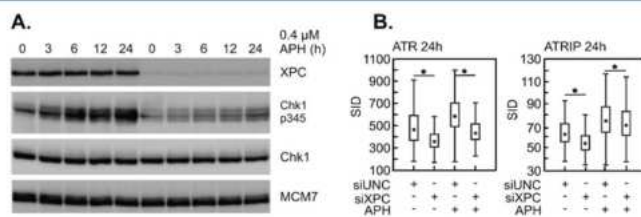


Figure 6. ATR-promoted checkpoint signaling is altered in XPC-depleted cells. (A) Western blot-based analysis of impaired phosphorylation of direct ATR target Chk1 in XPC-silenced cells. Cells were treated by APH and harvested at various time points. MCM7 served as a loading control. (B) Microscopy-based quantification of ATR and ATRIP recruitment to the chromatin shows a significant decrease in XPC-silenced cells under normal conditions and also after APH-induced replication stress.

barriers arising at CFS regions and promotes checkpoint activation.

XPC Influences Checkpoint Response after Replication Stress

To assess whether XPC depletion indeed influences checkpoint signaling after APH-induced replication stress, we tested phosphorylation of Chk1, the key ATR substrate and effector kinase promoting G2/M checkpoint arrest.⁶³ Consistent with our conceptual predictions, knockdown of XPC in two human cancer cell lines (U-2 OS, HeLa S3) and a diploid fibroblast

strain (TIG-3) resulted in a prominent negative impact on Chk1 phosphorylation at early time points after treatment with 0.4 μ M APH (Figure 6A and Figure S-3). In addition, the mitotic indices in such experiments, measured as the accumulation of nocodazole-arrested pH3 positive mitotic cells, were shifted toward unscheduled mitotic entry, pointing at impaired checkpoint function in the XPC-depleted cells (Figure S-4A,B). XPC-depleted U-2 OS cells treated with APH also showed elevated numbers of 53BP1 bodies in G1 phase after aberrant mitotic progression. Similarly, XPC-depleted

APH-treated TIG3 and HeLa S3 cells did not show a prominent elevation of G1 53BP1 bodies, suggesting that this type of readout is not manifested in all cell lines, probably due to rapid elimination of the damaged cells (data not shown). As the ATR-Chk1 cascade represents a major checkpoint signaling "unit", we also performed quantitative immunofluorescence microscopy analysis of chromatin-bound ATR and its partner ATRIP. The chromatin-bound signal of both proteins was decreased in XPC-depleted cells (Figure 6B). How XPC promotes binding of the ATR/ATRIP complex to chromatin remains elusive, but it is known that the binding of ATR is a necessary prerequisite for subsequent ATR-dependent checkpoint activation,⁶³ thereby providing a plausible explanation for the impaired Chk1 phosphorylation detected in our experiments with XPC-depleted cells under replication stress.

Altogether, the data set obtained in our present study supports the idea of the XPC/ATR-Chk1 pathway interaction in response to replication stress and their functional link in promoting activation of checkpoint signaling. Notably, a broadly analogous function of XPC was described for the lesions induced by UV radiation where cells depleted for XPC displayed impaired ATR activation and phosphorylation of its downstream target Chk1.⁵⁷ On the other hand, signaling of UV-induced lesions reportedly relied on XPC during G1 phase but not during S phase.⁶⁵ Our data in response to APH on the other hand demonstrate an S-phase relevant ATR/Chk1-promoting role of XPC in checkpoint signaling, most likely reflecting the different nature of the APH-induced relative to UV-induced DNA lesions as well as the differential requirement for XPC ubiquitylation, which are important mechanistic differences demonstrated in our present study. In terms of the impact on DNA, APH generates long stretches of single-stranded DNA by uncoupling of DNA polymerases and helicases, thereby creating vulnerable secondary structures, especially at CFSs that become the substrate for XPC and possibly GG-NER. Upon UV irradiation, on the other hand, DNA cross-links are formed and rapidly processed either by translesion synthesis⁶⁶ or converted into DNA double-strand breaks.⁶⁷

Overall, we propose that, in the absence of XPC, the replication problems that occur at CFSs are not properly recognized and/or processed during the S phase and become the source of subsequent genomic instability. Last but not least, our results also illustrate the power of innovative high-throughput screens based on quantitative proteomics and hypothesis-driven strategies to identify new components of fundamental mechanisms, such as cellular stress responses and maintenance of genomic integrity.

CONCLUSIONS

In this study, we performed the first unbiased proteome-wide screen to identify new putative proteins responsible for maintenance of CFS stability. Besides previously characterized WRN and MSH2 proteins, we also identified several additional candidates whose role in CFS maintenance warrants deeper characterization. Because of the fact that almost half of the identified proteins are implicated in NER, the XPC protein as the main initiator of the NER pathway was chosen for a follow-up functional study.

On the basis of our results, we propose a hypothesis for the role of XPC in preventing CFS expression by promoting checkpoint signaling under replication stress. We show that XPC deficient cells are incapable of proper checkpoint

activation in response to RS, leading to increased genomic instability manifested as accumulation of specific DNA lesions marked by 53BP1 bodies in G1 cells. We further suggest that this phenotype may reflect a new role for XPC, or possibly the whole GG-NER repair pathway, in sensing aberrant replication structures and providing the incision step, a role that is particularly required at hard-to-replicate structures in CFS loci formed after RS. Thus, XPC deficiency leads to impaired CFS-associated signaling through the ATR/ATRIP-Chk1 axis, thereby allowing for inappropriate passage of cells with aberrant structures associated with stalled replication forks through mitosis. The fate of such damaged cells depends on the respective genetic background and fitness of cellular DDR. In the next cell generation of U-2 OS cells passing through the unscheduled mitosis, such aberrant DNA structures can be detected as DNA double strand breaks marked by focal accumulation of 53BP1 in the form of the 53BP1 bodies. In some other cell lines, represented here by HeLa S3 or TIG-3 cells, this aberrant scenario during the metaphase/anaphase transition and/or immediately after mitosis of APH-exposed cells is "solved" by elimination of such abnormal cells through apoptosis. This is consistent with the notion that CFSs are important sites of the genome that may serve as alarm sensors for elimination of cells with unstable genetic material arising upon replication stress. Through this mechanism, CFSs may contribute to the intrinsic cellular barrier against tumorigenesis.⁶⁸

Apart from this important biological insight into the function of XPC protein and its relevance for chromosomal (in)stability and cancer, we also document that the strategy of using DNA structure-specific baits, which can be successfully combined with quantitative proteomics, can generate a wealth of results valuable for contemporary biomedicine.

ASSOCIATED CONTENT

Supporting Information

The Supporting Information is available free of charge on the ACS Publications website at DOI: 10.1021/acs.jproteome.6b00622.

Final structure of specific FRA16D fragment bait, verification of XPC ubiquitylation upon APH, 53BP1 bodies in G1 cells, checkpoint response and MI of TIG-3, HeLa XPC KD cells, illustration of automated evaluation of γ H2AX foci in mitosis, detection of γ H2AX in XPC-silenced U-2 OS shATR mitotic cells, and description of MS analyzer settings and gradient for peptide separation during LC-MS/MS (PDF)

Quantification of FRA16D interactors with APH treatment with a comparison of normal vs reverse experiment (XLSX)

Quantification of FRA16D interactors with MOCK treatment with a comparison of normal vs reverse experiment (XLSX)

Detailed protein report of APH treatment normal experiment (PDF)

Detailed protein report of APH treatment reverse experiment (PDF)

Detailed protein report of MOCK treatment normal experiment (PDF)

Detailed protein report of MOCK treatment reverse experiment (PDF)

Summary of complete protein identification and quantification MS data (XLSX)

AUTHOR INFORMATION

Corresponding Authors

*E-mail: martin.mistik@upol.cz.

*E-mail: jb@cancer.dk.

Notes

The authors declare no competing financial interest.

ACKNOWLEDGMENTS

We would like to thank our colleagues Juraj Kramara for discussion of experiments and Iva Protivankova for assistance with western blot analyses. L.B., I.C., and R.L. were supported by grant LO1204 from the National Program of Sustainability I, MEYS. M.M. and J.B. were supported by the Kellner Family Foundation. L.B. and E.V. were supported by the internal grant IGA-LF-2016-030. J.B. was supported by the Danish Council for Independent Research (DFR-1331-00262B), the Novo Nordisk Foundation (grant 16584), and the Swedish Research Council. M.M., J.B. and M.Y. were supported by the Grant Agency of the Czech Republic 13-17555S and the Norwegian Financial Mechanism CZ09 (Project PHOSCAN 7F14061); E.V., M.M., J.B., T.F., J.G., K.C., and J.V. were supported by the grant LO1304 from the National Program of Sustainability I, MEYS. M.M. was supported by Czech-BioImaging project (LM2015062 funded by MEYS, CR). K.K. was supported by the Endowment Fund of Palacky University.

ABBREVIATIONS

APH, aphidicolin; BER, base excision repair; CFS, common fragile site; DDR, DNA damage response; DSB, double-stranded break; FDR, false discovery rate; GG-NER, global genome nucleotide excision repair; GO, gene ontology; KEGG, Kyoto encyclopedia of genes and genomes; pH3, mitotically phosphorylated histone H3; RS, replication stress; SILAC, stable isotope labeling of amino acids in cell culture; MMR, mismatch repair; NER, nucleotide excision repair; NHEJ, nonhomologous end joining; γ H2AX, phosphohistone H2AX.

REFERENCES

- Glover, T. W.; Berger, C.; Coyle, J.; Echo, B. DNA polymerase alpha inhibition by aphidicolin induces gaps and breaks at common fragile sites in human chromosomes. *Hum. Genet.* **1984**, *67*, 136–142.
- Ruiz-Herrera, A.; Ponsá, M.; Gargá, F.; Egozcue, J.; García, M. Fragile sites in human and Macaca fascicularis chromosomes are breakpoints in chromosome evolution. *Chromosome Res.* **2002**, *10*, 33–44.
- Arlt, M. F.; Durkin, S. G.; Ragland, R. L.; Glover, T. W. Common fragile sites as targets for chromosome rearrangements. *DNA Repair* **2006**, *5*, 1126–1135.
- Durkin, S. G.; Ragland, R. L.; Arlt, M. F.; Mülle, J. G.; Warren, S. T.; Glover, T. W. Replication stress induces tumor-like microdeletions in FHIT/FRA3B. *Proc. Natl. Acad. Sci. U. S. A.* **2008**, *105*, 246–251.
- Schwartz, M.; Zlotorynski, E.; Kerem, B. The molecular basis of rare and common fragile sites. *Cancer Lett.* **2006**, *232*, 13–26.
- Zlotorynski, E.; Rahat, A.; Skaug, J.; Ben-Porat, N.; Ozeri, E.; Hershberg, R.; Levi, A.; Scherer, S. W.; Margalit, H.; Kerem, B. Molecular basis of expression of common and rare fragile sites. *Mol. Cell. Biol.* **2003**, *23*, 7143–7151.
- Zhang, H.; Freudenreich, C. H. An AT-Rich sequence in human common fragile site FRA16D causes fork stalling and chromosome breakage in *S. cerevisiae*. *Mol. Cell* **2007**, *27*, 367–379.

- Helmrich, A.; Ballarino, M.; Tora, L. Collisions between replication and transcription complexes cause common fragile site instability at the longest human genes. *Mol. Cell* **2011**, *44*, 966–977.
- Cheng, C. H.; Kuchta, R. D. DNA polymerase ϵ : Aphidicolin inhibition and the relationship between polymerase and exonuclease activity. *Biochemistry* **1993**, *32*, 8568–8574.
- Mrasek, K.; Schoder, C.; Teichmann, A. C.; Behr, K.; Franze, B.; Wilhelm, K.; Blaurock, N.; Claussen, U.; Liehr, T.; Weise, A. Global screening and extended nomenclature for 230 aphidicolin inducible fragile sites, including 61 yet unreported ones. *Int. J. Oncol.* **2010**, *36*, 929–940.
- Chang, D. J.; Lupardus, P. J.; Cimprich, K. A. Monoubiquitination of proliferating cell nuclear antigen induced by stalled replication requires uncoupling of DNA polymerase and minichromosome maintenance helicase activities. *J. Biol. Chem.* **2006**, *281*, 32081–32088.
- Casper, A. M.; Durkin, S. G.; Arlt, M. F.; Glover, T. W. Chromosomal instability at common fragile sites in Seckel Syndrome. *Am. J. Hum. Genet.* **2004**, *75*, 654–660.
- Casper, A. M.; Nghiem, P.; Arlt, M. F.; Glover, T. W. ATR regulates fragile site stability. *Cell* **2002**, *111*, 779–789.
- Durkin, S. G.; Arlt, M. F.; Howlett, N. G.; Glover, T. W. Depletion of Chk1, but not Chk2, induces chromosomal instability and breaks at common fragile sites. *Oncogene* **2006**, *25*, 4381–4388.
- Arlt, M. F.; Xu, B.; Durkin, S. G.; Casper, A. M.; Kastan, M. B.; Glover, T. W. BRCA1 is required for common fragile site stability via its G2/M checkpoint function. *Mol. Cell. Biol.* **2004**, *24*, 6701–6709.
- Howlett, N. G.; Taniuchi, T.; Durkin, S. G.; D'Andrea, A. D.; Glover, T. W. The Fanconi anemia pathway is required for the DNA replication stress response and for the regulation of common fragile site stability. *Hum. Mol. Genet.* **2005**, *14*, 693–701.
- Musio, A.; Montagna, C.; Mariani, T.; Tilenni, M.; Focarelli, M. L.; Brait, L.; Indino, E.; Benedetti, P. A.; Chessa, L.; Albertini, A.; Ried, T.; Vezoni, P. SMCI involvement in fragile site expression. *Hum. Mol. Genet.* **2005**, *14*, 525–533.
- Pirzio, L. M.; Pichierri, P.; Bignami, M.; Franchitto, A. Werner syndrome helicase activity is essential in maintaining fragile site stability. *J. Cell Biol.* **2008**, *180*, 305–314.
- Turner, B. C.; Ottey, M.; Zimonjic, D. B.; Potoczek, M.; Hauck, W. W.; Pequinot, E.; Keck-Waggoner, C. L.; Sevignani, C.; Aldaz, C. M.; McCue, P. A.; Palazzo, J.; Huebner, K.; Popescu, N. C. The Fragile histidine triad/commn chromosome fragile site 3B locus and repair-deficient cancers. *Cancer Res.* **2002**, *61*, 4054–4060.
- Di Micco, R.; Fumagalli, M.; Cicalese, A.; Piccinin, S.; Gasparini, P.; Luise, C.; Schurra, C.; Garre, M.; Nuciforo, P. G.; Bensimon, A.; Maestro, R.; Pelicci, P. G.; d'Adda di Fagnana, F. Oncogene-induced senescence is a DNA damage response triggered by DNA hyper-replication. *Nature* **2006**, *444*, 638–642.
- Bester, A. C.; Roniger, M.; Oren, Y. S.; Im, M. M.; Sarni, D.; Chaoat, M.; Bensimon, A.; Zamir, G.; Shewach, D. S.; Kerem, B. Nucleotide deficiency promotes genomic instability in early stage of cancer development. *Cell* **2011**, *145*, 435–446.
- Bartkova, J.; Horejsi, Z.; Koed, K.; Kramer, A.; Tort, F.; Zieger, K.; Gulberg, P.; Sehested, M.; Nesland, J. M.; Lukas, C.; Orntoft, T.; Lukas, J.; Bartek, J. DNA damage response as a candidate anti-cancer barrier in early human tumorigenesis. *Nature* **2005**, *434*, 864–870.
- Bartkova, J.; Rezaei, N.; Liontos, M.; Karakaidos, P.; Kletsas, D.; Issaeva, N.; Vassiliou, L. V.; Kolettas, E.; Niforou, K.; Zoumpourlis, V. C.; Takaoka, M.; Nakagawa, H.; Tort, F.; Fugger, K.; Johansson, F.; Sehested, M.; Andersen, C. L.; Dyrsjot, L.; Orntoft, T.; Lukas, J.; Kittas, C.; Helleday, T.; Halazonetis, T. D.; Bartek, J.; Gorgoulis, V. G. Oncogene-induced senescence is part of the tumorigenesis barrier imposed by DNA damage checkpoints. *Nature* **2006**, *444*, 633–637.
- Gorgoulis, V. G.; Vassiliou, L. V.; Karakaidos, P.; Zacharatos, P.; Kotsinas, A.; Liloglou, T.; Venere, M.; Dittullo, R. A., Jr.; Kastrinakis, N. G.; Levy, B.; Kletsas, D.; Yoneta, A.; Herlyn, M.; Kittas, C.; Halazonetis, T. D. Activation of the DNA damage checkpoint and genomic instability in human precancerous lesions. *Nature* **2005**, *434*, 907–913.

- (25) Lu, X.; Parvathaneni, S.; Hara, T.; Lal, A.; Sharma, S. Replication stress induces specific enrichment of RECQ1 at common fragile site FRA3B and FRA16D. *Mol. Cancer* **2013**, *12*, 1–12.
- (26) Bergoglio, V.; Boyer, A. S.; Walsh, E.; Naim, V.; Legube, G.; Lee, M. Y.; Rey, L.; Rosselli, F.; Cazaux, C.; Eckert, K. A.; Hoffmann, J. S. DNA synthesis by Pol η promotes fragile site stability by preventing under-replicated DNA in mitosis. *J. Cell Biol.* **2013**, *201*, 395–408.
- (27) Butter, F.; Scheibe, M.; Morl, M.; Mann, M. Unbiased RNA-protein interaction screen by quantitative proteomics. *Proc. Natl. Acad. Sci. U. S. A.* **2009**, *106*, 10626–10631.
- (28) Mittler, G.; Butter, F.; Mann, M. A SILAC-based DNA protein interaction screen that identifies candidate binding proteins to functional DNA elements. *Genome Res.* **2009**, *19*, 284–293.
- (29) Scheibe, M.; Arnoult, N.; Kappel, D.; Buchholz, F.; Decottignies, A.; Butter, F.; Mann, M. Quantitative interaction screen of telomeric repeat-containing RNA reveals novel TERRA regulators. *Genome Res.* **2015**, *23*, 2149–2157.
- (30) Trinkle-Mulcahy, L.; Boulon, S.; Lam, Y. W.; Urcia, R.; Boisvert, F. M.; Vandermeere, F.; Morrice, N. A.; Swift, S.; Rothbauer, U.; Leonhardt, H.; Lamond, A. Identifying specific protein interaction partners using quantitative mass spectrometry and bead proteomes. *J. Cell Biol.* **2008**, *183*, 223–239.
- (31) Hubner, N. C.; Bird, A. W.; Cox, J.; Spletstoesser, B.; Bandilla, P.; Poser, I.; Hyman, A.; Mann, M. Quantitative proteomics combined with BAC Transgene-Omics reveals in vivo protein interactions. *J. Cell Biol.* **2010**, *189*, 739–754.
- (32) Danielsen, J. M. R.; Larsen, D. H.; Schou, K. B.; Freire, R.; Falck, J.; Bartek, J.; Lukas, J. HCLK2 is required for activity of the DNA damage response kinase ATR. *J. Biol. Chem.* **2009**, *284*, 4140–4147.
- (33) Zuker, M. Mfold web server for nucleic acid folding and hybridization prediction. *Nucleic Acids Res.* **2003**, *31*, 3406–3415.
- (34) Schug, J. Using TESS to predict transcription factor binding sites in DNA sequence. *Curr. Protoc. Bioinformatics* **2008**, *1*.
- (35) Shevchenko, A.; Tomas, H.; Havlis, J.; Olsen, J. V.; Mann, M. In-gel digestion for mass spectrometric characterization of proteins and proteomes. *Nat. Protoc.* **2006**, *1*, 2856–2860.
- (36) Sebel, M.; Stosova, T.; Havlis, J.; Wielsch, N.; Thomas, H.; Zdrahal, Z.; Shevchenko, A. Thermostable trypsin conjugates for high-throughput proteomics: synthesis and performance evaluation. *Proteomics* **2006**, *6*, 2959–2963.
- (37) Rappsilber, J.; Mann, M.; Ishihama, Y. Protocol for micro-purification, enrichment, pre-fractionation and storage of peptides for proteomics using StageTips. *Nat. Protoc.* **2007**, *2*, 1896–1906.
- (38) Oppermann, F. S.; Gnad, F.; Olsen, J. V.; Hornberger, R.; Greff, Z.; Keri, G.; Mann, M.; Daub, H. Large-scale proteomics analysis of the human kinome. *Mol. Cell. Proteomics* **2009**, *8*, 1751–1764.
- (39) Bindea, G.; Mlecnik, B.; Hackl, H.; Charoentong, P.; Tosolini, M.; Kirilovsky, A.; Fridman, W. H.; Pages, F.; Trajanoski, Z.; Galon, J. ClueGO: a Cytoscape plug-in to decipher functionally grouped gene ontology and pathway annotation networks. *Bioinformatics* **2009**, *25*, 1091–1093.
- (40) Shannon, P.; Markiel, A.; Ozier, O.; Baliga, N. S.; Wang, J. T.; Ramage, D.; Amin, N.; Schwikowski, B.; Ideker, T. Cytoscape: a software environment for integrated models of biomolecular interaction networks. *Genome Res.* **2003**, *13*, 2498–2504.
- (41) Yamada, M.; Watanabe, K.; Mistrik, M.; Vesela, E.; Protivankova, I.; Mailand, N.; Lee, M.; Masai, H.; Lukas, J.; Bartek, J. ATR-Chk1-APC/C^{oh1}-dependent stabilization of Cdc7-ASK (Dbf4) kinase is required for DNA lesion bypass under replication stress. *Genes Dev.* **2013**, *27*, 2459–2472.
- (42) Ong, S. E.; Blagoev, B.; Kratchmarova, I.; Kristensen, D. B.; Steen, H.; Pandey, A.; Mann, M. Stable isotope labeling of amino acids in cell culture, SILAC, as a simple and accurate approach to expression proteomics. *Mol. Cell. Proteomics* **2002**, *1*, 376–386.
- (43) Ong, S. E.; Mann, M. A practical recipe for stable isotope labeling by amino acids in cell culture (SILAC). *Nat. Protoc.* **2007**, *1*, 2650–2660.
- (44) von Mering, C.; Huynen, M.; Jaeggi, D.; Schmidt, S.; Bork, S.; Snel, B. STRING: a database of predicted functional associations between proteins. *Nucleic Acids Res.* **2003**, *31*, 258–261.
- (45) Gillet, L. C. J.; Schärer, O. D. Molecular mechanisms of mammalian global genome nucleotide excision repair. *Chem. Rev.* **2006**, *106*, 253–276.
- (46) Sugawara, K.; Ng, J. M. Y.; Masutani, Ch.; Iwai, S.; van der Spek, P. J.; Eker, A. P. M.; Hanaoka, F.; Bootsma, D.; Hoeijmakers, J. H. J. Xeroderma pigmentosum group C protein complex is the initiator of Global Genome Nucleotide Excision repair. *Mol. Cell* **1998**, *2*, 223–232.
- (47) Sugawara, K.; Okuda, Y.; Saijo, M.; Nishi, R.; Matsuda, N.; Chu, G.; Mori, T.; Iwai, S.; Tanaka, K.; Hanaoka, F. UV-induced ubiquitylation of XPC protein mediated by UV-DDB-ubiquitin ligase complex. *Cell* **2005**, *121*, 387–400.
- (48) Nishi, R.; Okuda, Y.; Watanabe, E.; Mori, T.; Iwai, S.; Masutani, C.; Sugawara, K.; Hanaoka, F. Centrin-2 stimulates nucleotide excision repair by interacting with xeroderma pigmentosum group C protein. *Mol. Cell. Biol.* **2005**, *25*, 5664–5674.
- (49) Moser, J.; Kool, H.; Giakzidis, I.; Caldecott, K.; Mullenders, L. H. F.; Foustier, M. L. Sealing of chromosomal DNA nicks during nucleotide excision repair requires XRCC1 and DNA ligase III alpha in a cell-cycle-specific manner. *Mol. Cell* **2007**, *27*, 311–323.
- (50) Fitch, M. E.; Nakajima, S.; Yasui, A.; Ford, J. M. In vivo recruitment of XPC to UV induced cyclobutane pyrimidine dimers by the DDB2 gene product. *J. Biol. Chem.* **2003**, *278*, 46906–46910.
- (51) Sugawara, K.; Shimizu, Y.; Iwai, S.; Hanaoka, F. A molecular mechanism for DNA damage recognition by the xeroderma pigmentosum group C protein complex. *DNA Repair* **2002**, *1*, 95–107.
- (52) Krasikova, Y. S.; Rechkunova, N. Y.; Maltseva, E. A.; Anarbaev, R. O.; Pestryakov, P. E.; Sugawara, K.; Min, J. H.; Lavrik, O. L. Human and yeast DNA damage recognition complexes bind with high affinity DNA structures mimicking in size transcription bubble. *J. Mol. Recognit.* **2013**, *26*, 653–661.
- (53) Shell, S. M.; Hawkins, E. K.; Tsai, M. S.; Hlaing, A. S.; Rizzo, C. J.; Chazin, W. J. Xeroderma pigmentosum complementation group C protein (XPC) serves as a general sensor of damaged DNA. *DNA Repair* **2013**, *12*, 947–953.
- (54) Melis, J. P. M.; Kuiper, R. V.; Zwart, E.; Robinson, J.; Pennings, J. L. A.; van Oostrom, C. T. M.; Luijten, M.; van Steeg, H. Slow accumulation of mutations in (XPC^{-/-})mice upon induction of oxidative stress. *DNA Repair* **2013**, *12*, 1081–1086.
- (55) D'Errico, M.; Parlanti, E.; Teson, M.; de Jesus, B. M. B.; Degan, P.; Calcagnile, A.; Jaruga, P.; Bjoras, M.; Crescenzi, M.; Pedrini, A. M.; Egly, J. M.; Zambruno, G.; Stefanini, M.; Dizdaroğlu, M.; Dogliotti, E. New functions of XPC in the protection of human skin cells from oxidative damage. *EMBO J.* **2006**, *25*, 4305–4315.
- (56) Ray, A.; Mir, S. N.; Wani, G.; Zhao, Q.; Battu, A.; Zhu, Q.; Wang, Q. E.; Wani, A. A. Human SNF5/INI1, a component of the human SWI/SNF chromatin remodeling complex, promotes nucleotide excision repair by influencing ATM recruitment and downstream H2AX phosphorylation. *Mol. Cell. Biol.* **2009**, *29*, 6206–6219.
- (57) Ray, A.; Milum, K.; Battu, A.; Wani, G.; Wani, A. A. NER initiation factors, DDB2 and XPC, regulate UV radiation response by recruiting ATR and ATM kinases to DNA damage sites. *DNA Repair* **2013**, *12*, 273–283.
- (58) Le May, N.; Mota-Fernandes, D.; Velez-Cruz, R.; Iltis, I.; Biard, D.; Egly, J. M. NER factors are recruited to active promoters and facilitate chromatin modification for transcription in the absence of exogenous genotoxic attack. *Mol. Cell* **2010**, *38*, 54–66.
- (59) Stout, G. J.; Blasco, M. A. Telomere length and telomerase activity impact the UV sensitivity syndrome xeroderma pigmentosum C. *Cancer Res.* **2013**, *73*, 1844–1854.
- (60) Löffler, H.; Fechter, A.; Matuszewska, M.; Saffrich, R.; Mistrik, M.; Marhold, J.; Hornung, C.; Westermann, F.; Bartek, J.; Kramer, A. Cep63 recruits Cdk1 to the centrosome: Implications for regulation of mitotic entry, centrosome amplification and genome maintenance. *Cancer Res.* **2011**, *71*, 2129–2139.

- (61) Rogakou, E. P.; Pilch, D. R.; Orr, A. H.; Ivanova, V. S.; Bonner, W. M. DNA double-stranded breaks induce histone H2AX phosphorylation on Serine 139. *J. Biol. Chem.* **1998**, *273*, 5858–5868.
- (62) Ibuki, Y.; Shikata, M.; Toyooka, T. γ H2AX is a sensitive marker of DNA damage induced by metabolically activated 4-(methylnitrosamino)-1-(3-pyridyl)-1-butanone. *Toxicol. In Vitro* **2015**, *29*, 1831–1838.
- (63) Liu, Q. H.; Guntuku, S.; Cui, X. S.; Matsuoka, S.; Cortez, D.; Tamai, K.; Luo, G. B.; Carattini-Rivera, S.; DeMayo, F.; Bradley, A.; Donehower, L. A.; Elledge, S. J. Chk1 is an essential kinase that is regulated by ATR and required for the G(2)/M DNA damage checkpoint. *Genes Dev.* **2000**, *14*, 1448–1459.
- (64) Lukas, C.; Savic, V.; Bekker-Jensen, S.; Doil, C.; Neumann, B.; Pedersen, R. S.; Grøfte, M.; Chan, K. L.; Hickson, I. D.; Bartek, J.; Lukas, J. 53BP1 nuclear bodies form around DNA lesions generated by mitotic transmission of chromosomes under replication stress. *Nat. Cell Biol.* **2011**, *13*, 243–253.
- (65) Ray, A.; Blevins, Ch.; Wani, G.; Wani, A. A. ATR- and ATM-mediated DNA damage response is dependent on excision repair assembly during G but not in S phase of cell cycle. *PLoS One* **2016**, *11*, e0159344.
- (66) Shachar, S.; Ziv, O.; Avkin, S.; Adar, S.; Wittschieben, J.; Reißner, T.; Chaney, S.; Friedberg, E. C.; Wang, Z.; Carell, T.; Geacintov, N.; Livneh, Z. Two-polymerase mechanisms dictate error-free and error-prone translesion DNA synthesis in mammals. *EMBO J.* **2009**, *28*, 383–393.
- (67) Elvers, L.; Johansson, F.; Groth, P.; Erixon, K.; Helleday, T. UV stalled replication fork restart by re-priming in human fibroblasts. *Nucleic Acids Res.* **2011**, *39*, 7049–7057.
- (68) Georgakilas, A. G.; Tsantoulis, P.; Kotsinas, A.; Michalopoulos, I.; Townsend, P.; Gorgoulis, V. G. Are common fragile sites merely structural domains or highly organized functional units susceptible to oncogenic stress? *Cell. Mol. Life Sci.* **2014**, *71*, 4519–4544.

Report

Low-dose DNA damage and replication stress responses quantified by optimized automated single-cell image analysis

Martin Mistrik,^{1,2,†} Lenka Oplustilova,^{1,2,†} Jiri Lukas¹ and Jiri Bartek^{1,2,*}

¹Institute of Cancer Biology and Centre for Genotoxic Stress Research; Danish Cancer Society; Copenhagen, Denmark; ²Laboratory of Genome Integrity; Palacky University; Olomouc, Czech Republic

[†]These authors contributed equally to this work.

Abbreviations: ATM, ataxia telangiectasia mutated; ATR, ATM and Rad3-related; DDR, DNA damage response; DNA-PK, DNA-dependent protein kinase; DNA DSB, DNA double strand break; HR, homologous recombination; HU, hydroxyurea; IR, ionizing radiation; ssDNA, single-stranded DNA; γ -H2AX, serine 139-phosphorylated histone 2AX

Key words: DNA damage, replication stress, γ -H2AX, Rad51 foci, cancer cells, image analysis, homologous recombination, DNA breakage repair kinetics, cell cycle

Maintenance of genome integrity is essential for homeostasis and survival as impaired DNA damage response (DDR) may predispose to grave pathologies such as neurodegenerative and immunodeficiency syndromes, cancer and premature aging. Therefore, accurate assessment of DNA damage caused by environmental or metabolic genotoxic insults is critical for contemporary biomedicine. The available physical, flow cytometry and sophisticated scanning approaches to DNA damage estimation each have some drawbacks such as insufficient sensitivity, limitation to analysis of cells in suspension, or high costs and demand for trained personnel. Here we present an option how to transform a regular fluorescence microscope and personal computer with common software into a functional alternative to high-throughput screening devices. In two detailed protocols we introduce a new semi-automatic procedure allowing for very sensitive, quantitative, rapid and simple fluorescence image analysis in thousands of adherent cells per day. Sensitive DNA breakage estimation through analysis of phosphorylated histone H2AX (γ -H2AX), and homologous recombination (HR) assessed by a new RPA/Rad51 dual-marker approach illustrate the advantages and applicability of this technique. Our present data on assessment of low radiation doses, repair kinetics, spontaneous DNA damage in cancer cells, as well as constitutive and replication stress-induced HR events and their dependence on upstream factors within the DDR machinery document the versatility of the method. We believe this affordable approach may facilitate

mechanistic insights into the role of low-dose DNA damage in human diseases, and generally promote both basic and translational research in many areas of biomedicine where suitable fluorescence markers are available.

Introduction

DNA damaging insults, including exogenous agents such as various forms of radiation or environmental chemicals, or those arising from cell's own metabolic processes, pose a continuous threat to genomic integrity at the cellular level, and thereby potentially undermine organ homeostasis, health and longevity at the level of the whole organism. DNA lesions may lead to germline or somatic mutations, and genetic or epigenetic defects in the various cellular pathways that recognize, signal and repair the DNA lesions, are causally linked to a range of devastating diseases such as cancer, neurodegenerative and immunodeficiency diseases, and premature aging.¹⁻⁶ Given such fundamental role of the genome integrity maintenance in biology and pathology, intensive research has focused on better understanding of the molecular nature of the diverse types of DNA lesions, cellular pathways that deal with such lesions, and development of methods to detect the presence, and assess the extent, of DNA damage.

Among the diverse types of DNA lesions, arguably the most hazardous are DNA double-strand breaks (DSBs) that can destabilize the genome and have severe consequences for cell survival.^{1,4-7} DSBs may arise directly from impact of ionizing radiation or radiomimetic as well as some other anti-cancer drugs, for example, but also indirectly during processing of other types of lesions including those caused by ultraviolet light, oxidative stress or impaired DNA replication.^{1,4,6-9} In addition, DSBs arise also as part of the physiological programs of B and T lymphocytic cells, during genetic rearrangements of their immunoglobulin and T-cell receptor genes, respectively, and during meiotic recombination

*Correspondence to: Jiri Bartek; Centre for Genotoxic Stress Research; Danish Cancer Society; Strandboulevarden 49; Copenhagen DK:2100 Denmark; Tel.: +45.35.25.73.57; Fax: +45.35.25.77.21; Email: jb@cancer.dk

Submitted: 06/20/09; Accepted: 06/21/09

Previously published online as a Cell Cycle E-publication:
<http://www.landesbioscience.com/journals/cc/article/9331>

in the course of germ cell maturation.^{4,6,10} Upon detection of a DSB by sensor proteins such as the Mre11-Rad50-Nbs1 (MRN) complex or the Ku proteins, the apical DDR kinases ATM and DNA-PK, and later also ATR, become activated and phosphorylate serine 139 of histone H2AX, to generate what has become known as γ -H2AX.^{1,4-13} This chromatin mark then serves to recruit a plethora of DNA damage signaling and repair factors that process the DSBs and eventually seal the break.^{4-8,11,14} In practical terms, the so-called γ -H2AX foci can be conveniently identified by immunostaining, and this has become a popular surrogate marker to highlight the presence of DSBs.^{6-11,13,15-22}

Apart from γ -H2AX, numerous additional proteins that participate in the multifaceted genome maintenance network form subnuclear 'foci' through recruitment to, and accumulation at, the DNA damage sites.^{6-8,15,23-25} Such foci, for example those formed by the MRN complex proteins, 53BP1, MDC1,^{5,7,23-26} and the components of the recently identified ubiquitin ligase cascade including RNF8,²⁷⁻²⁹ RNF168,³⁰⁻³² and also BRCA1,³⁰ are often closely overlapping with the relatively large chromatin regions marked by γ -H2AX. Another type of foci, which are smaller and limited to stretches of single-stranded DNA (ssDNA) created as a result of DSB end resection or replication fork stalling, for example, are formed by proteins such as RPA, the ATR/ATRIP complex, Rad9 and components of the homologous recombination (HR) repair pathway, including Rad51.^{5,8,14,24,33,34} Broadly analogous to the γ -H2AX foci detection, these additional foci also provide convenient surrogate markers for monitoring DSB signaling (e.g., 53BP1 foci) and HR (e.g., Rad51 foci), respectively.

Critical for both basic research and clinical applications in the DNA damage field is the ability to detect, and ideally quantify in large numbers of cells, the amount of DNA lesions such as DSBs, to assess the dose of the genotoxic insult and/or their impact on the diverse model systems or human beings. This aspect of DDR research has a vast potential, ranging from mechanistic studies in cell culture systems, through high-throughput drug or genetic screening strategies, up to monitoring radiotherapy or even measurements of radiation dose exposure in case of a nuclear reactor accident or terrorist attack. The available methods to measure DNA damage in general, and DSBs in particular, encompass physical techniques such as pulsed-field gel electrophoresis, comet assay or neutral filter elution, as well as methods based on detection of the surrogate markers such as γ -H2AX. While the physical methods are able to detect the DNA breaks directly, they are considerably less sensitive, and require heat-exposed DNA free from histones, features that seriously limit their widespread use.⁹ In contrast, detection of γ -H2AX and some other DNA damage signaling or repair markers allows for very sensitive analysis of DNA damage, and directly in situ, thereby facilitating studies of genotoxic insults at physiologically and therapeutically relevant doses, and within the biologically more natural context of whole cells.⁹⁻¹¹

Techniques to assess the DDR markers are evolving, and particularly for nonadherent cells such as lymphocytes, recently optimized protocols based on flow cytometry are convenient, albeit not particularly sensitive means for measurements of γ -H2AX.³⁵

On the other hand, analysis of DNA damage at very low doses, and assessment of the vast majority of cell types that are naturally adherent (for which detachment from substratum is very stressful) require alternative methods which are however presently limited to very costly and sophisticated scanning instruments that require large investments and specially trained personnel. To overcome these limitations, we have developed and report here a versatile, highly sensitive method to quantify various parameters of the DDR in large numbers of adherent individual cells with statistical robustness, at very low cost affordable to most, if not all laboratories, with high degree of automation, and easily usable by the many researchers who are familiar with common fluorescence microscopes and personal computers.

In addition to providing the simple alternative for automated scanning systems, we also provide an alternative of automated fluorescence signal analysis in thousands of cells per day, based on standard software that is common for PC installations (Microsoft Windows XP, Adobe Photoshop, Microsoft Excel) or can be downloaded as freeware from the internet (Image J). Automation in our new system is ensured by coordinative linking of such software programs into a single analysis routine with multiple setting parameters. The critical linking and looping of the different MS Windows software together is achieved through application of Mouse recorder, a minimum-cost software the setting and usage of which is explained in detail. In this study, we present this innovative approach of DNA damage assessment through applications to quantification of low doses of ionizing radiation, assessment of DNA repair kinetics, response to replication stress, as well as detection of genetically defined differences in response to DNA damage, all in human adherent cells in situ. Furthermore, we discuss the merits and limitations of this approach, and highlight potential areas of its application, including quantitative assessment of the low-level endogenous DNA damage, as illustrated by our data on human cancer cells.

Results

Sensitive detection of DNA damage. To test the suitability of our method for evaluation of DNA damage levels that are below the limits of reliable detection for both the physical methods and flow cytometry approaches, we first examined the effects of ionizing radiation (IR), taking advantage of the known linear response of mammalian cells to increasing radiation doses^{9,17,36} and the possibility to expose the cells to precise doses of the clastogenic insult. In principle, however, virtually any type of DNA damaging agent can be used, as the readout we used, the induction of γ -H2AX visualized by antibodies to ser139-phosphorylated H2AX, is a universal marker for DDR created by all three major apical DDR kinases.^{4-13,37-39} IR causes a spectrum of DNA lesions including single stranded breaks (SSBs), base modifications and DSBs,³⁶ and although the activity of the ATM kinase is dominant in the response, the kinases DNA-PK and ATR also contribute to H2AX phosphorylation and activation of cell cycle checkpoints and DNA repair pathways.^{3-16,37-40}

In this initial series of experiments, we exposed the human U2OS osteosarcoma cells grown on coverslips to increasing doses

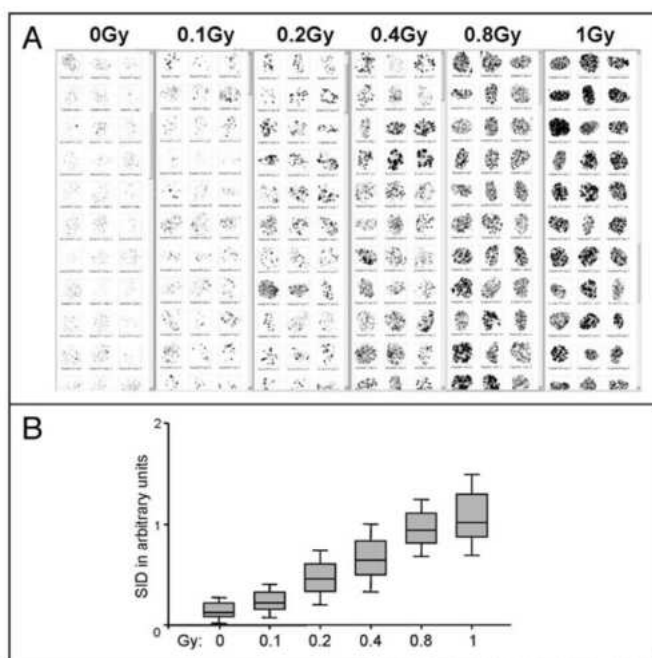


Figure 1. γ -H2AX signal integrated density (SID) quantification in U-2-OS cells after IR. (A) A Thumbnail comparison of image galleries of U-2-OS cells irradiated by indicated doses of ionizing radiation and stained for γ -H2AX. Fields with stained cells were photographed and the images analyzed using the automatic recognition routine based on DAPI co-staining of DNA. (B) Automatic signal quantification routine applied to the recognized cells, presented as a box plot chart summary. Minimum of 200 cells were analyzed for each sample. All differences between any two nearest samples are significant: *t*-test ($p < 0.0001$).

of ionizing radiation, spanning the 0–1 Gy range. Coverslips were fixed, stained and quantified for integrated signal density of the γ -H2AX immunofluorescence in each analyzed cell (see Supplement, Protocol A, for details). As can be seen from the data presented in Figure 1A and B, the values obtained with our method were consistent with the linear response within the entire 0–1 Gy range. In addition, the integrated signal values obtained for cells irradiated with increasing doses of 100 mGy-increments showed significant differences in the signal between the individual doses used (Fig. 1B). This result is noteworthy for at least two reasons. First, it documents the high sensitivity of the method. Second, the sensitive yet robust (as documented by the linearity of the values obtained across the entire 0–1 Gy dose range) readout even allowed the initial, spontaneous DNA damage that was present already in the mock (0 Gy)-treated cells to be well detected, an observation that inspired the next set of experiments.

Assessment of the endogenous constitutive DNA damage in cancer cells. The occurrence of constitutive DNA damage in premalignant or cancerous cells not exposed to any exogenous genotoxic insults, both in cell culture and in vivo in

clinical specimens, is an intriguing and recently often discussed phenomenon relevant for the molecular pathogenesis of cancer in general, and to oncogene-induced DNA breakage and genomic instability in particular.^{40,41} Encouraged by the data we obtained with the U2OS sarcoma cells (Fig. 1) that display a rather low degree of such spontaneous DNA damage, we asked whether our quantitative approach allows to distinguish differences in this parameter among different human cancer cell lines under unperturbed culture conditions.

Five human cancer cell lines representing four tumor types: U2OS osteosarcoma, HCT116 colon carcinoma (two variants), MCF7 breast carcinoma and CAPAN1 pancreatic carcinoma, were cultured in parallel under identical conditions, and the extent of their constitutive DNA damage without any genotoxic insult was examined, using the integrated signal density of the γ -H2AX marker as readout. The rationale for including the two isogenic HCT116 cell lines that either express wild-type p53 ($p53^{+/+}$) or lack the p53 gene ($p53^{-/-}$) was to see whether they display any differences in the extent of the constitutive DNA damage, given the original observation by DiTullio et al.⁴³ that the elevated endogenous damage was seen particularly among cancer cell lines with mutant p53. The results of these comparative experiments showed that there were indeed pronounced, reproducible differences among the cancer cell lines examined, ranging from the low level of spontaneous damage seen in U2OS cells, through intermediate level in MCF7 cells, up to an almost 10-fold higher (as compared to U2OS cells) signal in the CAPAN1 cells (Fig. 2). Interestingly, the deletion of the p53 gene from HCT116 cells correlated with a significant elevation of the constitutive DNA damage in otherwise isogenic HCT116 ($p53^{-/-}$) cells (Fig. 2). We conclude from these results that the new method we present is suitable to reliably detect and quantify also the low-level spontaneous DNA damage present in cancer cells. These results furthermore suggest that wild-type p53, when preserved in cancer cells, may at least partially limit the extent of such constitutive DNA damage.

Monitoring kinetics of γ -H2AX decay after IR. One of the key areas of application for techniques that assess the DNA damage is to monitor the kinetics of repair of the DNA lesions.^{6,9} To judge the suitability of our method for this purpose, we irradiated the U2OS cells with the therapeutically most relevant dose of 2 Gy, and followed the overall decrease of the γ -H2AX signal in a time course experiment. As is illustrated in Figure 3, our method was clearly capable of detecting the time-dependent decay of the γ -H2AX signal from its maximum by 30 min after irradiation until 8 hrs post IR. The timing of the peak value of γ -H2AX at approx. 30 min is known from various studies^{6,9} and agrees with our preliminary experiments using this method to assess the early time points after IR (data not shown). The data summary (Fig. 3)

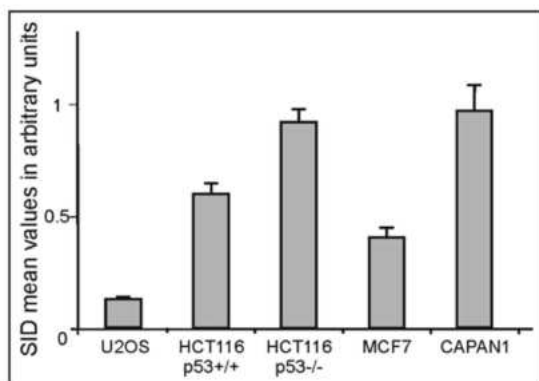


Figure 2. Panel of five human cancer cell lines evaluated for spontaneous DNA damage. Over 200 cells were scored for γ H2AX integrated signal density (SID) in two independent experiments for every cell line. Mean values and standard errors were calculated and are displayed in a single summary chart.

indicates that the bulk of the DSBs were repaired by 4 hrs after irradiation, and the high sensitivity of our method allowed us to conclude that even 8 hours after IR, there was a significant residual signal higher than the level in mock-treated cells, consistent with the notion that a fraction of difficult-to-rejoin DSBs may persist for a longer period of time.⁶

A dual-marker RPA/Rad51 assay to assess homologous recombination in S phase. While the data presented above were generated using the integrated signal density of γ -H2AX as a readout, we also wished to explore the potential of our method for evaluation of the number of the nuclear 'foci' that are formed by various DDR components and might serve as beacons for activated DNA damage signaling or repair pathways.^{4,8,33,34,44-48} The process we chose for this study was quantitative analysis of homologous recombination (HR), an important mechanism of DNA damage repair with high relevance to radiobiology and oncology.^{1,6,14} In our Protocol B (Supplementary Protocol B), we use the HR component Rad51 that forms foci at the sites of replication stress or other lesions that demand engagement of the HR repair.^{33,44} We used the Rad51 foci as a surrogate marker of individual HR events that are in progress, and set our image analysis routine to detect the individual foci, while subtracting the remaining background fluorescence. In addition, we adapted this Protocol to selectively analyze the subset of cells with ongoing DNA replication, i.e., those possibly experiencing replication stress, by concomitantly scoring the pattern of RPA, a protein that decorates regions of ssDNA at replicating forks.⁸

For the automatic selection of the maximally replicating cells and HR quantification we therefore developed a two-step procedure, based on double staining for RPA and Rad51. Upon optimized pre-extraction of the fixed cells, the RPA pattern of the major subset of fully replicating S-phase cells was selected based on a large number of very small 'micro-foci' evenly distributed

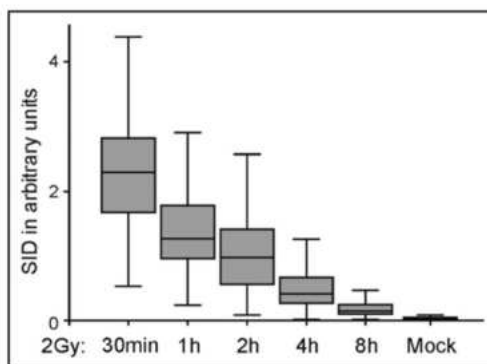


Figure 3. Analysis of DSB repair dynamics (γ H2AX signal decay) in U2OS cells after 2 Gy irradiation using quantification γ H2AX signal integrated density. Samples of U2OS cells were irradiated by 2 Gy of ionizing radiation, fixed at indicated times and stained for γ H2AX. Cells were analyzed by automatic recognition and quantification routine and data summarized using a box plot chart. Minimum 200 cells were analyzed for each sample. All differences between two nearest samples are significant: Hest ($p < 0.0001$).

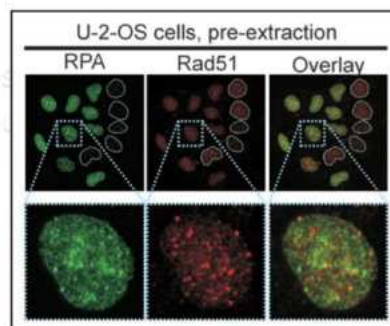


Figure 4. Example of paired immunofluorescence images used for automatic analysis of HR events in U2OS cells. Here, cells were exposed to 0.5 mM HU for 24 hours, pre-extracted and stained for RPA and Rad51. Pan-nuclear RPA signal indicating ongoing replication was used for recognition of cells to be further quantified for Rad51 foci. White silhouettes indicate cells likely outside S phase, which were automatically removed from the analysis based on low or heterogeneous RPA signal patterns.

throughout the nucleus (Fig. 4). We then set our automatic recognition routine to recognize only cells positive for this pan-nuclear pattern of RPA, and only in these cells the RAD51 signal was subsequently automatically quantified in the double-stained cell population.

Quantification of spontaneous and replication stress-induced HR events. Having established the combined RPA/Rad51 analysis approach, where pan-nuclear RPA identifies S-phase cells undergoing DNA replication, we decided to address the question whether in such cells, the Rad51-dependent HR is affected by the

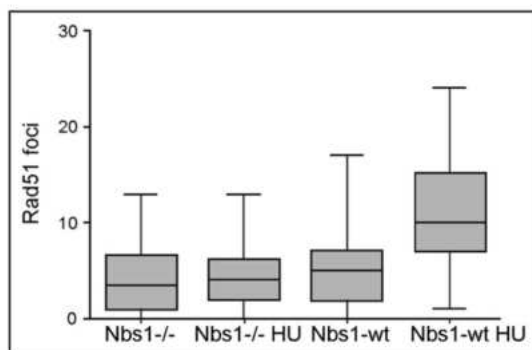


Figure 5. Graphical summary of HR events analysis in human fibroblasts lacking NBS1, and the HR-promoting effect of re-introduced wild-type NBS1. NBS1-tert (Nbs1^{-/-}) cells and NBS1-tert wtNBS1 (Nbs1-wt) complemented cells were left untreated or exposed to 0.5 mM of hydroxyurea (HU) for 24 hours and analyzed using automatic recognition and scoring routine of Rad51 foci in S-phase cells. Minimum 200 cells were analyzed for each sample. Differences between NBS1-tert and NBS1-tert-wtNBS1 cells are significant under both mock-treated (Htest: $p < 0.0666$) and HU treatment (Htest: $p < 0.0001$) conditions, as was the 4-groups ANOVA test comparison: $p < 0.0001$.

status of a candidate upstream regulator such as Nbs1.^{5,26,38,45,47} To examine the significance of intact Nbs1 for the Rad51-mediated HR, we employed the dual RPA/Rad51 protocol on human cells lacking functional NBS1 (cells derived from a patient with the Nijmegen breakage syndrome) and isogenic cells in which wild-type NBS1 was reconstituted through retrovirus-mediated stable expression.⁴⁹ This experiment showed that compared to their NBS1-reconstituted counterparts, the NBS1-defective cells displayed significantly fewer Rad51 foci ($p < 0.06$) when replicating their DNA in the absence of any exogenous insult (Fig. 5). In addition, the dependency of Rad51 foci/HR events on functional Nbs1 became even more apparent when the cells were treated with 0.5 mM HU for 24 hours ($p < 0.0001$), under conditions that induce replication stress and thereby increase the demand for more HR repair (Fig. 5).

To further demonstrate the suitability of the dual-marker assay to examine the impact of HU-induced replication stress, we next tested effects of HU treatment on the U2OS cell line. The question we asked was whether increasing concentrations of HU positively correlate with the amount of Rad51 foci in S-phase cells. The data from this series of experiments revealed positive correlation between Rad51 foci formation and HU within the range of 0–0.5 mM (Fig. 6). Surprisingly however, further increase of the HU concentrations to 1 mM and higher not only did not lead to further increase of Rad51 foci, but instead the number of such HR events was progressively inhibited (Fig. 6). Although the mechanistic basis of this intriguing phenomenon remains to be elucidated, we speculate that full inhibition of dNTP synthesis by higher concentrations of HU might also lead to inhibition of HR/Rad51 foci formation, possibly reflecting some feedback loop mechanisms involving sensors of inadequate dNTP supply and

the requirement of dNTPs for DNA synthesis associated with HR repair.

Discussion

In this study, we developed, and demonstrated the utility of, an innovative single-cell image analysis method that is potentially widely applicable in biomedical research, both basic and translational. While we demonstrate the key aspects of this approach on several examples from the DNA damage field, we would like to emphasize that this technology should be useful for analyses of any biological phenomena for which suitable fluorescence markers can be validated, including nucleic acid- and organelle-specific tags, and antibodies to a wide range of molecules including post-translationally modified proteins.

The advantages of our new method compared with the alternative, currently available approaches based on flow cytometry, physical methods such as electrophoresis, and expensive complex scanning devices^{9,18,19,30,35} include: (1) high sensitivity; (2) quantitative data output; (3) low investments for setting up the method (based on standard fluorescence microscope equipped with digital camera and common PC with software available in most laboratories); (4) automation of the routine that allows analysis of thousands of cells per day; and (5) relatively simple operation and high degree of transportability among laboratories, thanks also to our detailed protocols (see the Suppl. information) with both written guides and illustrative movies to facilitate the widespread use of the technique.

From the technical point of view, our method is highly versatile, as each nucleus is automatically recognized and evaluated separately for overall signal integrated density and amount of foci, and additional parameters such as area, circularity and signal density related to each focus can be also evaluated. The method allows immunofluorescence analysis to be performed selectively in subsets of tagged cells (see the RPA/Rad51 dual-marker approach introduced in this study as an example), and up to 3 additional channels can be exploited for combined analyses, using diverse antibody-, green fluorescence protein- and nucleotide analogs-based detection systems. Apart from the applicability for adherent cells, the method can easily be adapted for suspension cells, by examination of cytopsin or smear preparations. In addition, the image analysis system encompasses easily editable macros where every step is amenable to further creative modifications to meet specific requirements of the particular researcher and project.

Within the DNA damage research field, the high sensitivity of the method should make it particularly useful for applications in studies of spontaneous DNA damage,^{11,16,41} very low doses of genotoxic agents including assays for new carcinogens,¹⁹ analysis of long-term DNA repair dynamics and checkpoint recovery/adaptation mechanisms,^{5,6,20} to name just a few areas of wide interest.

For example, our experience with this new method (Fig. 2, and data not shown) indicates that it should significantly contribute to better understanding of the recently discovered role of the DDR machinery as an inducible biological barrier against oncogene-induced replication stress and progression of pre-malignant lesions into aggressive tumors.^{41,42,50-54} The oncogene-induced

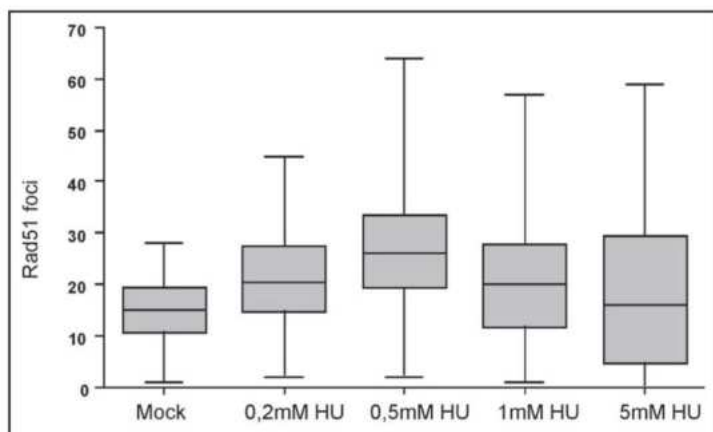


Figure 6. Effect of increasing HU concentration on HR events in U2OS cells. Cells were exposed to indicated doses of HU for 24 hours and analyzed using automatic recognition and scoring routine for Rad51 foci in S-phase (RPA-marked) cells. Note that within the range spanning 0–0.5 mM HU, the rate of HR repair events increased, however in higher HU concentrations of 1 mM–5 mM HU, the frequency of HR events decreased. Minimum 200 cells were analyzed for each sample: Hest (Mock-treated control vs. 0.2 mM HU: $p < 0.0001$; 0.2 mM vs. 0.5 mM HU: $p < 0.0001$; 0.5 mM vs. 1 mM HU: $p < 0.0001$; 1 mM vs. 5 mM HU: $p < 0.0092$). 5-groups ANOVA test: $p < 0.0001$.

endogenous DNA damage is of the extent clearly detectable and quantifiable by our method, and we believe this technique can also be adapted for analysis of immunostaining on tissue sections, since for example the γ -H2AX and 53BP1 foci are clearly detectable by immunohistochemistry.^{10,50,51} Furthermore, we believe that also additional applications in cancer research, such as monitoring the *in vivo* effects of genotoxic anti-cancer drugs, identification of carcinogens, or assessment of radiation dosage or exposure, may benefit from application of our method.

In terms of the RPA/Rad51 assay, we believe it can complement the currently used fluorescence assays for HR, based on reporter plasmid-encoded GFP fragments whose rejoining dependent on the HR activity in the cell can be assessed by flow cytometry.^{45,54} Given the limitations of this method, such as the fact that only relative values can be obtained, and the tested cells must undergo the same number of population doublings in order to be comparable, our surrogate marker approach with concomitant RPA pattern and Rad51 foci scoring should become a useful tool in the area of replication stress and HR research. As a 'by-product' of our Rad51 analysis in response to HU-induced replication stress, we identified a relatively narrow peak of HU concentration optimal for detection of HR events. Since many studies are based on HU concentrations around 5 mM^{8,55} that is already in the range when HR appears to be inhibited (Fig. 6), we propose that our approach may also help identify optimal range of diverse drugs, both for basic cell culture experiments, and possibly as an aid in designing personalized treatment regimens in the future.

Finally, given that high-throughput screens based on complex, high-cost fluorescence scanning instruments are becoming widely

used, our method may provide an option for how to transform a regular fluorescence microscope and common personal computer into a functional alternative to such demanding screening devices. Our detailed Supplementary guide with informative step-by-step movies provides an entire new platform open to further improvements and applications, and the examples documented by the results of the present study can be regarded as a guide for further user-tailored modifications. The broad range of potential applications of this new method is limited only by imagination (and by the spectrum of available fluorescence markers), and we very much hope that this approach will prove useful in the hands of many researchers.

Materials and Methods

Cell culture. Human U2OS, MCF7, CAPAN1 and HCT116 (both p53-proficient and deficient variants, kindly provided by B. Vogelstein) cell lines, as well as the human telomerase-immortalized fibroblasts from a Nijmegen breakage syndrome patient

(NBS-tert cells) were grown in DMEM supplemented with 10% fetal bovine serum (GIBCO). A NBS-tert + wtNBS1 derivative cell line expressing human WT NBS1 protein was generated as described.⁴⁹

Cell irradiation and drug treatment. Hydroxyurea was obtained from Sigma. Aqueous stock solution at a concentration of 1 M was kept light-shielded at -20°C and was diluted to the appropriate concentrations in culture medium shortly before treatment of the cells. Ionizing radiation at the desired dose was delivered by an X-ray generator (Pantak, Berkshire, United Kingdom; HF160; 150 kV, 15 mA, and dose rate of 2.18 Gy/min).

Immunofluorescence staining. For DSB evaluation, the cells were grown on glass coverslips, fixed by methanol:acetone (1:1) and then stained with primary antibodies against phospho-H2AX (ser139) (mouse or rabbit) or 53BP1, essentially as described previously.^{25,26} For RAD51 foci evaluation in replicating cells, the cells were grown on coverslips, washed in a buffer containing 10 mM PIPES pH 7, 100 mM NaCl, 300 mM sucrose, 3 mM and MgCl_2 (CSK buffer), then extracted 5 minutes in CSK + 0.5% Triton X, and rinsed with CSK and PBS before fixation in 4% formaldehyde. Immediately after fixation cells were stained with primary antibodies against RAD51 and RPA. As secondary antibodies were used goat anti-mouse and anti-rabbit coupled to Alexa Fluor dyes with excitation wavelengths of 488 or 568 nm (Molecular Probes). After the staining procedure the coverslips were dried by ethanol series and mounted on standard microscopic glass using Vecta Shield mounting medium with DAPI (Vector Laboratories) in case of DSB evaluation and without DAPI in case of RAD51 foci scoring. Examination was done using the fluorescence microscope

from Zeiss (model Axioplan II). Images were acquired through a PLAN-Neofluar 40x/1.3 oil immersion objective and photographed by a digital camera (Cool Snap). Each microscopic field was acquired twice through two different fluorescence filters. The exposition time, the binning, the setting of the microscope and the UV light source were kept constant for all the samples.

Computer based evaluation of γ H2AX signal integrated density. Each image photographed as described above was saved as a tiff file and later examined by combining Adobe Photoshop, Image J and Excel software using macro routines with fixed parameters for all samples. Adobe Photoshop was used for recognition of single cells based on DAPI staining and to subtract background in the corresponding DSB (usually γ -H2AX) signal image. In the Image J software the "Histogram" function was used to calculate the signal values and further processing of the numbers was achieved by mathematical operations in MS Excel. See Supplementary information for the protocol details. Statistical analysis of data set comparisons was performed using t-test (confidence interval 99%).

Computer based evaluation of RAD51 foci in DNA-replicating cells. Each image photographed as described above was saved as a tiff file and later examined by combining Adobe Photoshop, Image J and Excel software using macro routines with fixed parameters for all samples. Adobe Photoshop was used for recognition of single cells based on a pan-nuclear RPA signal pattern and to subtract background in the corresponding RAD51 image. In the Image J software "Analysis particles" function was used to analyze each focus for specialized parameters such as total amount and integrated density of each focus. The numerical data were further processed in MS-Excel by mathematical operations. See Supplementary information for the protocol details (Supplementary protocol B). Statistical analysis of paired data sets was performed using t-test (confidence interval 99%).

Antibodies. Antibodies used in this study included mouse monoclonal antibodies to phospho-histone H2A.X (Ser139) (Ab-cam, Upstate 05-636), to RPA (Neomarkers) and to 53BP1 (a generous gift from Thanos Halazonetis, University of Geneva) and rabbit polyclonal antibodies to phospho-histone H2A.X (Ser139) (Cell signaling Lot:2 #2577L) and to RAD51 (Santa Cruz).

Acknowledgements

We thank Professor David Morris for critical reading of the manuscript. This work was supported by grants from the Czech Ministry of Education (MSM6198959216), the Grant Agency of the Czech Academy of Sciences (IAA501370902), the Danish National Research Foundation, the Danish Cancer Society, the Danish Research Council, the Lundbeck Foundation (R13-A1287), and the European Community 7th Framework Program (Projects INFLA-CARE and GENICA).

Note

www.landesbioscience.com/supplement/MistrikCC8-16-Sup.pdf
www.landesbioscience.com/supplement/MistrikCC8-16-Sup1.swf
www.landesbioscience.com/supplement/MistrikCC8-16-Sup2.swf
www.landesbioscience.com/supplement/MistrikCC8-16-Sup3.swf
www.landesbioscience.com/supplement/MistrikCC8-16-Sup4.swf
www.landesbioscience.com/supplement/MistrikCC8-16-Sup5.swf

References

- Hoeijmakers JH. Genome maintenance mechanisms for preventing cancer. *Nature* 2001; 411:366-74.
- Schumacher B, Garinis GA, Hoeijmakers JH. Age to survive: DNA damage and aging. *Trends Genet* 2008; 24:77-85.
- Kastan MB, Bartek J. Cell cycle checkpoints and cancer. *Nature* 2004; 432:316-23.
- Harper JW, Elledge SJ. The DNA damage response: ten years after. *Mol Cell* 2007; 28:739-45.
- Bartek J, Lukas J. DNA damage checkpoints: from initiation to recovery or adaptation. *Curr Opin Cell Biol* 2007; 19:238-45.
- Jeggo PA, Lobrich M. DNA double strand breaks: their cellular and clinical impact? *Oncogene* 2007; 26:7717-9.
- Stucki M, Jackson SP. -H2AX and MDC1: anchoring the DNA-damage-response machinery to broken chromosomes. *DNA Repair* 2006; 5:534-43.
- Cimprich KA, Cortez D. ATR: an essential regulator of genome integrity. *Nat Rev Mol Cell Biol* 2008; 9:616-27.
- Kinner A, Wu W, Staudt C, Iliakis G. Gamma-H2AX in recognition and signaling of DNA double-strand breaks in the context of chromatin. *Nucleic Acids Res* 2008; 36:5678-94.
- Bartkova J, Bakkenist CJ, Rajpert-De ME, Skakkebaek NE, Sehested M, Lukas J, et al. ATM activation in normal human tissues and testicular cancer. *Cell Cycle* 2005; 4:838-45.
- Bonner WM, Redon CE, Dickey JS, Nakamura AJ, Sedelnikova OA, Solier S, et al. GammaH2AX and cancer. *Nat Rev Cancer* 2008; 8:957-67.
- Bakkenist CJ, Kastan MB. Initiating cellular stress responses. *Cell* 2004; 118:9-17.
- Rogakou EP, Pilch DR, Orr AH, Ivanova VS, Bonner WM. DNA double-stranded breaks induce histone H2AX phosphorylation on serine 139. *J Biol Chem* 1998; 273:5858-68.
- Hakem R. DNA-damage repair: the good, the bad and the ugly. *EMBO J* 2008; 27:589-605.
- Fernandez-Capetillo O, Celeste A, Nussenzweig A. Focusing on foci: H2AX and the recruitment of DNA-damage response factors. *Cell Cycle* 2003; 2:426-7.
- Sedelnikova OA, Bonner WM. GammaH2AX in cancer cells: a potential biomarker for cancer diagnostics, prediction and recurrence. *Cell Cycle* 2006; 5:2909-13.
- MacPhail SH, Banath JP, Yu TY, Chu EH, Lambur H, Olive PL. Expression of phosphorylated histone H2AX in cultured cell lines following exposure to X-rays. *Int J Radiat Biol* 2003; 79:351-8.
- Tanaka T, Halicka HD, Traganos F, Seiter K, Darzynkiewicz Z. Induction of ATM activation, histone H2AX phosphorylation and apoptosis by etoposide: relation to cell cycle phase. *Cell Cycle* 2007; 6:371-6.
- Albino AP, Huang X, Jorgensen E, Yang J, Gietl D, Traganos F, et al. Induction of H2AX phosphorylation in pulmonary cells by tobacco smoke: a new assay for carcinogens. *Cell Cycle* 2004; 3:1062-8.
- Bouquet F, Muller C, Salles B. The loss of gammaH2AX signal is a marker of DNA double strand breaks repair only at low levels of DNA damage. *Cell Cycle* 2006; 5:1116-22.
- Yu T, MacPhail SH, Banath JP, Klokov D, Olive PL. Endogenous expression of phosphorylated histone H2AX in tumors in relation to DNA double-strand breaks and genomic instability. *DNA Repair* 2006; 5:935-46.
- Zhao H, Traganos F, Albino AP, Darzynkiewicz Z. Oxidative stress induces cell cycle dependent Mre11 recruitment, ATM and Chk2 activation and histone H2AX phosphorylation. *Cell Cycle* 2008; 7:1490-5.
- Schultz LB, Chehab NH, Malikzay A, Halazonetis TD. p53 binding protein 1 (53BP1) is an early participant in the cellular response to DNA double-strand breaks. *J Cell Biol* 2000; 151:1381-90.
- Bekker-Jensen S, Lukas C, Kitagawa R, Melander F, Kastan MB, Bartek J, et al. Spatial organization of the mammalian genome surveillance machinery in response to DNA strand breaks. *J Cell Biol* 2006; 173:195-206.
- Bekker-Jensen S, Lukas C, Melander F, Bartek J, Lukas J. Dynamic assembly and sustained retention of 53BP1 at the sites of DNA damage are controlled by Mdc1/NFBD1. *J Cell Biol* 2005; 170:201-11.
- Lukas C, Falck J, Bartkova J, Bartek J, Lukas J. Distinct spatiotemporal dynamics of mammalian checkpoint regulators induced by DNA damage. *Nat Cell Biol* 2003; 5:255-60.

27. Kolas NK, Chapman JR, Nakada S, Ylanko J, Chahwan R, Sweeney FD, et al. Orchestration of the DNA-damage response by the RNF8 ubiquitin ligase. *Science* 2007; 318:1637-40.
28. Mailand N, Bekker-Jensen S, Fastrup H, Melander F, Bartek J, Lukas C, et al. RNF8 ubiquitylates histones at DNA double-strand breaks and promotes assembly of repair proteins. *Cell* 2007; 131:887-900.
29. Huen MS, Grant R, Manke I, Minn K, Yu X, Yaffe MB, Chen J. RNF8 transduces the DNA-damage signal via histone ubiquitylation and checkpoint protein assembly. *Cell* 2007; 131:901-14.
30. Doil C, Mailand N, Bekker-Jensen S, Menard P, Larsen DH, Pepperkok R, et al. RNF168 binds and amplifies ubiquitin conjugates on damaged chromosomes to allow accumulation of repair proteins. *Cell* 2009; 136:435-46.
31. Stewart GS, Panier S, Townsend K, Al-Hakim AK, Kolas NK, Miller ES, et al. The RIDDLE syndrome protein mediates a ubiquitin-dependent signaling cascade at sites of DNA damage. *Cell* 2009; 136:420-34.
32. Stewart GS. Solving the RIDDLE of 53BP1 recruitment to sites of damage. *Cell Cycle* 2009; 8:1532-8.
33. Yeykal CC, Greene EC. Visualizing the behavior of human Rad51 at the single-molecule level. *Cell Cycle* 2006; 5:1033-8.
34. Warmerdam DO, Freire R, Kanaar R, Smits VAJ. Cell cycle-dependent processing of DNA lesions controls localization of Rad9 to sites of genotoxic stress. *Cell Cycle* 2009; 8:1765-74.
35. Muslimovic A, Ismail IH, Gao Y, Hammarsten O. An optimized method for measurement of gamma-H2AX in blood mononuclear and cultured cells. *Nat Protoc* 2008; 3:1187-93.
36. Elkind MM. Repair processes in radiation biology. *Radiat Res* 1984; 100:424-5.
37. Burma S, Chen BP, Murphy M, Kurimasa A, Chen DJ. ATM phosphorylates histone H2AX in response to DNA double-strand breaks. *J Biol Chem* 2001; 276:42462-7.
38. Falck J, Coates J, Jackson SP. Conserved modes of recruitment of ATM, ATR and DNA-PKcs to sites of DNA damage. *Nature* 2005; 434:605-11.
39. Stiff T, O'Driscoll M, Rief N, Iwabuchi K, Lobrich M, Jeggo PA. ATM and DNA-PK function redundantly to phosphorylate H2AX after exposure to ionizing radiation. *Cancer Res* 2004; 64:2390-6.
40. Pilch DR, Sedelnikova OA, Redon C, Celeste A, Nussenzweig A, Bonner WM. Characteristics of gamma-H2AX foci at DNA double-strand breaks sites. *Biochem Cell Biol* 2003; 81:123-9.
41. Bartek J, Lukas J, Bartkova J. DNA damage response as an anti-cancer barrier: damage threshold and the concept of 'conditional haploinsufficiency'. *Cell Cycle* 2007; 6:2344-7.
42. Halazonetis TD, Gorgoulis VG, Bartek J. An oncogene-induced DNA damage model for cancer development. *Science* 2008; 319:1352-5.
43. DiTullio RA Jr, Mochan TA, Venere M, Bartkova J, Sehested M, Bartek J, et al. 53BP1 functions in an ATM-dependent checkpoint pathway that is constitutively activated in human cancer. *Nat Cell Biol* 2002; 4:998-1002.
44. Sorensen CS, Hansen LT, Dziegielewska J, Syljuasen RG, Lundin C, Bartek J, et al. The cell cycle checkpoint kinase Chk1 is required for mammalian homologous recombination repair. *Nat Cell Biol* 2005; 7:195-201.
45. Sartori AA, Lukas C, Coates J, Mistrik M, Fu S, Bartek J, et al. Human CtIP promotes DNA end resection. *Nature* 2007; 450:509-14.
46. Sorensen CS, Syljuasen RG, Lukas J, Bartek J. ATR, Claspin and the Rad9-Rad1-Hus1 complex regulate Chk1 and Gdc25A in the absence of DNA damage. *Cell Cycle* 2004; 3:941-5.
47. Jazayeri A, Falck J, Lukas C, Bartek J, Smith GC, Lukas J, et al. ATM- and cell cycle-dependent regulation of ATR in response to DNA double-strand breaks. *Nat Cell Biol* 2006; 8:37-45.
48. Liu S, Bekker-Jensen S, Mailand N, Lukas C, Bartek J, Lukas J. Claspin operates downstream of TopBP1 to direct the ATR signalling towards Chk1 activation. *Mol Cell Biol* 2006; 26:6056-64.
49. Horejsi Z, Falck J, Bakkenist CJ, Kastan MB, Lukas J, Bartek J. Distinct functional domains of Nbs1 modulate the timing and magnitude of ATM activation after low doses of ionizing radiation. *Oncogene* 2004; 23:3122-7.
50. Bartkova J, Horejsi Z, Koed K, Kramer A, Tort F, Zieger K, et al. DNA damage response as a candidate anti-cancer barrier in early human tumorigenesis. *Nature* 2005; 434:864-70.
51. Gorgoulis VG, Vassiliou LV, Karakaidos P, Zacharatos P, Kotsinas A, Liloglou T, et al. Activation of the DNA damage checkpoint and genomic instability in human precancerous lesions. *Nature* 2005; 434:907-13.
52. Bartkova J, Rezaei N, Liontos M, Karakaidos P, Kletsas D, Issaeva N, et al. Oncogene-induced senescence is part of the tumorigenesis barrier imposed by DNA damage checkpoints. *Nature* 2006; 444:633-7.
53. DiMicco, Fumagalli M, Cicalese A, Piccinin S, Gasparini P, Luise C, et al. Oncogene-induced senescence is a DNA damage response triggered by DNA hyper-replication. *Nature* 2006; 444:638-42.
54. Pierce AJ, Hu P, Han M, Ellis N, Jasin M. Ku DNA end-binding protein modulates homologous repair of double-strand breaks in mammalian cells. *Genes Dev* 2001; 15:3237-42.
55. Griffith E, Walker S, Martin C-A, Vagnarelli P, Stiff T, Vernay B, et al. Mutations in pericentrin cause Seckel syndrome with defective ATR-dependent DNA damage signaling. *Nature Genet* 2008; 40:232-6.

SCIENTIFIC REPORTS

OPEN

Cells and Stripes: A novel quantitative photo-manipulation technique

Received: 22 October 2015
Accepted: 10 December 2015
Published: 18 January 2016

Martin Mistrik^{1,*}, Eva Vesela^{1,*}, Tomas Furst¹, Hana Hanzlikova², Ivo Frydrych¹, Jan Gursky¹, Dusana Majera¹ & Jiri Bartek^{1,2,3}

Laser micro-irradiation is a technology widely used in the DNA damage response, checkpoint signaling, chromatin remodeling and related research fields, to assess chromatin modifications and recruitment of diverse DNA damage sensors, mediators and repair proteins to sites of DNA lesions. While this approach has aided numerous discoveries related to cell biology, maintenance of genome integrity, aging and cancer, it has so far been limited by a tedious manual definition of laser-irradiated subcellular regions, with the ensuing restriction to only a small number of cells treated and analyzed in a single experiment. Here, we present an improved and versatile alternative to the micro-irradiation approach: Quantitative analysis of photo-manipulated samples using innovative settings of standard laser-scanning microscopes. Up to 200 cells are simultaneously exposed to a laser beam in a defined pattern of collinear rays. The induced striation pattern is then automatically evaluated by a simple algorithm, which provides a quantitative assessment of various laser-induced phenotypes in live or fixed cells. Overall, this new approach represents a more robust alternative to existing techniques, and provides a versatile tool for a wide range of applications in biomedicine.

Confocal laser scanning microscopy (LSM) enables precise spatio-temporal photo-manipulations based on LSM-embedded lasers in defined regions of interest (ROIs). These techniques include induction of DNA damage in cell nucleus^{1,2} and various photo-bleaching/activating procedures such as fluorescence recovery after photobleaching (FRAP)³.

Among the research areas that exploit these techniques, live-cell monitoring of factors involved in cellular responses to DNA damage has been particularly prominent. Compared to standard conventional methods commonly employed in the DNA damage field, laser-induced DNA damage provides multiple advantages, such as the ability to damage DNA in a certain time-point and in only part of the nucleus while the surrounding DNA stays intact, a feature especially attractive for dynamic analyses of protein recruitment^{4–8}. Arguably the most deleterious lesions formed after laser micro-irradiation are DNA double strand breaks (DSB), a response to which involves a cascade of carefully orchestrated events, eventually leading to recruitment of factors participating in repair of DSBs via either homologous recombination or nonhomologous end joining pathways⁹. Among the main factors involved in the stepwise recruitment and assembly of the DSB response proteins is MDC1, a scaffold protein^{10,11} the GFP-tagged version of which was used as one of the DNA damage reporters in live-cell imaging experiments performed as part of our present study. MDC1 is one of the early-response proteins that forms a platform for recruitment of other important DDR factors (eg. RNF8, 53BP1, BRCA1, etc)^{12–14}. The other protein we used as a GFP-tagged reporter is 53BP1, a protein that plays an important role in DSB repair pathway choice¹⁵. Finally, as a representative of factors involved in DNA repair of non-DSB lesions, we also employed FANCD2, a protein that becomes activated by monoubiquitination and plays a central role in the so-called Fanconi anemia (FA) pathway implicated in repair of DNA interstrand crosslinks, translesion DNA synthesis, nucleolytic incision and homologous recombination¹⁶.

In general, current approaches to the photo-manipulation techniques involve manual definition of the ROI, which is then exposed to a particular laser resulting in the respective photo-effect. The ROI is followed over time

¹Institute of Molecular and Translational Medicine, Faculty of Medicine and Dentistry, Palacky University, Olomouc, Czech Republic. ²Institute of Molecular Genetics of the ASCR, v. v. i., Prague, Czech Republic. ³Danish Cancer Society Research Center, Copenhagen, Denmark. *These authors contributed equally to this work. Correspondence and requests for materials should be addressed to J.B. (email: jb@cancer.dk)

and its signal intensity is measured. The process is laborious and commonly requires constant attention for active repositioning of the readout area due to movement of cells over time³.

Here we propose a method to circumvent limitations of the manual approach by simultaneously exposing many cells to a co-linear pattern of laser rays. This is achieved by a particular set of LSM settings likely universally compatible with microscopes of various producers (tested on two types of LSM systems so far).

Results

Standard LSM systems can be adapted for photo-manipulation in a predefined striation pattern covering the entire acquisition area.

Once the LSM system is set to a very low resolution and slow scanning speed, it generates a specific striation pattern. In principle, the entire acquisition area is scanned with small resolution e.g. only 32 pixels in each dimension (x and y). Laser scanning microscope does not switch off the lasers during the bi-directional scanning process between points nor lines. Such settings then result into a pattern of 32 horizontal lines, rather than 32×32 dots. The total dose of light energy for each of the lines can be adjusted by altering the scanning speed (pixel dwell time) and further by repetitions of the scanning cycles (iterations). This effect can be visualized for example on a microscopic slide covered with a thin layer of fluorescent paint which is bleached by the laser only within the scanning lines (Fig. 1a). If the used laser wavelength and power has DNA-damaging properties, the same spatially defined DNA damage striation pattern can be induced in live cells and visualized for example by translocation of tagged responsive proteins towards the DNA lesions (Fig. 1b). If the laser is set to a bleaching mode, a similar negative striation pattern is achieved (Fig. 1c). A large number of cells (limited only by the numbers of cells that can grow within the acquisition area) can be exposed in a very short time and the induced striation pattern of known parameters is amenable to an automatic software evaluation.

In the LSM-based laser-induced DNA damage applications, the amount of recruited and/or modified responsive proteins (DNA damage recognition) and their subsequent release, degradation or de-modification (processes reflecting DNA repair) can be measured. This is applicable to immunofluorescence (IF)^{7,17} as well as live-cell imaging⁸. IF enables simultaneous detection of multiple proteins, including protein modifications (Supplementary Fig. S1), but has the disadvantages of an end-point assay. Live-cell analysis based on reporter cell lines tracks individual cells over time. The evolution of the striation pattern is followed providing a unique readout for various dynamic studies⁸ (Fig. 1d).

Principles of the signal quantification. The induced striation pattern is described by two pre-defined parameters: the stripe width and the inter-stripe distance (gauge). The stripe width is defined by the used hardware and cannot be manipulated by the user. On the other hand, the inter-stripe distance can be manipulated by changing the scanning resolution or objective magnification defining the total number of stripes per field (Supplementary Fig. S2). Simple software was developed for quantitative evaluation of the induced striation pattern. The algorithm first recognizes individual nuclei. In each nucleus, stripe(s) are automatically identified (see Fig. 1e and Methods for details and Supplementary information for the software code). A measure of striation (MS) is proposed to capture the excess signal in the stripes for each nucleus. Such an approach for DDR quantification was directly compared to a commonly used method measuring mean fluorescence signal per nucleus¹⁸. For fixed samples involving protein modifications at sites of DNA damage such as lesion-associated phosphorylation of histone H2AX, the MS provides better discrimination between positive and negative controls (Supplementary Fig. S1). For assessment of reporter protein recruitment, such as for MDC1-GFP accumulation at sites of DNA damage, only the MS value enables meaningful analysis of the DDR (Supplementary Fig. S1).

Method optimization. In live-cell reporters involving GFP-tagged DNA-damage responsive proteins, the dependence of MS on time can be captured by plotting the median MS for each time-point. Such dependence can be quantified by the following three parameters: amplitude, time to peak response, and relaxation speed (Fig. 1f, see Methods for details). These parameters reflect changes in the amount of DNA damage and subsequent processes such as lesion recognition and repair. If DNA damage/repair processes are studied in time, the response curve should be optimized for each reporter cell line by proper settings of the striping system to avoid saturation. In case of LSM systems, the total laser irradiation dose is affected by multiple parameters such as the laser wavelength and power, the pre-sensitization strategy (Supplementary Fig. S3) and hardware settings including the light path, scanning speed and used objectives (Supplementary Fig. S2). Despite not absolutely necessary¹⁹ (see also Supplementary Fig. S3), BrdU pre-sensitization of cells is the 'gold standard' for damaging DNA by UV-A lasers^{5,6,20}. The concentration of BrdU is one of the critical parameters affecting the induced damage²¹. Various BrdU concentrations were tested with the laser power fixed to cause minimal damage in non-presensitized cells (Supplementary Fig. S3). We found that the commonly used concentration range 1–10 μM of BrdU for 24 h is too high for quantitative readouts since levels above 1 μM cause saturation of the signal amplitude in various tested reporter cell lines and for both tested LSM systems (Supplementary Fig. S3). Moreover, concentrations above 1 μM cause unwanted interference with cell cycle progression (Supplementary Fig. S3). Thus, for further experiments, 24-hour pre-incubation with 0.5 μM BrdU was chosen as an optimum due to its minimal adverse effects and MS values below saturation.

Method validation for DNA damage analysis. Once properly set, the striping method together with the software solution were tested on a small panel of known chemicals to prove its potential utility for applications involving large numbers of cells such as high-content screens for compounds and/or factors relevant for DNA integrity maintenance (potential cancer therapeutics). The compounds we selected are known to interfere with processes contributing to genomic stability, DNA damage signaling and/or repair pathways. The experiment was performed using a 96-well plate format in a semi-automatic regimen with autofocus and automatic repositioning

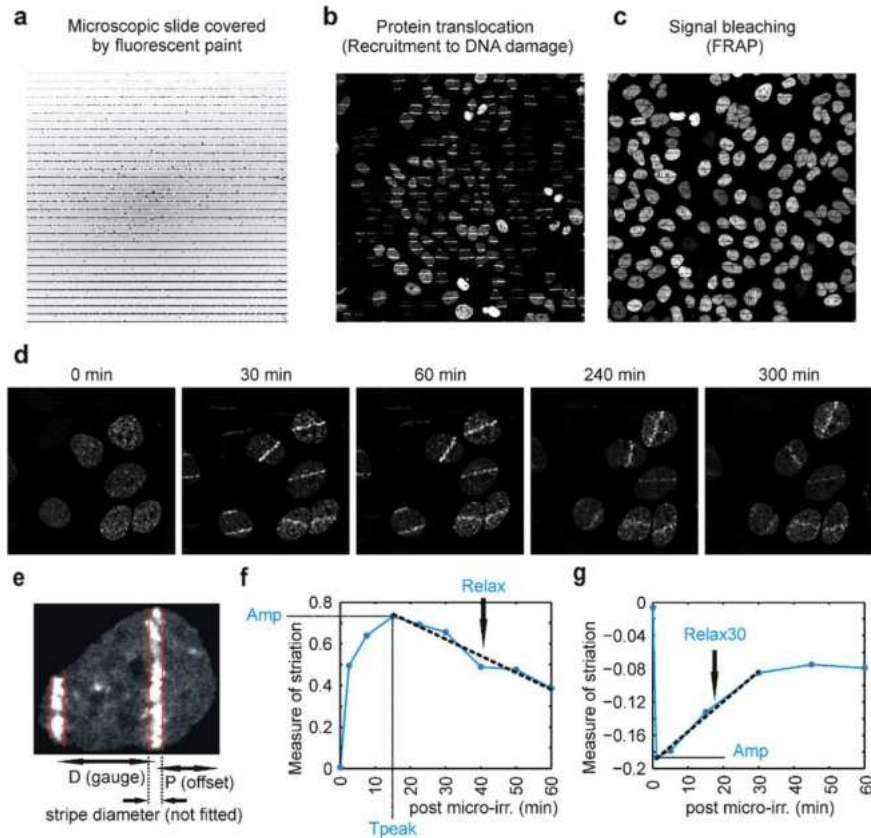


Figure 1. Method introduction. (a) Visualization of the striation pattern on a layer of fluorescent paint. (b) Striation pattern induced by a 355 nm laser (32 lines/field) in BrdU pre-sensitized U-2-OS-MDC1-GFP cells. DNA damage is visualized by recruitment of ectopically expressed MDC1-GFP protein. (c) Striation pattern bleached by a 488 nm laser (32 lines/field) in U-2-OS cells ectopically expressing histone H2B-GFP. (d) Evolution of the striation pattern over time. Cell line and DNA damage induction were the same as in (b). (e) Automatic stripe recognition by the software in the nucleus based on known values (gauge and position of the stripe) and additional fitting of recognized stripes. (f) Typical evolution of striation pattern after DNA damage caused by a 355 nm laser irradiation (32 lines/field, 1 iteration) in BrdU pre-sensitized U-2-OS-MDC1-GFP cells. The curve is plotted as medians of measure of striation (MS) values at indicated time points. The following parameters are used to describe the curve: Amp (amplitude, the maximum of MS over all time points), Tpeak (time to reach maximum MS), Relax (slope of the line fitted to MS values after Tpeak). (g) Typical evolution of striation pattern after bleaching. FRAP curve is formed by median values of MS at each time-point. The following parameters are used to describe the curve: Amp (amplitude, the minimum of MS), Relax30 (slope of the line fitted to MS values between 1 min and 30 min). Used cell line is the same as in (c).

and acquisition of striped regions in three different reporter cell lines. The tested compounds were added 2 hours before the experiment. For each compound, the cellular response at multiple time points after laser irradiation was compared with the mock treated sample. Four numerical parameters describing the MS curve (see Methods for details) were statistically evaluated (Fig. 2a). Notably, some of the compounds scored differentially for the MDC1-GFP, 53BP1-GFP and FANCD2-GFP reporters, respectively (Fig. 2a,b). Among the tested compounds only one (a PLK1 inhibitor) did not score in any of the measured parameters, in any of the reporter cell lines.

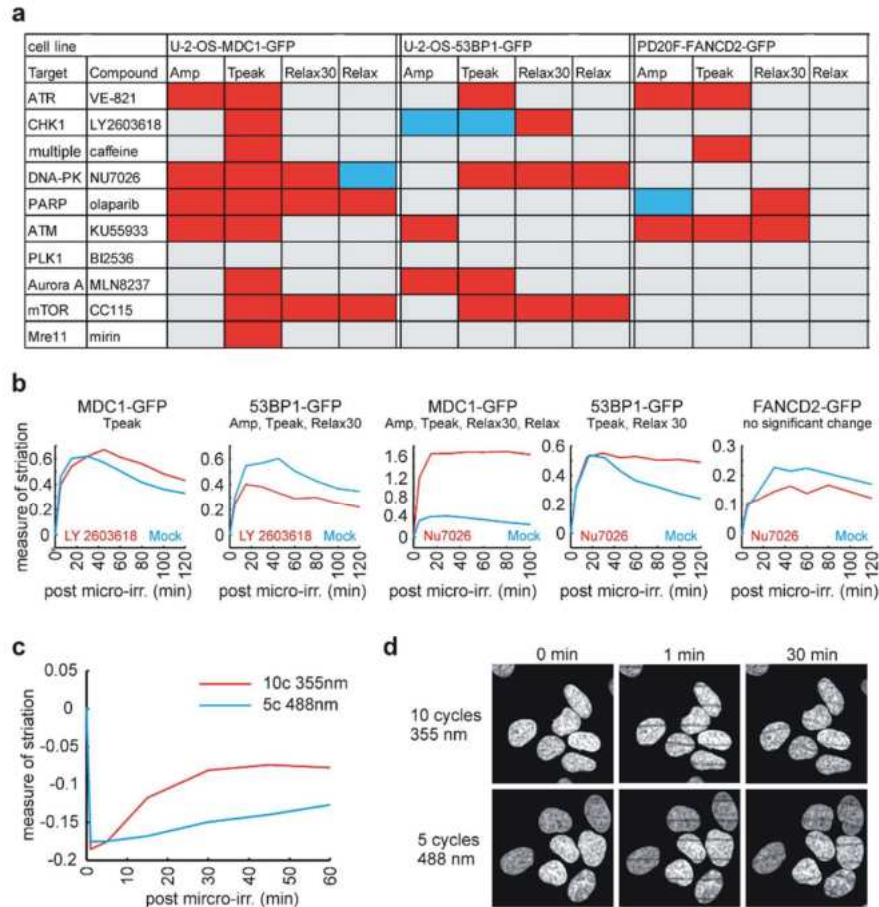


Figure 2. Method application. (a) Summary table for three reporter cell lines addressing parameters of DDR curve, Amp (amplitude, the maximum of MS over all time points), Tpeak (time to reach maximum MS), Relax (slope of the line fitted to DDR curve after Tpeak), Relax30 (slope of the line fitted to DDR curve after 30 min). The effects are color-coded: red – parameter upregulated, blue – downregulated, grey – no significant effect, Kruskal-Wallis test, $p < 0.05$. (b) Representative graphs of MS median values for selected compounds are showing differential reporter-dependent response (the parameters with significant change are listed in the graph titles), Kruskal-Wallis test, $p < 0.05$. (c) Illustrative graph of MS median values for H2B-GFP recovery after bleaching (FRAP). Bleaching was performed either with a 355 nm or 488 nm laser (32 lines/field) to the same level, Kruskal-Wallis test (difference in amplitude is non-significant, $p = 0.87$). Relax30 shows significant change ($p < 1.E-4$). (d) Illustrative images of U-2-OS-H2B-GFP cells bleached by a 355 nm or 488 nm laser and evolution of the striation pattern over time.

Method validation for FRAP analysis. The presented method including the software solution is easily adaptable for other photo-manipulation techniques. As an example of its utility, the FRAP method was tested in U-2-OS H2B-GFP reporter cells. The cells were pre-sensitized by $0.5 \mu\text{M}$ BrdU for 24 h and bleached by the co-linear stripes with either 488 nm laser or 355 nm laser. MS evaluation was performed along the same principle as for live-cell analysis after DNA damage. Despite the signal was initially bleached to the same level for both lasers, the H2B-GFP signal recovery was significantly faster after the UV-A laser bleaching (Fig. 2c,d). Apart from their technical merit, these results with the UV-A laser induced damage are novel and consistent with a published

report that DNA repair of lesions induced by UV-C lasers accelerates turnover of histones including H2B²³, suggesting that accelerated histone turnover is a common feature shared by multiple DNA repair pathways.

Discussion

The method presented in this study provides several advantages over currently used techniques, and offers a broad applicability in the area of LSM-based photo-manipulations in biomedicine. For the first time, a precisely defined striation pattern was used for simultaneous micro-irradiation of dozens of cells. Known parameters of striation patterns simplify software-based quantification of cellular responses. This enables an easy and unbiased evaluation of numbers of cells sufficient for robust statistical testing. Moreover, the method we present meets all requirements for full automation and application in high-content screens for new drugs and/or factors modulating diverse aspects of the DNA damage response. Several compounds that positively scored in our test panel are being intensively studied as potential anti-cancer therapeutics. Finally, the LSM system can produce the desired striation pattern rapidly because the laser path is ideally coordinated with the LSM scanning principle. This is particularly important for experiments where large numbers of cells are exposed simultaneously. Fast exposition speed allows also DNA damage experiments in non-pre-sensitized cells. Our data show that for DNA damage induction corresponding to pre-sensitization with 0.5 μ M BrdU, the non-pre-sensitized cells require approx. 6 times higher laser irradiation dose for the 355 nm, and a 10 times higher dose for the 405 nm laser (Supplementary Fig. S3). Thus either laser power or exposure time introduce serious limiting factors for presensitizer-free experiments if performed in a standard manner of manual laser path definition. Given all the advantages of the method we report here, we believe this new approach utilizing standard, widely used equipment could facilitate a broad range of biological and biomedical applications.

Methods

Microscopic devices. Microscopic station Zeiss Axioimager Z.1 with laser scanning LSM780 module. Lasers: UV-A 355 nm 65 mW (used for DNA damage induction, bleaching experiments and acquisition of Hoechst signal), argon-neon 458, 488, and 514 nm (used for acquisition of GFP and Alexa Fluor 488 signals) and 568 nm (used for acquisition of Alexa Fluor 568 signal). 40 \times objective (C-Apo, 1.2 DICIII, water immersion) was used for all experimental procedures unless stated otherwise in figure description. All other tested objectives are listed in Supplementary Fig. S2. Microscopic station Leica DMI 6000B with laser scanning TCS SP5 AOBIS TANDEM module. Lasers: UV-A 405 nm 100 mW (used for DNA damage induction), argon-ion 458, 488, and 514 nm (used for acquisition of GFP signal). Objective: 40 \times objective (HC PL APO 40 \times /1.30 OIL CS2, LP/0.17/D). Both microscopic stations were equipped with temperature-controlled incubator for live-cell support.

LSM settings for stripping procedure. ZEN 2011 software was used to control the Zeiss LSM780 device. For micro-irradiation 355 nm laser at maximum power (65 mW, 100% output) was used. To obtain desired striation pattern scan mode of very low resolution (size i.e. resolution 32 \times 32, 64 \times 64 or 128 \times 128 pixels) and the lowest possible scanning speed (pixel dwell time 709.27 μ s for 32 \times 32 pixels) was used. Striping at pixel resolution 32 \times 32 was chosen for most experiments with the 40 \times objective as it is causing approx. 1–2 stripes per cell nucleus. The scan was bidirectional, zoom 0.6. Number of iterations (means scanning cycles) is indicated in the figure legends (experiment dependent). Autofocus before each micro-irradiation was performed with 488 nm laser (the same settings as for respective GFP signal acquisition). For image acquisition in live-cell experiments with GFP-tagged reporters 488 nm laser was used. Images were acquired in 16 bit depth, zoom 0.6, five z-stack planes (0.6 μ m apart). To minimize bleaching the autofocus for image acquisition was based on reflected light of 561 nm laser which allows visualization of a thin contact layer between cells and the glass cultivation surface (also known as backscatter image). For bleaching experiments either 488 nm laser was used (100% output), or 355 nm laser (100% output). Autofocus was performed in the same manner as for micro-irradiation experiments.

For live-cell experiments performed on Leica SP5, Leica Application Suite Advanced fluorescence, FRET, FRAP, Live Data software was used. Micro-irradiation was done with acquisition resolution 32 \times 32 pixels, 10 Hz, bidirectional scan, 405 nm laser (68% output). Number of iterations (scanning cycles) is indicated in the figures. Acquisition of GFP signal was performed with following settings: resolution was set to 2048 \times 2048, 70 Hz, 488 nm laser, Hyd5 detector, 12 bit image depth, no z-stack. Autofocus was performed on GFP signal with the same settings as acquisition.

All live cell experiments were performed in pre-heated incubator (37 $^{\circ}$ C). Plates were placed into the incubator at least 45 min before the experiment to ensure proper temperature equilibration.

Visualization of the striation pattern using microscopic slide covered by fluorescent paint. Standard microscopic glass was covered by a homogeneous paint layer using red permanent marker (type: Permanent 8566, ink color 04, Centropen) and air dried. The paint layer was mounted by water and covered by a standard cover glass (0.17 mm). Signal was visualized using 561 nm laser and emission spectrum 570–710 nm. Micro-irradiation (stripping) procedure included 355 nm laser, 100%, 32 \times 32 pixels, 1 iteration, pixel dwell time 709.27 μ s, bi-directional scan.

Cell lines and treatments. All reporter cell lines were stably expressing the respective protein with a GFP tag. U-2-OS-MDC1-GFP, U-2-OS-53BP1-GFP and PD20F-FANCD2-GFP were obtained from Danish Cancer Society Research Centre, Copenhagen, Denmark²³, MRC-5 cells were obtained from ATCC and McCoy mouse fibroblasts were obtained from R-D Biotech. All cell lines were incubated under standard cultivation conditions (5% CO₂, 37 $^{\circ}$ C), in DMEM (Gibco) supplemented with 10% FBS (Invitrogen). Cells were pretreated by 0.5 μ M BrdU (Sigma) for 24 h before micro-irradiation unless stated otherwise (see figures description). For micro-irradiation procedures cells were seeded into 96 well plates with glass bottom (Corning) 18 hours before

laser irradiation. 2 hours before laser irradiation the medium was changed to DMEM CO₂ - independent medium without phenol red (Gibco) supplemented with 10% FBS and the tested chemicals. Cells were seeded in amounts to ensure sub-confluent density (proper cell cycle progression enables BrdU incorporation). After seeding the cells into 96 well plates the specimens were first placed on equilibrated bench for 20 min at RT to ensure equal cells distribution and then placed into incubator.

U-2-OS-H2B-GFP clone construction. Commercial plasmid pBOS-H2BGFP Vector was used. Cells were electroporated with Neon Transfection System (Life Technologies) with 15 µg of plasmid per 1.10⁶ cells (pulse voltage - 1230 V, pulse width 10 ms, pulse number 2). 72 h after transfection, GFP-positive cells were sorted for bulk culture stably expressing H2B-GFP. After proper cell culture propagation, 1 cell per well sorting was done to obtain individual clones (BD FACS Aria).

Quantitative analysis of the striation patterns. An in-house specialized software routine for the evaluation of the striation patterns was developed and implemented in MatLab. The first step of the routine consists of the segmentation of the images to find the individual nuclei. To be selected, a nucleus must satisfy certain conditions on its size and solidity. The process begins by segmenting the first image, acquired at the beginning of the experiment ($t = 0$, before laser irradiation). Standard thresholding algorithms (e.g. the Otsu's method) do not perform well here because there is a large variance in the signal intensity among the individual nuclei (a common problem in most live-cells based reporter systems). Consequently, a cascade of decreasing local thresholds is used. After the cascade has finished, usually all the nuclei of desirable characteristics are identified in the image. For the segmentation of the subsequent images, a tracking algorithm is used. The algorithm attempts to track each nucleus by searching the vicinity of its positions in the previous image. This tracking approach is necessary because the signal intensity in the inter-stripe regions of the nuclei may decrease all the way to the background level and thus become completely "invisible" for any simple thresholding procedure.

Several measures were proposed and tested to quantify the evolution of the striation patterns induced by the laser within each recognized and over the time tracked nucleus. In the end, the relative excess signal in the stripes, hereafter called the measure of striation and abbreviated "MS", proved to be the most useful. It is constructed as follows: Let us consider an image of an individual cell nucleus at time t . We start by rotating the image so that the (possible) stripes become vertical. This is done by taking the Radon Transform of the image and finding its maximum. If there are no stripes in the image, the nucleus gets usually rotated by a random angle.

Next, the position of the stripes and their diameter is found. This is done by fitting the stripes, i.e. maximizing a function of two variables $F(D,P)$ where D stands for the gauge (i.e. the distance between the centers of the stripes) and P stands for the horizontal offset of the stripes (i.e. the position of the center of the first stripe from the rightmost boundary point of the nucleus, see Fig. 1e). The function F measures the ratio of the mean intensity of the signal in the stripes to the mean intensity of the signal in the entire nucleus. The width of the stripes is a user-defined constant and it is not fitted. Although both the parameters D and P are known from the initial setting of the laser, the optimization (i.e. fitting) step is necessary due to elasticity of the nuclei and their movement in time. Without this optimization step, the measure of striation would automatically decrease in time as the nuclei move around and change shape. This would create a systematic error – a false decrease in the intensity of the stripes. The minimization is implemented by means of a trivial algorithm that fully evaluates all plausible values of D and P and selects the highest value for F . The parameter D is allowed to take only integer values from a pre-specified range and the parameter P is not allowed to depart too much from the point where the vertical sum of the signal reaches its maximum. More advanced optimization procedures may naturally be used, however, this optimization step takes much less time than the cell-tracking part of the algorithm. Moreover, the full evaluation of a single image (which may contain around 100 nuclei) takes only few seconds on a standard PC.

Once the position of the stripes is found, the measure of striation is computed according to equation (1):

$$MS = \frac{J_{meas} - J_{expt}}{J_{expt}}$$

Equation (1): J_{meas} (measured) stands for the actual signal integrated density of regions inside the stripes, and J_{expt} (expected) stands for the expected value of the signal integrated density in region of the stripes, if the nucleus was perfectly homogeneous and no stripes were present.

J_{expt} is computed according to equation (2):

$$J_{expt} = \frac{\text{Area inside the stripes}}{\text{Total area of the nucleus}} \text{SID of the nucleus}$$

Equation (2): SID stands for signal integrated density.

The measure MS thus captures the relative excess signal in the stripes. The baseline is zero which means there is no excess signal in the stripes, i.e. the stripes contain only as much signal as corresponds to their area, i.e. the signal is homogeneously distributed throughout the nucleus, i.e. there are no visible stripes. As the fluorescently labeled DNA-damage responsive proteins get recruited to the places of laser-induced damage (i.e. to the stripes), the measure of striation grows. After some time, the proteins are released, they begin to spread out again over the entire nucleus, and/or undergo degradation and the measure of striation decreases again. Thus, the measure of striation captures the dynamics of the DNA-repair processes. The construction of MS ensured that it is independent of the total SID of the nucleus. This is necessary because the total SID may vary greatly among individual nuclei.

DNA damage repair (DDR) curve parameters. By a DDR curve we mean the dependence of MS on time for a particular nucleus. To compare different DDR curves, the following three parameters were defined (Fig. 1f,g):

1. The amplitude of the response (Amp) which measures the maximum amount of the protein recruited to the stripes. It is computed as the maximum of MS over all observed time points.
2. The time to peak response (Tpeak) measures the speed of the protein recruitment. It is computed as the time (in minutes) from the micro-irradiation until the MS reaches its maximum.
3. The relaxation speed (Relax) which reflects the dynamics of the repair process after the peak response. It is calculated as the slope of the line fitted to the function $MS(t)$ for $t > T_{peak}$, where MS stands for the measure of striation, and t for time. For some samples treated by DNA damage/repair interfering compounds, the MS did not peak during the observed period and kept increasing. In these cases, the relaxation speed was measured by the slope of the line fitted to $MS(t)$ for $t > 30 \text{ min}$.

These parameters are computed for every nucleus within a sample and differences among samples are tested for statistical significance by means of the Kruskal-Wallis test. The significance level of all tests was set to 0.05. For illustrative graphs the median MS at each timepoint was computed and these medians were connected by lines (Figs 1f,g and 2b).

Screen for compounds potentially affecting DNA damage response. Panel of compounds including VE-821²⁴ (Selleck Chem.), LY2603618²⁵ (Selleck Chem.), Caffeine²⁶ (Sigma), NU7026²⁷ (Sigma), Olaparib²⁸ (Selleck Chem.), KU55933²⁹ (Sigma), BI2536³⁰ (Selleck Chem.), MLN8237³¹ (Selleck Chem.), CC115³² (Celgene Corporation) and Mirin³³ (Sigma) was tested in 3 reporter cell lines. Each compound was added to cells 2 hours before micro-irradiation in final concentration of 10 μM with the exception of BI2536 (100 nM). Respective DDR protein recruitment to sites of damage was evaluated as MS in each timepoint for every single cell. Four parameters characterizing the DDR curve (see above) were calculated and statistically tested against mock treated control (Fig. 2a). Every sample was tested in technical duplicate (i.e. in two separate wells on the same 96 well plate). Results from duplicates were pooled and tested against pooled mock treated sample. At least two independent biological replicates were performed for each tested compound. Only significant effects scored similarly in both biological replicates were marked in the table by a color change (Fig. 2a). Minimum of 100 cells were scored in each experiment.

FRAP experiment. Cells were seeded and treated in the same way as for the micro-irradiation experiments, including BrdU pre-sensitization. The FRAP curve (i.e. the evolution of MS in time) was constructed in the same way as the DDR curve. The first two DDR curve parameters (Amp, Tpeak) were defined similarly as above (taking the minimum of MS instead of a maximum). Tpeak was not used as the minimum MS (i.e. maximum striation) is always reached immediately after the bleaching. The relaxation speed was measured in a slightly different way. The parameter Relax30 denotes the slope of the line fitted to the FRAP curve between $t = 1 \text{ min}$ and $t = 30 \text{ min}$, the parameter Relax denotes the slope of the line fitted to the FRAP curve between $t = 1 \text{ min}$ and $t = 60 \text{ min}$ (Fig. 1g). Experiment was performed in two biological replicates. Minimum of 150 cells were scored in each experiment.

Immunofluorescence. Cells were seeded and treated with BrdU in the same way as described for the live-cell experiments (see above). At indicated timepoints after micro-irradiation, cells were fixed with 10% buffered formalin (Sigma) and permeabilized with 0.5% Triton X for 5 min. After 20 min blocking in 1% BSA in PBS, the samples were incubated with primary antibodies at 4 °C 18 h, followed by 1 h incubation with secondary antibodies at RT. DNA was stained by Hoechst33342 (Invitrogen) 5 $\mu\text{g}/\text{ml}$ in PBS. Acquisition of IF labeled samples was performed by the Zeiss LSM780 system. Scan mode was set to frame, size 1024 \times 1024, 16 bit image depth, zoom 0.6, five z-stack planes (0.6 μm apart). Autofocus was performed with settings used for acquisition of Hoechst stained nuclei. Acquired images were analyzed for measure of striation by slightly modified software routine described above. The modification included deactivation of tracking module and recognition of individual nuclei based on Hoechst stain channel. Following antibodies were used: phospho-H2AX (Ser139) JBW301 (Millipore, 500 \times), 53BP1 (Santa Cruz, 500 \times), BRCA1 (Santa Cruz, 300 \times), cyclin A (Leica, 50 \times), AlexaFluor488 and AlexaFluor568 (Invitrogen, 1000 \times).

Cell cycle analysis. Cells were seeded and treated in the same way as for the micro-irradiation experiment. After 24 h incubation with indicated concentrations of BrdU, cells were fixed with 10% formalin (Sigma) and stained with Hoechst33342 5 $\mu\text{g}/\text{ml}$ in PBS (Invitrogen) for 10 min. Cell cycle was evaluated using OlympusBX71 inverted microscope and ScanR Acquisition and Analysis software (Olympus).

References

1. Kong, X. *et al.* Comparative analysis of different laser systems to study cellular responses to DNA damage in mammalian cells. *Nucleic acids research* **37**, e68, doi: 10.1093/nar/gkp221 (2009).
2. Dinant, C. *et al.* Activation of multiple DNA repair pathways by sub-nuclear damage induction methods. *Journal of cell science* **120**, 2731–2740, doi: 10.1242/jcs.004523 (2007).
3. Ishikawa-Ankerhold, H. C., Ankerhold, R. & Drummen, G. P. Advanced fluorescence microscopy techniques—FRAP, FLIP, FLAP, FRET and FLIM. *Molecules (Basel, Switzerland)* **17**, 4047–4132, doi: 10.3390/molecules17044047 (2012).
4. Britton, S. *et al.* DNA damage triggers SAF-A and RNA biogenesis factors exclusion from chromatin coupled to R-loops removal. *Nucleic acids research* **42**, 9047–9062, doi: 10.1093/nar/gku601 (2014).
5. Lukas, C., Falck, J., Bartkova, J., Bartek, J. & Lukas, J. Distinct spatiotemporal dynamics of mammalian checkpoint regulators induced by DNA damage. *Nature cell biology* **5**, 255–260, doi: 10.1038/ncb945 (2003).

6. Galanty, Y. *et al.* Mammalian SUMO E3-ligases PIAS1 and PIAS4 promote responses to DNA double-strand breaks. *Nature* **462**, 935–939, doi: 10.1038/nature08657 (2009).
7. Bekker-Jensen, S. *et al.* Spatial organization of the mammalian genome surveillance machinery in response to DNA strand breaks. *The Journal of cell biology* **173**, 195–206, doi: 10.1083/jcb.200510130 (2006).
8. Bekker-Jensen, S., Lukas, C., Melander, F., Bartek, J. & Lukas, J. Dynamic assembly and sustained retention of 53BP1 at the sites of DNA damage are controlled by Mdc1/NFBD1. *The Journal of cell biology* **170**, 201–211, doi: 10.1083/jcb.200503043 (2005).
9. Jackson, S. P. & Bartek, J. The DNA-damage response in human biology and disease. *Nature* **461**, 1071–1078, doi: 10.1038/nature08467 (2009).
10. Lukas, C. *et al.* Mdc1 couples DNA double-strand break recognition by Nbs1 with its H2AX-dependent chromatin retention. *The EMBO journal* **23**, 2674–2683, doi: 10.1038/sj.emboj.7600269 (2004).
11. Lukas, J., Lukas, C. & Bartek, J. More than just a focus: The chromatin response to DNA damage and its role in genome integrity maintenance. *Nature cell biology* **13**, 1161–1169, doi: 10.1038/ncb2344 (2011).
12. Stucki, M. & Jackson, S. P. gammaH2AX and MDC1: anchoring the DNA-damage-response machinery to broken chromosomes. *DNA repair* **5**, 534–543, doi: 10.1016/j.dnarep.2006.01.012 (2006).
13. Coster, G. & Goldberg, M. The cellular response to DNA damage: a focus on MDC1 and its interacting proteins. *Nucleus (Austin, Tex.)* **1**, 166–178, doi: 10.4161/nucl.1.2.11176 (2010).
14. Doil, C. *et al.* RNF168 binds and amplifies ubiquitin conjugates on damaged chromosomes to allow accumulation of repair proteins. *Cell* **136**, 435–446, doi: 10.1016/j.cell.2008.12.041 (2009).
15. Panier, S. & Boulton, S. J. Double-strand break repair: 53BP1 comes into focus. *Nature reviews. Molecular cell biology* **15**, 7–18, doi: 10.1038/nrm3719 (2014).
16. Kim, H. & D'Andrea, A. D. Regulation of DNA cross-link repair by the Fanconi anemia/BRCA pathway. *Genes & development* **26**, 1393–1408, doi: 10.1101/gad.195248.112 (2012).
17. Xu, G. *et al.* REV7 counteracts DNA double-strand break resection and affects PARP inhibition. *Nature* **521**, 541–544, doi: 10.1038/nature14328 (2015).
18. Toledo, L. I. *et al.* ATR prohibits replication catastrophe by preventing global exhaustion of RPA. *Cell* **155**, 1088–1103, doi: 10.1016/j.cell.2013.10.043 (2013).
19. Epe, B. DNA damage spectra induced by photosensitization. *Photochemical & photobiological sciences: Official journal of the European Photochemistry Association and the European Society for Photobiology* **11**, 98–106, doi: 10.1039/c1pp05190c (2012).
20. Miller, K. M. *et al.* Human HDAC1 and HDAC2 function in the DNA-damage response to promote DNA nonhomologous end-joining. *Nature structural & molecular biology* **17**, 1144–1151, doi: 10.1038/nsmb.1899 (2010).
21. Fujii, Y. *et al.* Comparison of the bromodeoxyuridine-mediated sensitization effects between low-LET and high-LET ionizing radiation on DNA double-strand breaks. *Oncol Rep* **29**, 2133–2139, doi: 10.3892/or.2013.2354 (2013).
22. Dinant, C. *et al.* Enhanced chromatin dynamics by FACT promotes transcriptional restart after UV-induced DNA damage. *Molecular cell* **51**, 469–479, doi: 10.1016/j.molcel.2013.08.007 (2013).
23. Chirnomas, D. *et al.* Chemosensitization to cisplatin by inhibitors of the Fanconi anemia/BRCA pathway. *Molecular cancer therapeutics* **5**, 952–961, doi: 10.1158/1535-7163.mct-05-0493 (2006).
24. Reaper, P. M. *et al.* Selective killing of ATM- or p53-deficient cancer cells through inhibition of ATR. *Nature chemical biology* **7**, 428–430, doi: 10.1038/nchembio.573 (2011).
25. King, C. *et al.* Characterization and preclinical development of LY2603618: a selective and potent Chk1 inhibitor. *Investigational new drugs* **32**, 213–226, doi: 10.1007/s10637-013-0036-7 (2014).
26. Wang, G., Bhoopalan, V., Wang, D., Wang, L. & Xu, X. The effect of caffeine on cisplatin-induced apoptosis of lung cancer cells. *Experimental hematology & oncology* **4**, 5, doi: 10.1186/2162-3619-4-5 (2015).
27. Gurung, R. L., Lim, H. K., Venkatesan, S., Lee, P. S. & Hande, M. P. Targeting DNA-PKcs and telomerase in brain tumour cells. *Molecular cancer* **13**, 232, doi: 10.1186/1476-4598-13-232 (2014).
28. Hopkins, T. A. *et al.* Mechanistic Dissection of PARP1 Trapping and the Impact on *In Vivo* Tolerability and Efficacy of PARP Inhibitors. *Molecular cancer research: MCR* **13**, 1465–1477, doi: 10.1158/1541-7786.mcr-15-0191-t (2015).
29. Hickson, I. *et al.* Identification and characterization of a novel and specific inhibitor of the ataxia-telangiectasia mutated kinase ATM. *Cancer research* **64**, 9152–9159, doi: 10.1158/0008-5472.can-04-2727 (2004).
30. Lund-Andersen, C., Patzke, S., Nahse-Kumpff, V. & Syljuasen, R. G. PLK1 inhibition can cause radiosensitization or radioresistance dependent on the treatment schedule. *Radiotherapy and oncology: journal of the European Society for Therapeutic Radiology and Oncology* **110**, 355–361, doi: 10.1016/j.radonc.2013.12.014 (2014).
31. Liu, Y. *et al.* Targeting aurora kinases limits tumour growth through DNA damage-mediated senescence and blockade of NF-kappaB impairs this drug-induced senescence. *EMBO molecular medicine* **5**, 149–166, doi: 10.1002/emmm.201201378 (2013).
32. Jekimovs, C. *et al.* Chemotherapeutic compounds targeting the DNA double-strand break repair pathways: the good, the bad, and the promising. *Frontiers in oncology* **4**, 86, doi: 10.3389/fonc.2014.00086 (2014).
33. Muraki, K., Han, L., Miller, D. & Murnane, I. P. Processing by MRE11 is involved in the sensitivity of subtelomeric regions to DNA double-strand breaks. *Nucleic acids research* **43**, 7911–7930, doi: 10.1093/nar/gkv714 (2015).

Acknowledgements

This work was supported by grants from the Grant Agency of the Czech Republic 13–17555S, Czech National Program of Sustainability LO1304, the Kellner Family Foundation, EU operation program CZ.1.07/2.3.00/30.0004 and CZ.1.07/2.3.00/30.0041, the Novo Nordisk Foundation (NNF12OC0002290 and NN13331) and the Danish Council for Independent Research (DFR-1331-00262).

Author Contributions

M.M. and E.V. wrote the manuscript and performed most cell work and stripping experiments, T.F. designed the software script and performed all statistical analysis, H.H. performed parallel stripping experiments on LeicaSP5 LSM system, I.F. prepared and characterized the U-2-OS H2B-GFP cell line, J.G. and D.M. performed stripping experiments and contributed to data evaluation, J.B. wrote the manuscript and contributed to data evaluation.

Additional Information

Supplementary information accompanies this paper at <http://www.nature.com/srep>

Competing financial interests: The authors declare no competing financial interests.

How to cite this article: Mistrik, M. *et al.* Cells and Stripes: A novel quantitative photo-manipulation technique. *Sci. Rep.* **6**, 19567; doi: 10.1038/srep19567 (2016).



ARTICLE


<https://doi.org/10.1038/s41467-021-20989-9>

OPEN

Microthermal-induced subcellular-targeted protein damage in cells on plasmonic nanosilver-modified surfaces evokes a two-phase HSP-p97/VCP response

Martin Mistrik^{1,6}, Zdenek Skrott^{1,6}, Petr Muller², Ales Panacek³, Lucie Hochvaldova³, Katarina Chroma¹, Tereza Buchtova¹, Veronika Vandova², Libor Kvitek³ & Jiri Bartek^{1,4,5}

Despite proteotoxic stress and heat shock being implicated in diverse pathologies, currently no methodology to inflict defined, subcellular thermal damage exists. Here, we present such a single-cell method compatible with laser-scanning microscopes, adopting the plasmon resonance principle. Dose-defined heat causes protein damage in subcellular compartments, rapid heat-shock chaperone recruitment, and ensuing engagement of the ubiquitin-proteasome system, providing unprecedented insights into the spatiotemporal response to thermal damage relevant for degenerative diseases, with broad applicability in biomedicine. Using this versatile method, we discover that HSP70 chaperone and its interactors are recruited to sites of thermally damaged proteins within seconds, and we report here mechanistically important determinants of such HSP70 recruitment. Finally, we demonstrate a so-far unsuspected involvement of p97(VCP) translocase in the processing of heat-damaged proteins. Overall, we report an approach to inflict targeted thermal protein damage and its application to elucidate cellular stress-response pathways that are emerging as promising therapeutic targets.

¹Laboratory of Genome Integrity, Institute of Molecular and Translational Medicine, Faculty of Medicine and Dentistry, Palacky University, Olomouc, Czech Republic. ²Regional Centre for Applied Molecular Oncology, Masaryk Memorial Cancer Institute, Brno, Czech Republic. ³Regional Centre of Advanced Technologies and Materials, Department of Physical Chemistry, Faculty of Science, Palacky University, Olomouc, Czech Republic. ⁴Danish Cancer Society Research Center, Copenhagen, Denmark. ⁵Division of Genome Biology, Department of Medical Biochemistry and Biophysics, Science for Life Laboratory, Karolinska Institute, Stockholm, Sweden. ⁶These authors contributed equally: Martin Mistrik, Zdenek Skrott. [✉]email: martin.mistrik@upol.cz; jb@cancer.dk

NATURE COMMUNICATIONS | (2021)12:713 | <https://doi.org/10.1038/s41467-021-20989-9> | www.nature.com/naturecommunications

1

Exposure of cells and tissues to elevated temperatures is routinely used in research on protein thermal stability profiling, thermal therapies, treatments of accidental burns, and proteinopathies involving an accumulation of defective proteins. At the cellular level, the thermal damage primarily impairs proteins, causing their unfolding, aggregation, amyloidogenesis, and denaturation, phenomena particularly implicated in the pathobiology of Alzheimer's disease (AD), Huntington disease, Parkinson disease, amyotrophic lateral sclerosis and amyloidosis¹. Accumulation of defective proteins is also among the hallmarks of cancer with potentially causative roles, and cellular mechanisms of protein quality control represent anticancer therapeutic targets, as exemplified by clinically applicable inhibitors of the ubiquitin–proteasome system (UPS)².

Studying responses to thermal damage of proteins on the level of a single living cell or even subcellular level represents a significant challenge due to the lack of available methods allowing precise and fast delivery of the heat to the target structure at the micrometer scale. The temperature elevation is currently achieved by heating the cell culture media using various heat sources such as a water bath, an incubator with a pre-set target temperature, or by various energy emitters, including microwaves, ultrasound, and infra-red lamps and lasers³. However, such approaches have severe limitations, including, but not limited to: (i) a significant time delay in achieving the desired temperature as the media must be heated primarily; (ii) spatial restrictions as the whole cultivation vessel, or at least its large part is inevitably exposed to the heat; and (iii) overall precision issues including the inability to target selected single cells or subcellular compartments, thereby limiting the type of biological questions one can address.

Currently, the function of cellular chaperones is studied mainly by biochemical approaches under *in vitro* non-physiological conditions, mostly based on model substrates and simplified peptides, leaving the role and regulation of chaperones under physiological conditions of intact cell largely unexplored. Dramatic differences between cells and test tube should be taken into consideration, such as molecular crowding (300–400 mg ml⁻¹ of proteins in cells), presence of other (macro)molecules, or increased interactions between macromolecules leading to changes in protein aggregation or folding⁴. Moreover, the findings from biochemical experiments are challenging to validate in cellular experiments due to a lack of appropriate methods. Thus, some basic questions regarding the function of chaperones in cells, including their recruitment kinetics to the substrates, remain unanswered.

The emerging field of plasmonic nanoparticles (NPs) has opened, besides other possibilities, a way for localized thermal therapy due to the efficient and tunable photothermal properties. When illuminated by light, free electrons localized on the NP surface become excited, and the local electron cloud is asymmetrically distributed over the whole NP. This distribution produces a coulombic restoring force between positively charged nuclei and negatively charged electrons from the conduction band, which leads to collective oscillation of the electron cloud on the particle surface called localized surface plasmon (LSP). The localized surface plasmon resonance (LSPR) occurs if the frequency of the incident light matches the frequency of LSP oscillation. As a result, the light is absorbed much more efficiently and generates localized and highly amplified electric fields in the proximity of the NP surface^{5,6}. Absorption of light by NPs may be non-radiatively relaxed and simultaneously converted to heat energy. Surface plasmon resonance depends on many parameters of the NPs, including size, shape, composition, surface coatings, dielectric properties of the metal NP and the environment^{6–8}. Importantly, the absorption and scattering frequency of plasmonic NPs can be selectively changed by adjusting the

morphology and the structure of the NPs and tuned to be located in the desired wavelength. Silver NPs can be easily tailored to possess an intense SPR band at a suitable wavelength region, enabling them to produce heat after the irradiation with appropriate laser and makes them an excellent candidate for a photothermal therapeutic agent. Plasmon NPs convert energy from the light to heat immediately and efficiently, allowing localized heating of the surrounding environment^{9–11}.

In an attempt to remedy the lack of suitable techniques for inflicting targeted protein damage in live human cells, we exploit here the properties of the plasmonic nanosilver-modified surfaces as a cell culture substrate. The approach that we developed, and examples of its applications to study molecular pathways highly relevant for biomedicine, are presented below.

Results

Plasmon-coated cultivation surface as a tool for heat micro-irradiation. We adopted the NPs technology to directly focus the heat on the individual cells or subcellular compartments within a micrometer scale. The method is based on modified microscopic cell culture plates, pre-coated by a layer of anisotropic silver NPs allowing excitation through targeted irradiation by conventional lasers used in the laser scanning microscopes (LSM) and allowing controllable heating. The deposition of NPs with suitable plasmonic properties on the cultivation surface is based on the layer-by-layer self-assembly technique, which facilitates the binding of negatively charged silver NPs using positively charged thin polymeric film deposited on the surface of the cultivation plate (Fig. 1a). For this purpose, water dispersion of anisotropic silver NPs of various crystallinity and shapes such as spheres, plates, rods, and triangles (Supplementary Fig. 1a, b), were synthesized by a two-step reduction method, showing the typical UV/VIS absorption spectrum (Supplementary Fig. 1c). Next, the prepared NPs were coated on the bottom of standard cell culture 24-well plates, which were pre-coated by a thin polymeric film consisting of polyacrylic acid (PAA) and poly(diallyl dimethylammonium chloride) (PDMA) polyions, thereby ensuring higher wettability and strong electrostatic binding ability of silver NPs, respectively¹².

Notably, such modified cultivation surface is chemically stable, optically transparent, and fully compatible with standard tissue culture methods, including cell adherence, cell viability and growth (Supplementary Fig. 1e–g). The photothermal effect and heat emission of the plasmonic modified cultivation surface after irradiation with the LSM laser is detectable within the LWIR spectrum (7.5–14 μm) by thermal imaging (Fig. 1b and Supplementary Fig. 1h).

To analyze the ability of the modified surface to induce microthermal damage of proteins in live cells, we employed a human reporter U-2-OS cell line expressing a GFP-tagged HSP70 protein (Heat shock protein 70). HSP70 is the central cellular chaperone involved in the processing of unfolded or aggregated proteins⁴. Immediately (within 8 s) after the laser exposure, HSP70-GFP accumulated at the micro-thermal damage sites, forming the laser path's precise pattern demonstrating proximate recognition of heat-damaged proteins by HSP70 in cells (Fig. 1c). The HSP70-GFP signal within the damaged areas changed over time positionally, and also the intensity decreased within a few minutes, indicating dynamic processing (Supplementary Video 1). HSP70 interacting partners, E3 ubiquitin ligase CHIP, and co-chaperone HOP⁴ were also rapidly recruited to the sites of thermal damage with similar signal kinetics as HSP70 (Fig. 1c). Importantly, the same chaperone response was observed in another human reporter cell line (H1299) and on different plasmon layer-modified cell culture plates, thereby attesting to

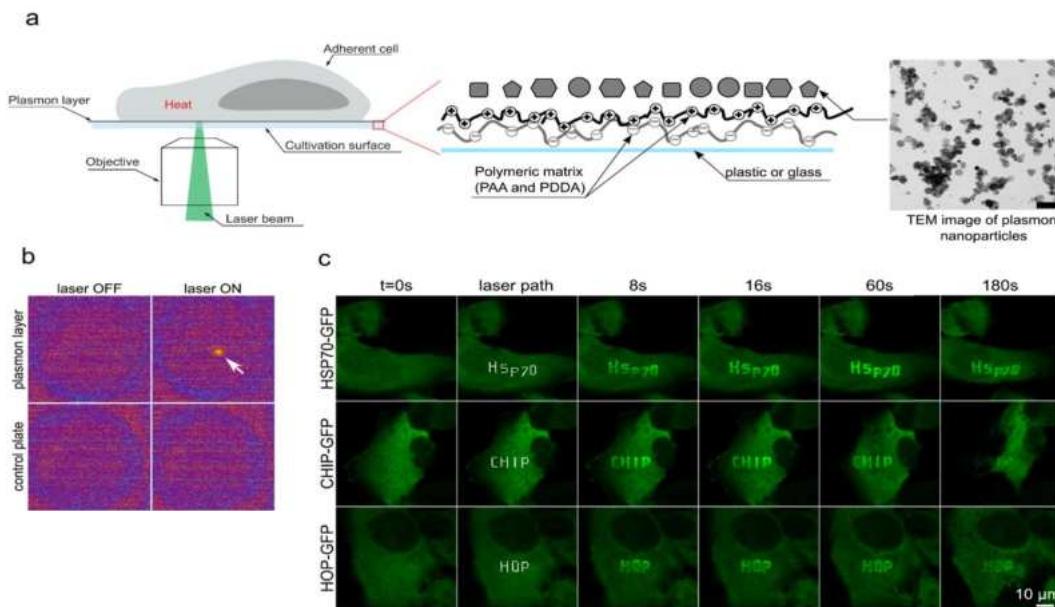


Fig. 1 Plasmonic cultivation surface activated by a laser of appropriate wavelength induces microthermal damage. **a** Schematic representation of the concept of microthermal damage inflicted on cellular proteins. The cell culture plate surface is modified by a thin polymeric film consisting of PAA (polyacrylic acid) and PDDA (poly(diallyl dimethylammonium chloride)) for the efficient binding of plasmonic silver NPs. Plasmon NPs convert energy from light (laser) immediately and efficiently to heat, enabling direct focusing of the heat on subcellular regions. **b** Thermal imaging shows emitted heat detected in the LWIR spectrum in plasmon-modified cell culture plate wells activated by 561 nm laser. **c** Recruitment of various GFP-tagged heat shock-related proteins to micro-heated regions in U-2-OS cells grown on a plasmon-modified Ibidi plate. Microheated regions were exposed to 561 nm laser (power 15%). The defined laser path is shown in white. Cells were followed in time. Representative results from two experiments. Scale bars = 10 μ m, for TEM micrograph 100 nm.

the method's universal applicability (Supplementary Fig. 2a, b). Another chaperone involved in the processing of heat-damaged proteins, HSP90, was less prominent but also detectable within the damaged sites (Supplementary Fig. 2c, d).

To rule out the possibility that the observed protein damage and cellular response might also involve the direct damaging effect of plasmon activating laser, we performed an additional control experiment. The plasmon layer was partially scratched from the cultivation surface using a pipet tip, which is also visible using transmission light microscopy (Supplementary Fig. 3). Importantly, only those cellular areas which are in direct contact with the plasmon layer, but not those in contact with the adjacent scratched surface, revealed the typical HSP70 protein response upon exposure to the plasmon activating laser (Supplementary Fig. 3).

Compatibility of the method with quantitative readouts.

Overall, the presented approach enables a so-far unprecedented analysis of the function and kinetics of chaperones or other factors involved in the processing of damaged proteins. In combination with a software-based ROI analysis, this setup also allows precise quantification of the process in time (Fig. 2a, b, and Supplementary Fig. 4a). The microthermal damage can also be induced by an adaptation of the so-called 'laser stripe' (laser micro-irradiation) approach, which is commonly used in the field of DNA damage^{13,14}. By this technique, dozens of cells can be

simultaneously and uniformly exposed to co-linear laser stripes of damaged chromatin containing DNA double-strand breaks, forming an easily recognizable pattern¹³. We adapted this approach and the HSP70-GFP reporter for characterization of dose-response aspects of our method. Indeed, the dosing can be precisely controlled to trigger responses ranging from relatively faint and transient recruitment of HSP70-GFP to stripes, up to clearly visible stripes persisting for several minutes, by adjusting the laser power (Fig. 2c). Importantly, these experiments do not require any specialized laser equipment as the real energy hitting the plasmon layer corresponds to values 0.23, 0.38 and 0.48 mW, respectively. Alternatively, the total emitted heat can also be increased by changing the number of laser exposure cycles with a fixed laser power (Supplementary Fig. 4b). These data confirm that the method does not require any unusual equipment, and generates predictably reproducible results in a dose-dependent manner.

Real-time kinetics and structural requirements of HSP70 recruitment.

As stated above, the current knowledge about chaperone function is based mainly on biochemical experiments with purified components under rather artificial conditions. HSP70 is known to form oligomeric structures, and recently, various oligomeric structures were proposed^{15,16}. Yet, the relevance of HSP70 dimerization is not fully understood, and it has not been studied in the context of live cells.

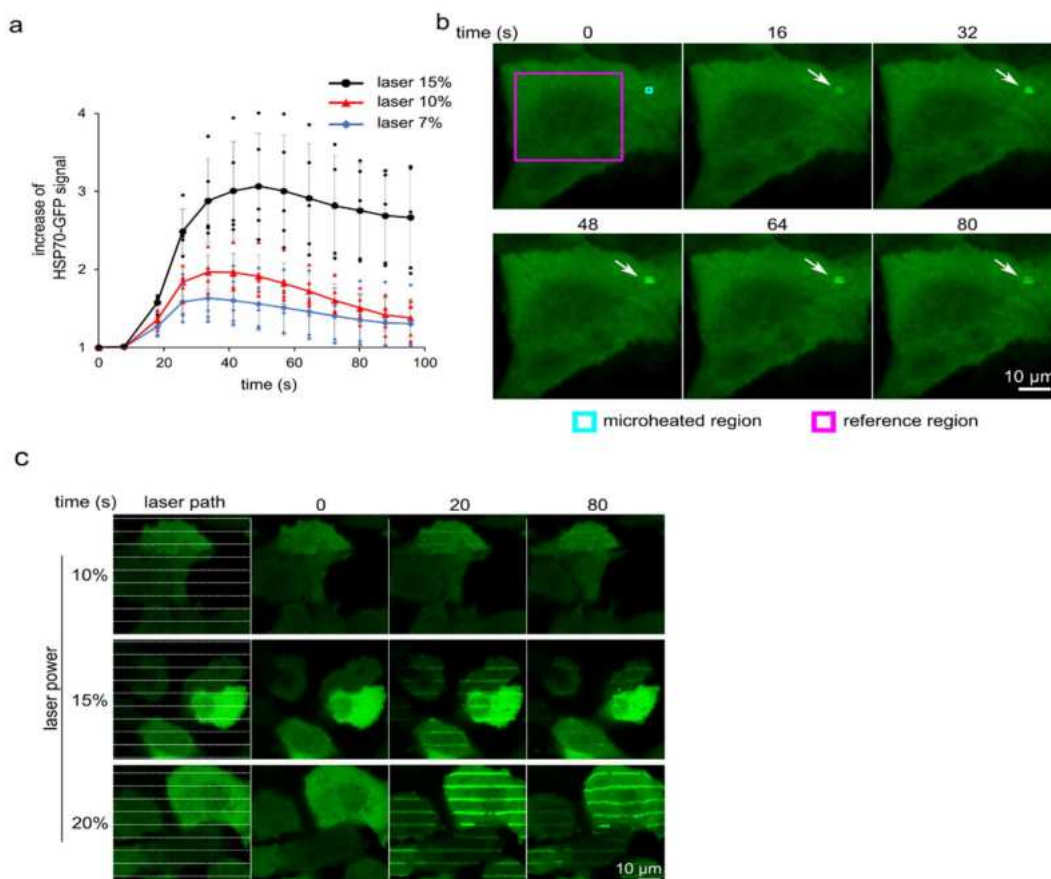


Fig. 2 Demonstration of dose-response dependence and quantification of the cellular response. **a** ROI-based quantitative analysis of the kinetics of HSP70-GFP recruitment to micro-heated proteins and the dependence of the process on the laser power used for plasmon layer activation (mean, SD, $n = 5$ cells). **b** Representative images depicting the evolution of the HSP70-GFP signal in the micro-heated ROI (white arrow, $n = 5$ cells). **c** H1299 cells grown on a plasmon-modified Ibidi plate expressing HSP70-GFP were exposed to collinear laser stripes of different laser power. The laser dose-response correlates with stronger and longer-persisting HSP70-GFP signals. Representative results from two experiments. Scale bars = 10 μm . Source data are provided as a Source Data file for Fig. 2a.

To assess the contribution of the HSP70 dimerization for its function, we employed three *HSP70* mutants known to impair the protein function *in vitro*^{17,18}, which have however so far not been tested in cells. Using the thermal micro-irradiation approach, we observed that, compared to the positive control of wild-type HSP70-GFP, the mutation that impairs the HSP70's binding ability to client substrates (V438F) strongly abrogated the recruitment to micro-heated regions. This outcome was consistent with the expected mode of HSP70 recruitment to damage sites through recognition of the substrates, and it further attested to the suitability of our approach for addressing physiologically relevant questions. Also, the mutation affecting HSP70's ATPase activity (T204A), robustly impaired the recruitment of the respective mutant HSP70-GFPs

to the localized damaged proteins. Importantly, the subtle mutations (N540A, E543A) that impair the dimerization of HSP70 robustly inhibited the recruitment as well (Fig. 3a). These results reveal critical roles of the ATPase activity and dimerization, respectively, for proper recruitment of HSP70 to client substrates. Furthermore, these results further validate the applicability of our method for precision analyses of chaperone activity in the cellular context. These data also demonstrate that the observed recruitment to the lesion site does not reflect any potential unspecific method artefact but rather reflects HSP70's physiological ability to bind denatured proteins actively, in an acute manner, an on-demand dictated by the cellular context under heat-inflicted damage in live human cells.

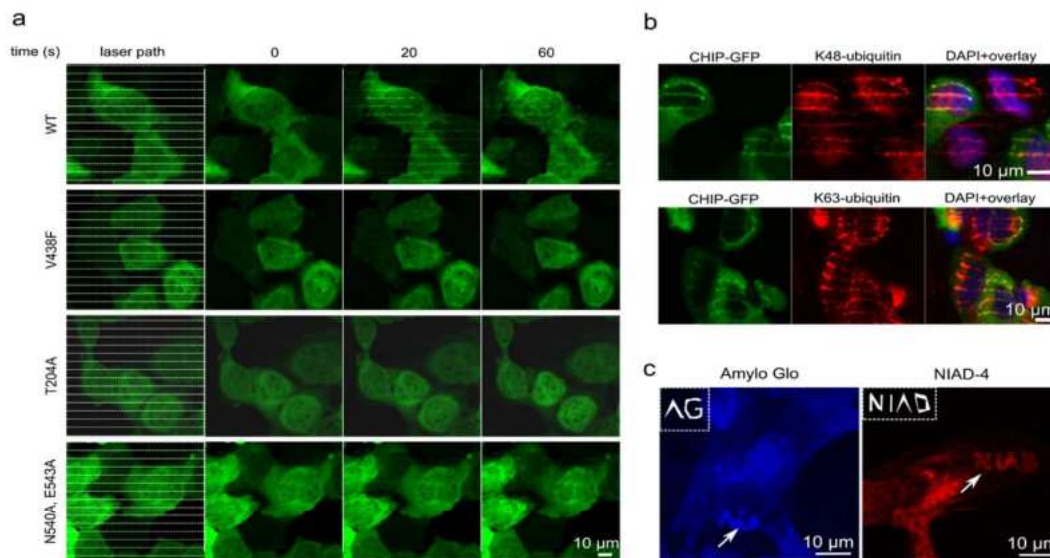


Fig. 3 Impaired recruitment of several HSP70 mutants and characterization of proteins damaged by micro-heating. **a** U-2-OS cells grown on a plasmon-modified ibidi plate expressing HSP70-GFP variants were micro-heated by laser stripes and followed in time, revealing impaired recruitment to micro-heated regions of the indicated HSP70 mutants, compared to wild-type (WT) HSP70 control. **b** U-2-OS CHIP-GFP cells were micro-heated in the form of colinear stripes, fixed and processed for immunofluorescence analysis of the accumulation of K48- and K63-ubiquitinated proteins. **c** Detection of amyloid aggregates by NIAD-4 and AmyloGlo dyes in U-2-OS cells in microheated regions. The defined laser path is shown in the upper left corner of each image. All panels show representative results from two experiments. Scale bars = 10 μ m.

Thermally damaged proteins are ubiquitinated and processed by p97 translocase. To provide further insights into the cellular response to micro-thermally damaged proteins and assess the method's compatibility with immunofluorescence, we next immunostained the exposed cells for ubiquitin. Using immunofluorescence, we observed a clear co-localization of the thermally damaged sites with signals from antibodies, specifically recognizing K48- and K63-ubiquitinated proteins (Fig. 3b). Such K48-linked ubiquitination of the damaged protein indicates ongoing processing by the UPS, while the K63-ubiquitin is mainly associated with pathway signaling or autophagy¹⁹, suggesting a potential involvement of additional mechanisms. Furthermore, we also tested specific fluorescent dyes recognizing unfolded or aggregated proteins. For example, NIAD-4 dye, commonly used as a detection reagent for β -sheet structures of AD-associated amyloid plaques, highlights the micro-heated proteins. Another dye accumulated within the thermally micro-irradiated regions is Amylo Glo (Fig. 3c), used for detecting amyloids. Thus, the amyloidogenesis of damaged proteins and the formation of β -sheets is induced within heated regions, consistent with previous publications reporting that heat stress triggers amyloid formation^{20,21}.

To elucidate the subsequent fate of the heat-damaged proteins, we considered their noticeable positional stability. It is well established that certain proteins dedicated to proteasomal degradation, which are part of insoluble cellular structures, require initial processing by p97 (VCP – Valosin Containing Protein, p97) as demonstrated for Endoplasmic reticulum-, chromatin-, or mitochondria-associated protein degradation²². Yet, any potential role of p97 in the processing of thermally

damaged proteins has remained unexplored. To investigate whether p97 is involved in handling heat-damaged proteins, we first analysed the recruitment of GFP-tagged p97 to thermally damaged sites. Indeed, we observed the accumulation of p97-GFP within the micro heated areas a few minutes after irradiation and the persistence there for around 20 min (Fig. 4a). We further validated this response for endogenous p97 in human cells using immunofluorescence, and confirmed co-localisation of p97 with accumulated GFP-ubiquitin (Fig. 4b). For a more in-depth mechanistic insight, we pretreated the cells with the UAE1 (Ubiquitin-activation enzyme 1) inhibitor (MLN7243), which is capable of blocking nearly all cellular ubiquitinations²³. Under the UAE1-inhibited conditions, we observed complete prevention of p97-GFP recruitment, indicating that ongoing ubiquitinations are required for the localisation of p97 within the heat-damaged sites (Fig. 4c). Interestingly, a specific inhibitor of ATPase activity of p97 (CB-5083)²⁴ also suppressed the recruitment of p97 to heat-damaged proteins (Fig. 4c), revealing that intact ATPase activity is required for proper accumulation of p97 within the heated subcellular regions.

To further study the active role of p97 in processing the heat-damaged proteins, we next studied a GFP-ubiquitin reporter cell line under p97 inhibition. In mock-treated cells, the GFP-ubiquitin was recruited to the micro heated regions within 5 min and persisted for up to 10 min. In contrast, cells pretreated with CB-5083 displayed stronger and longer-persisting GFP-ubiquitin signals within micro heated areas (at least for 20 min) (Fig. 4d). These data indicate direct and rate-limiting involvement of p97 in the proper processing kinetics of ubiquitinated proteins damaged by heat. We further confirmed these results under additional

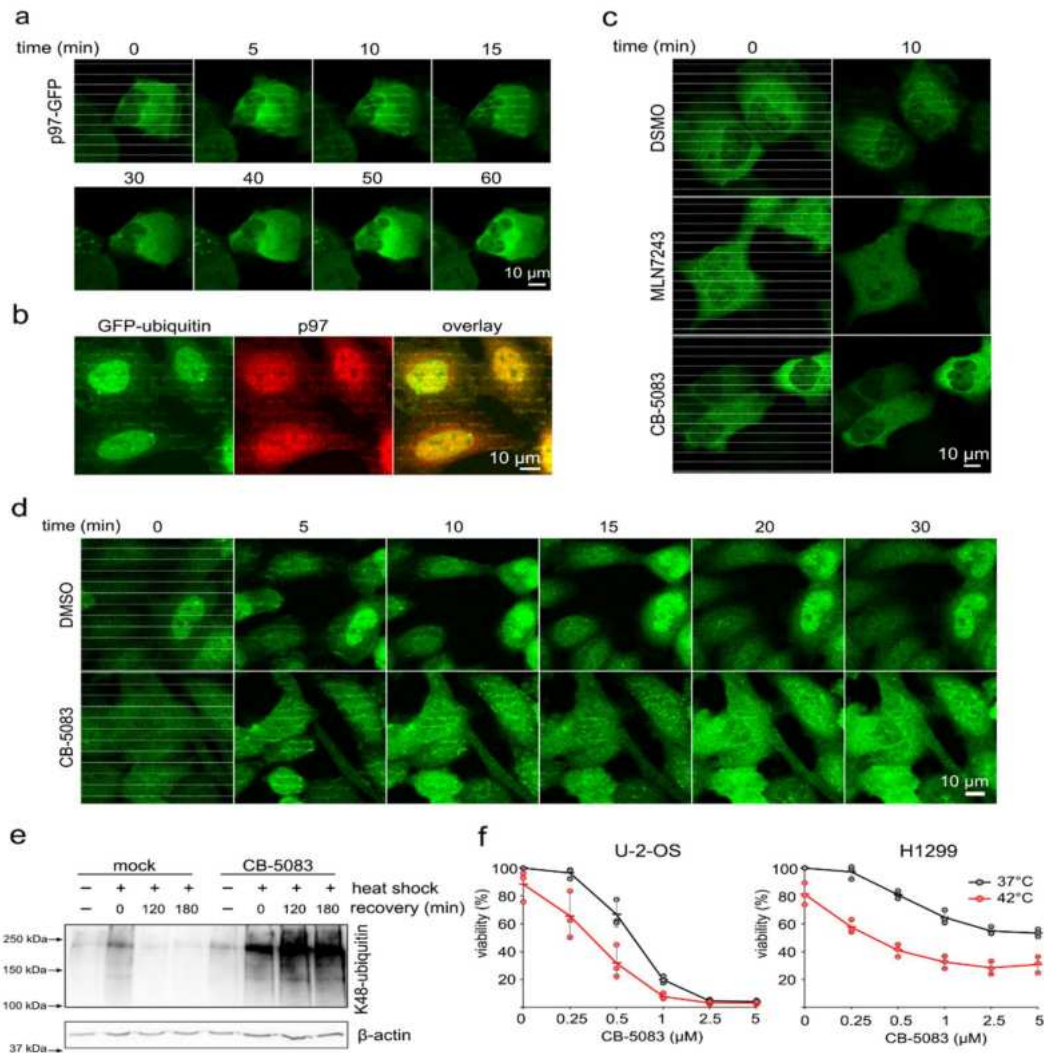


Fig. 4 p97 is recruited to thermally damaged proteins. **a** U-2-OS cells expressing p97-GFP grown on a plasmon-modified TPP plate were micro-heated by laser stripes and followed in time, revealing the kinetics of accumulation of p97-GFP in micro-heated regions. Representative results from three experiments. **b** U-2-OS cells expressing GFP-ubiquitin were micro-heated in the form of collinear stripes, fixed and processed for immunofluorescence analysis of the accumulation of endogenous p97 protein. Representative results from three experiments. **c** Pretreatment by UAE1 inhibitor MLN7243 (5 μ M for 30 min) or p97 inhibitor CB-5083 (5 μ M for 30 min) suppress recruitment of p97-GFP to micro-heated regions in the form of collinear stripes, which are visible only in mock-treated cells. Representative results from three experiments. **d** Inhibition of p97 by CB-5083 (5 μ M for 30 min) increased the accumulation and persistence of GFP-ubiquitin in micro-heated regions in the form of collinear stripes compared to the mock-treated control in U-2-OS cells stably expressing GFP-ubiquitin. Representative results from three experiments. **e** p97 inhibitor CB-5083 (5 μ M) increased the accumulation and persistence of K48-ubiquitinated proteins in insoluble cell fraction after heat shock (30 min at 43 $^{\circ}$ C). Cells were recovered at 37 $^{\circ}$ C for indicated times and cell pellets were analysed by WB. Representative results from two experiments. **f** Cell viability analysis after heat shock pulse (4 h at 42 $^{\circ}$ C) and recovery at 37 $^{\circ}$ C for 24 h (mean, SD from three independent experiments). Scale bars = 10 μ m. Source data are provided as a Source Data file for Fig. 4e, f.

settings, based on a standard experimental approach used for the heat shock induction. We treated cells with CB-5083 or mock and then exposed the whole cell population to a 43 °C heat-shock pulse using a pre-warmed water bath, after which the cells were allowed to recover at 37 °C for different periods of time. Western blot analysis of insoluble cell fractions confirmed the involvement of p97 translocase in the processing of heat-damaged proteins. Indeed, CB-5083-mediated inhibition of p97 caused a more robust and persisting accumulation of K48-ubiquitinated proteins, that otherwise dynamically disappeared in mock-treated cells during recovery at 37 °C (Fig. 4e). Moreover, using a similar experimental setup, we confirmed that the cytotoxic effect of a heat shock pulse was significantly enhanced in cells with inhibited p97 (Fig. 4f), indicating a contribution of p97 to better survival of cells exposed to thermal insults.

UPS compensates for the processing of thermally damaged proteins under HSP70 malfunction. Our data from the recruitment dynamics of various responsive factors suggest two temporally distinct, and potentially linked or cooperating mechanisms involved in processing thermally damaged proteins. The initial, more acute mechanism involves immediate action of cellular chaperones and co-chaperones, represented primarily by HSP70, involving also HSP90, CHIP and HOP. The second, delayed and more durable mechanism, involves UPS, characterized by massive poly-ubiquitination and recruitment of the p97 translocase. To gain more insight into any potential orchestration within this two-wave cellular heat stress response, we evaluated the effect of HSP70 impairment by the established chemical inhibitor of HSP70, VER155008^{21,25}. First, to validate the direct impact of VER155008 on HSP70 function in cells, we compared the HSP70 recruitment to damaged proteins in control and treated cells. VER155008 did not abrogate recruitment of HSP70 but rather resulted in prolonged HSP70 persistence at the heat damage sites, indicating inefficient chaperone-mediated processing of unfolded proteins, recognized, yet not further processed under HSP70 activity inhibitor treatment (Fig. 5a). To investigate the effect of HSP70 activity on the ubiquitination of damaged proteins, we then titrated damage intensity to the level at which the chaperones accomplished all the processing, i.e., without the apparent need for the subsequent involvement of p97. Under such settings, no GFP-ubiquitin signal was detectable. In contrast, under the same mild damaging conditions in cells with impaired HSP70 function (treated by VER155008), the accumulation of GFP-ubiquitin signal became detectable (Fig. 5b). Consistently, while under such mild conditions and proficient HSP70 response (mock treatment) p97-GFP did not recruit to sites of damage, in the VER155008-treated cells p97-GFP formed clearly visible stripes along the heat damaged subcellular areas (Fig. 5c). These results indicate that under a relatively mild heat damage conditions, the UPS pathway components including ubiquitin and p97, seem to provide a back-up compensatory role in case the primary chaperones (HSP70) are not fully operational. Furthermore, this two-wave mechanism becomes fully engaged, as a temporally coordinated cellular response, under conditions when the initial HSP-mediated pathway becomes overwhelmed by the severity of the damage.

Discussion

Our present study describes a highly versatile method suitable for induction and monitoring of cellular responses to conditions that lead to unfolded, aggregated proteins and β -sheet amyloids, aspects highly relevant for both basic and translational research on cellular protein quality control and its malfunction in a range of neurodegenerative disorders and cancer. First, we designed and

validated plasmonic silver NPs modification of various cell cultivation microscopic plates. Such products enable the researchers thermal micro-irradiation of small subcellular regions and concomitant monitoring of both the overall fate, and particularly the heat-triggered intracellular events in adherently growing cells using standard LSM. Notably, the laser equipment required to apply this method does not demand any uncommon or highly specialized setups with regard to the laser power. Also, the wavelengths needed for the plasmon layer activation do not have to be strictly 561 nm as used in this study, given that the plasmon layer's absorption peak covers more laser types used in the diverse LSM-type laboratory microscopes.

In addition to the method itself, we applied this approach to study behavior of selected protein chaperones in the physiological context of live cells in a spatiotemporally-controlled manner and at the level of unprecedented detail. Indeed, the information about the substrate recruitment kinetics in real time, and the effect of some of the functional mutants of one of the most studied protein chaperones - HSP70 (including the requirement for intact substrate recognition, ATPase and dimerization domains, respectively) are now revealed owing to the method described here. We also aimed at obtaining more insights into the characteristics, and particularly the further processing of the thermally damaged proteins. One of the important contributions of our study to the field are the results revealing the recruitment kinetics and variable residence time of the heat shock factors at the damage sites in a heat dose-dependent manner. Furthermore, apart from confirming that heat damage induces protein β -sheet amyloidogenesis in cells, we now report that the heat-damaged proteins are not only recognized by specific chaperones but can be further modified by poly-ubiquitylation and processed by the p97/VCP translocase pathway. The latter two-phase scenario is valid for more severe damage or conditions of chaperone insufficiency. Surprisingly, both types of the poly-Ub chains (K48- and K63-linked) are present at the same time within the heat-damaged subcellular sites, implying that a coordinated action of multiple E3 ubiquitin ligases is to be expected, likely linked to further processing by different protein-maintenance pathways, an intriguing concept that should inspire further work in this area, now amenable for experimentation thanks to the technique we report.

From the available literature on yeast and bacteria, it is known that in the processing of cellular protein aggregates, HSP70 cooperates with AAA+ (ATPase associated with diverse cellular activities) family members such as HSP104 disaggregase. However, such disaggregase is apparently lacking in metazoans²⁶. In this study using human cells, we discovered the involvement of the AAA+ translocase p97 in the processing of heat-damaged proteins. P97/VCP is an established component of the UPS machinery and generally protein quality control, promoting the degradation of ER-, mitochondria- or chromatin-associated proteins²². Despite mutations in the p97 gene are associated with various neurodegenerative diseases accompanied by accumulation of protein aggregates, the function of p97 in processing heat-damaged and aggregated proteins has not been studied²⁷. We show that p97 becomes recruited into the heat-damaged sites in the ubiquitin- and its own ATPase activity-dependent manner. The involvement of p97 becomes evident under more severe heat damage conditions, or in case the function of HSP70 is compromised (Fig. 6). After the p97 chemical blockade, we confirmed a substantial impact on the ubiquitin signal persistence within the heat-damage areas. Interestingly, the ubiquitin signal's disappearance was delayed, rather than completely blocked after p97 inhibition, suggesting that over time, spontaneous deubiquitylation of the damaged proteins or processing by alternative mechanisms such as autophagy or chaperone-mediated protein

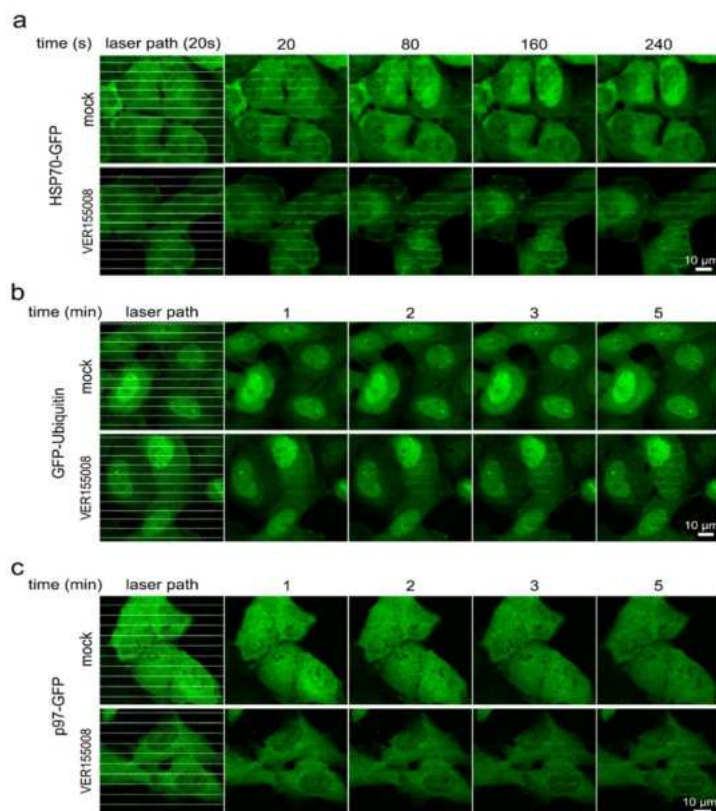


Fig. 5 The effect of HSP70 inhibition on recruitment of HSP70, ubiquitin and p97 translocase. **a** Pretreatment by HSP70 inhibitor (VER155008, 20 μ M for 30 min) increases the persistence of HSP70-GFP in micro-heated regions. **b** Inhibition of HSP70 by VER155008 (20 μ M for 30 min) promotes ubiquitination of heat-damaged proteins detected by GFP-ubiquitin reporter. **c** Inhibition of HSP70 by VER155008 (20 μ M for 30 min) increases the recruitment of p97-GFP to micro-heated regions. All panels show representative results from three experiments.

repair may further join this complex cellular response. Broadly analogous with multiple-pathway involvement associated with vital cellular responses to insults such as DNA damage or oxidative stress^{28,29}, our current results further attest to the biological significance of a multifaceted cellular response to thermal damage. This emerging concept is further supported by our result reported here, that experimental inhibition of the ubiquitin/p97 arm of the response exacerbates cytotoxicity of the otherwise well-tolerated degree of thermal damage.

Overall, we present a versatile methodology that may be broadly applicable in life sciences, including diverse screening strategies to search for chemical or cellular modulators of chaperone function, and generally in both basic/mechanistic and translational biomedical research. Application of this approach allowed us to provide insights into the molecular mechanisms of cellular responses to thermal damage in real time, including temporal orchestration of complementary stress-response pathways. Last but not least, our study raises multiple questions that should inspire further research dedicated to the processing of damaged cellular proteins, an essential aspect of cellular biology

with broad implications for neurodegenerative, prion-associated, and other life-threatening diseases.

Methods

Synthesis of plasmonic NPs. A step-by-step protocol describing the synthesis of plasmonic NPs can be found at Protocol Exchange³⁰. Water dispersion of anisotropic silver NPs (108 mg/L) was synthesized by two-step reduction process, involving partial reduction of the $[\text{Ag}(\text{NH}_3)_2]^+$ complex cation by sodium borohydride in the first step resulting in the formation of the silver nuclei, which were subsequently in the second step grown up by the reduction using weak reduction substance, e.g., hydrazine. All the reaction components were, at the laboratory temperature (23 °C), stirred continuously with a magnetic stirrer. Initially, 5 mL of aqueous silver nitrate (0.005 M), 1.25 mL of ammonia solution (0.1 M), 1.25 mL sodium citrate (1% w/w) and 13.425 mL distilled water were added into a 50 mL beaker and stirred while adding reducing agents. The reduction was initiated by the addition of 0.075 mL of sodium borohydride (0.001 M), which resulted in a reduction of silver complex cation, the formation of small NPs (seeds), and a change of the dispersion color to light yellow. Finally, 4 mL of hydrazine solution (0.05 M) was rapidly added into the dispersion of silver seeds under vigorous stirring, resulting in the growth of the seeds into final and stable silver anisotropic NPs followed by a change of the color of the dispersion from light yellow to typical purple. The final reaction concentrations of all the reaction components were as follows: silver nitrate 1×10^{-3} mol dm⁻³, ammonia 5×10^{-3} mol dm⁻³, citrate

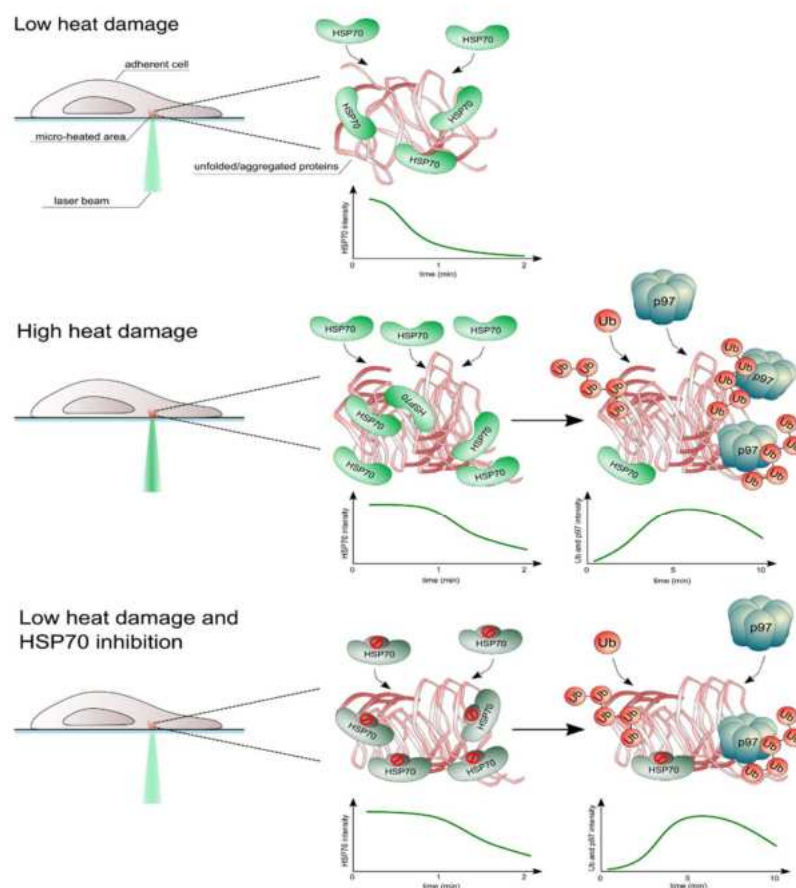


Fig. 6 Schematic representation of the cellular two-wave response to micro-heat damage. The intensity of micro-heat damage can be manipulated by laser power and defined regions enable detailed cellular response analysis. In case of low damage, the immediately recruited chaperones (such as HSP70, Heat shock protein 70) process the thermally damaged proteins within a minute and the activity of UPS is not needed. HSP70 persists for a longer time and ubiquitination (Ub) of damaged proteins is initiated in case of severe heat damage, followed by p97 recruitment and processing. In the case of HSP70 malfunction (inhibition), even low heat damage triggers ubiquitination and p97 recruitment as a compensatory response.

0.05% (w/w), sodium borohydride 3×10^{-6} mol dm^{-3} and hydrazine 8×10^{-3} mol dm^{-3} as a reducing agent. This way, prepared silver NPs were used for NP deposition on the cultivation surface. However, other plasmonic NPs with different shapes and optical properties (LSPR) can be prepared via the same method, but changing the ratio between citrate and hydrazine, using different amount of citrate varying from 0.25 to 4 ml (1% w/w) and adjusting the total volume to 25 ml. By this approach, the silver NPs with plasmon peak within the range of 440–725 nm can be synthesized. The prepared NPs have a negative surface charge ($\zeta = -38$ mV).

Deposition of silver NP on cell culture plates with plastic surfaces. A step-by-step protocol describing the deposition of silver NP can be found at Protocol Exchange³⁰. Silver NPs prepared by the above-mentioned method were subsequently coated onto the bottom of functionalized Ibidi 24-well plates (u-Plate, Ibidi, cat.n.: 82406), Greiner CELLSTAR® 96-well plates (Sigma, cat. n.: M0562) or TPP 24-well plates (TPP, cat. n.: 92424). The plates were first functionalized by 1% PAA (Sigma Aldrich) solution followed by 1% poly(diallyldimethylammonium chloride) (PDDA) (Sigma Aldrich) solution for 2 h each to coat them by thin polymeric film consisting of two layers of oppositely charged polyelectrolytes

(PAA and PDDA). After 4 h of the treatment, wells were washed with distilled water to remove non-bonded polymers and filled with the dispersion of silver NPs. Silver NPs were bonded within 45 min to thin polymeric PAA_PDDA film deposited on well surface through the electrostatic interactions between negatively charged silver NPs and positively charged PDDA forming the top layer of the thin polymeric film. In the end, wells were washed with distilled water to remove non-bonded NPs and air-dried.

Deposition of silver NP on cell culture plates with glass surface. A step-by-step protocol describing the deposition of silver NP can be found at Protocol Exchange³⁰. Due to the fact that the glass surface is already negatively charged, the modification with negatively charged PAA as described above for plastic bottoms was skipped. Instead, the glass surface (Cellvis glass-bottom plates, P24-1.5H-N) was cleaned and activated by the piranha solution ($\text{H}_2\text{SO}_4:\text{H}_2\text{O}_2$, 7:3) for 15 min, followed by washing with distilled water. After that, the plates were functionalized by 1% poly(diallyldimethylammonium chloride) (PDDA) (Sigma Aldrich) solution for 2 h to coat them by thin polymeric PDDA film. After the treatment, wells were washed with distilled water to remove non-bonded polymer and filled with the

dispersion of silver NPs. Silver NPs were bonded within 45 min to thin polymeric PDPA film deposited on well surface through the electrostatic interactions between negatively charged silver NPs and positively charged PDPA forming the top layer of the thin polymeric film. In the end, wells were washed with distilled water to remove unbonded NPs and air-dried.

Plasmids, cloning. All coding sequences were cloned by Gateway recombination technology (Invitrogen, Carlsbad, CA, USA). The full coding sequences of human Hsp70 (HSPA1A, UniProt ID: P0DMV8-1), CHIP (STUB1, UniProt ID: Q9UNE7-1) and HOP (STIIP1, UniProt ID: P31948-1) were cloned into PB-EF1a-N-EmGFP-PURO-GW-Dest vector containing an N-terminal GFP tag. Hsp70 point mutants were prepared by QuikChange Site-Directed Mutagenesis Kit (Agilent, Santa Clara, CA, USA) according to the manufacturer's manual. Following primers were used to create Hsp70 mutants: GACAACCAACCCGGGTTCTGATCCAGGTGTAC and GTACACCTGGATCAGGAACCCGGGTTGGTTGTC for V438F, TGGCGGGGGGGCCCTTCGACGTG and CACGTCGAAGGCGCCCGCCGCCA for T204A and GTGTGACCAAGCCGCGCTGGCGTCTACGCTTC and GAAGCGTAGGACGCCAGGCGGCGCTTGGCTGACAC for N540A, E543A.

Cell culture and transfection. Human osteosarcoma U-2-OS and human lung cancer H1299 cell lines (both from ATCC) were used for all studies. Cells were maintained in DMEM media (Lonza) supplemented with 10% fetal bovine serum (Thermo Fisher Scientific) and 1% penicillin/streptomycin (Sigma-Aldrich). The Piggy Bac transposon system (PB) has been used to generate a stable expression of GFP fused proteins. A total of 10^5 cells were transfected using Lipofectamine 3000 (Invitrogen, Carlsbad, CA, USA) with 1800 ng of transposon plasmid and 200 ng of transposase plasmid. Cells were selected in the same media supplemented with puromycin 5 μ g/ml (InvivoGen, San Diego, CA). Flow cytometry and cell sorting (FACS Aria-III, Becton Dickinson) was used to enrich cell populations with optimal GFP expression. U-2-OS expressing GFP-ubiquitin reporter and U-2-OS expressing p97-GFP were previously described³¹.

Cell viability. Cells were seeded on the original control multi-well plate (Greiner) or a plate modified by the plasmon NPs layer. Twenty-four hours after seeding, the cell viability was analyzed by XTT assay (Applchem) according to the manufacturer's instructions. XTT solution was added to the medium and incubated for 30–60 min, and then the dye intensity was measured at the 475 nm wavelength using a spectrometer (TECAN, Infinite M200PRO). To analyse the viability after heat shock, the cells were seeded on TPP 96-well plate. The next day, the cells were treated by CB-5083 or mock and placed in a water bath pre-heated to 42 °C for 4 h and then put back to cell culture incubator with standard conditions. Cell viability was analysed by XTT assay 24 h later.

Microscopy and microthermal damage induction. A step-by-step protocol describing the microthermal damage induction can be found at Protocol Exchange³⁰. For the visualization and delivery of the microthermal damage, we used a Zeiss Axioimager Z1 platform equipped with an LSM780 module for confocal laser scanning microscopy (CLSM). Used objectives included Zeiss objectives Alpha Plan-APOCHROMAT 40x water immersion for the lbiid plates and glass-bottom plates, and LD Plan-NEOFLUAR 40x/0.6 Korr for the TPP plates. CLSM setup included argon 488 nm and 355 nm lasers for visualization. For the plasmon layer activation, we used exclusively 561 nm 20 mW solid-state laser. The power range hitting the plasmon layer corresponded to 0.16–2.41 mW; exact values are stated in the main text (see also details of laser power measurements below). The laser irradiation times were defined by the pixel dwell time and the total irradiation time. For the FRAP-like experiments where irradiation ROI was pre-defined, the pixel dwell time was fixed at 100 μ s, and the whole irradiation time was dependent on the size of the ROI (–18–26 s for letter-like ROIs and 2 s for the square ROIs). For the stripping approach, the pixel dwell time was fixed at 709 μ s, and the total irradiation time was 0.85 s for one irradiation cycle resulting in 32 colinear stripes across the one microscopic field. See also ref.¹³ for details for setting up the laser stripping approach in LSM. All laser irradiations and acquisitions were performed using the Zeiss Zen 11 software.

Measurement of the laser power. PT-9610 optometer with PD-2D Laser Power Detector (Gigahertz-Optik) was used to obtain the values describing the laser power in watts hitting the plasmon layer. The optometer was set for 561 nm wavelength, and the detector was placed instead of the microscopic plate. Irradiation of the sensor was performed by 561 nm solid-state laser via the same objectives as used for the micro-irradiation process. The values were recorded at continuous laser mode at different laser power setups. Exact values for Alpha Plan-APOCHROMAT 40x water immersion objective were: 0.16 mW (7% laser power), 0.23 mW (10% laser power), 0.38 (15% laser power), 0.48 (20% laser power), 2.41 mW (100% laser power). The exact value for LD Plan-NEOFLUAR 40x/0.6 Korr objective was: 1.27 mW (100% laser power).

Quantitative ROI analysis. The analysis was performed by the Zeiss Zen 11 software employing an internal plugin for bleaching and FRAP (Fluorescence

recovery after photobleaching) analysis³¹. Control region (not exposed to the plasmon activating laser) was used for correction of baseline fluorescence and its potential change in time during acquisition and comparison with the microheated region (exposed to the plasmon activating laser). The data were exported to the Microsoft Excel 2016 and the increase of HSP70-GFP signal was calculated according to formula: increase of HSP70-GFP intensity = $(\text{mean}_{\text{Microheated region}(t=x)} / \text{mean}_{\text{Reference region}(t=x)}) / (\text{mean}_{\text{Microheated region}(t=0)} / \text{mean}_{\text{Reference region}(t=0)})$.

Immunofluorescence and dye staining. Cells were fixed 5 min after microthermal damage with 4% formaldehyde for 15 min at room temperature, washed with PBS, and permeabilized with 0.5% Triton X-100 in PBS for 5 min. After PBS washes, the cells on the plastic inserts were immunostained with primary antibody for 1 h at room temperature (anti-K48-ubiquitin, Apu2, Merck Millipore; anti-K63-ubiquitin, Apu3, Merck Millipore; anti-VCP, Abcam, ab11433), followed by PBS washes and staining with Alexa Fluor 568-conjugated secondary antibody for 60 min at room temperature. Nuclei were visualized by DAPI staining at room temperature for 2 min. For the beta-aggregates visualization, NIAD-4 (Sigma) dye was directly added to culture media (300 nM), and aggregates were detected in live cells after laser irradiation. AmyloGlo staining was performed according to the manufacturer's instruction (Biosensis). Briefly, cells were irradiated by the 561 nm laser, fixed with formaldehyde for 15 min at room temperature, washed with PBS, and permeabilized with 0.5% Triton X-100 in PBS for 5 min and washed. Next, the slide was incubated with 70% ethanol for 5 min, washed with distilled water, and stained with 1X AmyloGlo reagent for 15 min, followed by quick washes in 0.9% saline and distilled water.

Thermal camera imaging. The thermal camera (Therm-App®, Opgal Optronics Industries Ltd.) was placed in an in-house built holder keeping the camera at an ~5-cm distance from the top of the culture plate. The camera's germanium objective was manually focused on the bottom of a single well. The whole assembly was placed inside the Zeiss Axioimager Z1 platform equipped with LSM780 module for confocal laser scanning microscopy (CLSM) (see Supplementary Fig. 1h for the setup). The bottom of the well's inner surface was focused and exposed to the 561 nm laser working in the continuous mode while the thermal camera was used to acquire thermograms.

Western blotting. U2OS cells were seeded at 0.7×10^6 cells per 6 cm dish for 24 h before the experiment. P97 inhibitor- (CB-5083; 5 μ M; Selleckchem) or Mock-treated cells were exposed to 43 °C for 30 min in a water bath. Subsequently, dishes with cells were moved to an incubator with a standard set up of 37 °C and 5% CO₂. The cell lysates of pellet fraction were collected in time (0-, 2-, 3 h) by a quick wash with 0.5% Triton X-100 followed by resuspension in 1x Laemmli sample buffer. Equal amounts of cell lysates were separated by SDS-PAGE on hand casted gels and then transferred onto a nitrocellulose membrane. The membrane was blocked in Tris-buffered saline containing 5% milk and 0.1% Tween 20 for 1 h at room temperature, and then incubated overnight at 4 °C with the following primary antibodies: anti-ubiquitin lys48-specific (1:1000; Merck Millipore, clone Apu2), anti- β -actin (1:1000; Santa Cruz Biotechnology, sc-47778), followed by detection with secondary antibodies: goat anti-mouse IgG-HRP (GE Healthcare), goat anti-rabbit (GE Healthcare). Bound secondary antibodies were visualized by ELC detection reagent (Thermo Fisher Scientific) and images were recorded by an imaging system equipped with a CCD camera (ChemiDoc, Image Lab 6.1 software, Bio-Rad).

Characterization of plasmonic NPs. The synthesized water dispersion of silver anisotropic NPs and the deposited layer of silver anisotropic NPs were characterized by transmission electron microscopy (TEM) using a JEM 2010 TEM instrument (Jeol, Japan). In the case of water dispersion, a droplet of the sample with a silver concentration of 108 mol dm⁻³ was deposited on a carbon-coated copper grid and dried in a vacuum drier at 25 °C for 1 h. In the case of the silver NPs layer, carbon-coated copper grids were used and modified in the same way as cultivation plates. For this analysis, the carbon-coated copper grid was put in an Eppendorf tube and functionalized by PAA solution followed by poly(diallyldimethylammonium chloride) solution for 2 h each in order to coat them by the thin polymeric film. After 4 h of the treatment, carbon-coated grids were washed with distilled water in Eppendorf tube to remove non-bonded polymers and after that, Eppendorf tubes were filled with a dispersion of silver NPs. Silver NPs were bonded within 45 min to thin polymeric film deposited on carbon-coated copper grids and followed by washing with distilled water to remove un-bonded NPs and dried in a vacuum drier at 25 °C for 1 h. UV-vis spectra of silver NP dispersions were recorded on a Specord S 600 (Analytic Jena, Germany) spectrophotometer. Dispersions of silver anisotropic NPs were 10 times diluted prior to the measurements and layers of silver anisotropic NPs deposited on the cultivation plates were used as they were prepared. Zeta potential of silver NPs in water dispersion was obtained by electrophoretic mobility measurements using Zetasizer NanoZS (Malvern, UK).

Reporting summary. Further information on research design is available in the Nature Research Reporting Summary linked to this article.

Data availability

The data that support the findings of this study are available from the corresponding author upon reasonable request. Source data are provided with this paper.

Received: 26 August 2020; Accepted: 7 January 2021;

Published online: 29 January 2021

References

- Hartl, F. U. Protein misfolding diseases. *Annu. Rev. Biochem.* **86**, 21–26 (2017).
- Deshaies, R. J. Proteotoxic crisis, the ubiquitin-proteasome system, and cancer therapy. *BMC Biol.* **12**, 94 (2014).
- Guin, D., Gelman, H., Wang, Y. & Grubele, M. Heat shock-induced chaperoning by Hsp70 is enabled in-cell. *PLoS ONE* **14**, e0222990 (2019).
- Kim, Y. E., Hipp, M. S., Bracher, A., Hayer-Hartl, M. & Ulrich Hartl, F. Molecular chaperone functions in protein folding and proteostasis. *Annu. Rev. Biochem.* **82**, 323–355 (2013).
- Kim, M., Lee, J. & Nam, J. Plasmonic photothermal nanoparticles for biomedical applications. *Adv. Sci.* **6**, 1900471 (2019).
- Mayer, K. M. & Hafner, J. H. Localized surface plasmon resonance sensors. *Chem. Rev.* **111**, 3828–3857 (2011).
- Xue, C. & Mirkin, C. A. pH-switchable silver nanoprisms growth pathways. *Angew. Chem. - Int. Ed.* **46**, 2036–2038 (2007).
- Haes, A. J., Stuart, D. A., Nie, S. & Van Duyne, R. P. Using solution-phase nanoparticles, surface-confined nanoparticle arrays and single nanoparticles as biological sensing platforms. *J. Fluoresc.* **14**, 355–367 (2004).
- Jiang, K., Smith, D. A. & Pinchuk, A. Size-dependent photothermal conversion efficiencies of plasmonically heated gold nanoparticles. *J. Phys. Chem. C* **117**, 27073–27080 (2013).
- Plech, A., Kotaidis, V., Gréillon, S., Dahmen, C. & von Plessen, G. Laser-induced heating and melting of gold nanoparticles studied by time-resolved x-ray scattering. *Phys. Rev. B* **70**, 195423 (2004).
- Govorov, A. O. & Richardson, H. H. Generating heat with metal nanoparticles. *Nano Today* **2**, 30–38 (2007).
- Zhao, S., Zhang, K., An, J., Sun, Y. & Sun, C. Synthesis and layer-by-layer self-assembly of silver nanoparticles capped by mercaptosulfonic acid. *Mater. Lett.* **60**, 1215–1218 (2006).
- Mistrik, M. et al. Cells and stripes: a novel quantitative photo-manipulation technique. *Sci. Rep.* **6**, 19567 (2016).
- Lukas, C., Falck, J., Bartkova, J., Bartek, J. & Lukas, J. Distinct spatiotemporal dynamics of mammalian checkpoint regulators induced by DNA damage. *Nat. Cell Biol.* **5**, 255–260 (2003).
- Morgner, N. et al. Hsp70 forms antiparallel dimers stabilized by post-translational modifications to position clients for transfer to Hsp90. *Cell Rep.* **11**, 759–769 (2015).
- Mayer, M. P. & Gierasch, L. M. Recent advances in the structural and mechanistic aspects of Hsp70 molecular chaperones. *J. Biol. Chem.* **294**, 2085–2097 (2019).
- Trcka, F. et al. Human stress-inducible Hsp70 has a high propensity to form ATP-dependent antiparallel dimers that are differentially regulated by cochaperone binding. *Mol. Cell. Proteom.* **18**, 320–337 (2019).
- Vandova, V. et al. HSPA1A conformational mutants reveal a conserved structural unit in Hsp70 proteins. *Biochim. Biophys. Acta - Gen. Subj.* **1864**, 129458 (2020).
- Komander, D. & Rape, M. The ubiquitin code. *Annu. Rev. Biochem.* **81**, 203–229 (2012).
- Audas, T. E. et al. Adaptation to stressors by systemic protein amyloidogenesis. *Dev. Cell* **39**, 155–168 (2016).
- Frottin, F. et al. The nucleolus functions as a phase-separated protein quality control compartment. *Science* **365**, 342–347 (2019).
- Meyer, H., Bug, M. & Bremer, S. Emerging functions of the VCP/p97 AAA-ATPase in the ubiquitin system. *Nat. Cell Biol.* **14**, 117–123 (2012).
- Hyer, M. L. et al. A small-molecule inhibitor of the ubiquitin activating enzyme for cancer treatment. *Nat. Med.* **24**, 186–193 (2018).
- Anderson, D. J. et al. Targeting the AAA ATPase p97 as an approach to treat cancer through disruption of protein homeostasis. *Cancer Cell* **28**, 653–665 (2015).
- Schlecht, R. et al. Functional analysis of Hsp70 inhibitors. *PLoS ONE* **8**, e78443 (2013).
- Mogk, A., Bukau, B. & Kampinga, H. H. Cellular handling of protein aggregates by disaggregation machines. *Mol. Cell* **69**, 214–226 (2018).
- Tang, W. K. & Xia, D. Mutations in the human AAA+ chaperone p97 and related diseases. *Front. Mol. Biosci.* **3**, 79 (2016).
- Jackson, S. P. & Bartek, J. The DNA-damage response in human biology and disease. *Nature* **461**, 1071–1078 (2009).
- Sies, H., Berndt, C. & Jones, D. P. Oxidative Stress. *Annu. Rev. Biochem.* **86**, 715–748 (2017).
- Mistrik, M. et al. Protocol for subcellular targeted microthermal protein damage in cells cultivated on plasmonic nanosilver-modified surfaces. *Protoc. Exch.* <https://doi.org/10.21203/rs.3.pep-1314/v1> (2021).
- Skrott, Z. et al. Alcohol-abuse drug disulfiram targets cancer via p97 segregase adaptor NPLA. *Nature* **552**, 194–199 (2017).

Acknowledgements

The study was supported by MEYS CR (Large RI Project LM2018129 - Czech-BioImaging), ERDF (project No. CZ.02.1.01/0.0/0.0/16_013/0001775), EPOCH project (No. CZ.02.1.01/0.0/0.0/16_019/0000868), and project CZ.02.1.01/0.0/0.0/16_019/0000754, Grant agency of the Czech Republic: GACR 20-28685S, GACR 19-03796S and GACR 19-22720S, Technology Agency of the Czech Republic: TN01000013, Ministry of Health of the Czech Republic (MMCI, 00209805), Danish Cancer Society (R204-A12617-B153), Danish Council for Independent Research (DFF-7016-00313), Danish National Research Foundation (DNRF125 - project CARD), Swedish Research Council (VR-MH 2014-46602-117891-30), and Lundbeck Fonden (R266-2017-4289).

Author contributions

M.M., J.B. and Z.S. designed experiments, which were performed by M.M. and Z.S. A.P., L.H. and L.K. prepared and characterized plasmonic nanoparticle-modified surfaces. P.M. and V.V. prepared reporter cell lines. K.C. performed western blot analysis. T.B. performed cell viability tests. M.M., Z.S., P.M., A.P., and J.B. discussed and interpreted the results. M.M., Z.S., A.P., and J.B. wrote the manuscript, which was approved by all authors.

Competing interests

M.M., Z.S., L.H., A.P., L.K., and J.B. are inventors of the pending patent application (European Patent Office, application number EP20198904.3; patent applicants: Palacky University in Olomouc, Czech Republic). The patent application covers preparation of plasmon-modified cultivation surfaces and usage of thereof for induction of microthermal damage. The remaining authors declare no competing interests.

Additional information


Supplementary information The online version contains supplementary material available at <https://doi.org/10.1038/s41467-021-20989-9>.

Correspondence and requests for materials should be addressed to M.M. or J.B.

Peer review information *Nature Communications* thanks Anatoly Pinchuk and the other, anonymous, reviewer(s) for their contribution to the peer review of this work. Peer reviewer reports are available.

Reprints and permission information is available at <http://www.nature.com/reprints>

Publisher's note Springer Nature remains neutral with regard to jurisdictional claims in published maps and institutional affiliations.

 **Open Access** This article is licensed under a Creative Commons Attribution 4.0 International License, which permits use, sharing, adaptation, distribution and reproduction in any medium or format, as long as you give appropriate credit to the original author(s) and the source, provide a link to the Creative Commons license, and indicate if changes were made. The images or other third party material in this article are included in the article's Creative Commons license, unless indicated otherwise in a credit line to the material. If material is not included in the article's Creative Commons license and your intended use is not permitted by statutory regulation or exceeds the permitted use, you will need to obtain permission directly from the copyright holder. To view a copy of this license, visit <http://creativecommons.org/licenses/by/4.0/>.

© The Author(s) 2021

An efficient, non-invasive approach for *in-vivo* sampling of hair follicles: design and applications in monitoring DNA damage and aging

Natalie Kudlova^{1,*}, Hanus Slavik^{1,*}, Pavlina Duskova¹, Tomas Furst², Josef Srovnal¹, Jiri Bartek^{1,3,4}, Martin Mistrik¹, Marian Hajduch¹

¹Institute of Molecular and Translational Medicine, Faculty of Medicine and Dentistry, Palacky University and University Hospital Olomouc, Olomouc 779 00, Czech Republic

²Faculty of Science, Palacky University and University Hospital in Olomouc, Olomouc 779 00, Czech Republic

³Danish Cancer Society Research Center, Copenhagen DK-2100, Denmark

⁴Division of Genome Biology, Department of Medical Biochemistry and Biophysics, Science for Life Laboratory, Karolinska Institute, Stockholm 171 77, Sweden

*Equal contribution

Correspondence to: Martin Mistrik, Marian Hajduch; email: martin.mistrik@upol.cz, marian.hajduch@upol.cz

Keywords: hair follicle cells, non-invasive sampling, irradiation, cellular senescence, DNA damage response

Received: July 15, 2021

Accepted: November 22, 2021

Published: December 6, 2021

Copyright: © 2021 Kudlova et al. This is an open access article distributed under the terms of the [Creative Commons Attribution License](https://creativecommons.org/licenses/by/3.0/) (CC BY 3.0), which permits unrestricted use, distribution, and reproduction in any medium, provided the original author and source are credited.

ABSTRACT

In accordance with the 3 Rs principle (to replace, reduce and refine) animal models in biomedical research, we have developed and applied a new approach for sampling and analyzing hair follicles in various experimental settings. This involves use of a convenient device for non-invasive collection of hair follicles and processing methods that provide sufficient amounts of biological material to replace stressful and painful biopsies. Moreover, the main components of hair follicles are live cells of epithelial origin, which are highly relevant for most types of malignant tumors, so they provide opportunities for studying aging-related pathologies including cancer. Here, we report the successful use of the method to obtain mouse hair follicular cells for genotyping, quantitative PCR, and quantitative immunofluorescence. We present proof of concept data demonstrating its utility for routine genotyping and monitoring changes in quality and expression levels of selected proteins in mice after gamma irradiation and during natural or experimentally induced aging. We also performed pilot translation of animal experiments to human hair follicles irradiated *ex vivo*. Our results highlight the value of hair follicles as biological material for convenient *in vivo* sampling and processing in both translational research and routine applications, with a broad range of ethical and logistic advantages over currently used biopsy-based approaches.

INTRODUCTION

Hair follicles provide a very accessible source of biological material that can be non-invasively obtained from most mammals [1, 2]. Such material is particularly valuable for experiments with rodent models involving repeated sampling that currently require multiple invasive biopsies, which are relatively laborious and

stressful for the animals [3]. Replacement of blood or skin tissue collection would also be convenient for specific examinations in human medicine [4–6]. This micro-organ structure also has other advantages in biomarker studies, including suitability for investigations of circadian rhythms [5, 7], and the presence of numerous cell types in a small area, which can be easily distinguished, such as keratinocytes, melanocytes, or

perifollicular macrophages and mast cells [8–10]. However, the epithelial component of the follicles is the most promising for biomarker investigations because most neoplastic diseases have an epithelial origin.

Here, we present a proof of concept study involving use of a newly designed and constructed device allowing collection of large amounts of murine hairs with their hair roots containing follicular cells. We also demonstrate that DNA, RNA, and proteins in the collected hair follicle cells can be conveniently analyzed using standard cell and molecular biology methods such as genotyping, qPCR, and immunofluorescence analyses. The study focused on changes associated with the DNA damage response (DDR), especially double-strand breaks, and cellular senescence both in naturally aged tissue and induced using ionizing radiation (IR).

RESULTS

Design of the follicular cells' collector

The device we developed sucks hair from skin by vacuum suction. It uses removable disposable forceps of inert fixation-compatible material; forceps are made from a pair of modified pipette tips of different sizes (one inside the other). The bigger pipette tip is connected to a pistol-like device and covers the smaller tip connected to a piston. The smaller tip clicks into the bigger one by piston push, thereby firmly gripping the sucked hairs. The tip is removed from the pistol by a further push of the piston and stays attached to the skin via the squeezed hair. The forceps with gripped hairs are then manually removed. The removed hairs include follicles composed of multiple live follicular cells (Figure 1). Approximately 200 mice hairs can be

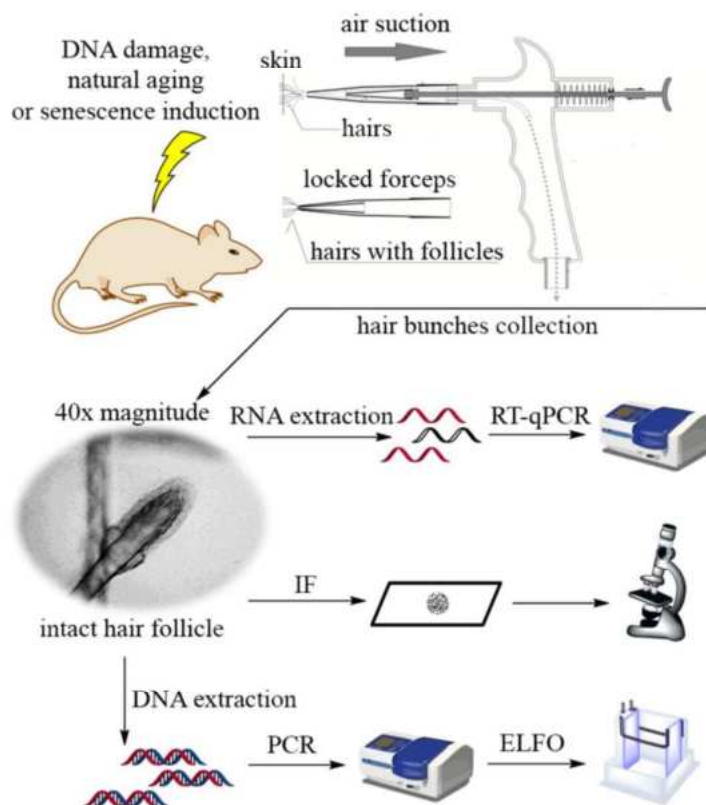


Figure 1. Design of the customized suction-based collector of hair follicle samples and scheme of the experimental workflow in the study.

removed in a single sample and each follicle contains approximately 50 cells. Inert and disposable forceps allow easy manipulation and immediate processing of the sample by fixation or lysis. The process is fast, easy, and does not involve touching the hair (Supplementary Video 1). Other advantages of the method include noninvasiveness, allowing many repetitive multi-site collections with minimal stress to the experimental animals.

Pre-processing of murine hairs

Hair follicles are morphologically intact and can be easily recognized during microscopic evaluation (Figure 2A). Collected hairs can be stored in a dry state or suitable medium, e.g. for nucleic acid extraction. We obtained median yields of 275 and 486 ng of total RNA and DNA per pluck of hairs obtained with our collection device according to analyses with a NanoDrop 1000 Spectrophotometer (Thermo Fisher Scientific). Moreover, the quality of RNA is usually high and suitable for further analyses with a RIN (RNA integrity number) of ca. 8 units according to analysis with an Agilent Bioanalyzer 2100. Thus, we consider DNA and RNA yields and qualities, presented in Figure 2B, sufficient for further experiments. There is no need for any special processing steps such as homogenization for isolating nucleic acids or cutting slices for microscopic analyses, and the material can be collected and processed repeatedly, within short times and in high amounts, from mice.

Genotyping of collected follicular cells fully replaces tail biopsies

Genotyping is one of the most common reasons for biopsy in research and commercial procedures involving genetically modified mice. Usually, a tip of the tail or an ear punch is collected from the examined mice to obtain DNA for analysis. To minimize pain and stress, the ethical standards of many countries require anesthesia before the collection, which complicates and prolongs the procedure. Here we show, that follicles collected by the specialized device described above can fully substitute tail tip biopsies. 5XFAD mice commonly used as a model for Alzheimer's and senescence-related diseases [11, 12], were used for proof of this concept. We compared the genotyping results from 151 tail biopsies and 151 hair samples from the offspring of 5XFAD transgenic males and C57Bl/6 females. For this, we assessed by PCR the presence or absence of two genes carried by the transgenic mice: *APP695* (*APP*, encoding an amyloid-beta [A4] mouse/human chimeric precursor protein) and *PSEN1* (*PST*, encoding human presenilin 1). Results obtained with DNA samples from hair bunches and tail biopsies were fully consistent (presence of both transgenes or absence of both, with no sample showing presence of only one of the transgenes). Thus, hair follicles could apparently fully replace tail biopsy for genotyping, with no loss of accuracy. Results of electrophoretic separation analysis demonstrating the transgenes' presence or absence are shown in Figure 3.

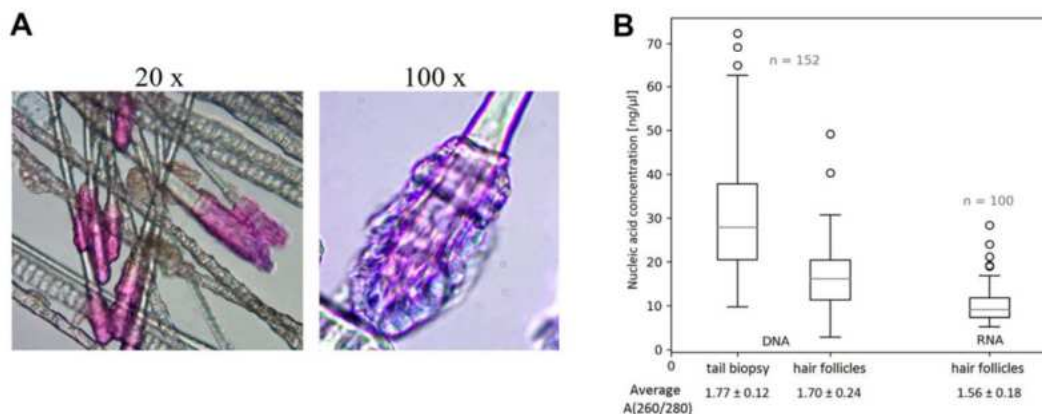


Figure 2. Murine hair follicles as starting material. (A) Representative images of hairs highlighted with Giemsa – Romanowsky staining (and indicated magnification) showing intact hair follicles obtained by sampling with our vacuum collector. (B) Comparison of DNA isolation results from hair follicles obtained with our device and common tail biopsies, and yields of RNA isolated from hair follicles. The quantity and quality of all nucleic acid samples, in 30 μl solutions, were measured using a ND 1000 Spectrophotometer. Data are presented as boxplots showing median, maximum and minimum values, their quartile distribution, interquartile range, and outlier values.

Downstream transcriptional DNA damage response in hair follicle cells after gamma irradiation *in-vivo*

Gamma irradiation, the most common mode of cancer treatment, causes complex responses in exposed cells called the DNA damage response (DDR). The DDR involves multiple transcriptional and posttranscriptional changes which are intensively investigated in cancer studies, and quantitative evaluation of DDR can be used for quick assessments of radiation exposure, radiotherapy monitoring, and identification of radiosensitive individuals [2, 13, 14]. Three commonly used markers (*p21*, *SESNI*, and *MDM2*) in the ATM/CHEK2/p53 pathway, which directly responds to DNA damage, were tested for acute radiation response by RT-qPCR. The

stability of their expression in the absence of IR was checked and *p21* showed the least variability between samples obtained on multiple occasions (significance of between-time differences: $p = 0.530$). In contrast, there were significant between-time differences in *SESNI* expression in irradiated samples and even in the absence of IR ($p = 0.025$). We also consider *SESNI* an inappropriate marker for monitoring hair follicles after IR because it has very low basal expression (late Ct values or negativity). However, there was significant upregulation of *SESNI* 30 minutes after IR and downregulation after 24 h, especially at the highest doses (Figure 4). In further contrast, *MDM2* showed a much more stable amplification pattern, but very weak dependence on IR. Thus, *p21* provided the most valuable

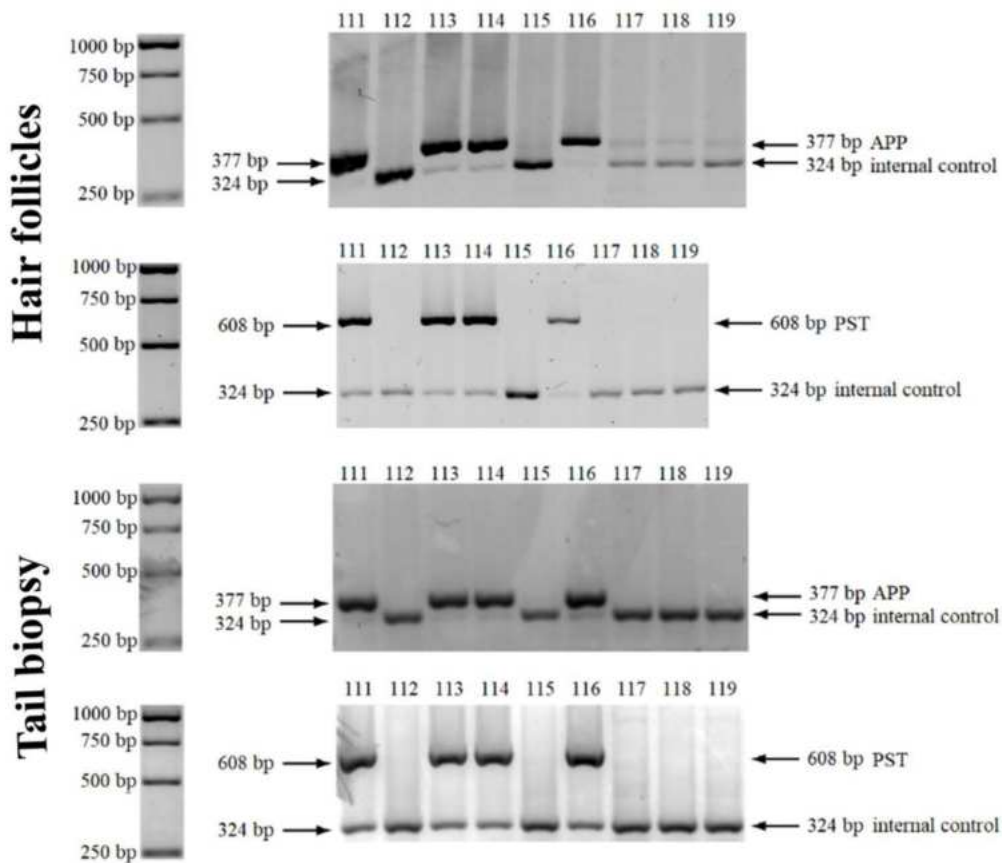


Figure 3. Genotyping using murine hair follicles. Results of PCR-agarose gel electrophoresis showing the presence or absence of *APP* and *PST* transgenes in representative samples (from mice 111 – 119), of both biological materials - hair follicles and tail biopsies. A 1 kb GeneRuler DNA ladder is presented on the left side.

amplification pattern, with the lowest variability and highest potential for distinguishing samples subjected to different IR doses and/or collected at different times. We observed a 2.5 median fold change (FC_m) 30 min after a 2 Gy dose, followed by a reduction to -1.54 after 24 h (Figure 4). A 6 Gy dose induced a longer response, with $FC_m = 1.81$ at 30 min after radiation, and no observed reduction until the 6 h time-point ($FC_m = 1.94$) and slight reduction to $FC_m = 1.24$ at the 24 h time point. The 10 Gy dose even induced an increase between the 30 min and 6 h time points ($FC_m = 2.25$ and 3.71, respectively). In summary, *p21* showed the most significant increase ($p < 0.01$) until 6 h after IR at all tested doses (Figure 4), with clear between-dose distinctions at some time points (with higher doses inducing higher FC_m values, except at the initial sampling point, 30 min after IR). In summary, our data provide some proof of concept by showing that our device and protocols can detect changes in expression patterns induced by external factors.

Immunofluorescence (IF) analysis of γ -H2AX lesions after gamma irradiation

In the previously mentioned ATM/CHEK2/p53 pathway and DDR, ATM kinase is directly recruited to DNA damage sites, where it phosphorylates histone H2AX on serine S139, forming γ -H2AX detectable as the immunofluorescent foci pattern in nuclei (Figure 5A - detail). We identified typical intense foci in the nuclei of irradiated hair follicles (Figure 5A). An IDD (intensity of DNA damage) value was calculated, as described in the methods section, for each hair follicle projection as averages from z-stack imaging (Figure 5B). Three to five morphologically intact follicles from each sample were scanned and analyzed. There were no statistically significant differences between measurements from either the same or different mice under defined conditions. Thus, we did not detect any inter-individual variability and there was no distinction between

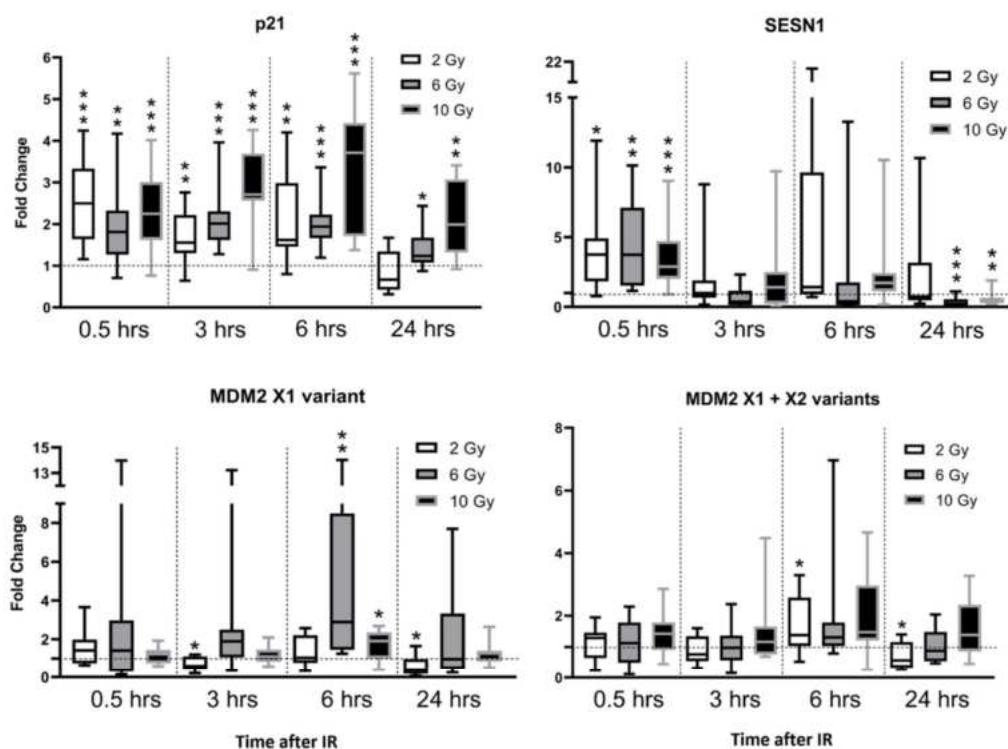


Figure 4. Gene expression changes (mRNA level) in murine hair follicles after *in vivo* ionizing irradiation. Data are expressed in boxplot graphs showing median, first quartile data distribution and maximum and minimum values of fold changes relative to expression at time zero (immediately before irradiation) normalized using *HPRT* mRNA levels. Results of paired t-tests of the significance of differences between indicated groups and times (relative to the zero-time point) are also depicted (* $p < 0.05$, ** $p < 0.01$, *** $p < 0.001$).

biological and technical replicates in further calculations. The low numbers of subjects in our experiments ($n = 5$ per condition) may have contributed to this, but they were sufficient for clear quantitative resolution of samples differing in radiation dose and/or time after IR. There was a strong increase in IDD shortly after irradiation, with a gradual reduction during the following 24 h. The IDD was also quantitatively dependent on dose, with clear separation between samples given 2 Gy from those given 6 and 10 Gy doses. Thus, the direct DDR after IR quantitatively differed between doses, but followed similar dynamic patterns under all three doses, in the murine hair follicles (Figure 5C). Not only recognizable foci were detected, but also areas with continuous green γ -H2AX signal, which we attributed to apoptotic lesions, based on previous reports [2] and their general occurrence in samples from mice given the 10 Gy treatment. The 10 Gy treatment also resulted in lower IDD values than the 6 Gy treatment, possibly due to cell damage exceeding thresholds allowing proper

quantification, although there was no significant difference between 6 Gy- and 10 Gy-treated samples at any time point. The other between-dose differences in samples collected 30 min, 3 h, and 6 h after IR were significant according to the Kruskal-Wallis non-parametric test with multiple comparisons.

Apart from gamma irradiation, we tested also the possibility to induce DDR after topical application of chemical clastogens. To address such an option, we dissolved DNA damaging agents bleomycin and cisplatin in DMSO and applied them directly to small areas of the skin of tested animals. Collected hair follicles from the exposed areas indeed showed increased γ -H2AX staining in the nuclei compared to the control areas (Supplementary Figure 3). These data confirm that the topical application of various chemical compounds and direct assessment of their effects in follicular cells *in-vivo* is possible which enriches the portfolio of applications of the method significantly.

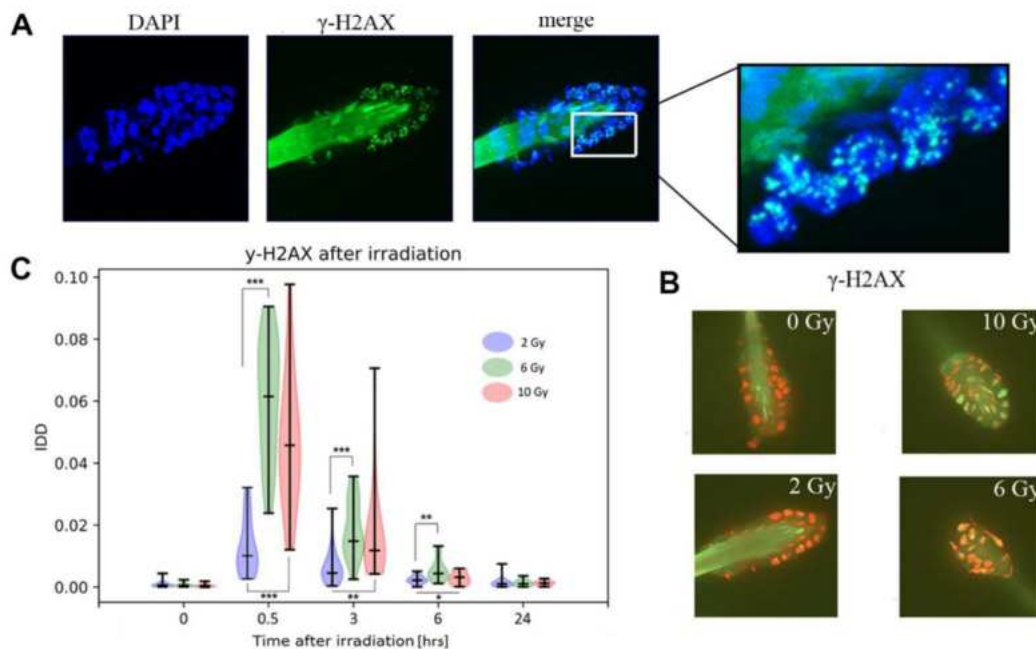


Figure 5. Immunofluorescent detection of γ -H2AX in murine hair follicles. (A) Representative images of a follicle after ionizing irradiation, extracted as maximum intensity projection from z-stack scanning by confocal spinning disc microscopy. Nuclei stained with DAPI and γ -H2AX foci and hair shaft autofluorescence are visible in the green channel. (B) Representative images used in the computational analyses of one z-stack layer, the red color of the nuclei (DNA) was selected artificially to maximize the visibility of green γ -H2AX foci. (C) Results of image analyses in terms of IDD (intensity of DNA damage), with each data point representing the area of the γ -H2AX signal related to the area of the nuclei in one scanned hair follicle in z-stack mode. Probability density of the data, maximal and minimal values, medians, and results of a multiple Kruskal-Wallis test (* $p < 0.05$, ** $p < 0.01$, *** $p < 0.001$) are showed in violin plots.

Expression patterns of selected markers in mice hair follicular cells reflect their biological age

Senescent cells are commonly identified by increases in senescence-associated β -galactosidase (SA- β -gal) activity [15–17], but assays of this activity have multiple limitations [18]. In contrast, *p16* and *p21* have known senescence-associated activities and functions [19–21], and their expression is highly elevated in a

wide variety of human and mouse senescent cell lines, so we used them as biomarkers for our age-related senescence measurements [22–24]. qPCR analyses of *p16* and *p21* expression levels using the acquired cDNA samples revealed significant differences in these two senescence biomarkers' expressions. *Inter alia*, there were strong differences in gene expression between young (6 months old, n=6) and old (2.5-3 years old, n=6) animals (Figure 6A) with $p < 0.05$, $p < 0.01$ or

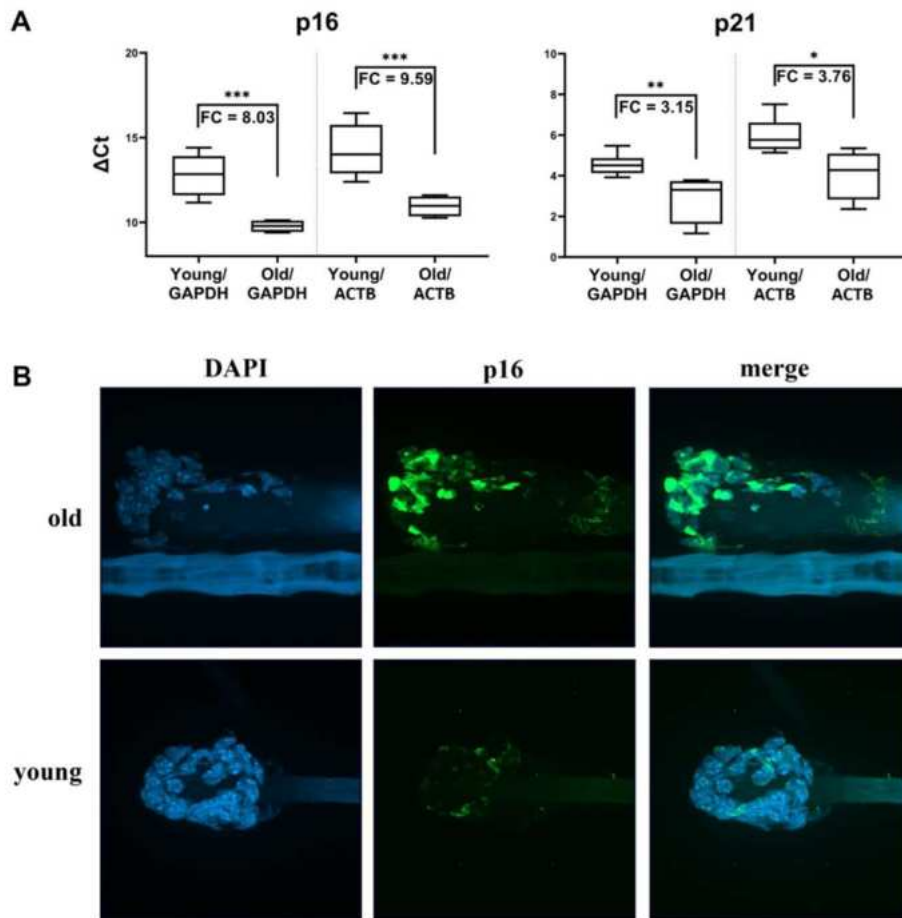


Figure 6. Markers of senescence analysis in hair follicular cells. (A) *p16* and *p21* gene expression (mRNA level) in hair follicles from young mice (6 months old) and old mice (2.5-3 years old) in boxplot graphs of Δ Ct values normalized using *GAPDH* or *ACTB*. Graphs show medians, first quartile data distribution, minimal and maximal points, and fold change values as a specifying detail. Results of a t-test are also shown (* $p < 0.05$, ** $p < 0.01$, *** $p < 0.001$). (B) Representative images showing the higher p16 protein levels in murine hair follicles of old animals relative to those of young animals. Images were obtained from z-stack scanning with a confocal spinning disc microscope. DAPI-stained nuclei are shown in the blue channel and p16 signals in the green channel. Autofluorescence can be seen in a hair shaft. Magnification 60x objective with oil immersion.

$p < 0.001$ depending on the housekeeping gene used for the data normalization and the target gene. Fold change differences in expression between the young and old animals of 8.03 and 9.58 ($p < 0.001$) were calculated for the *p16* marker, and 3.15 ($p < 0.01$) and 3.76 ($p < 0.05$) for *p21*. Naturally, no significant difference in expression of target senescence markers was detected using animals with the age difference of just a few months (data not shown). To support our qPCR data, we confirmed the changes in p16 expression at the protein level using immunofluorescence assays and the same mice cohort, which showed that cells from the older animals had higher levels of p16 protein (Figure 6B).

Radiation-induced senescence detection in murine hair follicles

The number of senescent cells in tissues can also be increased artificially by exposure to various DNA damaging factors. Gamma radiation is a very well-known inducer, and even mildly dosing of cells or animals can generate detectable senescence features [25, 26]. In addition, patients who have undergone anticancer chemo- and/or radiotherapy typically have higher numbers of senescent cells than non-treated counterparts of the same chronological age [27, 28]. We detected clear irradiation-dependent senescence induction in a mouse model, as irradiated soft tissue in the right hind leg acquired more senescent cells (according to expression levels of the *p16* and *p21* markers) than control tissue in the left hind leg. Hair follicles were collected at seven time-points (the first before IR) from the left and right hind legs of 10

mice. Significant elevation in expression of the selected *p16* and *p21* markers was observed in irradiated legs from 21 and 28 days after IR, respectively, relative to levels in samples collected directly before IR. Both markers remained constantly up-regulated until the last sampling time (35 days after IR), clearly indicating that senescence was induced in the irradiated tissue. The quantitative changes were not very strong, the highest observed FC_m was 2.26, for the *p16* marker 21 days after IR. However, the changes were significant ($p < 0.01$) at all of the last three sampling times for *p16* expression. The other marker, *p21*, showed weaker potential for discrimination between senescent and normal tissue in mice using hair follicle samples, with FC_m peaking at 1.25, 28 days after IR ($p = 0.05$). The expression of both markers remained unchanged in hair follicles of the control left legs during the experimental investigations (Figure 7). Those findings prompted the idea of using hair follicle cells as a murine irradiation-induced senescence model for studying senescence markers, aging experiments, and *in vivo* senolytic drug identification.

DISCUSSION

To meet ethical standards, experiments involving laboratory animals should be designed to obtain maximum information while minimizing stress, and ideally, they should be replaced wherever possible. Unfortunately, they cannot currently be replaced by alternative assays in numerous applications in basic and pre-clinical research. However, we present here a simple method for obtaining biological material in the

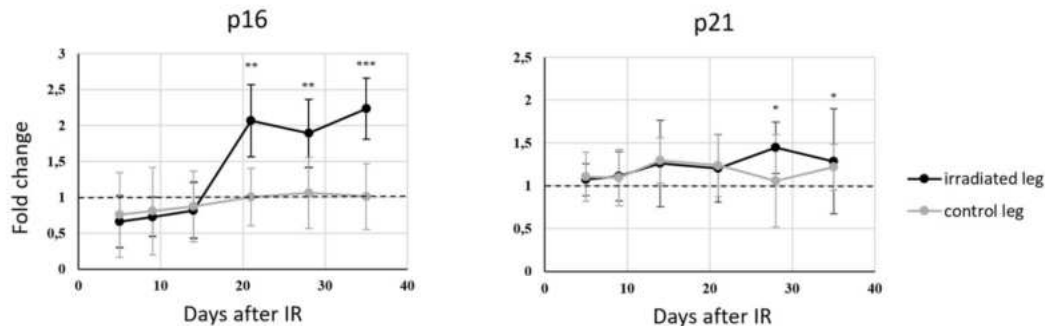


Figure 7. Changes with time in *p16* and *p21* gene expression (mRNA level) in murine hair follicles after a fractionated dose of 3 x 8 Gy applied *in vivo* to the right hind leg of a mouse, using each animal's left hind leg as a control. Data are expressed as fold changes relative to expression at the zero-time point (shortly before irradiation) normalized using *GAPDH* mRNA levels. Means and standard deviations are shown. ΔCt values from certain time points were compared using paired t-tests and relevant time points on curves are marked with asterisks (* $p < 0.05$, ** $p < 0.01$ and *** $p < 0.001$).

form of follicular cells from laboratory mice with sufficient quantities and quality for multiple analyses using standard modern molecular biology methods. The material has numerous advantages, including the convenience, non-invasiveness, and repeatability of the sample collection together with its contents of cells of epithelial origin and distal tissue, as well as the ease of exposing follicular tissue to test substances with topical applications (Supplementary Figure 3). The biggest limitations of follicular cell collection in the past were the complex logistics involved in processing the samples. Ordinary tweezers and forceps used in previous setups are extremely impractical with a high risk of cross-contamination, thus this material has been used in relatively few studies. We have circumvented these limitations by using our simple device, which enables a fast, convenient collection of follicular cells. The speed by which the samples can be collected and processed (e.g. by fixation) is among the biggest advantages of our solution as it can be performed within seconds. This fact limits any potential underlying cellular responses and additional DDR caused by confounding stressing factors related to the withdrawal process [2]. To corroborate the method's practical utility, we selected three applications. First, we proved that a sample of mouse hairs collected using disposable forceps in less than a minute (Supplementary Video 1) provides enough DNA for analysis by standard genotyping methods developed for tail tip biopsies or ear punches. As millions of laboratory mice are routinely genotyped globally every year this approach represents a major ethical and logistic breakthrough. Compared to such standard methods of biological biopsies (including phlebotomy) the amount of distress to the laboratory mice is relatively low caused mostly by the animal hand-grip as there is no visible pain reaction during the process of hair withdrawal (no twitching and/or squeaking). The absence of pain is supported also by the fact that the mice hair roots are, compared e.g. to humans, embedded relatively shallowly in upper skin layers [4, 10, 29] and very little strength is necessary for the withdrawal process.

Although hair samples have been previously used for that purpose [29–31], our sample collection approach may motivate researchers to use them more routinely and widely.

As we showed, mRNA can also be obtained from the collected samples in sufficient quantity and quality, so we designed another set of experiments in which we monitored changes in the expression of selected genes using qPCR. We targeted genes that respond to DNA damage caused by gamma irradiation and genes whose expression changes during oncogenesis. The DDR is intensively studied in carcinogenesis and cancer treatment research. IR markers often respond differently in different

biological materials, so there is no universally optimal marker that consistently provides quantitative responses, especially on the mRNA level. However, acute DDR has been detected accurately and dose-dependently by monitoring the dynamics of *p21* in previous studies [14, 32–34]. We dedicated *p21* as a suitable marker for gene expression measurements in hair follicles. It is also known that responses to IR differ and topically applied drugs can be more meaningfully evaluated using hair follicles than blood samples [2, 6]. Moreover, *p16* mRNA levels differ between samples of young and old human skin [35], which supports our use of its qPCR-based quantification to distinguish follicular cells of young and old mice. The marker has also been applied, for more than 10 years, in analyses of processes associated with senescence caused by G1 arrest, and thus oncogenesis [36], as well as for monitoring tissue degeneration (which can be regarded as premature tissue aging) caused by gamma irradiation or cytotoxic drugs [37]. Irradiation was used as the inducing factor in our artificially triggered senescence experiments, in which we applied fractionated doses of IR based on recent literature [38, 39], clinical experience together with our previous knowledge and optimization. We did not apply a single high IR dose as in previous studies [40] to avoid the formation of post-radiation skin lesions, which did not develop when using fractionated doses. Our approach opens new possibilities for research to find new drugs that can selectively eliminate senescent cells from organisms [41]. Thus, monitoring *p16* and *p21* mRNA levels by this method might replace laborious and less accurate methods, such as SA- β -gal assays in 'senolytics' research [42].

We also optimized the immunofluorescent (IF) approach for analyzing the collected follicular cells and thus monitoring selected proteins, including quantitative microscopy-based analysis of the DNA lesion marker γ -H2AX after gamma irradiation (Figure 5). For this, we developed software for routine evaluation of IDD by analysis of γ -H2AX foci in z-stack images of individual hair follicles and investigation of acute DDR after IR, which was made publicly available (<https://doi.org/10.6084/m9.figshare.14822643.v1>). The temporal dynamics we observed in our samples are consistent with previous results [2, 43] and generally, we proved that murine follicular cells can be used in IF assays of both nuclear and cytoplasmic proteins (Supplementary Figures 1, 2). It might be that the sensitivity of the method will be able to map functional differences between various GMO animals on the cellular level [4, 8]. For example, GMO mice harboring changes in genes involved in DDR could reveal differences in the DNA repair dynamics within the nuclei of follicular cells. Moreover, such tests could be also performed *ex-vivo*, because collected follicular cells are viable [5], without compromising genome

integrity [2], and can be kept alive for a significant time allowing various functional tests (Supplementary Figure 4). However, further research is needed to confirm such intriguing potential applications.

Last but not least, the method can be easily adapted for sampling other laboratory mammals, as hairs can be readily collected from rats, rabbits, dogs, monkeys, and even humans by the presented device (Supplementary Figure 4), opening a plethora of future research and biomedical applications.

MATERIALS AND METHODS

Ethics statement

All investigations were conducted following the ethical standards stated in the Declaration of Helsinki and other relevant national and international guidelines, with approval of the author's institutional review board.

Mouse hair collection

We collected each sample using an extraction device with modified pipette tips (described in patents EP2928382A1 and US 20150297253). We then placed the tips with the samples directly into 500 μ l portions of RNeasy (Qiagen, Hilden, Germany) for RT-qPCR analysis or 500 μ l of 10% neutral buffered formalin solution (Sigma-Aldrich, St. Louis, MO, USA) for immunofluorescence assays.

Human hair collection and *ex-vivo* irradiation

Hair follicles were collected from surface disinfected human calves and immediately put into the Dulbecco's modified Eagle's medium containing 4.5 g/l glucose (Biosera, Nuaille, France), supplemented with 10% fetal bovine serum (Gibco/Thermo Fisher Scientific, Grand Island, NY, USA) and 1% penicillin-streptomycin (Sigma-Aldrich). Samples were stored in the cell culture medium under normal cultivation conditions (5% CO₂, 37° C, 100% humidity) during the necessary incubation steps until the fixation for immunofluorescence assays. Human hair follicle samples were irradiated on Petri dishes with DMEM culture medium using X-ray RS225M Research Cabinet (Xstrahl, Suwanee, GA, USA) with a 2 Gy dose. Samples were fixed 30 min after irradiation and processed in the same way as described below in the „Immunofluorescence and image acquisition” chapter.

Irradiation

Thirty C57Bl/6 wild-type mice (Envigo, Huntingdon, UK) were used in the first part of the study, 10 mice for

each dose of ionizing radiation. An RS225M Research Cabinet (Xstrahl, Suwanee, GA, USA) was used to generate X-rays in all experiments. Each mouse was anesthetized with isoflurane (FORANE inhalation solution, Aescica, Hemel Hempstead, UK) before and during the application of the radiation. Only the right hind leg and adjacent parts of the body were irradiated, while the rest was covered by lead armor. Additionally, 10 mice Balb/cOlaHsd (Envigo, The Netherlands) were irradiated to induce senescence in muscle tissue with a fractionated dose of 3 x 8 Gy.

Topical application of chemical clastogens

HsdWin:NMRI mice (Envigo, Huntingdon, UK) females (3 animals per group) were treated with two clastogens (bleomycin or cis-platin) topically. Both compounds were dissolved in DMSO. We applied 16,6 μ l of bleomycin solution (5 μ g/ml) and 30 μ l of cis-platin solution (0,5 mg/ml). Each mouse was treated on the right body side by gentle rubbing of the compound into the skin. The treated spot had approximately 1,5 cm in diameter, each treated spot was marked. Bleomycin-treated animals were incubated in their homecages for 1 hour and animals treated with cisplatin were incubated for 5 hours. Then we collected hair samples (treated samples from the marked spot, control samples from the left body side). All samples underwent IF staining for γ -H2AX detection.

DNA isolation and genotyping

We genotyped the offspring (151 animals) of 5XFAD transgenic males (B6Cg-TgTg(APPswFLon, PSEN1*^{M146L}*^{L286V})6799Vas/Mmjax) obtained from The Jackson Laboratory and C57Bl/6 J01aHsd females from Envigo (Huntingdon, UK) as genetic background. Genomic DNA was isolated from both mouse hair follicles and mouse tail biopsies with a Cobas® DNA Sample Preparation Kit (Roche, Basel, Switzerland) according to the manufacturer's instructions. The presence of APP and PST transgenes was confirmed by optimized PCR, the reaction mixture contained 2 μ l of template sample, 2 μ l of 10 μ M APP or PST primer mix, 2 μ l of 10 μ M internal control primer mix, 5 μ l 5x GC buffer, 0.5 μ l 10 mM deoxyribonucleotide triphosphates (dNTPs), 0.75 μ l DMSO, 0.25 μ l Phusion® High-Fidelity DNA Polymerase and 12,5 μ l nuclease-free water (reagents from New England Biolabs, Ipswich, MA, USA). Primers are listed in Supplementary Table 1. Reactions were performed using the following program: 98° C for 30 s, followed by 30 amplification cycles of 98° C for 10 s, 63° C for 30 s, 72° C for 10 s, then 72° C for 5 min and cooling afterward. PCR products were visualized and checked using 1% agarose/TBE gels and an Odyssey Fc

electrophoresis system (LI-COR, Lincoln, NE, USA). The presence or absence of target genes was determined and animals were categorized as GMO-positive (with both transgenes present) or GMO-negative (lacking both genes). Each sample had to contain a band for internal control (bp).

RNA extraction and reverse transcription

Total RNA was extracted from hair stacks lysed in 700 μ l of QIAzol Lysis Reagent and processed immediately using a miRNeasy Mini Kit (Qiagen, Hilden, Germany) according to the manufacturer's recommended protocol, except the need to discard hair samples before solutions were transferred into columns. Finally, RNA from each sample was eluted into 30 μ l RNase-free water. RNA concentration and quality were assessed by a Nanodrop ND 1000 Spectrophotometer (ThermoScientific, Wilmington, DE, USA). To obtain cDNA, total RNA was used for reverse transcription using 18.9 μ l of each sample, mixed with 0.3 μ g of Random Primers (Promega, Madison, WI, USA) to a final volume of 19.5 μ l and incubated at 70° C for 5 min. Then, samples were cooled for 1 min. A solution containing 6 μ l of RevertAid 5x RT buffer (Fermentas, Vilnius, Lithuania), 3 μ l of 10 mM deoxyribonucleotide triphosphates (dNTPs), and 0.75 μ l of 40 U/ μ l RNasin ribonuclease inhibitor (Promega) was added to each sample. The mixed solutions were incubated for 5 min at room temperature. In the last step, 150 U (0.75 μ l) of RevertAid Moloney Murine Leukemia Virus reverse transcriptase (Fermentas) was added to each sample. The final 30 μ l mixtures were incubated at room temperature for 10 min, 42° C for 60 min, and 70° C for 10 min. The resulting samples of cDNA were stored at -20° C. RNA for the subsequent aging experiment was obtained from mouse hair follicles of the mouse strain used for genotyping.

Quantitative PCR (qPCR)

For quantification of *p21*, *SENS1*, *MDM2* expression, as studied markers, and expression of *HPRT* as a housekeeping gene for relative quantification in the radiation experiment, real-time PCR was performed using a LightCycler 480 instrument (Roche). SYBR Green intercalation chemistry was used to detect the fluorescence signal and supplied software was used for Ct data generation and Tm analyses. An 18 μ l volume solution of each sample was mixed with 12.43 μ l DEPC-treated water (Ambion, Austin, TX, USA), 2 μ l 10X Thermo-Start PCR Buffer, 1.6 μ l of 25 mM MgCl₂ and 0.2 μ l of 5 U/ μ l Thermo-Start Taq DNA Polymerase (Thermo Fisher Scientific, Waltham, MA, USA). A 0.61 μ l portion of SYBR® Green I nucleic acid gel stain (10 000 x in DMSO) diluted in 10 mM Tris-HCl buffer

pH 8 (Sigma-Aldrich) was added to each mixture, followed by 0.16 μ l of 25 mM dNTPs (Promega) and 1 μ l of a solution of specific primers for the selected marker and species. Specific oligonucleotides were custom synthesized by Generi Biotech (Hradec Králové, Czech Republic) and are presented in Supplementary Table 1. Reactions were performed in doublets using 2 μ l cDNA. Touch-down programs were chosen for murine samples with the following cycling parameters: 95° C for 10 min, then 95° C for 15 s and 67° C for 20 s with a target temperature of 62° C and 1° C steps for the first touchdown, and 95° C for 15 s and 60° C for 20 s with a target temperature of 58° C and 2° C steps for the second touchdown. Fluorescence signals were acquired during 50 cycles of 95° C for 15 s and 54° C (60° C for *MDM2*) for 45 s. For qPCR analyses of senescence marker (*p16* or *p21*) expression and housekeeping genes (*GAPDH* and *ACTB*), 2 μ l of cDNA of each sample was used within reaction mixtures further containing 10 μ l LightCycler 480 probes Master 2x conc. (Roche), 7 μ l LightCycler 480 Probes Master H₂O PCR grade (Roche) and 1 μ l FAM-MGB Taqman probe (ThermoFisher Scientific). Reactions were performed using the following program: 95° C for 10 min, followed by 50 amplification cycles of 95° C for 15 s and 60° C for 60 s.

Immunofluorescence and image acquisition

Murine hair follicles for IF assays were obtained from HsdWin:NMRI mice (Envigo, UK). All samples were fixed in 10% neutral buffered formalin (Sigma-Aldrich) for 20 min and permeabilized with 0.5% TritonX-100 (Carl Roth GmbH + Co. KG, Karlsruhe, Germany) in phosphate-buffered saline (PBS) for 10 min. After every step, samples were washed in PBS (2 x 2 min). Then they were blocked in PBS containing 1% bovine serum albumin (Sigma-Aldrich) for 20 min. The blocking solution was also used to dilute the antibodies. Samples were incubated in primary antibody solution overnight at 4° C. After washing with PBS, samples were incubated in secondary antibody solution for one hour. The primary and secondary antibodies are listed in Supplementary Tables 2, 3. Samples were washed in PBS and mounted using Vectashield antifade medium with DAPI (Vector Laboratories, Burlingame, CA, USA). Images of mouse hair follicles were obtained using an Axio Observer.Z1/Cell Observer Spinning Disc microscopic system (Zeiss, Oberkochen, Germany) with a 63x oil objective. All images were processed using ZEN Blue Image processing software (Zeiss).

Giemsa - Romanowsky staining

To investigate the mouse hair follicle cells' general morphology, we used classical Giemsa-Romanowsky

staining, as follows. Immediately after collecting samples of murine hairs in collection tips they were incubated in 4% methanol solution for 15 min, washed three times for 2 min in PBS, then soaked for 30 seconds in May - Grünwald solution (Penta, Prague, Czech Republic) and subsequently rinsed in distilled water for 2 min, gently dried and finally incubated in 10x diluted Giemsa-Romanowsky solution (Penta). The rest of the staining solution was discarded by washing the samples in distilled water for 2 min. Hair endings with follicles were cut and placed between a microscopic glass and coverslip in a water drop. Images were obtained at 20x or 100x magnification with a transmission light microscope (Zeiss, Primo Vert).

Data processing and statistical analyses

Matlab R2017a and Microsoft Excel were used for all data processing analyses and visualizations. Fold changes in gene expression were calculated from qPCR data using the $\Delta\Delta C_t$ method, with averages of raw technical measurements as the inputs. The Kruskal-Wallis test was used for irradiation-dependence verification of the results at zero doses. T-tests were used to investigate differences between irradiated and non-irradiated samples at each time point. T-tests were also used to generate p-values describing the significance of differences between old and young animals and between variables measured at the zero-time point and all other time points in both irradiated and control hind legs in the radiation-induced senescence experiment. In γ -H2AX analyses, green dots and areas were sought in z-stack images (in tiff format) of DAPI-stained tissues. Two median filters were used for automatic identification of the foci and suppression of background signals. The intensity of DNA damage (IDD) was calculated as shares of the signals and DAPI area, where one data point represents the average value from z-stack images from one hair follicle. The software with example 6 Gy data set is publically available on the Figshare platform at the following link: <https://doi.org/10.6084/m9.figshare.14822643.v1>. The Kruskal-Wallis test was used to test the null hypothesis that there was no treatment- or sample-related differences in technical measurements.

AUTHOR CONTRIBUTIONS

MH, MM, JB, and JS designed the experiments and interpreted data. qPCR experiments were performed by NK and HS. Microscopy experiments were performed by MM, HS, and NK. Animal handling, sample collection, and sample *ex-vivo* treatments were done by NK, HS, and PD. TF developed and programmed a method for quantitative analysis of microscopic images. MM, NK, HS, JB, and MH wrote the manuscript.

ACKNOWLEDGMENTS

We gratefully acknowledge expert assistance in sample collection by Katerina Frantikova and Tereza Schneiderova and partial assistance in sample preparation for RT-qPCR set-up by Petra Svarcova and Tereza Lausova during their internship at our institute.

CONFLICTS OF INTEREST

MM, JB, MH are co-inventors on patents EP2928382A1 and US 20150297253, utilizing the method for extraction of follicular cells and device for the pursuance of this method. All authors declare they have no conflicts of interest.

FUNDING

The study was supported by MEYS CR: (Large RI Project LM2018129 – Czech-BioImaging), ERDF (project No. CZ.02.1.01/0.0/0.0/16_013/0001775), ENOCH project (No. CZ.02.1.01/0.0/0.0/16_019/0000868), and Czech national node of the European infrastructure for translational medicine (LM2018133), Technological Agency of the Czech Republic (TN01000013), Grant of the Czech Ministry of Interior (VG20102014001), The Novo Nordisk Foundation (16854 and 0060590), The Swedish Research Council VR-MH 2014-46602-117891-30, The Swedish Cancer Foundation/Cancerfonden (# 170176) and The Danish National Research Foundation (project CARD, DNRF 125).

REFERENCES

1. Green MR, Clay CS, Gibson WT, Hughes TC, Smith CG, Westgate GE, White M, Kealey T. Rapid isolation in large numbers of intact, viable, individual hair follicles from skin: biochemical and ultrastructural characterization. *J Invest Dermatol.* 1986; 87:768–70. <https://doi.org/10.1111/1523-1747.ep12457348> PMID:3782859
2. Redon CE, Nakamura AJ, Goulliaeva K, Rahman A, Blakely WF, Bonner WM. The use of gamma-H2AX as a biodosimeter for total-body radiation exposure in non-human primates. *PLoS One.* 2010; 5:e15544. <https://doi.org/10.1371/journal.pone.0015544> PMID:21124906
3. Bhogal N, Kaspler P, Jalali F, Hyrien O, Chen R, Hill RP, Bristow RG. Late residual gamma-H2AX foci in murine skin are dose responsive and predict radiosensitivity *in vivo*. *Radiat Res.* 2010; 173:1–9. <https://doi.org/10.1667/RR1851.1> PMID:20041754

4. Wang GY, Wang J, Mancianti ML, Epstein EH Jr. Basal cell carcinomas arise from hair follicle stem cells in Ptc1(+/-) mice. *Cancer Cell*. 2011; 19:114–24.
<https://doi.org/10.1016/j.ccr.2010.11.007>
PMID:21215705
5. Yamaguchi A, Matsumura R, Matsuzaki T, Nakamura W, Node K, Akashi M. A simple method using *ex vivo* culture of hair follicle tissue to investigate intrinsic circadian characteristics in humans. *Sci Rep*. 2017; 7:6824.
<https://doi.org/10.1038/s41598-017-07268-8>
PMID:28755004
6. Randall KJ, Foster JR. The demonstration of immunohistochemical biomarkers in methyl methacrylate-embedded plucked human hair follicles. *Toxicol Pathol*. 2007; 35:952–57.
<https://doi.org/10.1080/01926230701748198>
PMID:18098041
7. Watts LM, Browne JA, Murphy BA. Investigation of a non-invasive method of assessing the equine circadian clock using hair follicle cells. *J Circadian Rhythms*. 2012; 10:7.
<https://doi.org/10.1186/1740-3391-10-7>
PMID:23039139
8. Chou WC, Takeo M, Rabbani P, Hu H, Lee W, Chung YR, Carucci J, Overbeek P, Ito M. Direct migration of follicular melanocyte stem cells to the epidermis after wounding or UVB irradiation is dependent on Mc1r signaling. *Nat Med*. 2013; 19:924–29.
<https://doi.org/10.1038/nm.3194> PMID:23749232
9. Aoki H, Hara A, Motohashi T, Kunisada T. Keratinocyte stem cells but not melanocyte stem cells are the primary target for radiation-induced hair graying. *J Invest Dermatol*. 2013; 133:2143–51.
<https://doi.org/10.1038/jid.2013.155> PMID:23549419
10. Paus R, Cotsarelis G. The biology of hair follicles. *N Engl J Med*. 1999; 341:491–97.
<https://doi.org/10.1056/NEJM199908123410706>
PMID:10441606
11. Griñán-Ferré C, Sarroca S, Ivanova A, Puigoriol-Illamola D, Aguado F, Camins A, Sanfeliu C, Pallàs M. Epigenetic mechanisms underlying cognitive impairment and Alzheimer disease hallmarks in 5XFAD mice. *Aging (Albany NY)*. 2016; 8:664–84.
<https://doi.org/10.18632/aging.100906>
PMID:27013617
12. Kritsilis M, V Rizou S, Koutsoudaki PN, Evangelou K, Gorgoulis VG, Papadopoulos D. Ageing, Cellular Senescence and Neurodegenerative Disease. *Int J Mol Sci*. 2018; 19:2937.
<https://doi.org/10.3390/ijms19102937>
PMID:30261683
13. Mayer C, Popanda O, Greve B, Fritz E, Illig T, Eckardt-Schupp F, Gomolka M, Benner A, Schmezer P. A radiation-induced gene expression signature as a tool to predict acute radiotherapy-induced adverse side effects. *Cancer Lett*. 2011; 302:20–28.
<https://doi.org/10.1016/j.canlet.2010.12.006>
PMID:21236564
14. Kabacik S, Ortega-Molina A, Efeyan A, Finnson P, Bouffler S, Serrano M, Badie C. A minimally invasive assay for individual assessment of the ATM/CHEK2/p53 pathway activity. *Cell Cycle*. 2011; 10:1152–61.
<https://doi.org/10.4161/cc.10.7.15231>
PMID:21389785
15. Gire V, Roux P, Wynford-Thomas D, Brondello JM, Dulic V. DNA damage checkpoint kinase Chk2 triggers replicative senescence. *EMBO J*. 2004; 23:2554–63.
<https://doi.org/10.1038/sj.emboj.7600259>
PMID:15192702
16. Campisi J. Cancer, aging and cellular senescence. *In Vivo*. 2000; 14:183–88.
PMID:10757076
17. Itahana K, Dimri G, Campisi J. Regulation of cellular senescence by p53. *Eur J Biochem*. 2001; 268:2784–91.
<https://doi.org/10.1046/j.1432-1327.2001.02228.x>
PMID:11358493
18. Evangelou K, Lougiakis N, Rizou SV, Kotsinas A, Kletsas D, Muñoz-Espín D, Kastrinakis NG, Pouli N, Marakos P, Townsend P, Serrano M, Bartek J, Gorgoulis VG. Robust, universal biomarker assay to detect senescent cells in biological specimens. *Aging Cell*. 2017; 16:192–97.
<https://doi.org/10.1111/acer.12545> PMID:28165661
19. Collado M, Serrano M. Senescence in tumours: evidence from mice and humans. *Nat Rev Cancer*. 2010; 10:51–57.
<https://doi.org/10.1038/nrc2772> PMID:20029423
20. Brown JP, Wei W, Sedivy JM. Bypass of senescence after disruption of p21CIP1/WAF1 gene in normal diploid human fibroblasts. *Science*. 1997; 277:831–34.
<https://doi.org/10.1126/science.277.5327.831>
PMID:9242615
21. Hall BM, Balan V, Gleiberman AS, Strom E, Krasnov P, Virtuoso LP, Rydkina E, Vujcic S, Balan K, Gitlin I, Leonova K, Polinsky A, Chernova OB, Gudkov AV. Aging of mice is associated with p16(Ink4a)- and β -galactosidase-positive macrophage accumulation that can be induced in young mice by senescent cells. *Aging (Albany NY)*. 2016; 8:1294–315.
<https://doi.org/10.18632/aging.100991>
PMID:27391570
22. Liu JY, Souroullas GP, Diekman BO, Krishnamurthy J, Hall BM, Sorrentino JA, Parker JS, Sessions GA,

- Gudkov AV, Sharpless NE. Cells exhibiting strong *p16^{INK4a}* promoter activation *in vivo* display features of senescence. *Proc Natl Acad Sci USA*. 2019; 116:2603–11.
<https://doi.org/10.1073/pnas.1818313116>
 PMID:30683717
23. Sherr CJ, DePinho RA. Cellular senescence: mitotic clock or culture shock? *Cell*. 2000; 102:407–10.
[https://doi.org/10.1016/S0092-8674\(00\)00046-5](https://doi.org/10.1016/S0092-8674(00)00046-5)
 PMID:10966103
24. Wright WE, Shay JW. Telomere dynamics in cancer progression and prevention: fundamental differences in human and mouse telomere biology. *Nat Med*. 2000; 6:849–51.
<https://doi.org/10.1038/78592> PMID:10932210
25. Rodier F, Coppé JP, Patil CK, Hoeijmakers WA, Muñoz DP, Raza SR, Freund A, Campeau E, Davalos AR, Campisi J. Persistent DNA damage signalling triggers senescence-associated inflammatory cytokine secretion. *Nat Cell Biol*. 2009; 11:973–79.
<https://doi.org/10.1038/ncb1909> PMID:19597488
26. Tsai KK, Stuart J, Chuang YY, Little JB, Yuan ZM. Low-dose radiation-induced senescent stromal fibroblasts render nearby breast cancer cells radioresistant. *Radiat Res*. 2009; 172:306–13.
<https://doi.org/10.1667/RR1764.1>
 PMID:19708779
27. Guillon J, Petit C, Moreau M, Toutain B, Henry C, Roché H, Bonichon-Lamichhane N, Salmon JP, Lemonnier J, Campone M, Verrière V, Lelièvre E, Guette C, Coqueret O. Regulation of senescence escape by TSP1 and CD47 following chemotherapy treatment. *Cell Death Dis*. 2019; 10:199.
<https://doi.org/10.1038/s41419-019-1406-7>
 PMID:30814491
28. Li M, You L, Xue J, Lu Y. Ionizing Radiation-Induced Cellular Senescence in Normal, Non-transformed Cells and the Involved DNA Damage Response: A Mini Review. *Front Pharmacol*. 2018; 9:522.
<https://doi.org/10.3389/fphar.2018.00522>
 PMID:29872395
29. Schmitteckert EM, Prokop CM, Hedrich HJ. DNA detection in hair of transgenic mice—a simple technique minimizing the distress on the animals. *Lab Anim*. 1999; 33:385–89.
<https://doi.org/10.1258/002367799780487922>
 PMID:10778788
30. Meldgaard M, Bollen PJ, Finsen B. Non-invasive method for sampling and extraction of mouse DNA for PCR. *Lab Anim*. 2004; 38:413–17.
<https://doi.org/10.1258/0023677041958981>
 PMID:15479556
31. Picazo M, García-olmo D. DNA from tissues of young mice is optimal for genotyping. *Electronic Journal of Biotechnology*. 2015; 18:83–87.
<https://www.sciencedirect.com/science/article/pii/S071734581400147X>
<https://doi.org/10.1016/j.ejbt.2014.12.002>
32. Paul S, Amundson SA. Development of gene expression signatures for practical radiation biodosimetry. *Int J Radiat Oncol Biol Phys*. 2008; 71:1236–44.
<https://doi.org/10.1016/j.ijrobp.2008.03.043>
 PMID:18572087
33. Kabacik S, Manning G, Raffy C, Bouffler S, Badie C. Time, dose and ataxia telangiectasia mutated (ATM) status dependency of coding and noncoding RNA expression after ionizing radiation exposure. *Radiat Res*. 2015; 183:325–37.
<https://doi.org/10.1667/RR13876.1> PMID:25738893
34. Albrecht H, Durbin-Johnson B, Yunis R, Kalanetra KM, Wu S, Chen R, Stevenson TR, Rocke DM. Transcriptional response of *ex vivo* human skin to ionizing radiation: comparison between low- and high-dose effects. *Radiat Res*. 2012; 177:69–83.
<https://doi.org/10.1667/rr2524.1> PMID:22029842
35. Ressler S, Bartkova J, Niederegger H, Bartek J, Scharffetter-Kochanek K, Jansen-Dürr P, Wlaschek M. p16^{INK4A} is a robust *in vivo* biomarker of cellular aging in human skin. *Aging Cell*. 2006; 5:379–89.
<https://doi.org/10.1111/j.1474-9726.2006.00231.x>
 PMID:16911562
36. Lukas J, Sørensen CS, Lukas C, Santoni-Rugiu E, Bartek J. p16^{INK4a}, but not constitutively active pRb, can impose a sustained G1 arrest: molecular mechanisms and implications for oncogenesis. *Oncogene*. 1999; 18:3930–35.
<https://doi.org/10.1038/sj.onc.1202777>
 PMID:10435615
37. Nasto LA, Wang D, Robinson AR, Clauson CL, Ngo K, Dong Q, Roughley P, Epperly M, Huq SM, Pola E, Sowa G, Robbins PD, Kang J, et al. Genotoxic stress accelerates age-associated degenerative changes in intervertebral discs. *Mech Ageing Dev*. 2013; 134:35–42.
<https://doi.org/10.1016/j.mad.2012.11.002>
 PMID:23262094
38. Seol MA, Jung U, Eom HS, Kim SH, Park HR, Jo SK. Prolonged expression of senescence markers in mice exposed to gamma-irradiation. *J Vet Sci*. 2012; 13:331–38.
<https://doi.org/10.4142/jvs.2012.13.4.331>
 PMID:23271173
39. Kim BC, Yoo HJ, Lee HC, Kang KA, Jung SH, Lee HJ, Lee M, Park S, Ji YH, Lee YS, Ko YG, Lee JS. Evaluation of

- premature senescence and senescence biomarkers in carcinoma cells and xenograft mice exposed to single or fractionated irradiation. *Oncol Rep.* 2014; 31:2229–35.
<https://doi.org/10.3892/or.2014.3069> PMID:24626611
40. Peng X, Wu Y, Brouwer U, van Vliet T, Wang B, Demaria M, Barazzuol L, Coppes RP. Cellular senescence contributes to radiation-induced hyposalivation by affecting the stem/progenitor cell niche. *Cell Death Dis.* 2020; 11:854.
<https://doi.org/10.1038/s41419-020-03074-9>
PMID:33056980
41. Lee S, Schmitt CA. The dynamic nature of senescence in cancer. *Nat Cell Biol.* 2019; 21:94–101.
<https://doi.org/10.1038/s41556-018-0249-2>
PMID:30602768
42. Capparelli C, Chiavarina B, Whitaker-Menezes D, Pestell TG, Pestell RG, Hulit J, Andò S, Howell A, Martinez-Outschoorn UE, Sotgia F, Lisanti MP. CDK inhibitors (p16/p19/p21) induce senescence and autophagy in cancer-associated fibroblasts, “fueling” tumor growth via paracrine interactions, without an increase in neo-angiogenesis. *Cell Cycle.* 2012; 11:3599–610.
<https://doi.org/10.4161/cc.21884>
PMID:22935696
43. Suzuki K, Nakashima M, Yamashita S. Dynamics of ionizing radiation-induced DNA damage response in reconstituted three-dimensional human skin tissue. *Radiat Res.* 2010; 174:415–23.
<https://doi.org/10.1667/RR2007.1>
PMID:20726705

ARTICLE

doi:10.1038/nature25016

Alcohol-abuse drug disulfiram targets cancer via p97 segregase adaptor NPL4

Zdenek Skrott^{1*}, Martin Mistrik^{1*}, Klaus Kaae Andersen², Søren Friis², Dusana Majera¹, Jan Gursky¹, Tomas Ozdian¹, Jirina Bartkova^{2,3}, Zsofia Turi¹, Pavel Moudry¹, Marianne Kraus⁴, Martina Michalova¹, Jana Vaclavkova¹, Petr Dzubak¹, Ivo Vrobel¹, Pavla Pouckova⁵, Jindrich Sedlacek⁶, Andrea Miklovcova⁷, Anne Kutt², Jing Li⁸, Jana Mattova⁵, Christoph Driessen⁴, Q. Ping Dou^{9,10}, Jørgen Olsen², Marian Hajduch¹, Boris Cvek^{6†}, Raymond J. Deshaies^{8,11‡} & Jiri Bartek^{2,3}

Cancer incidence is rising and this global challenge is further exacerbated by tumour resistance to available medicines. A promising approach to meet the need for improved cancer treatment is drug repurposing. Here we highlight the potential for repurposing disulfiram (also known by the trade name Antabuse), an old alcohol-aversion drug that has been shown to be effective against diverse cancer types in preclinical studies. Our nationwide epidemiological study reveals that patients who continuously used disulfiram have a lower risk of death from cancer compared to those who stopped using the drug at their diagnosis. Moreover, we identify the ditiocarb-copper complex as the metabolite of disulfiram that is responsible for its anti-cancer effects, and provide methods to detect preferential accumulation of the complex in tumours and candidate biomarkers to analyse its effect on cells and tissues. Finally, our functional and biophysical analyses reveal the molecular target of disulfiram's tumour-suppressing effects as NPL4, an adaptor of p97 (also known as VCP) segregase, which is essential for the turnover of proteins involved in multiple regulatory and stress-response pathways in cells.

Despite advances in the understanding of cancer biology, malignant diseases have a high global toll. Furthermore, the increasing average human life expectancy is predicted to have demographic consequences, including an increase in the incidence of cancer. The high cancer-associated morbidity and mortality highlight the need for innovative treatments. Given the high costs, failure rate and long testing periods of developing new medicines, using drugs that are approved for the treatment of diverse diseases as candidate anti-cancer therapeutics represents a faster and cheaper alternative¹, benefitting from available clinically suitable formulations and evidence of tolerability in patients. Among promising cancer-killing drugs² is disulfiram (tetraethylthiuram disulfide, DSF), a drug that has been used for over six decades as a treatment for alcohol dependence³, with well-established pharmacokinetics, safety and tolerance at the US Food and Drug Administration (FDA)-recommended dosage⁴. In the body, DSF is metabolized to ditiocarb (diethyldithiocarbamate, DTC) and other metabolites, some of which inhibit liver aldehyde dehydrogenase⁵. Because DSF showed anti-cancer activity in preclinical models^{3,6–9} and because adjuvant DTC was used to treat high-risk breast cancer in a clinical trial¹⁰, DSF emerges as a candidate for drug repurposing in oncology. Additional advantages of DSF include a broad spectrum of malignancies sensitive to DSF, and its ability to also target the stem-like, tumour-initiating cells¹¹. Although the mechanism of DSF's anti-cancer activity remains unclear and it has been suggested that the drug inhibits proteasome activity^{6,12}, it has been shown that DSF chelates bivalent metals and forms complexes with copper (Cu), which enhances its anti-tumour activity^{6,13}. In addition to the lack of a well-defined mechanism of action in cancer cells, the main obstacles for DSF repurposing have

been: (i) uncertainty about the active metabolite(s) of DSF *in vivo*; (ii) the lack of assays to measure these active derivative(s) in tumours; (iii) missing biomarker(s) to monitor the impact of DSF in tumours and tissues; (iv) the lack of insights into the preferential toxicity towards cancer cells compared to normal tissues; and (v) the absence of a specific molecular target that could explain the potent anti-tumour activity of DSF. Here, we combine experimental approaches and epidemiology to address the important characteristics of DSF in relation to cancer, pursuing the goal of repurposing DSF for cancer therapy. We identify the active metabolite of DSF, and provide biological validation and mechanistic insights, including the discovery of a biologically attractive protein that has previously not been considered as the target for the anti-cancer activity of DSF.

Epidemiological analyses of DSF and cancer

The relative lack of cancer-related clinical trials with DSF^{10,14} prompted us to explore whether DSF use might reduce cancer mortality at a population level. Using the Danish nationwide demographic and health registries, we estimated hazard ratios of cancer-specific mortality associated with DSF use among patients with cancer for the first time during 2000–2013 (see Methods, Table 1 and Extended Data Fig. 1a). DSF users were categorized as (i) previous users, who were patients that were prescribed DSF for alcohol dependency only before their cancer diagnosis or (ii) continuing users, who were patients that were prescribed DSF both before and after diagnosis. As expected from the increase in cancer risk and the deleterious effect on prognosis¹⁵ caused by alcohol abuse, cancer-specific mortality was higher among previous DSF users than among patients with cancer who had never

¹Institute of Molecular and Translational Medicine, Faculty of Medicine and Dentistry, Palacky University, Olomouc, Czech Republic. ²Danish Cancer Society Research Center, DK-2100 Copenhagen, Denmark. ³Science for Life Laboratory, Division of Genome Biology, Department of Medical Biochemistry and Biophysics, Karolinska Institutet, Stockholm, Sweden. ⁴Kantonsspital St Gallen, Department Oncology/Hematology, St Gallen, Switzerland. ⁵Institute of Biophysics and Informatics, First Faculty of Medicine, Charles University, 120 00 Prague 2, Czech Republic. ⁶Department of Cell Biology & Genetics, Palacky University, Olomouc, Czech Republic. ⁷Psychiatric Hospital, 785 01 Sternberk, Czech Republic. ⁸Division of Biology and Biological Engineering, Caltech, Pasadena, California 91125, USA. ⁹Barbara Ann Karmanos Cancer Institute and Department of Oncology, School of Medicine, Wayne State University, Detroit, Michigan, USA. ¹⁰School of Basic Medical Sciences, Affiliated Tumor Hospital of Guangzhou Medical University, Guangzhou 511436, China. ¹¹Howard Hughes Medical Institute, Caltech, Pasadena, California 91125, USA. [†]Present addresses: Olomouc University Social Health Institute, Palacky University, Olomouc, Czech Republic (B.C.); Amgen, Thousand Oaks, California 91320, USA (R.J.D.). ^{*}These authors contributed equally to this work.

Table 1 | Cancer-specific mortality associated with DSF use among Danish patients with cancer

Cancer type	Overall				Localized stage				Non-localized stage				Unknown stage			
	Number*	HR	95% CI	P value	Number*	HR	95% CI	P value	Number*	HR	95% CI	P value	Number*	HR	95% CI	P value
Any cancer†																
Previous users	3,038	1.00			1,429	1.00			1,054	1.00			555	1.00		
Continuing users	1,177	0.66	0.58–0.76	0.000	602	0.69	0.64–0.74	0.000	355	0.71	0.59–0.87	0.001	220	0.65	0.57–0.75	0.000
No prescriptions	236,950	0.68	0.64–0.73	0.000	113,354	0.59	0.57–0.61	0.000	73,933	0.80	0.73–0.88	0.000	49,663	0.66	0.62–0.71	0.000

Hazard ratios (HR) and 95% confidence intervals (CI) comparing continuing and previous users of DSF, relative to the time of their cancer diagnosis. For DSF exposure categories, statistics and clinical stages, see Methods.

*Number of patients included.

†Except cancers of the liver and kidney.

used DSF. Notably, we also found reduced cancer-specific mortality for cancer overall (Table 1), as well as for cancers of the colon, prostate and breast among continuing users compared to previous DSF users (Extended Data Fig. 1a). Stratification by clinical stage (Table 1) revealed reduced cancer-specific mortality with continuing use of DSF even among patients with metastatic disease. Although it is not possible to draw conclusions about causality, these findings supported the hypothesis that DSF may exert anti-cancer effects among patients suffering from common cancers, prompting us to perform pre-clinical analyses.

Anti-tumour activity of the DTC–copper complex

Because DSF anti-cancer activity has been suggested to be copper-dependent^{6,13}, we compared groups of mice injected with human MDA-MB-231 cancer cells, fed with a (i) normal diet; (ii) normal diet plus copper gluconate (CuGlu); (iii) normal diet plus DSF; or (iv) normal diet plus DSF and CuGlu (DSF/CuGlu); and tumour volume was measured over time (Fig. 1a and Extended Data Fig. 1b, c). Compared to matched controls, tumour volume in DSF- and DSF/CuGlu-treated groups at 32 days (at DSF doses equivalent to those used by alcoholics) were suppressed by 57% and 77%, respectively ($P=0.0038$ in favour of the DSF/CuGlu treatment versus DSF alone). These results validate previous *in vitro*^{6,11,13} and *in vivo*^{6–9,13,16} studies, which indicated that DSF is an efficient anti-cancer agent and that copper potentiates its activity. As the reactive metabolite DTC forms complexes with metals, particularly copper¹⁷, we argued that a DTC–copper complex (bis (diethyldithiocarbamate)–copper (CuET)) forms *in vivo* (Extended Data Fig. 1d), providing the anti-cancer metabolite. To test this hypothesis, we developed a high-resolution

approach based on high-performance liquid chromatography–mass spectrometry to measure CuET in tissues, and readily detected CuET after a single oral dose of DSF (Extended Data Fig. 1e, f). Extracts from plasma, liver, brain and MDA-MB-231-xenografted tumours contained CuET in samples from mice treated for five days with DSF or DSF/CuGlu. The CuET levels in plasma and liver were slightly higher after DSF/CuGlu treatment compared to DSF alone. Notably, the CuET levels in the tumour specimens were almost an order of magnitude higher compared to corresponding levels in liver and brain tissues from the same animals (Fig. 1b), suggesting preferential accumulation of CuET in tumours. Importantly, we also confirmed formation of CuET in humans undergoing DSF treatment for alcoholism (Fig. 1c).

Next, we synthesized CuET and performed comparative cell culture and animal studies. Short-term (24-h) assays and long-term (colony-forming assay, CFA) assays consistently showed higher cytotoxicity of CuET than of the primary DSF metabolite DTC in various cancer cell lines (Fig. 1d and Extended Data Fig. 1g). The half-maximal lethal dose (LD_{50}) values of CuET in CFA experiments were ≤ 100 nM in three out of three tested breast cancer cell lines and similar potency was observed among cell lines derived from human lung, colon and prostate tumours (Extended Data Fig. 2a). These data were corroborated by tetrazolium dye ((2,3-bis-(2-methoxy-4-nitro-5-sulphophenyl)-2h-tetrazolium-5-carboxanilide) (XTT))-based 48-h cytotoxicity tests on a wider panel of cell types (Extended Data Fig. 2b). Unexpectedly, only the most sensitive cell lines (for example, AMO-1, Capan1) showed markers of apoptosis¹⁸, which included annexin V and activated caspases, whereas in most cell lines, for example, MDA-MB-231 and U2OS cells, CuET induced apoptosis-independent cell death (Extended Data Fig. 2c–f).

Direct therapeutic effects of CuET *in vivo* were then investigated using the MDA-MB-231 breast cancer (Fig. 1e) and AMO-1 myeloma (Fig. 1f) xenograft models treated intraperitoneally with a CuET–albumin formulation, with which the anti-tumour activity and good tolerability of this DSF metabolite was confirmed (Extended Data Fig. 1h, i).

CuET inhibits p97-dependent protein degradation

Next, we investigated the interaction between CuET and cellular protein degradation, one of the suggested explanations for anti-tumour effects of DSF^{6,12}. We confirmed that CuET induces phenotypic features shared with proteasome inhibitors, such as MG132 or bortezomib (BTZ), including accumulation of poly-ubiquitylated (poly-Ub) proteins (Fig. 2a and Extended Data Fig. 3a), rapid deubiquitylation of histone H2A (uH2A)¹⁹ (Extended Data Fig. 3b) and accumulation of ubiquitylated proteins in the cytoplasm¹⁹ (Extended Data Fig. 3c). Furthermore, TNF (also known as TNF α)-induced degradation of I κ B α (ref. 20) was blocked after 1-h treatment with CuET or BTZ (Fig. 2b). Finally, CuET inhibited degradation of Ub(G76V)–GFP (an ubiquitin-fusion degradation substrate)²¹ in a dose-dependent manner (Fig. 2c). However, although these data confirmed a defect in protein degradation, CuET had no effect on the CT-like, C-like or T-like activity of the 20S proteasome²² (Extended Data Fig. 3d, e). This was further corroborated by the lack of a stabilizing effect of CuET on p53 tumour suppressor protein in dicoumarol-treated cells, in which

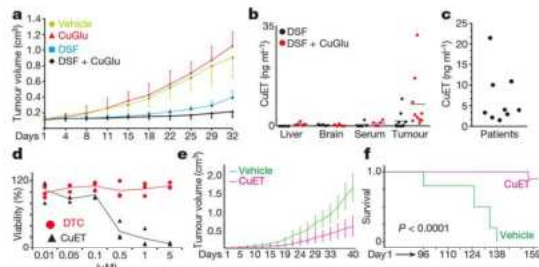


Figure 1 | Tumour-suppressing effects of DSF and CuET. a, Effects of orally administered DSF and CuGlu on subcutaneous growth of MDA-MB-231 tumours in mice. $n=8$ mice per group. b, CuET levels in mouse tumours and tissues. $n=5$ tissues, $n=10$ tumours. c, CuET levels in human plasma after DSF treatment ($n=9$ patients). d, Toxicity of DTC and CuET in MDA-MB-231 cells after 24 h treatment. $n=3$ experiments. e, Effect of CuET on subcutaneous growth of MDA-MB-231 tumours in mice. $n=20$ tumours. f, Survival of CuET- versus vehicle-treated mice with implanted AMO-1 xenografts. $n=10$ animals per group. P value from a log-rank test. Data are mean \pm s.d. (a, e) or mean (b) linked means with individual values (d) or individual values (c).

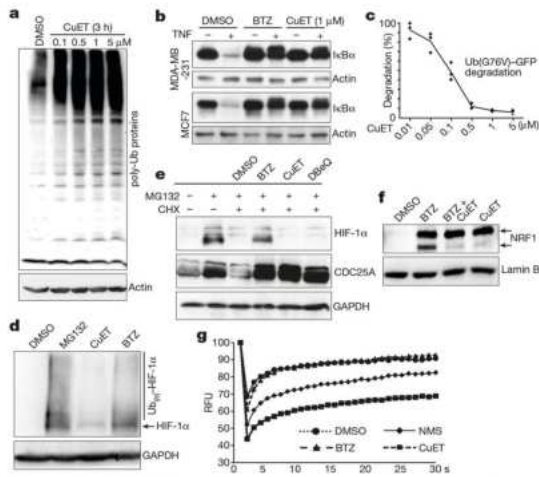


Figure 2 | CuET inhibits p97 segregase-dependent protein degradation. **a**, CuET causes accumulation of poly-ubiquitylated proteins in MCF7 cells. **b**, TNF-induced I κ B α degradation is compromised after 1-h treatment with CuET or BTZ. **c**, Dose-dependent inhibition of Ub(G76V)-GFP degradation by CuET. HeLa cells were treated for 3 h. $n = 3$ experiments. **d**, HIF-1 α levels after 2-h treatments with MG132 (5 μ M), CuET (1 μ M), BTZ (1 μ M) in HeLa cells. **e**, Differential effect of BTZ (1 μ M), CuET (1 μ M) and DBE (10 μ M) on CDC25A versus HIF-1 α in MG132-pretreated (4 h, 5 μ M), cycloheximide (CHX, 1 h, 50 μ g ml $^{-1}$)-exposed HeLa cells. **f**, BTZ (8 h, 1 μ M) induces NRF1 120-kDa (top arrow) and 110-kDa (bottom arrow) forms; whereas CuET (8 h, 0.5 μ M) only induced the non-cleaved 120-kDa form in NIH3T3 cells. **g**, FRAP quantification in U2OS Ub-GFP cells: slower mobility of accumulated cytoplasmic GFP-Ub after a 2-h pre-treatment with NMS873 (10 μ M), CuET (1 μ M) or BTZ (1 μ M). **a**, **b**, **d**–**g**, Data are representative of two independent biological experiments. Data are linked means and individual values (**c**) and relative mean signal of the bleached region from 12 cells per treatment (**g**).

p53 turnover depends on the core 20S proteasome independently of ubiquitin^{23,24}. In contrast to CuET, treatment with the 20S proteasome inhibitor BTZ stabilized p53 irrespective of dicoumarol (Extended Data Fig. 3f), indicating that 20S proteasome-dependent protein turnover remains operational with CuET treatment. Furthermore, CuET failed to inhibit 26S proteasome activity (Extended Data Fig. 3g), which was inferred from RPN11-dependent deubiquitylation²⁵. Collectively, these results suggest that CuET stabilizes ubiquitylated proteins by blocking a step upstream of the proteasome.

Next we considered p97-dependent processing of poly-Ub proteins, as this pathway operates upstream of the proteasome and its malfunction resembles phenotypes of proteasome inhibition²⁶. Unlike BTZ or MG132, CuET induced only modest accumulation (a small subfraction) of HIF-1 α (Fig. 2d), consistent with reported modest accumulation of HIF-1 α after knockdown of p97 compared to cells with inhibited proteasomes²⁷. Next, we pre-treated cells with MG132, followed by wash-off and 1-h cycloheximide (an inhibitor of translation) treatment combined with BTZ, CuET or DBE (a direct inhibitor of p97 ATPase activity)²⁸. All tested inhibitors prevented degradation of CDC25A (a known p97 target)²⁹, whereas degradation of the mostly p97-independent target, that is, most of HIF-1 α ²⁷, was inhibited only by BTZ (Fig. 2e). Furthermore, consistent with cleavage of the 120-kDa species of the endoplasmic reticulum-tethered transcription factor NRF1 into an active 110-kDa form being a p97-dependent process³⁰, appearance of the cleaved NRF1 form was inhibited by both CuET and NMS873 (another p97 ATPase inhibitor) (Fig. 2f and Extended Data Fig. 4a, b).

These results suggest that the p97 pathway is compromised in cells treated with CuET.

Next, we asked whether CuET impairs the p97 segregase activity that extracts poly-Ub proteins from cellular structures, such as the endoplasmic reticulum, Golgi apparatus or chromatin for subsequent proteasomal degradation³¹. Using fluorescence recovery after photobleaching (FRAP) to investigate the mobility of accumulated poly-Ub proteins, we found that whereas GFP-ubiquitin in DMSO- or BTZ-treated cells diffused rapidly into bleached areas, this diffusion was slower after treatment with CuET or NMS873 (Fig. 2g and Extended Data Fig. 4c). This suggests that after treatment with CuET or NMS873 at least a subset of the accumulated poly-Ub proteins remains immobile, probably embedded into cellular structures. Consistently, upon detergent pre-extraction of mobile proteins, we observed greater immunofluorescence signals of extraction-resistant poly-Ub(K48) proteins (destined for proteasomal degradation) in NMS873- and CuET-treated cells compared to BTZ- or DMSO-treated controls (Extended Data Fig. 4d). Western blot analysis of endoplasmic reticulum-rich microsomal fractions also revealed enrichment of poly-Ub proteins after CuET and NMS873 treatment (Extended Data Fig. 4e). Malfunction of p97 segregase is furthermore associated with a cellular unfolded protein response (UPR)³². We confirmed UPR in cells treated with CuET or NMS873 by detecting increased markers of UPR induction, including the spliced form of XBP1s, ATF4 and phosphorylated (p-) eIF2 α ³³ (Extended Data Fig. 4f).

These studies are also of clinical relevance, because inhibition of p97 was suggested as an alternative treatment strategy for myeloma patients who had relapsed after therapy with BTZ (also known by the trade name Velcade)³⁴ or carfilzomib (CFZ)³⁵. Thus, we performed cytotoxicity tests with CuET on a panel of BTZ- or CFZ-adapted and non-adapted human cell lines or on cells derived from samples of patients with myeloma before therapy and with BTZ therapy. All pairs of adapted and non-adapted cells showed similar sensitivity to CuET treatment, in contrast to BTZ (Extended Data Fig. 5a–d). These results suggest that treatment with DSF (best combined with copper) or CuET might become a feasible therapeutic option for patients with relapsed, BTZ-resistant multiple myeloma.

CuET binds and immobilizes NPL4

To elucidate how CuET inhibits the p97 pathway, we first used an assay of p97 ATPase activity²⁸. In contrast to treatment with NMS873, CuET had no effect on p97 ATPase activity (Extended Data Fig. 6a). Because NPL4 and UFD1 proteins are key components of the p97 segregase³¹, we examined whether CuET might target the pathway through these cofactors. Ectopic overexpression of NPL4-GFP, but not UFD1-GFP or p97-GFP, reduced CuET cytotoxicity, suggesting that NPL4 is a candidate target of CuET (Fig. 3a and Extended Data Fig. 6b). An analogous 'rescue effect' of ectopic NPL4-GFP was apparent from the reduction in accumulation of poly-Ub proteins caused by CuET (Extended Data Fig. 6c).

As shown by live-cell imaging, 2–3-h exposure to CuET induced prominent nuclear clustering of NPL4-GFP, but not of UFD1-GFP or p97-GFP (Fig. 3b). Within 2–3 h, most of cellular NPL4-GFP became immobilized in nuclear clusters and also in cytoplasmic areas, as shown by FRAP (Fig. 3c). CuET-induced immobilization of endogenous NPL4 was confirmed by accumulation, which was detectable by western blot, in the detergent-insoluble fractions from various cell lines (Fig. 3d) and by immunofluorescence on pre-extracted cells (Extended Data Fig. 6d). Notably, the immobilization of NPL4 was also detectable in pre-extracted sections of cryopreserved tumours from mice treated with DSF or DSF and CuGlu, thus providing a potential biomarker of CuET activity towards the p97 pathway *in vivo* (Fig. 3e).

NPL4 is an attractive candidate for CuET binding, because this protein contains two zinc finger domains: a C-terminal NZF (NPL4-zinc finger) and a putative zinc finger-NPL4³⁶, which bind bivalent metals and metal complexes that might chemically resemble CuET³⁷.

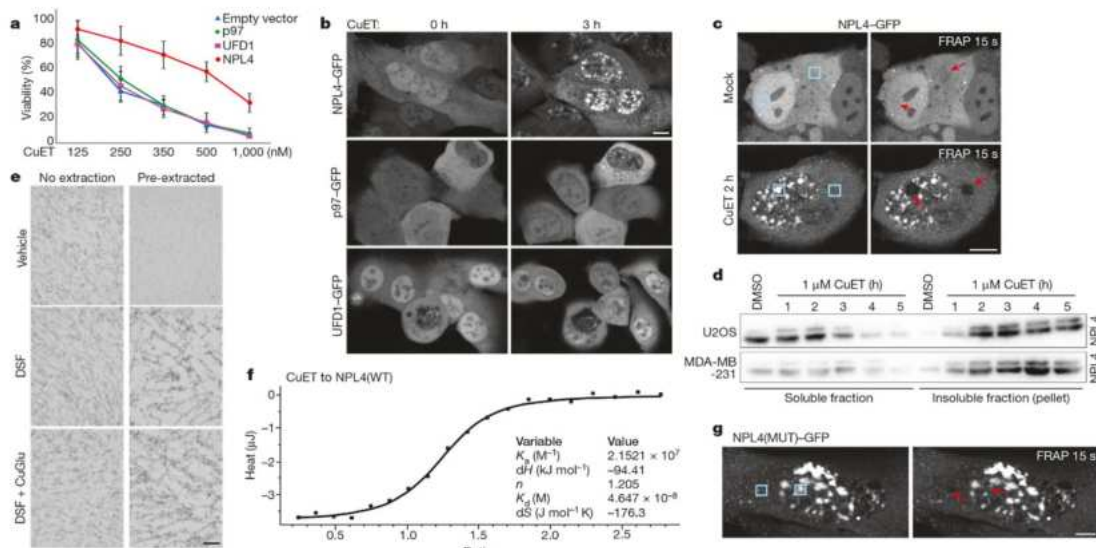


Figure 3 | CuET binds to and immobilizes NPL4. **a**, Ectopic NPL4-GFP, but not p97-GFP or UFD1-GFP rescues CuET toxicity in U2OS cells treated for 24 h. $n = 3$ experiments. Data are mean \pm s.d. **b**, CuET (1 μ M) induces intranuclear clustering of NPL4-GFP, but not p97-GFP or UFD1-GFP. **c**, CuET-induced (1 μ M) immobilization of NPL4-GFP (FRAP) in U2OS cells treated for 2 h. Blue boxes, areas before bleaching; arrows, after bleaching. **d**, NPL4 enrichment in Triton X-100-insoluble fractions

after CuET (1 μ M) treatment. **e**, Immunohistochemistry demonstrates the non-extractable NPL4 in MDA-MB-231 tumours from mice treated with DSF or DSF and CuGlu. **f**, ICT shows that CuET binds to purified NPL4(WT). **g**, Spontaneous intranuclear clustering and immobilization of NPL4(MUT)-GFP using FRAP in U2OS cells. Blue boxes, areas before bleaching; arrows, after bleaching. Scale bars, 10 μ m (**b**, **c**, **g**) or 50 μ m (**e**). **b**–**g**, Data are representative of two independent experiments.

Using isothermal calorimetry analysis (ITC)³⁸, we observed a standard dose–response-dependent binding curve (Fig. 3f) compatible with one binding site for CuET on wild-type NPL4 (NPL4(WT)), and a K_d in nanomolar concentrations for the NPL4–CuET interaction. Next, we used mutagenesis to test whether the putative ZF–NPL4 domain has any role in the potential NPL4–CuET interaction. The putative zinc finger domain was preferred, because an endogenous larger form of NPL4 that lacks the C-terminal NZF sequence exists in human cells. This larger NPL4 form is detectable as an upper band on western blots (Fig. 3d) and it is immobilized after CuET treatment, suggesting that the C-terminal NZF is not necessary for the interaction with CuET. No ITC interaction was found with a NPL4 mutant (NPL4(MUT)) (Extended Data Fig. 6f) in which both histidines and both cysteines in the putative zinc finger domain were substituted by alanines (Extended Data Fig. 6e). We used drug affinity responsive target stability (DARTS) as another, independent approach, which is based on altered protease susceptibility of target proteins upon drug binding³⁹. Consistently, exposure to CuET caused a differential pronase-dependent proteolysis pattern of NPL4(WT) but not NPL4(MUT) (Extended Data Fig. 6g). These results indicate that NPL4 is directly targeted by CuET and an intact putative zinc finger domain of NPL4 is essential for this interaction.

Notably, ectopically expressed NPL4(MUT)-GFP formed immobile nuclear clusters spontaneously in untreated cells, reminiscent of events seen in cells upon CuET treatment (Fig. 3c, g). Moreover, unlike ectopic NPL4(WT)-GFP, ectopically expressed NPL4(MUT)-GFP not only did not render cells resistant to CuET but also was toxic to the acceptor cells (Extended Data Fig. 6h). We also confirmed that multiple CuET-induced cellular phenotypes were mimicked by the ectopic NPL4(MUT)-GFP model, including accumulation of poly-Ub proteins and UPR activation (Extended Data Fig. 6i).

NPL4 aggregates trigger a heat-shock response

Although the nuclear NPL4 clusters occupied DAPI-unlabelled areas of chromatin (Extended Data Fig. 6d) co-localization with DAPI-excluded structures, such as nucleoli and nuclear speckles, were not found (Extended Data Fig. 7a). In late-G2 cells, NPL4 clusters were evidently excluded from the partially condensed chromatin (Extended Data Fig. 7b), suggesting that the NPL4 aggregates exclude chromatin rather than accumulating in specific nuclear areas. Both the nuclear clusters and the immobilized cytoplasmic NPL4 co-localized with poly-Ub proteins (confirmed by anti-Ub(K48) and FK2 antibodies), small ubiquitin-like modifiers (SUMOs) (only in nuclei) and with TDP43 protein⁴⁰ (Fig. 4a and Extended Data Fig. 7d), which are all features typical of aggregated defective proteins⁴¹. The same co-localization patterns were observed for spontaneous clusters formed by NPL4(MUT)-GFP showing that NPL4 aggregation is sufficient for the induction of these phenotypes even without CuET treatment (Extended Data Fig. 7c, e). Blockade of cellular ubiquitylation with a chemical inhibitor (MLN7243) of the E1 ubiquitin-activating enzyme failed to prevent either NPL4-GFP nuclear aggregation or cytoplasmic immobilization (Extended Data Fig. 7d), excluding the immobilization of NPL4 via recognition of ubiquitylated and SUMOylated substrates, but rather suggesting that immobilized NPL4 attracts ubiquitylated proteins or proteins that subsequently become ubiquitylated and/or SUMOylated. A key protein commonly associated with intracellular protein aggregates is HSP70, a chaperone implicated in aggregate processing⁴². Indeed, pre-extracted cells showed co-localization of HSP70 with both CuET-induced NPL4(WT)-GFP and spontaneous NPL4(MUT)-GFP aggregates (Fig. 4b, c). Both the CuET-induced NPL4(WT) aggregates and spontaneous NPL4(MUT) aggregates also co-localized with p97 (Extended Data Fig. 7f, g), as is particularly evident after pre-extraction. In the NPL4-GFP model, the amount of p97 immunoreactivity within

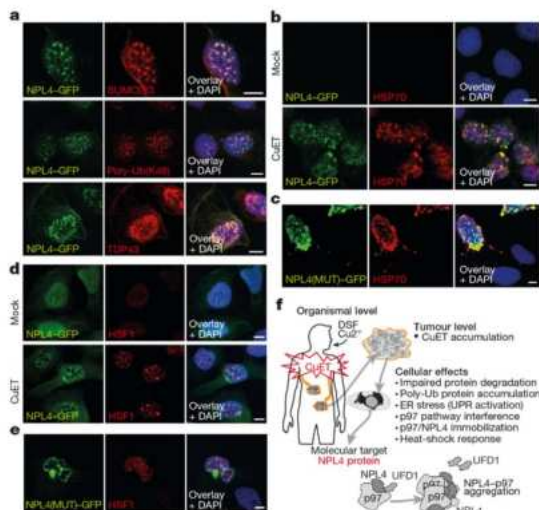


Figure 4 | NPL4 protein aggregation triggers HSR. **a**, NPL4-GFP co-localizes with SUMO2/3, poly-Ub(K48) and TDP43 in U2OS cells. Cells were treated with 1 μ M CuET for 3 h and pre-extracted. **b**, NPL4-GFP co-localizes with HSP70 in mock- and CuET-treated U2OS cells. Cells were treated with 1 μ M CuET for 3 h and pre-extracted. **c**, NPL4(MUT)-GFP co-localizes with HSP70 in U2OS cells after pre-extraction. **d**, CuET-induced HSF1 stress bodies. NPL4-GFP U2OS cells were treated with 1 μ M CuET for 3 h. **e**, HSF1 stress bodies in U2OS cells expressing NPL4(MUT)-GFP. **f**, Model of DSF anti-cancer activity in patients. Scale bars, 10 μ m. **a–e**, Data are representative of two independent experiments.

the NPL4-GFP clusters correlated with the GFP signal intensity, suggesting that p97 is immobilized via its interaction with NPL4. The other NPL4-binding partner, UFD1, was almost undetectable in detergent-insoluble pellets of CuET-treated or NPL4(MUT)-GFP-expressing cells despite clear p97 immobilization (Extended Data Fig. 8a, b), suggesting that UFD1 cannot bind to, or becomes only loosely attached to, the aggregated NPL4-p97 complex. Notably, non-extractable cellular p97 is detectable after CuET treatment (Extended Data Fig. 8c), including in stained tumour sections from mice treated with DSF or DSF and CuGlu, providing an additional candidate marker for CuET activity *in vivo* (Extended Data Fig. 8d).

Because aggregation of misfolded or damaged proteins triggers cellular heat-shock response (HSR) through an HSF1-dependent mechanism¹³, we confirmed that CuET treatment indeed triggered a robust HSR accompanied by characteristic HSF1 nuclear stress foci (Fig. 4d) that were also detectable in cells spontaneously aggregating NPL4(MUT)-GFP (Fig. 4e). HSR markers, including accumulation of heat-shock proteins and a phosphorylation shift in HSF1, were detectable by western blot (Extended Data Fig. 8e, f).

Discussion

Our results help to explain the anti-cancer activity of the alcohol-abuse drug disulfiram. We propose a model for DSF cytotoxic activity, featuring rapid conversion of DSF into CuET, which accumulates in tumours. After entering cells, CuET binds NPL4 and induces its aggregation, consequently disabling the vital p97-NPL4-UFD1 pathway and inducing a complex cellular phenotype leading to cell death (Fig. 4f). Supporting CuET as the active metabolite is the correlation of CuET concentrations (active in the nanomolar range) with the biological effects and functional impact on the targeted pathway(s) *in vivo*. In addition, CuET is the only known metabolite of DSF containing copper ions, a metal

that enhances the anti-tumour effects of DSF; it is unlikely that another DSF metabolite could represent the major anti-cancer agent as levels of non-CuET metabolites should be lowered by copper addition. We also present a method for CuET detection in tissues and plasma, as well as data suggesting that preferential accumulation of CuET in tumours may contribute to cancer cell toxicity, consistent with the high therapeutic tolerability of DSF³, as documented even after years of daily administration at doses comparable to those we used in our mouse experiments. Considering the numerous studies on DSF and diverse opinions about the potential target of its anti-cancer effects⁴⁴, identification of NPL4, a key component of the p97-NPL4-UFD1 segregase complex, as the molecular target of CuET is surprising. The CuET-NPL4 interaction leads to rapid formation of protein aggregates and immobilization of this otherwise very mobile multifunctional protein complex, resulting in a severe phenotype, induction of HSR and eventually cell death. While additional potential targets of CuET cannot be excluded, the malfunction of the p97 pathway due to the NPL4-p97 aggregate formation explains the major cell phenotypes and the consequent cell death. Our work also reconciles the controversial studies^{5,12}, suggesting that the proteasome is the DSF target, by demonstrating that neither 20S nor 26S proteasome, but the processing of ubiquitylated proteins by the NPL4-dependent segregase, is targeted by CuET. Our results support the notion that the p97-NPL4 pathway is a promising therapeutic target in oncology^{45,46}. Indeed, reports on p97 overabundance correlating with progression and metastasis of carcinomas of the breast, colon and prostate^{47–49} are consistent with our present nationwide epidemiological analysis, which revealed an association between continued use of DSF and favourable prognosis, an intriguing finding that should be investigated further, particularly given the currently limited therapeutic options for patients with metastatic cancer. From a broader perspective, our study illustrates the potential of multifaceted approaches to drug repurposing, providing novel mechanistic insights, identification of new cancer-relevant targets and encouragement for further clinical trials, here with DSF, an old, safe and public domain drug⁴ that might help to save lives of patients with cancer worldwide.

Online Content Methods, along with any additional Extended Data display items and Source Data, are available in the online version of the paper; references unique to these sections appear only in the online paper.

Received 1 October 2015; accepted 8 November 2017.

Published online 6 December 2017.

- Collins, F. S. Mining for therapeutic gold. *Nat. Rev. Drug Discov.* **10**, 397 (2011).
- Pantziarka, P. et al. The repurposing drugs in oncology (ReDO) project. *Eur. J. Cancer* **48**, 442 (2014).
- Ijijn, K. et al. High-throughput cell-based screening of 4910 known drugs and drug-like small molecules identifies disulfiram as an inhibitor of prostate cancer cell growth. *Clin. Cancer Res.* **15**, 6070–6078 (2009).
- Cvek, B. Nonprofit drugs as the salvation of the world's healthcare systems: the case of Antabuse (disulfiram). *Drug Discov. Today* **17**, 409–412 (2012).
- Shen, M. L., Johnson, K. L., Mays, D. C., Lipsky, J. J. & Naylor, S. Determination of *in vivo* adducts of disulfiram with mitochondrial aldehyde dehydrogenase. *Biochem. Pharmacol.* **61**, 537–545 (2001).
- Chen, D., Cui, Q. C., Yang, H. & Dou, Q. P. Disulfiram, a clinically used anti-alcoholism drug and copper-binding agent, induces apoptotic cell death in breast cancer cultures and xenografts via inhibition of the proteasome activity. *Cancer Res.* **66**, 10425–10433 (2006).
- Zha, J. et al. Disulfiram targeting lymphoid malignant cell lines via ROS-JNK activation as well as Nrf2 and NF- κ B pathway inhibition. *J. Transl. Med.* **12**, 163 (2014).
- Safi, R. et al. Copper signaling axis as a target for prostate cancer therapeutics. *Cancer Res.* **74**, 5819–5831 (2014).
- Liu, P. et al. Liposome encapsulated disulfiram inhibits NF- κ B pathway and targets breast cancer stem cells *in vitro* and *in vivo*. *Oncotarget* **5**, 7471–7485 (2014).
- Dufour, P. et al. Sodium dithiocarbamate as adjuvant immunotherapy for high risk breast cancer: a randomized study. *Biotherapy* **6**, 9–12 (1993).
- Yip, N. C. et al. Disulfiram modulated ROS-MAPK and NF- κ B pathways and targeted breast cancer cells with cancer stem cell-like properties. *Br. J. Cancer* **104**, 1564–1574 (2011).

12. Lövborg, H. *et al.* Inhibition of proteasome activity, nuclear factor- κ B translocation and cell survival by the anti-alcoholism drug disulfiram. *Int. J. Cancer* **118**, 1577–1580 (2006).
13. Allensworth, J. L. *et al.* Disulfiram (DSF) acts as a copper ionophore to induce copper-dependent oxidative stress and mediate anti-tumor efficacy in inflammatory breast cancer. *Mol. Oncol.* **9**, 1155–1168 (2015).
14. Nechushtan, H. *et al.* A phase IIb trial assessing the addition of disulfiram to chemotherapy for the treatment of metastatic non-small cell lung cancer. *Oncologist* **20**, 366–367 (2015).
15. Jin, M. *et al.* Alcohol drinking and all cancer mortality: a meta-analysis. *Ann. Oncol.* **24**, 807–816 (2013).
16. Li, Y. *et al.* Copper improves the anti-angiogenic activity of disulfiram through the EGFR/Src/VEGF pathway in gliomas. *Cancer Lett.* **369**, 86–96 (2015).
17. Suzuki, Y. *et al.* The origin of an EPR signal observed in dithiocarbamate-loaded tissues. Copper(II)-dithiocarbamate complexes account for the narrow hyperfine lines. *Biochim. Biophys. Acta* **1335**, 242–245 (1997).
18. Kepp, O., Galluzzi, L., Lipinski, M., Yuan, J. & Kroemer, G. Cell death assays for drug discovery. *Nat. Rev. Drug Discov.* **10**, 221–237 (2011).
19. Doll, C. *et al.* RNF168 binds and amplifies ubiquitin conjugates on damaged chromosomes to allow accumulation of repair proteins. *Cell* **136**, 435–446 (2009).
20. Li, J. M., Wu, H., Zhang, W., Blackburn, M. R. & Jin, J. The p97-UFD1L-NPL4 protein complex mediates cytokine-induced I κ B α proteolysis. *Mol. Cell. Biol.* **34**, 335–347 (2014).
21. Chou, T. F. & Deshaies, R. J. Quantitative cell-based protein degradation assays to identify and classify drugs that target the ubiquitin–proteasome system. *J. Biol. Chem.* **286**, 16546–16554 (2011).
22. Kisselev, A. F. & Goldberg, A. L. Monitoring activity and inhibition of 26S proteasomes with fluorogenic peptide substrates. *Methods Enzymol.* **398**, 364–378 (2005).
23. Asher, G., Lotem, J., Cohen, B., Sachs, L. & Shaul, Y. Regulation of p53 stability and p53-dependent apoptosis by NADH quinone oxidoreductase 1. *Proc. Natl Acad. Sci. USA* **98**, 1188–1193 (2001).
24. Asher, G., Tsvetkov, P., Kahana, C. & Shaul, Y. A mechanism of ubiquitin-independent proteasomal degradation of the tumor suppressors p53 and p73. *Genes Dev.* **19**, 316–321 (2005).
25. Verma, R. *et al.* Role of Rpn11 metalloprotease in deubiquitination and degradation by the 26S proteasome. *Science* **298**, 611–615 (2002).
26. Dai, R. M. & Li, C. C. Valosin-containing protein is a multi-ubiquitin chain-targeting factor required in ubiquitin–proteasome degradation. *Nat. Cell Biol.* **3**, 740–744 (2001).
27. Alexandru, G. *et al.* UBXD7 binds multiple ubiquitin ligases and implicates p97 in HIF1 α turnover. *Cell* **134**, 804–816 (2008).
28. Chou, T. F. *et al.* Reversible inhibitor of p97, DBE α , impairs both ubiquitin-dependent and autophagic protein clearance pathways. *Proc. Natl Acad. Sci. USA* **108**, 4834–4839 (2011).
29. Riemer, A. *et al.* The p97-Ufd1-Npl4 ATPase complex ensures robustness of the G2/M checkpoint by facilitating CDC25A degradation. *Cell Cycle* **13**, 919–927 (2014).
30. Radhakrishnan, S. K., den Besten, W. & Deshaies, R. J. p97-dependent retrotranslocation and proteolytic processing govern formation of active Nrf1 upon proteasome inhibition. *eLife* **3**, e01856 (2014).
31. Meyer, H., Bug, M. & Bremer, S. Emerging functions of the VCP/p97 AAA-ATPase in the ubiquitin system. *Nat. Cell Biol.* **14**, 117–123 (2012).
32. Magnaghi, P. *et al.* Covalent and allosteric inhibitors of the ATPase VCP/p97 induce cancer cell death. *Nat. Chem. Biol.* **9**, 548–556 (2013).
33. Samali, A., Fitzgerald, U., Deegan, S. & Gupta, S. Methods for monitoring endoplasmic reticulum stress and the unfolded protein response. *Int. J. Cell Biol.* **2010**, 830307 (2010).
34. Auner, H. W. *et al.* Combined inhibition of p97 and the proteasome causes lethal disruption of the secretory apparatus in multiple myeloma cells. *PLoS ONE* **8**, e74415 (2013).
35. Soriano, G. P. *et al.* Proteasome inhibitor-adapted myeloma cells are largely independent from proteasome activity and show complex proteomic changes, in particular in redox and energy metabolism. *Leukemia* **30**, 2198–2207 (2016).
36. Lass, A., McConnell, E., Fleck, K., Palamarchuk, A. & Wójcik, C. Analysis of Npl4 deletion mutants in mammalian cells unravels new Ufd1-interacting motifs and suggests a regulatory role of Npl4 in ERAD. *Exp. Cell Res.* **314**, 2715–2723 (2008).
37. Voráčková, I., Suchanová, S., Ulbrich, P., Diehl, W. E. & Ruml, T. Purification of proteins containing zinc finger domains using immobilized metal ion affinity chromatography. *Protein Expr. Purif.* **79**, 88–95 (2011).
38. Holdgate, G. *et al.* Biophysical methods in drug discovery from small molecule to pharmaceutical. *Methods Mol. Biol.* **1008**, 327–355 (2013).
39. Lomenick, B. *et al.* Target identification using drug affinity responsive target stability (DARTS). *Proc. Natl Acad. Sci. USA* **106**, 21984–21989 (2009).
40. Becker, L. A. *et al.* Therapeutic reduction of ataxin-2 extends lifespan and reduces pathology in TDP-43 mice. *Nature* **544**, 367–371 (2017).
41. Guo, L. *et al.* A cellular system that degrades misfolded proteins and protects against neurodegeneration. *Mol. Cell* **55**, 15–30 (2014).
42. Kim, Y. E., Hipp, M. S., Bracher, A., Hayer-Hartl, M. & Hartl, F. U. Molecular chaperone functions in protein folding and proteostasis. *Annu. Rev. Biochem.* **82**, 323–355 (2013).
43. Dai, C. & Sampson, S. B. HSF1: guardian of proteostasis in cancer. *Trends Cell Biol.* **26**, 17–28 (2016).
44. Cvek, B. Targeting malignancies with disulfiram (Antabuse): multidrug resistance, angiogenesis, and proteasome. *Curr. Cancer Drug Targets* **11**, 332–337 (2011).
45. Deshaies, R. J. Proteotoxic crisis, the ubiquitin–proteasome system, and cancer therapy. *BMC Biol.* **12**, 94 (2014).
46. Anderson, D. J. *et al.* Targeting the AAA ATPase p97 as an approach to treat cancer through disruption of protein homeostasis. *Cancer Cell* **28**, 653–665 (2015).
47. Cui, Y. *et al.* High expression of valosin-containing protein predicts poor prognosis in patients with breast carcinoma. *Tumour Biol.* **36**, 9919–9927 (2015).
48. Yamamoto, S. *et al.* Expression of valosin-containing protein in colorectal carcinomas as a predictor for disease recurrence and prognosis. *Clin. Cancer Res.* **10**, 651–657 (2004).
49. Tsujimoto, Y. *et al.* Elevated expression of valosin-containing protein (p97) is associated with poor prognosis of prostate cancer. *Clin. Cancer Res.* **10**, 3007–3012 (2004).

Supplementary Information is available in the online version of the paper.

Acknowledgements We thank J. Škvor, M. Zadinová, J. Večerka and D. Doležal for help with animal experiments, Jana Vrbkova for statistical analysis, D. Fridecky and T. Adam for help with HPLC, I. Protivankova and M. Grønvig Nielsen for technical assistance. This work was supported by grants from the Kellner Family Foundation, Czech National Program of Sustainability, Grant Agency of the Czech Republic, MEYS CR project Czech-Biologing, the Czech Health Research Council, of the Danish Cancer Society, the Danish National Research Foundation (project GARD), the Danish Council for Independent Research, the Novo Nordisk Foundation, the Czech Cancer League, the Swedish Research Council, Cancerfonden of Sweden, the European Commission (EATRIS), the Czech Ministry of Education, youth and sports (OPVKCZ), Cancer Research Czech Republic and the Howard Hughes Medical Institute.

Author Contributions Z.S., M.Mis., B.C., R.J.D. and J.Barte. conceived the study. Z.S. and M.Mis. performed most biochemical and microscopy experiments and wrote the manuscript. D.M. established the expression cell lines and performed most cytotoxicity tests. T.O., P.D. and I.V. performed the HPLC experiments. K.K.A., S.F. and J.O. performed the epidemiological analyses. J.Bartk. performed the immunohistochemical analyses. J.V. and P.D. performed DARTS experiments. P.M. performed cell death analyses. Z.T. performed cytotoxicity tests and heat-shock response analyses. A.K. performed cytotoxicity tests. A.M. designed and performed phlebotomies of patients treated with Antabuse. M.Mic. performed the ITC. J.G. performed FACS analyses, cell death assays and cell sorting. J.S. performed 20S proteasome assays. J.L. performed 26S proteasome assays. M.K. and C.D. performed the cytotoxicity experiments on myeloid- and patient-derived cell lines. P.P., J.M. and M.H. performed mouse experiments. J.Barte., B.C., Q.P.D. and R.J.D. helped to design the experiments, interpreted the data and wrote/edited the manuscript. All authors approved the manuscript.

Author Information Reprints and permissions information is available at www.nature.com/reprints. The authors declare competing financial interests: details are available in the online version of the paper. Readers are welcome to comment on the online version of the paper. Publisher's note: Springer Nature remains neutral with regard to jurisdictional claims in published maps and institutional affiliations. Correspondence and requests for materials should be addressed to J.Barte. (jb@cancer.dk), B.C. (cvekb@seznam.cz) and R.J.D. (deshai@caltech.edu).

Reviewer Information Nature thanks P. Brossart and the other anonymous reviewer(s) for their contribution to the peer review of this work.

METHODS

The experiments were not randomized.

Epidemiological analyses and access to health registers. We conducted a population-based cohort study by combining Danish nationwide demographic and health registers. This study was approved by the Danish Data Protection Agency and Statistics Denmark's Scientific Board. As the epidemiological study was based solely on register data and did not involve any contact with patients, no ethical approval was required from the Danish Scientific Ethical Committee⁵⁰. The cohort consisted of all Danes aged 35–85 years with a first-time diagnosis of cancer between January 2000 and December 2013. Because DSF (Antabuse) is a relative contra-indication among individuals with liver or kidney diseases, we excluded patients with cancers of the liver or kidney from the cohort. Cohort members were categorized according to use of DSF into two main groups: (i) those who filled at least one prescription of DSF within five years before the cancer diagnosis, but did not fill DSF prescription(s) during the first year after the diagnosis (previous users), that is, individuals suffering from alcoholism but taking DSF only before their cancer diagnosis; and (ii) those who used DSF before their cancer diagnosis and also filled one or more DSF prescriptions during the first year after the cancer diagnosis (continuing users), that is, individuals who underwent DSF therapy both before and after the cancer diagnosis. We also defined a category of patients with cancer who did not fill prescription(s) for DSF either before or after (≤ 1 year) the cancer diagnosis (never users). In the main analyses, we calculated hazard ratios and 95% confidence intervals estimating cancer-specific mortality among continuing DSF users compared to previous DSF users based on a Cox model regressing on both propensity scores and disulfiram use. By including propensity scores in the regression, we used demographic data and comorbid conditions/diagnostic codes as well as prescription data for selected concomitant drugs, to balance baseline characteristics of previous and continuing users of DSF and to adjust estimated hazard ratios of cancer-specific mortality associated with DSF use⁵¹. The patients with cancer were followed from one year after the diagnosis until death, migration or end of study (31 December 2014). The propensity scores thus estimate the probability of being treated with DSF in the exposure window 0–1 year after the cancer diagnoses conditional on the following other covariates in the calculation of propensity scores using logistic regression: gender, age at diagnosis, calendar time, highest achieved education and disposable income; medical histories of diabetes mellitus, chronic obstructive pulmonary disease, ischaemic heart disease, congestive heart failure, cerebrovascular disease, atrial fibrillation or atrial flutter, dementia and ulcer disease; and use of non-steroidal anti-inflammatory drugs (NSAIDs; including aspirin), non-aspirin antithrombotic agents (anticoagulants), statins, antihypertensive medication, other cardiovascular drugs, anti-diabetics and psychotropic drugs. In the Cox model, the propensity score is further included as a restricted cubic spline to model possible nonlinearities, in addition to the categorical disulfiram use, which is the variable of interest. Analyses were run for cancer overall and for breast, prostate and colon cancer, separately. Furthermore, all analyses were stratified by stage (localized, non-localized or unknown). Statistical significance of DSF use was evaluated by likelihood ratio tests. We used the software R for statistical computing⁵².

In vivo tumour experiments. The human breast cancer cell line MDA-MB-231 was injected (10^7 cells transplanted subcutaneously) to grow tumours in athymic NU/NU female mice (AnLab Ltd) with a body weight of 23.6–26.9 g, aged 12 weeks. Inclusion criteria were: female, appropriate age and weight (15–30 g). Exclusion criteria were: tumour size must not exceed 20 mm (volume $4,000 \text{ mm}^3$) in any direction in an adult mouse, the tumour mass should not proceed to the point where it significantly interferes with normal bodily functions, or causes pain or distress owing to its location, persistent self-induced trauma, rapid or progressive weight loss of more than 25%, for seven days. In none of the experiments were these approved ethical limits exceeded. After the tumours grew to $0.114\text{--}0.117 \text{ cm}^3$ on average, mice were randomly divided into four groups, each of eight mice, and treated as follows: (i) normal diet; (ii) normal diet plus oral administration of 0.15 mg kg^{-1} copper gluconate (CuGlu); (iii) normal diet plus oral administration of 50 mg kg^{-1} DSF; (iv) normal diet plus oral administration of 0.15 mg kg^{-1} CuGlu and 50 mg kg^{-1} DSF. Administration of compounds was carried out as a blinded experiment (all information about the expected outputs and the nature of used compounds were kept from the animal technicians). CuGlu was administered each day in the morning (08:00) and DSF each day in the evening (19:00) to mimic a clinical trial combining DSF and CuGlu in treatment of tumours involving the liver (NCT00742911). After treatment began, mice were weighed and their tumours measured twice per week. At day 32, mice were euthanized, and the tumours were removed and frozen at -80°C . The experiment was evaluated by comparing growth curves of tumours in the experimental groups with those in controls. The rates of tumour growth inhibition (TGI) were calculated by the formula $\text{TGI} = (1 - V_{\text{treated}}/V_{\text{control}})$ where V_{treated} is the mean of tumour volumes in the treated group and V_{control} is the mean of tumour volumes in the control group).

Mean tumour volume values at specific time intervals were statistically evaluated. To test directly the effect of CuET, we used MDA-MB-231 and AMO-1 models. MDA-MB-231 was injected (5×10^6 cells were transplanted subcutaneously) to grow tumours in SCID mice (ENVIGO) aged 10 weeks (± 2 weeks). AMO-1 xenografts were expanded in SCID mice. Each group consisted of 10 animals, each bearing two tumours. CuET was formulated in bovine serum albumin solution (1%) to a final concentration of 1 mg ml^{-1} . CuET was applied intraperitoneally with a schedule of five days on and two days off. All aspects of the animal study met the accepted criteria for the care and experimental use of laboratory animals, and protocols were approved by the Animal Research Committee of the 1st Faculty of Medicine Charles University in Prague and Ethical Committee of Faculty of Medicine and Dentistry, Palacky University in Olomouc. For HPLC-MS and immunohistochemistry analysis, we used MDA-MB-231 xenografted mice treated with the same DSF and DSF plus copper gluconate regime as described for the anti-cancer activity assessment with the notable difference that mice were euthanized after five days of treatment.

HPLC-MS analysis of CuET. The HR-MRM analysis was performed on a HPLC-ESI-QTOF system consisting of HPLC chromatograph Thermo UltiMate 3000 with AB Sciex TripleTOF 5600+ mass spectrometer, using the DuoSpray ESI source operated at an ion source voltage of 5,500 V, ion source gas flow rates of 40 units, curtain gas flow rate of 30 units, declustering potential of 100 V and temperature 400°C . Data were acquired in product ion mode with two parent masses (358.9 and 360.9) for analysis of CuET. Chromatographic separation was done by PTFE column, which was especially designed for analysis of strong metal chelators filled by C18 sorbent (IntellMed, IM_301). A analysis was performed at room temperature and with a flow rate of $1,500 \mu\text{l min}^{-1}$ with isocratic chromatography. Mobile phase consisted of HPLC grade acetone (Lachner) 99.9%, HPLC water (Merck Millipore) 0.1% and 0.03% HPLC formic acid (Sigma-Aldrich). Acquired mass spectra were evaluated in software PeakView 1.2. Extracted ion chromatograms of transitions 88.0 and 116.0 (common for both parent masses) with a 0.1 mass tolerance were Gaussian smoothed with width of two points. Peak area was then recorded and recalculated to ng ml^{-1} according to the calibration curve.

Sample preparation for HPLC-MS analysis. Liquid nitrogen-frozen biological samples were cut into small pieces using a scalpel. Samples (30–100 mg) were immediately processed by homogenization in 100% acetone in a ratio of 1:10 sample: acetone (for plasma or serum the ratio was 1:4). Homogenization was done in a table-top homogenizer (Retsch MM301) placed in a cold room (4°C) in 2-ml Eppendorf tubes with 2 glass balls (5 mm) for 1 min at 30 Hz. The tube was immediately centrifuged at 4°C , $20,000g$ for 2 min. Supernatant was decanted into a new 1.5-ml Eppendorf tube and immediately centrifuged for 30 min using a small table-top centrifuge (BioSan FVL-2400N) placed inside a -80°C freezer. Supernatant was quickly decanted into a glass HPLC vial and kept at -80°C for no longer than 6 h. Just before the HPLC analysis, the vial was placed into a pre-cooled (4°C) LC-sample rack and immediately analysed. To enable an approximate quantification of analysed CuET, a calibration curve was prepared. Various amounts of CuET were spiked in plasma, frozen in liquid nitrogen, and placed at -80°C to mimic sample processing. Standards were then processed as the samples described above. To measure circulating CuET concentrations, mice were given a single oral dose of DSF (50 mg kg^{-1}) and euthanized at different time points. Serum was collected and frozen for analysis.

Blood collection from humans for HPLC-MS analysis of CuET. Blood samples were collected before and 3 h after oral application of DSF (Antabuse, 400 mg) dissolved in water. Phlebotomy needles were specific for metal analysis—Sarstedt Safety Kanule $21G \times 1\frac{1}{2}$ inches, 85.1162.600. Collection tubes were specific for metal analysis—Sarstedt, S-Monovette 7.5 ml LH, 01.1604.400. Immediately after blood collection samples were centrifuged in a pre-cooled centrifuge (4°C at 1,300g for 10 min). After centrifugation, tubes were placed on ice and the plasma fraction was immediately aliquoted into the 1.5-ml Eppendorf tubes with approximately $500 \mu\text{l}$ per tube. The tubes with plasma were immediately frozen on dry ice and later stored in -80°C . Blood samples were collected from volunteers who gave informed consent and were undergoing Antabuse therapy because of alcohol abuse. Participants were four males (aged 34, 38, 41, 60 years) and five females (aged 37, 56, 46, 59, 63 years). All individuals were freshly diagnosed for alcohol-use disorder and were scheduled for Antabuse therapy. Blood samples were collected before and after the first use of Antabuse. All relevant ethical regulations were followed for the study. The study, including the collection of blood samples, was approved by the Ethical Committee of Faculty of Medicine and Dentistry, Palacky University in Olomouc.

Cell lines. Cell lines were cultured in appropriate growth medium supplemented with 10% fetal bovine serum (FBS) and penicillin–streptomycin; and maintained in a humidified, 5% CO_2 atmosphere at 37°C . Cell lines cultured in DMEM medium were: HCT116 (ATCC), DU145 (ECACC), PC3 (ECACC), T47D (NCI60),

HS578T (NCI60), MCF7 (ECACC), MDA-MB-231 (ATCC), U2OS (ECACC), HeLa (ATCC), NIH-3T3 (ATCC), CAPAN-1 (ATCC), A253 (ATCC), FaDu (ATCC), h-TERT-RPE1 (ATCC), HeLa-Ub(G76V)-GFP-ODD-Luc²¹. Cell lines cultured in RPMI1640 medium were: NCI-H358 (ATCC), NCI-H52 (ATCC), HCT-15 (ATCC), AMO-1 (ATCC), MM-1S (ATCC), ARH77 (ATCC), RPMI8226 (ATCC), OVCAR-3 (NCI60), CCRF-CEM (ATCC), K562 (ATCC), 786-0 (NCI60). Cell lines cultured in EMEM medium were: U87-MG (ATCC), SiHA (ATCC). Cell line A549 (ATCC) was cultured in F12K medium, HT29 (ATCC) in McCoy's medium and LAPC4 (provided by Z. Culig, University of Innsbruck) in IMDM medium supplemented with metribolone R1881 (Sigma-Aldrich). RWPE-1 (ATCC) cells were cultured in a keratinocyte serum-free medium supplemented with bovine pituitary extract and human recombinant epidermal growth factor (Thermo Fisher Scientific). BTZ- and CFZ-resistant multiple myeloma cell lines were previously described in ref. 35. Cell lines were tested for mycoplasma contamination and authenticated by STR method. None of the cell lines used in this study is listed in the database of commonly misidentified cell lines maintained by ICLAC.

Stable cell line construction. For construction of all stably transfected cell lines we used the U2OS cell line (ECACC). For U2OS Ub-GFP, we used the commercial Ub-GFP EGFP-C1 vector (Addgene); for U2OS NPL4-GFP, we used the commercial NPLOC4-GFP pCMV6-AC-GFP vector (Origene); for U2OS p97-GFP, we used the commercial VCP-GFP pCMV6-AC-GFP vector (Origene); and for U2OS UFD1-GFP, we used the commercial UFD1L-GFP pCMV6-AC-GFP vector (Origene). Cells were transfected using Promega FugeneHD according to the manufacturer's instructions. Cells were further cultured in the appropriate antibiotics (geneticin, 400 µg ml⁻¹). Medium with geneticin was replaced every 2–3 days until the population of resistant cells was fully established. Cells were further refined by sorting for cells expressing GFP (BD FACS Aria). For preparation of inducible NPL4(MUT)-GFP cells, U2OS cells were transfected with a pcDNA6/TR plasmid (Invitrogen, V1025-20) using the FugeneHD transfection reagent (Promega, E2311) according to the manufacturer's protocol. To generate a cell line that stably expressed the Tet repressor, U2OS cells were cultured in selective medium with blasticidin (10 µg ml⁻¹) for 10 days. Blasticidin-resistant colonies were picked, expanded and screened for clones that exhibited the lowest basal levels and highest inducible levels of expression. Next, the most suitable clones were transfected with the pCDNA4/TO expression vector encoding the mutated NPL4-GFP protein using the Fugene transfection reagent. Cells were cultured in medium with zeocin (500 µg ml⁻¹) to select clones that contain pcDNA4/TO-mutated NPL4-GFP. The NPL4(MUT)-GFP-encoding plasmid was obtained from Geneti Biotech. To induce expression of protein, cells were incubated with doxycycline (Sigma-Aldrich) 1 µg ml⁻¹ for 16–48 h.

Colony-formation assay. Cells were seeded into six-well plates at 100–300 cells per well (depending on the cell line). The next day, cells were treated with compounds as indicated in the specific experiments and kept in culture for 7–14 days. Colonies were visualized by crystal violet and counted.

XTT assay. Cells were plated at a density of 10,000 per well in a 96-well plate. The next day, cells were treated as indicated. After 24 h, an XTT assay was performed according to the manufacturer's instructions (Applchem). XTT solution was added to the medium and incubated for 30–60 min, and then the dye intensity was measured at the 475 nm wavelength using a spectrometer (TECAN, Infinite M200PRO). Results are shown as mean ± s.d. from three independent experiments, each performed in triplicate. For LD₅₀ analysis across the panel of cell lines listed in Extended Data Fig. 2b, cell lines were treated with various doses (at least five doses) for 48 h. LD₅₀ values were calculated using Graphpad Prism software based on survival curves from at least two independent experiments.

Annexin V staining. Cell cultures were treated as indicated and collected by trypsinization. Initial culture medium and washing buffer were collected to include detached cells. Cells were centrifuged (250g, 5 min) and re-suspended in a staining buffer (140 mM NaCl, 4 mM KCl, 0.75 mM MgCl₂, 10 mM HEPES) containing 2.5 mM CaCl₂, Annexin-V-APC (1:20, BD Biosciences) and 2.5 µg ml⁻¹ 7-AAD (BD Biosciences) for 15 min on ice in the dark. Samples were analysed by flow cytometry using BD FACSVerser (BD Biosciences) and at least 10,000 events were acquired per sample. Collected data were processed using BD FACSSuite (BD Biosciences) and exported into Microsoft Excel.

Caspases 3/7 assay. Activity of caspase-3 and -7 was quantified by cleavage of fluorogenic substrate CellEvent Caspase-3/7 Green Detection Reagent (Thermo Fisher Scientific). In brief, samples prepared in the same staining buffer as described for annexin V staining above, supplemented with 2% FBS, 0.5 µM CellEvent Caspase-3/7 Green Detection Reagent and incubated for 45 min at room temperature in the dark. Subsequently, 0.5 µg ml⁻¹ DAPI was added and samples were analysed by flow cytometry using BD FACSVerser (BD Biosciences) and at least 10,000 events were acquired per sample. Collected data were processed using BD FACSSuite (BD Biosciences) and exported into Microsoft Excel.

Viability assay of multiple myeloma cells. The CellTiter 96 MTS-assay (Promega) was used according to the manufacturer's instructions to determine the cell viability of BTZ (Janssen Cilag), CFZ and CuEt in cell lines and the absorbance of the formazan product was measured in 96-well microplates at 492 nm. The assay measures dehydrogenase enzyme activity found in metabolically active cells.

For patient cells, the more sensitive luminescent CellTiterGlo assay (Promega) was used to determine cell viability, measured by ATP production of metabolically active cells. The primary myeloma cell samples were obtained after written informed consent and approval by the independent ethics review board (St Gallen ethics committee—Ethikkommission Ostschweiz), in accordance with ICH-GCP and local regulations. Malignant plasma cells were retrieved by PBMC isolation from a patient with multiple myeloma progressing under BTZ-containing therapy, based on IMWG criteria (BTZ-resistant) and an untreated patient with multiple myeloma (BTZ-sensitive). The purity of the cell samples was >80% myeloma cells, as assessed by morphology.

Immunoblotting and antibodies. Equal amounts of cell lysates were separated by SDS-PAGE on hand-cast or precast tris-glycine gradient (4–20%) gels (Life Technologies), and then transferred onto a nitrocellulose membrane. The membrane was blocked with 5% bovine milk in Tris-buffered saline containing 0.1% Tween-20 for 1 h at room temperature, and then incubated overnight at 4 °C or for 1 h at room temperature, with one of the following primary antibodies (all antibodies were used in the system under study (assay and species) according to the instructions of the manufacturer): anti-ubiquitin (1:1,000; Cell Signaling, 3933), anti-H2A, acidic patch (1:1,000; Merck Millipore, 07-146), anti-monoubiquityl-H2A (1:1,000; Merck Millipore, clone E6C5), anti-IκBα (1:500; Santa Cruz Biotechnology, sc-371), anti-p53 (1:500; Santa Cruz Biotechnology, clone DO-1), anti-HIF-1α (1:1,000; BD Biosciences, 610958), anti-CDC25A (1:500; Santa Cruz Biotechnology, clone DCS-120), anti-NRF1 (1:1,000; Cell Signaling, clone D5B10), anti-VCP (1:2,000; Abcam, ab11433), anti-VCP (1:1,000; Novus Bio, NBP100-1557), anti-NPLOC4 (1:1,000; Novus Bio, NBP1-82166), anti-ubiquitin lys48-specific (1:1,000; Merck Millipore, clone Apu2), anti-β-actin (1:2,000; Santa Cruz Biotechnology, sc-1616; or 1:500, Santa Cruz Biotechnology, sc-87778), anti-GAPDH (1:1,000; GeneTex, clone 1D4), anti-lamin B (1:1,000; Santa Cruz Biotechnology, sc-6217), anti-calnexin (1:500; Santa Cruz Biotechnology, sc-11397), anti-α-tubulin (1:500; Santa Cruz Biotechnology, sc-5286), anti-XBP1 (1:500; Santa Cruz Biotechnology, sc-7160), UFD1 (1:500; Abcam, ab155003), cleaved PARP1 (1:500; Cell Signaling, 9544), p-eIF2α (1:500; Cell Signaling, 3597), ATF4 (1:500; Merck Millipore, ABE387), HSP90 (1:500; Enzo, ADI-SPA-810), HSP70 (1:500; Enzo, ADI-SPA-830), HSF1 (1:500; Cell Signaling, 4356), p-HSP27 (1:1,000; Abcam, 155987), HSP27 (1:1,000; Abcam, 109376) followed by detection by secondary antibodies: goat anti-mouse IgG-HRP (GE Healthcare), goat anti-rabbit (GE Healthcare), donkey anti-goat IgG-HRP (Santa Cruz Biotechnology, sc-2020). Bound secondary antibodies were visualized by ELC detection reagent (Thermo Fisher Scientific) and images were recorded by imaging system equipped with CCD camera (ChemIDoc, Bio-Rad) operated by Image Laboratory software or developed on film (Amersham).

Immunofluorescence staining. Cells were grown in 24-well plates with a 0.170-mm glass bottom (In Vitro Scientific). Where indicated, the cells were pre-extracted before fixation with pre-extraction buffer (10 mM PIPES pH 6.8, 100 mM NaCl, 1.5 mM MgCl₂, 300 mM sucrose, 0.5% Triton X-100, 1 mM DTT, 5 µg ml⁻¹ leupeptin, 2 µg ml⁻¹ aprotinin, 0.1 mM PMSF) for 20 min at 4 °C, washed by PBS and then immediately fixed with 4% formaldehyde for 15 min at room temperature. Cells were stained with primary antibodies: anti-ubiquitylated conjugated mouse FK2 antibody (1:500; Enzo, BML-PW8810), anti-VCP (1:500; Abcam, ab11433), anti-NPL4 (1:500; Novus Bio, NBP1-82166), HSP70 (1:100; Enzo, ADI-SPA-830), HSF1 (1:500; Cell Signaling, 4356), anti-ubiquitin lys48-specific (1:500; Merck Millipore, clone Apu2), SUMO2/3 (1:500; Abcam, ab3742), TDP43 (1:300; Proteintech, 10782-2-AP) and appropriate Alexa Fluor 488- and 568-conjugated secondary antibodies (Invitrogen, 1:1,000). Cytochrome c was stained using an Alexa Fluor 555-conjugated mouse anti-cytochrome c antibody according to the manufacturer's protocol (BD Pharmingen, 558700).

Microscopy, FRAP and image analysis. Samples were analysed using a Zeiss Axiomager Z.1 platform equipped with the Elyra PS.1 super-resolution module for structured illumination (SIM) and the LSM780 module for CLSM. High resolution images were acquired in super-resolution mode using a Zeiss Pln Apo100×/1.46 oil objective (total magnification, 1,600×) with appropriate oil (Immersion Oil 518F). SR-SIM setup involved five rotations and five phases for each image layer and up to seven z-stacks (101 nm) were acquired per image. The CLSM setup for FRAP and life cells acquisition had a c-Apo 40×/1.2 W water immersion objective. Bleaching of regions of interest (ROIs) was performed using an Argon 488 nm laser. Lower resolution images of fixed samples were acquired using a Plan Apo 63×/1.4 oil objective (total magnification 1,008×). FRAP and image acquisitions were performed using Zeiss Zen 11 software. For FRAP, internal Zen's 'Bleach'

and 'Regions' modules were used. Data from FRAP analysis involving multiple bleached ROIs were exported into Microsoft Excel and plotted. Basic processing of acquired images, such as contrast and brightness settings, was done in Adobe Photoshop on images exported as TIFFs. Quantitative microscopy-based cytometry of the immunofluorescence-stained samples was performed using an automatic inverted fluorescence microscope BX71 (Olympus) using ScanR Acquisition software (Olympus) and analysed with ScanR Analysis software (Olympus).

Cell fractionation on Triton-X100 insoluble pellets. Cells were treated as indicated, washed in cold PBS and lysed in lysis buffer (50 mM HEPES pH 7.4, 150 mM NaCl, 2 mM MgCl₂, 10% glycerol, 0.5% Triton X-100, protease inhibitor cocktail by Roche) for 10 min gently agitating at 4 °C. Then, cells were scraped into Eppendorf tubes and kept for another 10 min on ice with intermittent vortexing. After that, the lysate was centrifuged at 20,000g for 10 min at 4 °C. The insoluble fraction and supernatant were separately re-suspended in 1 × LSB buffer.

Isolation of microsomal fraction. After the desired treatment in cell culture, cells were washed with cold PBS and lysed (250 mM sucrose, 20 mM HEPES pH 7.4, 10 mM KCl, 1.5 mM MgCl₂, 1 mM EDTA, 1 mM DTT, protease inhibitor cocktail). Lysates were homogenized by Potter-Elvehjem PTFE homogenizer and kept on ice for 20 min. The homogenates were subjected to serial centrifugation steps (720g and 10,000g for 5 min each, and 100,000g for 1 h). Pellets and supernatants from the last ultracentrifugation step were resuspended in the 1 × LSB buffer and used for western blot analysis.

Immunoperoxidase staining of pre-extracted tissue sections. Frozen sections (4–5 μm thick) from xenograft-grown, cryopreserved tumour tissues were cut on a cryostat and placed on commercial adhesion slides (SuperFrost Plus, Menzel, Germany) and air-dried for 2 h at room temperature. The dried sections were carefully covered with the cold extraction buffer: 50 mM Tris-HCl (pH 7.5), 150 mM NaCl, 1 mM MgCl₂, 5% glycerol, 1 mM DTT, 1% Triton X-100, 1% IGEPAL, protease inhibitor cocktail (Phos Stop Easy pack, 04906837001, Roche) or cold PBS (controls) and incubated in a cold room for 20 min. Pre-extracted and control PBS-treated sections were gently washed three times in cold PBS, and fixed in 4% paraformaldehyde fixative for 15 min, followed by another three washes in PBS. Washed sections were then subject to a sensitive immunoperoxidase staining protocol, using the primary rabbit monoclonal antibody against VCP antibody (EPR3307(2)) (1:10,000; ab109240, Abcam) and rabbit polyclonal antibody against NPLC4 (1:500; NBPI-82166, Novus Biologicals) and Vectastain Elite kit as secondary reagents (Vector Laboratories, USA), followed by a nickel-sulfate-enhanced diaminobenzidine reaction without nuclear counterstaining, mounted and microscopically evaluated and representative images documented by an experienced oncopathologist.

Isothermal titration calorimetry (ITC). Experiments were performed at 25 °C with a Nano ITC Low Volume (TA Instruments) and analysed by Nano Analyze Software v.2.3.6. During all measurements, injections of 2.5 μl of ligand (16 μM) were titrated into 250 μl protein (2 μM) with time intervals of 300 s, a stirring speed of 250 r.p.m. All ITC experiments were conducted with degassed buffered solutions 20 mM HEPES buffer pH 7.3, in the presence of 1% DMSO. Purified GST-NPL4(WT) and GST-NPL4(MUT) proteins were used in ITC experiment.

Drug affinity responsive target stability (DARTS). DARTS was performed according to a modified published protocol³⁸. Purified GST-NPL4(WT) and GST-NPL4(MUT) proteins were diluted by 100 mM phosphate buffer, pH 7.4 to final concentration of 0.03 μg μl⁻¹. The proteins were treated with CuET (final concentration of 5 μM; dissolved in DMSO) for 1 h and equal amounts of DMSO were added to the solutions, which served as control samples. Pronase (Sigma-Aldrich) was dissolved in TNC buffer (50 mM Tris-Cl, 50 mM NaCl, 10 mM CaCl₂, pH 7.5). The 0.025 μg of pronase was added to 50 μl of protein solution and incubated for 1 h at 37 °C. Samples without pronase served as the non-digested controls. The pronase reaction was stopped by addition of 5 × SDS loading buffer; the samples were boiled at 95 °C for 15 min and loaded on SDS-PAGE gels. After SDS-PAGE, gels were silver-stained and scanned on a GS-800 Calibrated Densitometer (Bio-Rad) or used for western blot analysis.

20S proteasome activity. To measure proteasome activity in cell extracts, cell lines were seeded in 100-mm Petri dishes at a density of 3×10^6 cells per dish. After 24 h, cells were washed twice with 2 ml of ice-cold PBS and scraped in to 1,000 μl ice-cold PBS. The cells were then isolated and suspended in buffer (50 mM HEPES (pH 7.5), 150 mM NaCl, 1% Triton X-100 and 0.1 μM PMSF) and then centrifuged at 15,000 r.p.m. for 15 min at 4 °C. The cell lysates (10 μg) were incubated with 20 μM of substrates for measurement of chymotrypsin-like, trypsin-like and caspase-like activities (Suc-LIVT-AMC, Ac-RLR-AMC and Z-LLE-AMC (Boston Biochem)) in 90 μl of assay buffer (30 mM Tris-HCl, 0.035% sodium dodecylsulfate (pH 7.4)) in the presence CuET (1 μM and 5 μM) and BTZ (1 μM) for the investigation of proteasome inhibition; BTZ or an equivalent volume of solvent (DMSO) was used as a control. After 2 h of incubation at 37 °C, inhibition of proteasome activity was measured by the release of hydrolysed free AMC groups by fluorimeter at

380/460 nm (TECAN, Infinite M200PRO). To measure proteasome activity in live cells, the cells were seeded in 24-well plate at a density of 0.2×10^6 cells per well. Cell lines were treated with CuET (1 μM and 5 μM), vehicle control or 1 μM BTZ for 1 h. After incubation, cells were twice washed with 0.5 ml of 1 × ice-cold PBS and scraped into 100 μl ice-cold lysis buffer and then centrifuged at 15,000 r.p.m. for 15 min at 4 °C. Subsequently, the cell extract (10 μg) was incubated with 20 μM substrates to measure chymotrypsin-like, trypsin-like and caspase-like activities in assay buffer (30 mM Tris-HCl (pH 7.4)). After 2 h of incubation at 37 °C, inhibition of proteasome enzymatic activities was measured by the release of hydrolysed free AMC as described above.

Ub(G76V)-GFP degradation. HeLa Ub(G76V)-GFP-ODD-Luc cells expressing Ub(G76V)-GFP were seeded at a density of 10^4 cells per well in 96-well plates. The next day, cells were treated with 4 μM MG132 for 3 h. After that, the medium was discarded and cells were washed twice with PBS and then incubated with the tested compound in the presence of 30 μg ml⁻¹ cycloheximide for another 3 h. The GFP signal was acquired using an ImageXpress automated microscope. For each well, four images were taken (corresponding to 200–250 cells). Cells were analysed every 30 min during 3 h of treatment. Normalized GFP signal intensity was calculated using the following formula: (test compound – background)/(basal GFP signal intensity × background) where 'test compound' is defined as the mean GFP signal intensity of Ub(G76V)-GFP-expressing cells treated with the test compound. 'Background' is defined as the background GFP signal intensity of HeLa cells. 'Basal GFP signal intensity' is defined as mean GFP signal intensity of Ub(G76V)-GFP-expressing cells treated with DMSO. The degradation rate constant (*k*) was obtained from the slope of the linear range of plotting ln(normalized GFP signal intensity) versus time ranging from 90 to 180 min. The percentage of remaining *k* for each compound is calculated using the following formula (test compound/DMSO control) × 100.

p97 ATPase activity assay. p97 ATPase assay was performed as described previously²⁸. A total of 250 nM of p97 protein was diluted in assay buffer (50 mM Tris-HCl pH 7.4, 20 mM MgCl₂, 0.5 mM DTT). Test compounds were added in DMSO (final concentration of DMSO was 5%). After 10 min of incubation, the reaction was started with ATP (100 μM final concentration) followed by a 1-h incubation at room temperature. The reaction was stopped by adding Biolum green solution (Enzo) and free phosphate was measured according to the manufacturer's instructions. Results are expressed as the percentage of activity of the control (a well containing only DMSO).

26S proteasome activity. The RPN11 assay is described in PubChem (AID588493). In brief, a synthetic fluorescently labelled substrate, Ub4pepOG, was used to measure RPN11 activity. Fluorescence polarization assay was performed in a low-volume 384-well solid black plate in the presence of (i) 5 μl of the compound 1,10-phenanthroline or CuEt in 3% DMSO or 3% DMSO control; (ii) 5 μl of BioMol 26S proteasome; and (iii) 5 μl of substrate (15 nM Ub4pepOG). Fluorescence polarization is measured using a plate reader with excitation of 480 nm and emission of 520 nm filter set. The activity was normalized to DMSO control and fit to a dose-response curve.

Protein expression and purification. All proteins were expressed in *E. coli* BL21 (DE3) cells (Novagen). p97-His (pET28a vector) and Ufd1-His (pET28a vector) expression were induced by 1 mM IPTG (Life Technologies) at an OD₆₀₀ of 0.6 for 10 h at 22 °C. NPL4(WT) and NPL4(MUT) (pGEX-2TK) were induced by 0.4 mM IPTG at an OD₆₀₀ of 0.8 overnight at 16 °C. For p97 and UFD1, the bacterial pellet was suspended in buffer (50 mM Tris-HCl pH 8.0, 300 mM NaCl, 2.5 mM MgCl₂, 20 mM imidazole, 5% glycerol) and lysed by sonication and centrifuged (14,000g for 20 min). Proteins were purified by Ni-NTA chromatography (Qiagen) according to the manufacturer's instructions. For p97, the protein was further purified by gel filtration (Superdex 200, GE Healthcare). For GST-NPL4(WT) and GST-NPL4(MUT), the bacterial pellet was suspended in phosphate buffer (PBS, 0.1% Triton X-100, 300 mM NaCl) and lysed by sonication and centrifuged (14,000g for 10 min). Proteins were purified by glutathione sepharose 4B (Life Technologies) according to the manufacturer's protocol. The proteins were further purified by gel filtration (Superdex 200, GE Healthcare).

Chemicals. CuET was prepared by direct synthesis from water solutions of diethyldithiocarbamate sodium salt and copper(II) chloride as described previously⁵³. CuET for *in vivo* experiments was prepared equally with a slight modification. The reaction between diethyldithiocarbamate sodium salt and copper(II) chloride was performed in a sterile 1% aqueous solution of bovine serum albumin. The resulting solution was used directly. The following chemicals were purchased from commercial vendors: tetraethylthiuram disulfide (disulfiram, DSF) (Sigma-Aldrich), sodium diethyldithiocarbamate trihydrate (Sigma-Aldrich), copper D-gluconate (Sigma-Aldrich), BTZ (Velcade, Janssen-Cilag International N.V.), MG132 (Sigma-Aldrich), DBE (Sigma-Aldrich), NMS873 (Abmole), cycloheximide (Sigma-Aldrich), dicoumarol (Sigma-Aldrich), 1,10-phenanthroline (Sigma) and MLN7243 (Active Biochem).

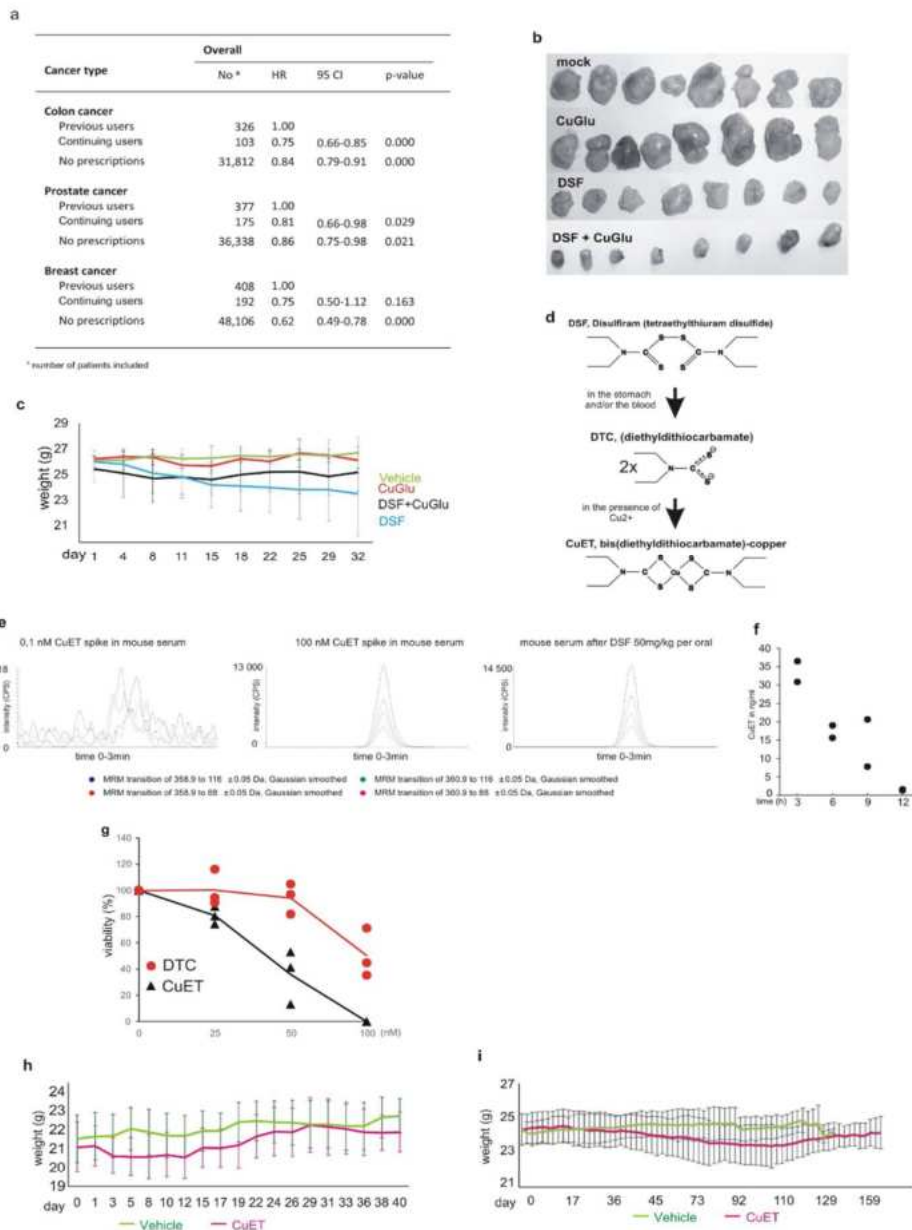
Statistical analyses and reproducibility. For the epidemiological study, we calculated hazard ratios and 95% confidence intervals estimating cancer-specific mortality, based on a Cox model regressing of both propensity scores and disulfiram use, balancing baseline characteristics of previous and continuing users of DSF and adjusting estimated hazard ratios of cancer-specific mortality associated with DSF use⁵¹. The propensity score estimates were conditional on multiple covariates, based on using logistic regression (see 'Epidemiological analyses and access to health registers' for specifics of cohorts and covariates). In the Cox model, the propensity score is further included as a restricted cubic spline to model possible nonlinearities, in addition to the categorical disulfiram use as the variable of interest. Statistical significance of DSF use was evaluated by likelihood ratio tests, using the software R for statistical computing⁵².

For evaluation of the animal studies, STATISTICA software, v.12 (StatSoft) was used to estimate sample size. For a power of 80%, the level of significance set at 5%, 4 groups and RMSSE = 0.8, seven mice per group were estimated. For usage of non-parametrical statistical methods, the number of eight mice per group was finally planned. The differences between tumour volumes were statistically analysed by non-parametrical Kruskal–Wallis test, not requiring any assumptions of normality and homoscedasticity. To test the effect of CuET treatment on survival of AMO-1-xenografted mice, a Kaplan–Meier graph and log-rank statistical test were

used. For other experiments, the statistics, such as number of repetitions, centre value and error bars, are specified in figure legends.

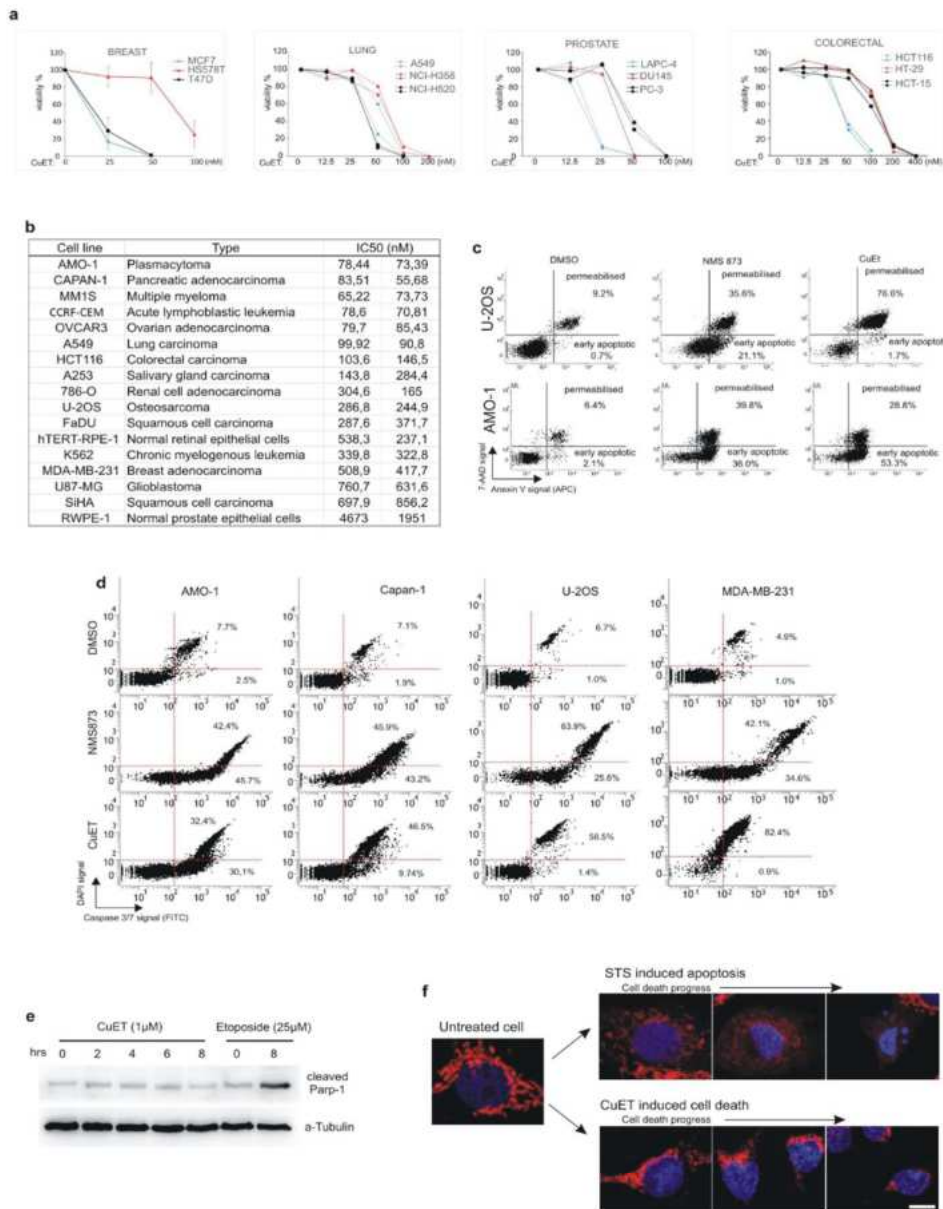
Data availability. Most data generated or analysed during this study are included in the article and its Supplementary Information. Uncropped images of all gels and blots can be found in Supplementary Fig. 1. Source Data for all graphs are provided in the online version of the paper. Additional datasets generated during and/or analysed during the current study and relevant information are available from the corresponding authors upon reasonable request.

50. Thygesen, L. C., Daasnes, C., Thaulow, I. & Brønnum-Hansen, H. Introduction to Danish (nationwide) registers on health and social issues: structure, access, legislation, and archiving. *Scand. J. Public Health* **39** (Suppl), 12–16 (2011).
51. Rosenbaum, P. R. & Rubin, D. B. The central role of the propensity score in observational studies for causal effects. *Biometrika* **70**, 41–55 (1983).
52. R Core Team. *R: A language and environment for statistical computing*. R Foundation for Statistical Computing <https://www.R-project.org/> R v.3.2.3 (2015–12–10) (R Foundation for Statistical Computing, 2016).
53. Čvek, B., Milacic, V., Taraba, J. & Dou, Q. P. Ni(II), Cu(II), and Zn(II) diethyldithiocarbamate complexes show various activities against the proteasome in breast cancer cells. *J. Med. Chem.* **51**, 6256–6258 (2008).



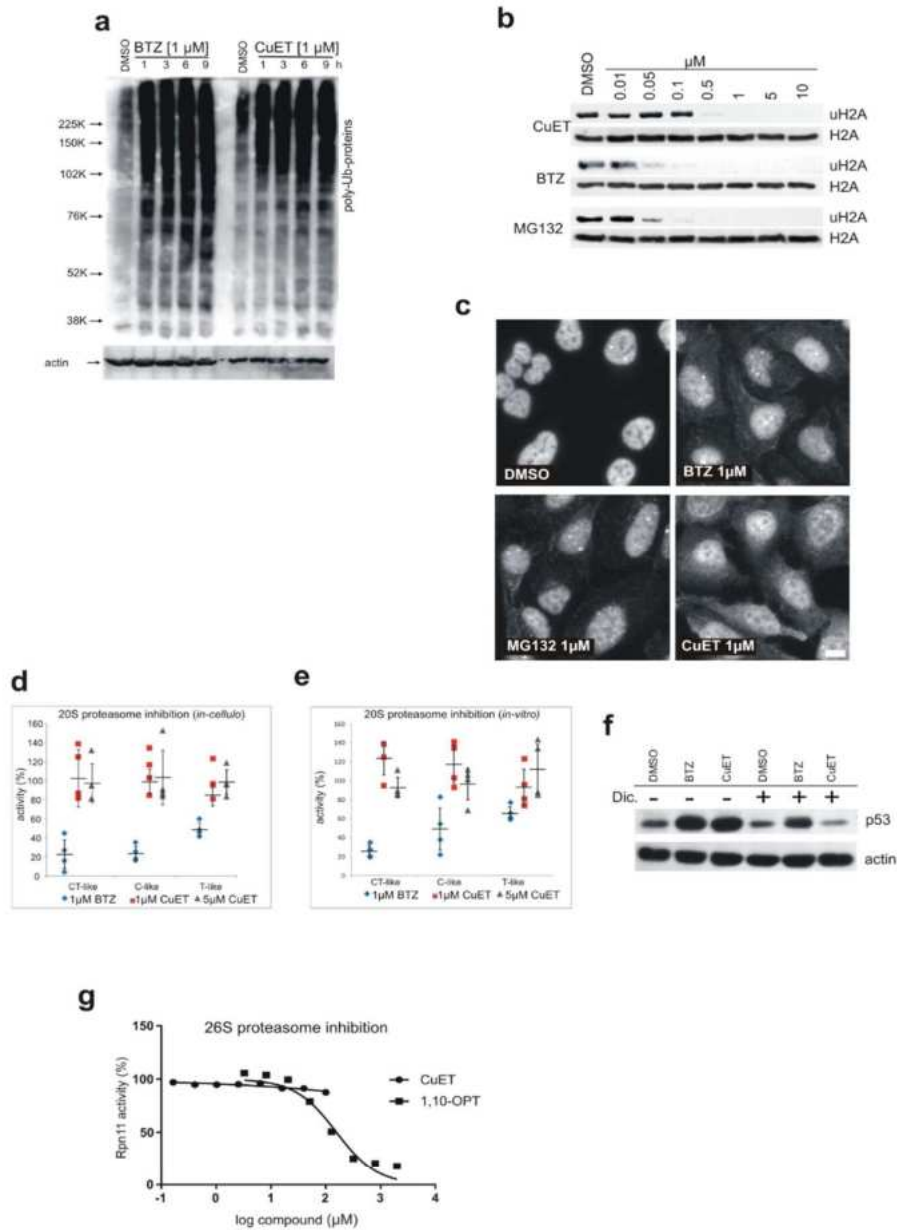
Extended Data Figure 1 | Epidemiological and pre-clinical data of the anti-cancer effects of DSF. **a**, Summary of hazard ratios (HR) and 95% confidence intervals (CI) for cancer-specific mortality among Danish patients with cancer, comparing continuing and previous users of DSF for selected types of cancer (for statistical analysis and definitions of DSF exposure categories, see Methods). **b**, Photographs of subcutaneously growing human MDA-MB-231 tumours extracted from mice at day 32. **c**, Time-course diagram of mouse weight. $n = 8$ animals per group. **d**, Model of CuET formation during metabolic processing of orally administered DSF in the human body. **e**, Examples of mass-spectrometry spectra of

CuET expressed as peaks of 4 MRM transitions in mouse serum after CuET spikes, compared to orally applied DSF (50 mg kg^{-1}). Data are representative of two independent experiments. **f**, Pharmacokinetic analysis of CuET levels in mouse serum after orally applied DSF (50 mg kg^{-1}). $n = 2$ animals per time point. **g**, Effect of DTC and CuET on MDA-MB-231 cells analysed by colony formation assay. $n = 3$ independent experiments. **h**, Time-course diagram of weight in CuET- and vehicle-treated mice. $n = 8$ animals per group. **i**, Extended time-course diagram of weight in CuET- and vehicle-treated mice. $n = 10$ animals per group. Data are mean \pm s.d. (**c**, **h**, **i**) or linked means (**g**).



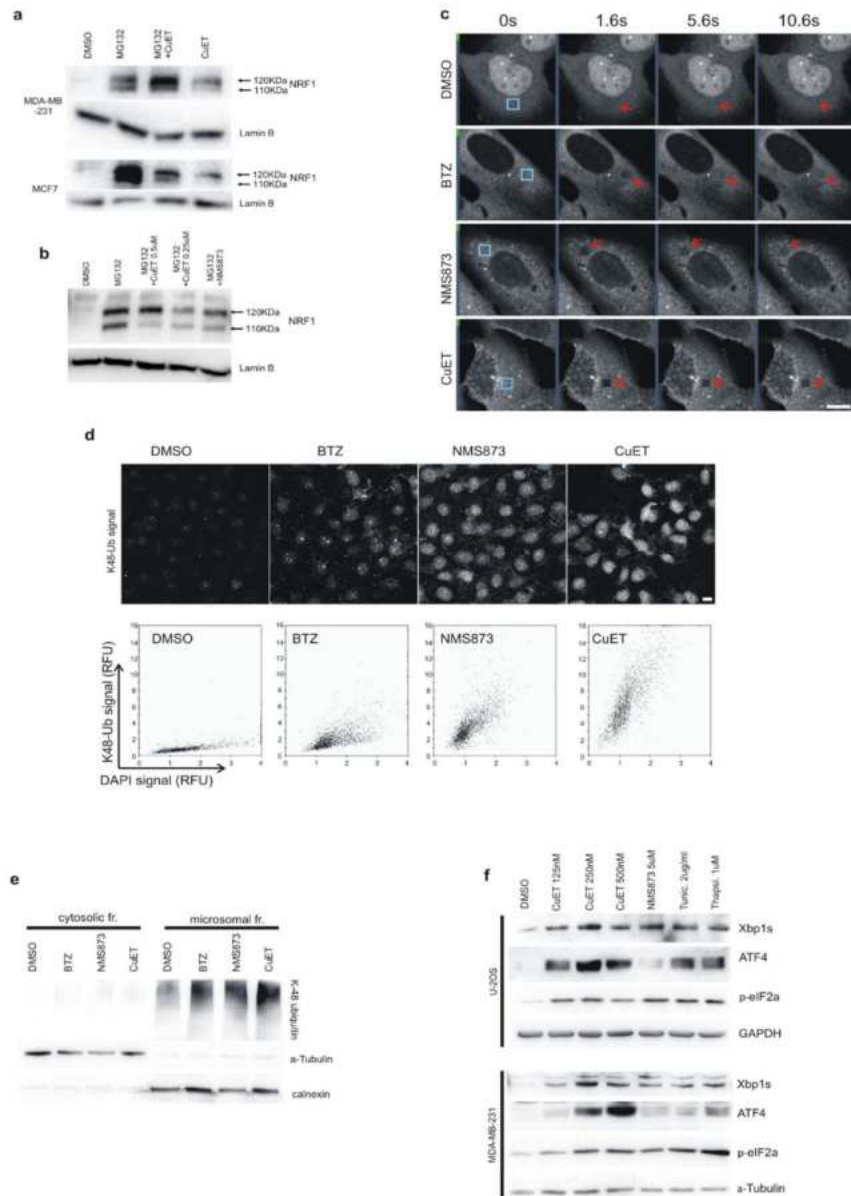
Extended Data Figure 2 | CuET is the major anti-cancer metabolite of DSE. **a**, CuET cytotoxicity measured by a colony-formation assay in human cell lines derived from breast, lung, colon and prostate carcinomas. Data are mean \pm s.d. of three independent biological experiments (breast) or presented individually for two independent biological experiments for each cell line (lung, colon and prostate). **b**, IC₅₀ values from two independent biological experiments documenting differential CuET-induced cytotoxicity across a panel of cancer and non-cancerous cell lines (48 h treatment). **c**, Analysis of annexin V signal in AMO-1 cells exposed to toxic doses of NMS873 (5 μ M, 16 h) or CuET (100 nM, 16 h) and in U2OS cell exposed to toxic doses of NMS873 (10 μ M, 16 h) or CuET

(1 μ M, 16 h). **d**, Analysis of caspase 3/7 activity in selected cell lines after apoptosis induction by NMS873 (AMO-1: 6 h, 5 μ M; Capan1: 16 h, 10 μ M; U2OS: 16 h, 10 μ M; MDA-MB-231: 24 h, 10 μ M) or CuET (AMO-1: 16 h, 100 nM; Capan1: 16 h, 250 nM; U2OS: 16 h, 1 μ M; MDA-MB-231: 24 h, 1 μ M). **e**, Absence of cleaved PARP1 after a toxic dose of CuET in U2OS cells, compared to etoposide treatment as a positive control. **f**, Analysis of cytochrome *c* (in red) release from mitochondria in U2OS cells during cell death induced by the positive control staurosporin (STS, 1 μ M) compared to cell death induced by CuET (1 μ M). Blue, DAPI. Scale bar, 10 μ m. **c–f**, Data are representative of two independent biological experiments.



Extended Data Figure 3 | CuET-induced proteasome inhibition-like response is not due to proteasome inhibition. a, Kinetics of poly-Ub protein accumulation in U2OS cells treated with CuET or the proteasome inhibitor BTZ. **b,** CuET treatment (1.5 h) induces rapid deubiquitylation of ubiquitylated histone H2A (uH2A) similarly to proteasome inhibitors BTZ or MG132 in U2OS cells. **c,** CuET treatment (1.5 h) induces rapid cytoplasmic accumulation of poly-ubiquitylated proteins (FK2 antibody staining) in U2OS cells, similar to BTZ and MG132 treatment.

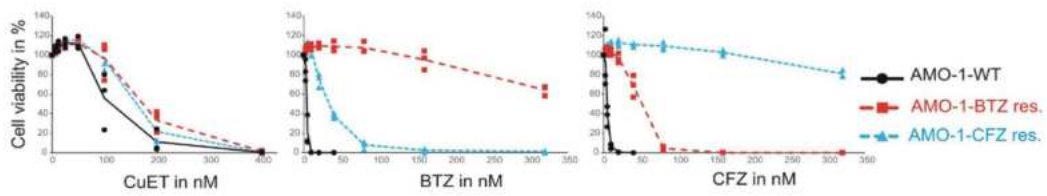
Scale bar, 10 μ m. **d, e,** 20S proteasome activity is not inhibited by CuET as examined in live MDA-MB-231 cells (**d**) or in lysates from MDA-MB-231 cells (**e**). Data are mean \pm s.d. of four independent experiments. **f,** CuET treatment (1 μ M, 6 h) does not cause accumulation of p53 in the presence of dicoumarol (300 μ M) in MCF7 cells. **g,** *In vitro* 26S proteasome function measured as RPN11 deubiquitylation activity, is not inhibited by CuET; 1,10-phenanthroline (1,10-OPT) served as a positive control. Data are representative of two (**a–c, f**) or three (**g**) independent experiments.



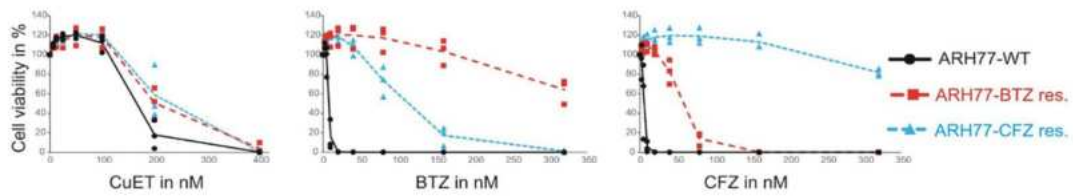
Extended Data Figure 4 | CuET inhibits the p97 pathway and induces cellular UPR. a, MG132-treated cells (5 μ M, 6 h) accumulate both forms of NRF1 (120-kDa and 110-kDa bands, top and bottom arrows, respectively), whereas CuET-treated cells (1 μ M, 6 h) accumulate only the non-cleaved 120-kDa form. b, Inhibition of the NRF1 cleavage process (appearance of the lower band) by CuET and NMS873 (a p97 inhibitor; 5 μ M) in mouse NIH3T3 cells co-treated with the proteasome inhibitor MG132 (5 μ M for 6 h). c, Time-course example images from a FRAP experiment, for which the quantitative analysis is shown in Fig. 2g (U2OS cells, blue boxes mark areas before bleaching, arrows after bleaching). d, U2OS cells pre-extracted with Triton X-100 and stained for poly-Ub(K48). The antibody

signal intensities for cells treated with DMSO, BTZ (1 μ M), NMS873 (10 μ M) and CuET (1 μ M) are analysed by microscopy-based cytometry and plotted below. e, Western blot analysis of accumulated poly-Ub proteins in the ultracentrifugation-separated microsomal fraction from U2OS cells treated with mock, CuET (1 μ M), NMS873 (10 μ M) or BTZ (1 μ M) for 3 h. f, UPR in U2OS and MDA-MB-231 cell lines induced by 6-h treatment with CuET (various concentrations) or positive controls (5 μ M NMS873, 2 μ g ml⁻¹ tunicamycin, 1 μ M thapsigargin) is shown by increased levels of XBP1s, ATF4 and p-eIF2 α . a–f, Data are representative of two independent experiments. All scale bars, 10 μ m.

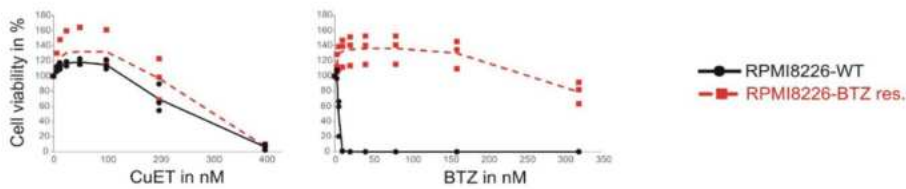
a



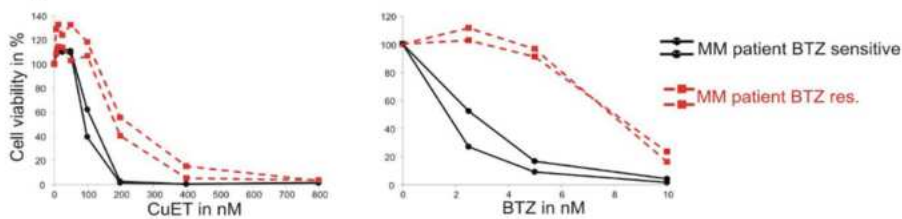
b



c

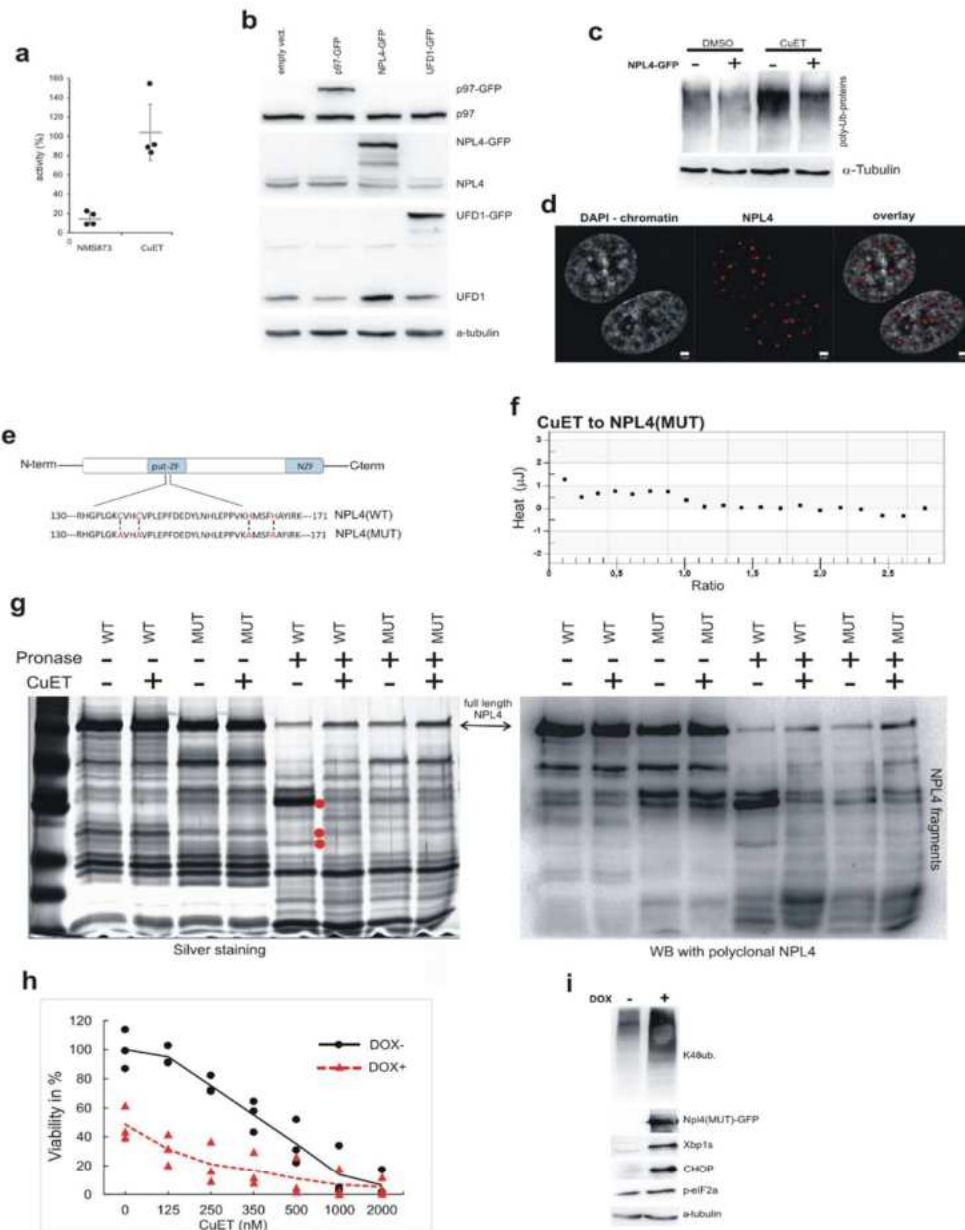


d



Extended Data Figure 5 | CuET kills BTZ-resistant cells. a, BTZ-adapted (BTZres), CFZ-adapted (CFZres) and non-adapted AMO-1 human myeloma cells are equally sensitive to treatment with CuET. b, BTZ-adapted, CFZ-adapted and non-adapted ARH77 human plasmacytoma cells are equally sensitive to treatment with CuET. c, BTZ-adapted and non-adapted RPMI8226 human myeloma cells are equally sensitive to

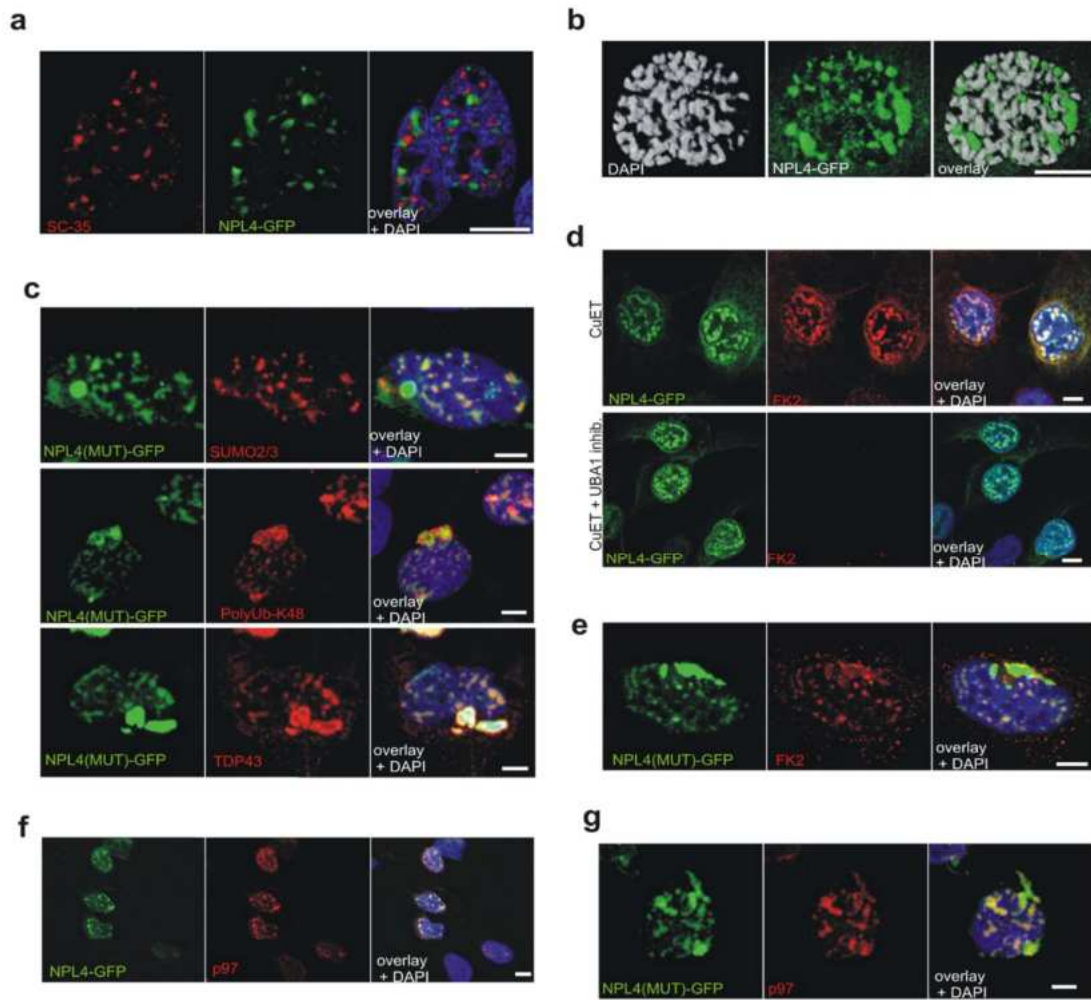
treatment with CuET. d, Human myeloma cells derived from a patient with BTZ-resistant myeloma show CuET sensitivity comparable to myeloma cells derived from a patient with BTZ-sensitive myeloma. Data are means linked of three independent experiments (a-c) or data are from two independent experiments (d).



Extended Data Figure 6 | See next page for caption.

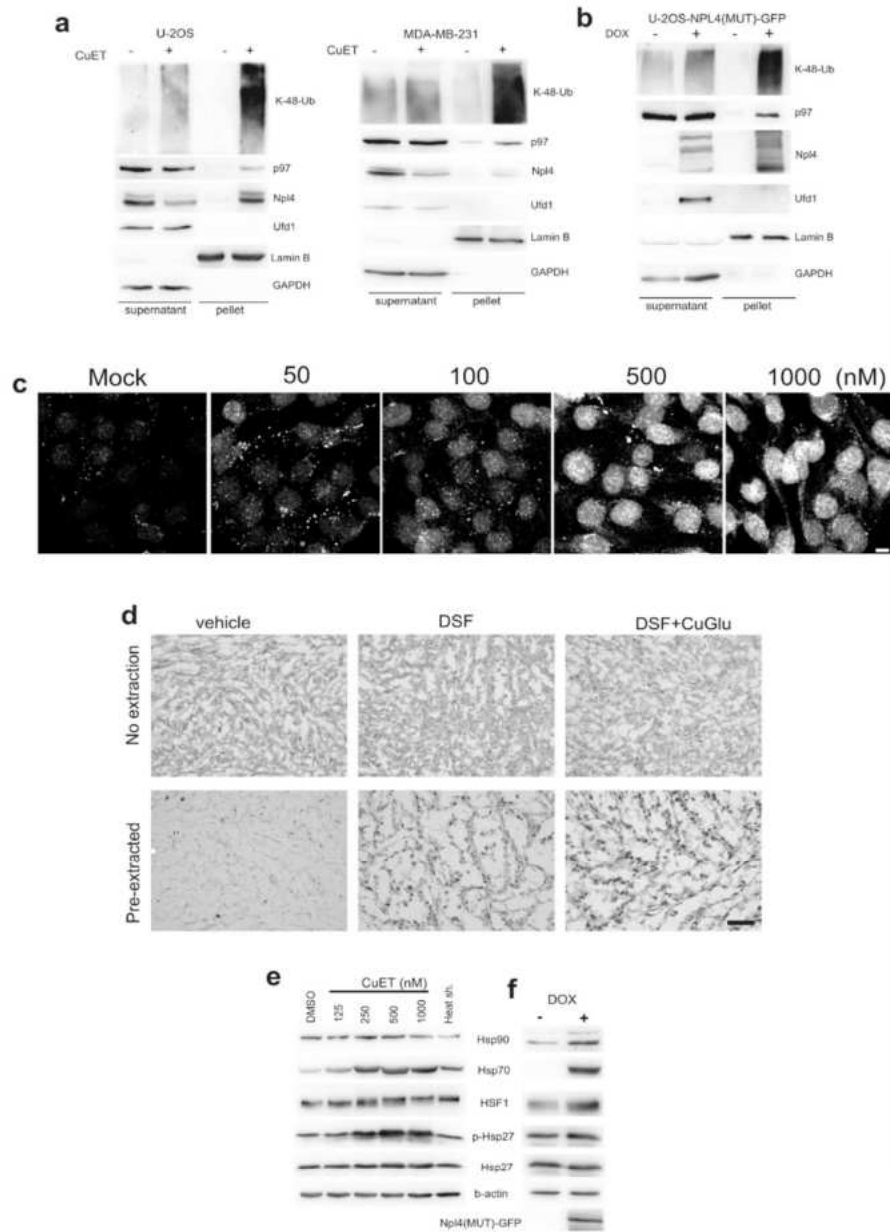
Extended Data Figure 6 | CuET targets NPL4, causing immobilization and nuclear clustering of NPL4. **a**, CuET (1 μ M) does not inhibit ATPase activity of p97. NMS873 (5 μ M) was used as a positive control. Data are mean \pm s.d. from four independent experiments. **b**, Western blotting analysis showing levels of ectopic p97-GFP, NPL4-GFP and UFD1-GFP in stable U2OS-derived cell lines used for the CuET-treatment rescue and cluster formation experiments. **c**, Ectopic expression of NPL4-GFP alleviates CuET-induced (125 nM, 4 h) accumulation of poly-Ub proteins in U2OS cells. **d**, Distribution of NPL4 nuclear clusters relative to chromatin in cells treated with CuET (1 μ M, 2 h). Scale bars, 2 μ m. **e**, Schematic representation of site-directed mutagenesis within the amino acid sequence of the putative zinc finger domain of NPL4.

f, ITC curve showing the lack of CuET binding to purified NPL4(MUT) protein. **g**, DARTS analysis of recombinant NPL4 proteins shows that differential pronase-mediated proteolysis after CuET addition is apparent for NPL4(WT) but not for NPL4(MUT); detected by either silver-stained SDS-PAGE (the most prominent differential bands are marked by red dots) or by blotting with an anti-NPL4 polyclonal antibody. **h**, Viability of cells expressing doxycycline-inducible NPL4(MUT)-GFP, treated with CuET for 48 h. Data are from three independent experiments, means are linked. **i**, Accumulation of K48-ubiquitinated proteins and activation of UPR in cells expressing the doxycycline-inducible NPL4(MUT)-GFP. **b-d, f, g, i**, Data are representative of two independent experiments.



Extended Data Figure 7 | Immobilized NPL4 forms insoluble protein aggregates. **a**, NPL4-GFP aggregates induced by CuET treatment (1 μM, 3 h) do not co-localize with nuclear speckles (stained by SC-35 antibody) or nucleoli (visible as a DAPI⁻ nuclear signal). **b**, NPL4-GFP nuclear aggregates induced by CuET (1 μM, 3 h) are excluded from chromatin in early prometaphase U2OS cells. **c**, Co-localization of spontaneous NPL4(MUT)-GFP aggregates with SUMO2/3, poly-UB(K48) and TDP43 in pre-extracted U2OS cells. **d**, NPL4-GFP aggregates are formed independently of ubiquitylation, as shown in CuET-treated (1 μM, 3 h)

cells pre-treated with a chemical UBA1 inhibitor (MLN7243, 10 μM, 1 h). The lack of cellular FK2 staining of ubiquitylated proteins validates the efficacy of the MLN7243 inhibitor. **e**, Co-localization of FK2 signal with the spontaneous NPL4(MUT)-GFP aggregates in pre-extracted U2OS cells. **f**, Analysis of p97 in CuET-induced (1 μM, 3 h) NPL4-GFP aggregates in pre-extracted U2OS cells. **g**, Analysis of p97 in spontaneous NPL4(MUT)-GFP aggregates in pre-extracted U2OS cells. **a-g**, Data are representative of two independent biological experiments. All scale bars, 10 μm.



Extended Data Figure 8 | NPL4 aggregation immobilizes the p97 binding partner and induces a global cellular HSR. a, Immobilization of selected proteins in Triton X-100-resistant pellet fractions of CuET-treated (1 μ M, 3 h) U2OS cells. **b,** Immobilization of selected proteins in Triton X-100-resistant pellet fractions from U2OS cells expressing doxycycline-inducible NPL4(MUT)-GFP (48 h after induction). **c,** CuET dose-dependent immobilization of p97 in Triton X-100 pre-extracted MDA-MB-231 cells (3 h). Scale bar, 10 μ m. **d,** Immunohistochemical

staining showing non-extractable p97 in MDA-MB-231 xenografts from mice treated with DSF or DSF and CuGlu, compared to vehicle. Scale bar, 50 μ m. **e,** HSR after CuET (8 h treatment) is shown by various HSR markers detected by western blotting of U2OS cell extracts. **f,** HSR markers in U2OS cells expressing doxycycline-inducible NPL4(MUT)-GFP (24 h after induction). **a-f,** Data are representative of two independent biological experiments.



Disulfiram's anti-cancer activity reflects targeting NPL4, not inhibition of aldehyde dehydrogenase

Zdenek Skrott¹ · Dusana Majera¹ · Jan Gursky¹ · Tereza Buchtova¹ · Marian Hajduch¹ · Martin Mistrik¹ · Jiri Bartek^{1,2,3}Received: 18 April 2019 / Revised: 27 June 2019 / Accepted: 22 July 2019 / Published online: 7 August 2019
© The Author(s), under exclusive licence to Springer Nature Limited 2019

Abstract

Aldehyde dehydrogenase (ALDH) is a proposed biomarker and possible target to eradicate cancer stem cells. ALDH inhibition as a treatment approach is supported by anti-cancer effects of the alcohol-abuse drug disulfiram (DSF, Antabuse). Given that metabolic products of DSF, rather than DSF itself inhibit ALDH *in vivo*, and that DSF's anti-cancer activity is potentiated by copper led us to investigate the relevance of ALDH as the suggested molecular cancer-relevant target of DSF. Here we show that DSF does not directly inhibit ALDH activity in diverse human cell types, while DSF's *in vivo* metabolite, S-methyl-N,N-diethylthiocarbamate-sulfoxide inhibits ALDH activity yet does not impair cancer cell viability. Our data indicate that the anti-cancer activity of DSF does not involve ALDH inhibition, and rather reflects the impact of DSF's copper-containing metabolite (CuET), that forms spontaneously *in vivo* and in cell culture media, and kills cells through aggregation of NPL4, a subunit of the p97/VCP segregase. We also show that the CuET-mediated, rather than any ALDH-inhibitory activity of DSF underlies the preferential cytotoxicity of DSF towards BRCA1- and BRCA2-deficient cells. These findings provide evidence clarifying the confusing literature about the anti-cancer mechanism of DSF, a drug currently tested in clinical trials for repositioning in oncology.

Introduction

Cancer stem cells (CSCs) are believed to represent a major challenge to successful cancer therapy [1], due to CSCs'

ability to resist standard-of-care treatment modalities and fuel post-treatment relapse and metastatic spread [2]. CSCs can be detected through expression of several markers including aldehyde dehydrogenases (ALDHs) [3]. There are 19 putatively functional *ALDH* genes in the human genome [4], and several ALDH isoenzymes are used as markers of stem cells including CSC [5]. ALDH have diverse functions in normal tissues, including the pivotal role in catalysing endogenous and exogenous aldehydes into carboxylic acids [6]. If aldehydes are not metabolized, they may cause severe toxicity to the cells, including DNA damage by forming adducts [7]. Numerous studies reported that ALDH is overexpressed in cancer cells and implicated in metastatic spread [8–10]. Despite the above-mentioned reports on ALDH in CSCs, however, it remains unclear whether ALDH may serve as an actionable target for cancer treatment, and whether tumours are indeed addicted to ALDH function.

Recent efforts to eradicate CSCs have exploited the old anti-alcoholism drug DSF, used for decades as an ALDH inhibitor in clinical care [4]. Eradication of CSCs by DSF has been reported in numerous studies, the first of which reported DSF's toxicity for breast cancer cells with CSC-

These authors contributed equally: Zdenek Skrott, Dusana Majera

Supplementary information The online version of this article (<https://doi.org/10.1038/s41388-019-0915-2>) contains supplementary material, which is available to authorized users.

✉ Martin Mistrik
martin.mistrik@upol.cz

✉ Jiri Bartek
jb@cancer.dk

¹ Institute of Molecular and Translational Medicine, Faculty of Medicine and Dentistry, Palacky University, Olomouc, Czech Republic

² Danish Cancer Society Research Center, Copenhagen, Denmark

³ Division of Genome Biology, Department of Medical Biochemistry and Biophysics, Science for Life Laboratory, Karolinska Institute, Stockholm, Sweden

like properties [11]. In recent years, multiple studies reported DSF as a drug toxic to cancer cells via inhibition of ALDH in a range of tumour types and models [12–20] and other studies have later build on these findings and used DSF combined with copper ions to target cancer cells [21–24]. However, the mechanism of ALDH inhibition by DSF is more complex, as metabolic products of DSF, not DSF itself, inhibit ALDH in vivo [4]. While well accepted in pharmacology, the latter fact has often been overlooked in the cancer-related studies focusing on DSF and ALDH, thereby causing potentially misleading interpretations of the results.

In vivo DSF is rapidly metabolized to diethyldithiocarbamate (DDTC), which is further converted to *S*-methyl-*N,N*-diethyldithiocarbamate (DETC) and *S*-methyl-*N,N*-diethyldithiocarbamate (Me-DDTC). Subsequent P450-catalyzed oxidation of DETC and Me-DDTC produces DETC-sulfoxide (DETC-SO) and *S*-methyl-*N,N*-diethyldithiocarbamate-sulfoxide (Me-DTC-SO) and -sulfone (Me-DTC-SO₂), metabolites that are most likely directly involved in ALDH inhibition [25–29]. Importantly, when downstream steps of DSF metabolism are blocked by a chemical P450 inhibitor, liver ALDH remains uninhibited [30], thus unambiguously proving that not DSF itself, but its metabolites are the genuine inhibitors of ALDH in vivo. Despite this knowledge is published and accepted in some research fields, most cancer-focused studies regard DSF as a direct ALDH inhibitor. Notably, there are no published data with regard to any anti-cancer effects of the DSF metabolites that are responsible for ALDH inhibition. Further fuelling the confusion in this field, the vast majority of cancer-related studies report that DSF inhibits ALDH only when combined with copper ions [12–16], a fact that further underlines the extent of misunderstanding and lack of logic behind such approach with respect to the known mechanism of ALDH inhibition, a process that does not involve copper at all. On the other hand, it is well known that copper does potentiate DSF's anti-cancer toxicity [12, 31, 32], and we have recently uncovered that this reflects the in vivo formation of a copper-containing CuET (bis-diethyldithiocarbamate-copper) complex, the ultimate anti-cancer metabolite derived from DSF [33]. This conundrum surrounding the links among DSF, ALDH, copper and cancer toxicity prompted us to assess the role of ALDH as a potential target of DSF's anti-cancer activity in more detail, using genuine validated inhibitors of ALDH enzymatic activity, and thereby help to reconcile the often mis-interpreted findings in this field, with the goal to facilitate the future repositioning of DSF for treatment of cancer.

Results

DSF's toxicity for cancer cells is mediated by CuET formed in the culture media

Despite numerous pre-clinical studies and ongoing clinical trials, the mechanism of anti-cancer activity of DSF is still debated, as several targets and hypotheses have been proposed. Among them, the inhibition of ALDH is probably currently the most prevalent and accepted theory. ALDH is attractive not only as a generally accepted marker of stem cells, but also as an important protective enzyme metabolising potentially harmful aldehydes. However, the hypothesis that ALDH may represent a promising avenue to target cancer stem cells or cancer in general, remains to be rigorously tested.

Recently, preferential cytotoxicity of DSF for homologous recombination (HR) deficient cells have been reported [20]. Since DSF is regarded by some as a direct inhibitor of ALDH, the reported cytotoxicity in this study was attributed to increased acetaldehyde levels ensuing ALDH inhibition, and subsequent DNA damage induced by the crosslinking activity of the aldehydes. As direct inhibition of cellular ALDH by DSF is in fact highly unlikely (see Introduction) we decided to reproduce and re-analyse those intriguing results. First, we tried to recapitulate the reported preferential sensitivity of BRCA1 and BRCA2-deficient cell lines to DSF [20]. Indeed, the H1299 cell lines with doxycycline (DOX)-inducible shBRCA1 or shBRCA2 show efficient knockdown of these genes after DOX induction (Fig. 1a) and both models show also hypersensitivity of BRCA-depleted cells to olaparib (Supplementary Fig. 1a) a PARP1 inhibitor effective against HR deficient cancers [34]. In agreement with Tacconi et al. [20], we confirmed that BRCA1- and BRCA2-deficient cells are indeed more sensitive to DSF treatment compared to their BRCA-proficient counterparts (Fig. 1b). Importantly, we have recently described a new metabolite of DSF, CuET, which is formed in vivo and is responsible for DSF's anti-cancer activity [33], providing a meaningful explanation for why is the toxicity of DSF potentiated by copper supplementation. Thus we sought to investigate whether the CuET complex forms also in vitro, since standard cell culture media contain significant amounts of copper ions [35] and the complex biochemical environment in the medium may allow spontaneous formation of such complex. Indeed, we have confirmed that CuET is detectable in DSF-containing medium even without any additional copper supplementation (Fig. 1c). As predicted, addition of more copper to the medium increased the amount of formed CuET; conversely chelation of copper ions by a metal chelator,

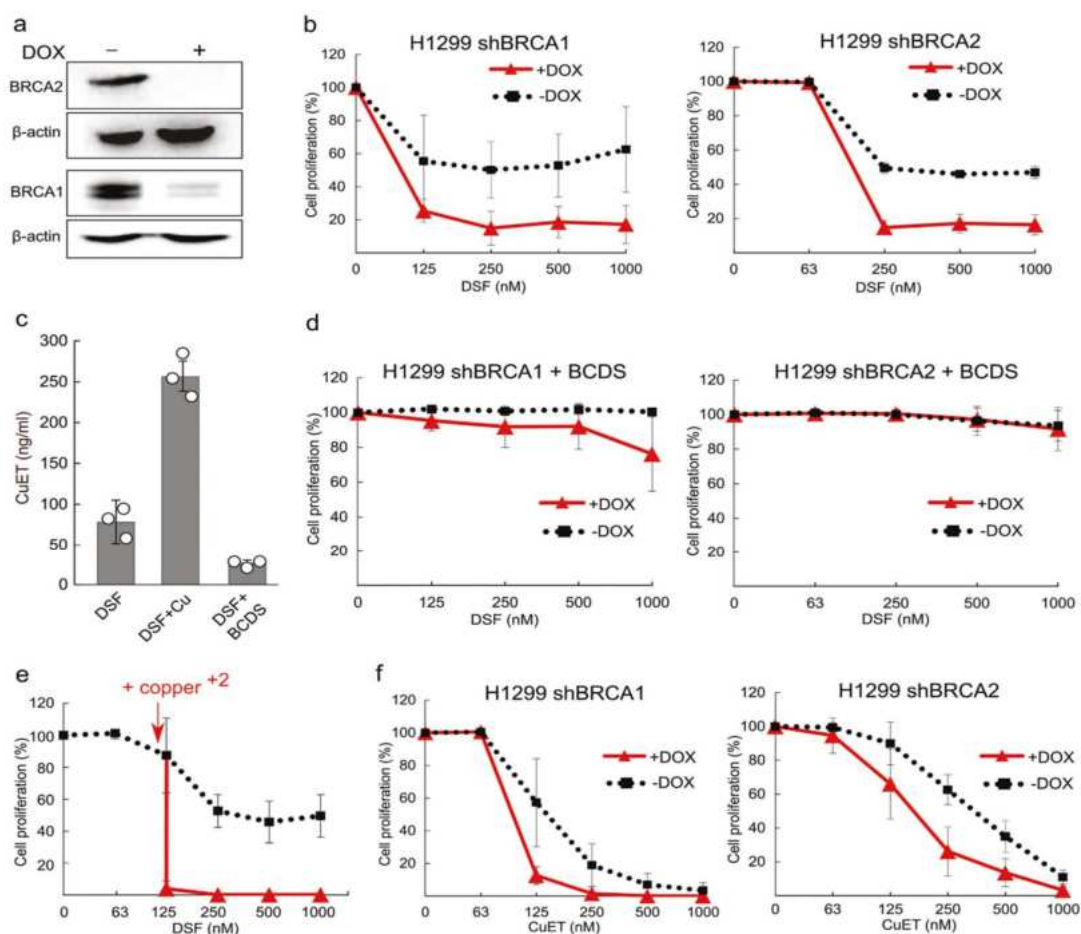


Fig. 1 Preferential cytotoxicity of disulfiram to BRCA1- and BRCA2-depleted H1299 cells is copper dependent. **a** H1299 cells expressing DOX-inducible shBRCA1 or shBRCA2 were cultivated for at least 3 days in DOX and protein expression was evaluated by Western blotting, confirming efficient knockdown of BRCA1 and BRCA2, respectively. **b** H1299 cells expressing DOX-inducible shBRCA1 or shBRCA2 were treated with DSF at indicated concentration for 5 days. **c** HPLC-MS analysis of CuET complex formed in the media

containing DSF, DSF with copper, or DSF with BCDS. **d** Cells as in **b** were treated with the combination of 10 μ M BCDS and DSF at indicated concentration for 5 days. **e** H1299 cells were treated with DSF or the combination of 1 μ M CuCl_2 and DSF at indicated concentrations for 5 days. **f** Cells as in **b** were treated with CuET at indicated concentration for 5 days. All graphs represent at least three independent experiments. Error bars represent SD

bathocuproinedisulfonic acid (BCDS), markedly reduced the levels of spontaneously formed CuET (Fig. 1c). Importantly, in line with our hypothesis and results of spontaneous formation of CuET, chelation of copper by BCDS completely reversed the cytotoxic effect of DSF in all tested cell lines irrespective of their BRCA1/2 status (Fig. 1d, Supplementary Fig. 1b). Another interesting aspect described by Tacconi et al. [20] was the observation that the cytotoxic effect of DSF reaches a certain plateau, which

cannot be overcome by increasing concentrations of the drug, a phenomenon attributed by the authors to limited solubility of the DSF. We also confirmed this plateau effect but we argued that this might be explained by an alternative mechanism, namely reflecting the limiting amounts of copper in culture media, which would enable only limited formation of CuET irrespective of increasing concentrations of DSF. To test the two alternative hypotheses, we added non-toxic extra amounts of copper ions to culture

medium. Supporting our hypothesis, we observed a reversal of the plateau effect, along with a striking potentiation of DSF toxicity (Fig. 1e). Finally, we directly tested the synthetic CuET complex. As expected, CuET treatment was highly potent and also recapitulated the preferential toxicity toward BRCA-impaired cell lines (Fig. 1f, Supplementary Fig. 1c). Taken together, these results demonstrate that DSF's cytotoxicity is fully dependent on copper ions and is mediated by the CuET complex, which is spontaneously formed in the medium, proportionally to the amounts of DSF and copper ions present in the cell culture environment.

Neither DSF nor CuET inhibit ALDH activity, contrary to DSF metabolite Me-DTC-SO

Given the fact that DSF's anti-cancer activity is commonly attributed to inhibition of ALDH, we wanted to test this hypothesis further. An important aspect of DSF as a drug is that it undergoes extensive metabolism resulting in several compounds, including S-methyl-N, N-diethylthiocarbamate-sulfoxide (Me-DTC-SO), which represents the most likely DSF's metabolite responsible for the inhibition of liver ALDH in vivo [25, 26]. However, no potential effect of Me-DTC-SO on cancer cells has so far been reported. First, we investigated the impact of CuET, DSF and Me-DTC-SO on ALDH activity. We selected two human cancer cell lines with high ALDH expression, K562 and A549, and used the well-established ALDEFLUOR assay to measure total ALDH activity in these cells [36]. Strikingly, in K562 cells ALDH activity was not impaired by either CuET or DSF treatment, in contrast to the Me-DTC-SO metabolite that inhibited ALDH with an efficacy similar to D-aminobenzaldehyde (DEAB), a commonly employed ALDH inhibitor used here as a positive control for ALDH inhibition (Fig. 2a, b). Consistently, neither CuET nor DSF decreased the percentage of ALDH positive cells, in contrast to Me-DTC-SO and DEAB (Fig. 2c). The same scenario was reproduced also in the A549 cells as neither CuET nor DSF mimicked the impact of the ALDH inhibitors, while Me-DTC-SO completely blocked the ALDH activity in all cells (Fig. 2d–f). Analogous data were seen in the BRCA1/2 knockdown H1299 cells whose overall ALDH activity is lower compared to K562 or A549 cell lines, again confirming that only Me-DTC-SO potently inhibited ALDH, while CuET and DSF had no direct measurable effect on ALDH activity (Supplementary Fig. 2a, b).

ALDH inhibitors are not toxic to cancer cells

Next, we tested the toxicity of Me-DTC-SO and DEAB, in concentrations efficiently inhibiting the ALDH activity. Strikingly, both compounds failed to suppress growth of

K562 and A549 cells (Fig. 3a). In contrast, CuET which does not inhibit ALDH reduced the growth of both cancer cell lines (Fig. 2b). Furthermore, the H1299 cells were highly responsive to CuET but fully resistant to both DEAB and Me-DTC-SO inhibitors, irrespectively of their BRCA1/2 status (Fig. 3c, d). Given the fact that DSF undergoes rapid transformation in vivo, it is very likely that both metabolites, CuET and Me-DTC-SO, exist in the body at the same time and their effects may potentially influence each other. To test if ALDH inhibition augments the toxicity of CuET, we combined CuET with Me-DTC-SO and DEAB at concentrations efficiently inhibiting ALDH and analysed the viability of cancer cells; however, no potentiation was observed (Fig. 3e). Taken together, these results clearly exclude ALDH inhibition as a possible explanation for DSF's anti-cancer activity and call for an alternative, mechanistically justified explanation. At the same time, our data caution that targeting the ALDH as an approach to cancer treatment should be further scrutinized.

Reduced ALDH activity readout of the ALDEFLUOR assay upon long-term exposure to DSF is an indirect consequence of toxicity

Our results excluding direct inhibition of ALDH by CuET and/or DSF sharply contrast with numerous previous studies claiming that DSF or DSF combined with copper inhibits ALDH activity in cultured cells [12–14, 19, 20], thereby raising the notion of how can such conflicting conclusions be reconciled. One key aspect shared by the studies that reported apparent effects of DSF or DSF/Cu treatments on ALDH activity were long exposure times to the drug (from many hours to several days). This seemed to us a rather odd approach for aiming to test direct enzymatic inhibitors for which a few-hour exposure should be sufficient. We argued that such long exposure times to a toxic and metabolized compound might generate confounding indirect effects and thereby complicate the interpretation of the final outcome, as many important cellular functions can be already hampered due to rather broad, non-specific phenotypes. Such late indirect effects could also bias the readout of the commonly used ALDEFLUOR assay, which requires cellular import of a fluorescent probe and its intracellular retention after cleavage by the ALDH enzyme. To test this idea, we compared ALDH activity at different time-points of drug exposure to evaluate the potential effect of reduced cellular fitness on the ALDEFLUOR assay readout. First, we measured ALDH activity after 3 h of incubation with the four relevant drugs, which was sufficient to suppress ALDH activity when the direct ALDH inhibitors DEAB and Me-DTC-SO were used, yet with no detectable ALDH-inhibitory effect of either CuET or DSF used in parallel experiments (Fig. 2a). Next, we tested not

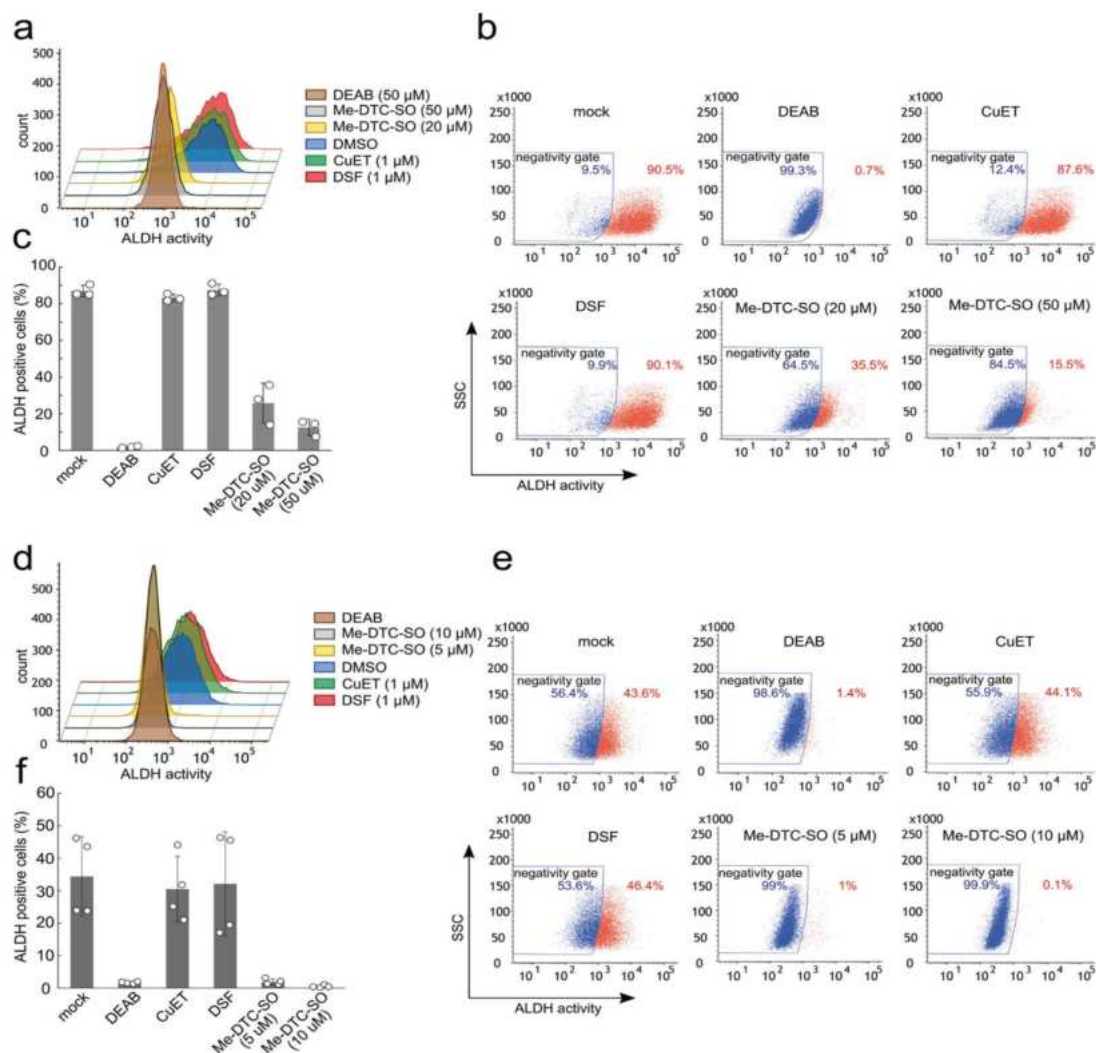


Fig. 2 ALDH activity in cells is inhibited by DSF's metabolite Me-DTC-SO, but not affected by DSF and CuET. **a, b** K562 cells were treated with indicated compounds and ALDH activity was quantified by ALDEFLUOR™ assay. Representative graphs and flow cytometry profile from three independent experiments are shown. **c** Number of

ALDH positive K562 cells. **d, e** A549 cells were treated with indicated compounds and ALDH activity was measured. Representative graphs and flow cytometry profile from four independent experiments are shown. **f** Number of ALDH positive A549 cells

only CuET as a compound of interest, but also bortezomib (BTZ), a compound that exerts its toxicity through specific inhibition of the 20 S proteasome and partly resembles the cellular effects induced by CuET [33]. Notably, BTZ's mechanism of action is completely unrelated to ALDH. Consistent with our previous results, DSF and CuET failed to inhibit ALDH activity after 3 h of exposure despite other

typical cellular phenotypes such as accumulation of poly-ubiquitinated proteins [33] are already well detectable in the cells treated for 3 h with the same concentration of DSF or CuET (Fig. 4a). As expected, also BTZ failed to score in the ALDH inhibition assay (Fig. 4b). Strikingly, however, after a prolonged treatment (20 h), both CuET and BTZ markedly reduced the ALDEFLUOR-assessed ALDH

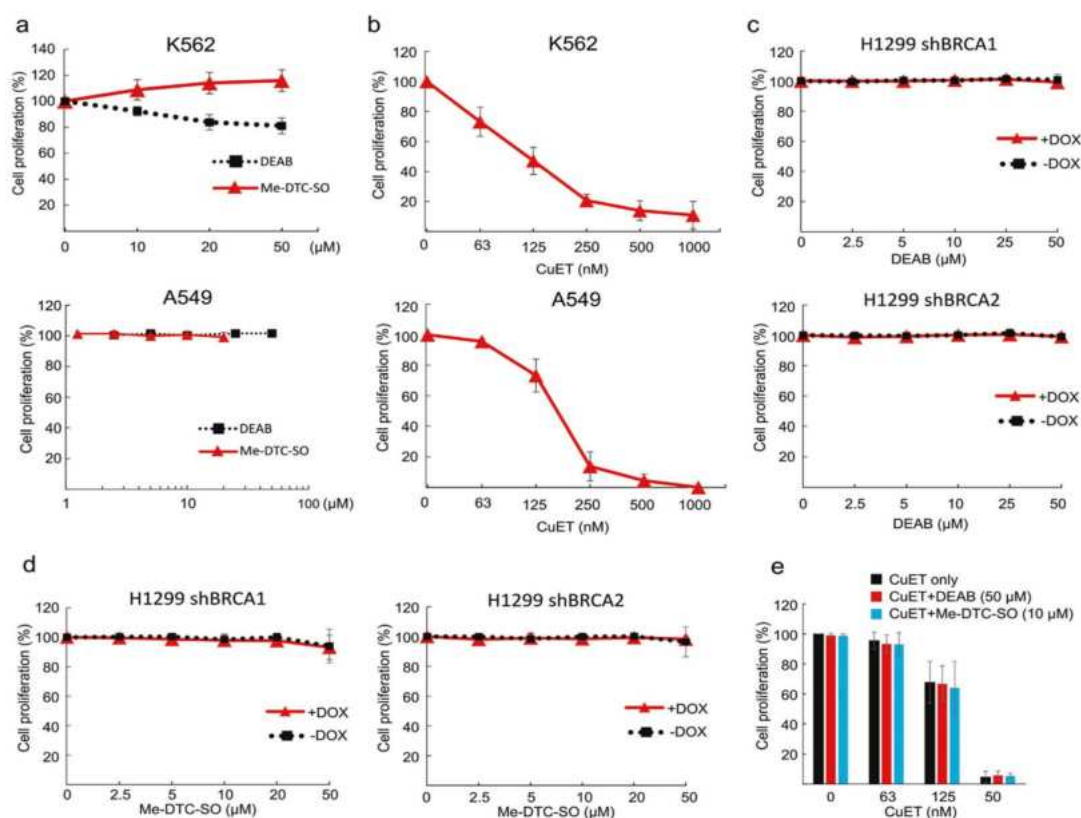


Fig. 3 Cytotoxicity of ALDH inhibitors and CuET. **a** Cytotoxicity of DEAB or Me-DTC-SO in A549 and K562 cells after 5 days of treatment. **b** Cytotoxicity of CuET in A549 and K562 cells after 5 days of treatment. All graphs represent at least three independent experiments. Error bars represent SD. **c** H1299 cells expressing

inducible shBRCA1 or shBRCA2 were treated with ALDH inhibitors DEAB and **d** Me-DTC-SO at indicated concentrations for 5 days. **e** Cytotoxicity of CuET, Me-DTC-SO and DEAB or their combination in A549 cells

activity readout (Fig. 4b) and clearly decreased the numbers of ALDH-positive cells (Fig. 4c, d). Such prolonged treatments also increased the numbers of permeabilised cells, an indirect marker of reduced cell fitness and increased cell death (Fig. 4e). Given that even BTZ, a compound never reported as an ALDH inhibitor, behaved similarly to CuET, we propose that the decrease of ALDH activity in such long-term treatment experiments is not caused by any direct interference with ALDH enzymatic activity, but it is rather a consequence of impaired cell fitness. All permeabilised cells were totally negative for ALDH activity (Supplementary Fig. 3b), which is understandable considering the principle of the ALDEFLUOR assay. Even the seemingly still ‘intact’ (nonpermeabilized) cells showed a lower ALDH activity readout suggesting that prolonged cellular stresses (at least the proteotoxic stress

caused by CuET- or BTZ-induced protein turnover impairment) is sufficient to indirectly affect the outcome of the ALDEFLUOR assay (Supplementary Fig. 3a), a fact that has been incorrectly interpreted by many as direct inhibition of ALDH by DSF. These results help explain the previous conflicting studies and exclude ALDH inhibition as a mechanism underlying DSF’s toxicity to cancer cells.

DSF toxicity is linked to NPL4 aggregation

We have recently reported that DSF is metabolised *in vivo* into the CuET complex, and showed that CuET represents the ultimate anti-cancer metabolite. CuET interferes with the cellular protein degradation machinery *via* targeting the NPL4 cofactor of the p97/VCP segregase, leading to NPL4

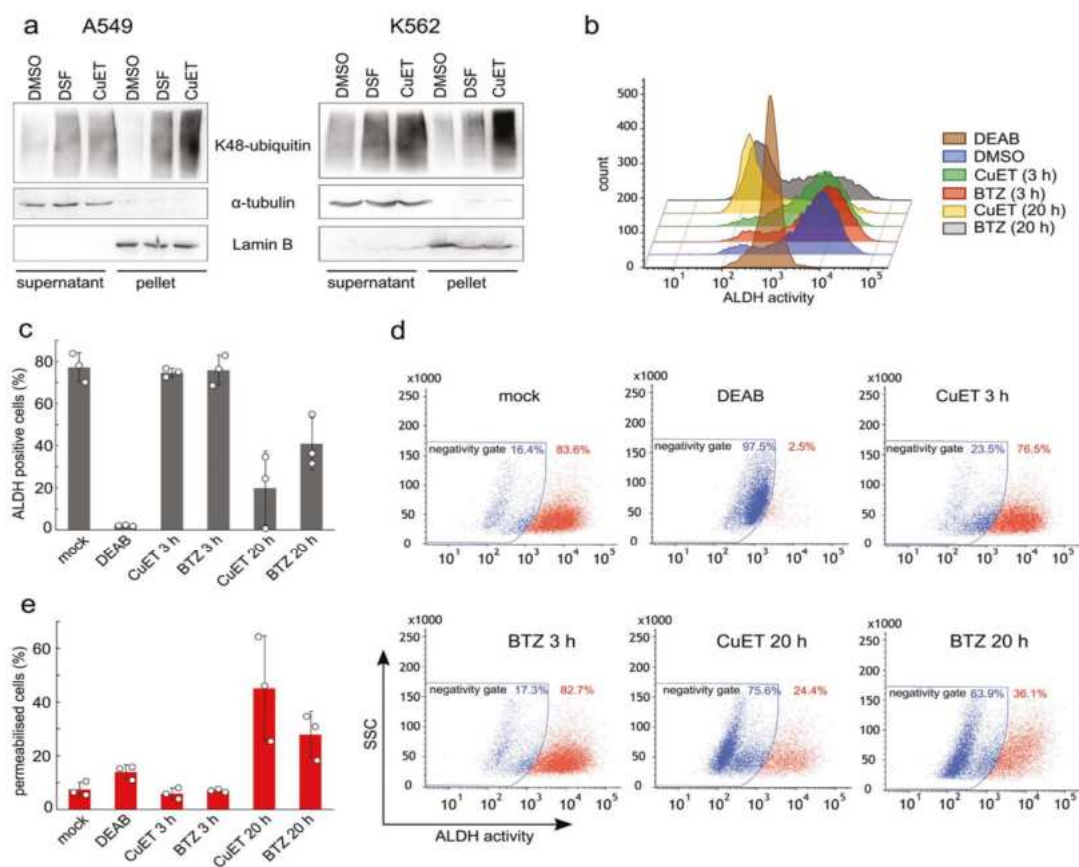


Fig. 4 CuET reduces ALDH activity after prolonged treatment. **a** Western blot analysis of immobilized and accumulated K48 poly-ubiquitin in CuET/DSF (1 μ M, 3 h) treated A549 and K562 cells. **b** K562 cells were treated with DEAB (50 μ M), CuET (1 μ M), BTZ (1 μ M) for indicated time and ALDH activity was quantified by ALDEFLUOR™ assay. Representative graphs from three independent

experiments are shown. **c** Number of ALDH positive K562 cells after indicated treatments. Error bars represent SD of three independent experiments. **d** Representative flow cytometry profile of K562 cells treated as in **b**. **e** Percentage of permeabilized K562 cells after indicated treatments was measured by DAPI staining using flow cytometry

aggregation, activation of stress responses and cell death [33]. Since CuET is formed from DSF also in vitro in culture media (Fig. 1c) and DSF's toxicity strictly depends on available copper ions (Fig. 1d, e), we examined whether DSF's cytotoxicity is also accompanied by NPL4 aggregation. We treated the cells with CuET, DSF, DSF combined with a copper chelator BCDS, and the two ALDH inhibitors: Me-DTC-SO and DEAB and assessed the NPL4 protein status. As expected, both CuET and DSF treatment led to formation of insoluble aggregated endogenous NPL4 resistant to pre-extraction (Fig. 5a). Chelation of copper ions by BCDS completely suppressed DSF's effect on NPL4 aggregation, thereby preserving the normal diffuse staining

pattern of NPL4 that was sensitive to cell pre-extraction. The same un-altered, extraction-sensitive diffuse staining of NPL4 was furthermore observed for mock treated cells, but also upon treatment by the two ALDH inhibitors Me-DTC-SO and DEAB (Fig. 5a, see Fig. 5b for signal quantification). These results were further corroborated using a NPL4-GFP expressing cell line showing the same effects on GFP tagged NPL4 protein (Supplementary Fig. 4a, b). Together with the other results of our present study, these data demonstrate that DSF's cytotoxicity does not involve ALDH inhibition, but rather it is attributable to CuET causing NPL4 aggregation, as recently described for the synthetic CuET complex [33].

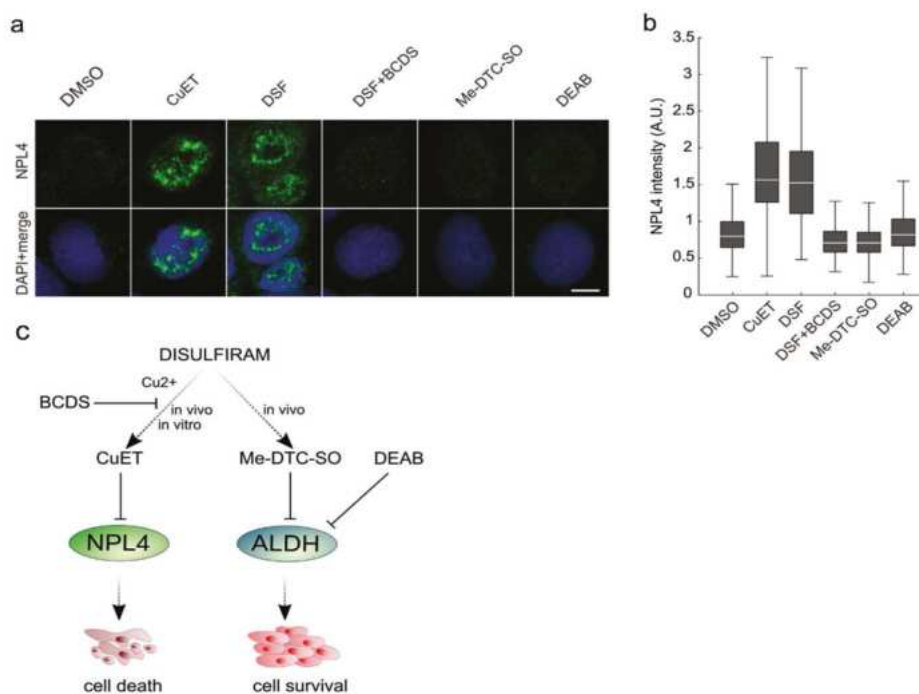


Fig. 5 DSF toxicity is caused by NPL4 aggregation. **a** A549 cells were treated with DMSO, DSF (1 μ M), CuET (500 nM), Me-DTC-SO (20 μ M), DSF with BCDS (10 μ M) and DEAB (50 μ M) for 4 h and NPL4 aggregation was visualized by immunofluorescence staining

after pre-extraction. **b** Quantification of nuclear NPL4 signal in more than 200 cells. **c** Schematic representation of the mechanism of action of disulfiram and its metabolites

Discussion

The alcohol-abuse drug DSF is a promising candidate for repurposing in cancer therapy, as documented by many pre-clinical studies and ongoing clinical trials. Proper knowledge of drug's mechanism of action is essential for both development of suitable biomarkers and selection of individual patients who might most benefit from such treatment. In this study, we therefore critically assessed the commonly accepted theory about DSF's mechanism of action in cancer cells, namely the inhibition of ALDH enzymes. Many publications attribute the anti-cancer effect of DSF to interference with ALDH, and others build their subsequent work on such conclusions. As ALDH was widely proposed to be a cancer target [37, 38], the hypothesis that DSF kills cancer cells *via* inhibition of ALDH seemed plausible and was widely accepted by experimental cancer researchers and oncologists. DSF is indeed well known as a drug averting alcoholism through ALDH enzyme inhibition in the human body. On the other hand, it is not DSF itself but rather some of its metabolites that directly inhibit ALDH, an

important fact that is much less appreciated and completely overlooked in cancer-related studies, thereby fuelling the misleading claims that DSF directly inhibits cellular ALDH. In sharp contrast, here we show that neither DSF nor CuET (which forms spontaneously both *in vivo* and *in cell culture* due to available copper ions) inhibits ALDH, contrary to the appropriate DSF's metabolite Me-DTC-SO that does inhibit ALDH. Importantly, the results of the cytotoxicity assays showed that the genuine ALDH inhibitors DEAB and Me-DTC-SO were not toxic to cancer cells at a concentration range that robustly inhibited the ALDH activity while treatments with CuET and DSF killed cancer cells efficiently. Furthermore, despite only a minor fraction of cells in culture (~20% in the H1299 cell line) are positive for ALDH activity, all cells respond well to CuET or DSF treatment. Furthermore, we have proven here that the cytotoxicity of DSF for human cancer cells requires the availability of copper and spontaneous formation of the CuET complex. The frequently observed potentiation of DSF activity by copper has been often attributed to ALDH inhibition, an unproven conclusion that lacks any rational

basis. Yet such major discrepancy has remained overlooked.

While some potential contribution of ALDH inhibition to the *in vivo* anti-cancer activity of DSF by the relevant metabolites cannot be entirely excluded, it should be emphasized that also under *in vivo* conditions, DSF's toxicity for cancer cells is potentiated by copper supplementation [12, 33] that leads to increased formation of CuET [33] at the expense of lower formation of the ALDH-inhibitory metabolites. Moreover, the ALDH hypothesis is also based only on results obtained in cell culture experiments, and it has so far not been proven under *in vivo* conditions, in tumour tissues. Importantly, in the Asian population a large number of people (approximately 540 million) carry a mutation in the *ALDH2* gene producing a defective enzyme [39] that causes alcohol-related symptoms largely resembling the therapeutic exposure to DSF. Yet, these people still suffer from common cancers with a similar frequency as the matched normal population [40]. In addition, normal stem cells physiologically express ALDH activity, but patients treated with DSF to prevent use of alcohol are medicated for many years with no evidence of stem cell exhaustion demonstrated by myelodysplasia or bone marrow failure [41]. As studies that employ DSF have become a key part of cancer research aiming to target ALDH in CSCs, our present results provide a fresh insight into this field that should motivate further thorough examination of the role played by ALDH in cancer cells. From the clinical perspective, inhibition of liver ALDH in cancer patients treated by DSF represents serious limitation for its widespread use. DSF must be excluded in all patients whose overall treatment requires administration of some alcohol-based substances. Those include patients receiving therapy with drugs where alcohol is used as an excipient (such as commonly used anti-cancer drugs gemcitabine or paclitaxel) or disinfectants (e.g., before surgery). Moreover, moderate alcohol consumption might be regarded by some patients as an important aspect of life quality, incompatible with a concomitant DSF treatment. Sensitive patients even do not tolerate alcohol-containing cosmetics or mouthwash under DSF therapy, again interfering with quality of life. Our results suggest that this limitation of DSF could be possibly overcome by direct application of CuET. However, on its own the CuET complex is highly lipophilic, water insoluble and thus unsuitable for clinical applications. In our previous work, we have overcome this limitation and developed an albumin-based formulation of CuET, which is prepared by single *in situ* reaction yielding CuET-albumin composition in an aqueous solution suitable for *in vivo* applications and demonstrating promising anti-tumour effects [33]. Consequently, other groups also reported formulations of CuET based on a similar principle and using

other pharmaceutically acceptable excipients [42, 43]. These results indicate, that direct application of CuET is in principle feasible and represents a potential strategy to target cancer. At the same time, our present study should inspire further research into the proposed ability of DSF to target CSCs, in light of our findings that the anti-cancer effect of DSF is mediated by CuET and involves NPL4 as the relevant target. Similarly, the observed hypersensitivity of BRCA1/2- deficient cancer cell models to CuET via NPL4 protein aggregation opens new avenues for further exploration in clinical scenarios associated with some DNA repair deficiencies.

Materials and methods

Cell lines

Human non-small cell lung carcinoma H1299 cells expressing a doxycycline (DOX)-inducible BRCA1 and BRCA2 shRNAs, U-2-OS cells expressing NPL4-GFP [33], human lung adenocarcinoma cells A549 (ATCC) and human chronic myelogenous leukemia K562 cells (ATCC) were cultured and maintained in DMEM medium (Lonza), supplemented with 10% fetal bovine serum (Thermo Fisher Scientific) and 1% penicillin/streptomycin (Sigma-Aldrich). H1299 expressing a DOX-inducible BRCA1 and BRCA2 shRNA were kindly provided [20]. For efficient BRCA1 and BRCA2 knockdown cells were cultivated in the presence of 2 µg/ml DOX for at least 3 days. Cell lines were tested for mycoplasma contamination and authenticated by CTR method.

Cell viability assays

H1299 and A549 cells were plated at a density 80,000–100,000 cells per well in six-well plates and in case of Olaparib treatment 20000 per well in 12-well plate. Next day cells were treated with compounds at indicated concentrations and left in culture for 5–7 days before analysing. On the day of analysing, growth medium was removed, cells were fixed in ice cold 70% ethanol and stained with 1% crystal violet in 96% ethanol and total growth area was calculated. Results are shown as mean values and standard deviations from at least three independent experiments.

K562 cell viability was analysed by XTT assay. Cells were plated at a density of 5000 per well in a 96-well plate. The next day, cells were treated as indicated. After 5 days, an XTT assay was performed according to the manufacturer's instructions (Applichem). XTT solution was added to the medium and incubated for 30–60 min, and then the dye intensity was measured at the 475 nm wavelength using a spectrometer (TECAN, Infinite M200PRO).

Immunoblotting

Equal amounts of cell lysates were separated by SDS-PAGE on NuPAGE™ 3–8% Tris-Acetate protein gels (Thermo Fisher Scientific) or hand-casted gels and then transferred onto nitrocellulose membrane. The membrane was blocked in Tris-buffered saline containing 5% milk in and 0.1% Tween 20 for 1 h at room temperature, and then incubated 1 h at room temperature with primary antibodies, followed by detection with secondary antibodies: Secondary antibodies were visualized by ELC detection reagent (Thermo Fisher Scientific).

Immunofluorescence

Cells were seeded on plastic inserts in 12-well dishes. Next day cells were treated with compounds at indicated concentrations and subsequently pre-extracted (0.1% Triton X 100 in PBS, for 2 min) and fixed with -20°C methanol for 15 min at room temperature, washed with PBS and permeabilized with 0.5% Triton X-100 in PBS for 5 min. After PBS washes, the cells on the plastic inserts were then immunostained with primary antibody for 120 min at room temperature, followed by a PBS washes and staining with fluorescently-conjugated secondary antibody for 60 min at room temperature. NPL4-GFP expressing cells were pre-extracted (0.2% Triton X 100 in PBS, for 2 min) and fixed with 4% formaldehyde for 15 min at room temperature, washed with PBS. Nuclei were visualized by DAPI staining at room temperature for 2 min. Dried plastic inserts with cells were mounted using Vectashield mounting medium (Vector Laboratories) and images were acquired using Zeiss Axioimager Z.1 platform.

Image quantification

Images were acquired using the Olympus IX81 fluorescence microscope and ScanR Acquisition software. The scans were quantified in automated image and data analysis software ScanR Analysis. The data were further analysed in the STATISTICA 13 software tool.

ALDEFLUOR assay

ALDH activity in cells were analysed by ALDEFLUOR assay (Stemcell) preformed according to manufacturer protocol. Briefly, cells were incubated with ALDH reagent in supplied buffer for 45 min at 37°C . After that, cells were centrifuged, resuspended in fresh assay buffer and kept on ice until measured by flow cytometry using BD FACSVerser (BD Biosciences), at least 10,000 events were acquired per sample. Collected data were processed by BD FACSSuite (BD Biosciences).

Measurement of CuET formation in vitro

To measure the formation of diethyldithiocarbamate-copper complex (CuET) in vitro, a complete cell culture medium (DMEM, 10% FBS) was incubated with $1\ \mu\text{M}$ DSF or $1\ \mu\text{M}$ DSF plus $1\ \mu\text{M}$ copper (ii) chloride, or DSF with BCDS ($20\ \mu\text{M}$). After 3 h of incubation in 37°C , the samples were vortexed and mixed with acetone in a ratio 1:4. The mixture was centrifuged $18\ 000\times g$ for 2 min at 4°C and immediately spinned for 30 min using small table centrifuge (Bio-San FVL-2400N) placed inside -80°C freezer. Supernatant was quickly transferred into glass HPLC vial and kept at -80°C not longer than 6 h. The CuET complex was analysed by HPLC-MS method described previously (Skrott et al. 2017). The quantification of CuET complex was calculated according to the calibration curve.

Cell fractionation for Triton X insoluble pellets

Cells were treated as indicated, washed in cold PBS and lysed in lysis buffer (50 mM Tris-HCl, pH 7.5, 150 mM NaCl, 2 mM MgCl_2 , 10% glycerol, 0.5% Triton-X100, protease inhibitor cocktail by Roche) for 2 min gently agitating at 4°C . Then, cells were scraped to eppendorf tubes and kept for another 10 min on ice with vortex steps. After that, the lysate was centrifuged at $20,000\times g$ for 10 min at 4°C . Insoluble fraction and supernatant were resuspended in LSB buffer.

Antibodies and chemicals

The following antibodies were used for immunoblotting: mouse monoclonal antibody against BRCA1 antibody (Santa Cruz, D-9, sc-6954), rabbit polyclonal antibody against BRCA2 (Bethyl, A300-005 A) antibody and mouse monoclonal antibody against β -actin (Santa Cruz, C4, sc-47778), lamin B (Santa Cruz, sc-6217), α -Tubulin (Santa Cruz, B-7, sc-5286), anti-ubiquitin lys48-specific (Merck Millipore, clone Apu2, 05-1307). For immunofluorescence were used following antibodies: mouse monoclonal antibody against NPL4 (Santa Cruz, D-1, sc-365796), AlexaFluor 488 goat anti-mouse (Invitrogen, A-11001). Chemicals used in this study were as follows: CuET (bisdiethyldithiocarbamate-copper complex, TCI chemicals), disulfiram (Sigma), copper chloride (Sigma), bortezomib (Velcade, Janssen-Cilag International N.V.), DEAB (Sigma), bathocuproinedisulfonic acid (Sigma), *S*-methyl-*N,N*-diethyldithiocarbamate-sulfoxide (Santa Cruz).

Acknowledgements We thank Dr. M. Tarsounas (Oxford, UK) for the human H1299 cell lines with regulatable expression of shBRCA1 and shBRCA2. The study was supported by grants from: Grant agency of Czech Rep. GACR 17-25976 S, MEYS CR (LM2015062 Czech-BioImaging and DRO-61989592), Internal grant of University of

Palacky IGA_LF_2019_026, Cancer Research Czech Republic, Ministry of School, Education, Youth and Sports of the Czech Republic (EATRIS-CZ No. LM2015064 and ENOC No. CZ.02.1.01/0.0/0.0/16_019/0000868), the Novo Nordisk Foundation (no. 16854), the Danish National Research Foundation (project CARD: no. DNRF125), the Danish Cancer Society (R204-A12617) the Swedish Research Council (VR-MH 2014-46602-117891-30), and the Swedish Cancer Society (no. 170176).

Compliance with ethical standards

Conflict of interest The authors declare that they have no conflict of interest.

Publisher's note Springer Nature remains neutral with regard to jurisdictional claims in published maps and institutional affiliations.

References

- Marques DS, Sandrini JZ, Boyle RT, Marins LF, Trindade GS. Relationships between multidrug resistance (MDR) and stem cell markers in human chronic myeloid leukemia cell lines. *Leuk Res*. 2010;34:757–62.
- Battle E, Clevers H. Cancer stem cells revisited. *Nat Med*. 2017;23:1124–34.
- Tirino V, Desiderio V, Paino F, De Rosa A, Papaccio F, La Noce M, et al. Cancer stem cells in solid tumors: an overview and new approaches for their isolation and characterization. *FASEB J*. 2013;27:13–24.
- Koppaka V, Thompson DC, Chen Y, Ellermann M, Nicolaou KC, Juvonen RO, et al. Aldehyde dehydrogenase inhibitors: a comprehensive review of the pharmacology, mechanism of action, substrate specificity, and clinical application. *Pharm Rev*. 2012;64:520–39.
- Pors K, Moreb JS. Aldehyde dehydrogenases in cancer: an opportunity for biomarker and drug development? *Drug Disco Today*. 2014;19:1953–63.
- Marchitti SA, Brocker C, Stagos D, Vasiliou V. Non-P450 aldehyde oxidizing enzymes: the aldehyde dehydrogenase superfamily. *Expert Opin Drug Metab Toxicol*. 2008;4:697–720.
- Brooks PJ, Theruvathu JA. DNA adducts from acetaldehyde: implications for alcohol-related carcinogenesis. *Alcohol*. 2005;35:187–93.
- van den Hoogen C, van der Horst G, Cheung H, Buijs JT, Lippitt JM, Guzmán-Ramírez N, et al. High aldehyde dehydrogenase activity identifies tumor-initiating and metastasis-initiating cells in human prostate cancer. *Cancer Res*. 2010;70:5163–73.
- Charafe-Jauffret E, Ginestier C, Iovino F, Tarpin C, Diebel M, Esterni B, et al. Aldehyde dehydrogenase 1-positive cancer stem cells mediate metastasis and poor clinical outcome in inflammatory breast cancer. *Clin Cancer Res*. 2010;16:45–55.
- Ginestier C, Hur MH, Charafe-Jauffret E, Monville F, Dutcher J, Brown M, et al. ALDH1 is a marker of normal and malignant human mammary stem cells and a predictor of poor clinical outcome. *Cell Stem Cell*. 2007;1:555–67.
- Yip NC, Fombon IS, Liu P, Brown S, Kannappan V, Armesilla AL, et al. Disulfiram modulated ROS-MAPK and NFκB pathways and targeted breast cancer cells with cancer stem cell-like properties. *Br J Cancer*. 2011;104:1564–74.
- Allensworth JL, Evans MK, Bertucci F, Aldrich AJ, Festa RA, Finetti P, et al. Disulfiram (DSF) acts as a copper ionophore to induce copper-dependent oxidative stress and mediate anti-tumor efficacy in inflammatory breast cancer. *Mol Oncol*. 2015;9:1155–68.
- Liu X, Wang L, Cui W, Yuan X, Lin L, Cao Q, et al. Targeting ALDH1A1 by disulfiram/copper complex inhibits non-small cell lung cancer recurrence driven by ALDH-positive cancer stem cells. *Oncotarget*. 2016;7:58516–30.
- Liu P, Kumar IS, Brown S, Kannappan V, Tawari PE, Tang JZ, et al. Disulfiram targets cancer stem-like cells and reverses resistance and cross-resistance in acquired paclitaxel-resistant triple-negative breast cancer cells. *Br J Cancer*. 2013;109:1876–85.
- Liu P, Brown S, Goktug T, Channathodiylil P, Kannappan V, Hugnot J-P, et al. Cytotoxic effect of disulfiram/copper on human glioblastoma cell lines and ALDH-positive cancer-stem-like cells. *Br J Cancer*. 2012;107:1488–97.
- Liu P, Wang Z, Brown S, Kannappan V, Tawari PE, Jiang W, et al. Liposome encapsulated Disulfiram inhibits NFκappaB pathway and targets breast cancer stem cells in vitro and in vivo. *Oncotarget*. 2014;5:7471–85.
- Jin N, Zhu X, Cheng F, Zhang L. Disulfiram/copper targets stem cell-like ALDH(+) population of multiple myeloma by inhibition of ALDH1A1 and Hedgehog pathway. *J Cell Biochem*. 2018;119:6882–93.
- Choi SA, Choi JW, Wang K-C, Phi JH, Lee JY, Park KD, et al. Disulfiram modulates stemness and metabolism of brain tumor initiating cells in atypical teratoid/rhabdoid tumors. *Neuro Oncol*. 2015;17:810–21.
- MacDonagh L, Gallagher MF, Ffrench B, Gasch C, Breen E, Gray SG, et al. Targeting the cancer stem cell marker, aldehyde dehydrogenase 1, to circumvent cisplatin resistance in NSCLC. *Oncotarget*. 2017;8:72544–63.
- Tacconi EM, Lai X, Folio C, Porru M, Zonderland G, Badie S, et al. BRCA1 and BRCA2 tumor suppressors protect against endogenous acetaldehyde toxicity. *EMBO Mol Med*. 2017;9:1398–414.
- Raha D, Wilson TR, Peng J, Peterson D, Yue P, Evangelista M, et al. The cancer stem cell marker aldehyde dehydrogenase is required to maintain a drug-tolerant tumor cell subpopulation. *Cancer Res*. 2014;74:3579–90.
- Wu L, Meng F, Dong L, Block CJ, Mitchell AV, Wu J, et al. Disulfiram and BKM120 in combination with chemotherapy impede tumor progression and delay tumor recurrence in tumor initiating cell-rich TNBC. *Sci Rep*. 2019;9:236.
- Wang N-N, Wang L-H, Li Y, Fu S-Y, Xue X, Jia L-N, et al. Targeting ALDH2 with disulfiram/copper reverses the resistance of cancer cells to microtubule inhibitors. *Exp Cell Res*. 2018;362:72–82.
- Bista R, Lee DW, Pepper OB, Azorsa DO, Arceci RJ, Aleem E. Disulfiram overcomes bortezomib and cytarabine resistance in Down-syndrome-associated acute myeloid leukemia cells. *J Exp Clin Cancer Res*. 2017;36:22.
- Lipsky JJ, Shen ML, Naylor S. In vivo inhibition of aldehyde dehydrogenase by disulfiram. *Chem Biol Inter*. 2001;130–132:93–102.
- Shen ML, Johnson KL, Mays DC, Lipsky JJ, Naylor S. Determination of in vivo adducts of disulfiram with mitochondrial aldehyde dehydrogenase. *Biochem Pharm*. 2001;61:537–45.
- Mays DC, Nelson AN, Fauq AH, Shriver ZH, Veverka KA, Naylor S, et al. S-Methyl N,N-diethylthiocarbamate sulfone, a potential metabolite of disulfiram and potent inhibitor of low Km mitochondrial aldehyde dehydrogenase. *Biochem Pharm*. 1995;49:693–700.
- Lam JP, Mays DC, Lipsky JJ. Inhibition of recombinant human mitochondrial and cytosolic aldehyde dehydrogenases by two candidates for the active metabolites of disulfiram †. *Biochemistry*. 1997;36:13748–54.
- Hart BW, Faiman MD. Bioactivation of S-methyl N,N-Diethylthiocarbamate to S-methyl N,N-diethylthiolcarbamate sulfoxide. *Biochem Pharm*. 1993;46:2285–90.

30. Yourick JJ, Faiman MD. Disulfiram metabolism as a requirement for the inhibition of rat liver mitochondrial low Km aldehyde dehydrogenase. *Biochem Pharm.* 1991;42:1361–6.
31. Chen D, Cui QC, Yang H, Dou QP. Disulfiram, a clinically used anti-alcoholism drug and copper-binding agent, induces apoptotic cell death in breast cancer cultures and xenografts via inhibition of the proteasome activity. *Cancer Res.* 2006;66:10425–33.
32. Majera D, Skrott Z, Bouchal J, Bartkova J, Simkova D, Gachechiladze M, et al. Targeting genotoxic and proteotoxic stress-response pathways in human prostate cancer by clinically available PARP inhibitors, vorinostat and disulfiram. *Prostate.* 2019;79:352–62.
33. Skrott Z, Mistrik M, Andersen KK, Friis S, Majera D, Gursky J, et al. Alcohol-abuse drug disulfiram targets cancer via p97 segregase adaptor NPL4. *Nature.* 2017;552:194–9.
34. Farmer H, McCabe N, Lord CJ, Tutt ANJ, Johnson DA, Richardson TB, et al. Targeting the DNA repair defect in BRCA mutant cells as a therapeutic strategy. *Nature.* 2005;434:917–21.
35. Bryan N, Andrews KD, Loughran MJ, Rhodes NP, Hunt JA. Elucidating the contribution of the elemental composition of fetal calf serum to antigenic expression of primary human umbilical-vein endothelial cells in vitro. *Biosci Rep.* 2011;31:199–210.
36. Zhou L, Sheng D, Wang D, Ma W, Deng Q, Deng L, et al. Identification of cancer-type specific expression patterns for active aldehyde dehydrogenase (ALDH) isoforms in ALDEFLUOR assay. *Cell Biol Toxicol.* 2019;35:161–77.
37. Huddle BC, Grimley E, Buchman CD, Chitchebinine M, Debnath B, Mehta P, et al. Structure-based optimization of a novel class of aldehyde dehydrogenase 1A (ALDH1A) subfamily-selective inhibitors as potential adjuncts to ovarian cancer chemotherapy. *J Med Chem.* 2018;61:8754–73.
38. Duan J-J, Cai J, Guo Y-F, Bian X-W, Yu S-C. ALDH1A3, a metabolic target for cancer diagnosis and therapy. *Int J Cancer.* 2016;139:965–75.
39. Lai C-L, Yao C-T, Chau G-Y, Yang L-F, Kuo T-Y, Chiang C-P, et al. Dominance of the inactive Asian variant over activity and protein contents of mitochondrial aldehyde dehydrogenase 2 in human liver. *Alcohol Clin Exp Res.* 2014;38:44–50.
40. Chang JS, Hsiao J-R, Chen C-H. ALDH2 polymorphism and alcohol-related cancers in Asians: a public health perspective. *J Biomed Sci.* 2017;24:19.
41. Suh JJ, Pettinati HM, Kampman KM, O'Brien CP. The status of disulfiram: a half of a century later. *J Clin Psychopharmacol.* 2006;26:290–302.
42. Chen W, Yang W, Chen P, Huang Y, Li F. Disulfiram copper nanoparticles prepared with a stabilized metal ion ligand complex method for treating drug-resistant prostate cancers. *ACS Appl Mater Interfaces.* 2018;10:41118–28.
43. Peng X, Pan Q, Zhang B, Wan S, Li S, Luo K, et al. Highly stable, coordinated polymeric nanoparticles loading copper(II) diethyldithiocarbamate for combinational chemo/chemodynamic therapy of cancer. *Biomacromolecules.* 2019;20:2372–83.



Article

Targeting the NPL4 Adaptor of p97/VCP Segregase by Disulfiram as an Emerging Cancer Vulnerability Evokes Replication Stress and DNA Damage while Silencing the ATR Pathway

Dusana Majera ^{1,†}, Zdenek Skrott ^{1,†}, Katarina Chroma ¹, Joanna Maria Merchut-Maya ², Martin Mistrik ^{1,†} and Jiri Bartek ^{1,2,3,*}

¹ Laboratory of Genome Integrity, Institute of Molecular and Translational Medicine, Faculty of Medicine and Dentistry, Palacky University, 77 147 Olomouc, Czech Republic; dusana.majera@upol.cz (D.M.); zdenek.skrott@upol.cz (Z.S.); katarina.chroma@upol.cz (K.C.)

² Danish Cancer Society Research Center, 2100 Copenhagen, Denmark; jomema@cancer.dk

³ Division of Genome Biology, Department of Medical Biochemistry and Biophysics, Science for Life Laboratory, Karolinska Institute, 171 77 Stockholm, Sweden

* Correspondence: martin.mistrik@upol.cz (M.M.); jb@cancer.dk (J.B.)

† These authors contributed equally to this work.

Received: 21 January 2020; Accepted: 17 February 2020; Published: 18 February 2020



Abstract: Research on repurposing the old alcohol-aversion drug disulfiram (DSF) for cancer treatment has identified inhibition of NPL4, an adaptor of the p97/VCP segregase essential for turnover of proteins involved in multiple pathways, as an unsuspected cancer cell vulnerability. While we reported that NPL4 is targeted by the anticancer metabolite of DSF, the bis-diethyldithiocarbamate-copper complex (CuET), the exact, apparently multifaceted mechanism(s) through which the CuET-induced aggregation of NPL4 kills cancer cells remains to be fully elucidated. Given the pronounced sensitivity to CuET in tumor cell lines lacking the genome integrity caretaker proteins BRCA1 and BRCA2, here we investigated the impact of NPL4 targeting by CuET on DNA replication dynamics and DNA damage response pathways in human cancer cell models. Our results show that CuET treatment interferes with DNA replication, slows down replication fork progression and causes accumulation of single-stranded DNA (ssDNA). Such a replication stress (RS) scenario is associated with DNA damage, preferentially in the S phase, and activates the homologous recombination (HR) DNA repair pathway. At the same time, we find that cellular responses to the CuET-triggered RS are seriously impaired due to concomitant malfunction of the ATRIP-ATR-CHK1 signaling pathway that reflects an unorthodox checkpoint silencing mode through ATR (Ataxia telangiectasia and Rad3 related) kinase sequestration within the CuET-evoked NPL4 protein aggregates.

Keywords: targeted cancer therapy; disulfiram; NPL4; replication stress; DNA damage; BRCA1; BRCA2; ATR pathway

1. Introduction

Recent advances in understanding of the altered wiring of cancer cell regulatory pathways, and hence vulnerabilities and dependencies of tumor cells have led to discoveries of new molecular targets potentially exploitable in cancer therapy. As the development of a new drug is time-consuming, very expensive, and prone to frequent failure, drug repurposing as a possible alternative approach to cancer treatment is currently undergoing serious consideration [1]. One of the candidate drugs for repurposing in oncology is disulfiram (tetraethylthiuram disulfide, DSF, commercially known as

Antabuse), a cheap and well-tolerated generic drug that has been used for decades to treat alcohol dependency. DSF has shown anticancer activity in preclinical models, and multiple clinical trials to treat various types of human malignancies by DSF are currently underway [2]. We have recently published that DSF is metabolized *in vivo* into the bis-diethyldithiocarbamate-copper complex (CuET), in a process that requires copper ions, and demonstrated that CuET represents the ultimate anticancer metabolite of DSF *in vivo* [3]. Furthermore, our nationwide epidemiological study in Denmark yielded results consistent with the emerging anticancer effects of DSF, documenting a lower risk of death from cancer in those cancer patients who were treated by DSF after their cancer diagnosis [3]. Mechanistically, we reported that CuET causes aggregation and thereby immobilization and dysfunction of NPL4, an essential cofactor of the p97/VCP segregase. This otherwise highly mobile protein complex is involved in the regulation of protein turnover upstream of the proteasome, with important roles in a wide range of cellular processes including fundamental pro-survival stress-tolerance pathways [3].

In a follow-up study devoted to target validation and further mechanistic insights into CuET effects [4], we explored the reported exceptional sensitivity to DSF of human cancer cell lines defective in BRCA1 or BRCA2 tumor suppressors, key components of the genome integrity maintenance machinery [4,5]. We found that CuET spontaneously forms from DSF and available copper ions also in cell culture media, and our experiments confirmed NPL4 as the molecular target while excluding the proposed inhibition of aldehyde dehydrogenase (ALDH) [5] and accumulation of toxic acetaldehydes causing DNA-protein and DNA interstrand cross-links [6], as the potential mechanistic explanation for the reported sensitivity of BRCA-defective tumors [4]. In addition to ALDH, we also excluded the proteasome, another previously suggested candidate target of DSF's anticancer effects, as a valid target. Indeed, we showed that the observed 'proteasome-inhibition-like features' triggered by DSF/CuET turned out to be fully attributable to the disabled NPL4 acting upstream of the proteasome [3]. Collectively, these mechanistic studies identified and validated NPL4 as the genuine, and possibly the only or dominant direct molecular target of DSF/CuET responsible for the widely appreciated tumor-inhibitory effects of DSF [3,4]. Indeed, the available evidence in the field now points to CuET-induced aggregation of NPL4 as the key anticancer mechanism of DSF under both *in vitro* and *in vivo* conditions, and a promising cancer vulnerability.

Relevant to the present study and the sensitivity of the BRCA-defective cancers to DSF/CuET, we and others previously discovered enhanced replication stress and endogenous DNA damage as a candidate hallmark of cancer [7–10], thereby pioneering the concept of the ATM-Chk2- and ATR-Chk1-mediated DNA damage response (DDR) checkpoints as important cell-intrinsic barriers against oncogene activation and tumor progression [10–12]. Currently, replication stress is recognized to play a prominent role in driving genomic instability and tumorigenesis, while further drug-mediated enhancement of replication stress or inhibition of replication stress-tolerance pathways such as ATR-Chk1 signaling may provide additional targetable vulnerabilities of cancer [13,14]. The main mechanistic consequence of replication stress is the accumulation of ssDNA and stalling of replication forks [15]. The ssDNA stretches become rapidly coated with replication protein A (RPA), thereby facilitating activation of the ATR-Chk1 signaling module and subsequent phosphorylation of hundreds of cellular proteins as substrates of ATR and Chk1 kinases [15,16]. These phosphorylation cascades also involve BRCA1 and BRCA2 and help to stabilize the stalled forks, thereby preventing fork collapse, while in parallel limiting the cellular entry into mitosis by activation of the S-M checkpoint [17]. Under inhibition or genetic deficiency of ATR, stalled replication forks tend to collapse, leading to a generation of DNA double-strand breaks (DSBs), which, if unrepaired or misrepaired, can cause chromosomal instability, severe pathologies or cell death [14,18].

With the above-mentioned knowledge as the starting point, here we examined potential mechanistic links between cancer-associated replication stress, DNA damage checkpoint signaling and the functional impact of DSF/CuET treatment on DNA replication and genome integrity maintenance, searching for possible explanations of the overall sensitivity of tumor cells, and the observed preferential sensitivity of cancer cells lacking BRCA1 and BRCA2, to treatment with DSF/CuET.

2. Materials and Methods

2.1. Cell Culture

Human non-small cell lung carcinoma H1299 cells expressing a doxycycline (DOX)-inducible BRCA1 and BRCA2 shRNAs, U2OS, MDA-MB-231, MDA-MB-436, U2OS cells expressing NPL4-GFP, U2OS expressing DOX-inducible MUT-NPL4-GFP [3] and U2OS cells expressing ATR-GFP [19] were cultured and maintained in DMEM (Dulbecco's Modified Eagle Medium, Lonza, Basel, Switzerland), supplemented with 10% fetal bovine serum (Thermo Fisher Scientific, Waltham, MA, USA) and 1% penicillin/streptomycin (Sigma-Aldrich, St. Louis, MO, USA). CAPAN-1 cells were grown in DMEM medium, supplemented with 20% fetal bovine serum and 1% penicillin/streptomycin. H1299 expressing a DOX-inducible BRCA1 and BRCA2 shRNA were kindly provided [5]. For efficient BRCA1 and BRCA2 knockdown cells were cultivated in the presence of 2 µg/mL DOX for at least three days.

2.2. Immunoblotting

Equal amounts of cell lysates were separated by SDS-PAGE on hand casted gels and then transferred onto the nitrocellulose membrane. The membrane was blocked in Tris-buffered saline containing 5% milk and 0.1% Tween 20 for 1 h at room temperature and then incubated 1 h at room temperature with primary antibodies, followed by detection with secondary antibodies. Secondary antibodies were visualized by ELC detection reagent (Thermo Fisher Scientific, Waltham, MA, USA).

2.3. Immunofluorescence

Cells were seeded on plastic inserts in 12-well dishes. The next day, cells were treated with compounds at indicated concentrations and subsequently either pre-extracted (0.1% Triton X 100 in Phosphate-Buffered Saline (PBS) for 2 min or fixed with formaldehyde for 15 min at room temperature, washed with PBS and permeabilized with 0.5% Triton X-100 in PBS for 5 min. After PBS washes, the cells on the plastic inserts were immunostained with primary antibody for 1 h at room temperature, followed by PBS washes and staining with fluorescently-conjugated secondary antibody for 60 min at room temperature. Nuclei were visualized by 4',6-diamidino-2-phenylindole (DAPI, 1 µg/mL) staining at room temperature for 2 min. For NPL4 staining, the cells were pre-extracted (0.1% Triton X 100 in PBS, for 2 min) and fixed with -20 °C methanol for 15 min at room temperature, washed with PBS and permeabilized with 0.5% Triton X-100 in PBS for 5 min. After PBS washes, the cells on the plastic inserts were immunostained with primary antibody for 120 min at room temperature, followed by PBS washes and staining with fluorescently-conjugated secondary antibody for 60 min at room temperature. Dried plastic inserts with cells were mounted using Vectashield mounting medium (Vector Laboratories, Burlingame, CA, USA), and images were acquired using the Zeiss Axioimager Z.1 platform.

2.4. Ethynyldeoxyuridine (EdU) and Bromodeoxyuridine (BrdU) Incorporation and Detection

To detect active DNA replication, cells were incubated with 10 µM EdU (Life Technologies, Carlsbad, CA, USA) for 30 min, fixed, permeabilized and stained using Click-iT reaction (100 mM Tris pH 8.5, 1 mM copper sulfate, 100 µM ascorbic acid, 1 µM azide Alexa fluor 488 (Life Technologies, Carlsbad, CA, USA) for 30 min at room temperature. To detect ssDNA, cells were incubated with 10 µM BrdU (Sigma) for 24 h, then BrdU was washed out, and cells were incubated with the tested compounds as indicated. After pre-extraction and fixation in buffered formol, the incorporated BrdU was detected by an anti-BrdU antibody (BD Biosciences, San Jose, CA, USA) without denaturation.

2.5. Image Quantification

Images were acquired using the Olympus IX81 fluorescence microscope and ScanR Acquisition software. The scans were quantified in automated image and data analysis software ScanR Analysis.

The data was further analyzed in the STATISTICA 13 software tool (Dell Software, Round Rock, TX, USA).

2.6. DNA Combing

H1299 cells were treated with 125 nM CuET for 5 h and subsequently pulsed with 5-Iodo-2'-deoxyuridine (IdU, 20 μ M) for 30 min, washed and pulsed with 5-Chloro-2'-deoxyuridine (CldU, 200 μ M) for additional 30 min. DNA replication was stopped by ice-cold PBS. Cells were collected and embedded in 0.5% insert agarose plugs. The plugs were incubated for 32 h in buffer containing proteinase K at 50 °C. Plugs were then washed with TE buffer and melted at 68 °C. The obtained solution was further digested overnight with Agarase I at 42 °C. The next day, the concentration of DNA was measured on nanodrop and combed on silanized cover glasses (Matsunami, Japan) with a speed of 0.3 mm/s. The cover glasses with combed DNA were baked at 60 °C, dehydrated with 70%, 90%, and 100% ethanol series for 3 min each. DNA was denatured at 75 °C in 2 \times SSC, 50% formamide for 2 min. Next, the cover glasses were dehydrated with a 70%, 90% and 100% ice-cold ethanol series for 5 min each, air dried, blocked using 1% BSA in PBS-Tween for 1 h at 37 °C and subsequently incubated with primary antibodies, mouse anti-BrdU for IdU detection (1:5) and rat anti-BrdU for CldU detection (1:25) for 1 h at 37 °C. After several washes with PBS-Tween, cover glasses were incubated with secondary antibodies goat anti-mouse A488 (1:100) and goat anti-rat A549 (1:100) for 30 min at 37 °C. After several washes with PBS-Tween, cover glasses were air-dried, mounted, and images of DNA fibers were acquired using the Zeiss Axioimager Z.1 platform.

2.7. Estimation of DNA Replication Origin Density

After the treatment by tested compounds, cells were pulsed with EdU (10 μ M) for 20 min, then harvested and resuspended in cold PBS (1 million of cells per 1 mL). 2 μ L of cell suspension was applied on glass slides (Superfrost Plus, Thermo Fisher) and allowed to partially evaporate for 5 min, then mixed with a lysis buffer (50 mM EDTA and 0.5% SDS in 200 mM Tris-HCl, pH 7.5) and incubated for 2 min. Slides were tilted to 15° to allow the spreading of fibers. After drying, the samples were fixed in methanol/acetic acid solution for 15 min and thoroughly washed. EdU was detected by click reaction using Alexafluor 488 azide. The signal was further enhanced by anti-Alexa fluor 488 antibody (A-11094, Thermo Fisher) and secondary antibody. DNA was visualized by YOYO-1 (Molecular Probes) staining (1 μ M for 20 min). Fiber images were acquired using the Zeiss Axioimager Z.1 platform, and the number of DNA replication origins was calculated on single well-stretched DNA fibers. A conversion factor of 2.59 kb/ μ m was used in calculations [20].

2.8. Cell Fractionation for Triton X Insoluble Pellets

Cells were treated as indicated, washed in cold PBS and lysed in lysis buffer (50 mM Tris-HCl, pH 7.5, 150 mM NaCl, 2 mM MgCl₂, 10% glycerol, 0.5% Triton-X100, protease inhibitor cocktail by Roche) for 2 min, under gentle agitation at 4 °C. Then, cells were scraped to Eppendorf tubes and kept for another 10 min on ice with vortex steps. Next, the lysate was centrifuged at 20,000 \times g for 10 min at 4 °C. Insoluble fraction and supernatant were re-suspended in Laemmli Sample Buffer (1X final concentration; 10% glycerol, 60 mM Tris-HCl, pH 6.8, 2% SDS, 0.01% bromophenol blue, 50 mM dithiothreitol).

2.9. Laser Micro-Irradiation

U2OS cells stably expressing GFP-ATR were seeded into 24-well plates with a glass-bottom (Cellvis) 24 h before laser micro-irradiation in a density of 6×10^5 cells/mL. After seeding the cells into the 24 well plates, the specimen was first placed on an equilibrated bench for 20 min at room temperature (RT) to ensure equal cell distribution and then placed into an incubator. CuET was added to cells 5 h before micro-irradiation in final concentrations of 250 nM and 500 nM. Twenty minutes before laser micro-irradiation, cells were pre-sensitized towards UV-A wavelength by 20 μ M 8-Methoxypsoralen

(8-MOP) and placed inside Zeiss Axioimager Z.1 inverted microscope combined with the LSM 780 confocal module. Laser micro-irradiation was performed at 37 °C via X 40 water immersion objective (Zeiss C-Apo 403/1.2WDICIII), using a 355 nm 65 mW laser set on 100% power to induce the DNA damage. The total laser dose that can be further manipulated by the number of irradiation cycles was empirically set to two irradiation cycles. Subsequent immunofluorescence detection and quantitative analysis of the striation pattern in photo-manipulated samples were essentially performed as described previously [21].

2.10. Antibodies and Chemicals

The following antibodies were used for immunoblotting: BRCA1 antibody (Santa Cruz Biotechnology, Dallas, TX, USA, D-9), rabbit polyclonal antibody against BRCA2 (Bethyl, Montgomery, TX, USA, A300-005A) antibody and mouse monoclonal antibody against β -actin (Santa Cruz Biotechnology, C4), lamin B (Santa Cruz Biotechnology, sc-6217), α -Tubulin (Santa Cruz Biotechnology, sc-5286), anti-ubiquitin lys48-specific (Merck Millipore, Burlington, MA, USA, clone Apu2) Chk1 (Santa Cruz, Biotechnology, sc-8404), phospho-Chk1 S317 (Cell Signalling, Danvers, MA, USA, 2344), phospho-Chk1 S345 (Cell Signalling, 2348), RPA (Abcam, ab16855, Cambridge, UK), phospho-RPA S33 (Bethyl, A300-246A), ATR (Santa Cruz Biotechnology, N-19). For immunofluorescence were used the following antibodies: γ H2AX (Merck Millipore, 05-636), cyclin A (Santa Cruz Biotechnology, H-3, Santa Cruz Biotechnology, sc-239), RPA (Abcam, ab16855), Rad51 (Abcam, ab63801), NPL4 (Santa Cruz Biotechnology, D-1), p97 (Abcam, ab11433), ATR (Santa Cruz Biotechnology, N-19). For DNA combing assay following antibodies were used: anti-BrdU (BD Biosciences, Franklin Lakes, NJ, USA, BD 347580) and rat anti-BrdU (Abcam ab6323).

Chemicals used in this study were as follows: CuET (bis-diethyldithiocarbamate-copper complex, TCI chemicals), disulfiram (Sigma, St. Louis, MO, USA), bortezomib (Velcade, Janssen-Cilag International N.V.), bathocuproinedisulfonic acid (Sigma, St. Louis, MO, USA), CB-5083 (Selleckchem, Houston, TX, USA), hydroxyurea (Sigma, St. Louis, MO, USA), AZD6738 (AstraZeneca, London, UK).

2.11. Field Inversion Gel Electrophoresis (FIGE)

Treated cells, as indicated in the main text, were trypsinized and melted into 1.0% InCert-Agarose inserts. Subsequently, agarose inserts were digested in a mixture of 10 mM Tris-HCl pH 7.5, 50 mM EDTA, 1% N-laurylsarcosyl, and proteinase K (2 mg/mL) at 50 °C for 24 hr and washed five times in Tris-EDTA (TE buffer, 10 mM Tris-HCl pH 8.0, 100 mM EDTA). The inserts were loaded onto a separation gel 1.0% agarose mixed with GelRed[®] solution (10,000x). Run conditions for the DNA fragments separation were: 110 V, 7.5 V/cm, 16 h, forward pulse 11 s, reverse pulse 5 s in 1X Tris-acetic acid-EDTA (TAE buffer 40 mM Tris, 20 mM acetic acid, 1 mM EDTA).

2.12. Alkaline Comet Assay

The alkaline comet assay was performed essentially as described in [22]. Briefly, CAPAN-1 and MDA-MB-436 cells were treated with 250 nM CuET or 2 mM hydroxyurea (HU) for 5 h, collected and resuspended in PBS (7500 cells/ μ L). Cells (7500) were then mixed with 37 °C low melting point agarose (Lonza, Basel, Switzerland), spotted on the normal melting point agarose (Invitrogen, Waltham, MA, USA) pre-coated slides and left to sit for 10 min at 4 °C. Slides were then immersed in the cold alkaline lysis buffer for 2 h at 4 °C. Slides were washed three times with the cold alkaline electrophoresis buffer and electrophoresis was performed (25 min, 4 °C, 0.6 V/cm). Slides were then washed with cold PBS and ddH₂O, dehydrated in cold graded ethanol, air-dried and stored at room temperature. For staining, slides were rehydrated with ddH₂O, stained with Sybr Gold (1:4000 in TE buffer; Thermo Fisher Scientific, Waltham, MA, USA), washed with PBS and mounted with Mowiol (Sigma-Aldrich, St. Louis, MO, USA). Images were acquired using a fluorescent microscope (Carl Zeiss, Oberkochen, Germany), a 20x air immersion objective (Carl Zeiss, Oberkochen, Germany) and Comet Assay IV software (Perceptive Instruments, Haverhill, UK). Presented results are from the technical duplicate.

Alkaline lysis buffer: 1.2 M NaCl, 100 mM Na₂EDTA, 0.1% sodium lauryl sarcosinate, 0.26 M NaOH (pH > 13, 4 °C, prepared fresh); alkaline electrophoresis buffer: 0.03 M NaOH, 2 mM Na₂EDTA (pH 12.3, 4 °C).

3. Results

3.1. CuET Causes DNA Damage Preferentially Detectable in S/G2-Phase Cells

To initiate our current study, we first wished to assess the impact of CuET on DNA damage in cultured human cancer cells, including isogenic cell pairs with experimentally altered components of the DDR machinery. To this end, we employed the established H1299 lung cancer model allowing for DOX-inducible shRNA-mediated depletion of BRCA1 or BRCA2 [4,5]. Indeed, treatment of these cell lines with CuET resulted in an increased formation of γ H2AX foci as well as enhanced overall γ H2AX signal intensity, established surrogate markers for chromatin response to DSBs and overall DNA damage signaling by the upstream DDR kinases, respectively (Figure 1A,B; Supplementary Figure S1A,B). Notably, the CuET-evoked increase of γ H2AX was more pronounced in the BRCA1- and BRCA2-depleted cells compared with their BRCA-proficient counterpart H1299 cells (unexposed to DOX) (Figure 1A,B; Supplementary Figure S1B). To clarify whether such DNA damage could also be caused by DSF itself, we treated the BRCA2-depleted H1299 cells with DSF in cell culture settings where the cells were first pre-treated by the copper chelator bathocuproinedisulfonic acid (BCDS), a manipulation that we previously reported prevents the otherwise spontaneous and rapid formation of CuET from DSF and copper in cell culture media [4]. As expected, when used alone, DSF caused a similar increase in DNA damage formation as CuET, however when DSF was combined with the copper chelator BCDS pre-treatment step, the γ H2AX-inducing effect of DSF was completely abrogated (Figure 1E). These results showed that the DNA damage observed after the treatment with DSF depends on the copper-dependent spontaneous formation of CuET in the culture media, thereby establishing that analogous to the anticancer effects, the active DNA damage-inducing compound is the CuET metabolite, rather than DSF itself.

Next, we pursued our observation that the increase of γ H2AX was apparent only in a subset of cells in a given exponentially growing cell population, suggesting that the DNA damage could be cell cycle-dependent. To examine this possibility, we again treated the above mentioned H1299 cells with CuET, yet in the subsequent immunofluorescence analysis, we double stained the cells for γ H2AX and cyclin A, an approach commonly used to distinguish cells in G1 phase (cyclin A negative) from those in S/G2 phases (cyclin A positive). Notably, the CuET-induced γ H2AX was preferentially seen in cyclin A positive cells, and this cell-cycle effect was even more pronounced in the BRCA1- and BRCA2-depleted cells (Figure 1C,D, Supplementary Figure S1C). The preference of elevated γ H2AX intensity in cyclin A positive cells was also confirmed in additional human cancer cell lines (Supplementary Figure S1D,E), thereby excluding a possibility that such genotoxic effects of CuET could be restricted to the H1299 cell model.

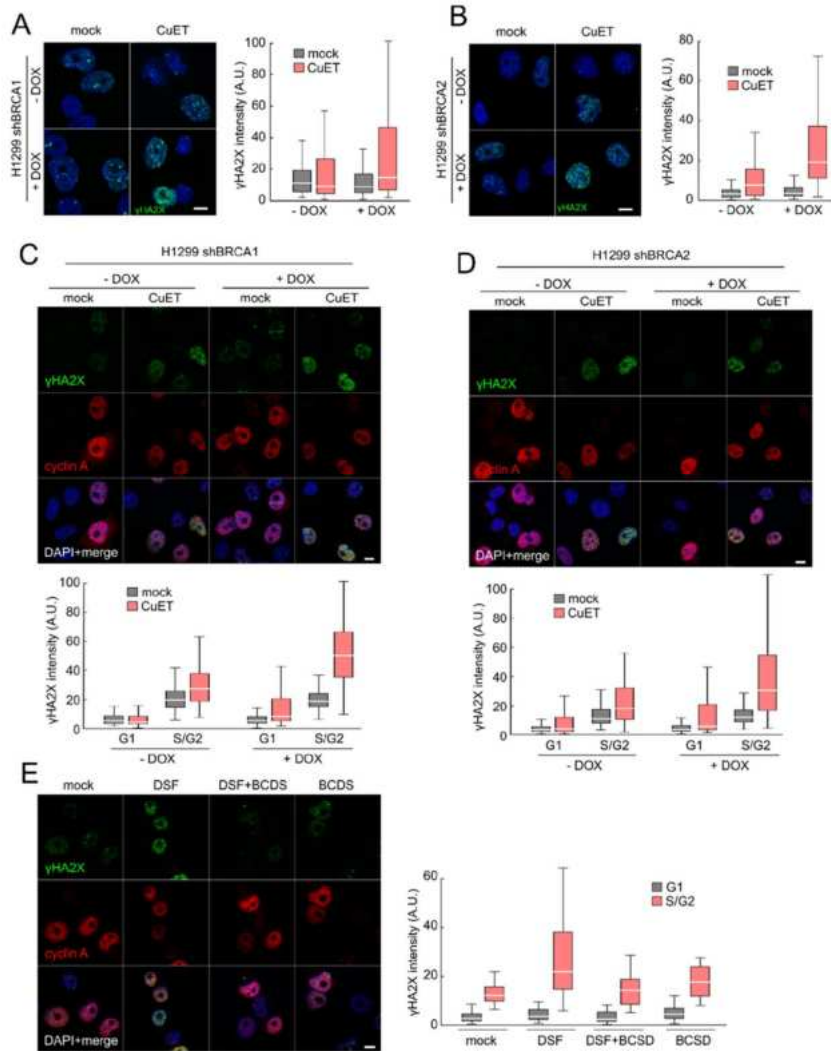


Figure 1. Disulfiram’s metabolite bis-diethylthiocarbamate-copper complex (CuET) causes DNA damage preferentially in S/G2 cells deficient for BRCA1 or BRCA2 proteins. H1299 cells expressing (doxycycline-) DOX-inducible shBRCA1 (A) or shBRCA2 (B) were cultivated for at least three days in DOX-containing media and then treated with CuET (250 nM) for 5 h, and γ H2AX intensity was analyzed by quantitative microscopy. (C) H1299 shBRCA1 cells or (D) H1299 shBRCA2 cells were treated as in (A) a γ H2AX intensity was quantified with respect to cyclin A positivity defining S/G2 phase. (E) H1299 shBRCA2 cells pre-incubated with DOX were treated with disulfiram (DSF) (500 nM), bathocuproinedisulfonic acid (BCSD) (50 μ M), or their combination for 5 h and γ H2AX intensity was quantified. Box plot represents 25–75 quartiles, median, and whiskers non-outlier range. Scale bars = 10 μ m.

Overall, we conclude from these results that the DNA damage-inducing effects of DSF are attributable to its CuET metabolite, include both elevated γ H2AX foci formation and overall γ H2AX signal intensity, and occur preferentially in cells traversing S/G2 phases.

3.2. CuET Treatment Decreases DNA Replication Fork Velocity and Increases the Number of Active Replication Origins

Since the CuET-induced DNA damage was more apparent in S/G2 cells, we argued that CuET might preferentially interfere with DNA replication. To examine this possibility, we pre-treated H1299 cells with CuET, followed by a pulse-treatment with the thymine analog EdU that becomes incorporated into newly synthesized DNA, allowing visualization of the rate of ongoing DNA replication using fluorescence readouts. Using this approach, we could indeed confirm severe impairment of DNA replication in CuET treated cells, manifested as a decreased EdU signal in H1299 cells (Figure 2A) and also other cell lines, such as human breast cancer MDA-MB-231 and osteosarcoma U2OS cells (Supplementary Figure S2A,B). DNA replication can be halted by the presence of DNA damage [23] and vice versa; replication interference can be the source of DNA damage [13,14]. To address what is the cause and consequence in this scenario, we performed a kinetic study showing that the decrease of EdU incorporation is an early event, preceding the γ H2AX foci formation (Figure 2B). This result indicated that the observed DNA damage most likely results from the CuET-induced impairment of DNA replication. To gain more detailed insights into the observed replication interference phenomenon, we employed DNA combing as an assay enabling us to directly assess the effect of CuET on DNA replication fork velocity. H1299 cells were first pre-treated with a rather low concentration of CuET and then pulsed with IdU and CldU thymine analogs to detect actively replicating DNA, the length of which can be evaluated by fluorescence microscopy-based measurements [24]. Our analysis of the obtained DNA fibers revealed a robust reduction of DNA replication fork velocity after CuET treatment (Figure 2C). Since such decreased DNA replication fork speed is known to trigger firing of dormant replication origins, we next tested the density of active origins using an established DNA fiber assay [22,25]. We quantified the number of origins per 1 Mb of DNA. Indeed, CuET treatment increased the number of active origins compared to untreated cells, similarly to treatment with the ATR kinase inhibitor AZD6738 (Figure 2D), a known activator of latent replication origin firing used here as a positive control [26].

We interpret these results as documenting a previously unsuspected negative impact of CuET on DNA replication, slowing down the fork velocity and concurrently leading to the firing of more dormant origins.

3.3. CuET-Induced Replication Stress Leads to DNA Damage that Triggers Homologous Recombination Repair Pathway

As replication stress is associated with accumulation of ssDNA stretches detectable by RPA32 protein foci or by staining for DNA-incorporated BrdU under non-denaturing conditions [18,27,28], we next assessed these parameters in human cells treated with CuET. Consistent with the CuET-impaired replication forks (see above), we found enhanced RPA32 foci in several cancer cell lines treated with CuET (Figure 3A,B) and also detected incorporated BrdU under non-denaturing conditions (Figure 3C,D). These data suggest that in CuET-treated cells, DNA helicase becomes uncoupled from DNA polymerases, generating stretches of ssDNA in a manner broadly analogous with effects of the replication stress-inducing drugs such as hydroxyurea or aphidicolin [28]. The RPA-coated ssDNA is known to recruit and activate the ATRIP-ATR-CHK1 signaling pathway [29] to stabilize the stalled replication structures, thereby avoiding fork collapse and formation of DSBs [30]. Importantly, these DNA lesions typically require repair by the homologous recombination (HR) repair pathway that encompasses, among other factors, also BRCA1 and BRCA2, the latter being critical for loading of the Rad51 HR repair protein [31–33]. To test whether Rad51 is involved in the repair process of lesions caused by the CuET treatment, we stained the cells for Rad51 and searched for the typical

DNA-associated Rad51 foci that form within the DSB-flanking chromatin regions under ongoing DNA repair. Indeed, in multiple tested cell lines, the CuET treatment increased the number of Rad51 foci (Figure 3E,F) except for the BRCA2-depleted cells, which are principally incapable of loading Rad51 both after CuET treatment and gamma-irradiation (here used as a positive control) (Figure 3G). The presence of DNA breaks in CuET treated cells was confirmed also by direct physical methods including Field Inversion Gel Electrophoresis (FIGE, detecting largely DSBs) (Figure 3H, Supplementary Figure S3D) and comet assay (Supplementary 3A,B,C, detecting a mixture of single-stranded and double stranded DNA breaks) in BRCA-deficient human cell lines derived from carcinomas of the breast (MDA-MB-436), lung (the H1299 series) and pancreas (CAPAN1), the latter reported by us previously as very sensitive to CuET treatment [3].

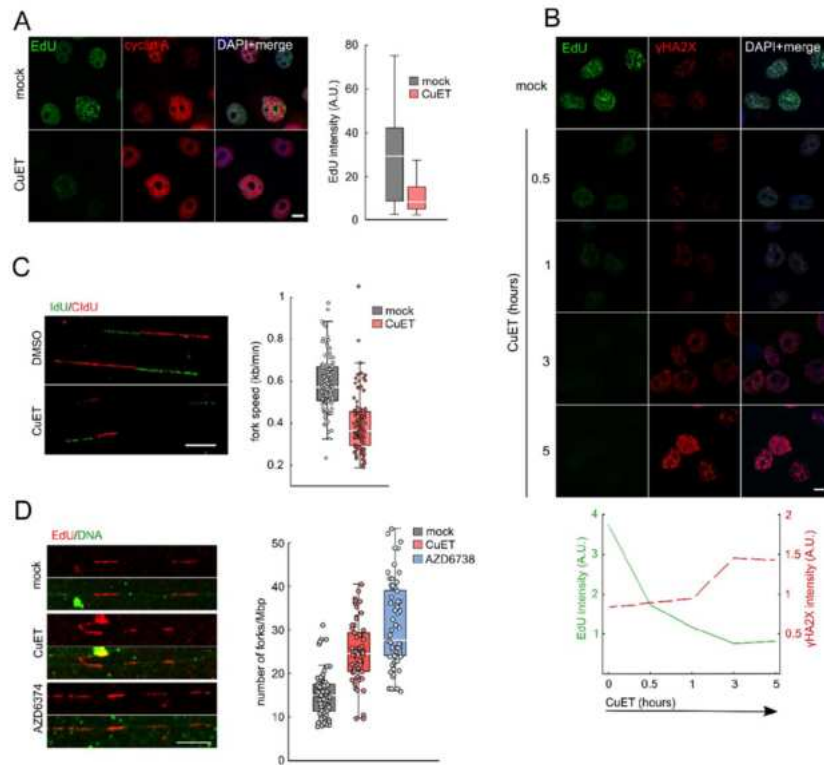


Figure 2. CuET impairs DNA replication. (A) H1299 cells were treated with CuET (250 nM) for 3 h, and ethynyldeoxyuridine (EdU) intensity was analyzed in cells positive for cyclin A. (B) H1299 cells were treated with CuET (250 nM) for different time points, and EdU and γ H2AX intensities were quantified. (C) H1299 cells were treated with CuET (125 nM) for 5 h, then pulse-labeled with 5-Iodo-2'-deoxyuridine (IdU) and 5-Chloro-2'-deoxyuridine (CldU) and processed for DNA combing. (D) H1299 cells were treated with CuET (250 nM) or AZD6374 (10 μ M) for 3 h and then pulsed with EdU and processed for DNA fiber assay. Box plot represents 25–75 quartiles, median, and whiskers non-outlier range. Scale bars = 10 μ m.

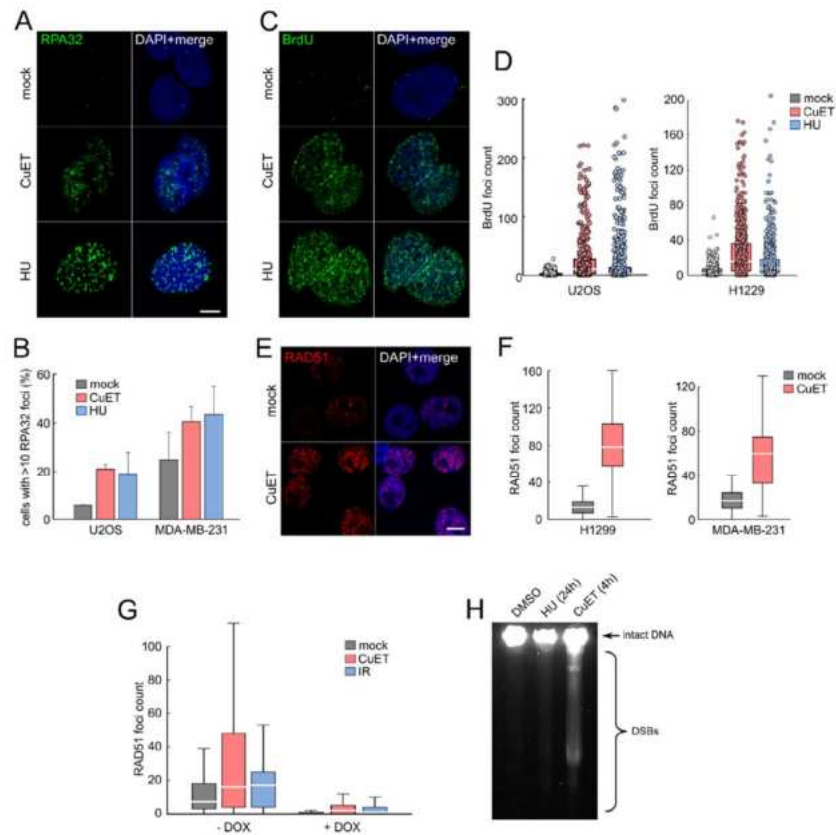


Figure 3. CuET induces replication stress. (A) RPA32 foci detection in pre-extracted U2OS cells treated with CuET (250 nM) or hydroxyurea (HU, 2 mM) for 5 h. (B) Quantification of cells with more than 10 RPA32 foci treated as in (A) (mean, SD from three independent experiments). (C) Formation of single-stranded DNA (ssDNA) visualized by BrdU detected under non-denaturing conditions in U2OS cells treated by CuET (250 nM) and HU (2 mM) for 5 h. (D) Quantification of bromodeoxyuridine (BrdU) foci in U2OS and H1299 cells treated as in C. (E) Detection of RAD51 foci in pre-extracted H1299 cells treated by CuET (250 nM) for 5 h. (F) Quantification of RAD51 foci in cyclin A positive H1299 and MDA-MB-231 cells treated by CuET (250 nM) for 5 h. (G) Quantification of Rad51 foci in BRCA2 proficient and deficient H1299 cells after 5-h treatment with 250 nM CuET or 4 Gray (Gy) irradiation. (H) FIGE analysis of DSBs in H1299 cells exposed to CuET or HU. Box plot represents 25–75 quartiles, median, and whiskers non-outlier range. Scale bars = 10 μ m.

Collectively, these results are consistent with CuET inducing replication stress-associated DNA damage that requires HR repair, including Rad51, a process that is defective in the absence of BRCA1 and BRCA2. Consequently, such DNA damage cannot be properly processed in cells lacking the BRCA factors, which explains the higher amount of DNA damage that contributes to the preferential sensitivity of BRCA-deficient cells to DSF [5] and CuET [4].

3.4. The ATR Signaling Pathway is Compromised in CuET-Treated Cells

In the context of the results obtained so far, we were intrigued by the fact that CuET treatment resulted in DNA breaks relatively quickly within 3–4 h. However, stalled or slowed replication forks should be rather stable for many more hours before turning into DSBs as reported in the U2OS cell line after HU treatment [31] (see also Supplementary Figure S3D). As the prominent role in the stabilization and protection of the stalled forks reflects the function of the RPA-ATRIP-ATR-Chk1 signaling pathway [29,30], we performed immunoblot analysis of extracts from various cell lines treated with CuET, to assess the status of the ATR signaling. In contrast to HU treatment which was used as a positive control, the RPA-ATRIP-ATR-Chk1 signaling pathway was not activated in response to CuET, as manifested by the absence of the ATR-mediated phosphorylations of the effector kinase Chk1: Chk1 S317 and Chk1 S345 (Figure 4A). This result was rather surprising as ssDNA is obviously present in the CuET treated cells (see Figure 3A–D) and also coated by the upstream factor RPA, thereby setting the initial stage for ATR activation and phosphorylation of ATR targets including Chk1. To further investigate whether CuET indeed impairs the RPA-ATRIP-ATR-Chk1 signaling, we treated cells with CuET in the presence of HU. While treatment with HU alone efficiently induced phosphorylation of Chk1 S317 and Chk1 S345, as expected, the combined treatment with CuET and HU revealed the lack of such Chk1 phosphorylations again, indicating that CuET exerted a dominant effect in suppressing the ATR pathway activity (Figure 4B). These unexpected results were then corroborated by the lack of Serine 33 phosphorylation of yet another ATR substrate, the replication stress marker RPA32, an event seen in the HU-treated control but not in CuET- or combined CuET- and HU-treated cells (Figure 4C).

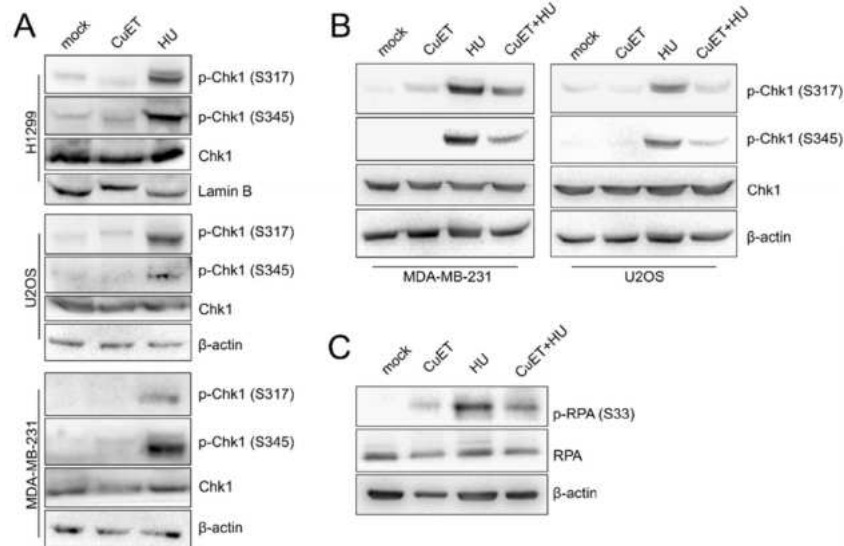


Figure 4. ATR signaling is compromised by CuET. (A) Western blot analysis of phosphorylated forms of Chk1 in various cell lines treated by CuET (250 nM) or HU (2 mM) for 5 h. (B) WB analysis of Chk1 phosphorylation in U2OS and MDA-MB-231 cells pre-treated by dimethylsulfoxide (DMSO, mock) or CuET (250 nM) for 2 h and then exposed to HU (2 mM) for additional 3 h. (C) WB detection of RPA32 phosphorylation in U2OS cells treated as in B.

Together these results suggest that CuET treatment not only causes replication stress by slowing down and/or stalling replication fork progression but at the same time, it also interferes with the activation of the RPA-ATRIP-ATR-Chk1 signaling cascade that is critical for proper cellular responses to replication stress.

3.5. The ATR Signaling Pathway is Compromised in CuET-Treated Cells

The fact that ATR kinase signaling was suppressed after CuET treatment despite ongoing robust replication stress that also included the formation of ssDNA inspired us to focus directly on the ATR protein and its behavior in response to CuET. As a general readout for analysis of ATR abundance, subcellular localization and function we employed the reporter U2OS cells expressing GFP-labeled ATR (U2OS ATR-GFP) that allowed us to directly assess also recruitment of the ATR protein to acutely inflicted DNA lesions induced by laser microirradiation of psoralen pre-sensitized cell nuclei [19,21]. While in control mock-treated cells, the ATR-GFP protein rapidly formed the expected pattern of fluorescent stripes matching the laser tracks, such recruitment of ATR was markedly impaired after CuET exposure (Figure 5A and Supplementary Figure S4). Moreover, we noticed that in CuET-treated cells without any laser exposure, the otherwise pan-nuclear and generally diffuse ATR-GFP fluorescence signal became altered, forming a pattern that was reminiscent of protein aggregates previously reported by us for the NPL4 protein after CuET treatment [3] (Figure 5B). Indeed, further immunofluorescence analysis confirmed co-localization of ATR-GFP with the NPL4/p97 aggregates formed after CuET treatment (Figure 5C) and general immobilization of the ATR protein was then confirmed by two additional complementary approaches: quantitative microscopy on cultured and pre-extracted U2OS ATR-GFP cells (Figure 5D), and immunoblotting identification of protein translocation from the mobile into the immobile (pre-extraction resistant) protein fraction. Notably, unlike the aggregated immobile ATR protein, the downstream component of the ATR cascade, namely the effector kinase Chk1 was not immobilized after CuET treatment (Figure 5E). To distinguish whether or not ATR immobilization was caused by CuET independently of CuET's key reported target, the NPL4 protein [3], we employed our U2OS cell model conditionally expressing a mutated form of NPL4-GFP, a protein which tends to aggregate spontaneously when expressed in cells due to the point mutation in the putative zinc-finger domain involved in the interaction with CuET [3]. We have already shown that such spontaneous aggregation of the NPL4-MUT protein mimics multiple aspects of CuET treatment including association and immobilization of various cellular stress-response proteins including HSP70, p97, SUMO, polyUb, and TDP43 with the NPL4 aggregates [3]. Indeed, using this model, we found the association and immobilization of ATR-GFP within the spontaneously formed NPL4-MUT aggregates (Figure 5F,H).

In summary, these experiments identified NPL4 aggregation, induced by either CuET in the case of wild-type NPL4, or mutation-caused conformational change of the NPL4-MUT protein in the absence of any added CuET, as the primary event and a pre-requisite for the subsequent sequestration of ATR in such NPL4 aggregates, with the ensuing signaling defect of the ATR-Chk1 signaling pathway.

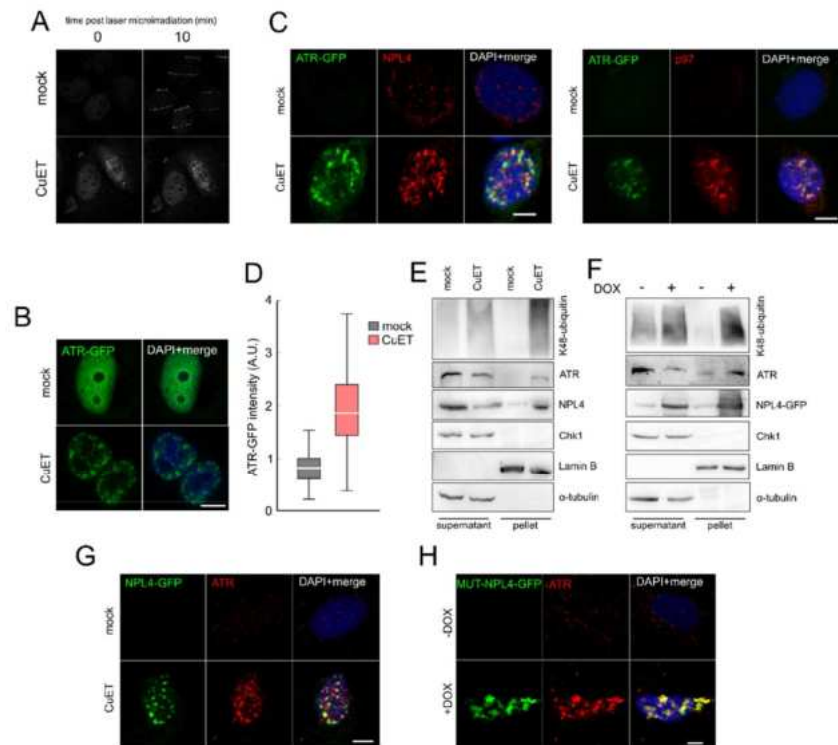


Figure 5. CuET induces immobilization of ATR and its localization to NPL4 aggregates. (A) ATR recruitment to sites of damage caused by laser-microirradiation is impaired after CuET treatment (250 nM for 5 h). (B) ATR-GFP forms typical nuclear clusters after CuET treatment (250 nM for 5 h). (C) Microscopic analysis of co-localization of ATR-GFP with NPL4 and p97 after CuET treatment (250 nM, 3 h) in pre-extracted U2OS cells. (D) Quantitative microscopic analysis of pre-extraction resistant ATR-GFP protein in U2OS cells in control and CuET treated cells (250 nM, 5 h). (E) WB analysis of immobilized ATR, K48 ubiquitinated proteins, and NPL4 in extracts of CuET-treated (250 nM, 3 h) U2OS cells. (F) WB analysis of immobilized ATR, K48 ubiquitinated proteins, and NPL4 in MUT-NPL4-GFP expressing U2OS (Doxycycline induction for 18 h). (G) Microscopic analysis of co-localization of NPL4-GFP with ATR after CuET treatment (250 nM, 3 h) in pre-extracted U2OS cells. (H) Microscopic analysis of co-localization of MUT-NPL4-GFP with ATR after 18 h doxycycline induction in pre-extracted U2OS cells. Scale bars = 10 μ m.

4. Discussion

The major advance provided by the results from our present study is the identification of a new mode of cancer cell cytotoxicity evoked by diethyldithiocarbamate-copper complex, CuET [3,4], the anticancer metabolite of the alcohol aversion drug DSF that is currently tested in clinical trials for repurposing in oncology. Indeed, after years of convoluted efforts to understand the tumor-inhibitory effects of DSF, the field has been aided by our discovery of CuET as the ultimate cancer-killing compound that rapidly forms as DSF becomes metabolized under both in vivo [3], and cell culture [4,34] conditions. At the mechanistic level, we found that CuET impairs the cellular protein degradation machinery

upstream of the proteasome, by inducing aggregation and immobilization of NPL4, an essential cofactor of the p97/VCP segregase complex [3]. This mechanism helps explain the observed preferential toxicity in cancer cells experiencing high levels of proteotoxic stress, such as multiple myeloma [3].

Inspired by the recent intriguing observation that human cancer cells lacking the BRCA1/2 DNA damage response genes are particularly sensitive to DSF [4,5], here we focused on potential genotoxic/replication stress as another aberrant cancer-associated trait [7–10] that could be triggered and/or enhanced by CuET. Indeed, we have found that CuET induces DNA damage preferentially in S-phase cells consistent with robust impairment of DNA replication, induction of replication stress, and impairment of ATR signaling. The same effects can be recapitulated with replacing CuET by DSF, as the culture media contain traces of copper that enable the spontaneous formation of CuET [34]. We validated the latter notion by combined treatment of cells with DSF and the copper chelator BCDS (Figure 1E), which efficiently precludes the spontaneous formation of CuET [4] and thereby the cellular phenotypes otherwise shared by CuET and DSF.

The fundamental question that emerges from our present study, and which we address only partially here, is the nature of the precise molecular mechanism behind the CuET-induced replication stress. As CuET impairs the p97/NPL4 pathway that is directly implicated in several processes linked to DNA repair and replication [35], it remains to be seen whether the replication interference could be explained by impacting such processes, including DNA replication, translesion synthesis, DNA-protein crosslinks repair, or termination of replication [36], possibly in a combination. Moreover, p97, together with diverse cofactors, is also directly involved in DSB repair, contributing to the recruitment of the 53BP1 repair factor [37] and also other DDR proteins [38–40]. On the other hand, also indirect effects of NPL4 aggregation, for example, the triggered heat-shock response, could plausibly contribute to the phenotypes observed here. In our previous work, we observed that apart from NPL4/p97, the CuET-induced aggregates contain several proteotoxic stress-related proteins, including HSP70, SUMO2/3, polyubiquitin chains, and TDP-43 [3]. Here, we have surprisingly found that also ATR kinase, a key factor required for proper cellular response to replication stress, is trapped and sequestered in the NPL4 aggregates, thus explaining the dysfunction of ATR signaling in CuET-treated cells. Conceptually, given that ATR dysfunction is known to trigger replication stress, a feature we see also after CuET treatment, one could argue that ATR aggregation could represent the primary and/or major cause of the CuET-induced replication stress. On the other hand, our time-course analysis suggests that DNA replication becomes impaired very quickly upon CuET addition, as judged from the EdU staining (Figure 2B), in fact preceding any detectable ATR aggregation. Therefore, we currently believe that the two processes, replication fork stalling, and ATR aggregation are possibly initiated independent of each other and act rather in a complementary manner to cause the observed robust replication stress phenotype. A related emerging question for future work is what brings ATR to the vicinity of the forming NPL4 aggregates in the first place? This issue is speculative at present, and it remains to be seen whether some structural features of ATR, possibly shared by additional proteins, such as unstructured regions or high dependency on chaperones, could be involved. Alternatively, the recruitment to aggregates might share the mechanism of the reported ATR recruitment into areas of high topological stress within the nuclear envelope [41]. ATR might be sequestered by the aggregates also through direct interaction with NPL4 or due to the global proteotoxic stress-related changes in the cell. The latter scenario would partially resemble the so-called β -sheets-containing protein aggregates that sequester and mislocalize several proteins involved in RNA metabolism and nucleocytoplasmic transport [42]. Alternatively, liquid–liquid phase separation might also be involved in this process. A recent study [43] revealed that acute hyperosmotic stress induces phase separation of the proteasomes and formation of discrete puncta in the nucleus. Interestingly, these structures also contained K48-ubiquitinated proteins or p97 segregase, the proteins also found in NPL4 clusters, raising the question of whether phase separation plays a role in the case of NPL4 aggregation or attraction of other proteins. These questions need to be addressed by dedicated future studies, to help us better understand the effects of

NPL4 aggregates on cellular physiology, providing clues about why so many seemingly unrelated phenotypes have so far been described after DSF treatment.

Last but not least, our present results are also highly relevant from the clinical point of view, not least because protein aggregation represents an unorthodox and so far largely unexplored mechanism of action for anticancer drugs. This rather unique mechanism may also contribute to the observed synergistic effects of DSF/copper with either ionizing radiation [44] or the DNA damage-inducing drug temozolomide [45] a combination currently tested in several clinical trials focusing on glioblastoma patients [46–48], as well as a combination of DSF with cisplatin [49]. We hope that the data we report here will inspire further research in this rapidly evolving area of biomedicine, and yield additional effective therapies based on combining DSF/copper (CuET) with other currently used DNA damage-related therapeutic modalities.

Overall, based on our present results we suggest that CuET (DSF/copper) evokes and/or exacerbates replication stress in tumor cells while concomitantly precluding the ATR-mediated pro-survival response to such stress, thereby collectively creating a toxic scenario (understandably more severe in BRCA1/2-defective cells) reminiscent of ‘killing two birds with one stone.’

Supplementary Materials: The following are available online at <http://www.mdpi.com/2073-4409/9/2/469/s1>, Figure S1: CuET is causing DNA damage preferentially in S/G2 cells. Figure S2: CuET impairs DNA replication in MDA-MB-231 and U2OS cells. Figure S3: Detection of DNA breaks after CuET treatment. Figure S4: Microscopy-based quantitative analysis of fluorescence signal in cells.

Author Contributions: D.M., Z.S., M.M., and J.B. conceived the study, D.M. and Z.S. designed and performed most experiments, K.C. contributed the laser microirradiation data. J.M.M.-M. performed alkaline comet assay. D.M., Z.S., M.M., and J.B. interpreted the results and wrote the manuscript, which was approved by all authors. All authors have read and agreed to the published version of the manuscript.

Funding: The study was supported by grants from Grant Agency of Czech Rep. GACR 17-25976S, The work was supported by the MEYS CR (Large RI Project LM2018129 Czech-Biolmaging) and ERDF (project No. CZ.02.1.01/0.0/0.0/16_013/0001775), Internal grant of the Palacky University IGA_LF_2019_026), Ministry of School, Education, Youth and Sports of the Czech Republic (ENOCN No. CZ.02.1.01/0.0/0.0/16_019/0000868), the Novo Nordisk Foundation (no. 16854), the Danish National Research Foundation (project CARD: no. DNRF125), the Danish Cancer Society (R204-A12617), the Swedish Research Council (VR-MH 2014-46602-117891-30), and the Swedish Cancer Society (no. 170176).

Acknowledgments: We thank M. Tarsounas (Oxford, UK) for the human H1299 cell lines with the regulatable expression of shBRCA1 and shBRCA2 and Mgr. Tatana Stosova for help with FIGE (Palacky University, Olomouc, Czech Republic).

Conflicts of Interest: The authors declare no conflict of interest.

References

- Collins, F.S. Mining for therapeutic gold. *Nat. Rev. Drug Discov.* **2011**, *10*, 397. [CrossRef] [PubMed]
- McMahon, A.; Chen, W.; Li, F. Old wine in new bottles: Advanced drug delivery systems for disulfiram-based cancer therapy. *J. Control. Release* **2020**, *319*, 352–359. [CrossRef] [PubMed]
- Skrott, Z.; Mistrik, M.; Andersen, K.K.; Friis, S.; Majera, D.; Gursky, J.; Ozdian, T.; Bartkova, J.; Turi, Z.; Moudry, P.; et al. Alcohol-abuse drug disulfiram targets cancer via p97 segregase adaptor NPL4. *Nature* **2017**, *552*, 194–199. [CrossRef] [PubMed]
- Skrott, Z.; Majera, D.; Gursky, J.; Buchtova, T.; Hajdich, M.; Mistrik, M.; Bartek, J. Disulfiram’s anti-cancer activity reflects targeting NPL4, not inhibition of aldehyde dehydrogenase. *Oncogene* **2019**, *38*, 6711–6722. [CrossRef]
- Tacconi, E.M.; Lai, X.; Folio, C.; Porru, M.; Zonderland, G.; Badie, S.; Michl, J.; Sechi, I.; Rogier, M.; Matia Garcia, V.; et al. BRCA1 and BRCA2 tumor suppressors protect against endogenous acetaldehyde toxicity. *EMBO Mol. Med.* **2017**, *9*, 1398–1414. [CrossRef]
- Lorenti Garcia, C.; Mechilli, M.; Proietti De Santis, L.; Schinoppi, A.; Katarzyna, K.; Palitti, F. Relationship between DNA lesions, DNA repair and chromosomal damage induced by acetaldehyde. *Mutat. Res. Mol. Mech. Mutagen.* **2009**, *662*, 3–9. [CrossRef]

7. Bartkova, J.; Hořejší, Z.; Koed, K.; Krämer, A.; Tort, F.; Zieger, K.; Guldberg, P.; Sehested, M.; Nesland, J.M.; Lukas, C.; et al. DNA damage response as a candidate anti-cancer barrier in early human tumorigenesis. *Nature* **2005**, *434*, 864–870. [[CrossRef](#)]
8. Bartkova, J.; Rezaei, N.; Lontos, M.; Karakaidos, P.; Klatsas, D.; Issaeva, N.; Vassiliou, L.-V.F.; Kolettas, E.; Niforou, K.; Zoumpourlis, V.C.; et al. Oncogene-induced senescence is part of the tumorigenesis barrier imposed by DNA damage checkpoints. *Nature* **2006**, *444*, 633–637. [[CrossRef](#)]
9. Gorgoulis, V.G.; Vassiliou, L.-V.F.; Karakaidos, P.; Zacharatos, P.; Kotsinas, A.; Liloglou, T.; Venere, M.; DiTullio, R.A.; Kastrinakis, N.G.; Levy, B.; et al. Activation of the DNA damage checkpoint and genomic instability in human precancerous lesions. *Nature* **2005**, *434*, 907–913. [[CrossRef](#)]
10. Halazonetis, T.D.; Gorgoulis, V.G.; Bartek, J. An Oncogene-Induced DNA Damage Model for Cancer Development. *Science* **2008**, *319*, 1352–1355. [[CrossRef](#)]
11. Bartek, J.; Bartkova, J.; Lukas, J. DNA damage signalling guards against activated oncogenes and tumour progression. *Oncogene* **2007**, *26*, 7773–7779. [[CrossRef](#)] [[PubMed](#)]
12. Jackson, S.P.; Bartek, J. The DNA-damage response in human biology and disease. *Nature* **2009**, *461*, 1071–1078. [[CrossRef](#)] [[PubMed](#)]
13. Gaillard, H.; García-Muse, T.; Aguilera, A. Replication stress and cancer. *Nat. Rev. Cancer* **2015**, *15*, 276–289. [[CrossRef](#)]
14. Bartek, J.; Mistrik, M.; Bartkova, J. Thresholds of replication stress signaling in cancer development and treatment. *Nat. Struct. Mol. Biol.* **2012**, *19*, 5–7. [[CrossRef](#)]
15. Zeman, M.K.; Cimprich, K.A. Causes and consequences of replication stress. *Nat. Cell Biol.* **2014**, *16*, 2–9. [[CrossRef](#)] [[PubMed](#)]
16. Berti, M.; Vindigni, A. Replication stress: Getting back on track. *Nat. Struct. Mol. Biol.* **2016**, *23*, 103–109. [[CrossRef](#)]
17. Eykelenboom, J.K.; Harte, E.C.; Canavan, L.; Pastor-Pedro, A.; Calvo-Asensio, I.; Llorens-Agost, M.; Lowndes, N.F. ATR Activates the S-M Checkpoint during Unperturbed Growth to Ensure Sufficient Replication Prior to Mitotic Onset. *Cell Rep.* **2013**, *5*, 1095–1107. [[CrossRef](#)]
18. Toledo, L.L.; Altmeyer, M.; Rask, M.-B.; Lukas, C.; Larsen, D.H.; Povlsen, L.K.; Bekker-Jensen, S.; Mailand, N.; Bartek, J.; Lukas, J. ATR Prohibits Replication Catastrophe by Preventing Global Exhaustion of RPA. *Cell* **2014**, *156*, 374. [[CrossRef](#)]
19. Bekker-Jensen, S.; Lukas, C.; Kitagawa, R.; Melander, F.; Kastan, M.B.; Bartek, J.; Lukas, J. Spatial organization of the mammalian genome surveillance machinery in response to DNA strand breaks. *J. Cell Biol.* **2006**, *173*, 195–206. [[CrossRef](#)]
20. Jackson, D.A.; Pombo, A. Replicon Clusters Are Stable Units of Chromosome Structure: Evidence That Nuclear Organization Contributes to the Efficient Activation and Propagation of S Phase in Human Cells. *J. Cell Biol.* **1998**, *140*, 1285–1295. [[CrossRef](#)]
21. Mistrik, M.; Vesela, E.; Furst, T.; Hanzlikova, H.; Frydrych, I.; Gursky, J.; Majera, D.; Bartek, J. Cells and Stripes: A novel quantitative photo-manipulation technique. *Sci. Rep.* **2016**, *6*, 19567. [[CrossRef](#)] [[PubMed](#)]
22. Maya-Mendoza, A.; Moudry, P.; Merchut-Maya, J.M.; Lee, M.; Strauss, R.; Bartek, J. High speed of fork progression induces DNA replication stress and genomic instability. *Nature* **2018**, *559*, 279–284. [[CrossRef](#)] [[PubMed](#)]
23. Budzowska, M.; Kanaar, R. Mechanisms of Dealing with DNA Damage-Induced Replication Problems. *Cell Biochem. Biophys.* **2009**, *53*, 17–31. [[CrossRef](#)] [[PubMed](#)]
24. Bianco, J.N.; Poli, J.; Saksouk, J.; Bacal, J.; Silva, M.J.; Yoshida, K.; Lin, Y.-L.; Tourrière, H.; Lengronne, A.; Pasero, P. Analysis of DNA replication profiles in budding yeast and mammalian cells using DNA combing. *Methods* **2012**, *57*, 149–157. [[CrossRef](#)]
25. Quinet, A.; Carvajal-Maldonado, D.; Lemacon, D.; Vindigni, A. DNA Fiber Analysis: Mind the Gap! *Methods Enzymology* **2017**, *591*, 55–82.
26. Couch, F.B.; Bansbach, C.E.; Driscoll, R.; Luzwick, J.W.; Glick, G.G.; Betous, R.; Carroll, C.M.; Jung, S.Y.; Qin, J.; Cimprich, K.A.; et al. ATR phosphorylates SMARCAL1 to prevent replication fork collapse. *Genes Dev.* **2013**, *27*, 1610–1623. [[CrossRef](#)]
27. Sogo, J.M. Fork Reversal and ssDNA Accumulation at Stalled Replication Forks Owing to Checkpoint Defects. *Science* **2002**, *297*, 599–602. [[CrossRef](#)]

28. Byun, T.S.; Pacek, M.; Yee, M.C.; Walter, J.C.; Cimprich, K.A. Functional uncoupling of MCM helicase and DNA polymerase activities activates the ATR-dependent checkpoint. *Genes Dev.* **2005**, *19*, 1040–1052. [[CrossRef](#)]
29. Lee, Z.; Elledge, S.J. Sensing DNA Damage Through ATRIP Recognition of RPA-ssDNA Complexes. *Science* **2003**, *300*, 1542–1548. [[CrossRef](#)]
30. Liao, H.; Ji, F.; Helleday, T.; Ying, S. Mechanisms for stalled replication fork stabilization: New targets for synthetic lethality strategies in cancer treatments. *EMBO Rep.* **2018**, *19*. [[CrossRef](#)]
31. Petermann, E.; Orta, M.L.; Issaeva, N.; Schultz, N.; Helleday, T. Hydroxyurea-Stalled Replication Forks Become Progressively Inactivated and Require Two Different RAD51-Mediated Pathways for Restart and Repair. *Mol. Cell* **2010**, *37*, 492–502. [[CrossRef](#)] [[PubMed](#)]
32. Whelan, D.R.; Lee, W.T.C.; Yin, Y.; Ofri, D.M.; Bermudez-Hernandez, K.; Keegan, S.; Fenyo, D.; Rothenberg, E. Spatiotemporal dynamics of homologous recombination repair at single collapsed replication forks. *Nat. Commun.* **2018**, *9*, 3882. [[CrossRef](#)] [[PubMed](#)]
33. Davies, A.A.; Masson, J.Y.; McIlwraith, M.J.; Stasiak, A.Z.; Stasiak, A.; Venkitaraman, A.R.; West, S.C. Role of BRCA2 in control of the RAD51 recombination and DNA repair protein. *Mol. Cell* **2001**, *7*, 273–282. [[CrossRef](#)]
34. Majera, D.; Skrott, Z.; Bouchal, J.; Bartkova, J.; Simkova, D.; Gachechiladze, M.; Steigerova, J.; Kurfurstova, D.; Gursky, J.; Korinkova, G.; et al. Targeting genotoxic and proteotoxic stress-response pathways in human prostate cancer by clinically available PARP inhibitors, vorinostat and disulfiram. *Prostate* **2019**, *79*, 352–362. [[CrossRef](#)]
35. Ramadan, K. p97/VCP- and Lys48-linked polyubiquitination form a new signaling pathway in DNA damage response. *Cell Cycle* **2012**, *11*, 1062–1069. [[CrossRef](#)] [[PubMed](#)]
36. Ramadan, K.; Halder, S.; Wiseman, K.; Vaz, B. Strategic role of the ubiquitin-dependent segregase p97 (VCP or Cdc48) in DNA replication. *Chromosoma* **2017**, *126*, 17–32. [[CrossRef](#)]
37. Meerang, M.; Ritz, D.; Paliwal, S.; Garajova, Z.; Bosshard, M.; Mailand, N.; Janscak, P.; Hübscher, U.; Meyer, H.; Ramadan, K. The ubiquitin-selective segregase VCP/p97 orchestrates the response to DNA double-strand breaks. *Nat. Cell Biol.* **2011**, *13*, 1376. [[CrossRef](#)]
38. Bergink, S.; Ammon, T.; Kern, M.; Schermelleh, L.; Leonhardt, H.; Jentsch, S. Role of Cdc48/p97 as a SUMO-targeted segregase curbing Rad51–Rad52 interaction. *Nat. Cell Biol.* **2013**, *15*, 526–532. [[CrossRef](#)]
39. Singh, A.N.; Oehler, J.; Torrecilla, I.; Kilgas, S.; Li, S.; Vaz, B.; Guérillon, C.; Fielden, J.; Hernandez-Carralero, E.; Cabrera, E.; et al. The p97-Ataxin 3 complex regulates homeostasis of the DNA damage response E3 ubiquitin ligase RNF8. *EMBO J.* **2019**, *38*, e102361. [[CrossRef](#)]
40. Davis, E.J.; Lachaud, C.; Appleton, P.; Macartney, T.J.; Näthke, I.; Rouse, J. DVC1 (C1orf124) recruits the p97 protein segregase to sites of DNA damage. *Nat. Struct. Mol. Biol.* **2012**, *19*, 1093–1100. [[CrossRef](#)]
41. Kumar, A.; Mazzanti, M.; Mistrik, M.; Kosar, M.; Beznoussenko, G.V.; Mironov, A.A.; Garrè, M.; Parazzoli, D.; Shivashankar, G.V.; Scita, G.; et al. ATR Mediates a Checkpoint at the Nuclear Envelope in Response to Mechanical Stress. *Cell* **2014**, *158*, 633–646. [[CrossRef](#)] [[PubMed](#)]
42. Woerner, A.C.; Frottin, F.; Hornburg, D.; Feng, L.R.; Meissner, F.; Patra, M.; Tatzelt, J.; Mann, M.; Winkhofer, K.F.; Hartl, F.U.; et al. Cytoplasmic protein aggregates interfere with nucleocytoplasmic transport of protein and RNA. *Science* **2016**, *351*, 173–176. [[CrossRef](#)] [[PubMed](#)]
43. Yasuda, S.; Tsuchiya, H.; Kaiho, A.; Guo, Q.; Ikeuchi, K.; Endo, A.; Arai, N.; Ohtake, F.; Murata, S.; Inada, T.; et al. Stress- and ubiquitylation-dependent phase separation of the proteasome. *Nature* **2020**, *578*, 296–300. [[CrossRef](#)] [[PubMed](#)]
44. Wang, Y.; Li, W.; Patel, S.S.; Cong, J.; Zhang, N.; Sabbatino, F.; Liu, X.; Qi, Y.; Huang, P.; Lee, H.; et al. Blocking the formation of radiation induced breast cancer stem cells. *Oncotarget* **2014**, *5*, 3743–3755. [[CrossRef](#)]
45. Lun, X.; Wells, J.C.; Grinshtein, N.; King, J.C.; Hao, X.; Dang, N.-H.; Wang, X.; Aman, A.; Uehling, D.; Datti, A.; et al. Disulfiram when Combined with Copper Enhances the Therapeutic Effects of Temozolomide for the Treatment of Glioblastoma. *Clin. Cancer Res.* **2016**, *22*, 3860–3875. [[CrossRef](#)]
46. Huang, J.; Campian, J.L.; Gujar, A.D.; Tsieng, C.; Anstas, G.; Tran, D.D.; DeWees, T.A.; Lockhart, A.C.; Kim, A.H. Final results of a phase I dose-escalation, dose-expansion study of adding disulfiram with or without copper to adjuvant temozolomide for newly diagnosed glioblastoma. *J. Neurooncol.* **2018**, *138*, 105–111. [[CrossRef](#)]

47. Huang, J.; Campian, J.L.; Gujar, A.D.; Tran, D.D.; Lockhart, A.C.; DeWees, T.A.; Tsien, C.I.; Kim, A.H. A phase I study to repurpose disulfiram in combination with temozolomide to treat newly diagnosed glioblastoma after chemoradiotherapy. *J. Neurooncol.* **2016**, *128*, 259–266. [[CrossRef](#)]
48. Jakola, A.S.; Werlenius, K.; Mudaisi, M.; Hylin, S.; Kinhult, S.; Bartek, J.J.; Salvesen, O.; Carlsen, S.M.; Strandeus, M.; Lindskog, M.; et al. Disulfiram repurposing combined with nutritional copper supplement as add-on to chemotherapy in recurrent glioblastoma (DIRECT): Study protocol for a randomized controlled trial. *F1000Research* **2018**, *7*, 1797. [[CrossRef](#)]
49. Nechushtan, H.; Hamamreh, Y.; Nidal, S.; Gottfried, M.; Baron, A.; Shalev, Y.I.; Nisman, B.; Peretz, T.; Peylan-Ramu, N. A Phase IIb Trial Assessing the Addition of Disulfiram to Chemotherapy for the Treatment of Metastatic Non-Small Cell Lung Cancer. *Oncologist* **2015**, *20*, 366–367. [[CrossRef](#)]



© 2020 by the authors. Licensee MDPI, Basel, Switzerland. This article is an open access article distributed under the terms and conditions of the Creative Commons Attribution (CC BY) license (<http://creativecommons.org/licenses/by/4.0/>).

Cannabidiol-induced activation of the metallothionein pathway impedes anticancer effects of disulfiram and its metabolite CuET

Tereza Buchtova¹ , Zdenek Skrott¹, Katarina Chroma¹, Jiri Rehulka¹, Petr Dzubak¹, Marian Hajduch¹, David Lukac¹, Stefanos Arampatzis², Jiri Bartek^{1,2,3}  and Martin Mistrik¹ 

¹ Faculty of Medicine and Dentistry, Institute of Molecular and Translational Medicine, Palacky University, Olomouc, Czech Republic

² Danish Cancer Society Research Center, Copenhagen, Denmark

³ Division of Genome Biology, Department of Medical Biochemistry and Biophysics, Science for Life Laboratory, Karolinska Institute, Stockholm, Sweden

Keywords

cancer; cannabidiol; CuET; disulfiram; metallothionein

Correspondence

J. Bartek and M. Mistrik, Faculty of Medicine and Dentistry, Institute of Molecular and Translational Medicine, Palacky University, 77 147 Olomouc, Czech Republic
 Tel: +420 773 458 536
 E-mails: jb@cancer.dk;
 martin.mistrik@upol.cz

(Received 2 July 2021, revised 21 September 2021, accepted 8 October 2021, available online 26 October 2021)

doi:10.1002/1878-0261.13114

Disulfiram (DSF), an established alcohol-aversion drug, is a candidate for repurposing in cancer treatment. DSF's antitumor activity is supported by preclinical studies, case reports, and small clinical trials; however, ongoing clinical trials of advanced-stage cancer patients encounter variable results. Here, we show that one reason for the inconsistent clinical effects of DSF may reflect interference by other drugs. Using a high-throughput screening and automated microscopy, we identify cannabidiol, an abundant component of the marijuana plant used by cancer patients to mitigate side effects of chemotherapy, as a likely cause of resistance to DSF. Mechanistically, in cancer cells, cannabidiol triggers the expression of metallothioneins providing protective effects by binding heavy metal-based substances including the bis-diethylthiocarbamate-copper complex (CuET). CuET is the documented anticancer metabolite of DSF, and we show here that the CuET's anticancer toxicity is effectively neutralized by metallothioneins. Overall, this work highlights an example of undesirable interference between cancer therapy and the concomitant usage of marijuana products. In contrast, we report that insufficiency of metallothioneins sensitizes cancer cells toward CuET, suggesting a potential predictive biomarker for DSF repurposing in oncology.

1. Introduction

Disulfiram (Antabuse), a drug used for almost 70 years to treat alcohol abuse, is an emerging candidate for repurposing in cancer therapy. Antitumor activity of disulfiram (DSF) is supported by numerous

preclinical studies, case reports, and small clinical trials [1–3], yet clinical data from larger randomized trials are still lacking. Despite several promising case reports about durable remissions of advanced-stage cancer patients after DSF therapy [1,4,5], results from clinical trials are still limited and less favorable [6], a trend

Abbreviations

5-HT1A, 5-hydroxytryptamine receptor subtype 1A; A2A, adenosine A2A receptor; BCDS, bathocuproine disulfonic acid; CB1, cannabinoid receptor 1; CB2, cannabinoid receptor 2; CBD, cannabidiol; Cd, cadmium; CuET, bis-diethylthiocarbamate-copper complex; DSF, disulfiram; GAPDH, glyceraldehyde 3-phosphate dehydrogenase; GPR55, G protein-coupled receptor 55; HPLC-MS, high-pressure liquid chromatography-mass spectrometry; MTF1, metal transcriptional factor 1; MTs, metallothioneins; NPL4, nuclear protein localization protein 4; PPAR γ , peroxisome proliferator-activated receptor γ ; PRISM, profiling relative inhibition simultaneously in mixtures; qPCR, quantitative polymerase chain reaction; TRPV1, transient receptor potential cation channel subfamily V members 1; TRPV2, transient receptor potential cation channel subfamily V members 2; Ub, ubiquitin; WB, western blotting; Zn, zinc.

that is shared with other repurposed drugs [7]. The results from the few clinical trials available so far suggest that DSF's anticancer effect may be limited to a subset of cancer patients [8,9], thereby raising a need for the identification of biomarkers that would help guide the patient selection in the future. A broader assessment of DSF in clinical oncology had been hindered mainly by the unknown identity of the active anticancer metabolite and its mechanism of action in cancer cells, including the key molecular target. Consequently, there is currently no reliable way to predict who among cancer patients is likely to benefit from the DSF treatment. In an effort to improve this situation, we have recently discovered that DSF is metabolized in the human body to bis-diethyldithiocarbamate-copper complex (CuET), that CuET represents the long-sought-after active compound that kills cancer cells, and that mechanistically, such toxicity to cancer cells reflects CuET-mediated impairment of NPL4, an essential cofactor of p97 segregase broadly involved in the degradation of cellular proteins [10,11]. We have also noticed that the CuET complex levels assessed after administration of the same dose of DSF vary significantly among patients [10]. We hypothesize that the observed variable clinical responses to DSF treatment might be attributable, at least in part, to the divergent extent of CuET formation, a process that is likely influenced by genetic and environmental factors, the latter including copper intake and the overall diet. Furthermore, the effectiveness of DSF treatment may be affected also by factors such as concomitant exposure to other drugs or pharmaceutically active compounds, a scenario particularly likely for advanced-stage cancer patients. With the primary mechanism of anticancer activity of DSF known, the identification of such factors that impact cellular responses to DSF/CuET is key to facilitate the repurposing of DSF in clinical oncology.

In this study, we identified cannabidiol (CBD), the most abundant nonpsychoactive compound and the second most abundant cannabinoid from the *Cannabis* sp. plant (known as marijuana), as a compound, strongly interfering with the anticancer activity of CuET. Apart from recreational use, marijuana and its products have been advocated for the treatment of a range of inflammatory, autoimmune and neurodegenerative conditions, epilepsy, multiple sclerosis, arthritis, and schizophrenia [12–14]. Mechanistically, CBD shows a low affinity for both cannabinoid receptors: CB1 and CB2, and while CBD exerts negative allosteric modulatory effects on CB1, it is an agonist of CB2. In addition to cannabinoid receptors, other potential targets of CBD have been reported, such as

the transient receptor potential cation channel subfamily V members 1 and 2 (TRPV1/2; agonist), peroxisome proliferator-activated receptor γ (PPAR γ ; agonist), G protein-coupled receptor 55 (GPR55; antagonist), 5-hydroxytryptamine receptor subtype 1A (5-HT1A, agonist), and adenosine A2A receptor (A2A, agonist) [12–15].

Notably, CBD is popular among cancer patients due to its ability to reduce the adverse effects of chemotherapy, including vomiting, nausea, and weight loss [16,17]. Various anticancer effects were also reported for cannabinoids including antiproliferative and proapoptotic properties, interference with angiogenesis, cancer cell migration, adhesion, and invasion [12,18,19], a notion which further motivates cancer patients to use CBD.

2. Materials and methods

2.1. Cell lines

Human osteosarcoma U-2-OS (ATCC), human breast adenocarcinoma MDA-MB-231 (ATCC), U-2-OS ectopically expressing NPL4-GFP [10], U-2-OS ectopically expressing MT-2A-GFP, and retinal pigment epithelia hTERT RPE-1 (ATCC) were maintained in DMEM (Lonza, Basel, Switzerland) supplemented with 10% fetal bovine serum (Thermo Fisher Scientific, Waltham, MA, USA) and 1% penicillin/streptomycin (Sigma-Aldrich, St. Louis, MO, USA). MCF 10A nontransformed human breast epithelial cell line and well-characterized breast cancer cell lines obtained from the ATCC repository, HCC1954 and SK-BR-3 (both HER+ve), ZR-75-1 and MCF7 (both luminal, ER+ve), MDA-MB-436, MDA-MB-231, CAL-51, MDA-MB-468, HCC70, MDA-MB-453, MDA-MB-157 (all triple-negative), used for metallothionein expression analysis were grown all grown under identical conditions in a mixture of 50% MEGM (Lonza) and 50% DMEM (Gibco, Amarillo, TX, USA) media, supplemented with 10% FBS (Gibco), 1% penicillin/streptomycin (Gibco), and SingleQuots supplement kit (Lonza) as recommended by the manufacturer.

2.2. High-throughput screening for CuET activity interferers

U-2-OS-NPL4-GFP was seeded into 384-well plates (PerkinElmer, CellCarrier-UltraPlate) at a concentration of 1250 cells per well in 30 μ L of media. The next day, the cells were pretreated with selected 1282 compounds (see enclosed Table S1) overnight (17 h). The

used concentration for each of the compounds was set to 10 μM . Subsequently, the cells were treated with 0.2 μM CuET for 3 h to induce aggregation and immobilization of the NPL4-GFP signal. Next, the cells were pre-extracted by 0.2% Triton X-100 buffer with 10 μM Hoechst 33342, washed by PBS, and fixed by 1% formalin for 10 min. After the fixation, the wells were washed by PBS and as the last step, the 30 μL of PBS was dispensed per well. Each well was acquired using an automated microscopic platform (Yokogawa CV7000, 10 \times air objective), with 4 microscopic fields per well. Images were analyzed by the Columbus image analysis pipeline (PerkinElmer, Waltham, MA, USA). Individual nuclei were recognized based on the Hoechst dye signal. In each nucleus, the level of the NPL4-GFP signal was scored and means of fluorescence intensity per nucleus were plotted.

2.3. RNA interference and overexpression experiments

siRNA against MTF1 (cat. no: SR302991, OriGene) and against MT-2A (cat. no: SR302987, OriGene) were used. For overexpression plasmids, Myc-DDK-tagged MT-2A (cat. no: RC202748, OriGene) and GFP-MT-2A (cat. no: RG202748, OriGene) were used. Transfection of siRNA was performed with Lipofectamine RNAiMAX (cat. n.: 13778-075, Invitrogen, Waltham, MA, USA) according to the manufacturer's instructions. The plasmid was transfected with Lipofectamine 2000 (cat. n.: 11668-027, Invitrogen) according to the manufacturer's instructions. The cells were reseeded to the required plate or dish 24 h after transfection. Treatments were started 72 h after transfections.

2.4. Stable cell line construction

Plasmid with TurboGFP-tagged MT-2A (cat. no: RG202748, OriGene) was transfected with Lipofectamine 2000 (cat. no: 11668-027, Invitrogen) according to the manufacturer's instruction. Cells were further cultivated in the presence of selective antibiotics (Geneticin, G418; Sigma, 400 $\mu\text{g}\cdot\text{mL}^{-1}$). Medium with Geneticin was replaced every 2–3 days until the population of resistant cells was fully established. Clonal cell lines were further produced from single cells.

2.5. XTT assay

5000 cells were seeded into a 96-well plate. The cells were treated as indicated in figure annotation. 72 h (24 h for RPE-1) after treatment, an XTT assay (AppliChem, Darmstadt, Germany) was performed

according to the manufacturer's instructions. Briefly, XTT solution was added to media and incubated for 30–120 min. The dye intensity was measured at the 475 nm wavelength using a spectrometer (TECAN, Infinite M200PRO). Results are shown as mean values and standard deviations from 3 independent experiments, each performed in 5 technical replicates.

2.6. Cell fractionation

Cells were treated as indicated in figure annotation. Before harvesting, the cells were washed by cold PBS. Lysis buffer (50 mM HEPES, pH 7.4, 150 mM NaCl, 2 mM MgCl_2 , 10% glycerol, 0.5% Triton X-100, and protease inhibitor cocktail by Roche) was applied to the cells and kept for 10 min gently agitating at 4 $^{\circ}\text{C}$. After that, cells were scraped and the whole mixture was placed inside Eppendorf tubes and kept for another 10 min on ice with intermittent vortexing. After that, the mixture was centrifuged at 20 000 \times g for 10 min at 4 $^{\circ}\text{C}$. Insoluble fraction and supernatant were each separately diluted in 2x LSB buffer and used for western blot analyses.

2.7. Western blot

Equal amounts of cell lysates were separated by SDS/PAGE on hand-cast (8%, 15%) or commercial gradient 4–15% Mini-PROTEAN TGX Precast Gel (cat. no: 4561083 or 4561086, BIO-RAD). Separated proteins were transferred onto a nitrocellulose membrane. The membrane was blocked with 5% bovine milk in Tris-buffered saline containing 0.1% Tween 20 for 1 h at room temperature and then incubated overnight at 4 $^{\circ}\text{C}$ with primary antibodies followed by detection by secondary antibodies. Secondary antibodies were visualized by Immobilon Forte Western HSR Substrate (cat. no: WBLUF0500, Merck Millipore, Burlington, MA, USA), and images were acquired by ChemiDoc imaging system (Bio-Rad, Hercules, CA, USA).

2.8. Immunofluorescence staining and quantitative microscopy

For microscopy, the cells were grown on glass coverslips. Cells were treated as indicated in figure annotation. Before fixation, the cells were pre-extracted with pre-extraction buffer (0.5% Triton X-100) for 1 min, after that quickly washed by PBS, and then immediately fixed with 4% formaldehyde for 15 min at room temperature. Alternatively, the pre-extraction step was bypassed and cells were directly fixed with 4% formaldehyde for 15 min and then permeabilized by

0.5% Triton X-100 for 20 min. In both protocols, nuclei were stained by DAPI ($1 \mu\text{g}\cdot\text{mL}^{-1}$) at room temperature for 5 min. Samples were visualized and acquired using fluorescence microscopes (Zeiss LSM780 or Olympus IX81 ScanR automated microscope). Quantitative analysis of microscopic data was performed in SCANR Analysis software. Acquired and ScanR processed data were further statistically tested in the STATISTICA 13 (TIBCO).

2.9. Quantitative polymerase chain reaction

The qPCR was performed in a 96-well plate or 8-tube strip (Roche, Basel, Switzerland). Reactions were performed in LightCycler Nano (Roche), LightCycler 480 Instrument II (Roche), or 7500 Fast Real-Time PCR System (Applied Biosystems, Waltham, MA, USA) with a 'gb SG PCR Master Mix' (cat. no: 3005, Geni Biotech) or 'Fast SYBR Green Master Mix' (cat. no: 4385612, Applied Biosystems). Following primers were used: HSPA1A forward 5'-GCCTTCCAAGATTGCTGTT-3'; reverse 5'-TCAACATTGCAAACACAGGA-3' [20]; MT-1E forward 5'-GCCTGACTGCTTGTTCGTCT-3'; reverse 5'-AAGAGCAGTTGGGGTCCATT-3'; MT-2A forward 5'-CCCCTCCAGATGTAAGA-3'; reverse 5'-TAGCAAACGGTCACGGTCAG-3'; GAPDH [21] forward 5'-AGCCACATCGCTCAGACAC-3'; reverse 5'-GCCCAATACGACCAATCC-3'. Gene expression was evaluated by the delta-delta CT method.

2.10. Measurement of CuET in culture medium and cells

To measure the formation of CuET in culture medium, a complete cell culture medium (DMEM, 10% FBS, 1% penicillin/streptomycin) was incubated with CuET or CuET + CBD combination as described. After incubation, the medium was vortexed and mixed with acetone in a ratio of 1 : 4. The mixture was centrifuged $18\,000\times g$ for 2 min at 4°C . The supernatant was transferred into glass HPLC vials for measurement. The CuET complex was analyzed by the HPLC-MS method described previously [10]. The quantification of the CuET complex was calculated according to the calibration curve.

To measure the concentration of CuET in cells, subconfluent U-2-OS cell culture was treated with CuET or CuET + CBD combination as described. After incubation, the medium was removed, cells were washed twice with PBS, and PBS was thoroughly aspirated. Cells were scraped and stored at -80°C . Cellular pellets were then homogenized with acetone and

centrifuged $18\,000\times g$ for 2 min at 4°C , and supernatant was transferred into a glass HPLC vial. The CuET complex was analyzed by the HPLC-MS method described previously [10]. The quantification of the CuET complex was calculated according to the calibration curve.

2.11. Statistical analysis

Separated bar graphs of qPCR experiments are plotted as mean \pm SD presenting 3 independent experiments. XTT assay with XY graphs comprising error bars is plotted as mean and error \pm SD. All the figures represent 3 independent experiments with each point presenting 5 replicates. 2D box plots of the quantitative microscopy analysis are plotted as median \pm SD. All the experiments were done in 3 independent experiments. The figure depicting the experiment represents a random selection from one of the experiments. Statistical significance was assessed by unpaired t-test, and the resulting *P*-value is shown in graphs and particular figure legends. The graphical processing was performed in Statistica 13 or GRAPHPAD Prism 8.0.1. Statistical significance, as well as IC50 values, was calculated in GRAPHPAD Prism 8.0.1 and 9.2.0.

2.12. Chemicals and antibodies

The following antibodies were used for immunoblotting: anti- β -actin (1 : 1000; Santa Cruz Biotechnology, cat. no: sc-47778), anti-DDK (1 : 1000; OriGene, cat. no: TA50011-100), anti-GAPDH (clone 1D4, 1 : 500; GeneTex, cat. no: GTX78213), antihistone H3 (1 : 2000; Cell Signaling, cat. no: 4499P), anti-MTF1 (1 : 1000; NOVUS Biologicals, cat. no: NBP1-86380), anti-NPLOC4 (1 : 1000; NOVUS Biological, cat. no: NBP1-82166), anti-Ubiquitin K48 (clone Apu 2, cat. no 05-1307, Millipore) goat-anti mouse IgG-HRP (1 : 1000; GE Healthcare, NA931, Chicago, IL, USA), goat-anti-rabbit (1 : 1000; GE Healthcare, NA934), and donkey-anti goat IgG-HRP (Santa Cruz Biotechnology, sc-2020, Dallas, TX, USA). The formulation of CuET (bis-diethyldithiocarbamate-copper complex) in water was based on direct synthesis in the presence of 1% bovine serum albumin as described previously [10,22]. Briefly, 10 mL of 2.8 mM CuET is prepared by adding 200 μL of 280 mM solution of sodium bis-diethyldithiocarbamate trihydrate (DTC, Sigma-Aldrich) and 28 μL of 1 M CuCl_2 (Sigma-Aldrich) into 9772 mL of 1% solution of bovine serum albumin in ddH₂O (Sigma-Aldrich). The resulting CuET formulation was kept at 4°C for no longer than a month. All solutions were sterile-filtered before synthesis. The

chelator bathocuproine disulfonic acid (Sigma-Aldrich) was used for copper chelation in a final concentration of 10 μM and was added to the sample just before the disulfiram (Sigma-Aldrich) treatment. CBD [(*-*-cannabidiol)] was ordered from Abcam (cat. n.: ab120448). 10 mM stock solution was prepared in methanol (Penta).

3. Results

3.1. NPL4-GFP cell reporter-based screen implicates CBD in resistance to CuET

We set up a high-throughput screening approach for the identification of CuET sensitivity modulators. The screen was based on a reporter human sarcoma U-2-OS cell line expressing GFP-tagged NPL4 protein, the molecular target of CuET's anticancer effects. Upon CuET treatment, NPL4 undergoes robust aggregation and immobilization, a phenotype exploited in our screen to search for NPL4-GFP fluorescence in the insoluble cell fraction [10]. Immobilized NPL4-GFP can be quantified using microscopy-based analysis after detergent (Triton X-100) pre-extraction of drug-exposed cultured cells. The pre-extraction procedure washes away soluble proteins from cells, thereby selectively enriching for insoluble proteins including the aggregated NPL4. For the screening setup, we pretreated cells with various chemicals from our library of 1282 pharmacologically active compounds overnight at the nontoxic concentration (for the list of compounds used in the screen, Table S1). The next day, the cells were exposed to 0.2 μM of CuET for 3 h, as the latter treatment leads to the insoluble aggregate formation of NPL4 and consequently to pre-extraction-resistant NPL4-GFP signal conveniently detected by high-throughput microscopy. Interestingly, several compounds substantially decreased the level of such CuET-immobilized NPL4-GFP signal suggesting possible interference with CuET treatment. Cannabidiol (CBD), the nonpsychotropic component of marijuana, was the strongest hit in our screen (Fig. 1A), moreover a hit with high clinical relevance due to its rather common use among cancer patients [23].

The CBD hit was then further validated by more detailed microscopy-based analysis in the U-2-OS-NPL4-GFP cell line (Fig. 1B,C). The same CBD-promoted rescuing effect from CuET-evoked aggregation of NPL4 was confirmed also for the endogenous NPL4 protein using immunoblotting analysis. Thus, CuET administered alone promotes accumulation of NPL4 within the nondissolvable cellular fraction, an

effect that was reduced in two cell lines, U-2-OS osteosarcoma and breast cancer-derived MDA-MB-231 when exposed to a combined CBD + CuET treatment (Fig. 1D, Fig. S1A). Next, we addressed whether the reduced aggregation of NPL4 by CBD affects also the CuET cancer cell toxicity profile. To this end, the cells were pretreated by CBD overnight and then treated with CBD along with increasing concentrations of CuET for 72 h. The significant rescue effect of CBD in terms of better cell survival was confirmed for both tested cell lines (Fig. 1E and Fig. S6C as part of the following siRNA combined experiments). Both cell lines pretreated by CBD also displayed decreased accumulation of K48 polyubiquitylated (poly-Ub) proteins, a surrogate marker for impaired protein degradation caused by malfunction of the p97-NPL4 segregase pathway [10] (Fig. 1F, Fig. S1B). The activation of the heat-shock pathway is yet another marker of CuET-induced proteotoxic stress [10] the effect of which can be quantified by qPCR by examination of mRNA levels of HSPA1A, the major stress-inducible member of the HSP70 family. Consistently, CuET highly induced HSPA1A mRNA levels which effect was significantly decreased in cells pretreated by CBD (Fig. S2A). These results indicate that CBD attenuates the CuET-promoted aggregation of NPL4 resulting in reduced toxicity of this compound toward cancer cells.

3.2. Both CBD and CuET induce expression of the metallothionein family members

To explore the mechanism of the rescue effect described above, we first tested for a potential direct interaction of CBD with CuET and/or reduced uptake of CuET as the most straightforward explanations. To address this possibility, we used the HPLC-MS-based detection allowing direct monitoring of the CuET levels in cells [10]. We detected similar levels of CuET in control and CBD-pretreated cells, suggesting that the observed drug interference in the CBD pretreated cells is unlikely to be attributable to a lower cellular uptake of CuET (Fig. S3A, B).

Available literature describes various cellular responses to CBD treatment [12–15] including activation of the so-called metallothionein pathway [24–26]. This particular pathway might plausibly explain the rescuing effect from the CuET-evoked NPL4 aggregation observed in our experiments as the proteins in the family of metallothioneins (MTs) are rich in cysteines that can chelate divalent metals via sulfhydryl groups. Metals that avidly bind to MTs include Cd, Zn, and Cu which are either used, stored, or removed from the cell [27]. The CuET molecule contains noncovalently

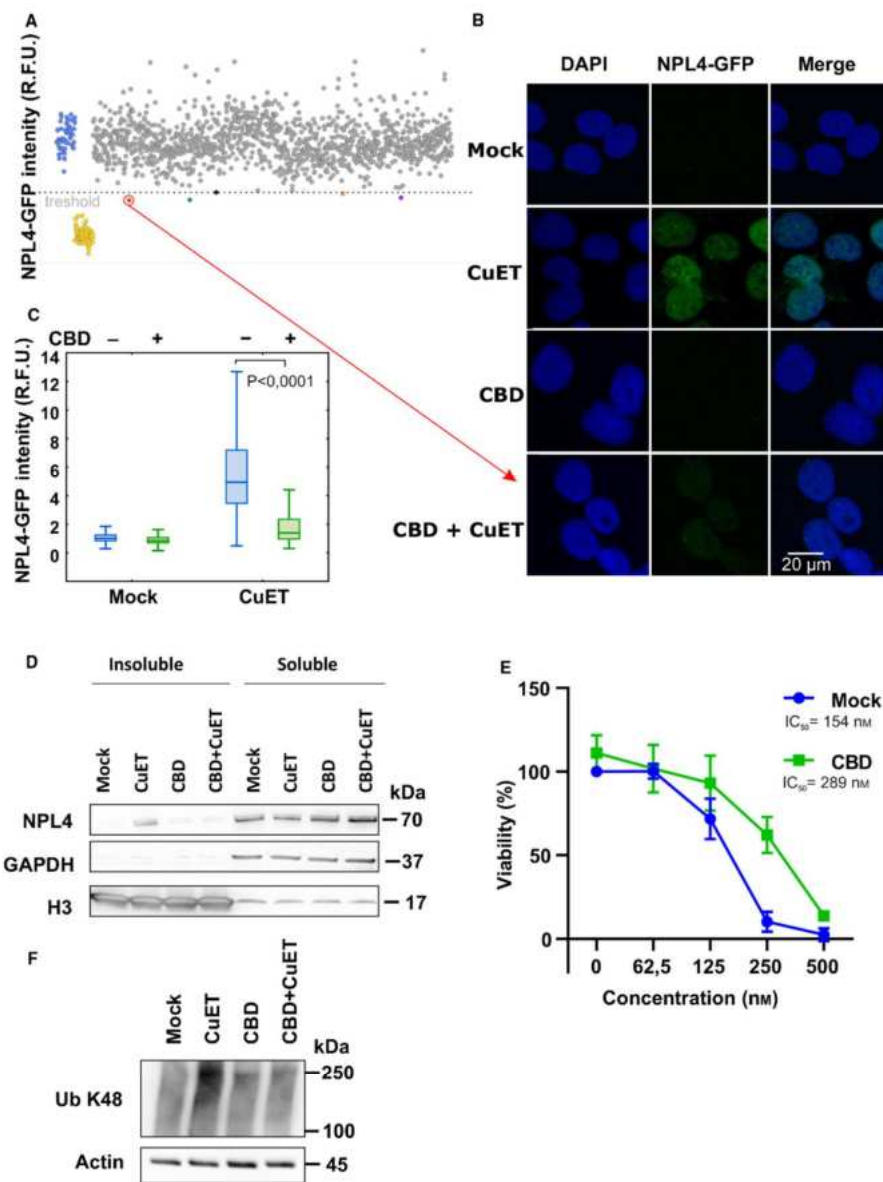


Fig. 1. Cannabidiol (CBD) protects cells from bis-diethylthiocarbamate-copper complex (CuET). (A) Dot plot depicting the results of high-throughput screening of the chemical library. CuET + mock-treated controls are in blue, and untreated controls are in yellow. Tested compounds overcoming the threshold of 0.5% positive hits are highlighted in red, green, black, orange, and violet colors. Cells were pretreated with compounds (10 μM) for 17 h and treated with 0.2 μM CuET for 3 h. The screening result represents one experiment ($n = 1$). (B,C) Microscopy-based confirmation of the strongest hit. Cells were pretreated with 10 μM CBD for 17 h and treated with 0.2 μM CuET for 3 h and analyzed by microscope including microscopy-based quantitative analysis (20 μm scale bar) of NPL4-GFP signal in Triton X-100 pre-extracted cells. Combined treatment shows significantly less accumulation of nondissolvable (pre-extraction resistant) NPL4 protein compared with CuET treatment only (two-tailed *t*-test). Pre-extraction was performed before the fixation step. The figures show results from one of three independent experiments ($n = 3$). (D) Cells pretreated with 10 μM CBD for 17 h and treated with 0.2 μM CuET for 3 h accumulate less endogenous NPL4 protein in insoluble fractions compared with CuET treatment only as observed by western blot (WB). The figure shows one of three independent experiments ($n = 3$). (E) Cells pretreated with 10 μM CBD for 17 h and treated with increasing concentration of CuET for 72 h are more resistant compared with CuET treatment only as observed by the XTT assay. The results represent the mean and standard deviation of three independent experiments ($n = 3$). (F) WB analysis of K48 polyubiquitinated (Ub K48) proteins reflecting differences in a malfunction of protein degradation in mock, CuET, CBD, and CBD + CuET-treated cells. For the experiment, the cells were treated for 3h by 0.2 μM CuET. In the combined treatment, CuET was added 17 h after 10 μM CBD. The figure shows one of three independent experiments ($n = 3$).

bound divalent copper, and thus, MTs might 'neutralize' this compound as part of their known toxic ion detoxification function [28].

To test the hypothesis that MT overexpression may explain the observed rescue effect, we first confirmed that CBD indeed induces the expression of metallothioneins using quantitative polymerase chain reaction (qPCR). The mRNA levels of *MT-1E* and *MT-2A* roughly doubled after overnight CBD treatment in U-2-OS cells (Fig. 2A,B, Fig. 4A,B). Interestingly, treatment by CuET for 3 h also evoked a robust increase in the mRNA levels for *MT-1E* and *MT-2A*, indicating that CuET can rapidly trigger this cellular heavy metal defense mechanism. In the combined treatment with CBD and CuET, using drug concentrations that parallel those used in our phenotype rescue experiments, the induced expression levels of the MTs were even higher than after exposure to either compound alone (Fig. 2A,B, Fig. 4A,B).

3.3. CBD-induced metallothioneins protect cells from CuET-mediated toxicity

Given the observed induction of metallothioneins, we next aimed at obtaining more mechanistic insights into the interplay among CBD, CuET, and MTs. Our strategy was to directly manipulate the metallothionein pathway and assess any impact in terms of potential modulation of the CuET-mediated cellular response. It is known that metal transcription factor 1 (MTF1) plays a pivotal role in MT gene expression [29]. Indeed, after the knockdown of MTF1 (Fig. S5A), we observed a significantly reduced ability of our model cell lines to induce expression of *MT-1E* and *MT-2A* after CuET exposure (Fig. 5B,C). Importantly, such experimentally achieved MTF1 insufficiency rendered the U-2-OS and MDA-MB-231 cells particularly sensitive to CuET treatment as confirmed in a 72-h XTT assay (Fig. 3A, Fig. S6A,B). This hypersensitivity was

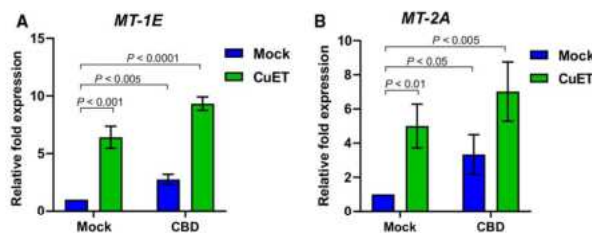


Fig. 2. Induction of metallothioneins *MT-1E*, *MT-2A* expression by cannabidiol (CBD), and bis-diethylthiocarbamate-copper complex (CuET) measured by quantitative polymerase chain reaction (qPCR) A) CBD and CuET increase the expression of *MT-1E* mRNA. B) CBD and CuET increase the expression of *MT-2A* mRNA. The experimental setup involved pretreatment with 10 μM CBD for 17 h and treatment with 0.2 μM CuET for 3 h. In the combined treatment, CuET was added 17 h after CBD. For both charts, a two-tailed *t*-test was used for *P*-value calculation. The result represents the mean and standard deviation of three independent experiments ($n = 3$).

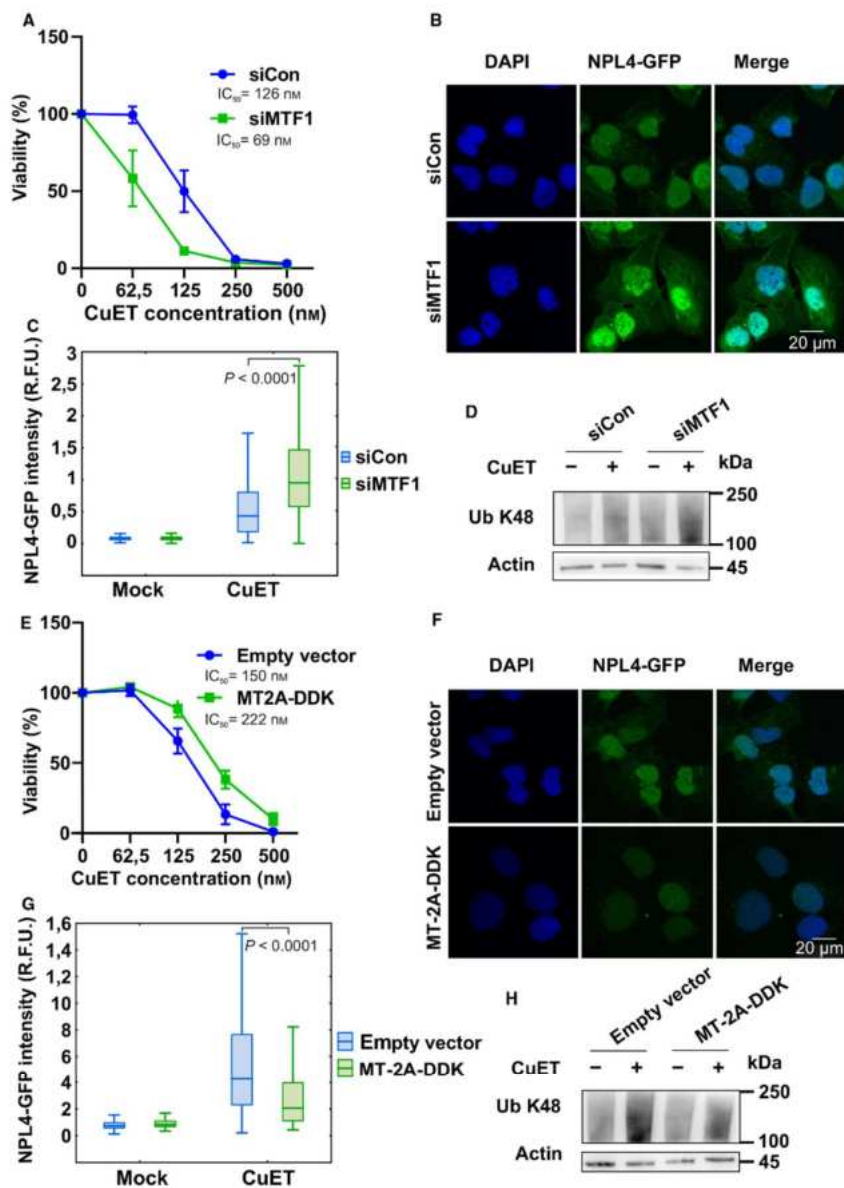


Fig. 3. Metallothionein level modulates the cellular responses to bis-diethyldithiocarbamate-copper complex (CuET) (A) MTF1-silenced cells are more sensitive to CuET. Cells were treated with increasing concentration of CuET for 72 h and analyzed by XTT assay. The result represents the mean and standard deviation of three independent experiments ($n = 3$). (B, C) MTF1-silenced cells accumulate significantly more of the nondissolvable NPL4 after CuET as depicted by microscopic images (20 μm scale bar) and corresponding quantitative microscopic analysis of NPL4-GFP signal in Triton X-100 pre-extracted cells. Cells were treated with 0.2 μM CuET for 3 h. A two-tailed t-test was used for P -value calculation. The results represent one of three independent experiments ($n = 3$). (D) MTF1-silenced cells accumulate more K48 polyubiquitinated (Ub K48) proteins after CuET treatment. Cells were treated with 0.2 μM CuET for 3 h and analyzed by western blot (WB). The figure shows one of three independent experiments ($n = 3$). (E) MT-2A-overexpressing cells are more resistant to CuET. Cells were treated with increasing concentrations of CuET for 72 h and analyzed by XTT assay. The result represents the mean and standard deviation of three independent experiments ($n = 3$). (F, G) MT-2A-overexpressing cells accumulate significantly less of the nondissolvable NPL4 as depicted by microscopic images (20 μm scale bar) and corresponding quantitative microscopic analysis of NPL4-GFP signal in Triton X-100 pre-extracted cells. Cells were treated with 0.2 μM CuET for 3 h. A two-tailed t-test was used for P -value calculation. The results represent one of three independent experiments ($n = 3$). (H) MT-2A-overexpressing cells accumulate fewer K48 polyubiquitinated proteins after CuET. Cells were treated with 0.2 μM CuET for 3 h and analyzed by WB. The figure shows one of three independent experiments ($n = 3$).

accompanied by an elevated amount of immobilized NPL4-GFP in the U-2-OS NPL4-GFP reporter model (Fig. 3B,C). This is an important finding which directly links the increased toxicity with CuET's primary cellular target. The toxic effect was further underlined also by the increased accumulation of poly-Ub proteins and increased expression of HSPA1A (Fig. 3D, Fig. S6D, Fig. S2B).

Next, we used a complementary approach and designed a cell line transiently overexpressing the

DDK-tagged (Flag-tagged) MT-2A protein (Fig. S5A). This cellular model was more resistant to the CuET treatment compared with the control, empty vector-transfected cells (Fig. 3E). Cells expressing the ectopic MT-2A also showed less immobilized NPL4-GFP (Fig. 3F,G) under otherwise standard CuET treatment conditions, and the rescue effect was further underlined by the decreased accumulation of poly-Ub proteins and decreased expression of HSPA1A (Fig. 3H, Fig. S2C). Next, we established a stable U-2-OS-MT-

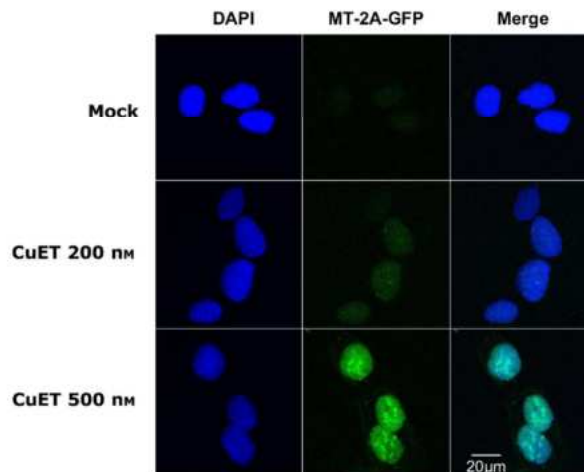


Fig. 4. Bis-diethyldithiocarbamate-copper complex CuET treatment immobilizes MT-2A-GFP. MT-2A-GFP protein is immobilized after CuET treatment revealed as depicted by microscopic images after Triton X-100 based pre-extraction. Cells were treated with 0.2 and 0.5 μM CuET for 3 h (20 μm scale bar). The figure represents one of two independent experiments ($n = 2$).

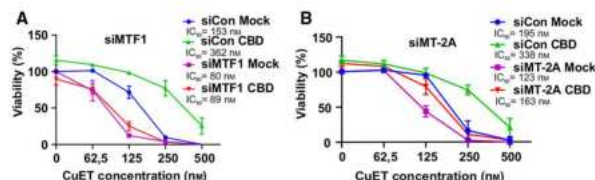


Fig. 5. Concomitant gene silencing with cannabidiol (CBD) treatment and role of metallothionein MT-2A in response to bis-diethyldithiocarbamate-copper complex (CuET) analyzed by XTT assay (A) CBD pretreatment does not protect MTF1-silenced cells from CuET toxicity. Cells were pretreated with 10 μ M CBD for 17 h and treated with 10 μ M CBD and increasing concentration of CuET for 72 h. The result represents the mean and standard deviation of three independent experiments ($n = 3$). (B) MT-2A-silenced cells are sensitized to CuET treatment. CBD pretreatment protects MT-2A-silenced cells from CuET toxicity only partially. Cells were pretreated with 10 μ M CBD for 17 h and treated with 10 μ M CBD and increasing concentration of CuET for 72 h. The result represents the mean and standard deviation of three independent experiments ($n = 3$).

2A-GFP cellular model to see any potential direct effects of CuET on MT-2A protein behavior. Indeed, we could detect MT-2A-GFP signal immobilization (i.e., resistance to pre-extraction) resembling the effect of CuET on NPL4-GFP protein, suggesting the direct interaction of MT-2A with CuET (Fig. 4).

To link the observed phenotypes more thoroughly with the CBD's mode of action, we also tested the rescue effect in MTF1-silenced cells. As expected, in the MTF1-silenced cells, the rescue effect of CBD treatment on the CuET-evoked phenotypes became negligible in both the U-2-OS and MDA-MB-231 cell lines (Fig. 5A, Fig. S6C). Analogous results were obtained also for primary human RPE-1 cells (Fig. S7A, B). Besides MTF1 knockdown, also direct silencing of *MT-2A* (Fig. S5D) was similarly able to render the U-2-OS cells more sensitive to CuET treatment (Fig. 5B).

Our findings that high levels of metallothioneins in tumor cells can cause resistance to CuET, while cancer cells harboring low-level MTs may be more sensitive to such treatment, raise a possibility that metallothionein expression levels might help predict responses to CuET (DSF) treatment in the future. One prediction for such candidate biomarker application is that the starting endogenous expression levels of MTs would vary among individual models or clinical specimens, preferably showing at least a subset of cases with expression levels below those in corresponding normal cell/tissue type. As the first step toward testing the landscape of MT expression patterns, we employed qPCR to assess mRNA levels of two relevant MTs: MT-1E and MT-2A, among a panel of 11 human cell lines derived from diverse types of breast cancer (2 luminal, 2 HER-positive, and 7 triple-negative, see Methods), compared with levels found in the nontransformed human MCF 10A cells as a reference (Fig. S8). Notably, the expression of both MT-1E and MT-2A

was more than an order of magnitude lower in the majority of these cancer cell models compared with MCF 10A cells, except for triple-negative cell lines, some of which expressed levels comparable with those in the control MCF 10A (Fig. S8). None of the 11 cancer cell lines showed levels of either MT that would exceed expression seen in the MCF 10A control.

Altogether, these results show that CBD induces the metallothionein pathway consistently in various cellular backgrounds, that this cellular response leads to enhanced MT expression which protects cancer cells against the DSF's anticancer metabolite CuET, and that low levels of MTs render cancer cells more sensitive to CuET treatment, raising a possibility to explore MT levels as candidate biomarkers for future clinical applications.

4. Discussion

In this work, we show how the high-throughput screening approach combined with the high content microscopy analysis can be used for addressing highly relevant clinical issues. By setting up the phenotypic screening involving the known drug target (NPL4) as the readout, we were able to identify a clinically relevant compound—cannabidiol (CBD), as the most likely cause of unwanted interference with ongoing cancer treatment with disulfiram (Antabuse), the anticancer effects of which are currently tested in multiple ongoing preclinical studies and clinical trials [30]. Furthermore, our present experiments also reveal the mechanistic basis of this CBD-mediated interference. It is known that DSF targets cancer cells via its direct metabolite CuET [10], chemically bis-diethyldithiocarbamate-copper complex. Inside cells, CuET binds and aggregates NPL4, an important factor for protein processing and degradation [10]. Concomitant

treatment with CBD induces overexpression of metallothioneins which compete with NPL4 for the available CuET, thereby ultimately lowering the efficacy of treatment by CuET.

CBD, the nonpsychotropic component of marijuana has become the focus of attention in medicine in recent years. Numerous studies have revealed the considerable potential of the substance for patients with diseases of the nervous system, inflammatory diseases, or cancer. In several countries, marijuana is now accepted as a medical drug, and CBD itself is sold with or without prescription in various forms. An example of the prescription-available form is Epidiolex used for the treatment of seizures in two types of epilepsy and tuberous sclerosis complex in the United States. In the context of this study, it is important that CBD and various cannabis products are becoming popular among cancer patients due to their potential to mitigate chemotherapy-induced side effects including chronic pain, nausea, vomiting, loss of appetite, and anxiety [16,17].

Interestingly, the potential of MTs as detoxifying proteins has been known for decades and this function has also been linked to possible resistance to some chemotherapeutics [31–33]. The detoxifying ability of MTs has been reported even for some nonmetal-based drugs. Chemotherapeutics that are sensed and bound by MTs are neutralized before reaching their intended target(s) and thereby become clinically ineffective. Thus, MT expression represents potential predictive biomarkers of resistance to specific treatments [34,35]. In light of these facts and our data presented here, CBD usage might be a relevant factor to be kept in mind for cancer patients not only undergoing the trials with DSF-repurposing therapy but also treated with some standard-of-care chemotherapy drugs.

Importantly, the effect of metallothioneins MT-1E and MT-2A and MTF1 transcription factor on the activity of DSF has been recently identified also in another independent study aimed at the high-throughput screening of antitumor effects of known drugs using a molecular barcoding method called PRISM (profiling relative inhibition simultaneously in mixtures) [36]. Disulfiram (DSF) was one of the tested substances and the screen revealed that cells with reduced or lost expression of *MT-1E* and *MT-2A* genes became more sensitive to DSF. The authors of this study did not realize that it was not DSF but rather its metabolite CuET against which the MTs protect the cells. It seems the fact that CuET is spontaneously formed from DSF and copper ions in culture media is underappreciated by the scientific community [11]. Indeed, after blocking this conversion

of DSF into CuET through chelation of copper ions from the cell culture media, DSF becomes a harmless molecule regardless of the MT expression status, as we also documented here (Fig. S9). Thus besides CBD, the copper availability for CuET formation during the trials with DSF will likely also represent one of the factors affecting the anticancer efficacy. For example, it is known that increased uptake of zinc negatively affects copper uptake and thus should be limited by the patients during such treatment [37]. Similarly, patients with celiac disease may be deficient in copper [38].

Yet another important aspect of our present study is the validation of the crucial role of the MT pathway in protecting cancer cells against the impact of DSF's metabolite CuET on NPL4 protein. Despite DSF is intensively tested in several ongoing clinical trials aiming at repurposing DSF for cancer treatment, there is currently no biomarker suitable for the selection of patients who could most benefit from DSF, a fact that unfortunately highly limits the potential success of DSF treatment in oncology. Together with the Corsetto *et al.* (2020) study, our present report highlights MTs and MTF1 as such candidate predictive biomarkers, which are upregulated and vary considerably among the patients as well as different cancer types [32,39–41]. In this context, while preliminary, our findings of substantially lower MT-1E and MT-2A expression levels among a panel of human breast cancer cell line models compared with nontransformed breast epithelial cell control suggest that such potential biomarker application may be worth pursuing further. While speculative at present, if future tissue validation analyses confirm that endogenous metallothionein levels are much lower in cancer cells *in vivo* compared with corresponding normal tissue, such a striking difference may highlight yet another contributing factor helping to explain why disulfiram (and CuET) is toxic for tumor cells yet largely without major negative side effects and well tolerated by both experimental animals and people [1,2,5,10]. Moreover, the link of MT pathway to CuET effectiveness can inspire new therapeutic approaches, which can be explored in future studies, such as a combination of DSF (and copper supplementation) with a compound APTO-253, an experimental drug inhibiting MTF1 function currently tested in phase I clinical trial (NCT02267863).

5. Conclusions

For the first time, we linked CBD-mediated activation of the metallothionein pathway with protection/resistance against CuET (an anticancer metabolite of DSF)

which we believe is highly relevant for the ongoing clinical trials with DSF. Patients undergoing such treatment should avoid concomitant usage of CBD-containing drugs. This finding may also provide a plausible explanation, at least in part, for some of the differential outcomes among cancer patients treated by DSF.

From a broader perspective, this discovery somewhat resembles the scenario of antioxidant supplements the increased uptake of which is also common among cancer patients and may potentially interfere with standard-of-care chemo-radiotherapy [42]. Similarly, CBD may reduce the effectiveness of all treatments, for which the reactivity with metallothioneins has been studied [31–33]. Thus, this work could motivate further research on CBD and its interaction with anticancer drugs as an issue highly relevant for biomedicine in general and oncology in particular.

Acknowledgment

The study was supported by MEYS CR: (Large RI Project LM2018129—Czech-BioImaging), ERDF (project No. CZ.02.1.01/0.0/0.0/16_013/0001775), ENOCH project (No. CZ.02.1.01/0.0/0.0/16_019/0000868), Grant agency of the Czech Republic: GACR 20-28685S, Technology Agency of the Czech Republic: TN01000013, Internal grant of University of Palacky IGA_LF_2021_030, by the Czech Ministry of Education, Youth and Sports (CZ-OPENSREEN—LM2018130), the Novo Nordisk Foundation (16854 and 0060590), the Swedish Research Council VR-MH 2014-46602-117891-30, the Swedish Cancer Foundation/Cancerfonden (#170176), and the Danish National Research Foundation (project CARD, DNRF 125).

Conflict of interest

MM, JB, ZS, and MH are co-inventors on patent EP 17193240.3 and patent application EP 18199181.1, both utilizing CuET formulation into nanoparticles as an anticancer agent. Other authors declare no competing interests.

Author contributions

JB, MM, TB, and ZS designed the experiments, interpreted the data, and write the manuscript; TB performed microscopic, qPCR, and most of the cellular experiments; MM contributed to the microscopic experiments; ZS performed mass spectroscopy experiments and the chelation cytotoxic tests; KCH contributed to the cytotoxicity tests and western blotting. JR, PJ, and MH designed, performed, and interpreted

the HTS screen; DL contributed to the cytotoxicity tests. SA performed metallothionein expression analysis in breast cancer cell lines.

Peer Review

The peer review history for this article is available at <https://publons.com/publon/10.1002/1878-0261.13114>.

Data accessibility

Supporting data of this study are in Table S1 and Figures S1–S9. Raw data are available from the corresponding author upon reasonable request.

References

- 1 Brar SS, Grigg C, Wilson KS, Holder WD, Dreau D, Austin C, Foster M, Ghio AJ, Whorton AR *et al.* (2004) Disulfiram inhibits activating transcription factor/cyclic AMP-responsive element binding protein and human melanoma growth in a metal-dependent manner *in vitro*, in mice and in a patient with metastatic disease. *Mol Cancer Ther* **3**, 1049–1060.
- 2 Chen D, Cui QC, Yang H & Dou QP (2006) Disulfiram, a clinically used anti-alcoholism drug and copper-binding agent, induces apoptotic cell death in breast cancer cultures and xenografts via inhibition of the proteasome activity. *Cancer Res* **66**, 10425–10433.
- 3 Dufour P, Lang JM, Giron C, Duclos B, Haehnel P, Jaecq D, Jung JM & Oberling F (1993) Sodium dithiocarb as adjuvant immunotherapy for high risk breast cancer: a randomized study. *Biotherapy* **6**, 9–12.
- 4 Karamanakos PN, Trafalis DT, Papachristou DJ, Panteli ES, Papavasiliopoulou M, Karatzas A, Kardamakis D, Nasioulas G & Marselos M (2017) Evidence for the efficacy of disulfiram and copper combination in glioblastoma multiforme - A propos of a case. *J BUON* **22**, 1227–1232.
- 5 Lewison EF (1976) Spontaneous regression of breast cancer. *Natl Cancer Inst Monogr* **44**, 23–26.
- 6 Huang J, Chaudhary R, Cohen AL, Fink K, Goldlust S, Boockvar J, Chinnaiyan P, Wan L, Marcus S *et al.* (2019) A multicenter phase II study of temozolomide plus disulfiram and copper for recurrent temozolomide-resistant glioblastoma. *J Neurooncol* **142**, 537–544.
- 7 Tran AA & Prasad V (2020) Drug repurposing for cancer treatments: a well-intentioned, but misguided strategy. *Lancet Oncol* **21**, 1134–1136.
- 8 Huang J, Campian JL, Gujar AD, Tsiens C, Anstas G, Tran DD, DeWees TA, Lockhart AC & Kim AH (2018) Final results of a phase I dose-escalation, dose-expansion study of adding disulfiram with or without

- copper to adjuvant temozolomide for newly diagnosed glioblastoma. *J Neurooncol* **138**, 105–111.
- 9 Nechushtan H, Hamamreh Y, Nidal S, Gotfried M, Baron A, Shalev YI, Nisman B, Peretz T & Peylan-Ramu N (2015) A phase IIb trial assessing the addition of disulfiram to chemotherapy for the treatment of metastatic non-small cell lung cancer. *Oncologist* **20**, 366–367.
 - 10 Skrott Z, Mistrik M, Andersen KK, Friis S, Majera D, Gursky J, Ozdian T, Bartkova J, Turi Z *et al.* (2017) Alcohol-abuse drug disulfiram targets cancer via p97 segregase adaptor NPL4. *Nature* **552**, 194–199.
 - 11 Skrott Z, Majera D, Gursky J, Buchtova T, Hajdich M, Mistrik M & Bartek J (2019) Disulfiram's anti-cancer activity reflects targeting NPL4, not inhibition of aldehyde dehydrogenase. *Oncogene* **38**, 6711–6722.
 - 12 Pellati F, Borgonetti V, Brighenti V, Biagi M, Benvenuti S & Corsi L. (2018) Cannabis sativa L. and nonpsychoactive cannabinoids: their chemistry and role against oxidative stress, inflammation, and cancer. *Biomed Res Int* **2018**, 1691428.
 - 13 Peres FF, Lima AC, Hallak JEC, Crippa JA, Silva RH & Abilio VC (2018) Cannabidiol as a promising strategy to treat and prevent movement disorders? *Front Pharmacol* **9**, 482.
 - 14 Pisanti S, Malfitano AM, Ciaglia E, Lamberti A, Ranieri R, Cuomo G, Abate M, Faggiana G, Proto MC *et al.* (2017) Cannabidiol: State of the art and new challenges for therapeutic applications. *Pharmacol Ther* **175**, 133–150.
 - 15 Massi P, Solinas M, Cinquina V & Parolaro D (2013) Cannabidiol as potential anticancer drug. *Br J Clin Pharmacol* **75**, 303–312.
 - 16 Mortimer TL, Mabin T & Engelbrecht A-M (2019) Cannabinoids: the lows and the highs of chemotherapy-induced nausea and vomiting. *Future Oncol* **15**, 1035–1049.
 - 17 Whiting PF, Wolff RF, Deshpande S, Di Nisio M, Duffy S, Hernandez AV, Keurentjes JC, Lang S, Misso K *et al.* (2015) Cannabinoids for medical use: a systematic review and meta-analysis. *JAMA* **313**, 2456–2473.
 - 18 Massi P, Vaccani A, Bianchessi S, Costa B, Macchi P & Parolaro D (2006) The non-psychoactive cannabidiol triggers caspase activation and oxidative stress in human glioma cells. *Cell Mol Life Sci* **63**, 2057–2066.
 - 19 Freimuth N, Ramer R & Hinz B (2010) Antitumorogenic effects of cannabinoids beyond apoptosis. *J Pharmacol Exp Ther* **332**, 336–344.
 - 20 Chung U, Seo J-S, Kim Y-H, Son GH & Hwang J-J (2012) Quantitative analyses of postmortem heat shock protein mRNA profiles in the occipital lobes of human cerebral cortices: implications in cause of death. *Mol Cells* **34**, 473–480.
 - 21 Evangelou K, Bartkova J, Kotsinas A, Pateras IS, Lontos M, Velimezi G, Kosar M, Liloglou T, Trougakos IP *et al.* (2013) The DNA damage checkpoint precedes activation of ARF in response to escalating oncogenic stress during tumorigenesis. *Cell Death Differ* **20**, 1485–1497.
 - 22 Chen W, Yang W, Chen P, Huang Y & Li F (2018) Disulfiram copper nanoparticles prepared with a stabilized metal ion ligand complex method for treating drug-resistant prostate cancers. *ACS Appl Mater Interfaces* **10**, 41118–41128.
 - 23 Koturbash I & MacKay D (2020) Cannabidiol and other cannabinoids: from toxicology and pharmacology to the development of a regulatory pathway. *J Diet Suppl* **17**, 487–492.
 - 24 Juknat A, Pietr M, Kozela E, Rimmerman N, Levy R, Coppola G, Geschwind D & Vogel Z (2012) Differential transcriptional profiles mediated by exposure to the cannabinoids cannabidiol and Δ^9 -tetrahydrocannabinol in BV-2 microglial cells. *Br J Pharmacol* **165**, 2512–2528.
 - 25 Scott KA, Dennis JL, Dalglish AG & Liu WM (2015) Inhibiting heat shock proteins can potentiate the cytotoxic effect of cannabidiol in human glioma cells. *Anticancer Res* **35**, 5827–5837.
 - 26 Juknat A, Rimmerman N, Levy R, Vogel Z & Kozela E (2012) Cannabidiol affects the expression of genes involved in zinc homeostasis in BV-2 microglial cells. *Neurochem Int* **61**, 923–930.
 - 27 Foster AW & Robinson NJ (2011) Promiscuity and preferences of metallothioneins: the cell rules. *BMC Biol* **9**, 25.
 - 28 Coyle P, Philcox JC, Carey LC & Rofe AM (2002) Metallothionein: the multipurpose protein. *Cell Mol Life Sci* **59**, 627–647.
 - 29 Radtke F, Heuchel R, Georgiev O, Hergersberg M, Gariglio M, Dembic Z & Schaffner W (1993) Cloned transcription factor MTF-1 activates the mouse metallothionein I promoter. *EMBO J* **12**, 1355–1362.
 - 30 Meraz-Torres F, Plöger S, Garbe C, Niessner H & Sinnberg T (2020) Disulfiram as a therapeutic agent for metastatic malignant melanoma—old myth or new logos? *Cancers* **12**, 3538.
 - 31 Casini A, Karotki A, Gabbiani C, Rugi F, Vašák M, Messori L & Dyson PJ (2009) Reactivity of an antimetastatic organometallic ruthenium compound with metallothionein-2: relevance to the mechanism of action. *Metallomics* **1**, 434–441.
 - 32 Merlos Rodrigo MA, Jimenez Jimenez AM, Haddad Y, Bodoor K, Adam P, Krizkova S, Heger Z & Adam V (2020) Metallothionein isoforms as double agents - Their roles in carcinogenesis, cancer progression and chemoresistance. *Drug Resist Updat* **52**, 100691.
 - 33 Wong DL & Stillman MJ (2018) Capturing platinum in cisplatin: kinetic reactions with recombinant human apo-metallothionein 1a. *Metallomics* **10**, 713–721.

- 34 Kasahara K, Fujiwara Y, Nishio K, Ohmori T, Sugimoto Y, Komiya K, Matsuda T & Saijo N (1991) Metallothionein content correlates with the sensitivity of human small cell lung cancer cell lines to cisplatin. *Cancer Res* **51**, 3237–3242.
- 35 Mangelinck A, da Costa MEM, Stefanovska B, Bawa O, Polrot M, Gaspar N & Fromigué O (2019) MT2A is an early predictive biomarker of response to chemotherapy and a potential therapeutic target in osteosarcoma. *Sci Rep* **9**, 12301.
- 36 Corsello SM, Nagari RT, Spangler RD, Rossen J, Kocak M, Bryan JG, Humeidi R, Peck D, Wu X *et al.* (2020) Discovering the anti-cancer potential of non-oncology drugs by systematic viability profiling. *Nat Cancer* **1**, 235–248.
- 37 Brewer GJ, Hill GM, Prasad AS, Cossack ZT & Rabbani P (1983) Oral zinc therapy for Wilson's disease. *Ann Intern Med* **99**, 314–319.
- 38 Halfdanarson TR, Kumar N, Hogan WJ & Murray JA (2009) Copper deficiency in celiac disease. *J Clin Gastroenterol* **43**, 162–164.
- 39 Krizkova S, Ryvolova M, Hrabeta J, Adam V, Stiborova M, Eckschlager T & Kizek R (2012) Metallothioneins and zinc in cancer diagnosis and therapy. *Drug Metab Rev* **44**, 287–301.
- 40 Shi Y, Amin K, Sato BG, Samuelsson SJ, Sambucetti L, Haroon ZA, Laderoute K & Murphy BJ (2010) The metal-responsive transcription factor-1 protein is elevated in human tumors. *Cancer Biol Ther* **9**, 469–476.
- 41 Si M & Lang J (2018) The roles of metallothioneins in carcinogenesis. *J Hematol Oncol* **11**, 107.
- 42 Jung AY, Cai X, Thoene K, Obi N, Jaskulski S, Behrens S, Flesch-Janys D & Chang-Claude J (2019) Antioxidant supplementation and breast cancer prognosis in postmenopausal women undergoing chemotherapy and radiation therapy. *Am J Clin Nutr* **109**, 69–78.

Supporting information

Additional supporting information may be found online in the Supporting Information section at the end of the article.

Fig. S1. Cannabidiol (CBD) pre-treatment modulates the cellular responses to bis-diethylthiocarbamate-copper complex (CuET) in the MDA-MB-231 cell line as observed by western blot.

Fig. S2. Expression of heat-shock protein *HSPA1A* after bis-diethylthiocarbamate-copper complex (CuET) is modulated by cannabidiol (CBD) and metallothioneins in U-2-OS cell line.

Fig. S3. Cannabidiol (CBD) does not directly interact with bis-diethylthiocarbamate-copper complex (CuET) neither affects its cellular uptake.

Fig. S4. Cannabidiol (CBD) and bis-diethylthiocarbamate-copper complex (CuET) induce expression of *MT-1E* and *MT-2A* mRNA in the MDA-MB-231 cell line.

Fig. S5. MTF1 silencing affects the cellular ability to express metallothioneins.

Fig. S6. Metallothionein level modulates the toxic responses to bis-diethylthiocarbamate-copper complex (CuET) in the MDA-MB-231 cell line.

Fig. S7. Primary cell line RPE-1 exhibits similar drug responsiveness compared to tested cancer cell lines.

Fig. S8. mRNA levels of metallothioneins *MT-1E* and *MT-2A* in human breast cancer cell lines measured by quantitative polymerase chain reaction (qPCR).

Fig. S9. Metallothioneins protect cells against bis-diethylthiocarbamate-copper complex (CuET) rather than disulfiram (DSF) as evaluated by XTT assay.

Table S1. A table summarizing data for screened compounds.



Cannabis-derived products antagonize platinum drugs by altered cellular transport

Tereza Buchtova^a, Lucie Beresova^a, Katarina Chroma^a, Tomas Pluhacek^b, Tibor Beres^c, Dominika Kaczorova^{c,d}, Petr Tarkowski^{c,d}, Jiri Bartek^{e,f}, Martin Mistrik^{a,*}

^a Faculty of Medicine and Dentistry, Institute of Molecular and Translational Medicine, Palacký University, Olomouc, Czech Republic

^b Department of Analytical Chemistry, Faculty of Science, Palacký University Olomouc, 17. listopadu 12, 771 46 Olomouc, Czech Republic

^c Czech Advanced Technology and Research Institute, Palacký University, Olomouc, Czech Republic

^d Centre of the Region Haná for Biotechnological and Agricultural Research, Department of Genetic Resources for Vegetables, Medicinal and Special Plants, Crop Research Institute, Olomouc, Czech Republic

^e Danish Cancer Society Research Center, DK 2100 Copenhagen, Denmark

^f Division of Genome Biology, Department of Medical Biochemistry and Biophysics, Science for Life Laboratory, Karolinska Institute, 171 77 Stockholm, Sweden

ARTICLE INFO

Keywords:

Platinum-based drugs
Cannabis
Cannabidiol
Cellular transport
Drug therapy efficacy

ABSTRACT

Cannabinoids, a class of compounds derived from *Cannabis sativa* L., have recently become more widely accessible for public consumption in the form of diverse cannabis products, in parallel with weakening the measures that so far restricted their availability. The US Food and Drug Administration has approved several cannabis-derived drugs for management of various diseases as well as chemotherapy-induced nausea and vomiting. Besides the attenuation of adverse effects of chemotherapy, numerous reports about cannabinoid-mediated anticancer effects further motivate cancer patients to support their therapy with such products. Here we present a set of preclinical data with human cell culture models, suggesting that cannabidiol and cannabis extracts may effectively counteract the anticancer effects of the clinically widely used standard-of-care platinum-based drugs. We show that even low concentrations of cannabinoids reduced the toxicity of cisplatin, oxaliplatin, and carboplatin, an effect which was accompanied by decreased platinum adduct formation and a set of commonly used molecular markers. Mechanistically, our results excluded the possibility that the observed enhanced survival of cancer cells was mediated transcriptionally. Instead, trace metal analyses strongly indicate an inhibitory impact of cannabinoids on intracellular platinum accumulation, thereby implicating changes in cellular transport and/or retention of these drugs as the likely cause of the observed biological effects. Our study raises the possibility that the desirable effect of counteracting adverse effects of chemotherapy might, at least for some cannabinoids, reflect impaired cellular availability, and consequently attenuation of the anticancer effects of platinum drugs.

Data availability: All data supporting the conclusions are available in the article and supplementary files. Raw data are available upon request from the corresponding author.

1. Introduction

Current standard-of-care cancer chemotherapy protocols commonly include cisplatin or other platinum-derived drugs as their key components [1]. Cisplatin was the first such compound, approved by the FDA in 1978 for the treatment of ovarian and testicular cancers [1], with the application spectrum later extended to cover also head and neck, esophageal, gastric, colon, bladder, and cervical cancers as the first-line therapy, as well as many other types of malignancies, including lung

cancer, as the second-line therapy, often combined with other chemotherapeutics and/or other treatment modalities [2,3]. Mechanistically, cisplatin becomes hydrolyzed in cells to become a potent electrophile that reacts with cysteine-rich proteins and purine bases at the N7 position. Ensuing DNA damage is the most widely accepted mechanism to which the antineoplastic properties of cisplatin have been attributed. Indeed, cisplatin forms DNA adducts and crosslinks, which can hinder DNA replication and hence cell division, inducing cell death [3].

However, cisplatin has multiple shortcomings, including dose-

* Correspondence to: Institute of Molecular and Translational Medicine, Faculty of Medicine and Dentistry, Palacký University, 77 147 Olomouc, Czech Republic.
E-mail address: martin.mistik@upol.cz (M. Mistrik).

<https://doi.org/10.1016/j.bioph.2023.114801>

Received 9 February 2023; Received in revised form 9 April 2023; Accepted 25 April 2023

Available online 1 May 2023

0753-3322/© 2023 The Authors. Published by Elsevier Masson SAS. This is an open access article under the CC BY license (<http://creativecommons.org/licenses/by/4.0/>).

limiting side effects and the development of resistance. Neuro-, nephron-, oto-, and gastrointestinal toxicity with myelosuppression are some of the most common negative side effects impacting patients, with nephrotoxicity as the major dose-limiting factor [2,4]. Although carboplatin, the second generation of platinum-based drugs, solved some of the challenging issues of cisplatin in oncology, carboplatin also has serious side effects, including dose-limiting myelosuppression [2,3]. Moreover, despite some improved attributes, carboplatin is unsuitable for certain cancers that can be treated by cisplatin but is approved for the treatment of ovarian and testicular cancer, as well as numerous other tumor types in the context of combined therapies [2,2,5]. Compared to cisplatin, the carboplatin molecule contains a bidentate dicarboxylate ligand instead of two chlorine atoms. The ligand provides carboplatin with new properties, including slower hydrolysis, lower reactivity, and longer retention. Although the reaction products of carboplatin are analogous to those of cisplatin, substantially higher concentrations of carboplatin are needed to achieve the same toxicity [3]. Furthermore, cross-resistance is inevitable due to the close similarity of these two substances [2,6].

Oxaliplatin, the third-generation platinum-based drug, was developed to respond to acquired resistance induced by cisplatin and carboplatin. Its ability to overcome resistance is attributable to the different constitution of the molecule, which contains a 1,2-diaminocyclohexane ligand instead of amine groups, and oxalate as a leaving group [5,6]. This composition makes oxaliplatin lipophilic, which provides additional routes for cellular transport and alters its reactivity and mechanism of action. Oxaliplatin has lower reactivity with DNA, but its toxicity and anticancer properties are strongly exacerbated by its ability to interfere with ribosome biogenesis and protein synthesis [2,5,6]. Oxaliplatin is commonly used to treat colorectal cancers [2,6]. However, similar to previous platinum drug generations, oxaliplatin causes severe adverse effects with dose-limiting neurotoxicity [2,4].

While many patients initially benefit from platinum-derived chemotherapy, a large proportion of tumors relapse, and the acquired resistance to further chemotherapy often results in treatment failure. Though far from being fully understood, such drug resistance mechanisms include modulation of drug transport, glutathione and metallothionein pathways, enhanced DNA-damage repair, inhibition of cell death, and altered cancer cell metabolism [6].

In this study, we identify cannabidiol and cannabis plant extracts as substances interfering with the toxicity of all three of the above-mentioned platinum-based drugs. Cannabinoids are a family of substances with a broad pharmacological profile, potentially applicable to numerous health conditions, from neurological to inflammatory and autoimmune diseases [7–9]. Importantly, cannabis products are clinically highly relevant due to their extensive use among cancer patients [10–12]. Cannabis products are generally accepted to attenuate chemotherapy-induced unwanted side effects. Several cannabinoid-based drugs, including Dronabinol and Nabilone, are indeed being prescribed for chemotherapy-induced nausea and vomiting [13,14]. The motivation of oncological patients to use cannabis-based products is further boosted by numerous studies that suggest their anticancer properties via various mechanisms of action. It has also been speculated that simultaneous consumption of cannabinoids may support ongoing anticancer therapy through some direct anticancer effects [7,9,15]. However, antagonistic effects were also suggested [16,17]. Indeed, our present results call for caution with regard to such combinatorial use, as the positive effects of cannabinoids on cancer chemotherapy may not be universally applicable. Indeed, when combined with some chemotherapeutics, such as platinum-derived drugs, cannabis may undermine their anticancer effects and thereby attenuate the treatment efficacy.

2. Materials and methods

2.1. Cell lines

Human osteosarcoma U-2-OS (ATCC), human lung carcinoma NCI-H1299 (ATCC), and human lung fibroblast MRC-5 (ATCC) cells were maintained in DMEM (Lonza) supplemented with 10% fetal bovine serum (Thermo Fisher Scientific) and 1% penicillin/streptomycin (Sigma-Aldrich). MRC-5 cells were further supplemented with 1% non-essential amino acids (MEM NEAA, Gibco).

2.2. Crystal violet assay

Cells were seeded on a 96-well plate with a seeding density of 5000 cells per well. On the same day, the cells were pretreated with 2.5 μ M cannabinoid. After 17 h, the cells were treated with increasing concentrations of the platinum-based drug. Cisplatin (CisPt) and oxaliplatin (OxPt) were used in concentrations 5, 10, 20, and 40 μ M. Carboplatin (CarboPt) was used in concentrations 50, 100, 200, and 400 μ M. In the wash-out experiment, the CBD (cannabidiol) pretreatment was removed by washing with new DMEM media before treatment with platinum-based drugs. After 72 h of treatment, the cells were fixed with 70% cold ethanol for 15 min and labeled with crystal violet solution (5 g Crystal Violet, Sigma Aldrich, C6158; 200 mL 96% ethanol, 800 mL H₂O) for 20 min. Next, the 96-well plates were thoroughly washed under running water and left to dry. The cell-incorporated crystal violet dye was solubilized by phosphate buffer saline containing 0.2% Triton X-100 and measured at 590 nm using a spectrometer (TECAN, Infinite M200PRO). The results are shown as the mean value and standard deviation from three independent experiments. Five technical repeats were performed per experiment.

2.3. Colony formation assay

Cells were seeded on a 12-well plate with a seeding density of 100 cells per well. On the day of seeding, the cells were pretreated with 2.5 μ M CBD, and after 17 h, the cells were treated with 2.5 μ M CisPt, 5 μ M CarboPt, or 5 μ M OxPt. After 12 days, the colonies were fixed with 70% cold ethanol and labeled with crystal violet solution. Cells were washed under running water and air dried. For better contrast, the wells were filled with powdered white edible sugar and scanned using a tabletop scanner (Epson Perfection V750 PRO). The mean area and colony count were evaluated using ImageJ (Wayne Rasband) software. The results are shown as the mean value and standard deviation from three independent experiments. Three technical repeats were performed per experiment.

2.4. Immunofluorescence staining and quantitative microscopy

The cells were seeded on glass coverslips or a 24-well glass bottom plate (Cellvis, P24-1.5H-N). Cells were pretreated with 10 μ M CBD on the day of seeding, before treating with 10 μ M platinum-based drug for 24 h. In the case of treatment with cycloheximide (Cycloheximide solution, Sigma Aldrich, C4859), the treatment was shortened to 17 h and chemicals (CBD, cycloheximide, platinum-based drugs) were administered concomitantly. The cells were fixed with 4% cold formaldehyde for 15 min, followed by permeabilization with phosphate buffer saline containing 0.5% Triton X-100 for 5 min. Subsequently, the cells were blocked with DMEM media containing 10% fetal bovine serum (FBS, Gibco) for 1 h, before staining with primary antibody dissolved in blocking media overnight at 4 °C. Secondary antibodies were added for 1 h at room temperature. Nuclei were stained with DAPI (Sigma) (1 μ g·mL⁻¹) for 5 min. Samples were visualized and acquired using fluorescence microscopes (Olympus IX81 ScanR and/or Zeiss LSM 980). Quantitative analysis was performed in ScanR Analysis software (Olympus).

For cisplatin-DNA adduct staining, the cells were blocked in 5% bovine serum albumin and incubated in 2 M HCl for 10 min at 37 °C consecutively. The remainder of the protocol was performed as described above.

The results are shown as the mean value and standard deviation from three independent experiments.

2.5. Immunoblotting

The cells were seeded on a 6-cm Petri dish, pretreated with 10 µM CBD on the day of seeding, and then treated with 10 µM platinum-based drug for 24 h. The cells were lysed in Laemmli sample buffer. The protein concentration was measured by Bradford assay (Pierce Detergent Compatible Bradford Assay Kit, Thermo Scientific, 1863028), and approximately 10 µg of protein was loaded into a precast gel (Mini-PROTEAN TGX Stain-Free Gels, Bio-Rad, 4568093) and run under the conditions with constant 20 mA per gel. The separated proteins were transferred to nitrocellulose membrane, which was blocked in 5% milk (edible dried low-fat milk) dissolved in Tris-buffer saline containing 0.1 Tween 20 for 1 h. Next, the membrane was incubated with primary antibodies overnight at 4 °C, followed by secondary antibodies for 1 h at room temperature. Proteins were visualized by HRP substrate (Immobilon Forte Western HSR Substrate, Merck Millipore, WBLUF0500), and images were acquired using the ChemiDoc imaging system (Bio-Rad). The figure used in the manuscript represents one of three independent experiments.

2.6. Determination of total platinum and zinc content

The cells were seeded in a 15-cm Petri dish and were pretreated with 10 µM CBD on the day of seeding. Subsequently, the cells were treated with 20 µM CisPt for indicated time-points or 20 µM OxPt and 200 µM CarboPt for 24 h. The cells were then quickly washed in phosphate buffer saline and removed to 2-mL Eppendorf tubes. The samples were normalized according to the protein concentration. To determine the protein concentration, the samples were frozen at -80 °C to rupture the cells and then centrifuged at 20,000 g for 10 min at 4 °C. The protein concentration was measured from the supernatant using the BCA assay (Pierce BCA Protein Assay Kit, Thermo Scientific, 23225).

The total Pt and Zn contents were determined by solution ICP-MS using an external calibration in the range of 5–100 µg.L⁻¹ for Zn and 0.1–100 µg.L⁻¹ for Pt. The aliquots of cell cultures were digested with 4 mL of concentrated nitric and hydrochloric acids (1:1, v/v) in the UltraWAVE digestion unit (Milestone, Italy) using a general temperature-control digestion method for biological samples. Following mineralization, the digests were quantitatively transferred to a 10-mL volumetric flask and filled with ultrapure water. The samples were subjected to ICP-MS analysis using the ORS-ICP-MS 7700x instrument (Agilent Technologies, Japan) in helium mode to overcome spectral interferences. The following isotopes were selected for quantitative ICP-MS analysis: ⁶⁶Zn, ¹⁹⁴Pt, and ¹⁹⁵Pt; and ⁸⁹Y and ²⁰⁹Bi as internal standards. The regular measurement of independently prepared quality control samples at the concentration level of 50 µg.L⁻¹ for Zn and 5 µg.L⁻¹ for Pt was adopted to ensure the reliability of the ICP-MS results. The results are shown as the mean value and standard deviation from three independent experiments.

2.7. 2,3-bis(2-methoxy-4-nitro-5-sulphophenyl)-2H-tetrazolium-5-carboxamide

For the XTT assay, 5000 cells per well were seeded on a 96-well plate. The cells were pretreated with 10 µM CBD and, after 17 h, treated with increasing concentrations of platinum-based drugs. After 72 h, the XTT assay was performed according to the manufacturer's instructions (AppliChem) and measured using a spectrometer (TECAN, Infinite M200PRO). The results are shown as the mean value and

standard deviation from three independent experiments. Five technical repeats were conducted per experiment.

2.8. RNA interference

siRNA against MTF1 (OriGene, SR302991) was used for RNA interference. The cells were transfected with siRNA using Lipofectamine RNAiMAX (Invitrogen, 13778) according to the manufacturer's instructions. The cells were reseeded to the required plate or dish 24 h after transfection. Treatments were started 72 h after transfection.

2.9. Cultivation of cannabis plants

Two genotypes of cannabis (*Cannabis sativa* L.) were used in this study. The genotype "Kosher Haze" (KH; Dutch Passion®, the Netherlands) was classified as chemotype I, which was THC dominant and grown from regular seeds. The seeds were cleaned with 0.03% v/v hydrogen peroxide and germinated on wet paper, in the dark, at laboratory temperature. During the vegetative phase of 8 weeks, the photoperiod was maintained at 18 h light/6 h dark, with a temperature of 24/18 °C, and relative humidity of 50%. During this phase, the plants underwent transplanting from germination soil (Florcom®, Czechia) to coconut coir (BioBizz, Spain) and topping. The genotype "Fantasy Bud" was classified as chemotype III, which was CBD dominant and grown from cuttings purchased from Konopex company (Ostrava, Czechia). Rooted clones were introduced directly into the flowering phase with 12 h of light. Both genotypes were cultivated in coconut coir (BioBizz, Spain). Plagron Cocos A + B, Power Roots, and Pure Zym (Plagron, the Netherlands) fertilizers were used for plant nutrition during the vegetative phase according to the manufacturer's instructions. Green sensation (Plagron, the Netherlands) was added to the nutrition scheme during the flowering stage. Full-spectrum 300 W LED Attis lights (Lumatek, UK) were used for illumination. Upon maturation (approx. 9 weeks), inflorescences were harvested and dried at 25 °C in the dark for 7 days, before curing and storing in glass jars in the dark at laboratory temperature.

2.10. Cannabis extraction

The dried inflorescences were sieved through a 1-mm mesh and decarboxylated for 30 min at 121 °C. Ethanolic extracts were prepared by adding 60 mL of 96% EtOH v/v to 6 g of decarboxylated material and sonicating for 30 min at 40 kHz. Upon centrifugation, the extraction solvent (1 mL supernatant aliquots) was evaporated on a centrifugal evaporator (Labconco, USA) at 40 °C. Phytocannabinoid profiling was accomplished according to methods recommended by the USP Cannabis expert panel [18] and according to the Dutch OMC (Office on Medicinal Cannabis, Analytical monograph Cannabis Flos (flowers/granulated); Version 7.1; Office of Medicinal Cannabis, Ministry of Health Welfare and Sport; Netherlands, 2014). The phytocannabinoid profiles of the extracts are shown in detail in ST1.

2.11. Statistical analysis

XY graphs comprising error bars are plotted as mean values and standard deviation from three independent experiments, each presented by five technical replicates. Interleaved and stacked bar graphs are plotted as mean values and standard deviation from three independent experiments. The scatter plot presents the mean values and standard deviation from three independent experiments, each presented by quantitative data obtained from ScanR Analysis software. Ordinary one-way ANOVA was used to assess statistical significance, and the resulting P-value is shown in the graphs. All graphical and analytic processing, including the calculation of the IC50 and IC75, were performed in GraphPad Prism 9.4.1.

2.12. Chemicals and antibodies

The following antibodies were used for immunofluorescence labeling for microscopy: anti-cisplatin modified DNA (1:1000, Abcam, ab103261), γ H2AX (1:500, Millipore, 05-636), anti-nucleolin (1:1000, Abcam, ab70493), p53 (1:500, Santa Cruz, sc-6243), Alexa Fluor 488 goat anti-mouse IgG (1:500, Invitrogen, A11001), Alexa Fluor 568 goat anti-rabbit IgG (1:500, Invitrogen, A11036), and Alexa Fluor 568 goat anti-rat IgG (1:500, Abcam, ab175476).

The following antibodies were used for immunoblotting: anti-b-actin (1:1000; Santa Cruz Biotechnology, sc-47778), anti-MTF1 (1:1000; NOVUS Biologicals, NBP1-86380), anti-p53 (1:500, Santa Cruz, sc-126), anti-SMC1 (1:1000, Abcam, ab9263), goat-anti mouse IgG-HRP (1:1000; GE Healthcare, NA931), and goat-anti-rabbit (1:1000; GE Healthcare, NA934).

The following cannabinoids were used for the abovementioned assays: CBD (-)-cannabinoid, 10 mM stock solution in DMSO; Abcam, ab120448), Δ^9 -THC (Δ^9 -Tetrahydrocannabinol solution 1 mg·mL⁻¹ in methanol; Sigma Aldrich, T4764), and CBG (Cannabigerol solution 1 mg·mL⁻¹ in methanol; Sigma Aldrich, C-141). Extract 1 (CBD enriched) and extract 2 (Δ^9 -THC enriched) were prepared and characterized at the Crop Research Institute (Olomouc, Czech republic) as stated in the Material and Methods. Information on the composition of the extracts is described in *ST1*. The extract was dissolved in DMSO to achieve a 10 mM solution of the dominant cannabinoid.

The following platinum-based drugs were used for the abovementioned assays: Cisplatin (Selleckchem, S1166), carboplatin (Selleckchem, S1215), and oxaliplatin (Selleckchem, S1224). Cisplatin and carboplatin were dissolved in water, with stock solutions of 1 mg·mL⁻¹ and 10 mg·mL⁻¹, respectively. Oxaliplatin was dissolved in N, N-dimethylformamide (Sigma Aldrich, 227056) at a 5 mg·mL⁻¹ stock concentration.

The following chemicals were used for ICP-MS: Certified reference material of aqueous calibration solution, ASTASOL® Pt and Zn (1000.0 ± 2.0 mg·L⁻¹), nitric acid (69%, ANALPURE® grade), internal standards mix, INT-MIX 1 Sc, Y, In, Tb, and Bi (10.0 ± 0.1 mg·L⁻¹) were purchased from Analytika, Ltd., Czech Republic. Ultrapure water with a resistivity of 18.2 M Ω cm was produced by a Milli-Q Reference purification system (Millipore Corporation, Molsheim, France).

3. Results

3.1. CBD protects cells from the toxicity of three clinically used platinum-based drugs

We have recently reported that cannabidiol (CBD)-triggered expression of metallothioneins can protect cancer cells against copper-containing substances such as CuET (an anticancer metabolite of disulfiram) [17]. Metallothioneins, in general, are cysteine-rich proteins that can protect cells against the toxic effects of various metals and metal-containing drugs. Here, we wished to determine whether a similar metallothionein-mediated resistance mechanism could be relevant for platinum-based drugs. First, we performed cytotoxicity tests with CBD combined with each of the three clinically used platinum cytostatics: cisplatin (CisPt), carboplatin (CarboPt), and oxaliplatin (OxPt), respectively. As the assay readout, we used the crystal violet staining analysis in human U-2-OS osteosarcoma cells pretreated with CBD and then treated with increasing concentrations of the 3 platinum drugs. As shown in *Fig. 1A*, even relatively low concentrations of CBD effectively interfered with the toxic effects of CisPt and CarboPt, while the toxicity profile of OxPt remained unchanged. The experiment was also performed with a human lung carcinoma HCl-H1299 cell line and with primary MRC-5 lung fibroblasts, respectively. Overall, the results obtained with all three cell models showed a similar trend (*Figs. 1A* and *S1*). Next, we employed a colony formation assay using the U-2-OS cells, to corroborate the CBD-protective effects in an approach that involves

long-term exposure to the drugs. In this case, the CBD-mediated protective effect was even more pronounced and also confirmed in the OxPt-treated cells (*Fig. 1B*). Next, we analyzed the response using commonly used cellular stress markers, which partly differ across the platinum drugs [19–21]. In the case of CisPt, we analyzed the DNA damage using the γ H2AX marker [19], the level of which was significantly reduced in the CBD-pretreated cells (*Figs. 2A* and *S2*) in a concentration-dependent manner (*S3*). Moreover, using quantitative fluorescence microscopy, we confirmed the CBD-mediated attenuation of p53 levels after CarboPt treatment (*Figs. 2A* and *S2*). In cells treated with OxPt, CBD pretreatment caused lower levels of nucleolar stress, as reflected by NCL-protein localization (*Figs. 2A* and *S2*). Interestingly, for the diploid MRC-5 cells, the extent of nucleolar stress remained unchanged upon pretreatment with CBD, suggesting that the protective effect of CBD is even greater in cancer cells compared to normal cells. We also performed a western blot analysis of the p53 protein as the shared stress response marker induced by all platinum-based drugs [22]. Consistently with the other markers, in all models, the CBD cotreatment resulted in an attenuation of the platinum drug-induced p53 accumulation (*Fig. 2B, S4*). For CisPt, we also quantified the signal from CisPt-modified DNA using specific antibodies for these structures, thus assessing directly the extent of the DNA adducts caused by the drug. This immunofluorescence method enables direct visualization of cis-platinated DNA, a readout that was found to be significantly decreased after CBD pretreatment (*Fig. 2C*), suggesting that the protective effect of CBD against CisPt-mediated toxicity is directly linked to the ability of the drug to reach its molecular target.

3.2. CBD affects the cellular transport of platinum drugs

Metallothioneins induced by CBD serve as intracellular heavy metal chelators and detoxicators, and therefore they might offer a potential explanation for the protective effects described above. To investigate this possibility, we employed an RNAi-mediated knockdown of MTF1, a transcription factor required for metallothionein expression, whose depletion abolished the CBD-triggered resistance of human cancer cells towards the copper-containing anticancer metabolite of disulfiram in our previous work [17]. In MTF1 deficient cells, the CBD-mediated protective effect remained unchanged for CisPt and CarboPt (*SSFig. 5A, B*), thereby disproving the hypothesis that metallothionein could be responsible for the observed CBD-induced resistance to platinum drugs. Next, we included a washing step in the CBD pretreatment toxicity experiment to determine whether the protective effect employed other transcriptional responses; the idea being that any such transcriptional response should be relatively stable, and therefore an acute removal of CBD from the culture medium immediately after pretreatment should minimally impact the protective effect of CBD. However, upon CBD wash-out, U-2-OS cells lost the resistance against platinum-based drugs (*S6*). We further excluded the transcription-promoted rescue effect of CBD by cotreatment with cycloheximide (CHX), an inhibitor of protein synthesis. Indeed, cells cotreated with CHX retained their resistance against CisPt in the presence of CBD, as shown by lower induction of γ H2AX and a reduced formation of CisPt-DNA adducts in the nuclei (*Fig. 3*). These data indicate that CBD may rather affect the cellular influx and/or efflux of platinum drugs. To address this possibility, we used the ICP-MS method to measure the intracellular levels of platinum after CBD pretreatment. Our results demonstrated significantly lower levels of intracellular platinum in CBD-cotreated cells, supporting the hypothesis that altered cellular transport may underlie the CBD-induced resistance to platinum drugs (*Fig. 4*).

3.3. Observed protective effect of CBD against platinum-based drugs is shared by cannabis plant extracts

Instead of pure CBD, many patients use more or less defined cannabis

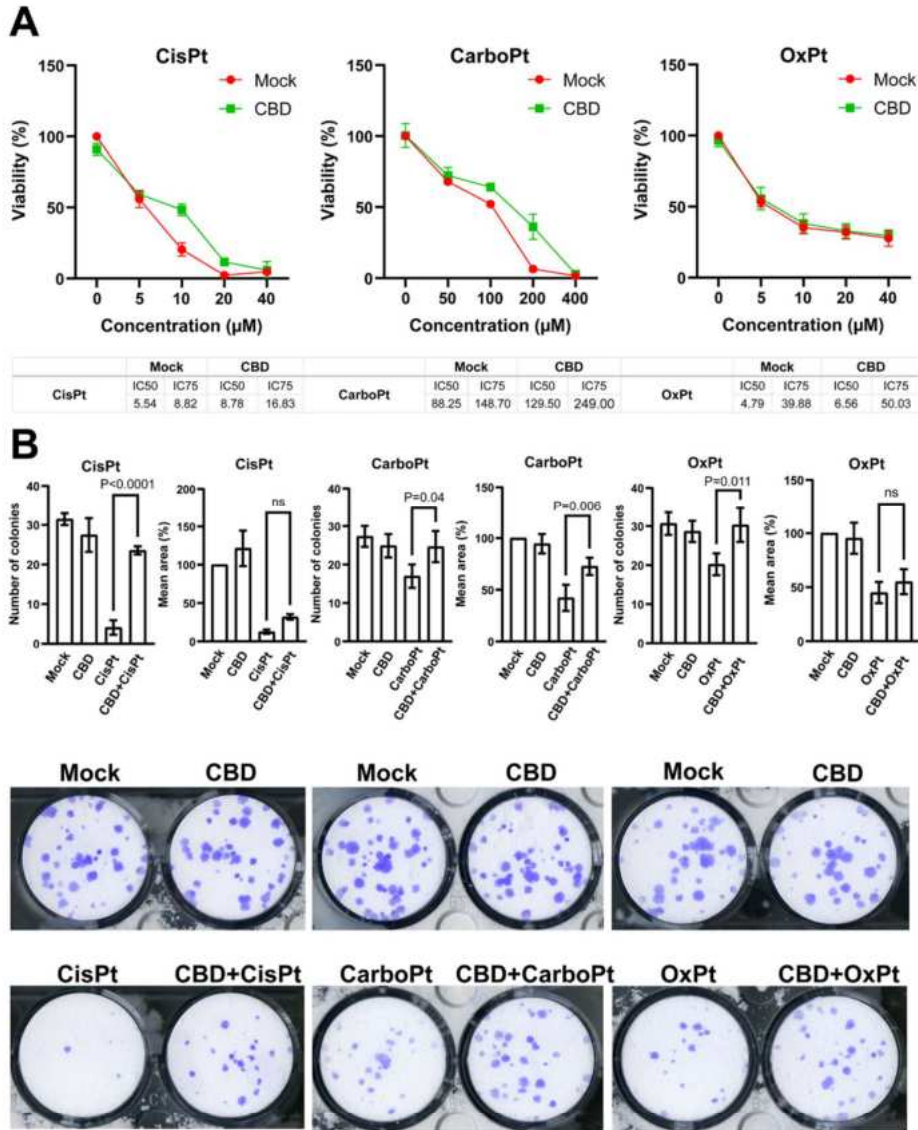


Fig. 1. Cannabidiol (CBD) protects U-2-OS cells against platinum-based drugs. A) Cells pretreated with 2.5 μ M CBD and treated with increasing concentrations of cisplatin (CisPt) and carboplatin (CarboPt) were more resistant to platinum-based drugs compared to mock-pretreated cells. Cells were pretreated for 17 h and treated for 72 h. The result was assessed by crystal violet assay. The IC50 and IC75 values (μ M), shown in the table below the graphs were calculated using logarithmic transformation and nonlinear regression. The final graphs present the mean and standard deviation of three independent experiments ($n = 3$). B) The results of the 12-day colony formation assay reveal substantial interference of CBD with all three tested platinum-based drugs (including oxaliplatin [OxPt]). Cells were pretreated with 2.5 μ M CBD for 17 h, before treating with CisPt (2.5 μ M), CarboPt (5 μ M), or OxPt (5 μ M) and grown for 12 days. The number of colonies and mean colony area were plotted on the graphs. For bar graphs, one-way ANOVA was used to calculate the P-value. The result represents the mean and standard deviation of three independent experiments ($n = 3$).

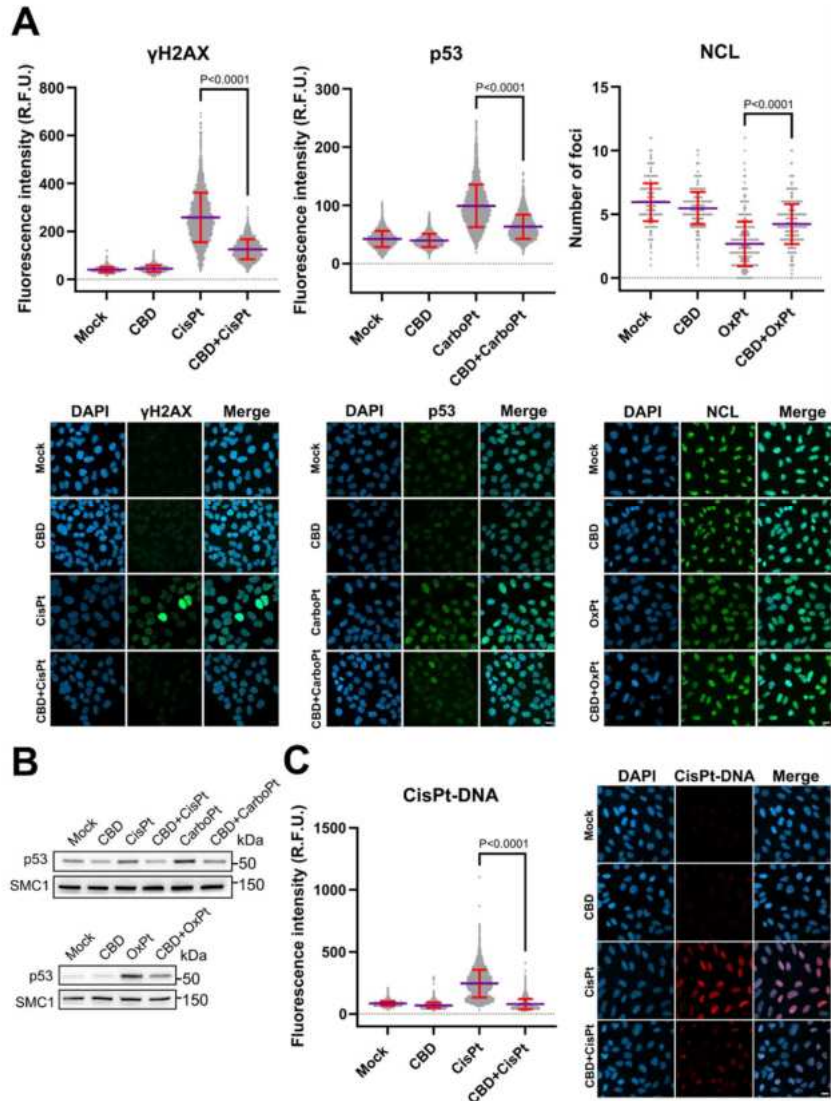


Fig. 2. Cannabidiol (CBD) protects U-2-OS cells from platinum-based drug-induced stress responses. **A)** CBD decreased DNA damage (measured as γ H2AX) after cisplatin (CisPt) treatment, attenuated induction of p53 after carboplatin (CarboPt) treatment, and increased the number of compact nucleoli after oxaliplatin (OxPt) treatment (as evaluated by nucleolin localization). The cells were pretreated with 10 μ M CBD for 17 h, before treating with CisPt (10 μ M), CarboPt (100 μ M), or OxPt (10 μ M) for 24 h. The cells were analyzed using fluorescence microscopy (scale bar: 20 μ m). For scatter plots, one-way ANOVA was used to calculate the P-value. The result represents the mean and standard deviation of three independent experiments (n = 3). **B)** Western blot analysis shows that CBD-pretreated cells accumulated less p53 after platinum-based drug treatment. Cells were pretreated with 10 μ M CBD for 17 h, before treating with CisPt (10 μ M), CarboPt (100 μ M), and OxPt (10 μ M) for 24 h. The result represents one of three independent experiments. **C)** CBD decreased CisPt-DNA adducts in CisPt-treated cells compared to mock-pretreated and CisPt-treated. Cells were pretreated with 10 μ M CBD for 17 h, before treating with CisPt (20 μ M) for 24 h, and analyzed by quantitative immunofluorescence microscopy (scale bar: 20 μ m). For scatter plots, one-way ANOVA was used to calculate the P-value. The result represents the mean and standard deviation of three independent experiments (n = 3).

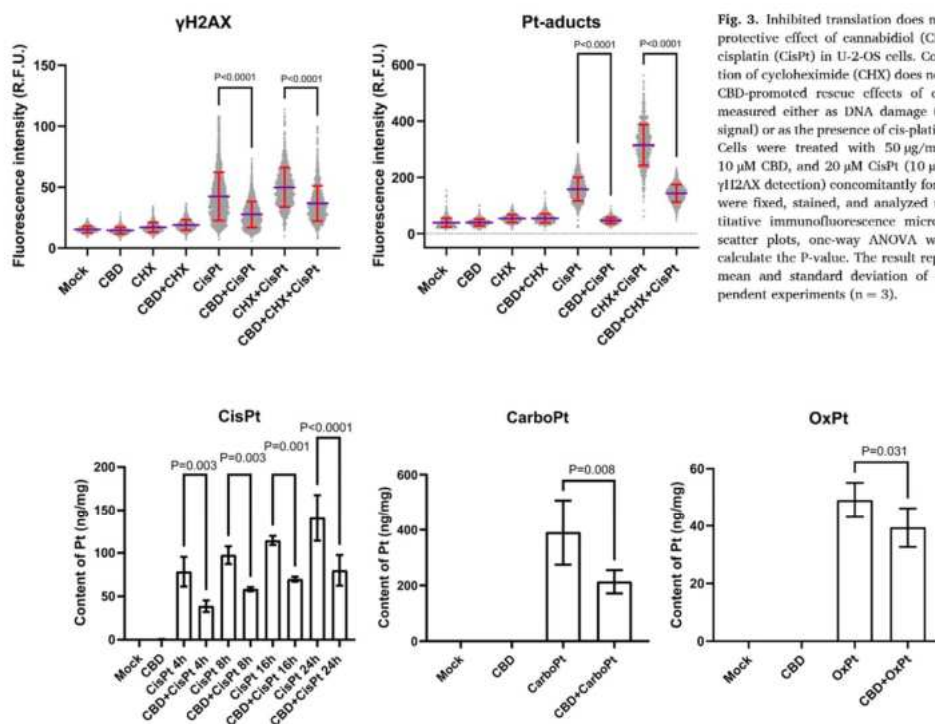


Fig. 3. Inhibited translation does not limit the protective effect of cannabidiol (CBD) against cisplatin (CisPt) in U-2-OS cells. Coadministration of cycloheximide (CHX) does not affect the CBD-promoted rescue effects of cis-platinum measured either as DNA damage (via γ H2AX signal) or as the presence of cis-platinated DNA. Cells were treated with 50 μ g/ml of CHX, 10 μ M CBD, and 20 μ M CisPt (10 μ M CisPt for γ H2AX detection) concomitantly for 17 h. Cells were fixed, stained, and analyzed using quantitative immunofluorescence microscopy. For scatter plots, one-way ANOVA was used to calculate the P-value. The result represents the mean and standard deviation of three independent experiments (n = 3).

Fig. 4. U-2-OS cells pretreated by cannabidiol (CBD) internalize less platinum. Trace elemental analysis showed a lower platinum content in cells subjected to combined treatment compared to those subjected to platinum-based drug only. Cells were pretreated with 10 μ M CBD for 17 h, before treating with CisPt (20 μ M) for 4, 8, 16, and 24 h, or CarboPt (200 μ M) and OxPt (20 μ M) for 24 h. The content of platinum was re-counted at 1 mg of protein. For bar graphs, one-way ANOVA was used to calculate the P-value. The result represents the mean and standard deviation of three independent experiments (n = 3).

plant extracts containing additional biologically active cannabinoids and other compounds. Therefore, we took advantage of the availability of cannabis extracts produced from two contrasting chemotypes (CBD dominant versus THC dominant), which were grown under defined conditions (see material and methods for more details and [ST1](#)). The protective effect against platinum drug toxicity that we observed for the CBD dominant variant was equally or even more potent than cell cotreatment by CBD-alone ([Fig. 5](#)). However, the extract from the Δ^9 -THC dominant variant was considerably less protective, suggesting that Δ^9 -THC itself may not be involved in the CBD-induced drug resistance. Consistently, further experiments with Δ^9 -THC pretreatment alone revealed no impact on the cellular sensitivity against platinum drugs ([Fig. 5](#)). Finally, we also tested the effect of cannabigerol (CBG), another cannabinoid typically present in cannabis plant extracts. CBG pretreatment displayed a significant, albeit less pronounced induction of resistance against CisPt and CarboPt ([Fig. 5](#)), indicating that protection against platinum-based drugs may be shared among diverse cannabinoids.

4. Discussion

Our present study sheds more light on the causes of acquired chemoresistance, one of contemporary oncology's most essential and challenging topics. Specifically, we have identified a so-far

unrecognized interference of CBD and cannabis extracts with the anti-cancer effects of three clinically commonly used platinum-based chemotherapeutics, resulting in acutely induced resistance of several human cancer cell models to these anticancer drugs. Furthermore, we also provide mechanistic insights into the observed cannabis product-induced chemoresistance. First, our functional assays aiming at better understanding this cannabinoid-induced chemoresistance phenomenon first excluded metallothioneins, a class of proteins that cause resistance to some other anticancer compounds [17] and which are transcriptionally induced by cannabinoids through the activity of the MTF1 transcription factor, as a potential mediator of resistance to platinum-derived drugs. Second, we further excluded that the acutely induced resistance to platinum drugs heavily relies on either ongoing transcription or protein translation in the target cells. Overall, our results narrowed the resistance mechanism using ICP-MS to cellular drug transport and/or retention in a translational-independent manner. We propose that cannabinoids limit the cellular uptake or accelerate the elimination of platinum-derived drugs from human cells and that this mechanism provides a major contribution to, though not necessarily the entire explanation for, the observed robust resistance to cytotoxic effects of clinically used platinum-derived chemotherapy in preclinical model experiments.

Previous studies of platinum-based medications examined a range of potentially involved membrane transporters, with OCT1-3, MATE1/2,

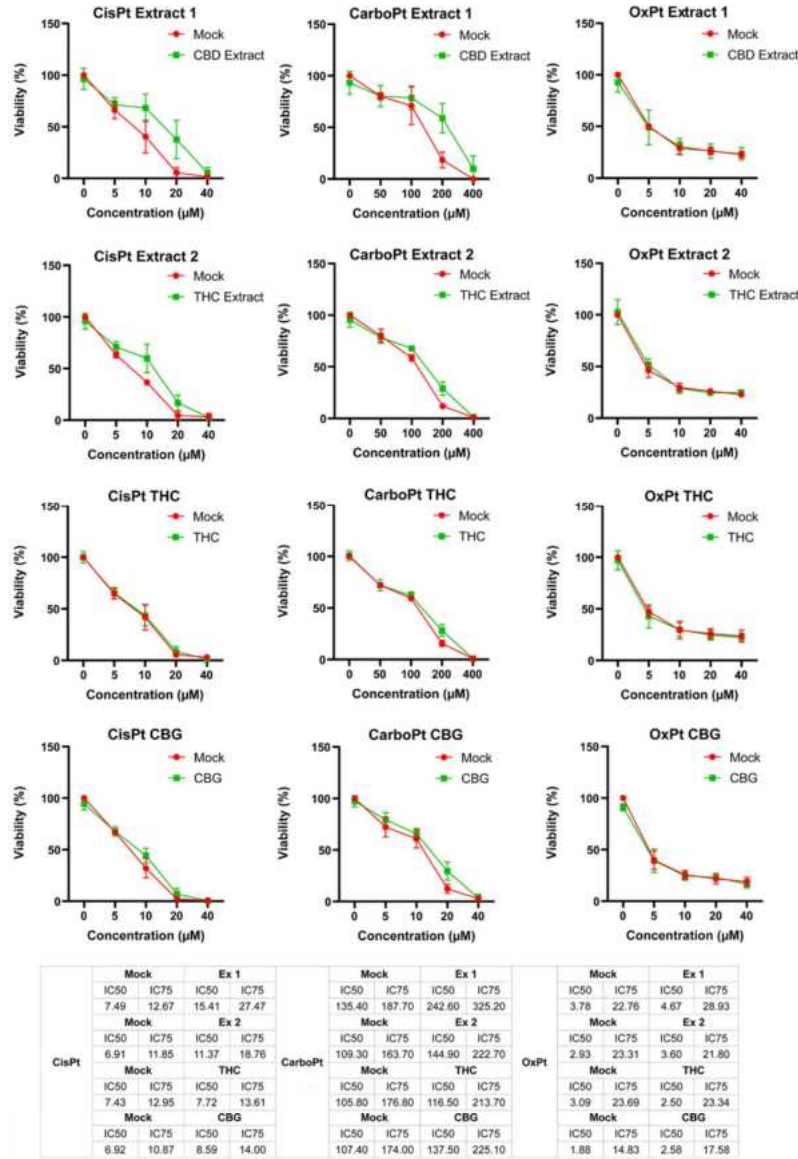


Fig. 5. Cannabis extracts and cannabigerol (CBG) provide similar rescue effects to cannabidiol (CBD) against cisplatin (CisPt) and carboplatin (CarboPt) in U-2-OS cells. CBD-enriched extract (Extract 1) induced a strong rescue effect against CisPt and CarboPt. Δ^9 -THC enriched extract (Extract 2) had a moderate protective effect against CisPt and CarboPt. Δ^9 -tetrahydrocannabinol (Δ^9 -THC) alone did not modulate cell sensitivity against platinum-based drugs. CBG had a protective effect on cells treated with CisPt and CarboPt, which was comparable to that observed with Extract 2. Cells were pretreated with extracts to reach a 2.5 μ M concentration of the primary cannabinoid for 17 h, followed by platinum-based drugs for 72 h. The result was assessed by crystal violet assay. The IC50 and IC75 values were calculated using logarithmic transformation and nonlinear regression. The final graphs present the mean and standard deviation of three independent experiments (n = 3).

CTR1, ATP7A/7B, and MRP2/4 among the most studied [6,23,24], and even more have been considered recently [25,26]. Whether or to what extent any of these transporters are direct CBD targets remains to be elucidated. Potential mechanisms by which CBD may influence the transport of platinum-based drugs in a transporter-independent manner include direct interaction with transporters, modulation of transporter phosphorylation, and altered transporter localization. Direct interaction with transporters could occur through competition with substrates, as has been shown for CBD and prazosin in the case of the BCRP transporter [27]. Posttranslational modification of transporters is another proposed mechanism by which CBD could interfere with transport. For example, Δ^9 -THC has been shown to indirectly modulate the phosphorylation of the divalent metal transporter-1 [28]. Lastly, altered transporter localization is another possibility. It has been shown that CBD can affect membrane composition [29]. Interestingly, our ICP-MS data revealed that CBD significantly increases the intracellular amount of zinc [37]. However, whether and how this phenomenon is related to platinum drug uptake requires further research. Nevertheless, the resulting increase in intracellular zinc levels provides a mechanistic explanation for the CBD-mediated expression of metallothioneins reported previously [30], linking this intriguing effect of cannabinoids with the known fact that increased intracellular zinc levels trigger MTF1-mediated expression of metallothioneins [31–33].

Importantly and highly relevant for oncology, our data suggest that simultaneous use of cannabis products, mainly those containing high amounts of CBD, has the potential to negatively affect the treatment of cancer patients with the widely used standard-of-care platinum-based drugs. This result is crucial because many cancer patients search for ways to support their treatment and/or relieve the adverse effects of standard chemotherapy, and cannabis products are often considered in such a context as an increasingly available option to provide both properties. Indeed, cannabis has been demonstrated to lessen several adverse conditions associated with cancer treatment, such as pain, nausea, vomiting, depression, and weight loss [16,34,35]. Moreover, direct anticancer effects of cannabis, through different proposed mechanisms, have also been suggested [7,9,15,16]. Two products, Nabilone (a synthetic cannabinoid) and Dronabinol (synthetic Δ^9 -THC), have been approved by the FDA for attenuation of chemotherapy-induced nausea and vomiting [14]. Additionally, Sativex (Δ^9 -THC:CBD) is a medicine under evaluation for relieving cancer-related pain [36–40]. In light of our data, cotreatment with these products under ongoing chemotherapy with platinum drugs should better be avoided, or at least Dronabinol should be the preferred choice in such clinical settings.

The potential interplay of platinum-based drugs with cannabis products has been studied to some extent at the preclinical level, including efficacy modulation. However, the results so far have been limited and inconsistent. For example, in line with our observation, CBD had been reported to attenuate CarboPt- and CisPt-mediated cytotoxic effects in canine urothelial carcinoma cells [41] and malignant melanoma cell lines [42], respectively. In contrast, some studies suggested that combined treatment might be more effective in regimens containing CisPt [43], while oxaliplatin combination with CBD was proposed to overcome OxPt resistance in colorectal cancer cell lines [44]. Furthermore, some relevant clinical studies that are presently at the early planning stage (NCT04585841 [45], NCT03607643 [46], NCT04582591 [47], NCT04398446 [48]) aim to evaluate CBD-mediated attenuation of OxPt-induced side effects. There is also a retrospective analysis suggesting the beneficial effects of cannabis on neuropathic pain in OxPt-treated patients [49]. However, our present results strongly suggest that this area of cancer research should first be very carefully evaluated before any widespread clinical applications should be recommended. Indeed, in the light of our present dataset, it is plausible that the attenuation of platinum-based drug-induced adverse effects in patients might reflect (at least partially) the overall decreased intracellular availability of the drugs, resulting in reduced treatment efficacy and, as a consequence, also reduced adverse effects.

Overall, we hope that our findings will motivate further research to identify the cellular transporter(s) affected by cannabinoids that are involved in platinum-based drug transport. Simultaneously, our results should serve as a warning for patients and physicians to carefully reconsider and better avoid combining platinum-based therapy and cannabis products containing high levels of CBD, at least until this drug interference phenomenon becomes better assessed in both preclinical and especially clinical settings.

5. Conclusion

In this study, we identified clinically relevant negative interactions between cannabis and the three most commonly used platinum-based anticancer chemotherapeutics. Additionally, we found that such cannabinoid-induced chemoresistance is translationally independent and reflects altered cellular drug transport. Our data should serve as a warning relevant for concurrent usage of some cannabis products by patients undergoing platinum-based treatment, to avoid (until more information on this issue becomes available) a potential negative impact of such combination on therapy outcome.

CRedit authorship contribution statement

Tereza Buchtova, Martin Mistrik, and Jiri Bartek designed the experiments, interpreted the data, and write the manuscript; Tereza Buchtova performed most of the cellular experiments; Lucie Beresova contributed to the cytotoxicity tests, microscopic experiments, and colony formation assays; Katarina Chroma, Martin Mistrik contributed to the microscopic experiments and cytotoxicity tests, Tomas Pluhacek performed measurements of platinum content, Tibor Beres, Dominika Kaczorova, and Petr Tarkowski prepared and analyzed cannabis extracts.

Conflicts of interest statement

The authors declare no conflict of interest.

Data availability

Data will be made available on request.

Acknowledgement

The work was supported by project ENOCH (No. CZ.02.1.01/0.0/0.0/16_019/0000868), an internal grant of the University of Palacký IGA_LF_2022_038, the National Institute for Cancer Research project (Programme EXCELES, ID Project No. LX22NPO5102) - Funded by the European Union - Next Generation EU, MEYS CR: (Large RI Project LM2018129 - Czech-BioImaging), the Novo Nordisk Foundation (grant # 0060590), the Swedish Research Council VR-MH 2014-46602-117891-30, the Danish National Research Foundation (project CARD, DNRF 125), and the Ministry of Agriculture of the Czech Republic (MZE-RO0423).

Ethics approval and consent to participate

Not applicable.

Appendix A. Supporting information

Supplementary data associated with this article can be found in the online version at doi:10.1016/j.biopha.2023.114801.

References

- [1] E. Wilshaw, Cisplatin in the treatment of cancer, *Platin. Met. Rev.* 23 (1979) 90–98.
- [2] D. Tsvetkova, S. Ivanova, Application of approved cisplatin derivatives in combination therapy against different cancer diseases, *Molecules* 27 (2022) 2466, <https://doi.org/10.3390/molecules27082466>.
- [3] S. Dassari, P.B. Tchounwou, Cisplatin in cancer therapy: molecular mechanisms of action, *Eur. J. Pharm.* 740 (2014) 364–378, <https://doi.org/10.1016/j.ejphar.2014.07.025>.
- [4] R. Oun, Y.E. Moussa, N.J. Wheate, The side effects of platinum-based chemotherapy drugs: a review for chemists, *Dalton Trans.* 47 (2018) 6645–6653, <https://doi.org/10.1039/c8dt00838b>.
- [5] S. Dibruba, G.V. Kalayda, Platinum-based drugs: past, present and future, *Cancer Chemother. Pharm.* 77 (2016) 1103–1124, <https://doi.org/10.1007/s00280-016-2976-z>.
- [6] J. Zhou, Y. Kang, L. Chen, H. Wang, J. Liu, S. Zeng, L. Yu, The drug-resistance mechanisms of five platinum-based antitumor agents, *Front Pharm.* 11 (2020) 343, <https://doi.org/10.3389/fphar.2020.00343>.
- [7] F. Pellati, V. Borgonetti, V. Brighenti, M. Biagi, S. Benvenuti, L. Corsi, Cannabis sativa L. and nonpsychoactive cannabinoids: their chemistry and role against oxidative stress, inflammation, and cancer, *Biomol. Res Int* 2018 (2018) 1691428, <https://doi.org/10.1155/2018/1691428>.
- [8] F.F. Peres, A.C. Lima, J.E.C. Hallak, J.A. Crippa, R.H. Silva, V.C. Abilio, Cannabidiol as a promising strategy to treat and prevent movement disorders? *Front Pharm.* 9 (2018) 482, <https://doi.org/10.3389/fphar.2018.00482>.
- [9] S. Pisanti, A.M. Malfitano, E. Giaglia, A. Lamberti, R. Ranieri, G. Cuomo, M. Abate, G. Faggiola, M.C. Proto, D. Fiore, C. Laezza, M. Bifulco, Cannabidiol: State of the art and new challenges for therapeutic applications, *Pharm. Ther.* 175 (2017) 135–150, <https://doi.org/10.1016/j.pharmthera.2017.02.001>.
- [10] M.C. Weiss, J.E. Hibbs, M.E. Buckley, S.R. Danese, A. Leitenberger, M. Bollmann-Jenkins, S.W. Meske, K.E. Aliano-Ruiz, T.W. McHugh, S.L. Larson, E.H. Le, N. L. Green, F.B. Gilman, V.G. Kulkarni, R.T. Chlebowski, D.M. Martinez, A. Coala T. Cannabis, Survey Study of breast, Cancer patients' Use Cannabis, *Treat. Cancer* 128 (2022) 160–168, <https://doi.org/10.1002/encr.38906>.
- [11] S.A. Pergam, M.C. Woodfield, C.M. Lee, G.-S. Cheng, K.K. Baker, S.R. Marquis, J. R. Fann, Cannabis use among patients at a comprehensive, Cancer Cent. a State Leg. Med. Recreat. Use, *Cancer* 123 (2017) 4488–4497, <https://doi.org/10.1002/cncr.30879>.
- [12] S. Pisanti, M. Bifulco, Medical Cannabis: A plurimillennial history of an evergreen, *J. Cell Physiol.* 234 (2019) 8342–8351, <https://doi.org/10.1002/jcp.27725>.
- [13] M.E. Badowski, P.K. Yanful, Dronabinol oral solution in the management of anorexia and weight loss in AIDS and cancer, *Ther. Clin. Risk Manag* 14 (2018) 643–651, <https://doi.org/10.2147/TCRM.S126849>.
- [14] B. Todaro, Cannabinoids in the treatment of chemotherapy-induced nausea and vomiting, *J. Natl. Compr. Canc Netw.* 10 (2012) 487–492, <https://doi.org/10.6004/jcncc.2012.0048>.
- [15] P. Müssi, M. Sollinas, V. Cincinno, D. Parolaro, Cannabidiol as potential anticancer drug, *Br. J. Clin. Pharm.* 75 (2013) 303–312, <https://doi.org/10.1111/j.1365-2125.2012.04299.x>.
- [16] T. Buchtova, D. Lukac, Z. Skrott, K. Chroma, J. Bartek, M. Mistrik, Drug-Drug Interactions of Cannabidiol with Standard-of-Care Chemotherapeutics, *Int. J. Mol. Sci.* 24 (2023) 2885, <https://doi.org/10.3390/ijms24032885>.
- [17] T. Buchtova, Z. Skrott, K. Chroma, J. Rehulka, P. Dzubak, M. Hajduch, D. Lukac, S. Arampatzis, J. Bartek, M. Mistrik, Cannabidiol-induced activation of the metallothionein pathway impedes anticancer effects of disulfiram and its metabolite CuET, *Mol. Oncol.* (2021), <https://doi.org/10.1002/1878-0261.13114>.
- [18] N.D. Sarma, A. Wayne, M.A. ElSohly, P.N. Brown, S. Elzinga, H.E. Johnson, R. J. Marles, J.E. Melanson, E. Russo, L. Deyton, C. Hudalla, G.A. Vrdoljak, J. H. Wurzer, L.A. Khan, N.-C. Kim, G.I. Giancaspro, Cannabis Inflorescence for Medical Purposes: USP Considerations for Quality Attributes, *J. Nat. Prod.* 83 (2020) 1334–1351, <https://doi.org/10.1021/acs.jnatprod.9b01200>.
- [19] P.L. Olive, J.P. Banáth, Kinetics of H2AX phosphorylation after exposure to cisplatin, *Cytom. B Clin. Cytom.* 76 (2009) 79–90, <https://doi.org/10.1002/cyto.b.20450>.
- [20] S. Siemer, D. Ornskov, B. Guerra, B. Boldyreff, O.G. Issinger, Determination of mRNA, and protein levels of p53, MDM2 and protein kinase CK2 subunits in P9 cells after treatment with the apoptosis-inducing drugs cisplatin and carboplatin, *Int. J. Biochem Cell Biol.* 31 (1999) 661–670, [https://doi.org/10.1016/s1357-2725\(99\)00020-5](https://doi.org/10.1016/s1357-2725(99)00020-5).
- [21] T. Ozdilli, D. Holub, Z. Maceckova, I. Varanasi, G. Rylkova, J. Rehulka, J. Vaclavkova, H. Slavik, P. Moudry, F. Znojek, J. Stankova, J.B. de Sanctis, M. Hajduch, P. Dzubak, Proteomic profiling reveals DNA damage, nuclear and ribosomal stress are the main responses to oxaliplatin treatment in cancer cells, *J. Proteom.* 162 (2017) 73–85, <https://doi.org/10.1016/j.jprot.2017.05.005>.
- [22] S. Schuch, S. Gajewski, J. Rothfuß, A. Hartwig, B. Köberle, Comparative study of the mode of action of clinically approved platinum-based chemotherapeutics, *Int. J. Mol. Sci.* 21 (2020) 6928, <https://doi.org/10.3390/ijms21186928>.
- [23] S. Harrach, G. Ciarraboli, Role of transporters in the distribution of platinum-based drugs, *Front Pharm.* 6 (2015) 85, <https://doi.org/10.3389/fphar.2015.00085>.
- [24] H. Burger, W.J. Loos, K. Eechoute, J. Verweij, R.H.J. Mathijssen, E.A.C. Wiemer, Drug transporters of platinum-based anticancer agents and their clinical significance, *Drug Resist Updat* 14 (2011) 22–34, <https://doi.org/10.1016/j.drup.2010.12.002>.
- [25] D. Wu, T. Liu, S. Deng, R. Han, Y. Xu, SLC39A4 expression is associated with enhanced cell migration, cisplatin resistance, and poor survival in non-small cell lung cancer, *Sci. Rep.* 7 (2017), <https://doi.org/10.1038/s41598-017-07830-4>.
- [26] M. Sobczak, M. Strachowska, K. Gronkowska, A. Robaszkiewicz, Activation of ABCG2 Genes by Cisplatin Depends on the CoREST Occurrence at Their Promoters in A549 and MDA-MB-231 Cell Lines, *Cancers (Basel)* 14 (2022) 894, <https://doi.org/10.3390/cancers14040894>.
- [27] L.L. Anderson, M.G. Etchart, D. Bahceci, T.A. Golembiewski, J.C. Arnold, Cannabis constituents interact at the drug efflux pump BCRP to markedly increase plasma cannabidiol concentrations, *Sci. Rep.* 11 (2021) 14948, <https://doi.org/10.1038/s41598-021-94212-6>.
- [28] Y.A. Seo, R. Kumara, H. Wetli, M. Wessling-Resnick, Regulation of divalent metal transporter-1 by serine phosphorylation, *Biochem J.* 473 (2016) 4243–4254, <https://doi.org/10.1042/BJC20160674>.
- [29] P. Bielawiec, S. Dziemiłko, K. Konstantynowicz-Nowicka, A. Chabowski, J. Dzięcioł, E. Harasim-Symbor, Cannabidiol improves muscular lipid profile by affecting the expression of fatty acid transporters and inhibiting de novo lipogenesis, *Sci. Rep.* 13 (2023) 3694, <https://doi.org/10.1038/s41598-023-30872-w>.
- [30] A. Jukna, N. Rimmnerman, R. Levy, Z. Vogel, E. Kozla, Cannabidiol affects the expression of genes involved in zinc homeostasis in BV 2 microglial cells, *Neurochem Int* 61 (2012) 923–930, <https://doi.org/10.1016/j.neuint.2011.12.002>.
- [31] B. Zhang, O. Georgiev, M. Hagmann, C. Günes, M. Cramer, P. Fallner, M. Vasić, W. Schaffner, Activity of Metal-Responsive Transcription Factor 1 by Toxic Heavy Metals and H2O2 In Vitro Is Modulated by Metallothionein, *Mol. Cell Biol.* 23 (2003) 8471–8485, <https://doi.org/10.1128/MCB.23.23.8471-8485.2003>.
- [32] F. Otsuka, Transcription Factor MTF-1 Involved in the Cellular Response to Zinc, *Yakugaku Zasshi* 141 (2021) 857–867, <https://doi.org/10.1248/yakushi.20.00247>.
- [33] V. Günther, U. Lindert, W. Schaffner, The taste of heavy metals: Gene regulation by MTF-1, *Biochim. Et. Biophys. Acta (BBA) - Mol. Cell Res.* 1823 (2012) 1416–1425, <https://doi.org/10.1016/j.bbancer.2012.01.005>.
- [34] T.L. Mortimer, T. Mabin, A.-M. Engelbrecht, Cannabinoids: the lows and the highs of chemotherapy-induced nausea and vomiting, *Future Oncol.* 15 (2019) 1035–1049, <https://doi.org/10.2217/fon.2018.0530>.
- [35] N. Montero-Oleas, I. Arevalo-Rodríguez, S. Nuñez-González, A. Viteri-García, D. Simancas-Racines, Therapeutic use of cannabis and cannabinoids: an evidence mapping and appraisal of systematic reviews, *BMC Complement Med Ther.* 20 (2020) 12, <https://doi.org/10.1186/s12906-019-2803-2>.
- [36] J.R. Johnson, M. Burnell-Nugent, D. Lossignol, E.D. Ganse Motan, R. Potts, M. T. Fallon, Multicenter, double-blind, randomized, placebo-controlled, parallel-group study of the efficacy, safety, and tolerability of THC/CBD extract and THC extract in patients with intractable cancer-related pain, *J. Pain. Symptom Manag.* 39 (2010) 167–179, <https://doi.org/10.1016/j.jpainsymman.2009.06.008>.
- [37] R.K. Portenoy, E.D. Ganse Motan, S. Allende, R. Yanagihara, L. Shioava, S. Weinstein, R. McQuade, S. Wright, M.T. Fallon, Nabiximols for opioid treated cancer patients with poorly controlled chronic pain: a randomized, placebo-controlled, graded-dose trial, *J. Pain.* 13 (2012) 438–449, <https://doi.org/10.1016/j.jpain.2012.01.003>.
- [38] J.R. Johnson, D. Lossignol, M. Burnell-Nugent, M.T. Fallon, An open-label extension study to investigate the long-term safety and tolerability of THC/CBD oromucosal spray and oromucosal THC spray in patients with terminal cancer-related pain refractory to strong opioid analgesics, *J. Pain. Symptom Manag.* 46 (2013) 207–218, <https://doi.org/10.1016/j.jpainsymman.2012.07.014>.
- [39] M.T. Fallon, E. Albert Lux, R. McQuade, S. Rossetti, R. Sanchez, W. Sun, S. Wright, A.H. Lichtman, E. Korniyeva, Sativex oromucosal spray as adjunctive therapy in advanced cancer patients with chronic pain unrelieved by optimized opioid therapy: two double-blind, randomized, placebo-controlled phase 3 studies, *Br. J. Pain.* 11 (2017) 119–133, <https://doi.org/10.1177/2049463717710042>.
- [40] A.H. Lichtman, E.A. Lux, R. McQuade, S. Rossetti, R. Sanchez, W. Sun, S. Wright, E. Korniyeva, M.T. Fallon, Results of a Double-Blind, Randomized, Placebo-Controlled Study of Nabiximols Oromucosal Spray as an Adjunctive Therapy in Advanced Cancer Patients with Chronic Uncontrolled Pain, *J. Pain. Symptom Manag.* 55 (2018) 179–188.e1, <https://doi.org/10.1016/j.jpainsymman.2017.09.001>.
- [41] J.M. Inkol, S.E. Hocker, A.J. Mutsaers, Combination therapy with cannabidiol and chemotherapeutics in canine urothelial carcinoma cells, *PLoS One* 16 (2021), e0255591, <https://doi.org/10.1371/journal.pone.0255591>.
- [42] P. Marzeda, P. Wróblewska-Luczka, M. Drozd, M. Florek-Luszczki, K. Zatuska-Ogryzek, J.J. Luszczki, Cannabidiol Interacts Antagonistically with Cisplatin and Additively with Mitoxantrone in Various Melanoma Cell Lines: An Isobolographic Analysis, *Int. J. Mol. Sci.* 23 (2022) 6752, <https://doi.org/10.3390/ijms23126752>.
- [43] O. Marinelli, M.B. Morelli, D. Annibali, C. Aguzzi, L. Zeppa, S. Tuyenerts, C. Amantini, F. Amant, B. Ferretti, F. Maggi, G. Santoni, M. Nabissi, The Effects of Cannabidiol and Prognostic Role of TRPV2 in Human Endometrial Cancer, *Int. J. Mol. Sci.* 21 (2020) 5409, <https://doi.org/10.3390/ijms21155409>.
- [44] S. Jeong, B.G. Kim, D.Y. Kim, B.R. Kim, J.L. Kim, S.H. Park, Y.J. Na, M.J. Jo, H. K. Yim, Y.A. Jeong, H.J. Kim, S.I. Lee, H.D. Kim, D.H. Kim, S.C. Oh, D. H. Lee, Cannabidiol Overcomes Oxaliplatin Resistance by Enhancing NO83- and SOD2-Induced Autophagy in Human Colorectal Cancer Cells, *Cancers (Basel)* 11 (2019), 1781, <https://doi.org/10.3390/cancers11060781>.
- [45] J.R. Andersen, The Effect of Medical Cannabidiol on Lean Body Mass in Patients Receiving Oxaliplatin or Paclitaxel Based Chemotherapy, *clinicaltrials.gov*, 2022, <https://clinicaltrials.gov/ct2/show/NCT04585841> (accessed January 16, 2023).

- [46] Leaf Vertical Inc, Randomized Double Blind, Placebo Controlled Parallel Multi Center Study to Assess the Efficacy of Cannabidiol (BRGX014) Combined With Standard Of Care Treatment in Subjects With Multiple Myeloma, Glioblastoma Multiforme, and GI Malignancies, clinicaltrials.gov, 2018. <https://clinicaltrials.gov/ct2/show/NCT03607643> (accessed April 18, 2022).
- [47] Zealand University Hospital, A Phase II Trial of Cannabidiol for Prevention of Chemotherapy induced Peripheral Neuropathy in Patients Receiving Oxaliplatin or Paclitaxel Based Chemotherapy, clinicaltrials.gov, 2022. <https://clinicaltrials.gov/ct2/show/study/NCT04582591> (accessed January 16, 2023).
- [48] Effect of Hemp CBD on Patients With CIPN - Tabular View - ClinicalTrials.gov, n.d. <https://clinicaltrials.gov/ct2/show/record/NCT04398446> (accessed January 18, 2023).
- [49] B. Weissengrin, D. Mirehman, S. Pelles, F. Bukstein, D.T. Blumenthal, I. Wolf, R. Geva, Effect of cannabis on oxaliplatin-induced peripheral neuropathy among oncology patients: a retrospective analysis, *Ther. Adv. Med Oncol.* 13 (2021), <https://doi.org/10.1177/1758835921990203>.

Review

Drug–Drug Interactions of Cannabidiol with Standard-of-Care Chemotherapeutics

Tereza Buchtova ¹, David Lukac ¹, Zdenek Skrott ¹ , Katarina Chroma ¹ , Jiri Bartek ^{2,3} and Martin Mistrik ^{1,*} ¹ Institute of Molecular and Translational Medicine, Faculty of Medicine and Dentistry, Palacký University, 77 147 Olomouc, Czech Republic² Danish Cancer Society Research Center, DK-2100 Copenhagen, Denmark³ Department of Medical Biochemistry and Biophysics, Science for Life Laboratory, Division of Genome Biology, Karolinska Institute, 171 77 Stockholm, Sweden

* Correspondence: martin.mistrik@upol.cz

Abstract: Cannabidiol (CBD) is an easily accessible and affordable Marijuana (*Cannabis sativa* L.) plant derivative with an extensive history of medical use spanning thousands of years. Interest in the therapeutic potential of CBD has increased in recent years, including its anti-tumour properties in various cancer models. In addition to the direct anticancer effects of CBD, preclinical research on numerous cannabinoids, including CBD, has highlighted their potential use in: (i) attenuating chemotherapy-induced adverse effects and (ii) enhancing the efficacy of some anticancer drugs. Therefore, CBD is gaining popularity as a supportive therapy during cancer treatment, often in combination with standard-of-care cancer chemotherapeutics. However, CBD is a biologically active substance that modulates various cellular targets, thereby possibly resulting in unpredictable outcomes, especially in combinations with other medications and therapeutic modalities. In this review, we summarize the current knowledge of CBD interactions with selected anticancer chemotherapeutics, discuss the emerging mechanistic basis for the observed biological effects, and highlight both the potential benefits and risks of such combined treatments. Apart from the experimental and preclinical results, we also indicate the planned or ongoing clinical trials aiming to evaluate the impact of CBD combinations in oncology. The results of these and future trials are essential to provide better guidance for oncologists to judge the benefit-versus-risk ratio of these exciting treatment strategies. We hope that our present overview of this rapidly advancing field of biomedicine will inspire more preclinical and clinical studies to further our understanding of the underlying biology and optimize the benefits for cancer patients.

Keywords: cannabidiol; drug–drug interaction; chemotherapy; cancer



Citation: Buchtova, T.; Lukac, D.; Skrott, Z.; Chroma, K.; Bartek, J.; Mistrik, M. Drug–Drug Interactions of Cannabidiol with Standard-of-Care Chemotherapeutics. *Int. J. Mol. Sci.* **2023**, *24*, 2885. <https://doi.org/10.3390/ijms24032885>

Academic Editor: Agata Kabala-Dzik

Received: 3 January 2023
Revised: 24 January 2023
Accepted: 30 January 2023
Published: 2 February 2023



Copyright: © 2023 by the authors. Licensee MDPI, Basel, Switzerland. This article is an open access article distributed under the terms and conditions of the Creative Commons Attribution (CC BY) license (<https://creativecommons.org/licenses/by/4.0/>).

1. Introduction

Understanding drug interactions is a fundamental yet challenging pharmacological issue that is especially problematic in oncology due to the usually narrow therapeutic window and potential serious toxicity profiles of drugs that are often applied to vulnerable patients and those with a long history of pre-treatment. Drug interactions may occur as a result of pharmacokinetic, pharmacodynamic, or biological factors, resulting in various outcomes, including decreased or increased therapeutic or adverse responses [1]. Despite extensive research and development work, most anticancer therapies have severe adverse effects. To mitigate such therapy-associated adverse effects, patients frequently use vitamins, dietary supplements, or herbal products, with *Cannabis* plant-based products occupying a prominent position. Indeed, a recent survey indicated that approximately two-thirds of patients with cancer had used *Cannabis* products during their ongoing therapy to alleviate adverse effects [2,3]. In these studies, cannabis products were mainly taken via inhalation, ingestion, or topically. These products were predominantly in the form of

edible, liquid, or smoked/vaporized cannabis. Additionally, a significant percentage of participants (22% and 21%) preferred CBD-only or -dominant products, respectively [3].

Cannabidiol (CBD), a product of *Cannabis sativa* L. (dominantly present in chemotypes II and III) [4], is particularly popular among patients with cancer because it is non-psychoactive, safe, and well-tolerated. CBD relieves therapy-induced issues, and some reports suggest it may even have direct anticancer properties. However, whether CBD improves or undermines, concomitant chemotherapy treatment has not yet been fully determined.

CBD belongs to the cannabinoid family and is a leading derivative of *Cannabis sativa* L.; CBD and tetrahydrocannabinol (THC) are the plant's main cannabinoid constituents [5] and have been extensively studied for years due to their therapeutic potential. Unlike THC, CBD is not psychoactive and is, therefore, a more suitable therapeutic candidate.

Based on the many studies showing the benefits of CBD, historical experience with cannabinoids, and current public interest, research into CBD for medical purposes has gained increasing attention. Currently, CBD is used as a medicine or complementary substance, and many CBD-based products are publicly available. However, it should be noted that most such products are off-label and often lack CBD-content verification. Currently, CBD is available in cosmetics, beverages, edibles, solutions, herbal extracts, and dried marijuana herbs and is easily accessible worldwide [6]. The anti-inflammatory, anti-oxidative, and other biological effects of CBD make it a promising therapeutic candidate for many diseases, including epilepsy, Alzheimer's disease, Parkinson's disease, and multiple sclerosis. Pure CBD solutions (under the commercial name Epidiolex/Epidyolex) for oral application are currently approved by the US Food and Drug Administration (FDA) to treat severe, orphan, early-onset, and treatment-resistant epilepsy syndromes [7–11]. Moreover, clinical trials examining the potential benefits of CBD in the context of Parkinson's disease, Crohn's disease, social anxiety disorder, and schizophrenia [12–16] have shown promising results.

CBD-related interactions with anticancer drugs are frequently linked to the transport of chemotherapeutics due to CBD's ability to modulate various receptors and transmembrane channels, including cannabinoid receptors 1 and 2 (CB1 and 2) [17], transient receptor potential vanilloid 1 and 2 (TRPV1 and 2) [18,19], peroxisome proliferator-activated receptor γ (PPAR γ) [20], 5-hydroxytryptamine receptor subtype 1A (5-HT1A) [21], G protein-coupled receptor 55 (GPR55) [22], and adenosine A2A receptor (A2A, agonist) [23]. CBD targets have been suggested to play a role in cancer therapy resistance, including breast cancer resistance protein (ABCG2/BRCP) [24], bile salt export pump (ABCB11/BSEP) [11], and p-glycoprotein (p-gp) [25,26]. Very relevant for drug–drug interactions, CBD also affects several biotransformation enzymes such as CYP3A4, UGT1A9, UGT2B7, CYP1A2, CYP2B6, CYP2C8, CYP2C9, and CYP2C19 [11]. Several studies have furthermore examined the ability of CBD to modulate the activity of other CYPs in vitro, including 3A5/7, 2D6, 2A6, 1A1, 1B1, and 2J2 [6]. Additionally, CBD appears to have bidirectional anti-oxidative [27] and pro-oxidative properties [28], potentially modulating drug efficacy. Moreover, CBD is metabolized by CYP3A4 and CYP2C19, making it a substrate shared by multiple oncology drugs. This circumstance may slow their respective metabolic processing in the organism, thereby potentially leading to dangerous outcomes [6].

CBD is generally perceived as a well-tolerated drug, beneficial for oncology patients due to its ability to attenuate some chemotherapy-induced side effects such as nausea, pain, and appetite loss [29]. Moreover, there is evidence to suggest that CBD has direct anti-proliferative and pro-apoptotic effects while also interfering with cancer-related processes, including angiogenesis, cell migration, adhesion, and invasion [30].

In this review, we summarize the current knowledge of CBD interactions with selected anticancer chemotherapeutics and discuss emerging mechanistic explanations of their biological effects.

2. CBD Interactions with Antimetabolites

Antimetabolites (Table 1) are small molecules resembling standard nucleotides—the building blocks of DNA. Because of this resemblance, they can be incorrectly incorporated into DNA or may inhibit DNA synthesis. Antimetabolites were among the first anticancer chemotherapeutics introduced in the late 1940s; a notable example is aminopterin, which was used to treat paediatric acute lymphoblastic leukaemia. Currently, antimetabolites represent a cornerstone of treatment for various cancer types [31,32].

2.1. 5-Fluorouracil

5-fluorouracil is a uracil analogue that inhibits thymidylate synthetase. The inhibited enzyme is incapable of deoxythymidine monophosphate conversion, which results in the depletion of deoxythymidine triphosphate used for DNA synthesis [32,33]. 5-fluorouracil is commonly used to treat a range of diverse solid tumours, including those of the gastrointestinal tract and head-and-neck, with common adverse effects such as gastrointestinal and oral mucositis [32,33]. Cuba et al. (2020) [33] evaluated the effect of CBD on oral mucositis inflicted by 5-fluorouracil in mice. Interestingly, CBD treatment reduced oral mucositis, probably as a consequence of its antioxidant properties, which were documented by the increased catalase and glutathione levels in CBD-cotreated mice. CBD with 5-fluorouracil and some other chemotherapeutics is planned to be tested for efficacy and safety in a randomized clinical trial on colon and rectal cancers (NCT03607643) [34].

2.2. Gemcitabine

Gemcitabine is a nucleoside analogue—specifically, a deoxycytidine. After intake, the drug is metabolized and incorporated into the DNA strand instead of the original nucleoside, which leads to inhibition of DNA polymerase and ribonucleotide reductase [32,35]. Gemcitabine is commonly used in patients with non-small cell lung, pancreatic, urinary bladder, and breast cancer, with haematological toxicity, oedema, and pulmonary, cutaneous, and gastrointestinal toxicity as common adverse effects [35]. Although the impact of CBD on gemcitabine-induced adverse effects is unknown, preclinical studies suggest an interesting potentiation of its anticancer toxicity. For example, combined treatment with CBD and gemcitabine significantly extended animal survival in the pancreatic ductal adenocarcinoma (PDAC) mouse model and also enhanced the inhibition of the proliferation of PDAC cell lines. This effect can be explained by CBD's antagonism of the GRP55 protein, a receptor of lysophosphatidylinositol, which is known to have a role in tumour progression [36–38]. GRP55 inhibition suppresses cell cycle progression and hence cell proliferation, reduces MAPK kinase activation, and lowers the overall abundance of ribonucleotide reductases in PDAC cells, all of which are associated with gemcitabine resistance [36,38]. The potentiation of gemcitabine toxicity by CBD was also confirmed in another PDAC cell line (MiaPaCa-2) [39]. Combined treatment with CBD and gemcitabine will be assessed for pancreatic cancer in a randomized clinical trial (NCT03607643) [34].

2.3. Methotrexate

Folates, compounds related to the vitamin D family, function via one-carbon metabolism, which is essential for purine, thymidylate, and polyamine synthesis. Folates are involved in the synthesis of S-adenosyl methionine, which is critical for the methylation of DNA, histones, lipids, and neurotransmitters [40]. Methotrexate is an antifolate antagonist targeting dihydrofolate reductase (DHFR), a key component of the folate pathway. Due to its structural similarity to folic acid, methotrexate can block the binding pocket of DHFR, leading to secondary inhibition of downstream enzymes in the folate pathway [32,40–42]. Methotrexate is used in combination with other chemotherapeutics to treat several types of cancer, including acute lymphocytic leukaemia, lymphoma, carcinomas of the breast and urinary bladder, and osteosarcoma [40,41]. Brown and Winterstein (2019) [6] suggested that CBD may interact with methotrexate treatment because it inhibits the ABCG2/BCRP transporter [24], which contributes to cellular efflux of methotrexate [43].

CBD cotreatment could thus lead to methotrexate accumulation, increasing the drug's efficacy but also potentially strengthening its adverse effects. However, this hypothesis awaits experimental confirmation.

Table 1. Summary of the drug–drug interactions of CBD with antimetabolites.

Antimetabolites									
CT	Aim	Model	Administration	CBD c	CT c	Evaluation Time	Special Condition	Results of Combined Treatment	References
5-FU	Attenuation of oral mucositis	CF-1 mouse strain	IP	3, 10, 30 mg/mL daily between days 4 and 7	60 mg/kg/day on days 0 and 2	Days 8 and 11	Mechanical trauma	Reduced oral mucositis	Cuba et al. (2020) [33]
	Chemotherapy efficiency	KPC mice with PDAC	IP	100 mg/kg daily	100 mg/kg every 3 days	Until death or pre-assigned endpoints are reached		Extended animal survival	Ferro et al. (2018) [36]
GEM	Signalling pathway acquiring resistance to GEM	PDAC cell line—HPAFII and PANC1		5, 10 μ M	20, 250, 500 nM	48–72 h		Decreased markers of resistance	
	Viability	PANC-1 and MiaPaCa-2		(6.25), 12.5, 25 μ M daily	(25), 50, 100 μ M single administration	72 h		Potentiated GEM toxicity	Luongo et al. (2020) [39]

5-FU: 5-fluorouracil; c: concentration; CBD: cannabidiol; CT: chemotherapeutics; GEM: Gemcitabine; IP: intraperitoneal; PDAC: pancreatic ductal adenocarcinoma.

3. Interactions of CBD with Alkylating Agents and Platinum-Based Drugs

Alkylating agents (Table 2) are reactive chemical substances that target DNA and proteins and belong to the oldest chemotherapeutics. Their ability to alter biological molecules is based on the transfer of alkyl groups to target molecules such as DNA, which often alters their structure or disrupts their function [44,45]. The alkylating agent mustard gas was first used as a chemotherapeutic in the early 1930s to treat skin cancer [45,46]. Mechlorethamine, an analogue of mustard gas, was approved as a chemotherapeutic in the late 1940s, followed by a number of related drugs [45].

Platinum-based drugs are commonly classified as alkylating agents even though they do not directly alkylate DNA; instead, they form covalent crosslinks between DNA strands and covalent DNA-protein adducts [45].

3.1. Carmustine

Carmustine (1,3-bis(2-chloroethyl)urea) belongs to the nitrosourea family. As a lipid-soluble, low molecular weight drug, it readily penetrates the blood–brain barrier and is therefore used to treat brain tumours, mainly glioblastoma multiforme as well as lymphomas and melanoma [45,47,48]. Reported adverse effects associated with carmustine include pulmonary, gastrointestinal, hepatic, renal, cardiovascular, haematological, and neurological toxicities, among others [48].

It has been hypothesized that CBD interferes with carmustine via the transient potential vanilloid 2 receptor (TRPV2), a nonselective cation channel that is usually activated by heat, altered osmolarity, or membrane stretching. As a TRPV2 agonist, CBD increases Ca^{2+} influx [19], possibly affecting the uptake and retention of some anticancer drugs. This theory was experimentally confirmed in glioblastoma cells, where CBD coadministration caused sensitization against carmustine. Interestingly, this effect was not observed in normal human astrocytes [49,50]. TRPV2 expression is also upregulated by a spliced variant of the AML1a (acute myeloid leukaemia) protein, induced by CBD treatment. As a transcription factor, AML1a impacts the expression of genes whose products are implicated in various biological processes, including hematopoietic self-renewal, cell proliferation,

and differentiation [51,52]. Although the function of AML1a in GBM (glioblastoma multiforme) remains poorly understood, AML1a is upregulated during GBM stem-like cell (GSC) differentiation, and downregulation of AML1a is associated with GBM chemoresistance. Thus, upregulation of AML1a by CBD may lead to GSC differentiation, resulting in restoration of carmustine sensitivity. This concept was experimentally validated at the level of GSC cell lines [52]. The potentiating effect of CBD on carmustine cytotoxicity was further examined by Deng et al. (2017) [53] in human GBMs, mouse primary GBMs, and mouse neural progenitor cells. Although CBD sensitized to carmustine both the murine and human GBM cells, a subsequent analysis of drug interactions between carmustine and CBD, their concentration dependence, and their effects on efficacy revealed a range of concentration-dependent synergistic, additive, or antagonistic effects on cell viability and proliferation among the three analysed model systems, overall indicating the complexity of such drug interactions [53].

3.2. Temozolomide

Temozolomide is an imidazotetrazine lipophilic prodrug that is activated and metabolized under physiological pH conditions. The resulting methyl diazonium salt is a lipophilic alkylating agent that passes through the blood–brain barrier. Consequently, temozolomide is particularly suitable for treating brain tumours [54,55]. Reported adverse effects of this drug include haematological, gastrointestinal, and neurological toxicities [56]. Experiments using the human U87MG glioma cell line, primary glioblastoma cells, and normal human astrocytes (NHAs) conducted by Nabissi et al. (2013) [49] suggested that temozolomide's efficacy is potentiated by CBD, again via TRPV2 activation. As in the case of carmustine, temozolomide cytotoxicity was potentiated in glioblastoma cells but not in NHAs.

The CBD-promoted potentiation of temozolomide's effects against GBM may also partly reflect effects on extracellular vesicles (EVs). Cells use EVs for drug efflux, pro-oncogenic signalling, invasion, and immunosuppression [57], and there is clear evidence that CBD is an effective modulator of EV properties. For example, CBD treatment of chemoresistant and chemosensitive patient-derived GBM cells led to the formation of EVs with reduced levels of pro-oncogenic miR21 and an elevated anti-oncogenic miR126 [58]. The same study suggested that, apart from its effects on EV properties, CBD treatment may reduce levels of prohibitin, a protein that protects mitochondrial function and may contribute to temozolomide chemoresistance.

In addition to the additive/synergistic effects observed between CBD and temozolomide toxicity, concentration-dependent antagonistic effects have been reported in human GBMs, mouse primary GBM cells, and mouse neural progenitor cells, suggesting a rather complex relationship [53]. In one study, the combination of CBD with temozolomide increased tumour growth in a mouse GBM model compared to temozolomide treatment alone [59]. However, the opposite effect was observed in another study using the same mouse model [60]. It is unclear why these two studies reached such highly discrepant results.

Notably, there are also limited clinical data. Likar et al. (2019) [61] evaluated brain tumours in patients who took CBD concomitantly with radiochemotherapy, including temozolomide. At the time of publication, patients taking CBD survived longer than expected. Currently, two clinical trials evaluate the effects of CBD and temozolomide combinations in patients with GBM (NCT03607643 and NCT03687034) [34,62].

3.3. Cisplatin

Cisplatin ((SP-4-2)-diamminedichloridoplatinum (II)) interacts with purines incorporated into DNA and causes DNA lesions. It is widely used as a chemotherapeutic agent for treating solid tumours despite having severe side effects, including renal toxicity, ototoxicity, hepatotoxicity, and gastrointestinal toxicity [45,63]. Several lines of evidence indicate that CBD is an effective attenuator of these cisplatin-induced adverse effects. For example, renal toxicity, a frequent limiting factor for cisplatin treatment, was effectively suppressed

by CBD in mice [64]. Indeed, CBD was shown to protect kidneys from cisplatin-induced effects by reducing oxidative and nitrosative stress, inflammation, and cell death, while improving renal function. Moreover, studies on cisplatin-induced emesis in shrews reported by Kwiatkowska et al. (2004) [65] showed that treatment with low doses of CBD attenuated cisplatin-induced vomiting, whereas high doses potentiated this adverse effect. Similar findings were obtained in another study on shrews by Rock et al. (2012) [66], which in a mouse model showed that the anti-emetic and anti-nausea effect of CBD was mediated by indirect activation of the somatodendritic serotonin autoreceptor 5-HT1A in the dorsal raphe nucleus. Activation of 5-HT1A reduces the excitability of serotonergic neurons and thus reduces serotonin release in terminal forebrain regions [66,67]. The same mechanism was confirmed in shrews and rats after treatment with cannabidiolic acid (CBDA), a compound similar to CBD that is effective at substantially lower concentrations [68].

Besides the ability to reduce adverse effects, CBD also seems to potentiate cisplatin toxicity in endometrial cancer cell lines. The enhanced response to cisplatin appeared to result from TRPV2 receptor activation and was strengthened in TRPV2 overexpression models [69]. Conversely, in the ovarian cancer cell line SKOV-3, CBD did not affect cisplatin-induced cytotoxicity, and a cell protective effect was observed at higher CBD concentrations [70]. Similarly, in GBM cell lines, combined treatment with CBD and cisplatin had mixed results; additive, synergistic, and antagonistic effects were all observed, depending on the drug concentrations used [53].

3.4. Oxaliplatin

Oxaliplatin is a third-generation platinum drug based on diaminocyclohexane (DACH) that can overcome cisplatin-induced resistance. Oxaliplatin is less reactive toward DNA than cisplatin, forming fewer protein-DNA adducts and DNA-DNA crosslinks. Despite its lower reactivity, oxaliplatin displays a similar cytotoxicity profile to cisplatin. It is believed that the DACH molecule causes specific DNA lesions that are difficult to detect and/or repair. Moreover, oxaliplatin interacts more strongly with proteins than cisplatin [71,72]. In addition to generating DNA lesions, oxaliplatin induces nucleolar and ribosomal stress, which may contribute significantly to its overall toxic effects [73]. Oxaliplatin is primarily used to treat colon cancer [63,72] and has less severe side effects than cisplatin; nephrotoxicity and ototoxicity are relatively rare. Moreover, while oxaliplatin treatment can cause gastrointestinal toxicity and hepatotoxicity, the main dose-limiting adverse effect is neurotoxicity [72] accompanied by mechanical allodynia. Importantly, CBD is a potent attenuator of oxaliplatin-induced neuropathy-associated pain in mice [74]. Pereira et al. (2021) [75] recently investigated the role of the endocannabinoid system in oxaliplatin-induced peripheral sensory neuropathy and showed that CBD has an analgesic effect that was partly attributed to interactions with the CB1 receptor. CBD treatment also attenuated mechanical hyperalgesia and c-Fos expression in the spinal cord's dorsal root ganglion and dorsal horn without cannabimimetic effects.

In another study on the potentiation of oxaliplatin by CBD, experiments using parental and oxaliplatin-resistant human colorectal cancer cell lines and their mouse xenografts conducted by Jeong et al. (2019) [76] showed that CBD restored oxaliplatin sensitivity tested in the resistant cancer cells. Mechanistically, this was attributed to a CBD-promoted decrease in NOS3 phosphorylation, which is otherwise elevated in oxaliplatin-resistant tumour cell lines. Reducing NOS3 phosphorylation lowered the level of NO and superoxide dismutase 2, resulting in ROS induction and mitochondrial dysfunction. Oxaliplatin combined with CBD is under evaluation in a randomized clinical trial of colorectal cancer (NCT03607643) [34].

3.5. Carboplatin

Carboplatin, or cis-diamine-1,1'-cyclobutane dicarboxylate platinum (II), is a second-generation platinum-based drug. Its mechanism of action resembles that of cisplatin, and its therapeutic effect is weaker than or equal to that of cisplatin itself [77,78]. Carboplatin is

used to treat testicular germ cell tumours as well as gynaecological, head-and-neck, thoracic, and urinary bladder cancers [79]. It has fewer adverse effects than cisplatin because of its different pharmacodynamics; its main adverse effects are myelosuppression, nausea, and vomiting [80]. Current knowledge of the interaction between CBD and carboplatin is limited because the combination of both drugs has only been tested in cellular models of canine urothelial carcinoma, in which the effect was antagonistic [81].

Table 2. Summary of the drug–drug interactions of CBD with alkylating agents and platinum-based drugs.

Alkylating Agents and Platinum-Based Drugs									
CT	Aim	Model	Administration	CBD c	CT c	Evaluation Time	Special Condition	Results of Combined Treatment	References
BCNU	Viability	U87MG, MZC, NHA		10 μ M	10^{-3} – 10^{-5} M/200 μ M	24, 72 h		Increased toxicity, except for NHA	Nabissi et al. (2013) [49]
	Colony formation	U87MG, MZC		10 μ M	200 μ M	Day 14		Decreased colony formation	
	Apoptosis	U87MG, MZC		10 μ M	200 μ M	6 h		Increased annexin	
	TRPV2 function	U87MG, MZC		10 μ M	200 μ M	Day 1		TRPV2 dependent	
	Cell viability, differentiation, apoptosis, mitochondrial activity	GCS lines of patients with cancer		10 μ M	200 μ M	24 h	Medium + EGF and bFGF	Restoration of BCNU sensitivity	Nabissi et al. (2015) [52]
Proliferation, viability	GBM (Hu, Ms), Ms NPCL		0.3–100 μ M	3 μ M to 1 mM	72 h		Concentration-dependent effect	Deng et al. (2017) [53]	
TMZ	Viability	U87MG, MZC, NHA		10 μ M	10^{-5} – 10^{-2} M/400 μ M	24, 72 h		Increased toxicity except for NHA	Nabissi et al. (2013) [49]
	Colony formation	U87MG, MZC		10 μ M	400 μ M	Day 14		Decreased colony formation	
	Apoptosis	U87MG, MZC		10 μ M	400 μ M	6 h		Increased annexin	
	TRPV2 function	U87MG, MZC		10 μ M	400 μ M	Day 1		TRPV2 dependent	
	EV release, miRs, prohibitin	LN18, LN229		5 μ M	800 μ M	1 h		Anti-oncogenic effect	Kosgodage et al. (2019) [58]
	Proliferation and viability (effect of CBD up to BCNU toxicity)	GBM (Hu, Ms) + Ms NPCL		0.3–100 μ M	1 μ M to 1 mM	72 h		Concentration-dependent effect	Deng et al. (2017) [53]
Survival	Patients with brain cancer	Capsule (CBD)		100 mg twice daily, increased up to 200 mg twice daily	Standard therapy		Surgical resection + radiotherapy	Prolonged life	Likar et al. (2019) [61]

Table 2. Cont.

Alkylating Agents and Platinum-Based Drugs									
CT	Aim	Model	Administration	CBD c	CT c	Evaluation Time	Special Condition	Results of Combined Treatment	References
	Tumour volume	Nude mice with U87 MG	Oral (CBD), IP (TMZ)	15 mg/kg/day	5 mg/kg/day	Day 15		Increased tumour growth	López-Valero et al. (2018) [59]
	Viability	Patient-derived GBM cells and four Glioma cell lines (U251, U87 MG, LN18)		10, 20, 30 µM	200, 500 µM	48 h		Synergic effect	
	Growth inhibition	U251, LN18, and GL261 sphere culture		30 µM	200 µM	24, 48 h		Synergic effect	
	Colony formation assay	U251, U87 MG		20 µM	500 µM	Day 7		Synergic effect	Huang et al. (2021) [60]
	Autophagy markers, mitophagy induction (U251)	U251, U87 MG		30 µM	500 µM	24, 48 h		Increased autophagy and mitophagy	
	Tumour growth, survival, markers of autophagy, mitophagy, and proliferation	Nude mice with U87 MG-GFP-luc	IP	15 mg/kg/once daily	25 mg/kg/once daily	Days 7, 14, 21, and 28		Decreased tumour growth	
CDDP	Renal function	Male C57BL/6j mice	IP	(2.5, 5), 10 mg/kg 1.5 h before (or 12 h after) CDDP, daily	20 mg/kg single administration	72 (+ 1.5) h		Decreased renal toxicity	
	Histopathological damage, ROS production, apoptosis, inflammation response, nitrosative stress	Male C57BL/6j mice	IP	10 mg/kg/day 1.5 h before CDDP	20 mg/kg single administration	72 (+ 1.5) h		Decreased renal toxicity	Pan et al. (2009) [64]
	CDDP-induced vomiting	Shrews	IP	5 (attenuation), 40 (potentiation) mg/kg 0.5 h before CDDP treatment	20 mg/kg	1 h observation	Mealworms 15 min before pre-treatment	Modulation according to the concentration of CBD	Kwiatkowska et al. (2004) [65]
	CDDP-induced vomiting	Shrews	SC (CBD), IP (CDDP)	5, 10 mg/kg 30 min before CDDP	20, (40) mg/kg	1 h observation	Mealworms 15 min before pre-treatment	Anti-emetic and anti-nausea effect	Rock et al. (2012) [66]
	CDDP-induced vomiting	Shrews	IP	CBCA: 0.5 mg/kg 45 min before CDDP	20 mg/kg	70 min observation	mealworms 15 min before pre-treatment	Attenuation of vomiting	Bolognini et al. (2013) [68]
	Viability	Ishikawa		3.92 µg/ml	0.25, 0.5 µg/ml	72 h		Increased CDDP toxicity	Marinelli et al. (2020) [69]

Table 2. Cont.

Alkylating Agents and Platinum-Based Drugs									
CT	Aim	Model	Administration	CBD c	CT c	Evaluation Time	Special Condition	Results of Combined Treatment	References
	Viability	SKOV-3		1, 10 μ M pre-treatment for 24 h; 10, 15, 20 μ M co-treatment	5–100 μ M	(24 +) 48 h		No effect (or antagonistic effect)	Fraguas-Sánchez et al. (2020) [70]
	Proliferation, viability	GBM (Hu, Ms) + Ms NPCL		0.3–100 μ M	0.1–100 μ M	72 h		Concentration-dependent effect	Deng et al. (2017) [53]
L-OHP	Mechanical allodynia	Male C57Bl6 mice	IP	1.25–10 mg/kg, 15 min before L-OHP	6 mg/kg single administration	Days 2, 4, 7, and 10		Attenuation of mechanical allodynia	King et al. (2017) [74]
	Chemotherapy efficiency—viability, cell death, autophagy, ROS, oxygen concentration, mitochondrial function	colo205 R, DLD-1 R		4 μ M	10 μ M	6, 12, 24 h		Sensitization of resistant cells	Jeong et al. (2019) [76]
	Tumour growth, autophagy	Female BALB/c nude mice with colo205 R	IP	10 mg/kg every 2 days	5 mg/kg every 2 days	Day 18		Lower tumour weight	
	Peripheral sensory neuropathy	Swiss male mice	PO (CBD), IV (L-OHP)	10 mg/kg, 3 times/week, 1 h before L-OHP or in mid-term between L-OHP injections	2 mg/kg twice a week	Days 28 and 56	Mechanical hyperalgesia—the tip of a rigid filament 1 week before drug injection, repeated once a week. Cold allodynia—tail immersed in cold water, once a week, 120 s cut-off time	Attenuation of peripheral sensory neuropathy	Pereira et al. (2021) [75]
CBDCA	Viability, combination index, apoptosis	AXA, Orig, and SH cell lines		0.03–300 μ M; IC50: 5.77, 5.30, and 5.48 μ M (and derived concentration series)	0.01–1 mM; IC50: 384, 529, and 398 μ M (and derived concentration series)	24 h	0.1% FBS	Antagonistic effect	Inkol et al. (2021) [81]

BCNU: carmustine; bFGF: basic fibroblast growth factor; CBD: cannabidiol; CBDCA: carboplatin; CBDA: cannabidiolic acid; CDDP: cisplatin; c: concentration; CT: chemotherapeutics; EGF: epithelial growth factor; EV: extracellular vesicles; GBM: glioblastoma; GSC: glioblastoma stem-like cells; Hu: human; IP: intraperitoneal; IV: intravenous; L-OHP: oxaliplatin; Ms: mouse; NHA: normal human astrocytes; NPCL: neural progenitor cell line; PO: per os; ROS: reactive oxygen species; SC: subcutaneous; TRPV2: transient receptor potential vanilloid 2; TMZ: temozolomide.

4. Interactions of CBD with Microtubule-Targeting Agents

Microtubules (Table 3) are components of the cytoskeleton that are dynamically polymerized and depolymerized. Microtubule-targeting agents inhibit one of these two processes, which has a profound impact on cytoskeleton morphology, cellular transport, motility, and mitosis, and thereby exert anticancer and anti-angiogenic effects [82,83]. The first microtubule-targeting agent used in the clinic was vinblastine, which was approved

for the treatment of lymphomas and various solid tumours in the early 1960s. Its success led to the discovery and development of a wider spectrum of agents with similar activity, with several of these drugs currently used to treat various types of malignancies [83].

4.1. Vinblastine

Vinblastine is an indole-containing alkaloid isolated from *Catharanthus roseus* and its endophytes [84] that shows microtubule-destabilizing properties. As an inhibitor of microtubule polymerization [82], it is widely used to treat Hodgkin's lymphoma, lymphosarcoma, choriocarcinoma, neuroblastoma, various carcinomas, leukaemia, Wilkins's tumour, and reticulum cell sarcoma [85]. Its known adverse effects include gastrointestinal, genitourinary, neurologic, haematological, and hepatic toxicities and patients treated with vinblastine are also prone to infections [86].

The effect of CBD on vinblastine-induced adverse effects is not yet known, but some studies suggest potentiation of the curative effect. For example, in leukaemia cells, CBD can help overcome vinblastine resistance that is caused by p-glycoprotein (p-gp) transporter overexpression. P-gp overexpression is responsible for multidrug resistance, and vinblastine is among its known substrates. CBD was shown to reduce the transporter's expression, reducing the efflux of vinblastine from cells. CBD cotreatment also increased vinblastine toxicity, but only in cells overexpressing the transporter. Notably, the effect was relatively mild, and verapamil, an established inhibitor of the p-gp transporter, was considerably more effective [25]. The synergistic effect of CBD and vinblastine manifested by reduced viability and increased apoptosis was further confirmed in canine urothelial carcinoma cells [81].

4.2. Paclitaxel

Paclitaxel, a member of the taxane family isolated from *Taxus brevifolia* [87], is a microtubule-stabilizing agent used to treat various solid tumours. Its common adverse effects include myelosuppression and peripheral neuropathy [88]. Ward et al. (2011; 2014) [89,90] used CBD to attenuate paclitaxel-induced peripheral neuropathy and showed that CBD cotreatment prevented this side effect in mice [89,90]. The neuroprotective activity of CBD was partially explained by its agonistic effect on the 5-HT_{1A} receptor, which is involved in central nervous system sensitization [89–91]. The same study also reported additive and synergistic effects in murine and human breast cancer cell lines [90]. The attenuating effect on paclitaxel-induced mechanical allodynia was also confirmed by King et al. (2017) [74] in mice. Apart from 5-HT_{1A}, the protective effect of CBD on paclitaxel-induced peripheral neuropathy might reflect the impact on mitochondrial Na⁺ Ca²⁺ exchanger-1 (mNCCX-1), which is primarily responsible for calcium homeostasis. Indeed, the knockdown of mNCCX-1 attenuated the protection conferred by CBD in dissociated dorsal root ganglia [92]. Another study confirmed CBD as an attenuator of paclitaxel-induced mechanical sensitivity and showed that CBD could not reverse previously established mechanical sensitivity in mice [93].

Other studies have examined the capacity of CBD to modulate the efficacy of paclitaxel. Synergistic or additive effects with CBD pre-/co-treatment on cytotoxicity were observed in breast cancer and ovarian cancer cell lines. These studies tested two CBD preparations—CBD in solution and CBD in polymeric microparticles—both of which were effective in the human MCF7, MDA-MB-231, and SKOV-3 cell lines and reduced tumour growth during in ovo studies on the chorioallantoic membrane of chicken embryos [70,94].

According to Luongo et al. (2020) [39], CBD and paclitaxel cotreatment had synergistic and additive effects in pancreatic cancer cell lines but only at relatively high CBD concentrations. Synergy was also observed in the MCF7 breast cancer cell line model [95]. CBD and paclitaxel cotreatment has also been investigated in human colorectal and gastric adenocarcinoma cell lines [96]. While CBD did not reduce viability after paclitaxel treatment in some cell lines, an additive effect on the inhibition of DNA replication was observed. Interestingly, the authors highlighted the importance of the foetal calf serum

content in cell culture media, leading to different results after CBD application, suggesting the potential influence of growth factors on the observed effects of CBD. In addition, CBD enhanced the cytotoxic effect of paclitaxel in endometrial cancer cell lines regardless of TRPV2 overexpression [69].

Finally, Brown and Winterstein (2019) [6] demonstrated that paclitaxel is a substrate of the ABCB1/BSEP transporter, which is another CBD target. Combined treatment with CBD may thus increase the efficacy of paclitaxel, albeit at the cost of a simultaneous increase in adverse effects.

4.3. Docetaxel

Docetaxel is a semisynthetic agent consisting of 10-diacetyl baccatin III derived from *Taxus baccata* that has been esterified with a synthetic side chain. Docetaxel is a microtubule stabilizer [97] that is used to treat metastatic breast, lung, prostate, gastric, and head-and-neck cancers; it seems to be more potent than paclitaxel. However, its poor solubility in water necessitates administration as a solution in ethanol and polysorbate 80, which introduces additional solvent-induced side effects. Docetaxel also has more severe adverse effects than paclitaxel, including neutropenia, musculoskeletal toxicity, and neurotoxicity [98].

De Petrocellis et al. (2013) [99] studied the pro-apoptotic effects of cannabinoids when combined with docetaxel in prostate carcinoma. Both CBD and CBD-DBS (extracts from *Cannabis sativa* L. strains enriched in particular cannabinoids) were examined. Interestingly, these researchers highlighted the importance of media composition (with/without sera) in experiments using CBD by showing that certain media can potentiate docetaxel toxicity in human LNCaP (androgen receptor AR-positive) cells. In the same study, CBD also potentiated the effect of docetaxel in AR-negative human DU-145 cells at lower concentrations but showed a tendency towards a protective effect at higher concentrations. In experiments using the DU-145 mouse xenograft model, CBD-DBS potentiated the effects of docetaxel, but a mild protective effect was observed following cotreatment with CBD and docetaxel in an LNCaP xenograft model. Combined treatment with docetaxel and CBD has also been examined in the MCF7 breast adenocarcinoma cell line, revealing that synergistic effects can be obtained at specific molar ratios [95].

4.4. Vincristine

Vincristine is a vinca alkaloid isolated from *Catharanthus roseus* that interferes with microtubule polymerization [100] and is used to treat cancers including leukaemia, lymphoma, central nervous system cancers, and sarcomas. Its common adverse effects include neuropathy and constipation [101].

While mechanical allodynia, a neurological condition induced by vincristine, was not attenuated by CBD pre-treatment [74], multiple lines of evidence suggest that CBD potentiates the anticancer effect of vincristine. First, as mentioned above, CBD targets the ATP-binding cassette (ABC) transporter (ABCC1/MRP1) responsible for multidrug resistance, including resistance to vincristine. In ovarian cancer cell lines overexpressing ABCC1/MRP1, CBD treatment attenuated the ABCC1/MRP1-mediated drug transport and increased the accumulation of vincristine inside the cells [102]. Second, combined CBD and vincristine treatment reduced cell proliferation in a synergic or additive manner in canine neoplastic cell lines. The authors suggested that this effect could be related to CBD-mediated induction of ERK and JNK kinase-mediated phosphorylation signalling leading to autophagy and apoptosis [103]. Third, a case report suggested a favourable impact of CBD on patients with high-grade gliomas treated with radiotherapy accompanied by a combination of vincristine, lomustine, and procarbazine. Importantly, two patients cotreated with CBD showed an improved health condition that exceeded expectations [104].

Table 3. Summary of the drug–drug interactions of CBD with microtubule-targeting agents.

Microtubule-Targeting Agents									
CT	Aim	Model	Administration	CBD c	CT c	Evaluation Time	Special Condition	Results of Combined Treatment	References
	Viability	CCRF-CEM, CEM/VLB100		10 μ M	0.1 nM to 10 μ M	72 h		Increased toxicity	Holland et al. (2006) [25]
VBT	Viability, combination index, apoptosis	AXA, Orig, and SH cell lines		0.03–300 μ M; IC50: 5.77, 5.30, and 5.48 μ M (and derived concentration series)	0.01–10 μ M; IC50: 2.51, 2.23, and 3.09 μ M (and derived concentration series)	24 h	0.1% FBS	Increased toxicity	Inkol et al. (2021) [81]
	Cold and mechanical allodynia	C57Bl/6 mice female and male	IP	5 or 10 mg/kg daily on days 1–14	1, 2, 4 or 8 mg/kg on days 1, 3, 5, and 7	Testing every 3–10 day (for 66 days)	Cold allodynia—acetone; mechanical allodynia—von Frey filaments	Attenuation of cold and mechanical allodynia	Ward et al. (2011) [89]
PTX	Mechanical allodynia	female C57Bl/6 mice	IP	2.5–10 mg/kg 15 min before PTX	4, 8 mg/kg on days 1, 3, 5 and 7	Weekly for 10 weeks	von Frey monofilaments	Attenuation of mechanical allodynia	Ward et al. (2014) [90]
	Viability	LN 231, 4T1		1–4 μ M	2.5–35 μ M	48 h		Increased toxicity	
	Mechanical allodynia	Male C57Bl/6 mice	IP	0.625–20 mg/kg 15 min before PTX	8 mg/kg on days 1, 3, 5, and 7	Reassessed on days 9, 14, and 21		attenuation of mechanical allodynia	King et al. (2017) [74]
	CBD-mediated protection against PTX	Dissociated DRG from embryonic rats		10 μ M	3 μ M	5 h		Knockdown of Mncx-1 attenuated CBD-mediated protection against PTX	Brenneman et al. (2019) [92]
	Viability, pre-administration strategy	MCF-7, MDA-MB-231		2.5, 5 and 10 μ M (MCF-7); 1.25, 2.5 and 5 μ M (MDA-MB-231) 24 h before PTX	10–500 nM	24 + 48 h		Increased toxicity	
	Viability, co-treatment strategy	MCF-7, MDA-MB-231		10, 15 and 20 μ M (MCF-7); 5, 7.5 and 10 μ M (MDA-MB-231)	10–500 nM	48 h		Increased toxicity	Fraguas-Sánchez et al. (2020) [94]
	Viability, combination studies	MCF-7, MDA-MB-231		CBD in solution 5 or 10 μ M daily; CBD-Mps (single administration), started 24 h before PTX	10–500 nM	24 + 48 h		Increased toxicity with both formulations	
	Tumour growth	MDA-MB-231 grafted onto CAM membrane	Topically	CBD in solution 100 μ M daily, CBD-Mps ones (single administration) 24 h before PTX	100 μ M	24 + 48 h		Reduced tumour growth	
	Viability, pre-administration study	SKOV-3		1 and 10 μ M for 24 h before PTX	10–500 nM	24 + 48 h		Increased toxicity with 10 μ M CBD	Fraguas-Sánchez et al. (2020) [70]

Table 3. Cont.

Microtubule-Targeting Agents									
CT	Aim	Model	Administration	CBD c	CT c	Evaluation Time	Special Condition	Results of Combined Treatment	References
	Viability, coadministration study	SKOV-3		10, 15, and 20 μ M	10–500 nM	48 h		Increased toxicity	
	Viability, pre- and coadministration study	SKOV-3		CBD in solution 10 μ M daily; CBD-Mps (single administration), started 24 h before paclitaxel	10–500 nM	24 + 48 h		Increased toxicity (Mps are more effective)	
	Tumour growth	SKOV-3	Topically	CBD in solution 100 μ M daily, CBD-Mps once (single administration) 24 before PTX	100 μ M	24 + 36 h		Reduced tumour growth	
	Viability	PANC-1 and MiaPaCa-2		6.25, 12.5, 25 μ M	1.75, 3.5, 7 μ M	72 h		Increased toxicity	Luongo et al. (2020) [39]
	Viability and synergy study	MCF7		CBD-PTX (1:9, 2:8, 3:7, 4:6, 5:5, 6:4, 7:3, 8:2, and 9:1, v/v)		72 h		Found the most synergistic ration	Absherbiny et al. (2021) [95]
	Apoptosis and necrosis	MCF7		64.6 μ M	0.1 μ M	24 h		Enhanced cell deaths (CBD toxic itself)	
	Viability, DNA synthesis	HT29		0.5–10 μ M	10 nM	72 h		No effect	
	Viability, DNA synthesis	AGS, SW480		0.5–10 μ M	2 and 10 nM	72 h		No effect at viability, increased inhibition of DNA synthesis	Sains-Cort et al. (2020) [96]
	Viability	Ishikawa		3.92 μ g/ml	0.0015 and 0.003 μ g/ml	72 h		Increased toxicity	Marinelli et al. (2020) [69]
	Mechanical sensitivity	Male C57Bl/6	IP	2.5 mg/kg on days 1, 3, 5 and 7; 15 min before PTX	8 mg/kg on days 1, 3, 5 and 7	Days –3, –2, –1, and 14	von Frey monofilaments	Prevention against the development of mechanical sensitivity	
	Mechanical sensitivity	Male C57Bl/6	PO, IP	0.25, 2.5, 25 mg/kg on days 1, 3, 5 and 7; 15 min before PTX	8 mg/kg on days 1, 3, 5 and 7	Days –3, –2, –1, and 14	von Frey monofilaments	Prevention against the development of mechanical sensitivity	Foss et al. (2021) [93]
	Mechanical sensitivity	Male C57Bl/6	IP	20 mg/kg on days 12, 13 and 14	8 mg/kg on days 1, 3, 5 and 7	Days –3, –2, –1, 11, and 14	von Frey monofilaments	CBD did not reverse mechanical sensitivity	
	Xenograft growth	Male MF-1 nude mice	IP+IV	100 mg/kg CBD-BDS daily	5 mg/kg once weekly	4–5 weeks observation		Different results according to xenograft origin	De Petrocellis et al. (2013) [99]
DTX	Viability and proliferation	LNCaP, DU-145		1–25 μ M	increasing concentration	72 h		Effect modulated by CBD concentration and sera presence	

Table 3. Cont.

Microtubule-Targeting Agents									
CT	Aim	Model	Administration	CBD c	CT c	Evaluation Time	Special Condition	Results of Combined Treatment	References
	Viability and synergy study	MCF7		CBD:DTX (1.9, 2.8, 3.7, 4.6, 5.5, 6.4, 7.3, 8.2, and 9.1, v/v)		72 h		Found the most synergistic ration	Alsherbiny et al. (2021) [95]
	Apoptosis, necrosis	MCF7		39.75 µM	0.5 µM	24 h		Increased apoptosis and necrosis	
VCT	Mechanical allodynia	Male C57Bl6 mice	IP	1.25–10 mg/kg 15 min before VCT	0.1 mg/kg daily for 7 days	Days 5, 10, 15, and 22		No effect	King et al. (2017) [74]
	VCT accumulation	Hu ovarian carcinoma cell line 2008/MRP1		2–100 µM 30 min before VCT	100 nM	30 + 90 min	Absence of serum	Increased VCT intracellular concentration	Holland et al. (2008) [102]
	Viability	Canine neoplastic cell lines		0.34, 0.67, 1.25, 2.5, 5, 10, 20 g/ml	0.25–6.6 nM	48 h		Reduced cell proliferation	Henry et al. (2021) [103]
	Disease progression	Patients with high-grade glioma		100–450 mg/day	Standard PCV therapy		Surgical resection + radiotherapy	Improved health condition	Dall’Stella et al. (2018) [104]

c: concentration; CAM: chicken chorioallantoic membrane; CBD: cannabidiol; CT: chemotherapeutics; DRG: dorsal root ganglion; DTX: docetaxel; Hu: human; IP: intraperitoneal; IV: intravenous; Mps: microparticles; PO: per os; PTX: paclitaxel; VBT: vinblastine; VCT: vincristine.

5. CBD Interactions with Anthracyclines

The anthracyclines (Table 4) are a class of compounds that intercalate into DNA, causing inhibition of DNA synthesis and interference with topoisomerase II [105]. The proto-typic anthracyclines, doxorubicin and daunorubicin, were isolated from *Streptomyces peuceitius* in the 1960s. Since then, several other compounds of this class have received clinical approval [106].

Doxorubicin

Doxorubicin has many therapeutic applications, including in the treatment of haematological malignancies, diverse types of carcinomas, and sarcomas. Its main adverse effects include cardiotoxicity, neurotoxicity, nephrotoxicity, and hepatotoxicity [107]. Doxorubicin has a complex molecular mechanism of action that involves both free radical induction and DNA intercalation leading to DNA breaks and chromosomal aberrations, often resulting in cell senescence or death [108].

Cardiomyopathy is the most severe doxorubicin-evoked adverse effect, which is manifested by myocardial injury, oxidative and nitrative stress, cardiac dysfunction, reduced mitochondrial biogenesis and function and decreased expression of medium-chain acyl-CoA dehydrogenase and uncoupling proteins 2 and 3 [109]. Preclinical studies have indicated that CBD may effectively attenuate these effects. For example, Fouad et al. (2013) [110] examined the effects of CBD on doxorubicin-mediated cardiotoxicity in rats, revealing that rats co-treated with CBD had attenuated cardiac injury, along with reduced levels of serum creatine kinase-MB, troponin T, lipid peroxidation, cardiac malondialdehyde, tumour necrosis factor- α , nitric oxide, calcium ions, nitric oxide synthase, nuclear factor- κ B, Fas ligand, and caspase-3. These CBD-mediated effects were accompanied by increased levels of cardiac glutathione (GSH), selenium, zinc ions, and survivin expression in cardiac tissue, all features that likely contributed to improved histological and biomarker readouts. A cardioprotective effect of CBD in doxorubicin-treated mice was also reported by Hao et al. (2015) [109], who observed reduced levels of cardiac oxidative and nitrative

stress markers, inflammation, and cell death together with enhanced expression of matrix metalloproteinases and improvements in cardiac biogenesis and mitochondrial function.

The potentiation of doxorubicin's anticancer activity by CBD has also been widely studied. Increased doxorubicin accumulation was observed after CBD treatment of Caco-2 and LLC-PK1/MDR1 cancer cell lines; this effect is probably attributable to the blocking of doxorubicin efflux by CBD-induced inhibition of the p-gp transporter [26]. CBD is also an agonist of the TRPV2 channel, which increases doxorubicin uptake, as shown in the U87MG glioma cell line [49] and hepatocellular carcinoma cell lines [111]. Positive modulation of TRPV2 by CBD and improved efficacy of doxorubicin were also confirmed in human triple-negative breast cancer cell lines, including their mouse xenografts [112]. Consistently, CBD enhanced the cytotoxic effect of doxorubicin in an endometrial cancer cell line overexpressing TRPV2 to a greater extent than was observed in parental cells with regular TRPV2 expression [69]. Synergic effects of CBD and doxorubicin were also confirmed in the MCF7 breast adenocarcinoma cell line [95].

Patel et al. (2021) [113] tested combined treatment with doxorubicin and free CBD or CBD encapsulated in EVs as a new delivery system in a model of triple-negative breast cancer (TNBC). Both formulations showed comparable potency in terms of sensitizing cancer cells to doxorubicin, which was manifested by the accumulation of cells in the G1 phase, and affected markers of inflammation, metastasis, and apoptosis. In the xenograft model, the combined treatment led to a reduction in tumour volume that was comparable for both CBD formulations.

CBD formulated in microparticles has also been tested with doxorubicin as a pre-/co-administration strategy, with several preclinical studies showing an enhanced cytotoxic effect in human breast cancer and ovarian cell lines, but only when using a pre-plus cotreatment strategy [70,94].

CBD-mediated potentiation of doxorubicin efficacy has recently been investigated in two TNBC cell lines [114]. The authors observed variable effects (without pre-treatment) as CBD cotreatment resulted in synergism or antagonism depending on the cell line and drug concentration used. Moreover, CBD was shown to effectively sensitize cells against doxorubicin in 3D cultures. Combining the two substances also potentiated the anti-migratory effect in human TNBC MDA-MB-231 cells. The authors suggested that this effect may reflect mechanisms involving integrins, LOX, ATG5, autophagy and ABCA2, all of which are downregulated by CBD.

Combined CBD and doxorubicin treatment have also been tested for potential veterinary cancer therapy applications, suggesting that they synergistically or additively reduce cell proliferation in canine neoplastic cell lines [103]. Additionally, an antagonistic effect was described for lower concentrations of CBD and doxorubicin [103].

Table 4. Summary of the drug–drug interactions of CBD with anthracyclines.

CT	Aim	Model	Administration	Anthracyclines		Evaluation Time	Special Condition	Results of Combined Treatment	References
				CBD c	CT c				
DOX	Cardiomyopathy	Male Sprague-Dawley rats	IP	5 mg/kg/day for 4 weeks	2.5 mg/kg 6x every 48 h for 2 weeks	4 weeks + 1 day		Attenuation of cardiomyopathy	Fouad et al. (2013) [110]
	Cardiomyopathy	Male C57BL/6j mice	IP	10 mg/kg 1.5 h before DOX and daily	20 mg/kg	5 days		Attenuation of cardiomyopathy	Hao et al. (2015) [109]
	Drug accumulation	Caco-2 cells		1, 3, 10, 30 μ M	1 μ M	1 h		Increased drug accumulation	Zhu et al. (2006) [26]
	Drug accumulation	LLC-PK1 and LLC-PK1/MDR1		5, 20, 100 μ M	1 μ M	1 h		Increased drug accumulation	

Table 4. Cont.

Anthracyclines									
CT	Aim	Model	Administration	CBD c	CT c	Evaluation Time	Special Condition	Results of Combined Treatment	References
DOX	Viability	U87MG, MZC, NHA		10 µM	10 ⁻⁵ –10 ⁻³ M	24, 72 h		Increased toxicity except for NHA	Nabissi et al. (2013) [49]
	Colony formation	U87MG, MZC		10 µM	200 µM	14 days		Decreased colony formation	
	Apoptosis	U87MG, MZC		10 µM	200 µM	6 h		Increased annexin	
	DOX uptake	MZC		10 µM 30 min before DOX	5 µM	0.5 + 2 h		TRPV2 dependent	
	TRPV2 function	U87MG, MZC		10 µM	200 µM	1 day		TRPV2 dependent	Neumann-Raizel et al. (2019) [111]
	TRPV2 function	Murine BNL1 ME A.7R.1 cells		10 µM co-treatment and after DOX washout	1 µM	Seconds		TRPV2 dependent	
	p-gp inhibition, viability, colony formation	Murine BNL1 ME A.7R.1 cells		10 µM	0.1 µM	24 h		Increased toxicity	
	DOX uptake	SUM159 and MDA-MB231		5 µM 2 h before DOX	5 µM	2 + 0.5 h		Higher DOX uptake	
	Viability	SUM159 and MDA-MB232		5 µM	0.025–64 µM	24 h		Increased toxicity	
	Apoptosis	SUM159		5 µM	0.5 µM	24 h		Increased apoptosis	
	Colony formation	SUM159 and MDA-MB232		5 µM	0.5 µM	6 days	Reduced serum	Decreased colony formation	
	Tumour growth/apoptosis	Female NU/NU nude mice with SUM159 xenograft	PT CBD; IP DOX	5 mg/kg once per week 2 h before DOX	5 mg/kg	4 weeks		Lower tumour volume, increased pro-apoptotic markers	Marinelli et al. (2020) [69]
	Viability	Ishikawa		3.92 µg/ml	0.015 and 0.03 µg/ml	72 h		Increased toxicity	
	Viability, pre-administration strategy	MCF-7, MDA-MB-231		2.5, 5 and 10 µM (MCF-7); 1.25, 2.5 and 5 µM (MDA-MB-231) 24 h before DOX	0.1–20 µM	24 + 48 h		Increased toxicity (more in MDA-MB-231)	Fraguas-Sánchez et al. (2020) [94]
	Viability, co-treatment strategy	MCF-7, MDA-MB-231		10, 15 and 20 µM (MCF-7); 5, 7.5 and 10 µM (MDA-MB-231)	0.1–20 µM	48 h		Increased toxicity (except 10 µM CBD in MCF7)	
	Viability, combination studies	MCF-7, MDA-MB-231		CBD in solution 5 or 10 µM daily; CBD-Mps (single administration), started 24 h before DOX	0.1–20 µM	24 + 48 h		Increased toxicity with both formulations	

Table 4. Cont.

Anthracyclines									
CT	Aim	Model	Administration	CBD c	CT c	Evaluation Time	Special Condition	Results of Combined Treatment	References
	Viability, pre-administration study	SKOV-3		1 and 10 μM for 24 h before DOX	1–60 μM	24 + 48 h		Not statistically significant	Fraguas-Sánchez et al. (2020) [70]
	Viability, coadministration study	SKOV-3		10, 15, and 20 μM	1–120 μM	48 h		Not statistically significant	
	Viability, pre- and coadministration study	SKOV-3		CBD in solution 10 μM daily; CBD-Mps (single administration), started 24 h before DOX	0.1–20 μM	24 + 48 h		Increased toxicity	
	Viability	MDA-MB-231		CBD and CBD EV 1 μM (24 h before DOX)	0.156–10 μM	24 + 48 h		Increased sensitivity	Patel et al. (2021) [113]
	Cell cycle, apoptosis, inflammatory, and metastatic markers	MDA-MB-231		CBD and CBD EV 1 μM (24 h before DOX)	500 nM	24 + 48 h		Increased G1 and apoptosis, decreased inflammation and metastasis	
	Cell migration	MDA-MB-231		CBD EV 1 μM	500 nM	40 h (reading every 10 min)		Decreased migration	
	Tumour volume, apoptosis, inflammatory and metastatic markers	Envigo nude mice (MDA-MB-231)	IP (CBD and CBD EV), IV (DOX)	CBD, CBD EV 5 mg/kg (1 day before DOX; twice weekly)	2 mg/kg (twice weekly)	Days 1, 4, 10, and 14		Lower tumour volume, increased apoptosis, decreased inflammation, and metastasis	Absherbiny et al. (2021) [95]
	Viability and synergy study	MCF7		CBD:DOX (1:9, 2:8, 3:7, 4:6, 5:5, 6:4, 7:3, 8:2, and 9:1, v/v)		72 h		Found the most synergistic ration	
	Apoptosis, necrosis	MCF7		38, 42 μM	0.2 μM	24 h		Increased apoptosis and necrosis	
	Viability	Canine neoplastic cell lines		0.34, 0.67, 1.25, 2.5, 5, 10, 20 g/ml	0.033–2 μM	48 h		Reduced cell proliferation	Henry et al. (2021) [103]
	Viability, combinatorial effect	MDA-MB-231, MDA-MB-468		1, 2.5 (2D); 5 (3D) μM	0.39–25 μM (2D); 5–100 μM (3D)	24 + 48h; 48h		Increased toxicity	Surapaneni et al. (2022) [114]
	Cell migration	MDA-MB-231		1 μM	500 nM	40 h (reading every 10 min)		Anti-migratory effect	
	Immunoblotting	MDA-MB-468		1 μM	1 μM	24 + 48 h		Increased cell sensitivity against DOX	

c: concentration; CBD: cannabidiol; CT: chemotherapeutics; D: dimensional; DOX: doxorubicin; EV: extracellular vesicles; IP: intraperitoneal; IV: intravenous; Mps: microparticles; NHA: normal human astrocytes; PT: peritumoural.

6. Interactions of CBD with Proteotoxic Stress-Inducing Drugs

Protein homeostasis involves protein synthesis, folding, and degradation in cells. Protein turnover is generally high in cancer cells due to uncontrolled cell divisions and growth as well as numerous genetic alterations that may give rise to proteins with altered structures or alter the composition of multimeric complexes [115]. Most cancer cells, therefore, experience elevated proteotoxic stress making them highly dependent on the proper function of protein-degradation machinery such as the ubiquitin-proteasome system (UPS). Protein homeostasis is therefore seen as a promising target for cancer therapy and has been studied extensively [116]. The first drug targeting this process, bortezomib, was approved for clinical use in 2003 [117].

6.1. Bortezomib

Bortezomib (Table 5) is one of the clinically used proteasome inhibitors and is commonly used to treat multiple myeloma (MM). It has a broad spectrum of adverse effects, including haematological and gastrointestinal toxicity and neurotoxicity [118]. CBD was shown to synergistically potentiate the anticancer effect of bortezomib, leading to increased growth inhibition, cell cycle arrest, and cell death through the ERK/AKT/NFκB pathway in human MM cell lines. The strongest cytotoxic response to bortezomib in combination with CBD was observed in TRPV2-overexpressing MM cells [119]. Bortezomib combined with CBD is about to be tested in phase II clinical trial of patients diagnosed with MM, GBM, and GI malignancies (NCT03607643) [34].

6.2. Disulfiram

Proteasome inhibitors aside, there are currently no approved anticancer drugs that directly target the UPS or protein homeostasis. However, some FDA-approved medicines targeting UPS that were initially approved for other indications are now being repurposed for cancer treatment. Disulfiram, which has been used for over 60 years to treat alcoholism, is an ideal candidate for repurposing as it is a well-tolerated drug with a substantial anticancer effect supported by numerous preclinical studies, case reports, and clinical trials, including several ongoing clinical trials (NCT04521335; NCT03323346; NCT03950830) [120–124]. The UPS-targeting effect of disulfiram is due to its metabolite, a copper-diethyldithiocarbamate complex (CuET), which targets the NPL4 protein, a cofactor of p97 segregase [125]. P97, with its cofactors, is a vital component of the UPS acting upstream of the proteasome through p97's ATPase activity that enables the segregation from diverse subcellular structures, unfolding, and translocation of ubiquitinated proteins for proteasome-mediated degradation [126]. CuET causes NPL4 aggregation leading to p97/NPL4 complex malfunction, triggering suprathreshold, irresolvable proteotoxic stress and consequently cancer cell death [125]. We recently showed that CBD effectively blocks CuET-mediated proteotoxic stress and toxicity in cancer cells by upregulating metallothioneins MT-1E and MT-2A, small proteins that are responsible for metal homeostasis and heavy metal detoxification, including copper. Because CuET is a copper complex, increased metallothionein expression reduces its activity against its primary target, NPL4, and thus reduces its toxicity [127]. These results indicate that the promising anticancer effect of the disulfiram/copper combination may be severely compromised by the simultaneous use of CBD products as supportive care.

Table 5. Summary of the drug–drug interactions of CBD with proteotoxic stress inducers and topoisomerase inhibitors.

Proteotoxic Stress Inducers									
CT	Aim	Model	Administration	CBD c	CT c	Evaluation Time	Special Condition	Results of Combined Treatment	References
BRT	Cytotoxicity, proliferation, cell cycle, necrosis, cell death	RPMI8226, U266		20 μ M	3 ng/ml	72 h		Synergistic activity	Morelli et al. (2014) [119]
	Mitochondrial activity	RPMI8226		20 μ M	3 ng/ml	1 h		Induced mitochondrial-dependent necrosis	
	ROS	RPMI8226		20 μ M	3 ng/ml	2 h		Increased ROS	
DSF/CuET	Viability	U2OS, MDA-MB-231		10 μ M 24 h pre-treatment + 10 μ M co-treatment	62.5–500 nM	24 + 72 h		Decreased sensitivity	Buchtova et al. (2021) [127]
	Proteotoxic stress markers, MTs induction	U2OS, MDA-MB-231, RPE-2		10 μ M 24 h before CuET	0.2 μ M	24 + 3 h		Decreased proteotoxic stress, increased MT expression	
Topoisomerase inhibitors									
CT	Aim	Model	Administration	CBD c	CT c	Time point	Special condition	Results of combined treatment	References
TPC	Viability	MEF3.8		10 μ M 1 h before TPC	1 nM–10 μ M	1 + 48 h		Increased toxicity	Holland et al. (2007) [24]

c: concentration; CBD: cannabidiol; CT: chemotherapeutics; DSF: disulfiram; BRT: bortezomib; TPC: topotecan.

7. CBD Interactions with Topoisomerase Inhibitors

Topoisomerases are essential modulators of DNA replication, recombination, repair, and transcription because of their role in releasing topological DNA stress. Topoisomerases catalyse single- or double-strand cleavage of DNA, and their proper function is crucial for cellular differentiation, proliferation, and survival. These enzymes were first identified as potential anticancer targets in the mid-1980s, and several topoisomerase inhibitors have since then been discovered and established in oncological praxis [128].

Topotecan

Topotecan (Table 5) selectively inhibits topoisomerase I, which catalyses single-strand DNA cleavage. Topotecan binds to the enzyme and prevents the re-ligation step, causing the formation of a single-strand DNA gap and simultaneously trapping the enzyme [129]. Topotecan is used as part of second-line therapy for metastatic ovarian cancers and relapsed small cell lung cancers. The most limiting adverse effect of topotecan is haematological toxicity; less severe effects include fatigue, nausea, vomiting, hypokalaemia, and increased γ -glutamyltransferase activity [130].

While the impact of CBD on adverse effects of topotecan is unknown, it seems that CBD may overcome resistance to topotecan mediated by the ABCG2/BCRP efflux transporter, which is directly targeted by CBD, as has been shown in the ABCG2/BCRP transporter-overexpressing MEF3.8 cell line [24].

8. Discussion

Currently, up to two-thirds of oncology practitioners say that they have discussed *Cannabis* product use with their patients but acknowledge that they do not have sufficient information to provide solid recommendations [131]. Indeed, recent surveys suggest con-

siderable use of CBD and *Cannabis*-derived products among patients with cancer [2,3]. This review aims to provide oncologists and cancer patients with an overview of the potential benefits and drawbacks, as well as some uncertainties, associated with concomitant CBD use during ongoing chemotherapy. We have focused on summarizing the available preclinical data concerning the drug–drug interactions of CBD with commonly used chemotherapeutics in cell cultures and animal models (Tables 1–5). However, the list of anticancer chemotherapeutics discussed herein is not exhaustive, and the effects of CBD in combination with other cannabinoids, which are discussed in several publications, were excluded due to the length restrictions and the focus of our present review.

Patients have two primary motivations for using CBD during ongoing anticancer therapy: (i) attenuation of adverse effects and (ii) enhancement of the therapeutic efficacy. Adverse effects are often limiting factors of chemotherapy treatment, and CBD, in combination with certain chemotherapeutics, can enable patients to withstand therapy for a longer time and/or at a higher dosage. According to available surveys [2,3], adverse effects are the main reason why patients with cancer use *Cannabis* products. Among the notable preclinical examples discussed in this review, CBD can alleviate 5-fluorouracil-induced oral mucositis, cisplatin-induced renal and gastric toxicities, oxaliplatin-induced neuropathic pain, paclitaxel-induced neuropathy, and doxorubicin-induced cardiotoxicity, as well as show some desirable anti-emetic and anti-nausea effects during chemotherapy. There is a consensus in most of the cited studies that CBD has good potential to improve the quality of life of patients with cancer undergoing standard chemotherapy.

The modulation of treatment efficacy by CBD is another fascinating issue that warrants further investigation. CBD has been proven to have a multi-target impact on various cellular processes, some of which are necessary for cancer-cell survival or modulate the toxic effects of various anticancer drugs. We collected and highlighted preclinical data illustrating these impacts. For example, CBD was shown to potentiate the effects of gemcitabine, carmustine, cisplatin, temozolomide, paclitaxel, and vincristine in various preclinical models. The mechanistic explanations for these combinatorial effects mainly involve effects on drug influx/efflux resulting from interactions with transporters and/or channels such as TRPV2, which is activated by CBD and increases the influx and retention of carmustine, cisplatin, temozolomide, doxorubicin, and bortezomib. The well-known p-gp efflux transporter, which is responsible for multidrug resistance, is yet another very relevant target of CBD in this context. CBD-mediated inhibition of the p-gp transporter leads to increased accumulation of vinblastine and doxorubicin in p-gp-overexpressing cell lines. CBD also inhibits the ABCC1/MRP1 and ABCG2/BCRP transporters and thereby facilitates the accumulation of methotrexate, vincristine, and topotecan, at least in cell lines overexpressing these transporters. Importantly, the ability of CBD to increase the accumulation of these drugs is not always cancer cell-/tissue-specific, a challenging aspect that raises the risk of unwanted increased adverse chemotherapy effects and overdose in patients using CBD in conjunction with these anticancer agents.

Other modes of chemotherapy potentiation by CBD that does not involve transporters have also been proposed. These include regulation of EV trafficking of anti- and pro-oncogenic miRNAs in temozolomide-treated glioblastoma [56]; induction of ERK and JNK kinase pathways, which promotes autophagy in vincristine- and doxorubicin-treated canine neoplastic cells [103]; GRP55 inhibition, which reduces growth and cell cycle progression in gemcitabine-treated PDAC cells [36]; and ROS induction in oxaliplatin-treated colorectal cell lines [76].

Importantly, there is also preclinical evidence that CBD might significantly reduce the efficacy of anticancer drugs in some cases. This serious issue remains relatively unexplored and has been mentioned in some studies as an unexpected finding without being actively studied mechanistically. However, one mechanistic explanation has been provided recently when it was shown that CBD efficiently protects cancer cells against certain metal-containing drugs by inducing the expression of specific detoxifying proteins known as metallothioneins [127]. Indeed, metallothioneins are involved in cellular defence against

multiple chemicals, and their effects are not limited to heavy metal complexes [132,133]. Consequently, this effect could be relevant for numerous anticancer drugs. Accordingly, antagonistic effects of CBD have been reported for carmustine, temozolomide, cisplatin, carboplatin, and doxorubicin. This suggests that concomitant use of CBD during anticancer therapy may be unsuitable for some drug combinations because it may appear to reduce adverse effects while actually reducing the likelihood of successful treatment.

Overall, based on the collected data here, it can be concluded that CBD shows exciting potential for improving cancer chemotherapy outcomes when combined with various standard-of-care drugs and not only in terms of side effect attenuation. For example, cancers with developed treatment resistance might benefit from concomitant CBD application due to its reported effects on transporters. In addition, combinations including carmustine, paclitaxel, and doxorubicin seem promising. However, some of the data are less conclusive, with conflicting findings involving, for example, temozolomide and cisplatin. Finally, CBD combined with carboplatin or disulfiram appears to be a potentially dangerous combination (decreasing the drug efficacy). The last two examples even raise an essential concern that some of the CBD-promoted side effect attenuation might reflect a reduced amount of available active drugs. Thus, given the lack of clinical data and only scheduled or ongoing clinical trials, the reported promising preclinical results need to be carefully evaluated and translated into meaningful clinical benefits.

Author Contributions: Conceptualization, T.B., M.M. and Z.S.; validation, T.B., D.L., K.C. and J.B.; investigation, T.B.; resources, T.B. and Z.S.; writing—original draft preparation, T.B. and Z.S.; writing—review and editing, T.B., D.L., K.C., J.B. and M.M.; visualization, T.B. and M.M.; supervision, M.M.; project administration, T.B. and M.M.; funding acquisition, M.M. All authors have read and agreed to the published version of the manuscript.

Funding: The work was supported by project ENOCH (No. CZ.02.1.01/0.0/0.0/16_019/0000868), Grant agency of the Czech Republic: GACR 20-28685S, Internal grant of the University of Palacky IGA_LF_2022_038, the Danish National Research Foundation (project CARD, DNRF 125), and the project National Institute for Cancer Research (Programme EXCELES, ID Project No. LX22NPO5102)—Funded by the European Union—Next Generation EU.

Conflicts of Interest: The authors declare no conflict of interest.

References

1. Scripture, C.D.; Figg, W.D. Drug Interactions in Cancer Therapy. *Nat. Rev. Cancer* **2006**, *6*, 546–558. [CrossRef] [PubMed]
2. Pergam, S.A.; Woodfield, M.C.; Lee, C.M.; Cheng, G.-S.; Baker, K.K.; Marquis, S.R.; Fann, J.R. Cannabis Use among Patients at a Comprehensive Cancer Center in a State with Legalized Medicinal and Recreational Use. *Cancer* **2017**, *123*, 4488–4497. [CrossRef] [PubMed]
3. Weiss, M.C.; Hibbs, J.E.; Buckley, M.E.; Danese, S.R.; Leitenberger, A.; Bollmann-Jenkins, M.; Meske, S.W.; Aliano-Ruiz, K.E.; McHugh, T.W.; Larson, S.L.; et al. A Coala-T-Cannabis Survey Study of Breast Cancer Patients' Use of Cannabis before, during, and after Treatment. *Cancer* **2022**, *128*, 160–168. [CrossRef] [PubMed]
4. Aizpurua-Olaizola, O.; Soydaner, U.; Öztürk, E.; Schibano, D.; Simsir, Y.; Navarro, P.; Etxebarria, N.; Usobiaga, A. Evolution of the Cannabinoid and Terpene Content during the Growth of *Cannabis Sativa* Plants from Different Chemotypes. *J. Nat. Prod.* **2016**, *79*, 324–331. [CrossRef]
5. ElSohly, M.A.; Radwan, M.M.; Gul, W.; Chandra, S.; Galal, A. Phytochemistry of *Cannabis Sativa* L. *Prog. Chem. Org. Nat. Prod.* **2017**, *103*, 1–36. [CrossRef]
6. Brown, J.D.; Winterstein, A.G. Potential Adverse Drug Events and Drug-Drug Interactions with Medical and Consumer Cannabidiol (CBD) Use. *J. Clin. Med.* **2019**, *8*, 989. [CrossRef]
7. Devinsky, O.; Patel, A.D.; Cross, J.H.; Villanueva, V.; Wirrell, E.C.; Privitera, M.; Greenwood, S.M.; Roberts, C.; Checketts, D.; VanLandingham, K.E.; et al. Effect of Cannabidiol on Drop Seizures in the Lennox-Gastaut Syndrome. *N. Engl. J. Med.* **2018**, *378*, 1888–1897. [CrossRef]
8. Devinsky, O.; Cross, J.H.; Wright, S. Trial of Cannabidiol for Drug-Resistant Seizures in the Dravet Syndrome. *N. Engl. J. Med.* **2017**, *377*, 699–700. [CrossRef]
9. Hess, E.J.; Moody, K.A.; Geoffrey, A.L.; Pollack, S.F.; Skirvin, L.A.; Bruno, P.L.; Paolini, J.L.; Thiele, E.A. Cannabidiol as a New Treatment for Drug-Resistant Epilepsy in Tuberous Sclerosis Complex. *Epilepsia* **2016**, *57*, 1617–1624. [CrossRef]

10. Thiele, E.A.; Marsh, E.D.; French, J.A.; Mazurkiewicz-Beldzinska, M.; Benbadis, S.R.; Joshi, C.; Lyons, P.D.; Taylor, A.; Roberts, C.; Somerville, K.; et al. Cannabidiol in Patients with Seizures Associated with Lennox-Gastaut Syndrome (GWPCARE4): A Randomised, Double-Blind, Placebo-Controlled Phase 3 Trial. *Lancet* **2018**, *391*, 1085–1096. [CrossRef]
11. Epidiolex: Highlights of Prescribing Information. Available online: [https://www.epidiolex.com/sites/default/files/pdfs/0222/0222-epidiolex_\(cannabidiol\)_uspi.pdf](https://www.epidiolex.com/sites/default/files/pdfs/0222/0222-epidiolex_(cannabidiol)_uspi.pdf) (accessed on 1 February 2023).
12. Leweke, F.M.; Piomelli, D.; Pahlisch, F.; Muhl, D.; Gerth, C.W.; Hoyer, C.; Klosterkötter, J.; Hellmich, M.; Koethe, D. Cannabidiol Enhances Anandamide Signaling and Alleviates Psychotic Symptoms of Schizophrenia. *Transl. Psychiatry* **2012**, *2*, e94. [CrossRef] [PubMed]
13. Chagas, M.H.N.; Zuardi, A.W.; Tumas, V.; Pena-Pereira, M.A.; Sobreira, E.T.; Bergamaschi, M.M.; dos Santos, A.C.; Teixeira, A.L.; Hallak, J.E.C.; Crippa, J.A.S. Effects of Cannabidiol in the Treatment of Patients with Parkinson's Disease: An Exploratory Double-Blind Trial. *J. Psychopharmacol.* **2014**, *28*, 1088–1098. [CrossRef] [PubMed]
14. Naftali, T.; Mechulam, R.; Marii, A.; Gabay, G.; Stein, A.; Bronshtain, M.; Laish, I.; Benjaminov, F.; Konikoff, F.M. Low-Dose Cannabidiol Is Safe but Not Effective in the Treatment for Crohn's Disease, a Randomized Controlled Trial. *Dig. Dis. Sci.* **2017**, *62*, 1615–1620. [CrossRef] [PubMed]
15. Crippa, J.A.S.; Derenusson, G.N.; Ferrari, T.B.; Wichert-Ana, L.; Duran, F.L.S.; Martin-Santos, R.; Simões, M.V.; Bhattacharyya, S.; Fumar-Poli, P.; Atakan, Z.; et al. Neural Basis of Anxiolytic Effects of Cannabidiol (CBD) in Generalized Social Anxiety Disorder: A Preliminary Report. *J. Psychopharmacol.* **2011**, *25*, 121–130. [CrossRef] [PubMed]
16. Larsen, C.; Shahinas, J. Dosage, Efficacy and Safety of Cannabidiol Administration in Adults: A Systematic Review of Human Trials. *J. Clin. Med. Res.* **2020**, *12*, 129–141. [CrossRef]
17. Thomas, A.; Baillie, G.L.; Phillips, A.M.; Razdan, R.K.; Ross, R.A.; Pertwee, R.G. Cannabidiol Displays Unexpectedly High Potency as an Antagonist of CB1 and CB2 Receptor Agonists in Vitro. *Br. J. Pharmacol.* **2007**, *150*, 613–623. [CrossRef]
18. Bisogno, T.; Hanuš, L.; De Petrocellis, L.; Tchilibon, S.; Ponde, D.E.; Brandi, I.; Moriello, A.S.; Davis, J.B.; Mechoulam, R.; Di Marzo, V. Molecular Targets for Cannabidiol and Its Synthetic Analogues: Effect on Vanilloid VR1 Receptors and on the Cellular Uptake and Enzymatic Hydrolysis of Anandamide. *Br. J. Pharmacol.* **2001**, *134*, 845–852. [CrossRef]
19. Qin, N.; Neeper, M.P.; Liu, Y.; Hutchinson, T.L.; Lubin, M.L.; Flores, C.M. TRPV2 Is Activated by Cannabidiol and Mediates CGRP Release in Cultured Rat Dorsal Root Ganglion Neurons. *J. Neurosci.* **2008**, *28*, 6231–6238. [CrossRef]
20. O'Sullivan, S.E.; Sun, Y.; Bennett, A.J.; Randall, M.D.; Kendall, D.A. Time-Dependent Vascular Actions of Cannabidiol in the Rat Aorta. *Eur. J. Pharmacol.* **2009**, *612*, 61–68. [CrossRef]
21. Russo, E.B.; Burnett, A.; Hall, B.; Parker, K.K. Agonistic Properties of Cannabidiol at 5-HT1a Receptors. *Neurochem. Res.* **2005**, *30*, 1037–1043. [CrossRef]
22. Ryberg, E.; Larsson, N.; Sjögren, S.; Hjorth, S.; Hermansson, N.-O.; Leonova, J.; Elebring, T.; Nilsson, K.; Drmota, T.; Greasley, P.J. The Orphan Receptor GPR55 Is a Novel Cannabinoid Receptor. *Br. J. Pharmacol.* **2007**, *152*, 1092–1101. [CrossRef] [PubMed]
23. Carrier, E.J.; Auchampach, J.A.; Hillard, C.J. Inhibition of an Equilibrative Nucleoside Transporter by Cannabidiol: A Mechanism of Cannabinoid Immunosuppression. *Proc. Natl. Acad. Sci. USA* **2006**, *103*, 7895–7900. [CrossRef] [PubMed]
24. Holland, M.L.; Lau, D.T.T.; Allen, J.D.; Arnold, J.C. The Multidrug Transporter ABCG2 (BCRP) Is Inhibited by Plant-Derived Cannabinoids. *Br. J. Pharmacol.* **2007**, *152*, 815–824. [CrossRef] [PubMed]
25. Holland, M.L.; Panetta, J.A.; Hoskins, J.M.; Bebawy, M.; Roufogalis, B.D.; Allen, J.D.; Arnold, J.C. The Effects of Cannabinoids on P-Glycoprotein Transport and Expression in Multidrug Resistant Cells. *Biochem. Pharmacol.* **2006**, *71*, 1146–1154. [CrossRef]
26. Zhu, H.-J.; Wang, J.-S.; Markowitz, J.S.; Donovan, J.L.; Gibson, B.B.; Gefroh, H.A.; Devane, C.L. Characterization of P-Glycoprotein Inhibition by Major Cannabinoids from Marijuana. *J. Pharmacol. Exp. Ther.* **2006**, *317*, 850–857. [CrossRef] [PubMed]
27. Borges, R.S.; Batista, J.; Viana, R.B.; Baetas, A.C.; Orestes, E.; Andrade, M.A.; Honório, K.M.; da Silva, A.B.F. Understanding the Molecular Aspects of Tetrahydrocannabinol and Cannabidiol as Antioxidants. *Molecules* **2013**, *18*, 12663–12674. [CrossRef]
28. Wu, H.-Y.; Chu, R.-M.; Wang, C.-C.; Lee, C.-Y.; Lin, S.-H.; Jan, T.-R. Cannabidiol-Induced Apoptosis in Primary Lymphocytes Is Associated with Oxidative Stress-Dependent Activation of Caspase-8. *Toxicol. Appl. Pharmacol.* **2008**, *226*, 260–270. [CrossRef]
29. Mortimer, T.L.; Mabin, T.; Engelbrecht, A.-M. Cannabinoids: The Lows and the Highs of Chemotherapy-Induced Nausea and Vomiting. *Future Oncol.* **2019**, *15*, 1035–1049. [CrossRef]
30. Pisanti, S.; Malfitano, A.M.; Ciaglia, E.; Lamberti, A.; Ranieri, R.; Cuomo, G.; Abate, M.; Faggiana, G.; Proto, M.C.; Fiore, D.; et al. Cannabidiol: State of the Art and New Challenges for Therapeutic Applications. *Pharmacol. Ther.* **2017**, *175*, 133–150. [CrossRef]
31. Farber, S.; Diamond, L.K. Temporary Remissions in Acute Leukemia in Children Produced by Folic Acid Antagonist, 4-Aminopteroyl-Glutamic Acid. *N. Engl. J. Med.* **1948**, *238*, 787–793. [CrossRef]
32. Luengo, A.; Gui, D.Y.; Vander Heiden, M.G. Targeting Metabolism for Cancer Therapy. *Cell Chem. Biol.* **2017**, *24*, 1161–1180. [CrossRef] [PubMed]
33. Cuba, L. de F.; Salum, F.G.; Guimarães, F.S.; Cherubini, K.; Borghetti, R.L.; de Figueiredo, M.A.Z. Cannabidiol on 5-FU-Induced Oral Mucositis in Mice. *Oral Dis.* **2020**, *26*, 1483–1493. [CrossRef] [PubMed]
34. Leaf Vertical Inc. *Randomized Double-Blind, Placebo-Controlled Parallel Multi-Center Study to Assess the Efficacy of Cannabidiol (BRCX014) Combined with Standard-of-Care Treatment in Subjects with Multiple Myeloma, Glioblastoma Multiforme, and GI Malignancies*; Clinicaltrials.gov: Bethesda, MD, USA, 2018.
35. Toschi, L.; Finocchiaro, G.; Bartolini, S.; Gioia, V.; Cappuzzo, F. Role of Gemcitabine in Cancer Therapy. *Future Oncol.* **2005**, *1*, 7–17. [CrossRef] [PubMed]

36. Ferro, R.; Adamska, A.; Lattanzio, R.; Mavrommati, I.; Edling, C.E.; Arifin, S.A.; Fyffe, C.A.; Sala, G.; Sacchetto, L.; Chiorino, G.; et al. GPR55 Signalling Promotes Proliferation of Pancreatic Cancer Cells and Tumour Growth in Mice, and Its Inhibition Increases Effects of Gemcitabine. *Oncogene* **2018**, *37*, 6368–6382. [[CrossRef](#)]
37. Oka, S.; Nakajima, K.; Yamashita, A.; Kishimoto, S.; Sugiura, T. Identification of GPR55 as a Lysophosphatidylinositol Receptor. *Biochem. Biophys. Res. Commun.* **2007**, *362*, 928–934. [[CrossRef](#)]
38. Piñeiro, R.; Maffucci, T.; Falasca, M. The Putative Cannabinoid Receptor GPR55 Defines a Novel Autocrine Loop in Cancer Cell Proliferation. *Oncogene* **2011**, *30*, 142–152. [[CrossRef](#)]
39. Luongo, M.; Marinelli, O.; Zeppa, L.; Aguzzi, C.; Morelli, M.B.; Amantini, C.; Frassinetti, A.; di Costanzo, M.; Fanelli, A.; Santoni, G.; et al. Cannabidiol and Oxygen-Ozone Combination Induce Cytotoxicity in Human Pancreatic Ductal Adenocarcinoma Cell Lines. *Cancers* **2020**, *12*, 2774. [[CrossRef](#)]
40. Hagner, N.; Joerger, M. Cancer Chemotherapy: Targeting Folic Acid Synthesis. *Cancer Manag. Res* **2010**, *2*, 293–301. [[CrossRef](#)]
41. Kozmiński, P.; Halik, P.K.; Chesori, R.; Gniazdowska, E. Overview of Dual-Acting Drug Methotrexate in Different Neurological Diseases, Autoimmune Pathologies and Cancers. *Int. J. Mol. Sci.* **2020**, *21*, 3483. [[CrossRef](#)]
42. Purcell, W.T.; Ettinger, D.S. Novel Antifolate Drugs. *Curr. Oncol. Rep.* **2003**, *5*, 114–125. [[CrossRef](#)]
43. Mao, Q.; Unadkat, J.D. Role of the Breast Cancer Resistance Protein (ABCG2) in Drug Transport. *AAPS J.* **2005**, *7*, E118–E133. [[CrossRef](#)]
44. Fu, D.; Calvo, J.A.; Samson, L.D. Balancing Repair and Tolerance of DNA Damage Caused by Alkylating Agents. *Nat. Rev. Cancer* **2012**, *12*, 104–120. [[CrossRef](#)]
45. Puyo, S.; Montaudon, D.; Pounquier, P. From Old Alkylating Agents to New Minor Groove Binders. *Crit. Rev. Oncol. Hematol.* **2014**, *89*, 43–61. [[CrossRef](#)]
46. Adair, F.E.; Bagg, H.J. Experimental and clinical studies on the treatment of cancer by dichlorethylsulphide (mustard gas). *Ann. Surg.* **1931**, *93*, 190–199. [[CrossRef](#)]
47. Brandes, A.A.; Bartolotti, M.; Tosoni, A.; Franceschi, E. Nitrosoureas in the Management of Malignant Gliomas. *Curr. Neurol. Neurosci. Rep.* **2016**, *16*, 13. [[CrossRef](#)]
48. Weiss, R.B.; Issell, B.F. The Nitrosoureas: Carmustine (BCNU) and Lomustine (CCNU). *Cancer Treat. Rev.* **1982**, *9*, 313–330. [[CrossRef](#)]
49. Nabissi, M.; Morelli, M.B.; Santoni, M.; Santoni, G. Triggering of the TRPV2 Channel by Cannabidiol Sensitizes Glioblastoma Cells to Cytotoxic Chemotherapeutic Agents. *Carcinogenesis* **2013**, *34*, 48–57. [[CrossRef](#)]
50. Likar, R.; Nahler, G. The Use of Cannabis in Supportive Care and Treatment of Brain Tumor. *Neurooncol. Pract.* **2017**, *4*, 151–160. [[CrossRef](#)]
51. Chuang, L.S.H.; Ito, K.; Ito, Y. RUX Family: Regulation and Diversification of Roles through Interacting Proteins. *Int. J. Cancer* **2013**, *132*, 1260–1271. [[CrossRef](#)]
52. Nabissi, M.; Morelli, M.B.; Amantini, C.; Liberati, S.; Santoni, M.; Ricci-Vitiani, L.; Pallini, R.; Santoni, G. Cannabidiol Stimulates Aml-1a-Dependent Glial Differentiation and Inhibits Glioma Stem-like Cells Proliferation by Inducing Autophagy in a TRPV2-Dependent Manner. *Int. J. Cancer* **2015**, *137*, 1855–1869. [[CrossRef](#)]
53. Deng, L.; Ng, L.; Ozawa, T.; Stella, N. Quantitative Analyses of Synergistic Responses between Cannabidiol and DNA-Damaging Agents on the Proliferation and Viability of Glioblastoma and Neural Progenitor Cells in Culture. *J. Pharmacol. Exp. Ther.* **2017**, *360*, 215–224. [[CrossRef](#)] [[PubMed](#)]
54. Arora, A.; Somasundaram, K. Glioblastoma vs Temozolomide: Can the Red Queen Race Be Won? *Cancer Biol. Ther.* **2019**, *20*, 1083–1090. [[CrossRef](#)] [[PubMed](#)]
55. Singh, N.; Miner, A.; Hennis, L.; Mittal, S. Mechanisms of Temozolomide Resistance in Glioblastoma—A Comprehensive Review. *Cancer Drug Resist.* **2021**, *4*, 17–43. [[CrossRef](#)] [[PubMed](#)]
56. Baumert, B.G.; Hegi, M.E.; van den Bent, M.J.; von Deimling, A.; Gorlia, T.; Hoang-Xuan, K.; Brandes, A.A.; Kantor, G.; Taphoorn, M.J.B.; Hassel, M.B.; et al. Temozolomide Chemotherapy versus Radiotherapy in High-Risk Low-Grade Glioma (EORTC 22033-26033): A Randomised, Open-Label, Phase 3 Intergroup Study. *Lancet Oncol.* **2016**, *17*, 1521–1532. [[CrossRef](#)]
57. Chang, W.-H.; Cerione, R.A.; Antonyak, M.A. Extracellular Vesicles and Their Roles in Cancer Progression. *Methods Mol. Biol.* **2021**, *2174*, 143–170. [[CrossRef](#)]
58. Kosgodage, U.S.; Uysal-Onganer, P.; MacLatchy, A.; Mould, R.; Nunn, A.V.; Guy, G.W.; Kraev, I.; Chatterton, N.P.; Thomas, E.L.; Inal, J.M.; et al. Cannabidiol Affects Extracellular Vesicle Release, MiR21 and MiR126, and Reduces Prohibitin Protein in Glioblastoma Multiforme Cells. *Transl. Oncol.* **2019**, *12*, 513–522. [[CrossRef](#)]
59. López-Valero, I.; Saiz-Ladera, C.; Torres, S.; Hernández-Tiedra, S.; García-Ibaoda, E.; Rodríguez-Fornés, F.; Barba, M.; Dávila, D.; Salvador-Tormo, N.; Guzmán, M.; et al. Targeting Glioma Initiating Cells with A Combined Therapy of Cannabinoids and Temozolomide. *Biochem. Pharmacol.* **2018**, *157*, 266–274. [[CrossRef](#)]
60. Huang, T.; Xu, T.; Wang, Y.; Zhou, Y.; Yu, D.; Wang, Z.; He, L.; Chen, Z.; Zhang, Y.; Davidson, D.; et al. Cannabidiol Inhibits Human Glioma by Induction of Lethal Mitophagy through Activating TRPV4. *Autophagy* **2021**, *17*, 3592–3606. [[CrossRef](#)]
61. Likar, R.; Koestenberger, M.; Stultsch, M.; Nahler, G. Concomitant Treatment of Malignant Brain Tumours With CBD—A Case Series and Review of the Literature. *Anticancer Res.* **2019**, *39*, 5797–5801. [[CrossRef](#)]
62. Leaf Vertical Inc. A Phase I Study of BRX014 to Investigate Dose-Ranging Safety and Pharmacokinetics in Adults with Glioblastoma (GBM) and Non-Methylated MGMT Gene Status; Clinicaltrials.gov: Bethesda, MD, USA, 2019.

63. Ghosh, S. Cisplatin: The First Metal Based Anticancer Drug. *Bioorg. Chem.* **2019**, *88*, 102925. [CrossRef]
64. Pan, H.; Mukhopadhyay, P.; Rajesh, M.; Patel, V.; Mukhopadhyay, B.; Gao, B.; Haskó, G.; Pacher, P. Cannabidiol Attenuates Cisplatin-Induced Nephrotoxicity by Decreasing Oxidative/Nitrosative Stress, Inflammation, and Cell Death. *J. Pharmacol. Exp. Ther.* **2009**, *328*, 708–714. [CrossRef] [PubMed]
65. Kwiatkowska, M.; Parker, L.A.; Burton, P.; Mechoulam, R. A Comparative Analysis of the Potential of Cannabinoids and Ondansetron to Suppress Cisplatin-Induced Emesis in the Suncus Murinus (House Musk Shrew). *Psychopharmacology* **2004**, *174*, 254–259. [CrossRef] [PubMed]
66. Rock, E.M.; Bolognini, D.; Limebeer, C.L.; Cascio, M.G.; Anavi-Goffer, S.; Fletcher, P.J.; Mechoulam, R.; Pertwee, R.G.; Parker, L.A. Cannabidiol, a Non-Psychotropic Component of Cannabis, Attenuates Vomiting and Nausea-like Behaviour via Indirect Agonism of 5-HT_{1A} Somatodendritic Autoreceptors in the Dorsal Raphe Nucleus. *Br. J. Pharmacol.* **2012**, *165*, 2620–2634. [CrossRef] [PubMed]
67. Parker, L.A.; Rock, E.M.; Limebeer, C.L. Regulation of Nausea and Vomiting by Cannabinoids. *Br. J. Pharmacol.* **2011**, *163*, 1411–1422. [CrossRef]
68. Bolognini, D.; Rock, E.M.; Cluny, N.L.; Cascio, M.G.; Limebeer, C.L.; Duncan, M.; Stott, C.G.; Javid, F.A.; Parker, L.A.; Pertwee, R.G. Cannabidiolic Acid Prevents Vomiting in Suncus Murinus and Nausea-Induced Behaviour in Rats by Enhancing 5-HT_{1A} Receptor Activation. *Br. J. Pharmacol.* **2013**, *168*, 1456–1470. [CrossRef]
69. Marinelli, O.; Morelli, M.B.; Annibaldi, D.; Aguzzi, C.; Zeppa, L.; Tuyaerts, S.; Amantini, C.; Amant, F.; Ferretti, B.; Maggi, F.; et al. The Effects of Cannabidiol and Prognostic Role of TRPV2 in Human Endometrial Cancer. *Int. J. Mol. Sci.* **2020**, *21*, 5409. [CrossRef]
70. Fraguas-Sánchez, A.I.; Fernández-Carballido, A.; Delie, F.; Cohen, M.; Martin-Sabroso, C.; Mezzananza, D.; Figini, M.; Satta, A.; Torres-Suárez, A.I. Enhancing Ovarian Cancer Conventional Chemotherapy through the Combination with Cannabidiol Loaded Microparticles. *Eur. J. Pharm. Biopharm.* **2020**, *154*, 246–258. [CrossRef]
71. Raymond, E.; Faivre, S.; Chaney, S.; Woynarowski, J.; Cvitkovic, E. Cellular and Molecular Pharmacology of Oxaliplatin. *Mol. Cancer Ther.* **2002**, *1*, 227–235.
72. Riddell, I.A. Cisplatin and Oxaliplatin: Our Current Understanding of Their Actions. *Met. Ions Life Sci.* **2018**, *18*. [CrossRef]
73. Ozdian, T.; Holub, D.; Maceckova, Z.; Varanasi, L.; Rylava, G.; Rehulka, J.; Vaclavkova, J.; Slavik, H.; Moudry, P.; Znojek, P.; et al. Proteomic Profiling Reveals DNA Damage, Nucleolar and Ribosomal Stress Are the Main Responses to Oxaliplatin Treatment in Cancer Cells. *J. Proteomics* **2017**, *162*, 73–85. [CrossRef]
74. King, K.M.; Myers, A.M.; Soroka-Monzo, A.J.; Tuma, R.F.; Tallarida, R.J.; Walker, E.A.; Ward, S.J. Single and Combined Effects of Δ^9 -Tetrahydrocannabinol and Cannabidiol in a Mouse Model of Chemotherapy-Induced Neuropathic Pain. *Br. J. Pharmacol.* **2017**, *174*, 2832–2841. [CrossRef] [PubMed]
75. Pereira, A.F.; Lisboa, M.R.P.; de Freitas Alves, B.W.; da Silva, C.M.P.; Dias, D.B.S.; de Menezes, K.L.S.; Cesário, F.R.A.S.; de França, J.C.; de Oliveira, A.R.; Hallak, J.E.C.; et al. Endocannabinoid System Attenuates Oxaliplatin-Induced Peripheral Sensory Neuropathy Through the Activation of CB1 Receptors. *Neurotox Res.* **2021**, *39*, 1782–1799. [CrossRef] [PubMed]
76. Jeong, S.; Kim, B.G.; Kim, D.Y.; Kim, B.R.; Kim, J.L.; Park, S.H.; Na, Y.J.; Jo, M.J.; Yun, H.K.; Jeong, Y.A.; et al. Cannabidiol Overcomes Oxaliplatin Resistance by Enhancing NOS3- and SOD2-Induced Autophagy in Human Colorectal Cancer Cells. *Cancers* **2019**, *11*, 781. [CrossRef] [PubMed]
77. Lokich, J.; Anderson, N. Carboplatin versus Cisplatin in Solid Tumors: An Analysis of the Literature. *Ann. Oncol.* **1998**, *9*, 13–21. [CrossRef] [PubMed]
78. Wilkins, A.C.; Rosenfelder, N.; Schick, U.; Gupta, S.; Thway, K.; Nutting, C.M.; Harrington, K.J.; Newbold, K.; Bhide, S.A. Equivalence of Cisplatin and Carboplatin-Based Chemoradiation for Locally Advanced Squamous Cell Carcinoma of the Head and Neck: A Matched-Pair Analysis. *Oral Oncol.* **2013**, *49*, 615–619. [CrossRef] [PubMed]
79. Ho, G.Y.; Woodward, N.; Coward, J.I.G. Cisplatin versus Carboplatin: Comparative Review of Therapeutic Management in Solid Malignancies. *Crit. Rev. Oncol. Hematol.* **2016**, *102*, 37–46. [CrossRef] [PubMed]
80. Oun, R.; Moussa, Y.E.; Wheate, N.J. The Side Effects of Platinum-Based Chemotherapy Drugs: A Review for Chemists. *Dalton Trans.* **2018**, *47*, 6645–6653. [CrossRef]
81. Inkol, J.M.; Hocker, S.E.; Mutsaers, A.J. Combination Therapy with Cannabidiol and Chemotherapeutics in Canine Urothelial Carcinoma Cells. *PLoS ONE* **2021**, *16*, e0255591. [CrossRef]
82. Dumontet, C.; Jordan, M.A. Microtubule-Binding Agents: A Dynamic Field of Cancer Therapeutics. *Nat. Rev. Drug Discov.* **2010**, *9*, 790–803. [CrossRef]
83. Steinmetz, M.O.; Prota, A.E. Microtubule-Targeting Agents: Strategies To Hijack the Cytoskeleton. *Trends Cell Biol.* **2018**, *28*, 776–792. [CrossRef]
84. Parthasarathy, R.; Shanmuganathan, R.; Pugazhendhi, A. Vinblastine Production by the Endophytic Fungus *Curvularia Verruculosa* from the Leaves of *Catharanthus roseus* and Its In Vitro Cytotoxicity against HeLa Cell Line. *Anal. Biochem.* **2020**, *593*, 113530. [CrossRef]
85. Aslam, J.; Khan, S.H.; Siddiqui, Z.H. *Catharanthus roseus* (L.) g. don. an important drug: Its applications and production. *Pharm. Glob.* **2010**, *4*, 1–16.
86. Earhart, R.H.; Khandekar, J.D.; Faraggi, D.; Schinella, R.A.; Davis, T.E. Phase II Trial of Continuous Drug Infusions in Advanced Ovarian Carcinoma: Acivicin versus Vinblastine. *Investig. New Drugs* **1989**, *7*, 255–260. [CrossRef]

87. Wani, M.C.; Taylor, H.L.; Wall, M.E.; Coggon, P.; McPhail, A.T. Plant Antitumor Agents. VI. The Isolation and Structure of Taxol, a Novel Antileukemic and Antitumor Agent from *Taxus Brevifolia*. *J. Am. Chem. Soc.* **1971**, *93*, 2325–2327. [CrossRef] [PubMed]
88. Marupudi, N.I.; Han, J.E.; Li, K.W.; Renard, V.M.; Tyler, B.M.; Brem, H. Paclitaxel: A Review of Adverse Toxicities and Novel Delivery Strategies. *Expert Opin. Drug Saf.* **2007**, *6*, 609–621. [CrossRef] [PubMed]
89. Ward, S.J.; Ramirez, M.D.; Neelakantan, H.; Walker, E.A. Cannabidiol Prevents the Development of Cold and Mechanical Allodynia in Paclitaxel-Treated Female C57Bl6 Mice. *Anesth Analg.* **2011**, *113*, 947–950. [CrossRef] [PubMed]
90. Ward, S.J.; McAllister, S.D.; Kawamura, R.; Murase, R.; Neelakantan, H.; Walker, E.A. Cannabidiol Inhibits Paclitaxel-Induced Neuropathic Pain through 5-HT_{1A} Receptors without Diminishing Nervous System Function or Chemotherapy Efficacy. *Br. J. Pharmacol.* **2014**, *171*, 636–645. [CrossRef]
91. Baron, R.; Binder, A.; Wasner, G. Neuropathic Pain: Diagnosis, Pathophysiological Mechanisms, and Treatment. *Lancet Neurol* **2010**, *9*, 807–819. [CrossRef]
92. Brennehan, D.E.; Kinney, W.A.; Ward, S.J. Knockdown siRNA Targeting the Mitochondrial Sodium-Calcium Exchanger-1 Inhibits the Protective Effects of Two Cannabinoids Against Acute Paclitaxel Toxicity. *J. Mol. Neurosci.* **2019**, *68*, 603–619. [CrossRef]
93. Foss, J.D.; Farkas, D.J.; Huynh, L.M.; Kinney, W.A.; Brennehan, D.E.; Ward, S.J. Behavioural and Pharmacological Effects of Cannabidiol (CBD) and the Cannabidiol Analogue KLS-13019 in Mouse Models of Pain and Reinforcement. *Br. J. Pharmacol.* **2021**, *178*, 3067–3078. [CrossRef]
94. Fraguas-Sánchez, A.I.; Fernández-Carballido, A.; Simancas-Herbada, R.; Martín-Sabroso, C.; Torres-Suárez, A.I. CBD Loaded Microparticles as a Potential Formulation to Improve Paclitaxel and Doxorubicin-Based Chemotherapy in Breast Cancer. *Int. J. Pharm.* **2020**, *574*, 118916. [CrossRef] [PubMed]
95. Alsherbiny, M.A.; Bhuyan, D.J.; Low, M.N.; Chang, D.; Li, C.G. Synergistic Interactions of Cannabidiol with Chemotherapeutic Drugs in MCF7 Cells: Mode of Interaction and Proteomics Analysis of Mechanisms. *Int. J. Mol. Sci.* **2021**, *22*, 10103. [CrossRef]
96. Sainz-Cort, A.; Müller-Sánchez, C.; Espel, E. Anti-Proliferative and Cytotoxic Effect of Cannabidiol on Human Cancer Cell Lines in Presence of Serum. *BMC Res. Notes* **2020**, *13*, 389. [CrossRef] [PubMed]
97. Cortes, J.E.; Pazdur, R. Docetaxel. *J. Clin. Oncol.* **1995**, *13*, 2643–2655. [CrossRef]
98. Zhang, E.; Xing, R.; Liu, S.; Li, P. Current Advances in Development of New Docetaxel Formulations. *Expert Opin. Drug Deliv.* **2019**, *16*, 301–312. [CrossRef]
99. De Petrocellis, L.; Ligresti, A.; Schiano Moriello, A.; Iappelli, M.; Verde, R.; Stott, C.G.; Cristino, L.; Orlando, P.; Di Marzo, V. Non-THC Cannabinoids Inhibit Prostate Carcinoma Growth in Vitro and in Vivo: Pro-Apoptotic Effects and Underlying Mechanisms. *Br. J. Pharmacol.* **2013**, *168*, 79–102. [CrossRef] [PubMed]
100. Mohammadgholi, A.; Rabbani-Chadegani, A.; Fallah, S. Mechanism of the Interaction of Plant Alkaloid Vincristine with DNA and Chromatin: Spectroscopic Study. *DNA Cell Biol.* **2013**, *32*, 228–235. [CrossRef] [PubMed]
101. Michlitsch, J.; Larkin, S.; Vichinsky, E.; Kuypers, F.A. Vincristine-Induced Anemia in Hereditary Spherocytosis. *Exp. Biol. Med.* **2019**, *244*, 850–854. [CrossRef]
102. Holland, M.L.; Allen, J.D.; Arnold, J.C. Interaction of Plant Cannabinoids with the Multidrug Transporter ABCB1 (MRP1). *Eur. J. Pharmacol.* **2008**, *591*, 128–131. [CrossRef]
103. Henry, J.G.; Shoemaker, G.; Prieto, J.M.; Hannon, M.B.; Wakshlag, J.J. The Effect of Cannabidiol on Canine Neoplastic Cell Proliferation and Mitogen-Activated Protein Kinase Activation during Autophagy and Apoptosis. *Vet. Comp. Oncol.* **2021**, *19*, 253–265. [CrossRef]
104. Dall’Stella, P.B.; Docema, M.F.L.; Maldaun, M.V.C.; Feher, O.; Lancellotti, C.L.P. Case Report: Clinical Outcome and Image Response of Two Patients With Secondary High-Grade Glioma Treated With Chemoradiation, PCV, and Cannabidiol. *Front. Oncol.* **2018**, *8*, 643. [CrossRef]
105. Douedi, S.; Carson, M.P. Anthracycline Medications (Doxorubicin). In *StatPearls*; StatPearls Publishing: Treasure Island, FL, USA, 2022.
106. Minotti, G.; Menna, P.; Salvatorelli, E.; Cairo, G.; Gianni, L. Anthracyclines: Molecular Advances and Pharmacologic Developments in Antitumor Activity and Cardiotoxicity. *Pharmacol. Rev.* **2004**, *56*, 185–229. [CrossRef] [PubMed]
107. Carvalho, C.; Santos, R.X.; Cardoso, S.; Correia, S.; Oliveira, P.J.; Santos, M.S.; Moreira, P.I. Doxorubicin: The Good, the Bad and the Ugly Effect. *Curr. Med. Chem.* **2009**, *16*, 3267–3285. [CrossRef] [PubMed]
108. Speth, P.A.; van Hoesel, Q.G.; Haanen, C. Clinical Pharmacokinetics of Doxorubicin. *Clin. Pharm.* **1988**, *15*, 15–31. [CrossRef] [PubMed]
109. Hao, E.; Mukhopadhyay, P.; Cao, Z.; Erdélyi, K.; Holovac, E.; Liaudet, L.; Lee, W.-S.; Haskó, G.; Mechoulam, R.; Pacher, P. Cannabidiol Protects against Doxorubicin-Induced Cardiomyopathy by Modulating Mitochondrial Function and Biogenesis. *Mol. Med.* **2015**, *21*, 38–45. [CrossRef]
110. Fouad, A.A.; Albuali, W.H.; Al-Mulhim, A.S.; Jresat, I. Cardioprotective Effect of Cannabidiol in Rats Exposed to Doxorubicin Toxicity. *Environ. Toxicol. Pharmacol.* **2013**, *36*, 347–357. [CrossRef]
111. Neumann-Raizel, H.; Shilo, A.; Lev, S.; Mogilevsky, M.; Katz, B.; Shneur, D.; Shaul, Y.D.; Leffler, A.; Gabizon, A.; Karni, R.; et al. 2-APB and CBD-Mediated Targeting of Charged Cytotoxic Compounds Into Tumor Cells Suggests the Involvement of TRPV2 Channels. *Front. Pharmacol.* **2019**, *10*, 1198. [CrossRef]
112. Elbaz, M.; Ahirwar, D.; Xiaoli, Z.; Zhou, X.; Lustberg, M.; Nasser, M.W.; Shilo, K.; Ganju, R.K. TRPV2 Is a Novel Biomarker and Therapeutic Target in Triple Negative Breast Cancer. *Oncotarget* **2016**, *9*, 33459–33470. [CrossRef]

113. Patel, N.; Kommineni, N.; Surapaneni, S.K.; Kalvala, A.; Yaun, X.; Gebeyehu, A.; Arthur, P.; Duke, L.C.; York, S.B.; Bagde, A.; et al. Cannabidiol Loaded Extracellular Vesicles Sensitize Triple-Negative Breast Cancer to Doxorubicin in Both in-Vitro and in Vivo Models. *Int. J. Pharm.* **2021**, *607*, 120943. [\[CrossRef\]](#)
114. Surapaneni, S.K.; Patel, N.; Sun, L.; Kommineni, N.; Kalvala, A.K.; Gebeyehu, A.; Arthur, P.; Duke, L.C.; Nimma, R.; G Meckes, D.; et al. Anticancer and Chemosensitization Effects of Cannabidiol in 2D and 3D Cultures of TNBC: Involvement of GADD45 α , Integrin-A5, -B5, -B1, and Autophagy. *Drug Deliv. Transl. Res.* **2022**. [\[CrossRef\]](#)
115. Deshaies, R.J. Proteotoxic Crisis, the Ubiquitin-Proteasome System, and Cancer Therapy. *BMC Biol.* **2014**, *12*, 94. [\[CrossRef\]](#) [\[PubMed\]](#)
116. Bastola, P.; Oien, D.B.; Cooley, M.; Chien, J. Emerging Cancer Therapeutic Targets in Protein Homeostasis. *AAPS J.* **2018**, *20*, 94. [\[CrossRef\]](#) [\[PubMed\]](#)
117. Manasanch, E.E.; Orłowski, R.Z. Proteasome Inhibitors in Cancer Therapy. *Nat. Rev. Clin. Oncol.* **2017**, *14*, 417–433. [\[CrossRef\]](#)
118. Scott, K.; Hayden, P.J.; Will, A.; Wheatley, K.; Coyne, I. Bortezomib for the Treatment of Multiple Myeloma. *Cochrane Database Syst. Rev.* **2016**, *4*, CD010816. [\[CrossRef\]](#) [\[PubMed\]](#)
119. Morelli, M.B.; Offidani, M.; Alesiani, F.; Discepoli, G.; Liberati, S.; Olivieri, A.; Santoni, M.; Santoni, G.; Leoni, P.; Nabissi, M. The Effects of Cannabidiol and Its Synergism with Bortezomib in Multiple Myeloma Cell Lines. A Role for Transient Receptor Potential Vanilloid Type-2. *Int. J. Cancer* **2014**, *134*, 2534–2546. [\[CrossRef\]](#) [\[PubMed\]](#)
120. Meraz-Torres, F.; Plöger, S.; Garbe, C.; Niessner, H.; Sinnberg, T. Disulfiram as a Therapeutic Agent for Metastatic Malignant Melanoma—Old Myth or New Logos? *Cancers* **2020**, *12*, 3538. [\[CrossRef\]](#) [\[PubMed\]](#)
121. University of Utah. *A Phase I Study of Disulfiram and Copper Gluconate in Patients with Treatment-Refractory Multiple Myeloma*; Clinicaltrials.gov: Bethesda, MD, USA, 2022.
122. The Institute of Molecular and Translational Medicine, Czech Republic. *Phase II Open Labeled Trial of Disulfiram with Copper in Metastatic Breast Cancer*; Clinicaltrials.gov: Bethesda, MD, USA, 2021.
123. National Cancer Institute, Slovakia. *Phase II Study of Disulfiram and Cisplatin in Refractory TGCT*; Clinicaltrials.gov: Bethesda, MD, USA, 2020.
124. Chroma, K.; Skrott, Z.; Gursky, J.; Bacovsky, J.; Moudry, P.; Buchtova, T.; Mistrik, M.; Bartek, J. A Drug Repurposing Strategy for Overcoming Human Multiple Myeloma Resistance to Standard-of-Care Treatment. *Cell Death Dis.* **2022**, *13*, 1–11. [\[CrossRef\]](#) [\[PubMed\]](#)
125. Skrott, Z.; Mistrik, M.; Andersen, K.K.; Friis, S.; Majera, D.; Gursky, J.; Ozdian, T.; Bartkova, J.; Turi, Z.; Moudry, P.; et al. Alcohol-Abuse Drug Disulfiram Targets Cancer via P97 Segregase Adaptor NPL4. *Nature* **2017**, *552*, 194–199. [\[CrossRef\]](#)
126. Meyer, H.; Bug, M.; Bremer, S. Emerging Functions of the VCP/P97 AAA-ATPase in the Ubiquitin System. *Nat. Cell Biol.* **2012**, *14*, 117–123. [\[CrossRef\]](#)
127. Buchtova, T.; Skrott, Z.; Chroma, K.; Rehulka, J.; Dzubak, P.; Hajduch, M.; Lukac, D.; Arampatzis, S.; Bartek, J.; Mistrik, M. Cannabidiol-Induced Activation of the Metallothionein Pathway Impedes Anticancer Effects of Disulfiram and Its Metabolite CuET. *Mol. Oncol.* **2021**. [\[CrossRef\]](#)
128. Liang, X.; Wu, Q.; Luan, S.; Yin, Z.; He, C.; Yin, L.; Zou, Y.; Yuan, Z.; Li, L.; Song, X.; et al. A Comprehensive Review of Topoisomerase Inhibitors as Anticancer Agents in the Past Decade. *Eur. J. Med. Chem.* **2019**, *171*, 129–168. [\[CrossRef\]](#)
129. Staker, B.L.; Hjerrild, K.; Feese, M.D.; Behnke, C.A.; Burgin, A.B.; Stewart, L. The Mechanism of Topoisomerase I Poisoning by a Camptothecin Analog. *Proc. Natl. Acad. Sci. USA* **2002**, *99*, 15387–15392. [\[CrossRef\]](#)
130. Devriese, L.A.; Witteveen, P.E.O.; Mergui-Roelvink, M.; Smith, D.A.; Lewis, L.D.; Mendelson, D.S.; Bang, Y.-J.; Chung, H.C.; Dar, M.M.; Huitema, A.D.R.; et al. Pharmacodynamics and Pharmacokinetics of Oral Topotecan in Patients with Advanced Solid Tumours and Impaired Renal Function. *Br. J. Clin. Pharmacol.* **2015**, *80*, 253–266. [\[CrossRef\]](#)
131. McLennan, A.; Kerba, M.; Subnis, U.; Campbell, T.; Carlson, L.E. Health Care Provider Preferences for, and Barriers to, Cannabis Use in Cancer Care. *Curr. Oncol.* **2020**, *27*, e199–e205. [\[CrossRef\]](#)
132. Mangelinck, A.; da Costa, M.E.M.; Stefanovska, B.; Bawa, O.; Polrot, M.; Gaspar, N.; Fromigué, O. MT2A Is an Early Predictive Biomarker of Response to Chemotherapy and a Potential Therapeutic Target in Osteosarcoma. *Sci. Rep.* **2019**, *9*, 12301. [\[CrossRef\]](#)
133. Merlos Rodrigo, M.A.; Jimenez Jimenez, A.M.; Haddad, Y.; Bodoor, K.; Adam, P.; Krizkova, S.; Heger, Z.; Adam, V. Metallothionein Isoforms as Double Agents—Their Roles in Carcinogenesis, Cancer Progression and Chemoresistance. *Drug Resist. Updat.* **2020**, *52*, 100691. [\[CrossRef\]](#)

Disclaimer/Publisher's Note: The statements, opinions and data contained in all publications are solely those of the individual author(s) and contributor(s) and not of MDPI and/or the editor(s). MDPI and/or the editor(s) disclaim responsibility for any injury to people or property resulting from any ideas, methods, instructions or products referred to in the content.

A drug repurposing strategy for overcoming human multiple myeloma resistance to standard-of-care treatment

Katarina Chroma¹, Zdenek Skrott¹, Jan Gursky¹, Jaroslav Bacovsky², Pavel Moudry³, Tereza Buchtova³, Martin Mistrik^{1,4} and Jiri Bartek^{1,3,4}

© The Author(s) 2022

Despite several approved therapeutic modalities, multiple myeloma (MM) remains an incurable blood malignancy and only a small fraction of patients achieves prolonged disease control. The common anti-MM treatment targets proteasome with specific inhibitors (PI). The resulting interference with protein degradation is particularly toxic to MM cells as they typically accumulate large amounts of toxic proteins. However, MM cells often acquire resistance to PIs through aberrant expression or mutations of proteasome subunits such as PSMB5, resulting in disease recurrence and further treatment failure. Here we propose CuET—a proteasome-like inhibitor agent that is spontaneously formed in-vivo and in-vitro from the approved alcohol-abuse drug disulfiram (DSF), as a readily available treatment effective against diverse resistant forms of MM. We show that CuET efficiently kills also resistant MM cells adapted to proliferate under exposure to common anti-myeloma drugs such as bortezomib and carfilzomib used as the first-line therapy, as well as to other experimental drugs targeting protein degradation upstream of the proteasome. Furthermore, CuET can overcome also the adaptation mechanism based on reduced proteasome load, another clinically relevant form of treatment resistance. Data obtained from experimental treatment-resistant cellular models of human MM are further corroborated using rather unique advanced cytotoxicity experiments on myeloma and normal blood cells obtained from fresh patient biopsies including newly diagnosed as well as relapsed and treatment-resistant MM. Overall our findings suggest that disulfiram repurposing particularly if combined with copper supplementation may offer a promising and readily available treatment option for patients suffering from relapsed and/or therapy-resistant multiple myeloma.

Cell Death and Disease (2022)13:203; <https://doi.org/10.1038/s41419-022-04651-w>

INTRODUCTION

Multiple myeloma (MM), the second most frequent hematologic malignancy represents a still incurable plasma cell disease [1, 2]. MM cells originating from antibody-producing B cells usually maintain immunoglobulin production, thereby causing endogenous proteotoxic stress and sensitivity to drugs targeting protein degradation. For many MM patients, the first-line therapy includes the proteasome inhibitor (PI) bortezomib, which significantly improves patients' outcomes. However, disease relapse usually follows in bortezomib-treated patients. To overcome the acquired bortezomib resistance, the second and third generation of PIs were developed, including carfilzomib and ixazomib, or marizomib and oprozomib currently undergoing clinical evaluation. While these drugs differ from each other by pharmacodynamic properties or route of administration, all target the 20S proteasome, raising the possibility of cross-resistance among them if the mode of resistance reflects mutations of active proteasome subunits (e.g. PSMB5) or altered expression of proteasome subunit [3, 4]. To overcome this limitation, alternative approaches to target proteasome or more generally the

ubiquitin-proteasome degradation system (UPS) are under pre-clinical testing for MM treatment. These approaches include targeting 19S proteasome components such as deubiquitinases POH1 [5] and USP14/UCHL5 [6] or ubiquitin-binding receptor RPN13 [7]. These inhibitors were effective against MM in vitro and in vivo, induced accumulation of ubiquitinated proteins, and activation of the cellular unfolded protein response (UPR) – a stress pathway leading to cell death [8–10]. The UPS machinery can be therapeutically targeted also at other steps besides the proteasome, by inhibition of the ubiquitin-activating enzyme (UEA1) by TAK-243 [11] or inhibition of p97/VCP segregase upstream of the proteasome – by CB5083 [12]. Both these compounds showed robust anti-MM activities in vitro and in vivo, accompanied by accumulation of non-degraded proteins and activation of the UPR [13–15]. While these molecular targets could possibly overcome the bortezomib/carfilzomib resistance caused by mutations in the proteasome subunits, such prediction is uncertain concerning other modes of resistance. Moreover, the point mutation within proteasome subunits abolishing bortezomib activity was so far found only in one study [4] but not by

¹Laboratory of Genome Integrity, Institute of Molecular and Translational Medicine, Faculty of Medicine and Dentistry, Palacky University, Olomouc, Czech Republic. ²Department of Hemato-oncology, University Hospital Olomouc and Medical Faculty of Palacky University Olomouc, Olomouc, Czech Republic. ³Danish Cancer Society Research Center, Copenhagen, Denmark. ⁴Division of Genome Biology, Department of Medical Biochemistry and Biophysics, Science for Life Laboratory, Karolinska Institute, Stockholm, Sweden. [✉]email: martin.mistrik@upol.cz; jib@cancer.dk
Edited by Professor Gerry Melino

Received: 19 October 2021 Revised: 28 January 2022 Accepted: 14 February 2022
Published online: 04 March 2022

others [16, 17] suggesting the rarity of nonrecurring mutations or polyploidy of proteasome subunits [18]. Accumulating evidence indicates that therapy resistance can reflect complex metabolic changes and clonal evolution of MM cells. For example treatment resistance in some MM patients can reflect expansion of $Xbp1^{low}$ B tumor cells and pre-plasmablasts which are intrinsically resistant to bortezomib due to lower immunoglobulin production and decreased proteasome load [19], thus supporting the load-versus-capacity theory [20]. Others confirmed a correlation of the low-level XBP1s and immunoglobulin production with poor responses to bortezomib therapy [21] or decreased sensitivity in vitro [22]. In terms of the MM secretory status, patients with measurable disease responded to bortezomib better than oligo- or non-secretory MM patients [23] consistent with Ig production/secretion sensitizing MM to bortezomib [24]. Some studies reported MM cell dedifferentiation and clonal propagation of pre-plasma cells during therapy [25, 26]. In such cases of bortezomib resistance, it is unclear whether alternative approaches of targeting the proteasome or UPS, in general, might be effective because such treatments still rely on the induction of ER stress and UPR-mediated cell death, scenarios potentially difficult to trigger in dedifferentiated, less secretory pre-plasma MM cells.

Here, we assessed Disulfiram (Antabuse), a well-tolerated alcohol-abuse drug and a promising candidate for repurposing in oncology [27–30]. In the context of MM, DSF might be particularly interesting because its anticancer activity is related to the CuET metabolite which is spontaneously formed in-vivo and in-vitro in the presence of copper ions [31]. CuET shows proteasome-like inhibitory effects via aggregation of NPL4 (an essential adaptor of p97) and induction of UPR in a broad range of cell lines [31]. We previously reported anti-MM efficacy of CuET for both in-vitro and in-vivo models [31]. In this study, we examine whether CuET may act similarly to the p97 inhibitor CBS083 (not approved clinically) and overcome resistance to proteasome inhibitors mediated by mutations of active proteasome subunits (e.g. PSMB5) or altered expression of proteasome subunits. Moreover, as CuET induces aggregation of NPL4 and some other proteins directly, we propose that it might trigger the UPR independently of the extent of endogenous proteotoxic stress and/or disbalance of other, non-UPS cancer-relevant pathways, such as through triggering replication stress which was also reported among CuET-induced effects [32].

RESULTS

CuET immobilizes NPL4, activates UPR and HSP in MM cell lines

Previously, we reported higher CuET sensitivity of myeloma cells than cell lines from other types of cancer [31]. Here, we first verified the enhanced CuET responsiveness in human AMO1 and MM1.S myeloma cell lines compared with breast cancer-derived MDA-MB-231 and osteosarcoma U2OS cells (Supplementary Fig. S1A, S1B) which are good CuET responders [31]. To elucidate the mechanism behind the MM hypersensitivity we first assessed the endogenous levels of VCP/p97 and its adaptor NPL4, the known target of CuET [31]. Among a series of cancer cell lines (Supplementary Fig. S1C), the abundance of NPL4 was variable, yet without any obvious correlation explaining the sensitivity. Next, we compared the extent of endogenous proteotoxic stress using K48-ubiquitin (K48-Ub) smears as readouts. Both AMO1 and MM1.S cells showed elevated K48-Ub smears compared to MDA-MB-231 and U2OS cells suggesting a relationship to CuET-sensitivity (Supplementary Fig. S1C) as the p97/NPL4 pathway is directly involved in the processing of K48-ubiquitylated proteins [33]. As MM cells grow in suspension, we assessed whether CuET induces the same phenotypes as published for other cell lines including proteasome-inhibition-like response, UPR and heat-shock response (HSR) [31]. CuET-exposed MM cells indeed accumulate polyubiquitinated

(poly-Ub) proteins in a dose-dependent manner (Fig. 1A), a feature typically shared with PIs such as bortezomib or MG132. Also, UPR components were elevated, including the spliced form of XBP1s and ATF4 and overabundant chaperone HSP70, the key HSR component, in both CuET-treated MM cell lines (Fig. 1B). Next, we asked whether CuET immobilizes NPL4 in MM cells, as reported for U2OS and MDA-MB-231 cells [31]. Indeed, the CuET-induced immobilization of endogenous NPL4 was confirmed by immunoblotting analysis of detergent-insoluble cellular fractions in both MM cell lines (Fig. 1B). Consistently with published data, the insoluble fractions were also enriched for polyubiquitinated proteins and HSP70 (Fig. 1B).

Accumulation of poly-Ub proteins, UPR, and HSR activation are features of CuET treatment shared with PIs [34] clinically used for MM treatment [35]. However, the observed enrichment of insoluble poly-Ub proteins and HSP70 seems to be a unique effect induced only by CuET. This effect is well apparent by immunofluorescence analysis where the increased proteotoxic stress (elevated K48-Ub) and HSP70 are detectable for CuET and BTZ in non-pre-extracted cells but upon Triton-X-100 pre-extraction, only CuET-treated cells show such signals (Fig. 1C). Collectively, these data indicate that in AMO1 and MM1.S MM models, CuET induces phenotypes shared with adherent cancer cell lines, and despite these phenotypes share some features with PI effects, there are also responses unique to CuET.

CuET toxicity against MM is unaffected by PSMB5 mutation responsible for resistance to PI

DSF reacts with copper ions in-vitro and in-vivo, ultimately forming the active metabolite CuET with PI-like activity [36]. Despite some reports suggesting proteasome as the direct target of DSF/Copper treatment, we demonstrated that neither 20 S nor 26 S proteasome is affected by DSF or CuET [31]. Instead, CuET acts upstream of the proteasome by interference with the p97/NPL4 segregase involved in pre-processing of proteins destined for degradation [31]. Consistent with such mode of action, any acquired resistance that involves proteasome modification should not affect the sensitivity of MM cells towards CuET. Recently, Barrio and colleagues [4] identified three somatic point mutations in proteasome subunit *PSMB5* as the underlying cause for resistance in MM cells chronically exposed to BTZ. We obtained two such cell lines including Bortezomib (Carfilzomib, Ixazomib)-resistant variants of AMO1 and L363 [4]. The wild-type (wt) AMO1 and L363 cell lines together with their sublines bearing two somatic *PSMB5* mutations (A20T, M45I) were tested for sensitivity to BTZ and CuET. As expected, overexpression of mutant *PSMB5* in either cell line induced BTZ resistance (Fig. 2A). In contrast, CuET decreased the cell viability regardless of the mutations (Fig. 2A), increased K48-Ub in the *PSMB5*-mutant cell lines similarly to the wild-type and also induced the same amount of immobilized poly-Ub proteins. The insoluble fraction was also enriched similarly for NPL4, P97, and HSP70 in the wt and mutant models (Fig. 2B). These results show that the CuET-induced 20 S proteasome-independent blockade of the proteolysis machinery remains still effective in cells with the clinically relevant proteasome *PSMB5* subunit mutations.

The cytotoxic effect of CuET is unaffected by reduced protein synthesis

One of the suggested resistance mechanisms of MM cells towards PIs reflects attenuated proteosynthetic activity. In such settings, the clinically relevant PIs become inefficient because the proteasome workload/capacity and extent of protein synthesis are closely interconnected [20]. Notably, such a universal resistance mechanism of MM cells might impact also responses to inhibitors targeting the protein degradation upstream of proteasome, including p97 inhibitors. This idea has however never been tested. The proteosynthesis-based

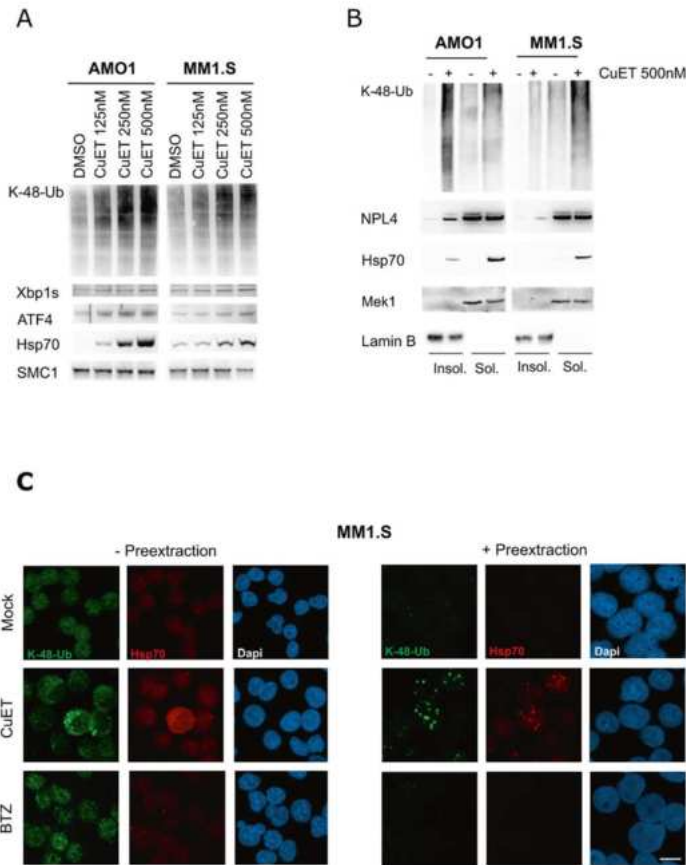


Fig. 1 Exposure to submicromolar CuET induces proteotoxic stress, protein aggregation, and activation of UPR and heat-shock pathways in MM cell lines. **A** CuET induces poly-ubiquitinated proteins (K-48-Ub), increases XBP1s and ATF4 proteins (markers of unfolded protein response, UPR), and accumulates heat shock protein HSP70 in AMO1 and MM1.S myeloma cell lines. **B** Immobilization of NPL4, HSP70, and K48-Ub- proteins in Triton X-100 pre-extracted pellet fraction of CuET-treated (500 nM, 5 h) AMO1 and MM1.S cells. **C** Immunofluorescence analysis of CuET (500 nM) and BTZ (10 nM) induced K48- poly-Ub proteins together with HSP70 in MM cell lines without/with pre-extraction step (5 h treatment). Scale 10 μ M.

resistance mechanism can be experimentally tested in MM cell lines by co-treatment with cycloheximide (CHX), an inhibitor of protein synthesis at translational level [37]. Indeed, co-treatment with CHX and BTZ indeed rescued the bulk of AMO1 and MM1.S cells from BTZ-induced reduction of cell viability (Fig. 3A and Supplementary Fig. S2). The same rescue effect was detected also for CB5083 (a selective inhibitor of p97) (Fig. 3A and Supplementary Fig. S2). Surprisingly, in contrast to this, the protective effect of CHX was not observed in MM cells treated by CuET, where the drop of cell survival almost recapitulated the outcome of treatment by CuET alone (Fig. 3A and Supplementary Fig. S2). To elucidate this effect, we examined the accumulation of K48-linked poly-Ub proteins in single-compound treated and co-treated cells. Interestingly, only CuET accumulated K48-linked poly-Ub proteins in combination with

CHX (Fig. 3B). Next, we employed yet another cellular model: the BTZ-adapted myeloma cell line AMO1-abzb, established by chronic exposure of AMO1 cells to bortezomib, displaying altered proteasome system and reduced proteo-synthesis [38]. First, we compared the AMO1-wt and AMO1-abzb cells' proteo-synthesis levels using the OPP click assay. As expected, AMO1-abzb showed reduced overall proteo-synthesis (Fig. 4A) and fewer K-48 poly Ub-proteins (Supplementary Fig. S3) suggesting an overall lower proteotoxic stress. Next, we examined the sensitivity of the AMO1-wt versus AMO1-abzb cells towards BTZ, CB5083, and CuET. As expected, AMO1-abzb cells were resistant to BTZ and cross-resistant to CB5083, at least at lower concentrations (Fig. 4B). Strikingly, both cell lines showed similar concentration-dependent decrease of cell viability when treated by CuET (Fig. 4B). In contrast to BTZ, CuET and also

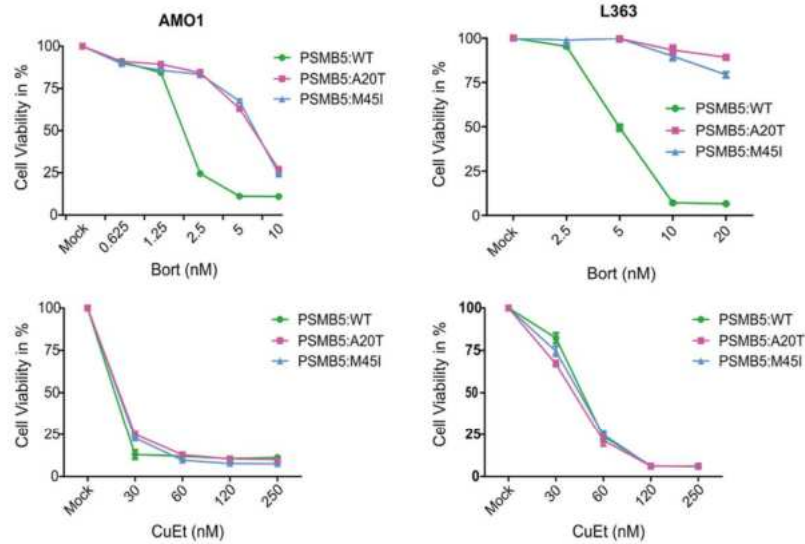
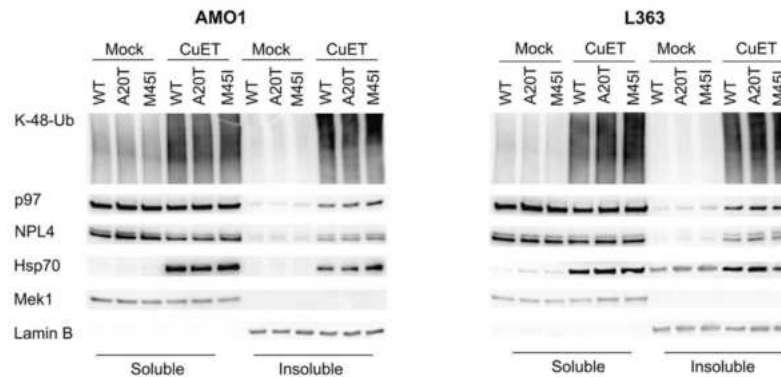
A**B**

Fig. 2 *PSMB5* mutations do not protect MM cells from CuET toxicity. **A** XTT-based viability test after 72 h treatment of indicated concentrations of BTZ or CuET in AMO1 (left) and L363 (right) sublines with mutated *PSMB5* proteasome subunit (A20T, M45I) compared to the WT counterparts. Data are mean \pm s.d. of three independent experiments. **B** CuET induces immobilization of NPL4, P97, poly-Ub proteins, and HSP70 in the insoluble fraction of WT, as well as *PSMB5*, mutated sublines of AMO1 and L363.

CB5083 treatments of both parental and BTZ-resistant AMO1 led to UPR activation detected by enhanced UPR-associated proapoptotic protein Chop (Fig. 4C) accompanied by apoptosis (Supplementary Fig. S4). Furthermore, in both cell lines, CuET induced additional accumulation of K-48 poly Ub-proteins and

enrichment of NPL4 and HSP70 in the insoluble fractions (Fig. 4D). Notably, the combined DSF + Cu treatment closely mimicked the cell survival effects obtained upon treatment with CuET (Fig. 4B), further confirming previous observations that these two treatment strategies are interchangeable [36].

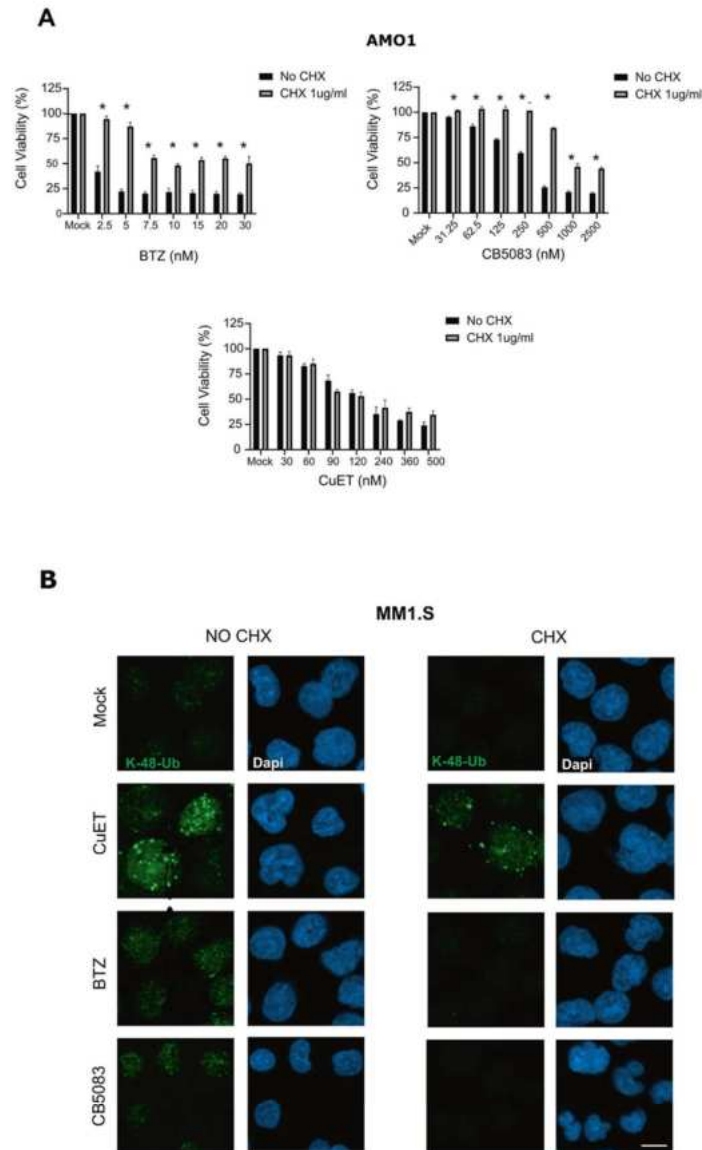
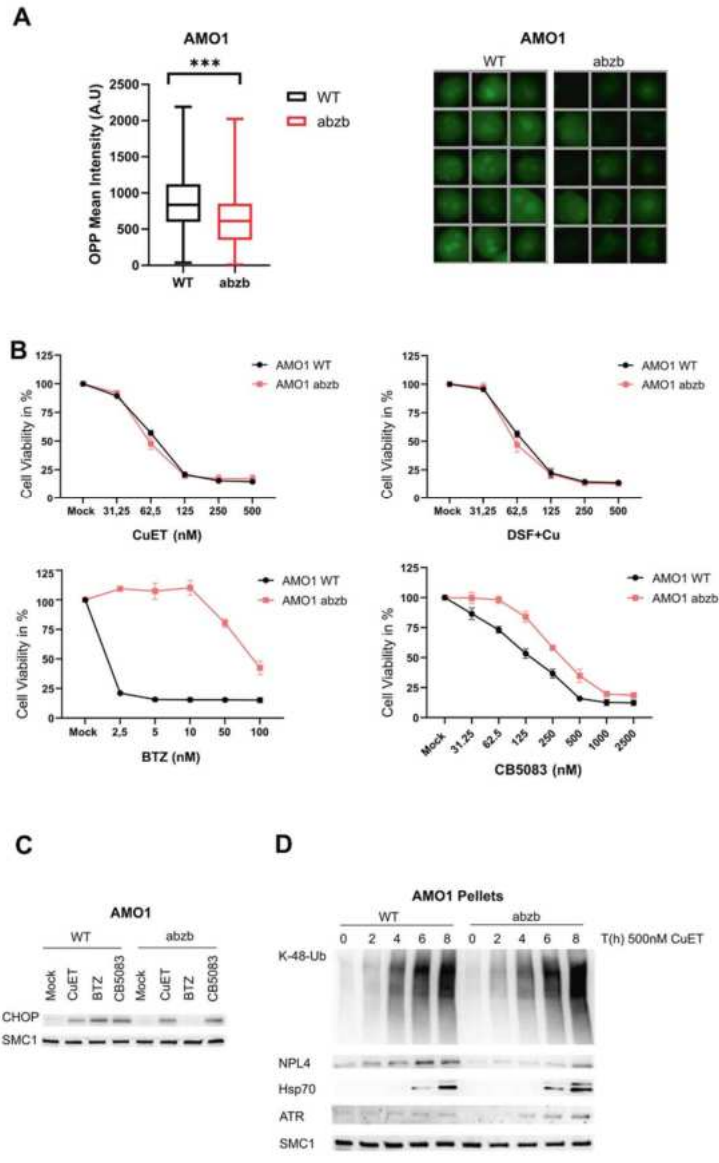


Fig. 3 Protein synthesis rate does not affect the cytotoxic impact of CuET. **A** Co-treatment with cycloheximide (CHX) does not rescue AMO1 cell death in CuET-treated samples in contrast to BTZ and p97 inhibitor (CBS5083). AMO1 cells were cultured for 24 h in the presence of the indicated doses of CuET, BTZ, and CBS5083 in the presence or absence of 1 μ g/ml CHX. Data are mean \pm s.d. of three independent experiments. Statistical significance was determined using T-test, * $P < 0,03$. **B** CHX does not reduce CuET-induced accumulation of poly-Ub proteins when compared to BTZ, CBS5083, and Mock (DMSO) treated samples. MM1.S were treated by 500 nM CuET, 2.5 nM BTZ or 10 μ M CBS5083 and co-treated with CHX 10 μ g/ml. After 3 h the cells were either pre-extracted and fixed or directly fixed and stained for K48-Ub. Scale 10 μ m.



CuET kills CD319⁺ MM patients' cells independently of disease stage and therapy

To validate the specific cytotoxic effect of CuET in MM seen in cell culture models also in clinical settings, we examined bone marrow samples from 14 patients (male and female) diagnosed with MM

or Monoclonal gammopathy of undetermined significance (MGUS). The ex-vivo testing setup involved depletion of red blood cells from fresh bone marrow biopsies followed by CuET treatment (100 nM and 500 nM for 24 h). In each sample, the MM cells were identified by flow cytometry using anti-CD-319-PE and

Fig. 4 MM cells adapted to bortezomib via decreased proteosynthesis remain sensitive to CuET treatment. **A** Bortezomib-adapted (BTZ res) AMO1 abzb cell line has reduced protein biosynthesis compared to parental AMO1, measured by OPP-Click assay. Representative microscopic images from the quantification of the OPP-Click signal are included. Results are mean \pm s.d. of three independent experiments. Statistical significance was determined using T-test, $***P \leq 0,0001$. **B** BTZ-adapted AMO1 abzb and non-adapted AMO1 cells are equally sensitive to treatment with CuET and DSF + Cu. Cells were cultured for 48 h with indicated doses of CuET, DSF, BTZ, and CB5083. **C** CuET and CB5083 activate the UPR pathway in AMO1 abzb similarly to the parental AMO1, measured by induction of pro-apoptotic protein CHOP. Cells were treated for 14 h with 250 nM CuET, 5 nM BTZ, and 250 nM CB5083 and subsequently lysed and probed for the level of CHOP protein. **D** CuET triggers the formation of protein aggregates in AMO1 abzb similar to the parental AMO1. Western blot detection of CuET-response associated K-48-Ub proteins, NPL4, HSP70 in Triton X-100 resistant protein fraction. Cells were treated with 500 nM CuET and lysed in indicated timepoints.

anti-CD-138-APC antibodies [39–42]. The separated noncancerous (CD319⁻) and cancerous (CD319⁺) cell fractions were examined for cell viability using plasma membrane permeabilization (DAPI positive). These results showed cytotoxic effect of CuET preferentially against the CD319⁺ MM cells independently of disease stage (MGUS or MM) and ongoing therapy (Fig. 5A–F). Thus, CuET induced cell death of CD319⁺ cells derived from patients diagnosed for MGUS (Fig. 5A), a patient diagnosed for MM having no previous therapy (Fig. 5B) as well as a MM patient under BTZ therapy (Fig. 5C). Importantly, we detected the cytotoxic effect of CuET also in the sample from a patient who relapsed after a 2-year disease-free period (Fig. 5D) and from two MM patients exhibiting resistance to all combinations of available clinically used anti-MM drugs (Fig. 5E, F). The latter included prior combinatory therapy by PIs, immunomodulatory and alkylating antineoplastic drugs usually prescribed to resistant, relapsed, and refractory myeloma patients. Overall, this data not only identify CuET as a plausible new therapeutic strategy for patients diagnosed with MM independently of disease stage and therapy history but also highlight an innovative and promising treatment approach for patients currently regarded as incurable, resistant to the full spectrum of currently available anti-MM drugs.

DISCUSSION

Proteasome inhibitors such as bortezomib constitute the first-line anti-MM therapy, however, acquired resistance occurs commonly [43]. Here, we provide evidence that the alcohol-abuse drug disulfiram could be a promising candidate for repurposing in treatment-resistant MM. The anticancer effect of DSF has been tested in numerous clinical trials [44]. From the mechanistic point of view, the hypothesis about DSF's anticancer effect being linked to inhibition of aldehyde dehydrogenase [45] was recently refuted [36]. Instead, the DSF's metabolite CuET represents the ultimate anticancer agent, explaining potentiation of DSF by copper [31]. Treatment of cells with CuET evokes phenotypes resembling inhibitors of protein degradation such as bortezomib or p97 [12, 31] via inhibition and aggregation of NPL4, an essential co-factor of p97 segregase [31, 46] involved in protein degradation upstream of the proteasome. Similar to other UPS blockers, CuET shows robust toxicity towards MM cells including preclinical models [31, 47]. Based on the rationale that CuET impairs UPS outside the proteasome we addressed here its toxic effect using the recently described clinically-relevant BTZ-resistant form of MM mutated in the proteasomal subunit *PSMB5*, responsible for resistance to BTZ and its derivatives ixazomib (IXA) and Carfilzomib (CARF) [4]. CuET potency was indeed unaffected by this mutation, analogous to the p97 inhibitor CB5083 [48]. Importantly, these data place CuET among the promising experimental anti-MM therapeutics such as p97 inhibitors.

The selection pressure imposed by PIs can also trigger adaptive mitigation of the otherwise intense immunoglobulin synthesis, elevated basal ER stress and expanded ER network, characteristic features that underlie the MM cell vulnerability to UPS blockers. Several studies highlighted the importance of immunoglobulin synthesis rate for MM sensitivity to BTZ [21, 24, 34]. Given frequently

observed dedifferentiation of MM cells and clonal propagation of pre-plasma cells during therapy [25, 26] the PIs resistance due to decreased immunoglobulin production [19] is clinically relevant. Moreover, this type of MM resistance may explain the observed cross-resistance among different PIs and the limited efficacy of second-generation PIs after the bortezomib-based regimen fails. This current state in the field raises the question of whether any of the UPS inhibitors, in general, may still retain their exceptional potency in such adapted MM cell populations. To test this hypothesis we experimentally mimicked the rescue effect of the decreased proteo-synthesis by concomitant treatment of MM cells with CHX [37], a drug limiting protein translation. This scenario protects MM cells from the toxicity of both BTZ and the p97 inhibitor CB5083. Strikingly, we could not see such CHX-mediated protective effect against treatment by CuET, a rather surprising result given the expected high mechanistic resemblance of CuET to CB5083. Next, we employed the BTZ-adapted AMO1 cell line (AMO1-abzb) as another model [38], in which resistance to BTZ reflects the downregulation of proteo-synthesis (Fig. 4A, 4B). In this BTZ- and partially CB5083-resistant system we confirmed the persistent sensitivity to CuET. Interestingly, in AMO1-abzb cells, both CuET and CB5083 were still capable of inducing the pro-apoptotic factor CHOP, a marker of activated UPR believed to be the main trigger of apoptosis in PI-treated MM cells [34]. Consistent with the role of p97/NPL4 in ER function, these results indicate that both compounds are efficient inducers of UPR, despite the reduced proteo-synthesis and the ensuing reduced proteasome load [37]. Due to endogenous ER stress, MM cells might be more prone to reaching supra-threshold UPR leading to apoptosis, contributing to the exceptional vulnerability to certain drugs. This conclusion is further supported by studies with classical ER-stressors such as thapsigargin and thapsigargin which are capable of UPR induction independently of UPS interference and are very toxic to MM [21, 49].

An important question raised from our data is why CuET is even more efficient in these resistant models than p97 inhibitors. We speculate that this might involve the triggering of additional toxic effects induced by CuET. Upon CuET treatment, NPL4 protein forms aggregates, which leads not only to impairment of protein degradation and p97 function but also activates massive HSR (Fig. 1, ref. [27]). Activated HSR by itself might contribute to the toxic effects in MM cells as suggested in a recent report [50]. Under treatment with CuET, the HSR is activated by NPL4 protein aggregates which can sequester and immobilize various other proteins [31] including the ATR kinase, with consequences for replication stress and DNA damage [32]. Importantly, MM cells display chromosomal abnormalities, a feature possibly linked to the hyperactivated proteolysis with high demands on ubiquitin, the insufficiency of which becomes a limiting factor in the proper function of DNA damage repair [51]. Related to enhanced endogenous stresses, MM also shows overabundance of RNA-DNA hybrids likely reflecting transcription-replication conflicts [52]. Consistent with these previous publications and hypotheses, human myeloma cell lines and a subset of myeloma patients with poor prognosis indeed exhibit high levels of replication stress and DNA damage [53]. High intrinsic DNA damage was confirmed by

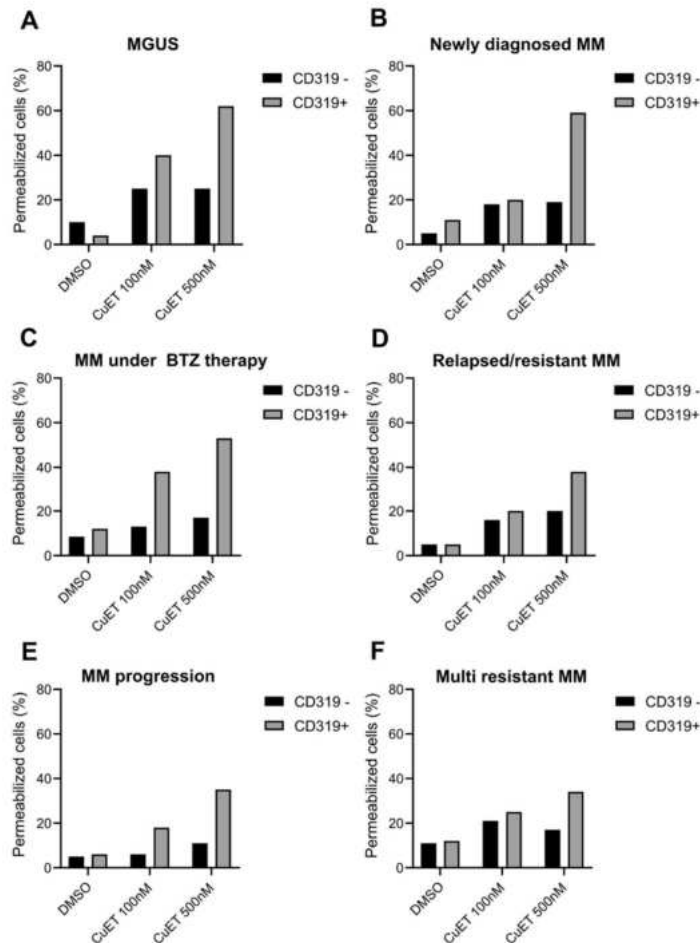


Fig. 5 CuET efficiently kills CD319⁺/CD138⁺ MM cancer cells isolated from patients independently of disease stage and ongoing/passed therapy. **A** Cytotoxic effect of CuET in a patient diagnosed for Monoclonal gammopathy of undetermined significance (MGUS; asymptomatic Multiple Myeloma). **B** Cytotoxic effect of CuET in a patient newly diagnosed with Multiple Myeloma without any passed therapy. **C** Cytotoxic effect of CuET in a patient diagnosed with Multiple Myeloma under Bortezomib therapy. **D** Cytotoxic effect of CuET in relapsed Multiple Myeloma patients after two years in remission. **E** Cytotoxic effect of CuET in a patient been in progression phase of the disease after a remission. **F** Cytotoxic effect of CuET in Multiple Myeloma patients being resistant to all available anti-MM therapies (proteasome inhibitors and immunomodulatory drugs). Each graph represents a single patient, samples treated for 24 h.

γ H2AX foci across the whole disease spectrum of MGUS to MM [54] including the samples used in our present study (Supplementary Fig. S5). Importantly, MM cells are addicted to the function of ATR making this kinase a new promising therapeutic vulnerability [55]. Thus, CuET might robustly enhance the high endogenous replication stress in MM cells due to the ATR depletion, thereby increasing DNA damage with lethal consequences. Importantly, in this study, we verified the immobilization of not only ATR but also ATM – yet another DNA-damage-related kinase [56] in insoluble fractions from CuET-treated AMO1 and

MM1.5 cells (Supplementary Fig. S6). These data suggest that besides affecting the cellular proteolytic machinery upstream of the proteasome, direct ER stress induction, and UPR activation, CuET evokes multiple mechanisms that target additional vulnerabilities of MM cells.

From the translational perspective, our data suggest that CuET works as an efficient anti-MM drug independently of the disease stage and resistance status. This notion is supported by our analyses of patients' bone marrow aspirates using an ex-vivo cytotoxicity test allowing direct comparison of the toxic effect of

CuET on MM (CD319⁺/CD138⁺ positive) vs normal plasma cells. This approach mimics the physiological environment since besides red blood cells the samples contain all blood and stromal cells and signaling molecules that might affect the therapy [57]. We examined 14 MM patient samples including newly diagnosed, under therapy, and resistant/relapsed. The number of viable CD319⁺/CD138⁺ MM cells was greatly reduced after treatment with CuET in a concentration-dependent manner, regardless of the patient donor or his/her stage of the disease. Importantly, CuET induced its cytotoxic effect preferentially in tumor cells (CD319⁺/CD138⁺). CuET efficiency was also confirmed in primary MM cells from patients resistant and/or relapsed after previous therapies with clinically used classes of drugs.

Altogether, our data suggest that DSF, particularly when combined with copper, is a candidate for an attractive and readily available treatment option for patients with relapsed and/or therapy-resistant MM. Gaps in our knowledge about the pharmacokinetics of CuET formation in patients, interference with other medications and the lack of predictive biomarkers currently preclude a wider application of DSF in oncology. On the other hand, some of the outstanding questions will hopefully be answered by the currently ongoing clinical trials with DSF repurposing in treatment of solid human malignancies, thereby also paving the way for use in therapy-refractory MM patients.

MATERIALS AND METHODS

Cell lines

Human multiple myeloma cell lines AMO1 (ATCC) and MM1.S (ATCC) were cultured in RPMI-1640 medium (Thermo Fisher Scientific) with 10% fetal bovine serum (Thermo Fisher Scientific) and 1% penicillin/streptomycin (Sigma-Aldrich). The wild type (WT) and BTZ-resistant AMO1 and L363 myeloma cell lines with point mutations in P5MB5 (A20T, M45I) as well as BTZ-adapted AMO1 abzb cell lines were provided by Department of Hematology, Kantonsspital St. Gallen, St. Gallen, Switzerland [4, 38]. The human osteosarcoma cell lines U2OS (ATCC) and breast cancer cell line MDA-MB-231 (ATCC) were cultured in DMEM (Dulbecco's Modified Eagle Medium, Lonza) with the same supplements as above. All cell lines were cultured under 5% CO₂ at 37 °C and tested for mycoplasma contamination.

XTT Viability assay of multiple myeloma cell lines

Approx. 10,000 cells were seeded per well in a 96-well plate. The next day, cells were treated as described in the figures. The XTT assay was performed according to the manufacturer's instructions (Applichem). The dye intensity was measured at the 475 nm wavelength using a spectrometer (TECAN, Infinite M200PRO).

Western blot

The whole-cell lysates were prepared by direct cell lysis in 1× Laemmli sample buffer (1× LSB). The insoluble pellet fraction used for the analysis of immobilized K48-Ubiquitin (Fig. 4D) was obtained by a quick wash of cells with 0.5% Triton X-100 followed by direct cell lysis in 1× LSB. Cell lysates were separated by SDS-PAGE on either hand-cast gels or pre-cast 4–12% gradient gels (SIGMA) and then transferred onto a nitrocellulose membrane. Blocking of the membrane, incubation with primary antibodies, detection with and visualization of secondary antibodies was performed as described previously [31]. Uncropped western blot results are included in the supplementary material.

Cell fractionation for Triton X insoluble pellets

Myeloma suspension cells were treated as indicated and the Triton X-100 soluble and insoluble MM cell fractions were collected by a procedure as described previously [31].

Immunofluorescence

Cells grown on coverslips were treated with compounds at indicated concentrations and subsequently either pre-extracted (0.1% Triton X 100 in PBS, for 2 min) and/or fixed with 4% paraformaldehyde for 15 min at room temperature, washed with PBS, and permeabilized with 0.5% Triton X-100 in PBS for 5 min. The following steps, including primary, secondary

antibody, and DNA staining were performed as described previously [31]. Samples were visualized using LSM 980 Zeiss Axioimager Z.1 microscope.

OPP Protein synthesis assay

Firstly, O-propargyl-puromycin (OPP; 20 μM) (Life Technologies) was added to the cells and incubated for 30 min. Next, cells were washed in ice-cold PBS, fixed, permeabilized by 0.5% Triton X 100 in PBS, and stained as described in the manufacturer's instructions (Click-iT™ Plus OPP Alexa Fluor™ 488 Protein Synthesis Assay Kit). Suspension AMO1 cells were fixed and cytospinned using the Cyto-Tek Sakura Instrument (Sakura Finetek, Torrance, CA, USA) onto microscopic slides, followed by permeabilization and staining as described in the manufacturer's instructions (Click-iT™ Plus OPP Alexa Fluor™ 488 Protein Synthesis Assay Kit). The fluorescent signal depicting active proteosynthesis was acquired via U-plan 5 Achromat 40x /0.9 NA objective using an automated microscopic acquisition system (ScanR, Olympus). The signal data from individual cells were processed in the STATISTICA 13.

Processing of MM patients' bone marrow aspirates for cell viability assays

Bone marrow (BM) aspirates from multiple myeloma patients were obtained by routine prognostic procedure at the Department of Hemato-oncology of the Faculty Hospital Olomouc (Czech Republic). Informed consent in accordance with the Declaration of Helsinki was obtained from all patients, and approval was obtained from the Ethics Committee of the University Hospital and the Faculty of Medicine Palacky University in Olomouc. Immediately after bone marrow aspiration, samples were mixed with 5 ml of RPMI-1640 containing 100U/ml heparin to prevent coagulation. The percentage of MM cells was identified by flow cytometry using anti-CD-319-PE and anti-CD-139-APC antibodies. The rest of the patients' bone marrow samples were passed through a 100 μm filter and spin down for 10 min at 20 °C and 445 G. For red blood cells removal, the cell pellets were re-suspended in pre-chilled red blood cell lysis buffer (RBC) (0.15MNH₄Cl; 10 mM KHCO₃; 0.1 mM EDTA; pH 7.3). The white blood cells including multiple myeloma plasma cells were re-suspended in RPMI-1640 and used for the cell viability experiments (see below).

Viability assay of MM patients' samples and flow cytometry analysis

Cells were seeded in duplicates in concentration 1×10⁵ cells/100 μl per well on 96 well plates and treated by CuET (100 and 500 nM), and Mock (0.5% DMSO). After 24 h, CuET- and Mock-treated cells were incubated with CD319-PE antibody for 30 min. After adding 1 ml of RPMI-1640 per sample, cells were centrifuged for 5 min at 200 G. The cell pellets were then re-suspended in RPMI-1640 with DAPI in concentration 0.5 μg/ml and incubated in dark for 15 min. Stained samples were analyzed by flow cytometry using BD FACS Verse (BD Biosciences) and at least 10 000 events were acquired per sample. Collected data were processed using BD FACS Suite (BD Biosciences).

Processing of MM patients' bone marrow aspirates for Western blot analysis

First steps of MM patients' BM aspirates processing were identical to those described above in "Processing of MM patients' bone marrow aspirates for cell viability assays". After red blood cells deprivation, samples were filtered through a 100 μm filter and centrifuged at 445 G for 10 min at 20 °C. Cell pellets were re-suspended in separation buffer (auto MACS Separation-Running Buffer, MACS Miltenyi Biotec). To obtain a single-cell suspension before magnetic labeling, cells were passed through 30 μm nylon mesh. Individual cells were magnetically labeled using CD138 microbeads (MACS Miltenyi Biotec) according to the manufacturer's instructions. Afterward, CD138 positive and CD138 negative cells were lysed in 1× LSB.

Patient's samples characteristics

BM samples were derived from 14 patients (6 men and 8 women) in the age of 52-78 years either diagnosed for MM driving stage- monoclonal gammopathy of undetermined significance (MGUS) or Multiple Myeloma (MM). Bone marrow (BM) aspirates from MM patients were obtained by routine prognostic procedure at the Department of Hemato-oncology of the Faculty Hospital Olomouc (Czech Republic) after an appropriate informed consent was signed. Six of the analyzed patients' samples were freshly diagnosed for MM having no passed therapy, 1 patient was under

Velcade (BTZ)-containing therapy, 5 patients were clinically diagnosed as relapsed after combinatory Velcade (BTZ), Revlimid (lenalidomide)/Thalidomid (thalidomide), Dexamethasone or Velcade (BTZ), Cytosan (Cyclophosphamide), Dexamethasone therapy. One patient was resistant to BTZ as well as to combinatory therapy by Velcade (BTZ), Revlimid (lenalidomide), and Dexamethasone.

Antibodies and chemicals

The following antibodies were used for immunoblotting: anti-ubiquitin lys48-specific (Merck Millipore, clone Apu2), anti-VCP (Novus Bio, NBP100-1557), anti NPOC4 (Novus Bio, NBP1-82166), HSP70 (Enzo, ADI-SPA-830), anti-XBP1 (Santa Cruz Biotechnology, sc-7160), ATF4 (Merck Millipore, ABE387), 1D4), anti-lamin B (Santa Cruz Biotechnology, sc-6217), MEK-1 Antibody (C-18) (Santa Cruz Biotechnology, sc-219), anti SMC1 antibody (Abcam, ab1276-50), CHOP (L63F7) (Cell Signaling, #2895), Caspase-3 antibody (Cell Signaling, #9662 S), Cleaved PARP (Asp214) antibody (Cell Signaling, #9544), Anti-GRP78 BiP antibody (Abcam, ab21685), ATR antibody (N-19) (Santa Cruz Biotechnology, sc-1887), ATM (D2E2) (Cell Signaling, #2873), Phospho-Histone H2A.X (Ser139) (20E3) (Cell Signaling, #9718), IRF-4 antibody (Cell Signaling, #4964). For immunofluorescence was the anti-ubiquitin lys48-specific antibody (Merck Millipore, clone Apu2), HSP70 antibody (Enzo, ADI-SPA-830). The antibodies used for detection of myeloma cells by flow cytometry measurement include PE anti-human CD319 (CRACC) antibody (BioLegend, 331806) and APC anti-human CD138 (44F9) antibody (Miltenyi Biotec, 130-117-544).

Chemicals used in this study: CuEt (bis-diethylthiocarbamate-copper complex, TCI chemicals), disulfiram (Sigma, St. Louis, MO, USA), bortezomib (PS-341, Sigma-Aldrich), CB5083 (Seleckchem), cycloheximide (Sigma-Aldrich).

DATA AVAILABILITY

The data used to support the findings of this study are available from the corresponding author upon request.

REFERENCES

- Anderson KC. Bortezomib therapy for myeloma. *Curr Hematol Rep.* 2004;3:65.
- Greenlee RT, Murray T, Bolden S, Wingo PA. Cancer statistics, 2000. *CA Cancer J Clin.* 2000;50:7–33.
- Allmeroth K, Horn M, Kroef V, Miethe S, Müller R-U, Denzel MS. Bortezomib resistance mutations in PSMB5 determine response to second-generation proteasome inhibitors in multiple myeloma. *Leukemia* 2021;35:887–92.
- Barrio S, Stühmer T, Da-Viá M, Barrio-García C, Lehners N, Besse A, et al. Spectrum and functional validation of PSMB5 mutations in multiple myeloma. *Leukemia* 2019;33:447–56.
- Li J, Yakushi T, Parlafi F, Mackinnon AL, Perez C, Ma Y, et al. Capzimin is a potent and specific inhibitor of proteasome isopeptidase Rpn11. *Nat Chem Biol.* 2017;13:486–93.
- D'Arcy P, Bmjic S, Olofsson MH, Fryknäs M, Lindsten K, De Cesare M, et al. Inhibition of proteasome deubiquitinating activity as a new cancer therapy. *Nat Med.* 2011;17:1636–40.
- Anchoori RK, Karaman B, Peng S, Wang JW, Jiang R, Tanno T, et al. A bis-benzylidene piperidone targeting proteasome ubiquitin receptor RPN13/ADRM1 as a therapy for cancer. *Cancer Cell.* 2013;24:791–805.
- Song Y, Ray A, Li S, Das DS, Tai YT, Carrasco RD, et al. Targeting proteasome ubiquitin receptor Rpn13 in multiple myeloma. *Leukemia* 2016;30:1877–86.
- Song Y, Li S, Ray A, Das DS, Qi J, Samur MK, et al. Blockade of deubiquitylating enzyme Rpn11 triggers apoptosis in multiple myeloma cells and overcomes bortezomib resistance. *Oncogene* 2017;36:5631–8.
- Tian Z, D'Arcy P, Wang X, Ray A, Tai Y-T, Hu Y, et al. A novel small molecule inhibitor of deubiquitylating enzyme USP14 and UCHL5 induces apoptosis in multiple myeloma and overcomes bortezomib resistance. *Blood* 2014;123:706–16.
- Hyer ML, Milhollen MA, Ciavarrì J, Fleming P, Traore T, Sappal D, et al. A small-molecule inhibitor of the ubiquitin activating enzyme for cancer treatment. *Nat Med.* 2018;24:186–93.
- Anderson DJ, Le Moigne R, Djakovic S, Kumar B, Rice J, Wong S, et al. Targeting the AAA ATPase p97 as an approach to treat cancer through disruption of protein homeostasis. *Cancer Cell.* 2015;28:653–65.
- Zhuang J, Shirazi F, Singh RK, Kulatase I, Wang H, Lee HC, et al. Ubiquitin-activating enzyme inhibition induces an unfolded protein response and overcomes drug resistance in myeloma. *Blood* 2019;133:1572–84.
- Le Moigne R, Aftab BT, Djakovic S, Dhimolea E, Valle E, Murnane M, et al. The p97 inhibitor CB-5083 is a Unique Disrupter of Protein Homeostasis in Models of Multiple Myeloma. *Mol Cancer Ther.* 2017;16:2375–86.
- Lichter DJ, Danaee H, Pickard MD, Tayber O, Sintchak M, Shi H, et al. Sequence analysis of β -subunit genes of the 20S proteasome in patients with relapsed multiple myeloma treated with bortezomib or dexamethasone. *Blood* 2012;120:4513–6.
- Politou M, Karadimitris A, Terpos E, Kotsianidis I, Apperley JF, Rahemtulla A. No evidence of mutations of the PSMB5 (beta-5 subunit of proteasome) in a case of myeloma with clinical resistance to Bortezomib. *Leuk Res.* 2006;30:240–1.
- Corre J, Cleynen A, Robiou du Pont S, Buisson L, Bolli N, Attal M, et al. Multiple myeloma clonal evolution in homogeneously treated patients. *Leukemia* 2018;32:2636–47.
- Ziccheddu B, Biancon G, Bagnoli F, De Philippis C, Maura F, Rustad EH, et al. Integrative analysis of the genomic and transcriptomic landscape of double-refractory multiple myeloma. *Blood Adv.* 2020;4:830–44.
- Leung-Hagesteijn C, Erdmann N, Cheung G, Keats JJ, Stewart AK, Reece DE, et al. Xbp1s-negative tumor B cells and pre-plasmablasts mediate therapeutic proteasome inhibitor resistance in multiple myeloma. *Cancer Cell.* 2013;24:289–304.
- Cenci S, Mezghrani A, Cascio P, Bianchi G, Cerruti F, Fra A, et al. Progressively impaired proteasomal capacity during terminal plasma cell differentiation. *EMBO J.* 2006;25:1104–13.
- Ling SCW, Lau EKK, Al-Shabeeb A, Nikolic A, Catalano A, Iland H, et al. Response of myeloma to the proteasome inhibitor bortezomib is correlated with the unfolded protein response regulator XBP-1. *1.* 2012;97:64–72.
- Zang M, Guo J, Liu L, Jin F, Feng X, An G, et al. Cdc37 suppression induces plasma cell immaturity and bortezomib resistance in multiple myeloma via Xbp1s. *Oncogenesis* 2020;9:1–13.
- Qin X-Q, An G, Li Z-J, Liu L-T, Xu Y, Yang L-H, et al. Secretary status of monoclonal immunoglobulin is related to the outcome of patients with myeloma: a retrospective study. *Blood Adv.* 2019;3:751–60.
- Meister S, Schubert U, Neubert K, Herrmann K, Burger R, Gramatzki M, et al. Extensive immunoglobulin production sensitizes myeloma cells for proteasome inhibition. *Cancer Res.* 2007;67:1783–92.
- Paiva B, Puig N, Cedena MT, de Jong BG, Ruiz Y, Rapado I, et al. Differentiation stage of myeloma plasma cells: biological and clinical significance. *Leukemia* 2017;31:382–92.
- Chaldos A, Barnes CP, Cowan G, Melo V, Hatjiharisi E, et al. Clinical drug resistance linked to interconvertible phenotypic and functional states of tumor-propagating cells in multiple myeloma. *Blood* 2013;121:318–28.
- Xu Y, Zhou Q, Feng X, Dai Y, Jiang Y, Jiang W, et al. Disulfiram/copper markedly induced myeloma cell apoptosis through activation of JNK and intrinsic and extrinsic apoptosis pathways. *Biomed Pharmacother.* 2020;126:110048.
- Meier S, Cantilena S, Niklison Chirov MV, Anderson J, Hargrave D, Salomoni P, et al. Alcohol-abuse drug disulfiram targets pediatric glioma via MLL degradation. *Cell Death Dis.* 2021;12:1–12.
- Chen D, Cui QC, Yang H, Dou QP. Disulfiram, a clinically used anti-alcoholism drug and copper-binding agent, induces apoptotic cell death in breast cancer cultures and xenografts via inhibition of the proteasome activity. *Cancer Res.* 2006;66:10425–33.
- Yoshino H, Yamada Y, Enokida H, Osako Y, Tsuruda M, Kuroshima K, et al. Targeting NPL4 via drug repositioning using disulfiram for the treatment of clear cell renal cell carcinoma. *PLoS ONE.* 2020;15:e0236119.
- Skrott Z, Mistrik M, Andersen KK, Friis S, Majera D, Gursky J, et al. Alcohol-abuse drug disulfiram targets cancer via p97 segregase adaptor NPL4. *Nature* 2017;552:194–9.
- Majera D, Skrott Z, Chroma K, Merchut-Maya JM, Mistrik M, Bartek J. Targeting the NPL4 Adaptor of p97/VCP Segregase by Disulfiram as an Emerging Cancer Vulnerability Evokes Replication Stress and DNA Damage while Silencing the ATR Pathway. *Cells.* 2020;18:9.
- Dai RM, Li CC. Valosin-containing protein is a multi-ubiquitin chain-targeting factor required in ubiquitin-proteasome degradation. *Nat Cell Biol.* 2001;3:740–4.
- Obeng EA, Carlson LM, Gutman DM, Harrington WJ, Lee KP, Boise LH. Proteasome inhibitors induce a terminal unfolded protein response in multiple myeloma cells. *Blood* 2006;107:4907–16.
- Shah JJ, Orłowski RZ. Proteasome inhibitors in the treatment of multiple myeloma. *Leukemia* 2009;23:1964–79.
- Skrott Z, Majera D, Gursky J, Buchtova T, Hajdich M, Mistrik M, et al. Disulfiram's anti-cancer activity reflects targeting NPL4, not inhibition of aldehyde dehydrogenase. *Oncogene* 2019;38:6711–22.
- Cenci S, Oliva L, Cerruti F, Milan E, Bianchi G, Raule M, et al. Pivotal Advance: protein synthesis modulates responsiveness of differentiating and malignant plasma cells to proteasome inhibitors. *J Leukoc Biol.* 2012;92:921–31.
- Rückrich T, Kraus M, Gogel J, Beck A, Ovaa H, Verdoes M, et al. Characterization of the ubiquitin-proteasome system in bortezomib-adapted cells. *Leukemia* 2009;23:1098–105.
- O'Connell FP, Pinkus JL, Pinkus GS. CD138 (syndecan-1), a plasma cell marker immunohistochemical profile in hematopoietic and nonhematopoietic neoplasms. *Am J Clin Pathol.* 2004;121:254–63.

40. Frigyesi I, Adolfsson J, Ali M, Christophersen MK, Johnsson E, Turesson I, et al. Robust isolation of malignant plasma cells in multiple myeloma. *Blood* 2014;123:1336–40.
41. Soh KT, Tario JD, Hahn T, Hillengass J, McCarthy PL, Wallace PK CD319 (SLAMF7) an alternative marker for detecting plasma cells in the presence of daratumumab or elotuzumab. *Cytometry Part B, Clinical Cytometry* [Internet]. 2020 Oct 6 [cited 2022 Jan 21]. Available from: <https://www.meta.org/papers/cd319-slamf7-an-alternative-marker-for-detecting/33017079>.
42. Zonder JA, Mohrbacher AF, Singhal S, van Rhee F, Bensinger WI, Ding H, et al. A phase 1, multicenter, open-label, dose escalation study of elotuzumab in patients with advanced multiple myeloma. *Blood* 2012;120:552–9.
43. Pinto V, Bergantim R, Cairas HR, Seca H, Guimarães JE, Vasconcelos MH. Multiple Myeloma: Available Therapies and Causes of Drug Resistance. *Cancers* (Basel). 2020;12.
44. Meraz-Torres F, Plöger S, Garbe C, Niessner H, Sinnberg T. Disulfiram as a Therapeutic Agent for Metastatic Malignant Melanoma-Old Myth or New Logos? *Cancers* (Basel). 2020;12.
45. Lipsky JJ, Shen ML, Naylor S. In vivo inhibition of aldehyde dehydrogenase by disulfiram. *Chem-Biol Interact*. 2001;130–132:93–102.
46. Pan M, Zheng Q, Yu Y, Ai H, Xie Y, Zeng X, et al. Seesaw conformations of Np14 in the human p97 complex and the inhibitory mechanism of a disulfiram derivative. *Nat Commun*. 2021;12:121.
47. Conticello C, Martinetti D, Adamo L, Buccheri S, Giuffrida R, Parrinello N, et al. Disulfiram, an old drug with new potential therapeutic uses for human hematological malignancies. *Int J Cancer*. 2012;131:2197–203.
48. Brunnert D, Kraus M, Stühmer T, Kirner S, Heiden R, Goyal P, et al. Novel cell line models to study mechanisms and overcoming strategies of proteasome inhibitor resistance in multiple myeloma. *Biochimica et Biophysica Acta (BBA) - Mol Basis Dis*. 2019;1865:1666–76.
49. Borjan B, Kern J, Steiner N, Gunsilius E, Wolf D, Untergasser G. Spliced XBP1 levels determine sensitivity of multiple myeloma cells to proteasome inhibitor bortezomib independent of the unfolded protein response mediator GRP78. *Front Oncol*. 2019;9:1530.
50. Sha Z, Goldberg AL. Multiple myeloma cells are exceptionally sensitive to heat shock, which overwhelms their proteostasis network and induces apoptosis. *PNAS* 2020;117:21588–97.
51. Chroma K, Mistrik M, Moudry P, Gursky J, Liptay M, Strauss R, et al. Tumors overexpressing RNF168 show altered DNA repair and responses to genotoxic treatments, genomic instability and resistance to proteotoxic stress. *Oncogene* 2017;36:2405–22.
52. Dutrieux L, Lin Y-L, Lutzmann M, Rodriguez R, Cogné M, Pasero P, et al. Transcription/replication conflicts in tumorigenesis and their potential role as novel therapeutic targets in multiple myeloma. *Cancers* 2021;13:3755.
53. Cottini F, Hideshima T, Suzuki R, Tai Y-T, Bianchini G, Richardson PG, et al. Synthetic lethal approaches exploiting DNA damage in aggressive myeloma. *Cancer Disco*. 2015;5:972–87.
54. Walters DK, Wu X, Tschumper RC, Arendt BK, Huddleston PM, Henderson KJ, et al. Evidence for ongoing DNA damage in multiple myeloma cells as revealed by constitutive phosphorylation of H2AX. *Leukemia* 2011;25:1344–53.
55. Botrugno OA, Bianchessi S, Zambroni D, Frenquelli M, Belloni D, Bongiovanni L, et al. ATR addiction in multiple myeloma: synthetic lethal approaches exploiting established therapies. *Haematologica* 2020;105:2440–7.
56. Bartek J, Bartkova J, Lukas J. DNA damage signalling guards against activated oncogenes and tumour progression. *Oncogene* 2007;26:7773–9.
57. Markovina S, Callander NS, O'Connor SL, Xu G, Shi Y, Leith CP, et al. Bone marrow stromal cells from multiple myeloma patients uniquely induce bortezomib resistant NF- κ B activity in myeloma cells. *Mol Cancer*. 2010;9:176.

ACKNOWLEDGEMENTS

The study was supported by MEYS CR (Large RI Project LM2018129 - Czech-BioImaging), ERDF (project No. CZ.02.1.01/0.0/0.0/16_013/0001/775), ENOCH project (No. CZ.02.1.01/0.0/0.0/16_019/0000868), Grant agency of the Czech Republic: GACR 20-28685 S, Technology Agency of the Czech Republic: TN01000013, Internal grant of Palacky University IGA_LF_2021_030, the Novo Nordisk Foundation (16854 and 0060590), the Swedish Research Council VR-MH 2014-46602-117891-30, the Swedish Cancer Foundation (# 170176) and the Danish National Research Foundation (project CARD, DNRF 125).

AUTHOR CONTRIBUTIONS

KCH, MM, and JBar designed experiments, which were performed mainly by KCH. KCH and JG performed viability assays of MM patients' samples enrolled by JB, PM and TB performed western blot analysis. KCH, ZS, PM, MM and JBar discussed and interpreted the results. KCH, ZS, MM and JBar wrote the manuscript which was approved by all authors.

COMPETING INTERESTS

The authors declare no competing interests.

ETHICS STATEMENT

This study has been approved by the Ethics Committee of the Faculty hospital and Medical faculty of the University of Palacky in Olomouc, Czech Republic. Reference number: 94/21.


ADDITIONAL INFORMATION

Supplementary information The online version contains supplementary material available at <https://doi.org/10.1038/s41419-022-04651-w>.

Correspondence and requests for materials should be addressed to Martin Mistrik or Jiri Bartek.

Reprints and permission information is available at <http://www.nature.com/reprints>

Publisher's note Springer Nature remains neutral with regard to jurisdictional claims in published maps and institutional affiliations.

 **Open Access** This article is licensed under a Creative Commons Attribution 4.0 International License, which permits use, sharing, adaptation, distribution and reproduction in any medium or format, as long as you give appropriate credit to the original author(s) and the source, provide a link to the Creative Commons license, and indicate if changes were made. The images or other third party material in this article are included in the article's Creative Commons license, unless indicated otherwise in a credit line to the material. If material is not included in the article's Creative Commons license and your intended use is not permitted by statutory regulation or exceeds the permitted use, you will need to obtain permission directly from the copyright holder. To view a copy of this license, visit <http://creativecommons.org/licenses/by/4.0/>.

© The Author(s) 2022



Contents lists available at ScienceDirect

European Journal of Medicinal Chemistry

journal homepage: www.elsevier.com/locate/ejmech

Research paper

Identification of novel dithiocarbamate-copper complexes targeting p97/NPL4 pathway in cancer cells

Martin Loffelmann^a, Zdeněk Škrott^a, Dušana Majera^a, Pavel Štarha^b, Vladimír Krýštof^{c,*},
Martin Mistrík^{a,**}

^a Institute of Molecular and Translational Medicine, Faculty of Medicine and Dentistry, Palacký University Olomouc, Hnevotínska 1333/5, Olomouc, 779 00, Czech Republic

^b Department of Inorganic Chemistry, Faculty of Science, Palacký University Olomouc, 17. listopadu 1192/12, Olomouc, 779 00, Czech Republic

^c Department of Experimental Biology, Faculty of Science, Palacký University Olomouc, Šlechtitelů 27, Olomouc, 783 71, Czech Republic

ARTICLE INFO

Keywords:
Dithiocarbamates
Copper complex
CuET
NPL4 protein
Proteotoxic stress
Cancer

ABSTRACT

Dithiocarbamates (DTCs) are simple organic compounds with many applications in industry and medicine. They are potent metal chelators forming complexes with various metal ions, including copper. Recently, bis (diethyldithiocarbamate)-copper complex (CuET) has been identified as a metabolic product of the anti-alcoholic drug Antabuse (disulfiram, DSF), standing behind DSF's reported anticancer activity. Mechanistically, CuET in cells causes aggregation of NPL4 protein, an essential cofactor of the p97 segregase, an integral part of the ubiquitin-proteasome system. The malfunction of p97/NPL4 caused by CuET leads to proteotoxic stress accompanied by heat shock and unfolded protein responses and cancer cell death. However, it is not known whether the NPL4 inhibition is unique for CuET or whether it is shared with other dithiocarbamate-copper complexes. Thus, we tested 20 DTCs-copper complexes in this work for their ability to target and aggregate NPL4 protein. Surprisingly, we have found that certain potency against NPL4 is relatively common for structurally different DTCs-copper complexes, as thirteen compounds scored in the cellular NPL4 aggregation assay. These compounds also shared typical cellular phenotypes reported previously for CuET, including the NPL4/p97 proteins immobilization, accumulation of polyubiquitinated proteins, the unfolded protein, and the heat shock responses. Moreover, the active complexes were also toxic to cancer cells (the most potent in the nanomolar range), and we have found a strong positive correlation between NPL4 aggregation and cytotoxicity, confirming NPL4 as a relevant target. These results show the widespread potency of DTCs-copper complexes to target NPL4 with subsequent induction of lethal proteotoxic stress in cancer cells with implications for drug development.

1. Introduction

Drug repurposing became an exciting strategy for finding new oncological drugs [1]. One such candidate is the long-term approved drug disulfiram (DSF) (commercial name Antabuse). Originally, DSF was introduced as an aldehyde dehydrogenase (ALDH) inhibitor, which causes severe alcohol intolerance, and has been used for alcoholism treatment until now. Numerous case reports and preclinical studies reported the anticancer potential of DSF, which triggered scientific interest in its mechanism of action. ALDH was among the suggested anticancer targets [2,3]. Still, DSF cannot directly inhibit ALDH in cells

[4], and its reported anticancer activity in cellular assays depends entirely on copper ions in culture media [4], indicating another target (s). It is known that DSF is quickly reduced in the human body to diethyldithiocarbamate (DDTC) [5], which is not only the precursor of metabolic products targeting ALDH [6–8] but also a very potent chelator of copper, forming diethyldithiocarbamate-copper complex (CuET) [9] also found in the human body [10]. Notably, such conversion of DSF to DDTC and CuET also occurs spontaneously in the culture media [4]. Without copper ions, DSF is an in-vitro non-toxic compound in straight contrast with CuET, where even nanomolar concentrations induce prominent phenotypes resembling inhibitors of the proteasome, potent

* Corresponding author.

** Corresponding author.

E-mail addresses: vladimir.krystof@upol.cz (V. Krýštof), martin.mistrik@upol.cz (M. Mistrík).

<https://doi.org/10.1016/j.ejmech.2023.115790>

Received 5 July 2023; Received in revised form 26 August 2023; Accepted 1 September 2023

Available online 4 September 2023

0223-5234/© 2023 Elsevier Masson SAS. All rights reserved.

anticancer drugs used clinically [4]. Closer insights revealed that CuET interferes with the p97 pathway [10], a central component of the ubiquitin-proteasome system, which works upstream of proteasomal degradation [11]. The nature of this interference is extraordinary, as CuET seems to work as an aggregation inducer targeting protein(s) such as NPL4 [10]. NPL4 (NPLOC4) is an essential cofactor of p97 AAA-ATPase, also called Valosin-containing protein (VCP) or Cdc48, a translocase extracting ubiquitinated proteins from various structures so they can be delivered to the proteasome or degraded via the autophagic-lysosomal pathway [11]. Importantly, cancer cells are particularly dependent on functional mechanisms responsible for proteostasis and protein degradation [12,13].

The way the CuET molecule turns otherwise mobile NPL4 protein into non-dissolvable aggregates forming typical nuclear clusters and fibrous cytoplasmic deposits [10] is not understood. It seems that either the whole CuET molecule or the copper ions it carries bind to the zinc-finger domain of the NPL4 protein, causing a conformational change and aggregation [10,14]. Moreover, it has been shown that additional proteins colocalize together with the aggregated NPL4, including p97, ubiquitin, and various structurally unstable proteins such as TDP43, p53, p21, MDM2, ATR, ATM, and more [10,15,16]. The nature or purpose of such co-localizations is unknown, but trapping multiple essential proteins in non-dissolvable aggregates likely contributes to the overall toxic effects [10,16,17].

Apart from CuET, no other dithiocarbamate-copper complexes were so far studied for their ability to target NPL4 protein in cells. Dithiocarbamates (DTCs) are organosulphur compounds with the molecular formula $R_2NCS_2^-$ (Fig. 1A). They possess a wide variety of applications, from being used as pesticides in agriculture to medicinal applications as antiparasitic, alcohol-abuse and oncological drugs [18,19]. One of their prominent features is that they readily form stable complexes with transition metals, such as copper (Fig. 1B), nickel, iron, zinc, or gold [19]. From the medicinal chemistry perspective, the most studied were complexes with copper, which are generally very stable and show good potency in cancer models. Most studies focused on CuET (Fig. 1B), leaving other DTCs somewhat overlooked, except for pyrrolidine-DTC, which was studied for its anti-proteasomal and NF- κ B (Nuclear Factor kappa B) activities [20,21]. However, the mechanism standing behind their anticancer activity remains largely unknown. Here, we explored a group of 20 DTCs-copper complexes for their ability to induce NPL4 protein aggregation/immobilization and how this translates to cancer cell toxicity.

2. Results and discussion

2.1. Various DTCs-copper complexes induce NPL4 aggregation in cancer cells

To test the biological activity of DTC-copper complexes, we chose 20 different DTCs that were either commercially available (1–7) or synthesized (8–20 – see Material and Methods for the synthesis details) (Fig. 2). Before the experiments, DTCs were mixed with $CuCl_2$ in a molar ratio of 2:1. The resulting complexes 3, 9, 13 and 16 were further characterized in details by analytical methods (see Material and Methods for more information). The primary focus of our study was to analyze the effect on NPL4 protein. For these studies, we employed reporter U-2-OS human osteosarcoma-derived cell line constitutively

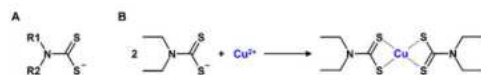


Fig. 1. (A) Structural formula of dithiocarbamates (DTCs). (B) The reaction of diethyldithiocarbamate with copper ions results in stable bis (diethyldithiocarbamate)-copper(II) complex (CuET).

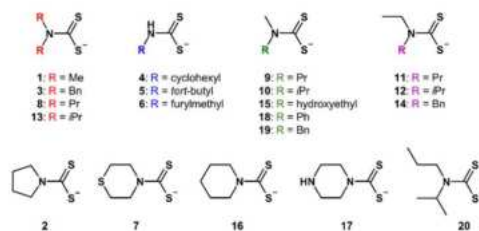


Fig. 2. List of tested DTCs. Structural formulas of DTCs whose copper complexes were used in the following biological experiments. Compounds 1–7 are commercially available and 8–20 were synthesized.

expressing human GFP-tagged NPL4 protein (U-2-OS-NPL4-GFP) [10]. The NPL4-GFP is fully extractable in mock-treated cells by detergent-based (Triton X-100) pre-extraction buffer, as most NPL4 is a freely mobile protein. After CuET treatment, the NPL4-GFP changes its properties. It becomes pre-extraction resistant (immobilized), forming typical nuclear clusters and fibrous cytoplasmic deposits indicative of protein aggregation (Fig. 3). For quantitative purposes, we developed a flow cytometry-based method confirming that after pre-extraction in CuET-treated cells, NPL4-GFP signal remains immobilized. In contrast, in mock-treated cells, the signal is lost (Fig. 4A).

We used this method to screen 20 DTC-copper complexes. We found that most complexes (13 out of 20) caused immobilization of NPL4-GFP comparable with CuET, used as a positive control (Fig. 4B), indicating interesting widespread sensitivity of NPL4 protein to structurally diverse DTCs-copper complexes. So far, it is not known whether the whole DTC-Cu complex binds to NPL4 or just copper ions, as suggested by *in vitro* studies showing strong inhibitory activity of cupric ions against purified NPL4 [14]. Our present data indicate that due to the widespread activity, DTC-copper complexes likely serve mainly as copper carriers towards proteins with high copper affinity instead of directly binding to the target protein(s). Such a scenario would also explain the previously reported protective effect of metallothioneins, cysteine-rich cellular copper chelators, from CuET treatment [22]. The inactivity of other DTC-copper complexes may be well explained by the inability to induce robust intracellular copper overload. However, interestingly, inactive compound 3 (R = dibenzyl) suggests that likely other factors also determine the efficacy of DTC-copper complexes, as this compound was shown to induce a significant accumulation of copper inside the cells comparable to CuET [23].

In the following experiment, we tested the concentration-dependency of positive hits from the primary screen and identified 9 potent compounds showing strong immobilization of NPL4 at sub-micromolar concentrations (Fig. 5).

The flow-cytometry results were further corroborated using confocal microscopy examination of cells treated with selected three active (1, 11, 16) and three inactive (6, 13, 18) compounds. The microscopic analysis of pre-extracted cells revealed the presence of typical NPL4-GFP aggregates in the nucleus and cytoplasmic deposits in all cells treated by the active compounds. At the same time, no such GFP signal was detectable in cells exposed to inactive compounds (Fig. 6). These data confirmed that diverse DTCs-copper complexes closely mimic the effect of CuET on NPL4 and induce the same pattern of pre-extraction-resistant protein aggregates.

2.2. DTCs-copper complexes capable of targeting NPL4 induce unfolded protein and heat shock cellular responses

CuET has been reported as a robust proteotoxic stress inducer due to its harmful effects on the NPL4/p97 pathway resulting in the accumulation of ubiquitinated and defective proteins in cells [10]. Cells

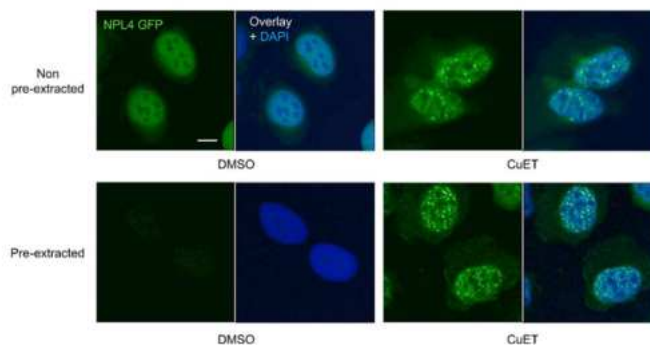


Fig. 3. NPL4-GFP protein aggregation after CuET treatment. NPL4-GFP protein becomes aggregated and immobilized (pre-extraction resistant) in U-2-OS-NPL4-GFP cells after treatment by CuET (1 μ M for 3 h).

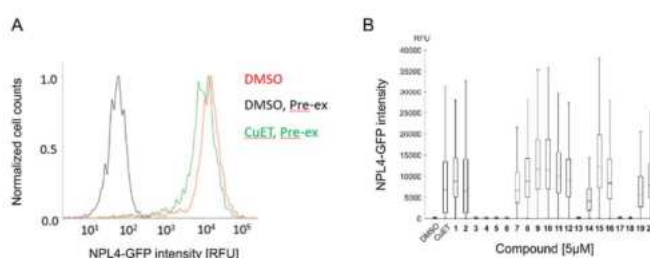


Fig. 4. Flow cytometric analysis of NPL4-GFP immobilization in U-2-OS-NPL4-GFP cells (A) Normalized cytometric histograms of GFP signal in U2OS-NPL4 GFP cells without pre-extraction, with pre-extraction and with pre-extraction after CuET treatment (5 μ M CuET for 3 h). (B) Screening of 20 DTC-copper complexes (5 μ M for 3 h) was performed in pre-extracted cells as in (A). Thirteen of twenty tested compounds immobilized NPL4 protein in the cells.

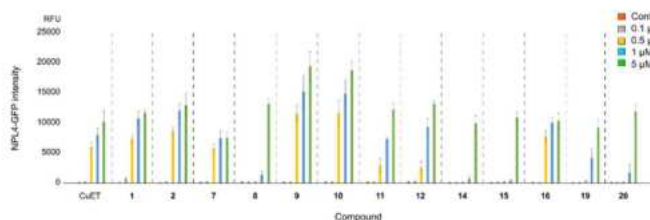


Fig. 5. Dose-dependent effect of selected DTC-copper complexes on NPL4-GFP immobilization. Selected compounds were tested at different concentrations using flow-cytometric analysis of NPL4-GFP signal in pre-extracted U-2-OS-NPL4-GFP cells (3 h). Data are means \pm s.d. of three independent biological experiments.

typically respond to proteotoxic stress via Heat-Shock Response (HSR) activation. This protective signaling pathway comprises phosphorylation and activation of transcription factor HSF1, a master regulator of HSR. In the nucleus, HSF1 triggers the transcription of genes encoding heat shock proteins – specialized chaperones such as HSP70, binding and stabilizing defective proteins [24]. The phosphorylation of HSF1 is well detectable as a shift of the protein band on the Western blot and is used as the typical proteotoxic stress marker [25].

Furthermore, HSF1, once activated and translocated into the nucleus, forms specific foci known as HSF1 stress bodies which can be detected using immunofluorescence microscopy as typical nuclear foci [26,27]. The proteotoxic stress is also often accompanied by the

accumulation of defective proteins within the endoplasmic reticulum, triggering another stress pathway known as Unfolded Protein Response (UPR). In general, activated UPR protects cells by reducing total proteosynthesis via phosphorylation of translation initiation factor 2 α (eIF2 α) to decrease global requirements on protein homeostasis. At the same time, it also upregulates the expression of UPR genes by activating transcription factors such as ATF4. UPR can also trigger apoptosis if the proteotoxic stress is beyond the resolvable threshold [28].

Activation of both HSR and UPR pathways was reported previously for cells treated by CuET [10,13]. To check if the same cellular responses underline the toxic impact of DTCs-copper complexes which scored in the NPL4-GFP immobilization screen, we selected the two most active

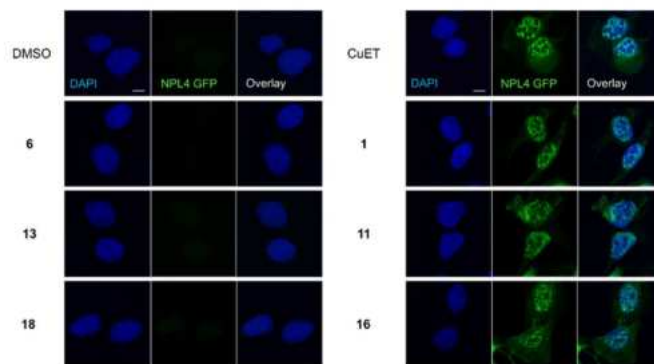


Fig. 6. Microscopic analysis of NPL4 aggregation induced by selected DTC-copper complexes. U-2-OS-NPL4-GFP cells were treated (1 μ M, for 3 h) by selected DTC-copper complexes and pre-extracted. Compounds 1, 11 and 16 induce the same NPL4-GFP aggregation pattern as CuET. Scale bar = 10 μ m.

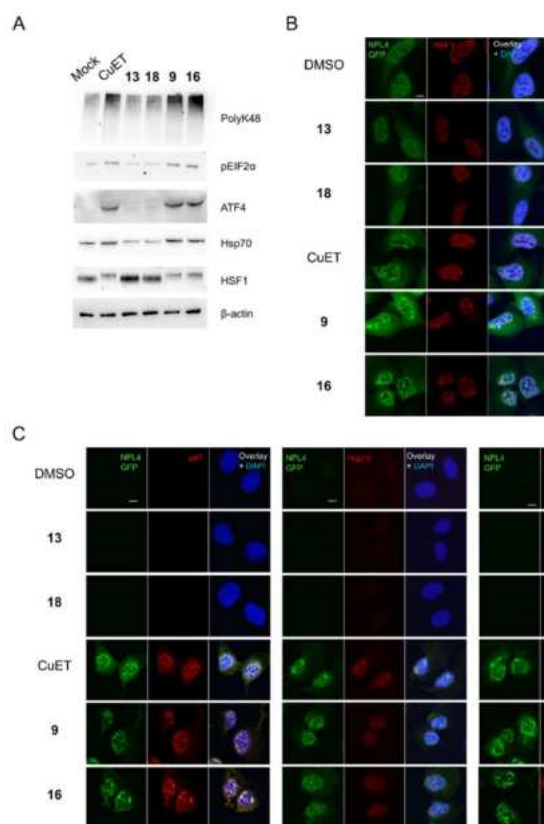


Fig. 7. DTC-copper complexes aggregating NPL4-GFP trigger Unfolded Protein Response (UPR) and Heat Shock Responses (HSR). (A) U-2-OS cells were treated by selected DTC-copper complexes (1 μ M for 3 h) and evaluated for UPR and HSR markers, including phosphorylation shift of HSF1 and accumulation of pEIF2 α , ATF4, Hsp70 and poly-ubiquitinated proteins. (B) U-2-OS-NPL4-GFP cells were treated by selected DTC-copper complexes (1 μ M for 3 h) and examined for HSF1 stress bodies in nuclei. (C) U-2-OS-NPL4-GFP cells were treated by selected DTC-copper complexes (1 μ M for 3 h) and analyzed for the presence of pre-extraction resistant p97, Hsp70 and poly-ubiquitinated proteins and co-localization of these proteins with aggregated NPL4-GFP.

compounds regarding NPL4 aggregation (9, 16) and two inactive ones (13, 18). Western blot analysis confirmed the accumulation of polyubiquitinated proteins, HSP70 chaperone and HSF1 phosphorylation shift in cells treated by the active compounds. Also, markers of UPR, p-eIF2, and ATF4 proteins were elevated (Fig. 7A). We also detected typical nuclear HSF1 stress bodies in cellular nuclei treated by the active compounds (Fig. 7B).

Next, we looked in more detail at the nature of the NPL4 aggregates induced by the active compounds. We detected that NPL4 aggregates colocalize and immobilize p97 segregase and HSP70 chaperone and are heavily marked by polyubiquitin K48 chains, just as it was previously reported for CuET [10] (Fig. 7C). Taken together, these results show that NPL4 aggregates induced by diverse DTCs-copper complexes share the same properties and leads to the same cellular stress responses involving activation of HSR and UPR.

2.3. NPL4 aggregation correlates with cytotoxicity in cancer cells

As excessive UPR and HSR typically lead to cell death, we next analyzed the viability of cells exposed to DTCs-copper complexes. We performed cytotoxic screening of all 20 compounds at a fixed concentration (5 μ M, 48 h) using the XTT assay on two cancer cell lines – U-2-OS and H1299. Notably, the cytotoxic data showed that only the DTC-copper complexes, which efficiently aggregated NPL4-GFP were also toxic for both cancer cell lines and vice versa (Fig. 8A). The ability of the complexes to immobilize NPL4 protein was directly compared to their cytotoxicity by Pearson's correlation, confirming significant positive correlation ($R^2 = 0.80$, $p < 0.001$) (Fig. 8B). The compound 6 (R = furylmethyl) was the only exception, as it was moderately toxic in U-2-OS cells despite the lack of measurable effect on NPL4. Still, this data strongly supports NPL4 protein as the primary and crucial target of various DTCs-copper complexes, which stands behind and determines their anticancer activity.

In the following experiments, we aimed to identify the most potent compounds. We selected 4 active compounds with the best NPL4 immobilization activity (9, 10, 11, 16), performed their cytotoxic

profiling and calculated IC_{50} values. All four compounds were highly toxic in both cell lines, with IC_{50} well below 500 nM in the short-term (48 h) experiment (Fig. 9A and B). In a more relevant colony-formation assay, which measures the toxicity in a long-term fashion (7 days), we identified compounds 9, 10 and 16 as highly toxic with IC_{50} 's below 50 nM (U-2-OS: 9 - $IC_{50} = 27.5 \pm 7.1$ nM; 10 - $IC_{50} = 23.4 \pm 4.4$ nM; 16 - $IC_{50} = 22.5 \pm 3.5$ nM; H1299: 9 - $IC_{50} = 33.9 \pm 7.9$ nM; 10 - $IC_{50} = 28.5 \pm 6.3$ nM; 16 - $IC_{50} = 43.4 \pm 9.5$ nM) (Fig. 9C and D). Overall, these results show that apart from CuET, there are more available DTCs-copper complexes with nanomolar activity and promising potential to target cancer cells via impairment of NPL4/p97 system leading to unresolvable proteotoxic stress.

3. Conclusion

CuET, a metabolite of disulfiram, was studied by many groups due to its anticancer properties [14,29–31]. Here we showed that many structurally diverse DTCs-copper complexes are toxic to cancer cells within the nanomolar range and share the CuET-associated mechanism of action involving proteostasis failure caused by aggregation of NPL4 protein, an essential component of the p97 pathway, for which we confirmed a strong positive correlation with cytotoxicity. Importantly, targeting proteostasis is an established approach of modern oncological treatments, as elevated proteotoxic stress belongs among cancer hallmarks [12], and various proteasome inhibitors are used to treat cancers [32]. Our work further confirmed the targeting of NPL4 protein as a promising anticancer strategy. Also, it sheds more light on the somewhat enigmatic molecular mechanism behind the NPL4 protein aggregation by DTCs-copper complexes. Due to the structural differences, it seems unlikely that all could bind directly to the NPL4 protein and instead suggest they serve as delivery molecules for cupric ions, which bind to and poison the NPL4 protein. The questions to be answered are why some DTCs-copper complexes cannot do that and whether such copper delivery towards NPL4 is an ability specific to DTC-based copper chelators only.

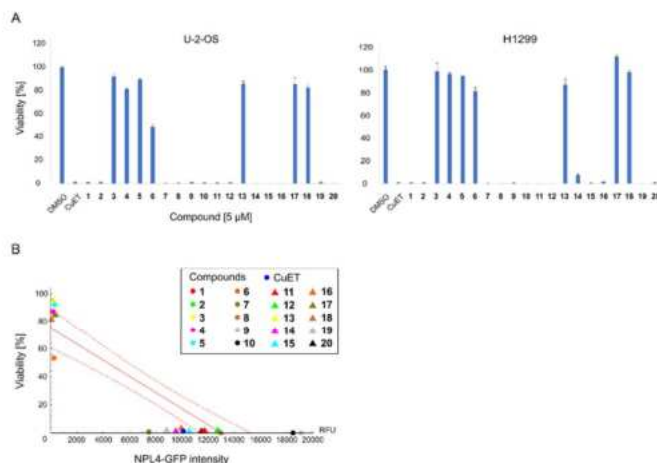


Fig. 8. Cytotoxicity of DTC-copper complexes correlates with their ability to aggregate NPL4 protein. (A) Primary cytotoxic screening of DTC-copper complexes at the fixed concentration and time (5 μ M, 48 h) using the XTT assay as readout in two cancer cell lines – U-2-OS and H1299. (B) Pearson's correlation analysis compares the ability of DTC-copper complexes to aggregate NPL4-GFP and cytotoxicity ($R^2 = 0.79$, $p < 0.001$, dashed lines represent the 95% confidence interval).

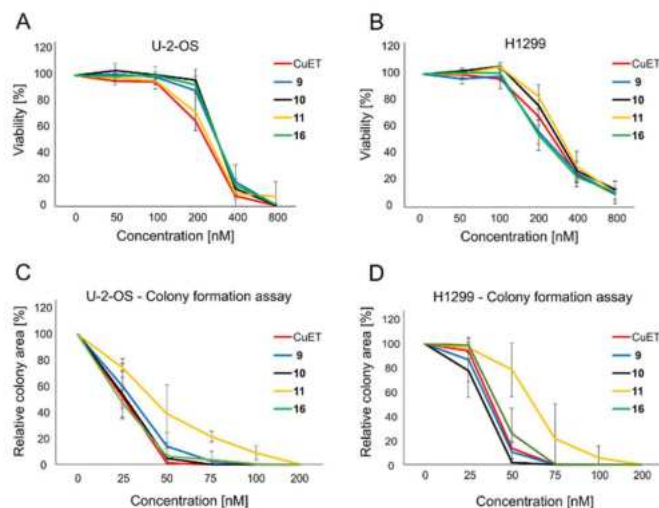


Fig. 9. Detailed cytotoxicity profiling of selected DTC-copper complexes. (A) Cytotoxicity analysis after 48 h in U-2-OS cells using XTT assay. (B) Cytotoxicity analysis after 48 h in H1299 cells using XTT assay. (C) Colony-formation assay analysis in U-2-OS cells and H1299 (D) after 7 days.

4. Materials and methods

4.1. Chemicals

Most chemicals were of ACS grade and purchased from Sigma-Aldrich. Chemicals dipropylamine, diisopropylamine, *N*-methylpropylamine, *N*-isopropylmethylamine, *N*-ethyl-*N*-propylamine, *N*-ethylisopropylamine, *N*-ethylbenzylamine, 2-(methylamino)ethanol, piperidine, piperazine, *N*-methylaniline, *N*-benzylmethylamine, *N*-isopropylpropylamine, sodium hydroxide, carbon disulphide and solvents ethanol, *n*-hexane and cyclohexane were purchased from Merck Life Science Ltd., Avantor - VWR International Ltd. and Litolab Ltd. (Chudobín, Czech Republic).

4.2. Commercially available DTCs

CuET and compounds 1–7 were purchased from various companies. CuET - copper(II) diethyldithiocarbamate, D0487, TCI, CAS: 13681-87-3; Compound 1 - sodium dimethyldithiocarbamate hydrate, D156604, Sigma-Aldrich, CAS: 207233-95-2; Compound 2 - ammonium pyrrolidinedithiocarbamate, P8765, Sigma-Aldrich, CAS: 5108-96-3; Compound 3 - sodium dibenzylidithiocarbamate hydrate, D0156, TCI, CAS: 55310-46-8; Compound 4 - sodium cyclohexyldithiocarbamate, BBL033928, Vitas-M Laboratory; Compound 5 - sodium *tert*-butyldithiocarbamate, EN300-1067046, Enamine, CAS: 882878-69-5; Compound 6 - 2-furylmethylcarbamodithioic acid, 085298, Matrix Scientific, CAS: 45815-80-3; Compound 7 - sodium thiomorpholine-4-dithiocarbamate, EN300-1085871, Enamine, CAS: 92754-62-6.

4.3. Synthesis of DTCs

Compounds 8–20 were synthesized *de novo*. Compounds sodium dipropylcarbamodithioate (8) [33], sodium methyl(propyl)carbamodithioate (9) [34], sodium methyl(propan-2-yl)carbamodithioate (10) [35], sodium ethyl(propan-2-yl)carbamodithioate (12) [36], sodium

dipropylcarbamodithioate (13) [33], sodium benzyl(ethyl)carbamodithioate (14) [37], sodium (2-hydroxyethyl)methylcarbamodithioate (15) [38], sodium piperidine-1-carbodithioate (16) [39], sodium piperazine-1-carbodithioate (17) [40], sodium methyl(phenyl)carbamodithioate (18) [41] and sodium benzyl(methyl)carbamodithioate (19) [42] were formerly reported in the literature. They were prepared according to the generalized synthetic procedure as described below. To the best of our knowledge, compounds sodium ethyl(propyl)carbamodithioate (11) and sodium propan-2-yl(propyl)carbamodithioate (20) are reported here for the first time, while compounds 8–10 and 12–19 have been previously prepared.

10 mmol of appropriate amine was mixed with 1 M aqueous NaOH (1 eq.; 10 mL), cooled to 0 °C and stirred for 30 min. After that, 0.665 mL of carbon disulfide (1.1 eq.) in 10 mL of ethanol was added dropwise over 2 min period. After the next 30 min of stirring at 0 °C, the reaction mixture was allowed to warm to RT and stirred overnight. The solvent was removed and the crude product was recrystallized from ethanol, filtered off, washed with *n*-hexane or cyclohexane (2 × 3 mL) and dried overnight at 50 °C.

The composition and purity of compounds 8–20 were studied by elemental analysis (Flash 2000 CHNS Elemental Analyser; Thermo Scientific) and ¹H nuclear magnetic resonance (NMR) spectroscopy (DMSO-*d*₆ solutions, 298 K, Varian spectrometer at 400.00 MHz). ¹H NMR spectra were calibrated against the residual DMSO ¹H NMR signal at 2.50 ppm. The splitting of proton resonances in the reported ¹H spectra is defined as s = singlet, d = doublet, t = triplet, q = quadruplet, sext = sextet, sep = septet, m = multiplet and bs = broad signal. ¹H-¹H COSY spectra were recorded where necessary for a precise assignment of the detected hydrogen atoms; gs = gradient selected, COSY = homonuclear correlated spectroscopy. ¹H NMR spectra are shown in the Supplementary data.

Sodium dipropylcarbamodithioate (8). ¹H NMR (DMSO-*d*₆, δ, ppm): 3.85 (t, *J* = 7.8 Hz, 2H), 1.61 (sext, *J* = 7.5 Hz, 2H), 0.78 (t, *J* = 7.2 Hz, 3H). Anal. Calcd. for C₇H₁₄NS₂Na (M_r = 199.31): C, 42.18; H, 7.08; N, 7.03%; found: C, 42.07; H, 6.82; N, 7.16%.

Sodium methyl(propyl)carbamodithioate (9). ^1H NMR (DMSO- d_6 , δ , ppm): 3.95 (t, $J = 7.8$ Hz, 2H), 3.32 (s, 3H), 1.56 (sext, $J = 7.5$ Hz, 2H), 0.79 (t, $J = 7.4$ Hz, 3H). *Anal. Calcd.* for $\text{C}_5\text{H}_{10}\text{NS}_2\text{Na}$ ($M_r = 171.26$): C, 35.07; H, 5.89; N, 8.18%; found: C, 34.86; H, 5.51; N, 7.96%.

Sodium methyl(propan-2-yl)carbamodithioate (10). ^1H NMR (DMSO- d_6 , δ , ppm): 6.16 (sep, $J = 6.7$ Hz, 1H), 3.15 (s, 3H), 1.00 (d, $J = 6.7$ Hz, 6H). *Anal. Calcd.* for $\text{C}_5\text{H}_{10}\text{NS}_2\text{Na}$ ($M_r = 171.26$): C, 35.07; H, 5.89; N, 8.18%; found: C, 35.39; H, 5.93; N, 7.91%.

Sodium ethyl(propyl)carbamodithioate (11). ^1H NMR (DMSO- d_6 , δ , ppm): 3.98 (q, $J = 6.8$ Hz, 2H), 3.84 (t, $J = 7.8$ Hz, 2H), 1.61 (sext, $J = 7.5$ Hz, 2H), 1.08 (t, $J = 7.0$ Hz, 3H), 0.78 (t, $J = 7.4$ Hz, 3H). *Anal. Calcd.* for $\text{C}_6\text{H}_{12}\text{NS}_2\text{Na}$ ($M_r = 185.29$): C, 38.89; H, 6.53; N, 7.56%; found: C, 38.53; H, 6.31; N, 7.23%.

Sodium ethyl(propan-2-yl)carbamodithioate (12). ^1H NMR (DMSO- d_6 , δ , ppm): 6.32 (sep, $J = 6.7$ Hz, 1H), 3.80 (q, $J = 6.7$ Hz, 2H), 1.15 (t, $J = 6.8$ Hz, 3H), 1.04 (d, $J = 6.7$ Hz, 6H). *Anal. Calcd.* for $\text{C}_6\text{H}_{12}\text{NS}_2\text{Na}$ ($M_r = 185.29$): C, 38.89; H, 6.53; N, 7.56%; found: C, 38.64; H, 6.77; N, 7.64%.

Sodium dipropan-2-ylcarbamodithioate (13). ^1H NMR (DMSO- d_6 , δ , ppm): 6.32 (bs, 1H), 3.67 (bs, 1H), 1.61 (bs, 6H), 1.01 (bs, 6H). *Anal. Calcd.* for $\text{C}_7\text{H}_{14}\text{NS}_2\text{Na}$ ($M_r = 199.31$): C, 42.18; H, 7.08; N, 7.03%; found: C, 41.94; H, 6.94; N, 6.75%.

Sodium benzyl(ethyl)carbamodithioate (14). ^1H NMR (DMSO- d_6 , δ , ppm): 7.26 (m, 5H), 5.42 (s, 2H), 3.92 (q, $J = 6.8$ Hz, 2H), 1.04 (t, $J = 7.0$ Hz, 3H). *Anal. Calcd.* for $\text{C}_{10}\text{H}_{12}\text{NS}_2\text{Na}$ ($M_r = 233.33$): C, 51.48; H, 5.18; N, 6.00%; found: C, 51.39; H, 4.96; N, 5.63%.

Sodium (2-hydroxyethyl)methylcarbamodithioate (15). ^1H NMR (DMSO- d_6 , δ , ppm): 4.72 (t, $J = 4.9$ Hz, 1H), 4.10 (t, $J = 6.3$ Hz, 2H), 3.59 (t, $J = 5.9$ Hz, 2H), 3.38 (s, 3H). *Anal. Calcd.* for $\text{C}_4\text{H}_8\text{NOS}_2\text{Na}$ ($M_r = 173.23$): C, 27.73; H, 4.65; N, 8.09%; found: C, 27.65; H, 4.32; N, 7.81%.

Sodium piperidine-1-carbodithioate (16). ^1H NMR (DMSO- d_6 , δ , ppm): 4.26 (t, $J = 5.5$ Hz, 4H), 1.54 (m, 2H), 1.39 (m, 4H). *Anal. Calcd.* for $\text{C}_6\text{H}_{10}\text{NS}_2\text{Na}$ ($M_r = 183.27$): C, 39.32; H, 5.50; N, 7.64%; found: C, 38.97; H, 5.43; N, 7.41%.

Sodium piperazine-1-carbodithioate (17). ^1H NMR (DMSO- d_6 , δ , ppm): 4.23 (bs, 5H), 2.70 (bs, 4H). *Anal. Calcd.* for $\text{C}_5\text{H}_9\text{N}_2\text{S}_2\text{Na}$ ($M_r = 184.26$): C, 32.59; H, 4.92; N, 15.20%; found: C, 32.67; H, 4.73; N, 14.86%.

Sodium methyl(phenyl)carbamodithioate (18). ^1H NMR (DMSO- d_6 , δ , ppm): 7.17 (m, 5H), 3.61 (s, 3H). *Anal. Calcd.* for $\text{C}_8\text{H}_8\text{NS}_2\text{Na}$ ($M_r = 205.28$): C, 46.81; H, 3.93; N, 6.82%; found: C, 46.57; H, 3.62; N, 6.71%.

Sodium benzyl(methyl)carbamodithioate (19). ^1H NMR (DMSO- d_6 , δ , ppm): 7.24 (m, 5H), 5.45 (s, 2H), 3.27 (s, 3H). *Anal. Calcd.* for $\text{C}_9\text{H}_{10}\text{NS}_2\text{Na}$ ($M_r = 219.30$): C, 49.29; H, 4.60; N, 6.39%; found: C, 48.91; H, 4.49; N, 6.08%.

Sodium propan-2-yl(propyl)carbamodithioate (20). ^1H NMR (DMSO- d_6 , δ , ppm): 6.12 (sep, $J = 6.9$ Hz, 1H), 3.61 (m, 2H), 1.65 (sext, $J = 7.8$ Hz, 2H), 1.01 (d, $J = 7.0$ Hz, 6H), 0.77 (t, $J = 7.4$ Hz, 3H). *Anal. Calcd.* for $\text{C}_7\text{H}_{14}\text{NS}_2\text{Na}$ ($M_r = 199.31$): C, 42.18; H, 7.08; N, 7.03%; found: C, 41.91; H, 6.89; N, 6.74%.

4.4. Chemical analysis of selected compounds

The representative complexes **3**, **9**, **13** and **16** were analyzed by elemental analysis, mass spectrometry, ultraviolet-visible (UV-Vis) spectroscopy and Fourier-transform infrared (FTIR) spectroscopy. Electrospray ionization mass spectrometry (ESI-MS; acetonitrile (ACN) solutions) was carried out with an LCQ Fleet ion trap spectrometer (Thermo Scientific; QualBrowser software, version 2.0.7) in both positive (ESI+) and negative (ESI-) ionization modes. A Jasco FT/IR-4700 spectrometer (Jasco, Easton, MD, USA) was used for the collection of the Fourier-transform infrared (FTIR) spectra in the range of 400–4000 cm^{-1} by using the attenuated total reflection (ATR) technique on a diamond plate. A Cintra 3030 dual beam automatic UV-Vis spectrometer

(GBC Scientific Instruments) was used for the recording of the UV-Vis spectra at the 190–900 nm region; UV-Vis = ultraviolet-visible. Complexes were dissolved in ACN to 1 mM concentration.

For 3: Light-brown solid. *Anal. Calcd.* for $\text{C}_{30}\text{H}_{28}\text{N}_2\text{CuS}_4$ ($M_r = 608.36$): C, 59.23; H, 4.64; N, 4.60%; found: C, 59.31; H, 4.63; N, 4.65%. ESI + MS (ACN, m/z): 607.0 (calc. 607.0 for $[\text{M}]^+$). IR (ATR, ν , cm^{-1}): 3351, 3310, 3295, 3280, 3265, 3025, 2925, 2876, 1604, 1583, 1494, 1452, 1431, 1353, 1306, 1258, 1223, 1146, 1078, 1030, 984, 941, 872, 823, 792, 739, 625, 552, 517, 447. UV-Vis (ACN, λ_{max} , nm (ϵ , $\text{M}^{-1}\text{cm}^{-1}$ in parentheses)): 435 (2370).

For 9: Brown solid. *Anal. Calcd.* for $\text{C}_{10}\text{H}_{20}\text{N}_2\text{CuS}_4$ ($M_r = 360.08$): C, 33.36; H, 5.60; N, 7.78%; found: C, 33.25; H, 5.57; N, 7.66%. ESI + MS (ACN, m/z): 359.0 (calc. 359.0 for $[\text{M}]^+$). IR (ATR, ν , cm^{-1}): 2953, 2925, 2868, 1517, 1462, 1446, 1430, 1396, 1366, 1303, 1261, 1208, 1145, 1103, 1063, 1032, 976, 922, 883, 745, 609, 569, 496, 413. UV-Vis (ACN, λ_{max} , nm (ϵ , $\text{M}^{-1}\text{cm}^{-1}$ in parentheses)): 432 (2200).

For 13: Yellow solid. *Anal. Calcd.* for $\text{C}_{14}\text{H}_{28}\text{N}_2\text{CuS}_4$ ($M_r = 416.19$): C, 40.40; H, 6.78; N, 6.73%; found: C, 40.09; H, 6.47; N, 6.84%. ESI + MS (ACN, m/z): 415.0 (calc. 415.0 for $[\text{M}]^+$). IR (ATR, ν , cm^{-1}): 3273, 2931, 2883, 1610, 1587, 1462, 1438, 1362, 1259, 1169, 1086, 1032, 967, 872, 834, 793, 618, 453, 408. UV-Vis (ACN, λ_{max} , nm (ϵ , $\text{M}^{-1}\text{cm}^{-1}$ in parentheses)): 408 (2240).

For 16: Light-brown solid. *Anal. Calcd.* for $\text{C}_{12}\text{H}_{20}\text{N}_2\text{CuS}_4$ ($M_r = 384.11$): C, 37.52; H, 5.25; N, 7.29%; found: C, 37.69; H, 5.25; N, 7.33%. ESI + MS (ACN, m/z): 383.0 (calc. 383.0 for $[\text{M}]^+$). IR (ATR, ν , cm^{-1}): 2943, 2926, 2853, 1503, 1438, 1363, 1284, 1256, 1238, 1135, 1110, 1065, 1022, 996, 975, 951, 881, 855, 615, 518, 471, 406. UV-Vis (ACN, λ_{max} , nm (ϵ , $\text{M}^{-1}\text{cm}^{-1}$ in parentheses)): 434 (1710).

5. Biological experiments

5.1. Cell culture and XTT assay

U-2-OS (human osteosarcoma, 92022711), H1299 (human non-small cell lung carcinoma, CRL-5803TM), U-2-OS cell line was purchased from the European Collection of Authenticated Cell Cultures (ECACC) and H1299 from the American Type Culture Collection (ATCC[®]). Cells were cultivated in sterile and filtered DMEM High Glucose medium w/Stable Glutamine, w/Sodium Pyruvate (Biosera), which contained 10% Fetal Bovine Serum (FBS, Gibco[™]) and 1% Penicillin-Streptomycin (Sigma-Aldrich). The incubation conditions were 37 °C and 5% CO_2 .

Five thousand cells per well were seeded in 96-well plates and after 24 h, the treatment was performed according to the described experiments. The cells were placed in the incubator (37 °C, 5% CO_2) for 48 h. Then the XTT assay was performed according to the manufacturer's instructions. XTT activator with XTT reagent (AppliChem) was mixed and added to the cells. After 30–90 min of incubation, the absorbance was measured at 475 nm using a plate reader (Infinite[®] 200 Pro, TECAN). Data were analyzed in Microsoft[®] Excel[®] for Microsoft 365 MSO (Version 2211). Results are shown as means \pm s. d. from three independent experiments that were performed in triplicates.

5.2. Colony-formation assay

Fifty cells per well were seeded in 24-well plates and after 24 h, the treatment was performed according to the described experiments. Cells were incubated for 7 days. Crystal violet was used for the staining of colonies and air dried. After the staining, a white powder (kitchen sugar) was added to the wells to enhance the contrast. Whole plates were scanned using a table scanner. The colony area for each well was calculated using ImageJ software. Results are shown as means \pm s. d. of three independent experiments, when each was performed in a technical triplicate.

5.3. Flow cytometric assay and screening

Three hundred thousand U-2-OS-NPL4-GFP cells were seeded in tissue culture dishes (growth surface 22.1 cm², TPP) in 4 ml of medium. After 24 h of incubation (37 °C, 5% CO₂), the treatment was performed according to the described experiments. Cells were incubated for 3 h (37 °C, 5% CO₂). Then the medium was removed, cells were washed with PBS, scraped, resuspended in PBS and transferred into 1.5 ml micro test tubes. Cells were pre-extracted with 0.1% Triton X-100 and subsequently stained with DAPI 0.5 µg/ml. After 15 min of incubation on ice, the measurement was performed on a flow cytometer (BD FACS Verse, BD Life Sciences) with GFP signal detection. Data were analyzed in the CytoSpec software (Version 11.6), Microsoft® Excel® for Microsoft 365 MSO (Version 2211), Statistica (Version 13.4.0.14).

5.4. Immunoblotting and antibodies

Four hundred thousand U-2-OS cells were seeded in tissue culture dishes (growth surface 22.1 cm², TPP) in 4 ml of medium and after 24 h, the cell lysates were prepared. The lysates were separated by SDS-PAGE using hand-cast gels (8%). The transfer to a nitrocellulose membrane was performed and the membrane was blocked with 5% milk in Tris-buffered saline containing 0.1% Tween-20 for 1 h. The incubation with primary antibodies took place at room temperature for 1 h. The list of primary antibodies: anti-β-actin (C4) (1:500; Santa Cruz Biotechnology, sc-47778), anti-ubiquitin Lys48, clone Apu2 (1:1000; Merck Millipore, 05–1307), ATF4 (1:1000; Merck Millipore, ABE387), HSP70/HSP72 (C92F3A-5) (1:1000; Enzo Life Sciences, ADI-SPA-810F), p-eIF2α (S51) (1:1000; Cell Signalling, 3597S), HSF1 (1:1000; Cell Signalling, 4356S). The detection was performed using the following secondary antibodies after 45 min incubation at room temperature: anti-mouse HRP-IgG (1:1000; GE Healthcare, NA931V), anti-rabbit HRP-IgG (1:1000; GE Healthcare, NA934). The chemiluminescent substrate (Thermo Fisher Scientific, 34580) was used for visualization. Images were recorded using ChemiDoc System (Bio-Rad) and analyzed with Image Lab Software (Bio-Rad).

5.5. Microscopy

Samples were analyzed using the LSM780 confocal microscope system (Zeiss). Images of fixed samples were acquired using a C Apo 40x/1.2 W water immersion objective. Image analysis was performed in Zeiss ZEN software (2011 SP7 FP3 black).

5.6. Immunofluorescence staining

One hundred thousand U-2-OS-NPL4-GFP cells per well were seeded in 12-well plates. After 24 h, the treatment was performed according to the described experiments. The cells were incubated (37 °C, 5% CO₂) for 3 h. Where indicated, the pre-extraction before fixation was performed with PBS containing 0.2% Triton X-100 for 1 min at room temperature. Then the cells were PBS washed and fixed with cold 4% formaldehyde for 15 min at room temperature. Primary antibodies were applied and the cells were incubated for 1 h at room temperature: anti-ubiquitin Lys48, clone Apu2 (1:500; Merck Millipore, 05–1307), HSP70/HSP72 (C92F3A-5) (1:500; Enzo Life Sciences, ADI-SPA-810F), HSF1 (1:500; Cell Signalling, 4356S). Secondary antibodies were applied and the cells were incubated for 1 h at room temperature: Goat anti-rabbit IgG (H + L) Alexa Fluor™ 568 (1:1 000, Invitrogen, A-11036), Goat anti-mouse IgG (H + L) Alexa Fluor™ 568 (1:1 000, Invitrogen, A-11004). Cells were subsequently stained with DAPI (1 µg/ml).

Declaration of competing interest

The authors declare that they have no known competing financial interests or personal relationships that could have appeared to influence

the work reported in this paper.

Data availability

Data will be made available on request.

Acknowledgments

The study was supported by the Czech Science Foundation (GA20-28685S) and by MEYS CR (Large RI Project LM2018129 Czech-BioImaging).

Appendix A. Supplementary data

Supplementary data to this article can be found online at <https://doi.org/10.1016/j.ejmech.2023.115790>.

References

- [1] M.S. Boguski, K.D. Mandl, V.P. Sukhatme, Repurposing with a difference, *Science* (2009), <https://doi.org/10.1126/science.1169920>.
- [2] P. Liu, S. Brown, T. Goktug, P. Channathodiyil, V. Kannappan, J. P. Hugnot, P.-O. Guichet, X. Bian, A.L. Arnesilla, J.L. Darling, W. Wang, Cytotoxic effect of disulfiram/copper on human glioblastoma cell lines and ALDH-positive cancer-stem-like cells, *Br. J. Cancer* 107 (2012) 1488–1497, <https://doi.org/10.1038/bjc.2012.442>.
- [3] X. Liu, L. Wang, W. Cai, X. Yuan, L. Lin, Q. Cao, N. Wang, Y. Li, W. Guo, X. Zhang, C. Wu, J. Yang, Targeting ALDH1A1 by disulfiram/copper complex inhibits non-small cell lung cancer recurrence driven by ALDH-positive cancer stem cells, *Oncotarget* 7 (2016) 58516–58530, <https://doi.org/10.18632/oncotarget.11305>.
- [4] Z. Skrott, D. Majera, J. Gursky, T. Buchtova, M. Hajdúch, M. Mistrík, J. Bartek, Disulfiram's anticancer activity reflects targeting NPL4, not inhibition of aldehyde dehydrogenase, *Oncogene* 38 (2019) 6711–6722, <https://doi.org/10.1038/s41388-019-0915-2>.
- [5] B. Johansson, Z. Stankiewicz, Bis-(diethylthiocarbamate) copper complex: a new metabolite of disulfiram? *Biochem. Pharmacol.* 34 (1985) 2989–2991, [https://doi.org/10.1016/0006-2952\(85\)90026-7](https://doi.org/10.1016/0006-2952(85)90026-7).
- [6] J.J. Lipsky, M.L. Shen, S. Naylor, In vivo inhibition of aldehyde dehydrogenase by disulfiram, *Chem. Biol. Interact.* 130–132 (2001) 93–102, [https://doi.org/10.1016/S0009-2797\(00\)00225-8](https://doi.org/10.1016/S0009-2797(00)00225-8).
- [7] J.P. Lam, D.C. Mays, J.J. Lipsky, Inhibition of recombinant human mitochondrial and cytosolic aldehyde dehydrogenases by two candidates for the active metabolites of disulfiram, *Biochemistry* 36 (1997) 13748–13754, <https://doi.org/10.1021/b970994e>.
- [8] B.W. Hart, M.D. Faiman, Bioactivation of S-methyl N,N-Diethylthiocarbamate to S-methyl N,N-diethylthiocarbamate sulfide, *Biochem. Pharmacol.* 46 (1993) 2285–2290, [https://doi.org/10.1016/0006-2952\(93\)90619-8](https://doi.org/10.1016/0006-2952(93)90619-8).
- [9] Z. Skrott, B. Cvek, Diethylthiocarbamate complex with copper: the mechanism of action in cancer cells, *Mini-Rev. Med. Chem.* 12 (2012) 1184–1192, <https://doi.org/10.2174/1389557128032762068>.
- [10] Z. Skrott, M. Mistrík, K.K. Andersen, S. Friis, D. Majera, J. Gursky, T. Ozdian, J. Bartkova, Z. Turi, P. Moudry, M. Kraus, M. Michalova, J. Vackova, P. Dzubak, I. Vrobel, P. Pouckova, J. Sedlacek, A. Miklovicova, A. Kutt, J. Li, J. Mattova, C. Driessen, Q.P. Dou, J. Olsen, M. Hajdúch, B. Cvek, R.J. Deshaies, J. Bartek, Alcohol-abuse drug disulfiram targets cancer via p97 segregase adaptor NPL4, *Nature* 552 (2017) 194–199, <https://doi.org/10.1038/nature25016>.
- [11] H. Meyer, M. Bug, S. Brenner, Emerging functions of the VCP/p97 AAA-ATPase in the ubiquitin system, *Nat. Cell Biol.* 14 (2012) 117–123, <https://doi.org/10.1038/ncb2407>.
- [12] R.J. Deshaies, Proteotoxic crisis, the ubiquitin-proteasome system, and cancer therapy, *BMC Biol.* 12 (2014) 94, <https://doi.org/10.1186/s12915-014-0094-0>.
- [13] K. Chroma, Z. Skrott, J. Gursky, J. Bacovsky, P. Moudry, T. Buchtova, M. Mistrík, J. Bartek, A drug repurposing strategy for overcoming human multiple myeloma resistance to standard-of-care treatment, *Cell Death Dis.* 13 (2022) 203, <https://doi.org/10.1038/s41419-022-04651-w>.
- [14] M. Pan, Q. Zheng, Y. Yu, H. Ai, Y. Xie, X. Zeng, C. Wang, L. Liu, M. Zhao, Sessaw conformations of Np4 in the human p97 complex and the inhibitory mechanism of a disulfiram derivative, *Nat. Commun.* 12 (2021) 121, <https://doi.org/10.1038/s41467-020-20359-x>.
- [15] D. Majera, Z. Skrott, K. Chroma, J.M. Mercht-Mayra, M. Mistrík, J. Bartek, Targeting the NPL4 adaptor of p97/VCP segregase by disulfiram as an emerging cancer vulnerability evokes replication stress and DNA damage while silencing the ATR pathway, *Cells* 9 (2020) 469, <https://doi.org/10.3390/cells9020469>.
- [16] D.C. Kanelis, A. Zisi, Z. Skrott, B. Lemmens, J.A. Espinoza, M. Kosar, A. Björkman, X. Li, S. Arampatzis, J. Bartkova, M. Andújar Sánchez, O. Fernandez-Capetillo, M. Mistrík, M.S. Lindström, J. Bartek, Actionable cancer vulnerability due to translational arrest, p53 aggregation and ribosome biogenesis stress evoked by the disulfiram metabolite CuIT, *Cell Death Differ.* (2023), <https://doi.org/10.1038/s41418-023-01167-4>.

- [17] A.C. Woerner, F. Protin, D. Hornburg, L.R. Feng, F. Meissner, M. Patra, J. Tatzelt, M. Mann, K.F. Winklhofer, F.L. Haril, M.S. Hipp, Cytoplasmic protein aggregates interfere with nucleocytoplasmic transport of protein and RNA, *Science* 351 (2016) 173–176, <https://doi.org/10.1126/science.1250333>.
- [18] L. Kaul, R. Süss, A. Zannettino, K. Richter, The revival of dithiocarbamates: from pesticides to innovative medical treatments, *iScience* 24 (2021), <https://doi.org/10.1016/j.isci.2021.102092>.
- [19] G. Hogarth, Metal-dithiocarbamate complexes: chemistry and biological activity, *Mini Rev. Med. Chem.* 12 (2012) 1202–1215, <https://doi.org/10.2174/138955712802762095>.
- [20] D. Cheu, F. Peng, Q.C. Cui, K.G. Daniel, S. Orlu, J. Liu, Q.P. Dou, Inhibition of prostate cancer cellular proteasome activity by a pyrrolidine dithiocarbamate-copper complex is associated with suppression of proliferation and induction of apoptosis, *Front. Biosci. - J. Vis. Literacy* 10 (2005) 2932–2939.
- [21] H. Löfberg, F. Öberg, L. Rickardson, J. Guillo, P. Nygren, R. Larsson, Inhibition of proteasome activity, nuclear factor KB translocation and cell survival by the antialcoholism drug disulfiram, *Int. J. Cancer* 118 (2006) 1577–1580, <https://doi.org/10.1002/ijc.21534>.
- [22] T. Buchtova, Z. Skrott, K. Chroma, J. Rehulka, P. Dzubak, M. Hajduch, D. Lukac, S. Arampatzis, J. Bartek, M. Mistrik, Camabidol-induced activation of the methionine pathway impedes anticancer effects of disulfiram and its metabolite CaT, *Mol. Oncol.* 16 (2022) 1541–1554, <https://doi.org/10.1002/1878-0261.13114>.
- [23] T. Fujie, M. Murakami, E. Yoshida, T. Tachinami, Y. Shinkai, Y. Fujiwara, C. Yamamoto, Y. Kusagai, H. Naka, T. Kaji, Copper diethyldithiocarbamate as an activator of Nr2f2 in cultured vascular endothelial cells, *JBC, J. Biol. Inorg. Chem.* 21 (2016) 263–273, <https://doi.org/10.1007/s00775-016-1337-z>.
- [24] K. Richter, M. Haslbeck, J. Buchner, The heat shock response: Life on the verge of death, *Mol. Cell* 40 (2010) 253–266, <https://doi.org/10.1016/j.molcel.2010.10.006>.
- [25] T. Guetouche, F. Boellmann, W.S. Lane, R. Voellmy, Analysis of phosphorylation of human heat shock factor 1 in cells experiencing a stress, *BMC Biochem.* 6 (2005) 4, <https://doi.org/10.1186/1471-2091-6-4>.
- [26] D. Majera, Z. Skrott, J. Bouchal, J. Bartkova, D. Simkova, M. Gachechiladze, J. Steigerova, D. Kurfurstova, J. Gursky, G. Korinkova, K. Cwierka, Z. Hodny, M. Mistrik, J. Bartek, Targeting genotoxic and proteotoxic stress-response pathways in human prostate cancer by clinically available PARP inhibitors, vorinostat and disulfiram, *Prostate* 79 (2019) 352–362, <https://doi.org/10.1002/pros.23741>.
- [27] G. Blamont, C. Vourc'h, Nuclear Stress Bodies, *Cold Spring Harbor Perspectives in Biology*, vol. 2, 2010, <https://doi.org/10.1101/cshperspect.a000695>.
- [28] C. Hetz, The unfolded protein response: controlling cell fate decisions under ER stress and beyond, *Nat. Rev. Mol. Cell Biol.* 13 (2012) 89–102, <https://doi.org/10.1038/nrm3270>.
- [29] B. Cvek, V. Milacic, J. Taraba, Q.P. Dou, Ni(II), Cu(II), and Zn(II) diethyldithiocarbamate complexes show various activities against the proteasome in breast cancer cells, *J. Med. Chem.* 51 (2008) 6256–6258, <https://doi.org/10.1021/jm9007807>.
- [30] W. Chen, W. Yang, P. Chen, Y. Huang, F. Li, Disulfiram copper nanoparticles prepared with a stabilized metal ion ligand complex method for treating drug-resistant prostate cancers, *ACS Appl. Mater. Interfaces* 10 (2018) 41118–41128, <https://doi.org/10.1021/acsami.8b14940>.
- [31] R.A. Pann, D.C. Dumut, A. Centorame, T. Thuraingam, M. Hajduch, M. Mistrik, P. Dzubak, J.B. De Sanctis, D. Radzich, M. Tabrizian, One-step synthesis of nanoliposomal copper diethyldithiocarbamate and its assessment for cancer therapy, *Pharmaceutics* 14 (2022) 640, <https://doi.org/10.3390/pharmaceutics14030640>.
- [32] E.E. Manasanch, R.Z. Orlovski, Proteasome inhibitors in cancer therapy, *Nat. Rev. Clin. Oncol.* 14 (2017) 417–433, <https://doi.org/10.1038/nrclinonc.2016.206>.
- [33] H.L. Klöpping, G.J.M. van der Kerk, Investigations on organic fungicides: IV. Chemical constitution and fungistatic activity of dithiocarbamates, thiram sulphides and structurally related compounds, *Recl. Trav. Chim. Pays Bas* 70 (2010) 917–939, <https://doi.org/10.1002/RECL.1951071008>.
- [34] H. Golzar, Heavy-metal immobilization Agents Having Good Metal-Chelating Properties, *Patent JP10076240 A*, 1998.
- [35] V. Konecny, Synthesis and biological properties of dithiocarbamic acid derivatives. 12. Biological properties of mixed anhydrides of N-methyl-IV-methoxycarbonylcarbamate and N,N'-dialkylidithiocarbamic acids, *Chem. Zvesti* 38 (1984) 839–849.
- [36] M. Afzal, K. Ellwood, N.L. Pickett, P. O'Brien, J. Rafferty, J. Waters, Growth of lead chalcogenide thin films using single-source precursors, *J. Mater. Chem.* 14 (2004) 1310–1315, <https://doi.org/10.1039/B313063K>.
- [37] K. Chandra, A.K. Garg, M.C. Jain, N. Kumar, B.S. Garg, Preparation and characterization of bis dithiocarbamate complexes of bis biphenyl tin(IV), *J. Indian Chem. Soc.* 57 (1980) 378–381, <https://doi.org/10.5281/ZENODO.6361397>.
- [38] Y. Tanaka, J. Odo, K. Kariya, Direct chelatometric titration of mercury(II) using sodium bis(4-sulfobenzyl)dithiocarbamate, *Bunseki Kagaku* 26 (1977) 60–63.
- [39] J.F. Thomson, J. Savit, E. Goldwasser, Tests of 2,3-dimercaptopropanol and related dithiols for decontamination of lewisite on human skin, *J. Pharmacol. Exp. Therapeut.* 89 (1947).
- [40] K. Hayano, H. Yoneyama, Y. Hayashi, Y. Noda, Syntheses of piperazines. I. Synthesis of N-methylpiperazine, *Yakugaku Kenkyu* 30 (1958) 256–261.
- [41] Y. Watanabe, E. Hirai, Fungicidal 2,4,6-cycloheptatrien-1-yl dithiocarbamates, *Patent DE2224597 A*, 1972.
- [42] E.A. Kreider, 2-(2-Methyl-5-nitro-1-imidazolyl)ethyl-N-aryldithiocarbamates, *Patent US3910945 A*, 1975.



Received: 24 September 2018 | Accepted: 24 October 2018
 DOI: 10.1002/pros.23741

ORIGINAL ARTICLE

WILEY **The Prostate**

Targeting genotoxic and proteotoxic stress-response pathways in human prostate cancer by clinically available PARP inhibitors, vorinostat and disulfiram

Dusana Majera PhD¹ | Zdenek Skrott MSC¹ | Jan Bouchal PhD² |
 Jirina Bartkova MD, PhD^{3,4} | Dana Simkova PhD² | Mariam Gachechiladze MD, PhD² |
 Jana Steigerova PhD² | Daniela Kurfurstova MD, PhD² | Jan Gursky PhD¹ |
 Gabriela Korinkova PhD² | Karel Cwiertka MD, PhD⁵ | Zdenek Hodny MD, PhD⁶ |
 Martin Mistrik PhD¹ | Jiri Bartek MD, PhD^{1,3,4,6}

¹Laboratory of Genome Integrity, Institute of Molecular and Translational Medicine, Faculty of Medicine and Dentistry, Palacky University, Olomouc, Czech Republic

²Department of Clinical and Molecular Pathology, Institute of Molecular and Translational Medicine, Faculty of Medicine and Dentistry, Palacky University, Olomouc, Czech Republic

³Danish Cancer Society Research Center, Copenhagen, Denmark

⁴Division of Genome Biology, Department of Medical Biochemistry and Biophysics, Science for Life Laboratory, Karolinska Institute, Stockholm, Sweden

⁵Department of Oncology, Faculty of Medicine and Dentistry, Palacky University, University Hospital, Olomouc, Czech Republic

⁶Department of Genome Integrity, Institute of Molecular Genetics of the CAS, v.v.i., Prague, Czech Republic

Correspondence

Jiri Bartek, MD, PhD, Danish Cancer Society Research Center, Copenhagen, Denmark
 Email: jb@cancer.dk

Jan Bouchal, PhD, Department of Clinical and Molecular Pathology, Institute of Molecular and Translational Medicine, Faculty of Medicine and Dentistry, Palacky University, Olomouc, Czech Republic
 Email: jan.bouchal@upol.cz

Martin Mistrik, PhD, Laboratory of Genome Integrity, Institute of Molecular and Translational Medicine, Faculty of Medicine and Dentistry, Palacky University, Olomouc, Czech Republic
 Email: martin.mistrik@upol.cz

Funding information

The Danish cancer society; the Novo Nordisk Foundation; Palacky University, Grant numbers: IGA-LF-2018-001, IGA-LF-2018-034; the Swedish research council and Cancer Fonden; the Danish council for independent research; Czech Ministry of Education, Grant number: DRO-61989592; Czech National Program of Sustainability, Grant number: LO1304; Czech Ministry of Health, Grant numbers: AZV 16-32030, DRO-FNOL00098892, NV15-28628A;

Background: Castration-resistant prostate cancer (PCa) represents a serious health challenge. Based on mechanistically-supported rationale we explored new therapeutic options based on clinically available drugs with anticancer effects, including inhibitors of PARP1 enzyme (PARPi), and histone deacetylases (vorinostat), respectively, and disulfiram (DSF, known as alcohol-abuse drug Antabuse) and its copper-chelating metabolite CuET that inhibit protein turnover.

Methods: Drugs and their combination with ionizing radiation (IR) were tested in various cytotoxicity assays in three human PCa cell lines including radio-resistant stem-cell like derived cells. Mechanistically, DNA damage repair, heat shock and unfolded protein response (UPR) pathways were assessed by immunofluorescence and immunoblotting.

Results: We observed enhanced sensitivity to PARPi/IR in PC3 cells consistent with lower homologous recombination (HR) repair. Vorinostat sensitized DU145 cells to PARPi/IR and decreased mutant p53. Vorinostat also impaired HR-mediated DNA repair, as determined by Rad51 foci formation and downregulation of TOPBP1 protein, and overcame radio-resistance of stem-cell like DU145-derived cells. All PCa models responded well to CuET or DSF combined with copper. We demonstrated that DSF interacts with copper in the culture media and forms adequate levels of CuET indicating that DSF/copper and CuET may be considered as comparable treatments. Both DSF/copper and CuET evoked hallmarks of UPR in PCa cells, documented by upregulation of ATF4, CHOP and phospho-eIF2 α , with ensuing heat

Kellner Family Foundation; Czech-Bioluming.
Grant number: LM2015062

shock response encompassing activation of HSF1 and HSP70. Further enhancing the cytotoxicity of CuET, combination with an inhibitor of the anti-apoptotic protein survivin (YM155, currently undergoing clinical trials) promoted the UPR-induced toxicity, yielding synergistic effects of CuET and YM155.

Conclusions: We propose that targeting genotoxic and proteotoxic stress responses by combinations of available drugs could inspire innovative strategies to treat castration-resistant PCa.

KEYWORDS

disulfiram, PARP, prostate cancer, proteotoxic stress, vorinostat

1 | INTRODUCTION

Prostate cancer (PCa) is the most frequently diagnosed malignancy in men and one of the major causes of cancer-related death in developed countries.¹ PCa is initially androgen-dependent and responds to androgen deprivation therapies, however, the disease ultimately progresses into a hormone-independent and largely incurable stage with metastases to the bones, lung, brain, or liver.

Aberrations in the DNA damage response (DDR) machinery are common in cancer and represent potential targets for therapeutic intervention.² PARP1 activity is important in sensing and signaling DNA damage that arises both endogenously, for example, through generation of oxidative DNA lesions and DNA single-strand breaks (SSBs), or exogenously, such as due to ionizing radiation (IR) exposure or treatment with various chemotherapeutics. Exposure of cycling cells to inhibitors of PARP1 (PARPi) causes excessive unrepaired SSBs and acceleration of DNA replication³ leading to replication stress and formation of DNA double-strand breaks (DSBs), toxic lesions preferentially repaired by homologous recombination (HR). HR defects due to mutations or silencing of factors such as BRCA1/2 sensitize cells to PARPi, as shown for ovarian, breast and also metastatic prostate cancer.⁴

Defects in DNA damage sensors, signaling kinases or nucleotide excision repair also sensitize to PARPi⁴ suggesting that the therapeutic potential of PARPi might extend beyond the BRCA1/2-defective tumors. There is also an urgent need to identify and validate potential biomarkers to predict sensitivity of individual tumors to PARPi, exemplified for PCa by the fusion oncogene TMRSS2-ERG or loss of the PTEN tumor suppressor.^{5,6}

PCa is a heterogeneous disease reflecting both genetic and epigenetic alterations.⁷ Six epigenetics-modulating drugs targeting DNA methylation or histone deacetylation have been approved for cancer treatment.⁷ Since epigenetic regulation is complex, preclinical studies are required to generate patient stratification hypotheses and identify predictive biomarkers. Epigenetic reprogramming after loss of Rb and p53 tumor suppressors diminishes androgen receptor expression and is associated with resistance to antiandrogen therapy.^{8,9} From this point of view, both PC3 and DU145 cells,

lacking AR and possessing mutations in tumor suppressors, represent relevant models of a subgroup of aggressive prostate cancer.

Another approach to PCa treatment could be drug repurposing, with potentially multifaceted benefits for clinical implementation of new treatment options. DSF is among such possible candidates, showing anti-tumor activity in multiple studies. Recently, we discovered the molecular target and mode of action of DSF, thereby strengthening DSF's potential as an anticancer drug.¹⁰ Many cancers become resistant to monotherapy through diverse mechanisms, posing a major challenge in contemporary oncology. Drug combination could overcome resistance to single compounds, thus it is vital to find the drugs that act synergistically and are well tolerated.¹¹

Here, we describe differential responses to PARPi and IR in cellular models of aggressive PCa: PC3 (typical for loss of p53 and PTEN), DU145 (mutated p53 and Rb) and radioresistant stem-like PCa cells.¹² Moreover, we show that HDAC inhibition alters expression of HR proteins and potentiates cytotoxicity of IR, and that DSF's active metabolite, diethyldithiocarbamate-copper complex (CuET), activates heat shock response and UPR, showing synergistic toxic effect in combination with a survivin inhibitor-YM155 in human PCa models.

2 | MATERIAL AND METHODS

2.1 | Cell lines

DU145 and PC3 cell lines were cultured in DMEM medium, LNCaP in RPMI medium and LAPC4 in IMDM. DMEM, RPMI, and IMDM media were supplemented with 10% fetal bovine serum and penicillin/streptomycin. IMDM medium was additionally supplemented with 1 nM R1881. RWPE-1 cells were cultured in a keratinocyte serum-free medium supplemented with the bovine pituitary extract and human recombinant epidermal growth factor (Thermo Scientific, Waltham, MA). EP156T cells were cultured as described previously.¹³ All cell cultures were maintained in humidified 5% CO₂ atmosphere at 37°C. LAPC4, EP156T and RWPE1 cells were kindly provided by Prof. Zoran Culig and Prof. Helmut Klocker (Innsbruck Medical University). Other cell lines were purchased from the European Collection of Cell

Cultures (ECACC) and authenticated by AmpflSTR™ Identifier PCR Amplification Kit (Applied Biosystems, Foster City, CA).

2.2 | Colony forming and cell viability assays

For clonogenic cell survival assay, cells were plated in 6-well plates at 200–500 cells per plate. Next day the cells received appropriate treatment and kept in culture for 7–14 days. Colonies of approximately 50 cells were visualized by 1% crystal violet in 96% ethanol, and their number and total area were counted. Results were confirmed in three independent experiments. For XTT assay, cells were plated at a density of 10 000 per well in a 96-well plate. The next day, cells were treated as indicated. After 48 h, an XTT assay was performed according to the manufacturer's instructions (Applchem, Darmstadt, Germany). XTT solution was added to the medium and incubated for 30–60 min, and then the dye intensity was measured at the 475 nm wavelength using a spectrometer (TECAN, Infinite M200PRO, Mannedorf, Switzerland).

2.3 | Ionizing radiation and chemicals

The KU58948 inhibitor was obtained from AstraZeneca (London, UK). Vorinostat, MK132, nutlin 3, DSF, tunicamycin, thapsigargin and CuCl₂ were purchased from Sigma-Aldrich, YM155 from Selleckchem and copper diethyldithiocarbamate (CuET) from TCI Chemicals. Ionizing radiation was delivered using Xstrahl RS research cabinet gamma irradiator.

2.4 | Immunoblotting

Equal amounts of cell lysates were separated by SDS-PAGE on handcast or precast gel (Invitrogen, Carlsbad, CA), and then transferred onto nitrocellulose membrane. The membrane was blocked with 5% milk in Tris-buffered saline containing 0.1% Tween 20 for 1 h at room temperature, and then incubated overnight at 4°C or 1 h at room temperature with one of the following primary antibodies against: p53 (FL-393, Cell Signaling, Danvers, MA), Rad51 (ab63801, Abcam, Cambridge, UK), GAPDH (GTX30666, GeneTex), alpha-tubulin (H-300, Santa Cruz, Dallas, TX), BRCA1 (D-9, Santa Cruz), KU70 (N3H10, Santa Cruz), KU80 (ab3107, Abcam), DNA-PKcs (clone 18-2 Thermo Scientific), lamin B (M-20, Santa Cruz), TopBP1 (A300-111A, Bethyl, Montgomery, TX), BRCA2 (A300-005A, Bethyl), ATF4 (ABE387, Merck-Millipore), CHOP (L63F7, Cell Signaling), p-eIF2α (S51, Cell signalling), HSP70 (C92FBA-5, Enzo), followed by detection by secondary antibodies: goat-anti mouse and goat-anti rabbit (GE Healthcare). HRP conjugated secondary antibodies were visualized by ECL detection reagent (Thermo Scientific).

2.5 | Immunofluorescence staining

After appropriate treatment cells were fixed with 4% formaldehyde for 15 min at room temperature, washed with PBS and permeabilized with 0.5% Triton X-100 in PBS for 5 min. The samples on the plastic inserts cutted directly from cultivation plates using CNC machine were then immunostained with primary antibodies against Rad51 (ab63201,

Abcam), cyclin A (6E6, Leica), BRCA1 (D-9, Santa Cruz), p53 (FL-393, Santa Cruz), HSF1 (43565 Cell Signaling), followed by a fluorochrome-conjugated secondary antibodies: Alexa Fluor-488 or Alexa Fluor-568 (Invitrogen). Nuclei were visualized by Hoechst 33342 at room temperature for 5 min before mounting. Images were automatically recorded using an inverted fluorescence microscope BX71 (Olympus) and ScanR Acquisition software (Olympus), analyzed with ScanR Analysis software (Olympus), and evaluated with Statistica software (StatSoft).

2.6 | Small RNA interference

DU145 cells were transfected with anti-p53 siRNA (Eurofins Genomics-GUC CAG AUG AAG CUC CCA GAA) and NT siRNA (Eurofins Genomics-UAA UGU AUU GGA ACG CAU A) using Lipofectamine RNAiMAX transfection reagent (Invitrogen) according to manufacturer's recommended protocol. After 24 h, cells were either collected for Western blot analysis or used for immunofluorescence analysis.

2.7 | Cell cycle analysis

Cells were harvested at indicated times after treatment (both adherent and detached cells were collected) and fixed in cold 70% ethanol. After treatment with RNaseA, samples were stained with propidium iodide (PI). Cellular DNA content was analyzed using flow cytometer BD FACSVerser (BD Biosciences), and collected data were processed using BD FACSuite (BD Biosciences). At least 10 000 cells per sample were analyzed.

2.8 | Caspases 3/7 assay

Activity of caspase-3 and -7 was quantified by cleavage of fluorogenic substrate CellEvent™ Caspase-3/7 Green Detection Reagent (ThermoFisher Scientific). Briefly, samples were prepared in staining buffer (140 mM NaCl, 4 mM KCl, 0.75 mM MgCl₂, 10 mM HEPES) supplemented with 2% FBS, 0.5 μM CellEvent™ Caspase-3/7 Green Detection Reagent and incubated for 45 min at room temperature in the dark. Subsequently, 0.5 μg/mL DAPI was added and samples were analyzed by flow cytometry using BD FACSVerser (BD Biosciences), at least 10 000 events were acquired per sample. Collected data were processed by BD FACSuite (BD Biosciences).

2.9 | Measurement of CuET formation in vitro

To measure the formation of diethyldithiocarbamate-copper complex (CuET) in vitro a complete cell culture medium (DMEM, 10% FBS, 1% penicillin/streptomycin) was incubated with 1 μM disulfiram or 1 μM disulfiram plus 1 μM copper (ii) chloride, and 1 μM CuET as a control. After 3 h of incubation in 37 °C, 5% CO₂, the samples were vortexed and mixed with acetone in a ratio 1:250. The mixture was centrifuged 18 000g for 2 min at 4°C. The CuET complex in supernatant was analyzed by HPLC-MS method as described previously.¹⁰ The quantification of CuET complex was calculated according to the calibration curve.

3 | RESULTS

3.1 | DU145 cells show more efficient HR repair after PARPi and IR compared to more responsive PC3 cells

The standard-of-care therapy for localized PCa is radical prostatectomy followed by fractionated radiotherapy. In patients with disseminated PCa, androgen deprivation is achieved either by surgical or chemical castration. However, tumors often become castration-resistant as

disease progresses.¹⁴ Human PC3 and DU145 cell lines both lack androgen receptors and thus represent useful models for PCa patients with androgen-independent tumor growth.⁸

Recent findings showed high response rates to PARPi treatment in patients with PCa defective in DNA repair genes.⁴ Using colony formation assays that mimic effects of long-lasting therapy, we found PC3 cells more sensitive to the PARPi than DU145 cells (Figure 1A), while normal prostate epithelial RWPE1 and EP156T cells did not respond within the 1000 nM range (Supplementary Figures S1A and S1B). As PARP inhibitors are also candidate radiosensitizers, we tested

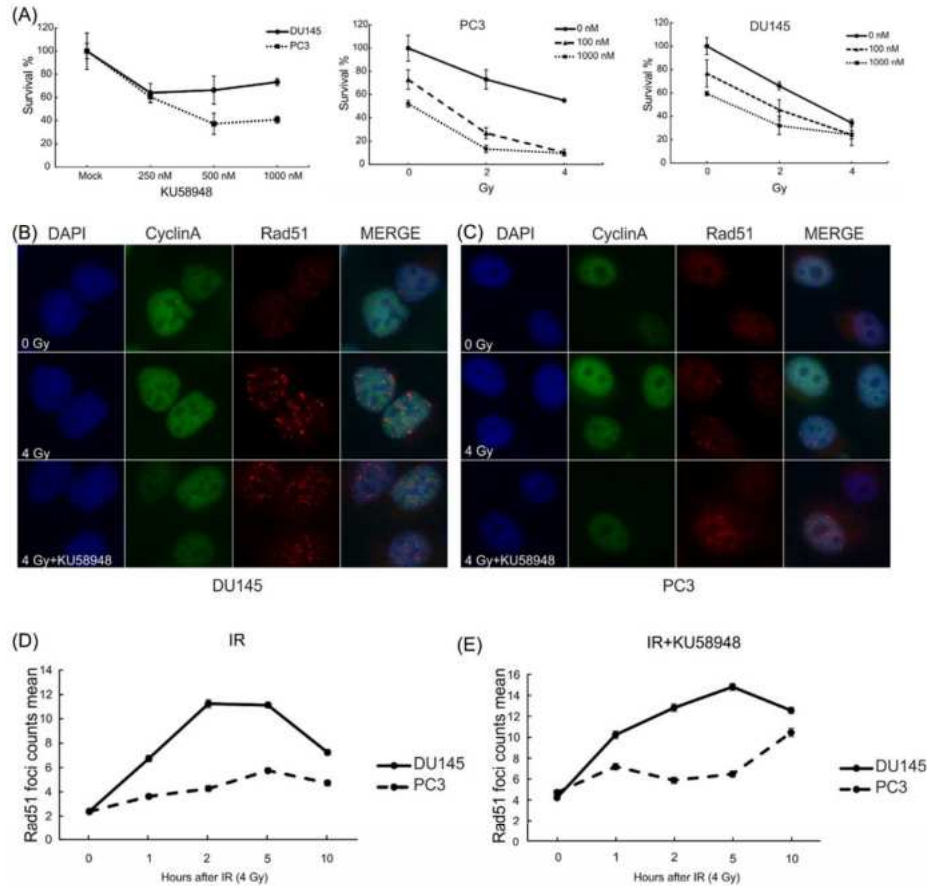


FIGURE 1 Rad51 foci formation is more effective in DU145 than in more responsive PC3 cells after KU58948 pre-treatment and IR. (A) PC3 and DU145 cells were treated with various concentrations of KU58948 and incubated for 8 days in colony formation assay. Next, cells were irradiated with different doses after 24 h pre-treatment with the KU58948 and incubated for 8-days in colony formation assay. Error bars represent SD of mean ($n = 3$). For immunofluorescence analysis, DU145 (B) and PC3 (C) cells were treated with 1 μ M KU58948 inhibitor for 24 h followed by IR (4 Gy) and fixed at different time points (0, 1, 2, 5, and 10 h). Images are representative from 2 h time points. Rad51 foci formation in cyclin A-positive DU145 cells was more effective than in PC3 cells (D and E). [Color figure can be viewed at wileyonlinelibrary.com]

combined PARPi and IR to explore potential additive/synergic effects. DU145 and PC3 cells were pre-treated with 100 nM and 1 μ M PARPi and irradiated after 24 h. Although PC3 cells were less responsive than DU145 to IR alone, the combination with PARPi was more effective in PC3 than in DU145 cells (Figure 1A). These data suggest that PC3 cells respond well to PARPi monotherapy or combined with IR, while DU145 respond rather poorly, a phenomenon which we decided to study further mechanistically.

PARPi is particularly effective in treatment of breast and ovarian cancer with BRCA1/2 mutations.¹⁵ BRCA1 along with Rad51 and other factors mediate HR, a high-fidelity DNA repair of DNA DSBs during S and G2 phases of the cell cycle. As PC3 cells responded well to PARPi and the combination with IR compared to DU145 cells, the functional status of HR-repair was examined using immunofluorescence analysis of RAD51 foci as marker of active HR. These experiments involved pre-treatment of cells with PARPi for 24 h, subsequent IR (4 Gy) and further incubation for 1, 2, 5, or 10 h. Fixed cells were then co-stained for RAD51 and the 5/G2 marker cyclin A to focus on the HR-relevant cell-cycle phases (Figures 1B and 1C).¹⁶ Quantification showed reduced RAD51 foci in PC3 cells compared to DU145 in cyclin A-positive cells (Figures 1D and 1E) supporting the hypothesis of insufficient HR to explain higher sensitivity of PC3 cells to PARPi. These data are consistent with the notion that HR defects sensitize cancer cells to PARPi, alone or combined with IR¹⁷ and extend this concept to PCa.

3.2 | Vorinostat treatment overcomes DU145 cell resistance towards IR and PARPi

Since DU145 cells display relative resistance to PARPi and the combined PARPi/IR treatment (Figure 1A), we sought to identify a drug able to sensitize this PCa model to PARPi. DU145 harbours p53 mutations (P223L and V274F) thereby providing a model matching PCa patients harbouring p53 mutation with limited treatment options and adverse prognosis.¹⁸ We chose the FDA-approved histone deacetylase inhibitor vorinostat (also known as SAHA), reportedly preferentially cytotoxic towards cancer cells with mutated p53.¹⁹ Indeed, DU145 cells responded well to vorinostat (Figure 2A) and were more sensitive compared to PC3 (Supplementary Figure S2A). In DU145 cells, vorinostat caused activation of apoptosis markers caspases 3/7 (Supplementary Figure S2E) and G2/M arrest, as determined by flow cytometry (Supplementary Figure S2D) and accumulation of prometaphase cells (Supplementary Figure S2B). Unfortunately, in the short-term viability assay normal prostate epithelial cells RWPE-1 and EP156T respond similarly, thereby questioning the therapeutic window of vorinostat monotherapy (Supplementary Figures S2F and S2G). Mechanistically, vorinostat treatment should evoke degradation of the accumulated mutant p53 protein reverting its anti-apoptotic effect.¹⁹ Indeed, downregulation of p53 by vorinostat (Figures 2C and 2E) was mediated by increased p53 degradation, rescuable by proteasome inhibitor MG132 or nutlin, an inhibitor of MDM2 ubiquitin ligase for p53 (Figure 2D). Importantly, pre-treatment with vorinostat also sensitized the DU145 cells to IR and PARPi (Figures 2B and S2C) suggesting possible impact of

vorinostat on the DDR machinery. This phenomenon was further explored as combinations of IR and/or PARPi with vorinostat could potentially represent feasible treatment strategies.

3.3 | Vorinostat downregulates HR factors and sensitizes radio-surviving PCa cells to IR

To elucidate how vorinostat potentiates the effects of IR and PARPi, we assessed its impact on the DDR pathways. First, as HDACs regulate gene expression, we examined the levels of multiple HR factors after vorinostat treatment, and observed modest yet noticeable decreases of BRCA1, BRCA2, Rad51, and TopBP1 proteins (Figure 3G). Interestingly, despite the lower total BRCA1 level (Figure 2F), the ability to form IR-induced BRCA1 foci remained unchanged (Figures 2G and 2H). Notably, vorinostat pre-treatment prevented formation of IR-induced Rad51 foci in cyclin A-positive cells (Figures 3A and 3B), suggesting robust impairment of HR explaining the acquired sensitivity to PARPi. This effect is unlikely attributable to vorinostat-mediated downregulation of mutant p53, because direct downregulation of mut-p53 in DU145 cells by siRNA did not reproduce such phenotype (Figures 3C-E). Interestingly, Ku70, Ku80, and DNA-PK, proteins involved in DSB repair via non-homologous end joining (NHEJ), remained unaffected upon vorinostat treatment (Figure 3F) consistent with differential transcription control of genes involved in distinct DNA repair pathways.²⁰ As radio-resistance in PCa represents a significant issue that lacks suitable cellular models, our team developed a model of radiosurviving PCa cells obtained by exposure of parental DU145 cells to clinically relevant daily fractions of IR to a cumulative dose of 64 Gy (2 Gy applied every 24 h for 32 days). This treatment is not 100% toxic and selects for a radiation-surviving, stem-like cell population.^{12,21} Importantly, pre-treatment with vorinostat sensitised such cells to IR in colony formation assay (Supplementary Figure S2H) further suggesting vorinostat as an interesting option for combined IR treatment.

3.4 | Disulfiram as a candidate drug for PCa treatment

Prostate, as a mainly secretory organ, is especially dependent on proper function of endoplasmic reticulum (ER) and ER-associated degradation (ERAD). ERAD malfunction or insufficiency leads to ER stress and activation of the unfolded protein response (UPR).²² Several factors of ERAD machinery are upregulated in PCa,²³ and UPR activation in PCa has been recently demonstrated, providing a possible vulnerability exploitable therapeutically.²⁴ We have recently shown that DSF targets cancer via inhibition of the p97/NPL4 pathway, essential for ERAD.¹⁰ DSF's anticancer activity depends on copper²⁵ and we showed that in vivo, DSF becomes converted into diethyldithiocarbamate, a strong copper chelator forming a stable (CuET) the ultimate anticancer metabolite of DSF.¹⁰ CuET accumulates in tumors and paralyzes p97/NPL4-dependent processing of proteins, leading to strong proteotoxic stress, UPR and heat shock

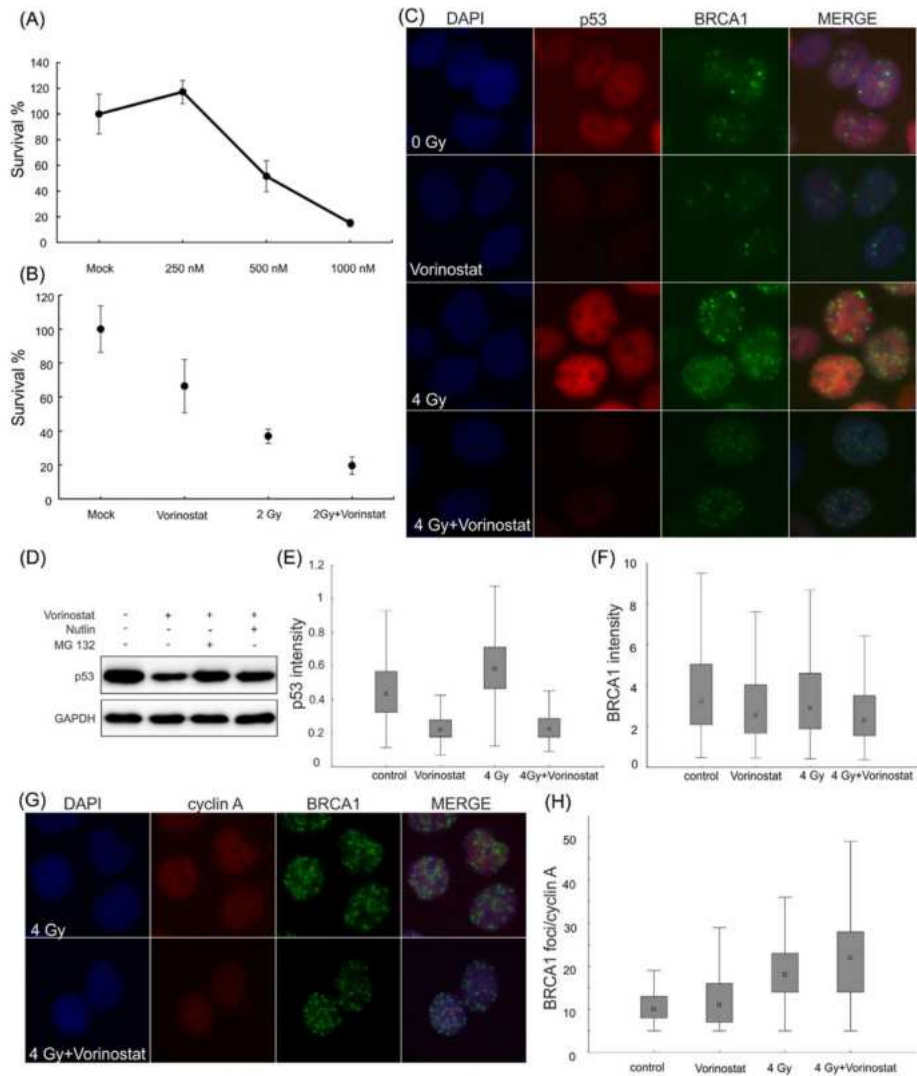


FIGURE 2 BRCA1 foci are formed in cyclin A-positive DU145 cells upon DNA damage after IR and vorinostat treatment, whereas p53 is downregulated. DU145 cell line was treated with vorinostat at indicated concentrations (A) and in combination with IR (2 Gy) and 500 nM vorinostat (B). Cell viability was measured by clonogenic cell survival assay for 8 days. Error bars represent SD of mean ($n = 3$). Next, cells were treated with 5 μ M vorinostat for 24 h, irradiated with 4 Gy and fixed after 5 h. Immunofluorescent staining of p53 and BRCA1 (C) was quantified for their intensity (E and F). One-day treatment with 5 μ M vorinostat downregulated p53 levels in DU145 cells which was abrogated by proteasome inhibitor MG132 or MDM2 inhibitor nutlin (D). Quantification of BRCA1 foci formation in cyclin A-positive DU145 cells (H) after IR and/or vorinostat was evaluated by immunofluorescence analysis (G). [Color figure can be viewed at wileyonlinelibrary.com]

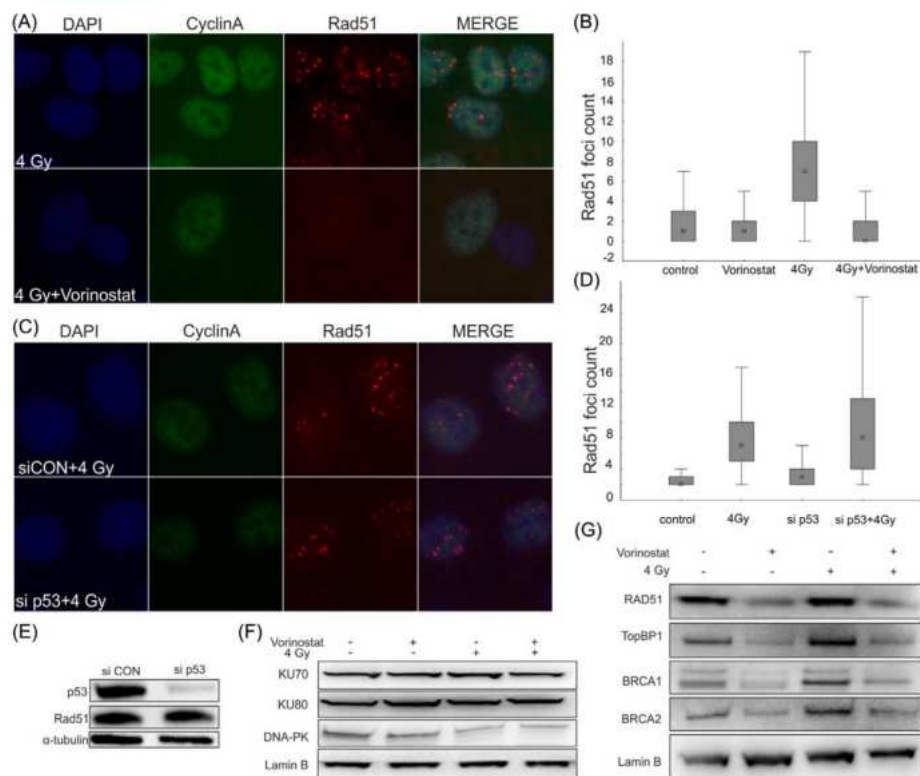


FIGURE 3 Vorinostat downregulates BRCA1 and Rad51 proteins. (A) Cells were treated with 5 μ M vorinostat for 24 h, irradiated with 4 Gy and fixed after 5 h. Rad51 foci were determined by immunofluorescence analysis. (B) Quantification of Rad51 foci formation was assessed in cyclin A-positive cells. (C) Next, cells were treated with siRNA (control or p53-targeting) for 48 h and formation of Rad51 was determined after IR (4 Gy) followed by 5 h of incubation. (D) Quantification of Rad51 foci was measured in cyclin A-positive cells after downregulation of p53. (E) Downregulation of mutated p53 had no impact on Rad51 protein levels. (G) Rad51, TopBP1, BRCA1 and BRCA2 were downregulated after 24 h of treatment with 5 μ M vorinostat, whereas Ku70, Ku80 and DNA-PK remained unchanged (F) as determined by Western blotting analysis. [Color figure can be viewed at wileyonlinelibrary.com]

responses (HSR).¹⁰ Since this drug is clinically used and well tolerated, it is an ideal candidate for repurposing. Specifically for PCa, DSF might be an interesting therapeutic candidate as it scored highly in PCa cell line models.²⁶

First, we treated DU145, PC3 and radiosurviving DU145 cells by DSF, DSF + CuCl₂, CuCl₂ alone or CuET for 48 h to test for cytotoxicity. All cell lines responded with similar sensitivity within nanomolar range (IC₅₀ around 200 nM) to DSF + CuCl₂ and CuET (Figure 4A). To further explore the comparable potencies of DSF + CuCl₂ and CuET, we assessed whether CuET forms also in vitro, in media containing DSF and CuCl₂. Indeed, we confirmed that CuET complex forms efficiently, indicating that the cell culture effects under DSF + CuCl₂ treatment are attributable to CuET (Figure 4B). DSF treatment alone was moderately toxic, likely

reflecting the presence of copper ions in standard growth media, forming some CuET. Notably, unlike treatments with PARPI or HDACi there was an obvious lack of differential responses among the otherwise very heterogeneous cell lines, suggesting a mechanism of action independent of the p53 status or DNA repair defects. To confirm that PCa cells treated by DSF + CuCl₂ and CuET are experiencing stress phenotypes similar to other cellular models,¹⁰ PCa cells were first examined for activation of HSR. Immunofluorescence analysis confirmed a robust HSR manifested by formation of HSF1 nuclear stress foci²⁷ (Figures 4C and 4D) and increase of heat shock protein 70 (HSP70), the main HSR effector, in all tested cell lines (Figure 4E). The PCa cells also strongly activate UPR manifested by elevated ATF4, CHOP, and phospho-eIF2 α , established UPR markers²² (Figures 5A and 5B).

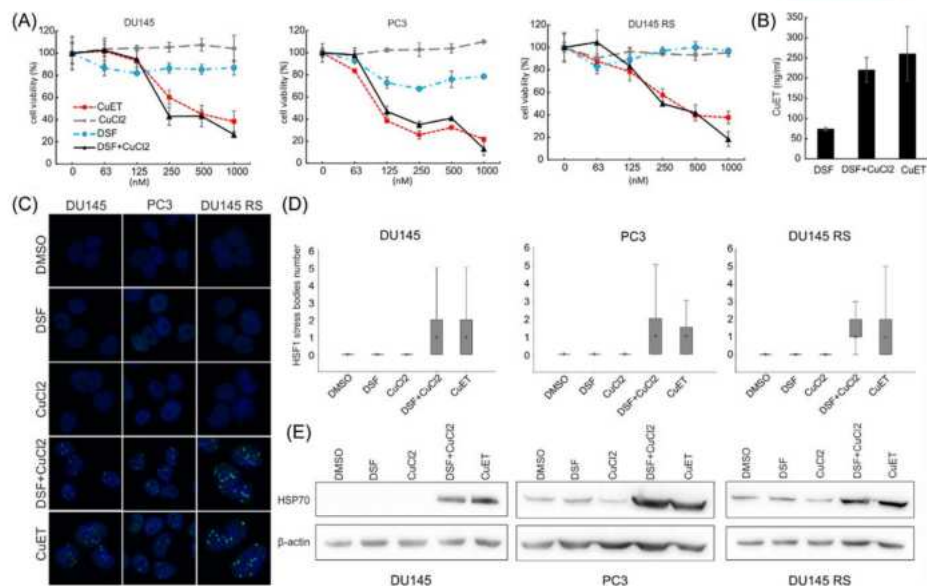


FIGURE 4 Disulfiram plus copper and CuET show cytotoxic effect in prostate cancer cell lines and activates heat shock response. (A) DU145, PC3 and radiosurviving DU145 cell lines were treated with DSF, copper chloride, DSF plus copper chloride or CuET with indicated concentrations and evaluated in 48 h by XTT assay. (B) Amount of CuET complex in the media was analyzed by HPLC-MS. (C) Cells were treated with indicated compounds (500 nM all) or their combinations and stained for HSF1. (D) HSF1 stress nuclear foci were quantified using ScanR. (E) Western blotting analysis revealed increase of HSP70, the main HSR effector, after the treatment with CuET or DSF + CuCl₂. [Color figure can be viewed at wileyonlinelibrary.com]

3.5 | Disulfiram toxicity synergizes with chemical inhibition of survivin

DSF's toxicity for PCa cell lines^{26,28} inspired a small pharmacodynamic clinical trial in PCa patients with non-metastatic recurrent prostate cancer.²⁹ The trial failed to show either global demethylation as a presumed pharmacodynamic marker²⁸ or significant changes in PSA levels, consequently concluding that such DSF monotherapy was inefficient in PCa patients. Such failure might reflect, at least in part, the fact that copper was not included into this trial, thus limiting DSF's anticancer activity that is otherwise apparent from preclinical studies including mouse models.^{10,30} A new Phase Ib study of intravenous copper loading combined with oral DSF administration in metastatic castration resistant prostate cancer was launched recently, which should provide more conclusive information about DSF efficacy in patients (ClinicalTrials.gov Identifier: NCT02963051). As DSF alone could be insufficient for eradication of PCa cells in vivo combined therapy could provide a better option. Because UPR, robustly induced by DSF + CuCl₂ and CuET treatments, strongly activates cell death, such candidate combinational treatment strategy could exploit inhibition of pro-survival proteins that are known to be overexpressed in cancers, such as survivin.³¹ Chemical inhibitor of survivin, YM155, showed anticancer activity in preclinical cancer models including

PCa³² and is being evaluated in clinical trials.³³ Interestingly, synergistic toxicity between YM155 and common UPR inducers thapsigargin and tunicamycin has been recently reported.³⁴ However, these two UPR inducers are very toxic and unsuitable for clinical applications.³⁵ On the other hand, DSF (combined with copper) is relatively well tolerated and thus provides a viable option to potentiate survivin inhibitors. Motivated by this rationale, DSF + CuCl₂ and CuET were first compared with thapsigargin and tunicamycin and very good potency in UPR induction was confirmed (Figures 5A and 5B). Next, DU145 and PC3 cells were treated with indicated combinations of DSF (with copper) and YM155. Combination of the drugs led to reduced survival of both DU145 and PC3 cells, (Figures 5C and 5D) revealing moderate synergy as computed using CompuSyn algorithm³⁶ (Figure 5E). Thus combination of two clinically available drugs, YM155 and DSF (supplemented with copper) represents a readily available and potentially efficient treatment option for PCa and also other cancer patients.

4 | DISCUSSION

Therapy of advanced PCa still poses a serious challenge in oncology, making any innovative and better alternative treatments highly

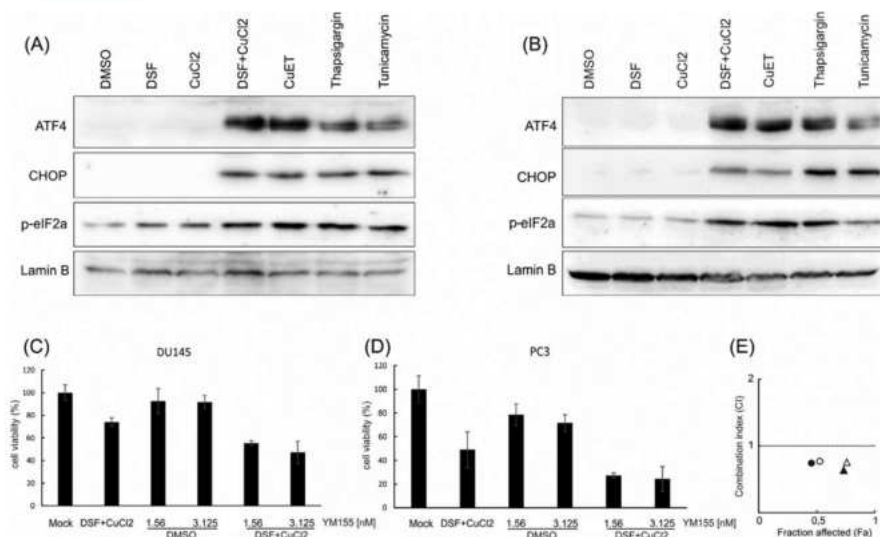


FIGURE 5 Disulfiram activates UPR and kills DU145 and PC3 cell lines in a synergistic manner with survivin inhibitor YM155. DU145 (A) and PC3 (B) cells were treated with 500 nM concentration of indicated compounds for 8 h and cell lysates were analyzed for ATF4, CHOP, p-eIF2a and lamin B. (C and D) Next, cells were treated with 500 nM DSF + CuCl₂ and with indicated concentrations of survivin inhibitor and analyzed for synergy in CompuSyn (E). Circles and triangles refer to DU145 and PC3 cells, respectively. Fill and empty objects indicate combinations of DSF + CuCl₂ with lower and higher concentration of survivin inhibitor, respectively

desirable. Here we chose two well-characterized cellular models (PC3, DU145) and one experimentally derived model (termed radio-surviving DU145) of castration resistant PCa to explore new therapeutic options. We concentrated on anticancer drugs currently entering or in clinical trials such as PARPi, vorinostat, and DSF, the latter with recently revealed mechanism of action through interference with p97/NPL4-mediated protein turnover. IR was added in some experimental setups as it is known that the standard androgen deprivation treatment may benefit from combination with radiotherapy in locally advanced prostate cancer.³⁷

Compared to DU145, PC3 cells showed higher sensitivity to PARPi and IR. Analogous observations were published by others and the differential sensitivity was associated in part with PTEN loss and induction of senescence in PC3 cells.^{38–40} Here, we add another clue as PC3 cells show low Rad51 foci formation after PARPi and IR suggesting defects in HR-promoted DNA repair. Defects in HR are regarded as a major prerequisite for synthetic lethality in combination with PARPi.⁴¹ Based on a phase II clinical trial, combined with next-generation sequencing of DNA repair genes, the PARPi olaparib (Lynparza) received an FDA designation of breakthrough therapy.^{4,42} Our present results suggest a potential for PARPi in treating PCa, guided by immunohistochemical and/or ex vivo biopsy evaluation of HR biomarkers such as RAD51 foci formation.⁴³ These approaches, while technically challenging, have a potential for clinical implementation as

predictive biomarkers for treatment with PARPi, complementary to genetic analyses of *BRCA1/2*, *ATM* or *TPR52-ERG*.^{4,6,42} Olaparib has also been recently reported to be effective in combination with, and as maintenance therapy after, first-line endocrine therapy of prostate cancer.⁴⁴

Different therapeutic approaches will be required for castration-resistant PCa cases that are HR repair proficient. Based on our current data, we propose another treatment strategy, involving HDAC inhibitors such as vorinostat. DU145 are among the cell lines with gain-of function p53 mutations,^{18,45} associated with preferential sensitivity to HDAC inhibition.¹⁹ Indeed, these cells responded well to vorinostat, particularly when combined with IR, as also noticed by others.⁴⁶ Consistent with the literature, we observed reduced p53, and modest downregulation of *BRCA1*, *BRCA2* and *Rad51* after vorinostat treatment by immunoblotting. For the first time, we report that vorinostat downregulates also TOPBP1 which is important for *Rad51* loading to chromatin during HR.⁴⁷ Indeed, pre-treatment with vorinostat resulted in less efficient DNA repair by HR, as documented by lower counts of *Rad51* foci in cyclin A-positive cells. Downregulation of mutated p53 by siRNA altered neither *Rad51* foci nor the *RAD51* protein level, indicating that the effect of HDAC inhibition by vorinostat is more pleiotropic affecting also the HR-promoted DNA repair processes. Consistently, other HDAC inhibitors, MS-275 and FK228, impaired HR repair.⁴⁸ The vorinostat-induced DNA repair defect was further corroborated in our experiments of combined treatment with IR and PARPi.

As targeting proteotoxic stress pathways represents an emerging promising therapeutic approach for PCa,²⁴ we also tested DSF that impairs protein degradation.¹⁰ DSF repurposing for cancer treatment is currently tested in at least eight clinical trials (according to ClinicalTrials.gov) involving various cancers including PCa. Despite DSF monotherapy failed in a clinical trial in PCa patients with non-metastatic recurrent PCa,²⁹ this study did not combine DSF with copper, which is required for DSF's anticancer activity in vitro^{25,49} and potentiates its activity in vivo.^{10,30} Another intriguing option for future treatment is concomitant DSF (ideally supplemented with copper) with other anticancer drugs or IR. Such combinations show promising results in preclinical models^{50,51} and also in a few clinical trials.^{52,53} In this study, we demonstrated toxicity of the CuET complex, the main anticancer metabolite of disulfiram in vivo¹⁰ as well as potency of DSF in combination with copper. These treatments also induced cellular responses which were reported for other cell lines, including UPR and HSR pathway activation. Such strong activation of UPR prompted us to test the combination of DSF with a survivin inhibitor YM155, reported as being highly potent in combination with UPR inducers thapsigargin and tunicamycin.³⁴ YM155 is a novel anticancer drug undergoing clinical trials and it was already tested as a monotherapy in castration-resistant PCa patients, yet with a rather limited effect.³³ The observed synergy between YM155 and CuET/DSF + CuCl₂, reported in our present study, provides a further rationale for additional preclinical and/or clinical investigations, with potential implications also for other human malignancies, beyond the treatment of PCa.

5 | CONCLUSIONS

Combined IR/PARPi effectively killed HR-impaired PCa cells. Vorinostat treatment reduced levels of HR factors including TOPBP1, with ensuing enhanced sensitivity to IR and PARPi. DSF/copper was effective against all PCa models, triggering proteotoxic stress, UPR and heat shock pathway activation, highlighting a rationale for combinatorial therapy blocking anti-apoptotic responses by survivin inhibitors. We propose that targeting genotoxic stress and proteotoxic stress responses by combinations of available drugs could inspire innovative strategies to treat castration-resistant PCa.

ACKNOWLEDGMENTS

We thank Kamila Nemcova for technical assistance with cell culture and immunoblotting. PARPi was kindly provided by Astra Zeneca. The study was supported by grants from the Kellner Family Foundation, Czech National Program of Sustainability LO1304, MEYS CR (LM2015062 Czech-Biolmaging and DRO-61989592), Czech Ministry of Health NV15-28628A, DRO-FNOL00098892 and AZV 16-32030A, University of Palacky IGA-LF-2018-001 and 034, the Danish cancer society, the Novo Nordisk Foundation, the Danish council for independent research, the Swedish research council and Cancer Fonden.

CONFLICTS OF INTEREST

The authors have no conflicts of interest to disclose.

ORCID

Dusana Majera  <http://orcid.org/0000-0002-9238-3437>

Jan Bouchal  <http://orcid.org/0000-0003-4842-1720>

REFERENCES

- Torre LA, Bray F, Siegel RL, Ferlay J, Lortet-Tieulent J, Jemal A. Global cancer statistics, 2012. *CA Cancer J Clin*. 2015;65:87–108.
- Kurfurstova D, Bartkova J, Vrtel R, et al. DNA damage signalling barrier, oxidative stress and treatment-relevant DNA repair factor alterations during progression of human prostate cancer. *Mol Oncol*. 2016;10:879–894.
- Maya-Mendoza A, Moudry P, Merchut-Maya JM, Lee M, Strauss R, Bartek J. High speed of fork progression induces DNA replication stress and genomic instability. *Nature*. 2018;559:279–284.
- Mateo J, Carreira S, Sandhu S, et al. DNA-repair defects and olaparib in metastatic prostate cancer. *N Engl J Med*. 2015;373:1697–1708.
- Mendes-Pereira AM, Martin SA, Brough R, et al. Synthetic lethal targeting of PTEN mutant cells with PARP inhibitors. *EMBO Mol Med*. 2009;1:315–322.
- Brenner JC, Ateeq B, Li Y, et al. Mechanistic rationale for inhibition of Poly(ADP-Ribose) polymerase in ETS gene fusion-positive prostate cancer. *Cancer Cell* 2011;19:664–678.
- Graça I, Pereira-Silva E, Henrique R, Packham G, Crabb SJ, Jerónimo C. Epigenetic modulators as therapeutic targets in prostate cancer. *Clin Epigenetics*. 2016;8:98.
- Ku SY, Rosario S, Wang Y, et al. Rb1 and Trp53 cooperate to suppress prostate cancer lineage plasticity, metastasis, and antiandrogen resistance. *Science*. 2017;355:78–83.
- Mu P, Zhang Z, Benelli M, et al. SOX2 promotes lineage plasticity and antiandrogen resistance in TP53- and RB1-deficient prostate cancer. *Science*. 2017;355:84–88.
- Skrott Z, Mistrik M, Andersen KK, et al. Alcohol-abuse drug disulfiram targets cancer via p97 segregase adaptor NPL4. *Nature*. 2017;552:194–199.
- Al-Lazikani B, Banerji U, Workman P. Combinatorial drug therapy for cancer in the post-genomic era. *Nat Biotechnol*. 2012;30:679–692.
- Kyjacova L, Hubackova S, Krejčíková K, et al. Radiotherapy-induced plasticity of prostate cancer mobilizes stem-like non-adherent, Erk signaling-dependent cells. *Cell Death Differ*. 2015;22:898–911.
- Kogan I, Goldfinger N, Milyavsky M, et al. HERT-immortalized prostate epithelial and stromal-derived Cells. *Cancer Res*. 2006;66:3531–3540.
- Santer FR, Erb HH, McNeill RV. Therapy escape mechanisms in the malignant prostate. *Semin Cancer Biol*. 2015;35:133–144.
- Fong PC, Boss DS, Yap TA, et al. Inhibition of poly(ADP-Ribose) polymerase in tumors from BRCA mutation carriers. *N Engl J Med*. 2009;361:123–134.
- Mistrik M, Oplustilova L, Lukas J, Bartek J. Low-dose DNA damage and replication stress responses quantified by optimized automated single-cell image analysis. *Cell Cycle*. 2009;8:2592–2599.
- Oplustilova L, Wolanin K, Mistrik M, et al. Evaluation of candidate biomarkers to predict cancer cell sensitivity or resistance to PARP-1 inhibitor treatment. *Cell Cycle*. 2012;11:3837–3850.
- Gurova KV, Rokhlin OW, Budanov AV, et al. Cooperation of two mutant p53 alleles contributes to Fas resistance of prostate carcinoma cells. *Cancer Res*. 2003;63:2905–2912.

19. Li D, Marchenko ND, Moll UM. SAHA shows preferential cytotoxicity in mutant p53 cancer cells by destabilizing mutant p53 through inhibition of the HDAC6-Hsp90 chaperone axis. *Cell Death Differ*. 2011;18:1904–1913.
20. Polkinghorn WR, Parker JS, Lee MX, et al. Androgen receptor signaling regulates DNA repair in prostate cancers. *Cancer Discov*. 2013;3:1245–1253.
21. Guggenberger F, van de Werken HJG, Erb HH, et al. Fractionated radiation of primary prostate basal cells results in downplay of interferon stem cell and cell cycle checkpoint signatures. *Eur Urol*. 2018;74:847–849.
22. Storm M, Sheng X, Arnoldussen YJ, Saatcioglu F. Prostate cancer and the unfolded protein response. *Oncotarget*. 2016;7:54051–54066.
23. Erzurumlu Y, Ballar P. Androgen mediated regulation of endoplasmic reticulum-associated degradation and its effects on prostate cancer. *Sci Rep*. 2017;7:40719.
24. Nguyen HG, Conn CS, Kye Y, et al. Development of a stress response therapy targeting aggressive prostate cancer. *Sci Transl Med*. 2018;10:e2036.
25. Chen D, Cui QC, Yang H, Dou QP. Disulfiram, a clinically used anti-alcoholism drug and copper-binding agent, induces apoptotic cell death in Breast cancer cultures and xenografts via inhibition of the proteasome activity. *Cancer Res*. 2006;66:10425–10433.
26. Ijijn K, Ketola K, Vainio P, et al. High-throughput cell-based screening of 4910 known drugs and drug-like small molecules identifies disulfiram as an inhibitor of prostate cancer cell growth. *Clin Cancer Res*. 2009;15:6070–6078.
27. Biamonti G, Vourc'h C. Nuclear stress bodies. *Cold Spring Harb Perspect Biol*. 2010;2:a000695.
28. Lin J, Haffner MC, Zhang Y, et al. Disulfiram is a DNA demethylating agent and inhibits prostate cancer cell growth. *Prostate*. 2011;71:333–343.
29. Schweizer MT, Lin J, Blackford A, et al. Pharmacodynamic study of disulfiram in men with non-metastatic recurrent prostate cancer. *Prostate Cancer Prostatic Dis*. 2013;16:357–361.
30. Safi R, Nelson ER, Chitneni SK, et al. Copper signaling axis as a target for prostate cancer therapeutics. *Cancer Res*. 2014;74:5819–5831.
31. Altieri DC. Survivin, cancer networks and pathway-directed drug discovery. *Nat Rev Cancer*. 2008;8:61–70.
32. Nakahara T, Takeuchi M, Kinoyama I, et al. YM155, a novel small-molecule survivin suppressant, induces regression of established human hormone-refractory prostate tumor xenografts. *Cancer Res*. 200;80:8014–8021.
33. Tolcher AW, Quinn DI, Ferrari A, et al. A phase II study of YM155, a novel small-molecule suppressor of survivin, in castration-resistant taxane-pretreated prostate cancer. *Ann Oncol*. 2012;23:968–973.
34. Lelli NM, Dey S, Brady L, Koumenis C. Identifying novel regulators of the Unfolded Protein Response (UPR) by genome-scale CRISPR-Cas9 knockout screens. *Cancer Res*. 2017;77:Abstract nr 1247.
35. Foufelle F, Fromenty B. Role of endoplasmic reticulum stress in drug-induced toxicity. *Pharmacol Res Perspect*. 2016;4:e00211.
36. Chou T-C. Theoretical basis, experimental design, and computerized simulation of synergism and antagonism in drug combination studies. *Pharmacol Rev*. 2006;58:621–681.
37. Warde P, Mason M, Ding K, et al. Combined androgen deprivation therapy and radiation therapy for locally advanced prostate cancer. *Lancet*. 2011;378:2104–2111.
38. Barreto-Andrade JC, Efimova EV, Mauceri HJ, et al. Response of human prostate cancer cells and tumors to combining PARP inhibition with ionizing radiation. *Mol Cancer Ther*. 2011;10:1185–1193.
39. Chatterjee P, Choudhary GS, Sharma A, et al. PARP inhibition sensitizes to low dose-Rate radiation TMPRSS2-ERG fusion gene-Expressing and PTEN-Deficient prostate cancer cells. Tofilon PJ, ed. *PLoS ONE*. 2013;8:e60408.
40. Fraser M, Zhao H, Luoto KR, et al. PTEN deletion in prostate cancer cells does not associate with loss of RAD51 function. *Clin Cancer Res*. 2012;18:1015–1027.
41. Lord CJ, Ashworth A. The DNA damage response and cancer therapy. *Nature*. 2012;481:287–294.
42. Helleday T. PARP inhibitor receives FDA breakthrough therapy designation in castration resistant prostate cancer: beyond germline BRCA mutations. *Ann Oncol*. 2016;27:755–757.
43. Naipal KAT, Verkaik NS, Ameziane N, et al. Functional ex vivo assay to select homologous recombination-deficient breast tumors for PARP inhibitor treatment. *Clin Cancer Res*. 2014;20:4816–4826.
44. Feiersinger GE, Trattng K, Leitner PD, et al. Olaparib is effective in combination with, and as maintenance therapy after, first-line endocrine therapy in prostate cancer cells. *Mol Oncol*. 2018;12:561–576.
45. Goh AM, Coffill CR, Lane DP. The role of mutant p53 in human cancer. *J Pathol*. 2011;223:116–126.
46. Chinnaiyan P, Vallabhaneni G, Armstrong E, Huang S-M, Harari PM. Modulation of radiation response by histone deacetylase inhibition. *Int J Radiat Oncol*. 2005;62:223–229.
47. Moudry P, Watanabe K, Wolanin KM, et al. TOPBP1 regulates RAD51 phosphorylation and chromatin loading and determines PARP inhibitor sensitivity. *J Cell Biol* 2016;212:281–288.
48. Fukuda T, Wu W, Okada M, et al. Class I histone deacetylase inhibitors inhibit the retention of BRCA1 and 53BP1 at the site of DNA damage. *Cancer Sci*. 2015;106:1050–1056.
49. Brar SS, Grigg C, Wilson KS, et al. Disulfiram inhibits activating transcription factor/cyclic AMP-responsive element binding protein and human melanoma growth in a metal-dependent manner in vitro, in mice and in a patient with metastatic disease. *Mol Cancer Ther*. 2004;10:49–1060.
50. Wang Y, Li W, Patel SS, et al. Blocking the formation of radiation induced breast cancer stem cells. *Oncotarget*. 2014;5:3743–3755.
51. Lun X, Wells JC, Grinshtein N, et al. Disulfiram when combined with copper enhances the therapeutic effects of temozolomide for the treatment of glioblastoma. *Clin Cancer Res*. 2016;22:3860–3875.
52. Nechushtan H, Hamamreh Y, Nidal S, et al. A phase IIb trial assessing the addition of disulfiram to chemotherapy for the treatment of metastatic non-small cell lung cancer. *Oncologist*. 2015;20:366–367.
53. Huang J, Campian JL, Gujar AD, et al. Final results of a phase I dose-escalation, dose-expansion study of adding disulfiram with or without copper to adjuvant temozolomide for newly diagnosed glioblastoma. *J Neurooncol*. 2018;138:105–111.

SUPPORTING INFORMATION

Additional supporting information may be found online in the Supporting Information section at the end of the article.

How to cite this article: Majera D, Skrott Z, Bouchal J, et al. Targeting genotoxic and proteotoxic stress-response pathways in human prostate cancer by clinically available PARP inhibitors, vorinostat and disulfiram. *The Prostate*. 2019;79:352–362. <https://doi.org/10.1002/pros.23741>